ABSTRACT

Title of Dissertation: TOPOLOGICAL QUANTUM MATTER: BRIDGING THEORY AND EXPERIMENT

Gautam Nambiar
Doctor of Philosophy, 2025

Dissertation Directed by: Professor Victor Galitski
Department of Physics

and

Professor Mohammad Hafezi
Department of Physics
Department of Electrical and Computer Engineering

Quantum many-body systems host a variety of exotic phases which can be described as the deconfined phase of an emergent gauge theory. Such phases in the context of spin systems go by the name Quantum Spin Liquids (QSLs). Often, the same features that make them interesting also make them hard to detect experimentally. This thesis is a collection of works aimed at connecting the defining theoretical properties of such phases to experimentally accessible observables, both in the setting of solid state materials and quantum devices.

The main theme of the first part of the thesis is magnetic monopoles of emergent compact $U(1)$ gauge theories that describe certain QSLs, namely Quantum Spin Ice and Dirac Spin Liquid in three and two spatial dimensions respectively. The condensation of monopoles drives a deconfinement-confinement phase transition in the gauge theory, and in the context of spin sys-

tems, drives transitions from QSL to ordered phases. We exploit this understanding to propose a "Monopole Josephson Junction" scheme to test if a candidate material is a Dirac Spin Liquid. A key component of our detection scheme is Raman Scattering. Next, we provide a proposal to prepare and diagnose Quantum Spin Ice (deconfined phase of $U(1)$ gauge theory in three spatial dimensions) in Rydberg atom arrays.

In the second part of the thesis, we explore quantum optics techniques to probe correlated quantum materials. In optical experiments, the photonic observable measured is usually the intensity or photon number operator of inelastically scattered light. We ask a general question – what can we learn about a material, given access to other photonic observables like quadrature and correlation between pairs of photons ($G^{(2)}$)? We develop a general formalism to map such photonic correlation functions to electronic ones. Focusing on the Hubbard model at half-filling, we show that such correlators can be used to probe spin-charge correlations, and to detect QSLs by detecting spin chirality and existence of fractional statistics.

TOPOLOGICAL QUANTUM MATTER: BRIDGING THEORY AND EXPERIMENT

by

Gautam Nambiar

Dissertation submitted to the Faculty of the Graduate School of the
University of Maryland, College Park in partial fulfillment
of the requirements for the degree of
Doctor of Philosophy
2025

Advisory Committee:
Professor Victor Galitski, Chair/Co-Advisor
Professor Mohammad Hafezi, Co-Chair/Co-Advisor
Professor Ichiro Takeuchi
Professor Alexey Gorshkov
Professor Victor Albert

© Copyright by
Gautam Nambiar
2025

Dedication

To Achhan, Amma, and Gayathri

Acknowledgments

While consulting other PhD theses, I am often fascinated by the Acknowledgements section. It is only now that I am facing the reality of having to write one for myself. Perhaps it is because the upcoming finish line still feels surreal. My PhD journey started in 2018. From the two-year scramble to find an advisor, followed by the COVID-19 pandemic, and then culminated by a two year saga of job hunt, this PhD has been quite a roller coaster-ride, to put it mildly. Consequently, my scattering cross-section with the University of Maryland has been quite large. This means that there are a large number of people who have been part of my journey and who I am grateful to.

I thank my co-advisors Victor Galitski and Mohammad Hafezi for their support. I am also grateful to have worked closely with Alexey Gorshkov and Maissam Barkeshli. At some point, if I am able to pick up even a small fraction of Mohammad's confidence and versatility, Alexey's efficiency and meticulousness, and Maissam's intensity and clarity, I will be happy with myself. I also thank Michael Gullans and Zohreh Davoudi for our collaboration, and my other committee members Victor Albert and Ichiro Takeuchi for their time.

Over these years, the discussions I had with several grad students and postdocs have molded the way I now think about physics. A big shout-out to Daniel Bulmash, who was effectively my advisor for a large chunk of the COVID lockdown. I thank my long-time friend and collaborator Naren Manjunath for many things – from his cool-headed yet assertive presence, to teaching

me classification of topological phases, to accidentally leading us to Georgetown while biking to Great Falls. It is during one such biking meetup, that we discovered the connection between monopole quantum numbers and classification of crystalline topological phases. I am grateful to Naren and Yuxuan Zhang for our intense collaboration that followed. Jeet Shah has been a long-time collaborator and friend, who led by example with his work ethic. I am also grateful to Andrey Grankin for our collaboration. Despite our ways of thinking being almost diametrically opposite, I learn something from each discussion with him. Six-seventh part of my PhD journey was spent being a roommate of Amit Vikram. Our unending discussions stochastically sampled (in a Markovian manner) typical trajectories in the space of all possible conversations. As I write this, I can almost hear Amit go on a rant on the nuances of ergodicity vs k-mixing and why my above sentence is imprecise.

I am fortunate to have overlapped with several other postdocs and grad students – Abu Saleh Musa Patoary, Alexander Schuckert, Ali Lavasani, Ali Rad, Alireza Parhizkar, Beini Gao, Benji Remez, Brayden Ware, Chris Baldwin, Chris Fechisin, Christopher White, Colin Rylands, Daniel Suarez, Deric Session, Eleanor Crane, En-Jui Kuo, Hossein Dehghani, Jacob Lin, Jon Kunjummen, Laura Shou, Mahdi Ghafariasl, Martin Ritter, Masoud Mohammadi, Mike Winer, Pranshoo Upadhyay, Soumadeep Saha, Stuart Thomas, Supratik Sarkar, Tsung-Sheng Huang, Yu-Xin Wang, Yunxiang Liao, Ze-Min Huang – it is inevitable that I am forgetting many, but thank you everyone!

Participating in mentorship initiatives at UMD Physics and mentoring Mayank Gupta and Noemi Ricotti was a delight. Also, working with Donna Hammer, Don Lynch, Clay Daetwyler and Logan Anbinder for the 2019 summer camps was quite an enriching experience. I am grateful to Josiland Chambers, Johnna Schmidt and Melissa Britton for all the administrative help.

I also thank friends I made at summer schools and conferences for all the physics and fun – (again incomplete list): Adarsh Patri, Amogh Anakru, Ananth Malladi, Arkya Chatterjee, Divyoj Singh, Marvin Qi, Nandu Manoj, Nish Verma, Rimika Jaiswal, Rushikesh Patil, Sandeep Joy, G. Shankar.

Further, I am grateful to Professors Ajit Balram, G. Baskaran, Diptiman Sen, Sreejith GJ, and Sumilan Banerjee for the physics discussions and their hospitality during my visits to Indian institutes during my PhD. My expedition in condensed matter physics can be traced back to my first year undergrad days when I approached my Quantum Chemistry professor at IISc, Prof. KL Sebastian for a summer project. He in turn connected me with Prof. R. Ganesh (then at IMSc). Ganesh took me on (then a naive eighteen year old with no research experience) and managed to both get me excited about magnetism and mentored me towards successfully finishing a research project. I am grateful to Professors Sebastian and Ganesh for teaching me many things and starting off my physics carreer.

While academics was an important aspect of grad school, it is the friendships I fostered which I will cherish for the longest. The long bike rides, road trips, hikes, potlucks and house parties in the company of friends are what really made grad school memorable. I should especially mention some friends who have been a vital part of my journey – from help with settling in, to support during difficult times, to all the shared fun moments: Arghya Sadhukhan, Amit Vikram, Subhayan Sahu, Naren Manjunath, Tamoghna Barik, Saurav Das, Sohitri Ghosh, Abu Saleh Musa Patoary, and Aritra Das. There were many other friends and roommates who I was fortunate to share this journey with. I apologize for the names I will inevitably miss, but let me try my best with the following incomplete list: Amitava Banerjee, Aniruddha Bapat, Aranya Chakraborty, Arinjoy De, Arushi Bodas, Deepak Sathyan, Gaurang Sriramanan, Jeet Shah, Jessica Bodosa,

Katelyn Rempe, Keshav Srinivasan, Khoi Hoang, Martin Ritter, Navya Gupta, Prakhar Gupta, Prathyush Poduval, Rajrupa Mondal, Rahul Shreshtha, Sagar Airen, Sagnik Mondal, Saipriya Satyajit, Sandesh Kalantre, Sanket Doshi, Saurabh Kadam, Sharoon Austin, Shourya Mukherjee, Shubham Jain, Stefano Antonini, Tapan Goel, Vasanth Pidaparthy, Vinay Vikramaditya, Vinu Sankar, Xiaozhen Fu. I thank my newfound Malayali community in whom I found a home away from home – Sijil PV and family, Gaurang, Maneesha Pradeep, and Srijit Paul. I was also fortunate to participate in many trips with the Adventure Program at UMD. Besides being a much needed stress buster, these trips taught me important outdoors skills, which I probably would not have learned otherwise. I thank the trip leaders and co-participants for this. I am grateful to have had access to the full network of biking trails in the greater DC area, which is where a sizable fraction of my PhD was spent.

I also thank the many friends back from my undergrad days for staying connected over Zoom meetings, in-person meetups and outdoor trips – Alistair Lewis, Ameya Prabhune, Aravind Baby, Avinash Mandaiya, P.S. Ganesh Subramanian, Gautam Aditya Kavuri, Gokul G Nair, Prathitha Kar, Shadab Ahamed, Shreyas Gopalakrishnan, Vishikh Athawale.

I am grateful to my extended family for all the support – Ammu, Ettan, Achamma, Muthachan, Ammamma, Valiamma, Ammaaman, Ammayi and Anju. Finally and most importantly, I would like to thank my father Satish Kumar Ambat, mother Jayasree TP and sister Gayathri Nambiar for everything. I don't think I can get myself to articulate in words how invaluable their support has been, but they will understand.

Citations to previously published work

Much of this dissertaion has appeared in print elsewhere. Here, we list the references that each chapter is based on.

- Chapter 2 is mostly based on "*Monopole Josephson effects in a Dirac spin liquid*" by Gautam Nambiar, Daniel Bulmash and Victor Galitski (Phys. Rev. Research 5, 013169) [1]. Additionally, in Sec. 2.6, we connect to the results of the following two papers:

  "*Fractional Disclination Charge and Discrete Shift in the Hofstadter Butterfly*" (Phys. Rev. Lett. 129, 275301) [2],

  and "*Quantized Charge Polarization as a Many-Body Invariant in (2+1)D Crystalline Topological States and Hofstadter Butterflies*" (Phys. Rev. X 13, 031005) by Yuxuan Zhang, Naren Manjunath, Gautam Nambiar, and Maissam Barkeshli [3].

- Chapter 3 is based on "*Diagnosing electronic phases of matter using photonic correlation functions*" (arXiv:2410.24215) by Gautam Nambiar, Andrey Grankin and Mohammad Hafezi [4].

- Chapter 4 is based on "*Quantum Spin Ice in Three-Dimensional Rydberg Atom Arrays*" by Jeet Shah, Gautam Nambiar, Alexey Gorshkov and Victor Galitski [5].

Table of Contents

List of Tables

List of Figures

Chapter 1: Introduction

The existence of a large variety of quantum phases of matter we see around us, such as metals, insulators, magnets and superconductors is ultimately due to a grand tug of war that determines the ground state of a given many-body Hamiltonian. A many-body Hamiltonian is a sum of kinetic and interaction energies which do not commute with each other. In most conventional phases of matter, the ground state can be understood by continuously deforming the Hamiltonian such that one of the terms wins the tug of war. For example, if the kinetic energy of electrons dominates over electron-electron interactions, then the resulting state is a Fermi gas with a Fermi surface (if the electrons partially fill a band). Fermi liquids which describe most metals are continuously connected to such a Fermi gas. Similarly, if a ferromagnetic spin-exchange interaction wins the tug of war, then the resulting state is a ferromagnet.

Exotic states emerge when there is no clear winner in this tug of war. A limiting case of such a scenario is when the ground state subspace of one part of the Hamiltonian is exponentially (in system size) degenerate. Then, any competing term added to the Hamiltonian can lift the degeneracy in interesting ways. A hallmark example is that of electrons in a magnetic field with a filling such that a flat Landau level is partially filled. In the exponentially degenerate subspace of electronic states, electron-electron repulsion can select a topologically ordered ground state with a fractionally quantized Hall conductance.

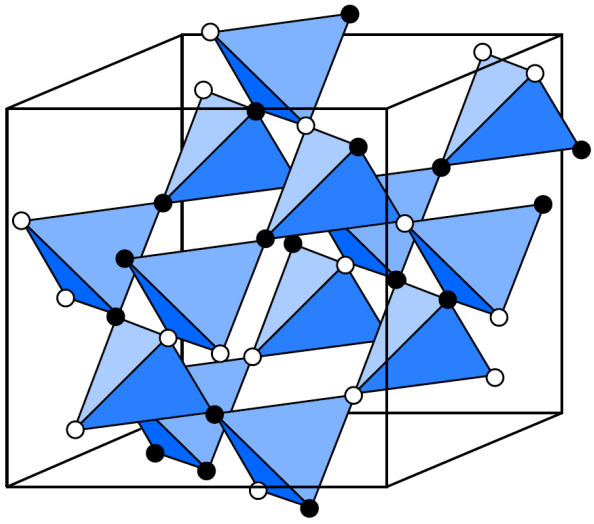

Figure 1.1: A typical ice-rule configuration on the Pyrochlore lattice. Black circles denote down $S^z = -1/2$ and empty circles denote $S^z = 1/2$.

A similar outcome in spin systems was pointed out by Anderson [19] where the ground state is a superposition of several almost-degenerate states, and the excitations are "fractional"[20]. Broadly, a common feature tying together such systems dubbed Quantum Spin Liquids is that, at low energies, they can be described as lying in a deconfined phase of an emergent gauge theory.

1.1 Motivating emergent gauge theories

To motivate how gauge theory emerges in spin systems, consider the following example of nearest neighbor Ising model with antiferromagnetic coupling on the Pyrochlore lattice made of corner sharing tetrahedra (Fig. 1.1). The spins live on the vertices of tetrahedra. Up to additive constant terms, the Hamiltonian can be rearranged to be a sum over individual tetrahedra (as opposed to a sum over the vertices):

$$\hat{H}_0 = \frac{V}{2} \sum_{\text{△}_\mathbf{r}} \left(\sum_{i \in \text{△}_\mathbf{r}} \hat{S}_i^z \right)^2 , \tag{1.1}$$

For $V > 0$, this energy is minimized by setting $\sum_{i \in \text{⏢}_{\mathbf{r}}} \hat{S}_i^z = 0$ for each tetrahedron centered at $\mathbf{r}$, a condition termed "ice rule". As shown by Pauling [21], there are $\sim (\sqrt{3/2})^N$ configurations satisfying this condition (where N is the number of spins). So, in any state obeying the ice rule, each tetrahedron consists of two $-1/2$ spins and two $+1/2$ spins, which can be interpreted as two spins pointing in and two pointing out of the tetrahedron. So, spins can be viewed as electric field $\hat{e}_{\mathbf{r},\mathbf{r}'}$ between a pair of neighboring tetrahedra. Thus, the ice rule is a Gauss's law constaint: $\text{div}\hat{e}_{\mathbf{r},\mathbf{r}'} = 0$. Flipping a spin results in violation of this Gauss's law on the two tetrahedra that share this spin. We then say that there is a "charge" on each of these tetrahedra. Now, let us imagine starting with a state that is a superposition of all ice rule configurations. Flipping a string of alternating (up/down) spins creates a pair of charges at the ends of the string. These charges are said to be "fractional" because any local operator can only create them in pairs.

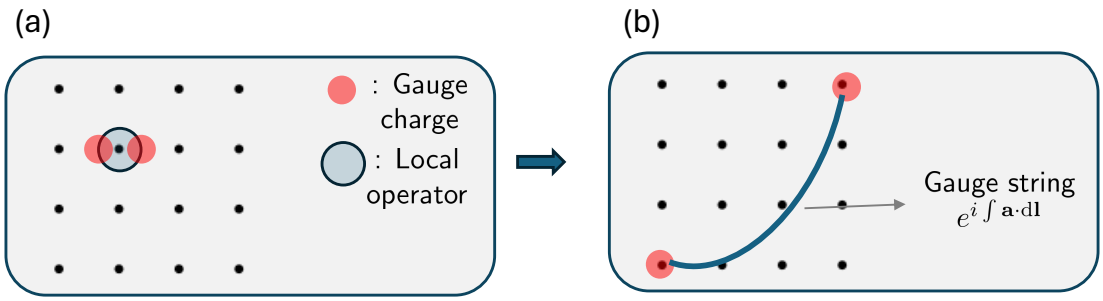

Figure 1.2: (a) Consider applying a local operator (pale blue circle) which we represent (perhaps by hand) as a composite made of two "gauge charge" creation operators. (b) There is a gauge string connecting these charges that remind us of the redundancy involved in splitting a local operator into two. If the gauge theory is in the deconfined phase, then the gauge charges have existence of their own, and the system supports fractional excitations.

Now, we can begin to see why gauge theory is a good description of states supporting "fractional" excitations. We explain this using a cartoon in Fig. 1.2. Let us suppose a local operator is rewritten as a composite operator that creates a pair of "fractional" excitations with a gauge field that encodes this redundancy. It makes sense to talk about each fractional

charge on its own if the gauge theory is in the deconfined phase. If the gauge theory is in the confined phase, then the fractional charges are bound back together. In this case, the gauge theory description ceases to be useful for the low-energy physics, and the system is better described as a more conventional ordered phase. A deconfined to confined phase transition is driven by proliferation of "flux/monopole"-like excitations of this gauge theory (reviewed in Appendix A.1). From this point of view, transitions from a spin liquid to conventional ordered phases are understood as a confinement-deconfinement transition, driven by a proliferation of "flux/monopole"-like excitations, or a Higgs transition, driven by a proliferation of "charge"-like excitations [22, 23, 24, 25, 26, 27]. Gauge theories and their phase transitions are of fundamental importance in physics [28, 29, 30, 31]. The prospect of this physics emerging in many-body systems provides an important motivation for studying quantum spin liquids. They are also interesting due to their possible role in the physics of strongly correlated materials [32] and possible application in quantum computing [33, 34].

1.2 Kinds of Quantum Spin Liquids

At this point, to prevent a common confusion regarding terminology, we remark that "Quantum Spin Liquid" is a loose umbrella term with the general theme being that it admits a low energy description involving matter coupled to a deconfined phase of a gauge theory. But this term encompasses phases that can be theoretically rather disparate. Here is a short summary:

- Quantum Spin Ice, i.e., $U(1)$ gauge theory in $3+1$ dimensions [6] : This is a gapless spin liquid and is the example we started with in this chapter. In Chapter 4 of this dissertation, we propose a scheme to prepare and detect this state in a Rydberg atom quantum simulator.

- In $2+1$ dimensions, gapped quantum spin liquids are topologically ordered, i.e., the ground state has a topological degeneracy that depends on the genus of the manifold in real space, and excitations are anyons with fractional statistics [34]. In Chapter 3 of this dissertation, we propose a technique to detect the existence of fractional statistics in a candidate spin liquid material by studying the correlations between photons in an optical scattering experiment.

  Below are a few examples of such gapped spin liquids:

  - $\mathbb{Z}_2$ gauge theory: Kitaev's Toric Code is an exactly solvable fixed point [33].
  - Chiral spin liquids: Described by a $U(1)$ level 2 Chern Simons theory (a bosonic version of a Fractional Quantum Hall state). [35]. Such states are characterized by a nonzero spin chirality. Detecting spin chirality experimentally is an open problem. In Sec. 3.7 of this dissertation, we propose an optical scheme to measure spin chirality.
  - Kitaev Spin Liquids: Kitaev wrote down an exactly solvable model [36] on a Honeycomb lattice that is effectively $\mathbb{Z}_2$ gauge theory coupled to Majorana fermions. This model hosts a variety of spin liquid phases. One is the regular Toric Code phase. Another is a spin liquid with Ising topological order. Yet another is a gapless (not topologically ordered) spin liquid described by gapless Majorana fermions coupled to gapped $\mathbb{Z}_2$ gauge theory.

- Dirac Spin Liquids [11, 23, 37]: It is described by QED_3, i.e., $U(1)$ gauge theory in $2+1$ dimensions coupled to gapless Dirac fermions. This theory is believed to flow to a strongly coupled Conformal Field Theory [9, 10, 38], and is not fully theoretically understood. Chapter 2 of this dissertation proposes novel ways to test if a candidate material is described

by this theory.

- Spinon Fermi Surface: It is described by $U(1)$ gauge theory in $2+1$ dimensions coupled to a Fermi surface. The theory is believed to be a non-Fermi liquid without quasiparticles [39, 40, 41, 42, 43], and is not well understood theoretically.

1.3 This dissertation: Bridging Theory and Experiment

The hallmark example of experimentally observed phases of matter described by a gauge theory are the Integer and Fractional Quantum Hall Effects (described by Chern-Simons theories). However, beyond these successes, at the time of writing, there is no conclusive experimental realization of other many-body systems described by deconfined phases of gauge theories. Ref. [44] provides a review of experimental progress on quantum spin liquids. Traditionally, in the solid state setting, experiments have focused on negative signatures, i.e., on ruling out conventional ordered states. For example, spin structure factor measured via neutron scattering would show broadening in a spin liquid because local operators create composite excitations. However, there could be other explanations for this broadening that are not due to fractionalization. Similarly, linear, or quadratic in T specific heat behavior is used as a signature of an emergent Fermi sea or emergent Dirac fermions respectively, but again this signature is not conclusive. A single probe cannot by itself conclusively diagnose a quantum spin liquid.

The approach taken in this dissertation is two-fold: (1) identify the key features of the field theory and propose a scheme to directly measure these features; and (2) propose a novel set of experimental probes, specifically making use of light-matter interactions.

We use this approach both in the solid state setting (Chapters 2 and 3) as well as in the set-

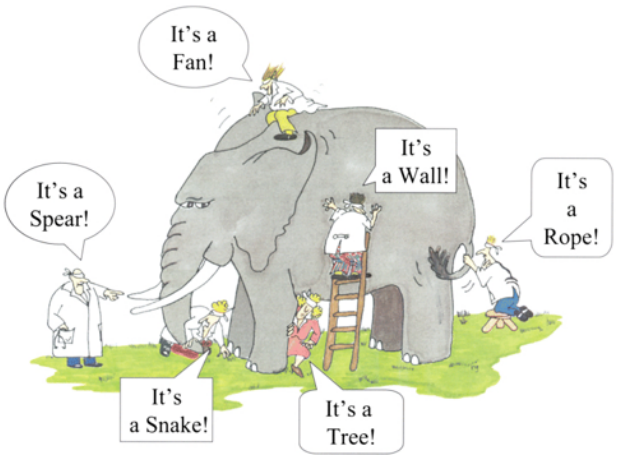

Figure 1.3: What an attempt to identify a putative Quantum Spin Liquid looks like. Figure from [13].

ting of quantum devices (Chapter 4). In Chapter 2, we first use our field theoretical understanding to propose a test for a Dirac Spin Liquid. The final observables in Chapter 2 are well-suited for measurement via Raman scattering. In Chapter 3, we answer a more general question – for a general electronic/spin system, what can we learn by measuring higher order correlations between Raman-scattered photons? In solid state systems, there is the prospect of truly realizing the thermodynamic limit, and thereby the field theoretic limit. But the disadvantage there is that one only has access to degrees of freedom at a highly coarse-grained level. In quantum devices on the other hand, qubit numbers at the time of writing are on the order of a few hundreds. But one has a major advantage of having microscopic access to each of these qubits. We exploit this access in Chapter 4 to propose a scheme to prepare and diagnose Quantum Spin Ice (deconfined phase of $U(1)$ gauge theory) in a three dimensional Rydberg atom simulator. In the remainder of this Introduction, we provide a more detailed outline of each Chapter.

1.3.1 Outline of Chapter 2

The central question of this chapter is – how do we know if a given piece of material is described by QED_3, i.e., how do we detect a Dirac Spin Liquid (DSL)? More precisely, can we induce and detect an emergent electric field inside a candidate DSL? We exploit the parent state picture of a DSL to argue that the answer is yes. This picture is that a DSL is known to be a "parent state" of various seemingly unrelated ordered states, such as antiferromagnets and valence bond solids in the sense that one can obtain ordered states by condensing magnetic monopoles of the emergent gauge field. We propose a range of "monopole Josephson effects" that arise when two ordered states are separated by a region of the parent DSL. In particular, we show that one can induce an AC monopole Josephson effect, which manifests itself as an AC emergent electric field in the spin liquid, accompanied by a measurable spin current. Further, we show that this AC emergent electric field can be measured as a sharp tunable peak in Raman scattering. This work provides a theoretical proof of principle that emergent gauge fields in spin liquids can be externally induced, manipulated, and probed using more conventional states.

The quantum numbers of monopoles under lattice symmetries can be used to characterize topological phases of matter under crystalline symmetries. We use this idea to establish a surprising connection between the DC Monopole Josephson effect and the characterization of topological phases in the presence of discrete lattice symmetries.

1.3.2 Outline of Chapter 3

In Chapter 2, we use Raman scattering as a probe to detect the emergent electric field in a spin liquid. In Chapter 3, we zoom out and ask a more general question – Raman intensity is re-

lated to the number operator of inelastically scattered photons, and is just one possible photonic correlator. But the modern quantum optics toolbox gives one access to a range of other photonic correlation functions such as $G^{(2)}$ (two-photon correlation) and phase sensitive quadrature correlations. Given access to these *photonic* correlators, what can we learn about the *electronic* properties of a Mott insulator off which the photons got scattered?

Specifically, we show that it is possible to probe certain spin, charge, and topological orders in an electronic system by measuring the correlation functions of scattered photons. We construct a mapping from the correlators of the scattered photons to those of a correlated insulator, particularly for Mott insulators described by a single-band Fermi-Hubbard model at half-filling. We show that frequency filtering before photodetection plays a crucial role in determining this mapping. We find that if the ground state of the insulator is a gapped spin liquid, a photon-pair correlation function, i.e., $G^{(2)}$, can detect the presence of anyonic excitations with fractional mutual statistics. Moreover, we show that correlations between electromagnetic quadratures can be used to detect expectation values of static spin chirality operators on both the kagome and triangular lattices, thus being useful in detecting chiral spin liquids. More generally, we show that a series of hitherto unmeasured spin-spin and spin-charge correlation functions of the material can be extracted from photonic correlations. This chapter opens up access to probe correlated materials, beyond the linear response paradigm, by detecting quantum properties of scattered light.

1.3.3 Outline of Chapter 4

In this chapter, we switch gears from the solid state setting to quantum devices. With the recent experiment showing preliminary signs of $\mathbb{Z}_2$ topological order [45], Rydberg atom

arrays have emerged as a promising platform to realize a quantum spin liquid. We present a proposal to access a confinement-deconfinement transition in a $U(1)$ quantum spin liquid in three spatial dimensions on a Rydberg-based quantum simulator. We study the ground state phase diagram of the proposed Pyrochlore Rydberg atom array as a function of experimentally relevant parameters. Within our calculation, we find that by tuning the Rabi frequency, one can access both the confinement-deconfinement transition driven by a proliferation of "magnetic" monopoles and the Higgs transition driven by a proliferation of "electric" charges of the emergent gauge theory. We suggest experimental probes for distinguishing the deconfined phase from ordered phases.

Chapter 2: Detecting a Dirac Spin Liquid: Monopole Josephson Effects

2.1 Introduction

Consider a spin-$1/2$ system in its ground state. Flipping a single spin creates a spin-1 excitation. If the ground state is conventional, such an excitation would disperse creating a superposition of spin-wave modes with spin 1. However, there is strong theoretical reason [46, 47] to expect exotic systems where, in addition to creating spin-1 modes, the spin-flip can fractionalize into two spin-1/2 excitations, which can then move away from each other. One interesting class of such systems in 2+1D are Dirac spin liquids (DSLs). The effective field theory describing DSLs is usually written in terms of Dirac fermions strongly coupled to an emergent $U(1)$ gauge field. This strongly coupled theory is believed to flow at low energies to a conformally invariant fixed point QED_3 [11, 48, 49].

To detect such an exotic state in a given physical system, say a material with spins, we would need to probe the low energy degrees of freedom of the effective field theory describing the state in question. For example, the low energy excitations of gapped spin liquids in 2+1D are anyonic quasiparticles. There have been proposals in the past for accessing emergent degrees of freedom in such gapped spin liquids with the assistance of more conventional ordered phases, which is helpful because one typically has better control over ordered phases. Examples of these include Refs. [50, 51, 52] for $\mathbb{Z}_2$ spin liquids, and Ref. [53] for Kitaev spin liquids.

For a strongly coupled field theory in 2+1D, such as QED_3 on the other hand, the low energy degrees of freedom are not well-defined quasiparticles, but instead the primary operators of the conformal field theory (CFT). Previous works have proposed ways to measure correlation functions of such operators in the ground state of a DSL [11, 54, 55]. However there appears to be a lack of proposals to directly control such operators externally and measure them. In this chapter, we explore this direction and propose a way to induce and measure an emergent electric field in a DSL. Our proposal relies crucially on coupling to monopole operators.

Monopole operators insert an integer multiple of 2π flux of the emergent $U(1)$ gauge field. Polyakov showed [56] that in 2+1 D, monopoles are always relevant in the renormalization group (RG) sense and proliferate in a pure $U(1)$ gauge theory, leading to confinement of test charges. Such a theory would not describe a spin liquid phase. However, including gapless fermions in the theory increases the scaling dimension of the monopoles, and in the limit of large number of fermion flavors N_f, monopoles can become irrelevant [9, 48]. Indeed, using a symmetry analysis followed by a large N_f analysis, Ref. [57] found that on the triangular lattice, monopoles are either disallowed by symmetry or irrelevant, suggesting that a DSL could be a stable phase. Such a phase has an emergent $U(1)_{\text{top}}$ symmetry corresponding to the conservation of total emergent flux (the subscript "top" is used to differentiate $U(1)_{\text{top}}$ from $U(1)$ gauge redundancy). In fact, monopoles are charged under an enlarged emergent internal symmetry $G_{IR} = SO(6) \times U(1)_{\text{top}}/\mathbb{Z}_2$ (see Sec. 2.2 for a review). Because spatial symmetries have a nontrivial action in G_{IR}, the monopoles transform under the microscopic symmetries like order parameters for magnetic orders including the 120° antiferromagnet and the $\sqrt{12} \times \sqrt{12}$ valence bond solid. Therefore, if the 2π monopoles somehow do proliferate (say as a result of spontaneous symmetry breaking, or due to a symmetry-breaking perturbation), the system exits the DSL

phase. The resulting phase is an ordered phase determined by which combination of monopoles proliferates. In this sense, it was suggested that the DSL is a parent state for several seemingly unrelated magnetic and VBS orders [23, 24].

Can this parent state picture guide us towards finding experimental probes for the low energy theory (QED_3) that describes the DSL? Can ordered states in proximity to a spin liquid have an interesting effect on the spin liquid, and vice-versa? In this chapter, we argue that the answer to both these questions is yes, by proposing a Josephson junction-like setup shown in Fig. 2.1 with two ordered phases separated by a middle region in the DSL phase. The main idea is that since the ordered states can be viewed as monopole condensates, monopoles can tunnel between the ordered states through the DSL.

We show that in certain circumstances, applying a Zeeman field gradient across the junction has the same effect as a voltage difference across a regular Josephson junction (between superconductors) and thus gives rise to an AC monopole current flowing across the DSL. In $2+1$ dimensions, a monopole current is equivalent to an electric field but in the perpendicular direction. Therefore, this "monopole Josephson effect" provides a way to externally induce an emergent electric field through the DSL. We suggest a way to measure the AC emergent electric field optically as a peak in Raman scattering intensity by identifying microscopic operators corresponding to the emergent electric field. In addition to this signature within the DSL region, we show that when the ordered phases are 120° antiferromagnets, the same monopole Josephson effect leads to a spin current across the junction. This spin current can in principle be measured on both the ordered side and the DSL using techniques proposed in [58, 59]. We also discuss three other conceptually related effects which all fall under the umbrella of the monopole Josephson effect.

The rest of the chapter is organized as follows. In Sec. 2.2, we provide a brief review of DSLs, emphasizing the relevant features of monopole operators and the parent state picture. In Sec. 2.3, we show that an emergent electric field in the DSL can be induced via the monopole Josephson effect. In Sec. 2.4, we propose a way to detect this emergent electric field using Raman scattering. In Sec. 2.5, we discuss other phenomena related to the monopole Josephson effect. In Sec. 2.6, we make a surprising connection to the classification of Chern insulators in the presence of crystalline symmetries. Finally, we offer some general conclusions and discussion in Sec. 2.7.

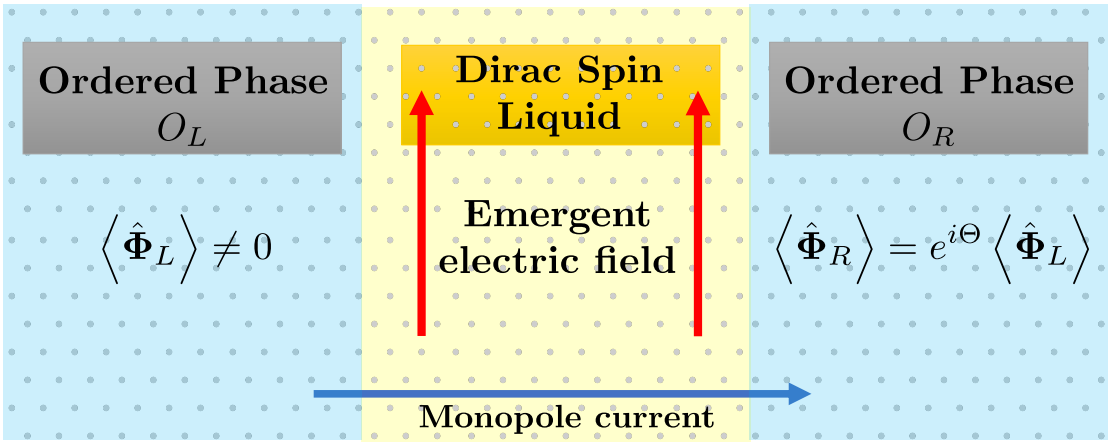

Figure 2.1: Monopole Josephson effect, general idea: We consider a junction of two ordered phases (O_L and O_R) separated by a DSL. O_L and O_R are viewed as monopole condensates such that their expectation values are related by a generalized phase (unitary matrix) $e^{i\Theta}$ (possibly time-dependent). This leads to a monopole current across the junction, which is equivalent to an electric field in the emergent $U(1)$ gauge field in the perpendicular direction inside the DSL.

2.2 Review of Dirac Spin Liquids

DSLs are described by an effective field theory with $N_f = 4$ flavors of gapless Dirac fermions at zero equilibrium density strongly coupled to a compact $U(1)$ gauge field. The fermions carry spin-$1/2$ under the microscopic $SO(3)$ spin rotation symmetry. One way to get to this theory is the parton construction, which we will briefly review below.

Before proceeding, we explain some notation. We use $\vec{V}$ for 2-component vectors in real-space, $\vec{\mathbf{V}}$ for 3-component vectors in internal spin or valley space, and $\mathbf{V}$ for vectors in other internal spaces such as $SO(6)$ (see Appendix B.2.4 for other remarks on notation).

Consider a spin system whose microscopic Hilbert space consists of spin-$1/2$ at each lattice site. We assume that the Hamiltonian realizes a DSL ground state and respects some set of symmetries G_{UV} which include lattice symmetries, time-reversal, and spin-rotation symmetry. We will work on the triangular lattice for concreteness, but the results are general except where otherwise noted. The objective of the parton construction is to come up with a mean-field theory even in the case when the spin operators $\left\langle \hat{\vec{\mathbf{S}}}_i \right\rangle = 0$ (likewise for other local spin operators) for all sites i. In this approach, the Hilbert space at each site i is doubled by writing spin operators in terms of fictitious spin-$1/2$ fermionic "spinon" operators $\hat{f}_{i,\alpha}$:

$$\hat{\vec{\mathbf{S}}}_i = \frac{1}{2} \sum_{\alpha,\beta \in \{\uparrow,\downarrow\}} \hat{f}^\dagger_{i\alpha} \vec{\boldsymbol{\sigma}}_{\alpha\beta} \hat{f}_{i\beta}. \tag{2.1}$$

Here $\vec{\sigma}$ is a vector of Pauli matrices. This description has a $U(1)$ gauge redundancy

$$\hat{f}_{i\alpha} \to e^{i\lambda_i} \hat{f}_{i\alpha}, \tag{2.2}$$

in the sense that the physical spin operators are invariant under such a transformation. The spin Hilbert space is recovered by imposing the constraint that there is exactly one fermion at each site. One now rewrites the spin Lagrangian in terms of these fermions. A quadratic term in spins becomes a quartic term in fermions, which is then decoupled so that the fermion hopping coefficients $\left\langle \sum_{\alpha=\uparrow,\downarrow} \hat{f}^\dagger_{i\alpha} \hat{f}_{j\alpha} \right\rangle$ acquire mean-field expectation value χ_{ij}. For a DSL on the triangular

lattice, the mean-field configuration for $\{\chi_{ij}\}$ consists of alternating π-flux and 0-flux on upward and downward triangles respectively. Diagonalizing this quadratic mean-field Hamiltonian gives a spectrum with two Dirac cones (valleys). To zeroth order, the single-occupancy-per-site constraint is relaxed to demanding single-occupancy on average, i.e., that the fermions are at half filling. This forces the chemical potential to lie exactly at the Dirac points. So, to zeroth order, the low-energy theory has 4 flavors of Dirac fermions — 2 valleys for each spin. $U(1)$ gauge fluctuations $\chi_{ij} \to \chi_{ij} e^{i a_{ij}}$ are now reintroduced. The single particle per site constraint is reintroduced only weakly as a Gauss's law by assuming a finite coupling constant g:

$$\sum_{\alpha=\uparrow,\downarrow} \hat{f}^\dagger_{i\alpha} \hat{f}_{i\alpha} - 1 = \frac{1}{g^2} \sum_j \hat{e}_{ij}, \tag{2.3}$$

where e_{ij} is the emergent electric field, i.e., the electric flux of a_{ij}. This leads us to a field theory Lagrangian density, which schematically is

$$\mathcal{L} = \sum_{i=1}^{N_f=4} \bar{\psi}_i \gamma^\mu \left(\partial_\mu - i a_\mu\right) \psi_i + \frac{1}{8\pi g^2} (\epsilon^{\mu\nu\lambda} \partial_\mu a_\nu)^2, \tag{2.4}$$

where each ψ_i is a 2-component spinor and a_0 has been introduced as a Lagrange multiplier enforcing Eq. 2.3. The theory of the DSL is then described by the low-energy fixed point, called QED_3, of Eq. (2.4). By itself, Eq. (2.4) is not useful to understand the fixed point because the coupling constant g^2 has dimensions of $\left[\text{Length}^{-1}\right]$. So, at low energies g^2 flows to ∞ making gauge fluctuations uncontrolled. However, progress can be made by treating $1/N_f$ as a small parameter. Then, because of screening of gauge fluctuations by the many gapless fermions, g^2 approaches a fixed point value which scales as Λ/N_f where Λ is an inverse length scale of order

of the lattice spacing [48]. Most of the current understanding of the QED$_3$ fixed point comes from this limit — thinking of the spinons ψ_i essentially as almost free fermions with gauge fluctuations controlled by the large N_f expansion. At the same time, one should keep in mind that the most important low energy operators to study are primary operators of the CFT with the lowest scaling dimensions.

The essential features of the nontrivial fixed point theory QED$_3$ are:

1. Monopole operators: Among the primary operators in QED$_3$ are magnetic monopoles $\hat{\Phi}_i^\dagger$. These operators insert 2π flux of the emergent gauge field a, that is,

$$\left[\hat{b}(x), \hat{\Phi}_i^\dagger(x')\right] = 2\pi\delta(x-x')\hat{\Phi}_i^\dagger(x'), \tag{2.5}$$

where $\hat{b}(x) = (\partial_1\hat{a}_2 - \partial_2\hat{a}_1)$(x). In a path integral, the insertion of these operators corresponds to instanton events whose role is to restore the compactness of the gauge field in the low energy theory.

2. Enlarged emergent symmetry group: [24, 57] While the microscopic Hamiltonian has the symmetries listed above, the DSL theory (QED$_3$) has an enlarged internal symmetry $G_{IR} = \frac{SO(6)\times U(1)_{\text{top}}}{\mathbb{Z}_2}$. The $U(1)_{\text{top}}$ symmetry corresponds to the conservation of total emergent magnetic flux through the plane: $\hat{b}_{\text{tot}} \equiv \frac{1}{2\pi}\int d^2x\hat{b}(x)$. Clearly monopole operators are charged under $U(1)_{\text{top}}$. The total flux is conserved because the monopole operators (i.e. flux creation/annihilation operators) have zero expectation value in the wave function described by DSL theory. The $SO(6)$ symmetry corresponds to the internal rotation between the spin and valley indices, and the monopole operators transform as a vector under $SO(6)$.

More concretely, inserting 2π flux leads to one Landau zero-mode per fermion flavor, and to maintain half filling, 2 out of 4 zero-modes need to be filled. The resulting 6 choices lead to 6 independent monopole creation operators $\hat{\Phi}_i^\dagger$ ($i \in \{1, \ldots 6\}$) which together transform as a vector under $SO(6)$. A complementary way to understand this is to observe that the fermionic partons enjoy an $SU(4)$ symmetry near the Dirac points. Upon carefully keeping track of redundant factors of $\mathbb{Z}_2$[1], one arrives at G_{IR} above. While the microscopic $SO(3) \subset G_{UV}$ spin-rotation symmetry is directly $SO(3)_{\text{spin}} \subset G_{IR}$, elements of the space group generally embed nontrivially into $SO(3)_{\text{valley}} \times U(1)_{\text{top}} \subset G_{IR}$ (in addition to the spatial transformation).

3. Parent state of competing orders [23, 24, 57] If a monopole operator condenses, i.e., acquires a nonzero expectation value, then the spinons confine, and the low-energy excitations are un-fractionalized spin-1 modes. The resultant phase is simply a conventional magnetically ordered phase. Many seemingly-unrelated ordered phases can appear depending on which monopole operator condenses and what the microscopic symmetries are. For example, on the triangular lattice, a 120° coplanar order can be obtained by condensing spin triplet monopoles, and valence bond solids with a unit-cell area of 12 times the elementary unit cell can be obtained by condensing spin singlet monopoles. The DSL thus serves as a "parent state" for many ordered states, in the sense that one mechanism (monopole condensation) in the DSL is responsible for driving transitions to many different ordered states.

   Such a transition could happen for multiple reasons. A monopole operator may be relevant

[1] The $\mathbb{Z}_2$ subgroup of $SU(4)$ generated by fermion parity is actually a $U(1)$ gauge transformation rather than a symmetry, reducing the $SU(4)$ symmetry to $SO(6) \cong SU(4)/\mathbb{Z}_2$. The element $-1 \in SO(6)$ is identical to a π rotation in $U(1)_{top}$.

in the renormalization group (RG) sense and symmetry allowed; in this case, the DSL represents a critical point separating ordered phases. On the other hand, if there are no relevant monopole operators that are symmetry allowed, then the DSL is a stable phase of matter — a gapless spin liquid. However, if there is explicit or spontaneous breaking of a symmetry which was previously forbidding some monopole operator from condensing, this would also lead to a transition to an ordered state.

2.2.1 Monopole condensation and unbroken symmetries

The goal of this section is to highlight one fact that will play a crucial role in our work — in a 120° AFM, applying spin rotation about a certain axis on the condensed monopoles is equivalent to applying a $U(1)_{\text{top}}$ phase rotation.[2] To do so, we will review a particular mechanism for driving monopole condensation. We first summarize the key facts:

1. Under this mechanism, a phase transition occurs when a certain linear combination of 2π monopole operators that is an eigenvector of a specific $SO(6)$ generator condenses.

2. From the G_{IR} transformation properties of the condensed monopole operator, one can determine which ordered phase arises.

3. The G_{IR} symmetry is not fully broken in the ordered state.

In Appendix B.1, we review previous works on the stability of DSLs, which suggest that a DSL could be a stable phase on the triangular lattice. In this case, 2π monopole operators are symmetry-disallowed in the Langrangian. However, they are still the operators with the lowest scaling dimensions in the low-energy theory. The following mechanism was proposed

[2] The reader can skip to Sec. 2.3, and return to this section when required.

[24, 60, 61] for destroying the DSL by proliferating 2π monopoles. First, due to interactions, a fermion bilinear, or mass term, spontaneously acquires a nonzero expectation value. Although other possibilities can occur, we will generally assume that a single bilinear

$$\langle \bar{\psi} \sigma^{\alpha} \tau^{\beta} \psi \rangle \neq 0 \tag{2.6}$$

where σ^{α} and τ^{β} are Pauli matrices acting in the spin and valley spaces respectively (here $\alpha, \beta \in \{0, 1, 2, 3\}$ but α and β are not both 0). This fermion bilinear serves as a mass term that splits the degeneracy of the fermionic Landau zero modes associated with adding a 2π magnetic flux, lowering the energy (and hence scaling dimension) of one specific linear combination of monopole operators. In particular, given a choice of generator $\sigma^{\alpha}\tau^{\beta}$ of $SU(4)$, we can find a corresponding generator $T\left[\sigma^{\alpha}\tau^{\beta}\right]$ of $SO(6)$. This linear combination of monopoles then becomes the most relevant operator and condenses, i.e., acquires a nonzero expectation value. The resulting state is an ordered state in which the fermions are confined [56] and the condensed monopole operator serves as an order parameter.

The linear combination of monopoles which condenses corresponds to the eigenvector of $T\left[\sigma^{\alpha}\tau^{\beta}\right]$ with the largest eigenvalue. As an example, suppose that the bilinear $\bar{\psi}\sigma^{3}\psi$ has a nonzero expectation value. One can check that three monopole operators, which we shall call $\hat{\Phi}_{1,2,3}$, transform as $SO(3)_{\text{spin}}$ singlets, and the other three transform as an $SO(3)_{\text{spin}}$ triplet $\hat{\vec{\Phi}}$. In

this basis, the $SO(6)$ generator corresponding to σ^3 is

$$T[\sigma^3] = \begin{pmatrix} 0_{3\times 3} & \cdots & & \\ \vdots & 0 & -i & 0 \\ & i & 0 & 0 \\ & 0 & 0 & 0 \end{pmatrix}. \tag{2.7}$$

The eigenvector of $T[\sigma^3]$ with maximal eigenvalue (equal to 1) is

$$\begin{aligned} \left\langle \hat{\mathbf{\Phi}} \right\rangle &= \begin{pmatrix} \left\langle \hat{\Phi}_1 \right\rangle & \left\langle \hat{\Phi}_2 \right\rangle & \left\langle \hat{\Phi}_3 \right\rangle & \left\langle \hat{\Phi}_4 \right\rangle & \left\langle \hat{\Phi}_5 \right\rangle & \left\langle \hat{\Phi}_6 \right\rangle \end{pmatrix}^T \\ &= |\Phi| \begin{pmatrix} 0 & 0 & 0 & 1 & i & 0 \end{pmatrix}^T. \end{aligned} \tag{2.8}$$

The interpretation of this fact is that the fermion mass term makes the energy of the monopole $(\hat{\Phi}_4^\dagger + i\hat{\Phi}_5^\dagger)\,|GS\rangle$ negative, where $|GS\rangle$ is the ground state of the DSL in the absence of the fermion mass term (whose energy we set to 0). Accordingly, the DSL ground state becomes unstable and a transition occurs to a state with $\left\langle \hat{\Phi}_4^\dagger + i\hat{\Phi}_5^\dagger \right\rangle \neq 0$.

Although the fermion mass terms pick up nonzero expectation values, the fact that the monopole operators have a lower scaling dimension means that we should treat the condensed monopole operator as the order parameter. Different approaches can be used to determine a microscopic order parameter corresponding to each monopole operator. Refs. [24, 57] used a symmetry analysis combined with a Wanner center study of mean-field free fermion bands. In Appendix B.2.2, we combine symmetry analysis with operator algebra constraints to independently motivate the same results. The key results are as follows. First suppose that a spin-triplet monopole operator condenses. If $\left\langle \hat{\vec{\mathbf{\Phi}}} \right\rangle$ (the vector notation refers to a vector under $SO(3)_{\text{spin}}$) is

given by the eigenvector with positive eigenvalue of $\vec{\mathbf{d}}_{\text{spin}} \cdot \vec{\mathbf{T}}_{\text{spin}}[\sigma]$ for a unit 3-vector in spin-space, $\vec{\mathbf{d}}_{\text{spin}}$, then the ordered state is a 120° coplanar AFM order in the plane (in spin-space) normal to $\vec{\mathbf{d}}_{\text{spin}}$. Similarly, various $\sqrt{12} \times \sqrt{12}$ VBS phases can be obtained if the condensed spin-singlet monopole is an eigenvector of $\vec{\mathbf{d}}_{\text{valley}} \cdot \vec{\mathbf{T}}_{\text{valley}}[\tau]$ for some unit 3-vector $\vec{\mathbf{d}}_{\text{valley}}$ in valley-space. In this VBS phase, the area of the unit cell is 12 times the area of the unit cell of a triangular lattice. [3]

Having identified the monopole order parameters, we now notice that the G_{IR} symmetry is not completely broken. Suppose that the condensed monopole is an eigenvector (in the sense of Eq. 2.8) of a generator $\hat{Q}$ of $SO(6)$. We focus for later use on the case where $\hat{Q} \in SO(3)_{\text{spin}}$. Then

$$\left\langle e^{i\theta\hat{Q}}\ \hat{\mathbf{\Phi}}\ e^{-i\theta\hat{Q}} \right\rangle = e^{-i\theta Q} \left\langle \hat{\mathbf{\Phi}} \right\rangle = e^{-i\theta} \left\langle \hat{\mathbf{\Phi}} \right\rangle . \tag{2.9}$$

Note also that under a $U(1)_{\text{top}}$ phase rotation,

$$\left\langle e^{-i\theta\hat{b}_{\text{tot}}}\ \hat{\mathbf{\Phi}}\ e^{i\theta\hat{b}_{\text{tot}}} \right\rangle = e^{i\theta} \left\langle \hat{\mathbf{\Phi}} \right\rangle . \tag{2.10}$$

Hence $\left\langle \hat{\mathbf{\Phi}} \right\rangle$ is invariant under $e^{-i\theta\hat{b}_{\text{tot}}} e^{i\theta\hat{Q}}$. Such a transformation generates a $SO(2)$ diagonal subgroup of $SO(2)_{\text{spin}} \times U(1)_{\text{top}}$ that is an unbroken symmetry. This "redundancy" between spin rotations and $U(1)_{\text{top}}$ phase rotation in the 120° AFM state will play a crucial role in the AC Josephson setup proposed in Section 2.3.

For completeness, we mention the concrete connection between the 120° AFM order pa-

[3] One could also consider condensation channels that are eigenvectors of the mixed generators $T\left[\sigma^i \tau^j\right]$. These "unconventional orders" were considered in Suppl. Note. 5 of [24]. We will not consider these in this chapter.

rameter and $\vec{\Phi}$:

$$\hat{\vec{\mathbf{\Phi}}} = \sum_{\vec{n}} e^{-i\vec{Q}.\vec{n}} \left(\hat{\vec{\mathbf{S}}}_{\vec{n}} + \ldots \right), \tag{2.11}$$

where $\vec{Q} = \frac{2\pi}{3}(\vec{\mathrm{b}}_1 - \vec{\mathrm{b}}_2)$. Here $\vec{\mathrm{b}}_1 \equiv \frac{\sqrt{3}}{2}\hat{x} - \frac{1}{2}\hat{y}$ and $\vec{\mathrm{b}}_2 \equiv \hat{y}$ are reciprocal lattice vectors satisfying $\vec{\mathrm{a}}_i \cdot \vec{\mathrm{b}}_2 = \delta_{ij}$, where $\vec{\mathrm{a}}_1 \equiv \hat{x}, \vec{\mathrm{a}}_2 \equiv \frac{1}{2}\hat{x} + \frac{\sqrt{3}}{2}\hat{y}$ are the basis vectors for the triangular lattice. In Eq. 2.11, the "..." refers to operators supported on three or more sites.

From Eq. 2.11, we can see that the ordering pattern

$$\left\langle \hat{\vec{\mathbf{S}}}_{\vec{n}} \right\rangle = \left(\cos\left(\vec{Q}.\vec{n}\right), \quad -\sin\left(\vec{Q}.\vec{n}\right), \quad 0 \right), \tag{2.12}$$

corresponds to $\left\langle \hat{\vec{\mathbf{\Phi}}} \right\rangle = |\Phi| \begin{pmatrix} 1 & i & 0 \end{pmatrix}^T$, which was the example we considered in Eq. 2.8.

2.3 Monopole Josephson effects

In the previous sections we reviewed how various ordered states can be obtained from a DSL by condensing combinations of 6 monopole operators related to each other by the enlarged $(SO(6) \times U(1)_{\text{top}})/\mathbb{Z}_2$ symmetry. Now we will argue how this can have physical consequences in the form of "monopole Josephson effects", by which we mean a flow of monopole current between two symmetry-broken regions of a system. Consider the setup shown in Fig. 2.1 where a lattice is split into three regions — two ordered phases (O_L and O_R) separated by a DSL region in the middle. Instead of considering three different materials kept next to each other, we assume that within the *same* sample, perturbations localized to regions L and R drive those regions to ordered phases. This allows us to view the ordered states O_L and O_R as being obtained via monopole condensation from the DSL. Monopoles can now tunnel from O_L to O_R through the

middle DSL resulting in a monopole current.

We note that the net monopole current (, i.e., current of $U(1)_{\text{top}}$ charge) is just the emergent electric field rotated by $90°$. This is because Faraday's law takes the form of a conservation law in 2+1 D:

$$\partial_t \frac{\hat{b}}{2\pi} + \partial_i \frac{\epsilon_{ij}\hat{e}_j}{2\pi} = 0. \tag{2.13}$$

So, $\hat{Q}[U(1)_{\text{top}}](x) = \frac{\hat{b}(x)}{2\pi}$ and $\hat{J}^i[U(1)_{\text{top}}](x) = \frac{\epsilon_{ij}\hat{e}_j(x)}{2\pi}$. Therefore this monopole Josephson setup provides a way to induce an emergent electric field inside the DSL (see Fig. 2.1). We will show in Sec. 2.4 that if this induced emergent electric field is time-dependent, it can be optically detected via Raman scattering.

For a given configuration of O_L and O_R, our goal is to make predictions for the resulting monopole currents. Since the monopoles are charged under $G_{IR} = SO(6) \times U(1)_{\text{top}}/\mathbb{Z}_2$, there are 16 different conserved currents in principle, corresponding to each generator of G_{IR}. These are $\hat{\vec{J}}[U(1)_{\text{top}}]$ (analogous to electric Josephson current across superconductors), and 15 currents for each generator of $SO(6)$, of which 3 are spin currents. Deep inside the DSL, since G_{IR} is a symmetry, all 16 currents are conserved at low energies. However, outside the DSL and at the boundaries, generically only the 3 spin currents will be conserved (assuming that $SO(3)_{\text{spin}}$ is respected throughout the system). So we will make statements about two kinds of quantities — (1) Spin currents that can be measured in either the ordered phases or the DSL, for example using techniques proposed in [58, 59], and (2) Currents corresponding to the emergent symmetries of the DSL, which can be probed only within the DSL. The most interesting result of this work is a time dependent (AC) $U(1)_{\text{top}}$ current in the DSL arising due to either a gradient in Zeeman field or due to a gradient in staggered spin chirality applied across the junction.

In this work, we focus on qualitatively determining, for a given configuration of O_L and O_R and external fields, which monopole currents are non-zero and their dependence on the external fields. In principle, one might also want to calculate the way that the magnitude of the currents $\left|\left\langle \hat{\vec{J}}_{\text{Josephson}}(\vec{x})\right\rangle\right|$ scale with the width of the DSL region and thickness of the boundaries. Qualitatively, we expect the currents to decay as a power law in the width w of the DSL region since the DSL is a critical phase. Since the scaling dimension of a conserved current is d in a $d+1$ dimensional CFT, we expect

$$\left|\left\langle \hat{\vec{J}}_{\text{Josephson}}(\vec{x})\right\rangle\right| \propto \frac{\left|\left\langle \hat{\mathbf{\Phi}}_L\right\rangle\right|\left|\left\langle \hat{\mathbf{\Phi}}_R\right\rangle\right|}{w^{2-\Delta_{b,L}-\Delta_{b,R}}} \equiv \mathcal{E}, \tag{2.14}$$

where $\Delta_{b,L}$ and $\Delta_{b,R}$ are the boundary scaling dimensions of the monopole operators on the left and right boundaries respectively. (Here, we have also defined the RHS of Eq. (2.14) as $\mathcal{E}$ for later convenience.) If the details of the interface provide an additional length scale, this could modify the above scaling. Calculating $\Delta_{b,L}$, $\Delta_{b,R}$ and any additional interface effects is a complicated boundary CFT problem beyond the scope of this work, so we will not address this issue in any more quantitative detail.

2.3.1 Effective Hamiltonian

Our first task is to write a low energy Hamiltonian coupling the two ordered regions L and R to the DSL. In the DSL, monopole operators are the most relevant in the RG sense, and hence coupling terms involving monopole tunneling should be the most important at low energy (we expect this from the large N_f scaling dimensions of monopole operators when one sets $N_f = 4$;

see Table B.1). This motivates the following coupling Hamiltonian (see Fig. 2.2(a))

$$H_{\text{c}} = -\sum_{i,j=1}^{6}\Big(\Gamma_{ij,L}\int dy\ \hat{\Phi}^{\dagger}_{iL}(x_L,y)\hat{\Phi}_{jD}(x_L,y) + \Gamma_{ij,R}\int dy\ \hat{\Phi}^{\dagger}_{iD}(x_R,y)\hat{\Phi}_{jR}(x_R,y)\Big) + \text{h.c.}, \tag{2.15}$$

where the left (right) interface is at $x = x_L$ ($x = x_R$) and y runs parallel to the boundary (in both terms above). A remark on notation — to emphasize a monopole-tunneling interpretation, we have used the same symbol $\hat{\Phi}_i$ for both the monopole operator in the DSL side ($\hat{\Phi}_{iD}$) and on the ordered sides $\hat{\Phi}_{i,L/R}$. But we note that in general, they would have different scaling dimensions. For example, as one crosses the interface, the system goes through a phase transition and the monopole scaling dimension at the transition is known to be smaller at the phase transition than deep in the DSL (from a large N_f calculation [60, 62]).

Since we assumed that the coupling matrix $\Gamma_{ij,L/R}$ preserves spin rotation symmetry,

$$\Gamma_{ij,L/R} \equiv \Gamma_S\delta_{ij},\ \text{for}\ 4 \le i,j \le 6. \tag{2.16}$$

Now, since the boundary breaks spatial symmetries, but preserves spin-rotation symmetries, we are also allowed to add single monopole terms for the spin-singlet monopoles, but not spin triplet monopoles:

$$\hat{H}_{\text{source}} = \sum_{i=1}^{3}\int dy\Big(V_{i,L}\hat{\Phi}_i(x_L,y) + V_{i,R}\hat{\Phi}_i(x_R,y)\Big) + \text{h.c.} \tag{2.17}$$

We argue in Appendix B.3 that $\hat{H}_{\text{source}}$ does not contribute significantly to the currents we are interested in. Then the full Hamiltonian without $\hat{H}_{\text{source}}$, i.e., $\hat{H} = \hat{H}_{DSL} + \hat{H}_{O_L} + \hat{H}_{O_R} + \hat{H}_c$ has

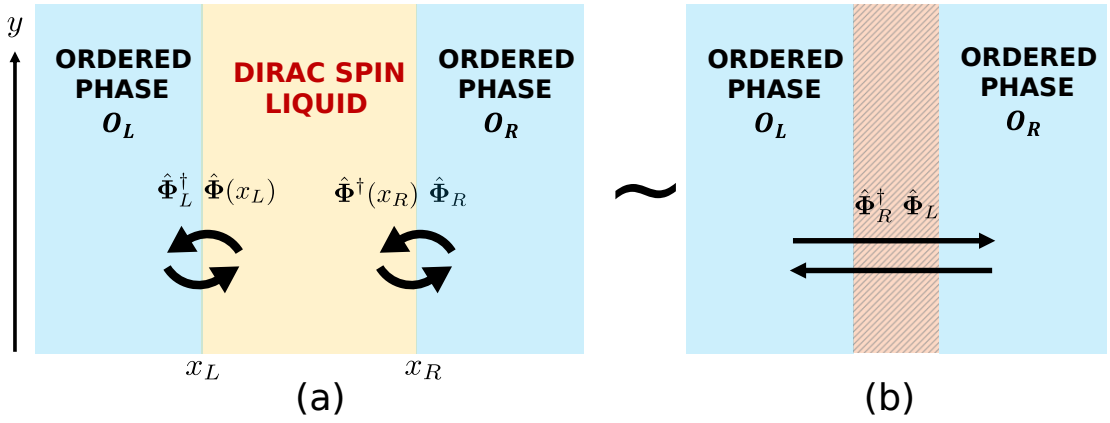

Figure 2.2: Schematic of the (a) effective monopole tunneling Hamiltonian Eq. (2.15) and (b) our proxy Hamiltonian Eq. (2.18) used to capture qualitative features of the Josephson currents obtained by schematically "integrating out" the DSL.

a global spin rotation $SO(3)$ symmetry, and formally, also a global $U(1)_{\text{top}}$ symmetry. We will now use the following strategy — we first write a schematic Hamiltonian for monopole tunneling between O_L and O_R, where the DSL region is assumed to have been "integrated out" (we ignore any potential retardation effects coming from integrating out gapless modes in the DSL):

$$\begin{aligned}\hat{H}_{\text{eff}} = \hat{H}_{O_L} + \hat{H}_{O_R} - \Gamma_S^{\text{eff}} \sum_{i=4}^{6} \left(\hat{\Phi}_{iL}^\dagger \hat{\Phi}_{iR} + \text{ h.c.} \right) \\ - \sum_{i,j=1}^{3} \left(\Gamma_{ij}^{\text{eff}} \hat{\Phi}_{iL}^\dagger \hat{\Phi}_{jR} + \text{ h.c.} \right),\end{aligned} \tag{2.18}$$

where we have neglected the spatial dependence of $\hat{\Phi}_{iL}$ (see Fig. 2.2 (b)). The parameter

$$\Gamma_S^{\text{eff}} \sim \mathcal{E} L, \tag{2.19}$$

where the factor of L, the system length along y, comes from the integration along the y direction and $\mathcal{E}$ was estimated in Eq. (2.14). We compute the conserved spin current and $U(1)_{\text{top}}$ current flowing from O_L to O_R using the above Hamiltonian, and assume that by current conservation

(justified in Appendix B.3), the *same* current also flows through the spin liquid.

2.3.2 Brief review of the generalized Josephson effects

Eq. (2.18) is of the form which is usually used to derive generalized Josephson currents between ordered phases which break symmetries belonging to a continuous group G [63, 64, 65]. Here, we provide a brief review of this formalism which computes the DC and AC Josephson currents of a given symmetry generator, following Ref. [63]. Let $\hat{Q}^r$ for $r \in \{1, \dots M\}$ be quantum operators corresponding to the M generators of G. For our problem, $\hat{Q}^r$ are the 15 $SO(6)$ charges $\hat{Q}_{\text{tot}}\left[\sigma^\alpha \tau^\beta\right]$ (where α and β are not both 0) and the emergent flux $\hat{b}_{\text{tot}}$. Now suppose the system is divided into left and right parts L and R (Fig. (2.2)). We assume that each $\hat{Q}^r$ can be written as a sum of local operators (see Appendix B.2 for a discussion). This allows us to define $\hat{Q}^r_{L/R}$ as the restriction of $\hat{Q}^r$ to the respective region L/R. Let $\hat{\Phi}_i$ be N operators charged under G, i.e. they transform under the group action. The group action is

$$\left[\hat{Q}^r, \hat{\Phi}_i\right] = \sum_{j=1}^{N} -T^r_{ij} \hat{\Phi}_j, \tag{2.20}$$

where T^r is an $N \times N$ Hermitian matrix of c-numbers and is a representation of $\hat{Q}^r$ on $\mathbb{C}^N$. When r above corresponds to $U(1)_{\text{top}}$, $T[U(1)_{\text{top}}] = 1_{6\times 6}$. For explicit formulas for T^r when $G = SO(6)$, see Eq. (B.13).

The set of operators $\hat{\Phi}_i$ will serve as the order parameter. They will acquire expectation value when the symmetry is broken. Assuming that $\hat{\Phi}_i$ is a sum of local operators, Eq. (2.20) holds approximately even when the operators are restricted to small regions. Suppose the expectation value $\left\langle \hat{\Phi}_{iR} \right\rangle$ on the right differs from that on the left $\left\langle \hat{\Phi}_{iL} \right\rangle$. We now compute the current

for each generator $\hat{Q}^r$ from left to right.

To do this, let us write an effective Hamiltonian. It is identical to Eq. (2.18), except that the following Hamiltonian assumes that the coupling respects the full symmetry G:

$$\hat{H} = \hat{H}_L + \hat{H}_R - \Gamma \sum_{i=1}^{N} \left(\hat{\Phi}^\dagger_{iL} \hat{\Phi}_{iR} + \hat{\Phi}^\dagger_{iR} \hat{\Phi}_{iL} \right), \tag{2.21}$$

where Γ is an effective coupling constant depending on the details of the intermediate region between L and R. The current of generator r from left to right $\hat{I}^r_{L\to R}$ can be calculated from the Heisenberg equation of motion

$$\hat{I}^r_{L\to R} \equiv -\frac{\mathrm{d}\hat{Q}^r_L}{\mathrm{d}t} = i\left[\hat{Q}^r_L, \hat{H}\right]. \tag{2.22}$$

Q^r_L commutes with H_L because it is conserved, and with H_R because H_R has support only on side R. The only nonzero contribution comes from the coupling term.

$$\hat{I}^r_{L\to R} = -i\Gamma \sum_{i,j} \hat{\Phi}^\dagger_{iL} T^r_{ij} \hat{\Phi}_{jR} + \text{ h.c.}. \tag{2.23}$$

The expectation value of the RHS above has a disconnected component and a connected component. Since the two sides of the system are symmetry breaking, $\left\langle \hat{\Phi}_{jL/R} \right\rangle$ is macroscopic. So, to lowest order, we will ignore the connected piece. Thus,

$$\left\langle \hat{I}^r_{L\to R} \right\rangle \approx -i\Gamma \sum_{i,j} \left\langle \hat{\Phi}^\dagger_{iL} \right\rangle T^r_{ij} \left\langle \hat{\Phi}_{jR} \right\rangle + \text{ h.c.}. \tag{2.24}$$

This is the DC Josephson effect. The same formula can also be used for the AC Josephson effect

as follows. A term is added to the Hamiltonian that couples to the *difference* in a conserved charge across the two sides: $\hat{H}_\mu = \frac{\mu}{2}(\hat{Q}^s_R - \hat{Q}^s_L)$ (for example, the electric potential difference between the two superconductors). As we will see below, this results in an oscillatory time dependence for $\left\langle \hat{\Phi}_{i(L/R)} \right\rangle$, and therefore according to Eq. (2.24), the current $\hat{I}^r_{L\to R}$ also acquires an oscillatory time dependence,

$$\frac{\mathrm{d}\hat{\Phi}_{iR}}{\mathrm{d}t} = -i\frac{\mu}{2}\left[\hat{\Phi}_{iR}, \hat{Q}^s_R\right] = +i\frac{\mu}{2}\sum_j (T^s)_{ij}\hat{\Phi}_{jR}, \tag{2.25}$$

$$\frac{\mathrm{d}\hat{\Phi}_{iL}}{\mathrm{d}t} = +i\frac{\mu}{2}\left[\hat{\Phi}_{iL}, \hat{Q}^s_L\right] = -i\frac{\mu}{2}\sum_j (T^s)_{ij}\hat{\Phi}_{jL}. \tag{2.26}$$

The solution is (suppressing the indices of $\hat{\mathbf{\Phi}}_{L/R}$ and T^r)

$$\hat{\mathbf{\Phi}}_R(t) = e^{i\frac{\mu}{2}tT^s}\hat{\mathbf{\Phi}}_R(0) \text{ and } \hat{\mathbf{\Phi}}_L(t) = e^{-i\frac{\mu}{2}tT^s}\hat{\mathbf{\Phi}}(0). \tag{2.27}$$

Substituting in Eq. (2.24), we get

$$\begin{aligned}\left\langle \hat{I}^r_{L\to R}(t)\right\rangle \approx &- i\Gamma \left\langle \hat{\mathbf{\Phi}}^\dagger_L(0)\right\rangle e^{i\frac{\mu}{2}tT^s}T^r e^{i\frac{\mu}{2}tT^s}\left\langle \hat{\mathbf{\Phi}}_R(0)\right\rangle \\ &+ \text{ h.c.}\end{aligned} \tag{2.28}$$

If T^r commutes with T^s, then from Eq. (2.28), the current oscillates at frequency μ — the familiar AC Josephson effect.

2.3.3 Monopole Josephson currents in a DSL

We will now use the above framework to qualitatively determine the Josephson currents in the setup shown in Fig. 2.1. The symmetry generators $\hat{Q}^r$ are the total magnetic flux $\hat{b}_{\text{tot}}$ and

the 15 generators of $SO(6)$, namely $\hat{Q}_{\text{tot}}\left[\sigma^{\alpha}\tau^{\beta}\right]$ (where α and β are not both 0. Note that for $\beta = 0$ and $\alpha \in \{1, 2, 3\}$, $\hat{Q}_{\text{tot}}[\sigma^{\alpha}]$ is just the total conserved spin $\hat{S}^{\alpha}_{\text{tot}}$). The operators charged under $\hat{Q}_r$ are the 6 monopoles $\hat{\Phi}_i$ which transform as an $SO(6)$ vector. In Sec. 2.2.1, we saw that the monopoles serve as order parameters for 120° AFMs and $\sqrt{12} \times \sqrt{12}$ valence bond solids. Now consider the scenario shown in Fig. 2.1. Deep inside the DSL, we assume that G_{space} of the triangular lattice is obeyed. Therefore, $\left\langle \hat{\mathbf{\Phi}} \right\rangle = 0$ here. At the same time, deep inside O_L and O_R, monopoles are condensed and acquire macroscopic expectation value $\left\langle \hat{\mathbf{\Phi}}_L \right\rangle$ and $\left\langle \hat{\mathbf{\Phi}}_R \right\rangle$ respectively. These ordered phases act as a source of monopoles which can tunnel through the DSL. We show below how one can get DC and AC Josephson effects for the setup where both O_L and O_R are in the 120° AFM phase.

2.3.3.1 $O_L = 120°$ AFM, $O_R = 120°$ AFM with angle mismatch: DC Josephson effect

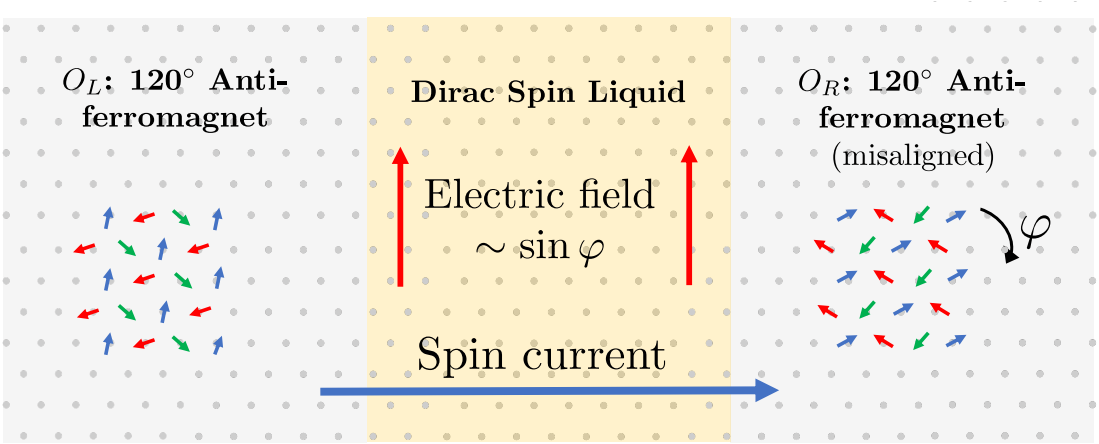

Figure 2.3: DC Josephson effect: a (120° AFM — DSL — 120° AFM) arrangement induces a DC electric field inside the DSL. The spins of the 120° AFM on the left obey Eq. (2.12), while those on the right are rotated with respect to Eq. (2.12) by angle φ. This results in a spin current, whose carriers inside the DSL are monopoles. The resulting monopole current is equivalent to an emergent electric field.

Assume both ordered phases are in a 120° AFM state, in which the spin triplet monopoles have acquired nonzero expectation value. Suppose the plane of ordering in spin-space is the same for O_L and O_R, which we take to be the xy plane. Now consider the situation where the ordering pattern on O_R is misaligned with respect to O_L by an angle φ (see Fig. 2.3). By this, we mean that if the spins in O_L form the ordering pattern given in Eq. (2.12), all the spins in O_R are rotated by angle φ about the $z-$axis with respect to the configuration dictated by Eq. (2.12). (Here, we have assumed that the lattice does not contain any defects.) For this situation, the expectation values of the spin triplet monopoles on either side take the form

$$\left\langle \hat{\vec{\mathbf{\Phi}}}_L \right\rangle = |\Phi_L| \begin{pmatrix} 1 & i & 0 \end{pmatrix}^T , \left\langle \hat{\vec{\mathbf{\Phi}}}_R \right\rangle = e^{i\varphi} |\Phi_R| \begin{pmatrix} 1 & i & 0 \end{pmatrix}^T . \tag{2.29}$$

Now, we can apply the formula for Josephson current Eq. (2.24). Due to the redundancy between $\hat{S}^z$ spin rotation and $U(1)_{\text{top}}$ phase rotation that we observed in Eq. (2.9) and Eq. (2.10), we get both a $U(1)_{\text{top}}$ current and a spin current that are equal to each other:

$$\left\langle \hat{I}[U(1)_{\text{top}}] \right\rangle = \left\langle \hat{I}\left[\sigma^3\right] \right\rangle = 2\Gamma_S^{\text{eff}} |\Phi_L||\Phi_R| \sin(\varphi). \tag{2.30}$$

Physically, the reason the two currents are the same is that the carriers of conserved spin and the carriers for conserved $U(1)_{\text{top}}$ charge are the same — the spin triplet monopoles. The total current $\left\langle \hat{I}^r \right\rangle$ is related to the current density $\left| \left\langle \hat{\vec{J}}^r \right\rangle \right|$ as $\left| \left\langle \hat{\vec{J}}^r \right\rangle \right| = \left\langle \hat{I}^r \right\rangle / L$ where L is the length of the boundary. These currents are perpendicular to both the O_L-DSL and O_R-DSL boundaries.

Therefore the emergent electric field is parallel to the boundaries. Since $\Gamma_S^{\text{eff}} \sim \mathcal{E}L$, we have

$$\langle \hat{e} \rangle \text{ and } \left\langle \hat{J}\left[\sigma^3\right] \right\rangle \sim \mathcal{E}\sin(\varphi), \tag{2.31}$$

where $\mathcal{E}$ has been estimated in Eq. (2.14). As we remarked previously, Eq. (2.31) should not be taken quantitatively, hence the $\sim$ symbol. The important takeaway is the $\sin\varphi$ dependence on the angle mismatch and the observation that the Josephson currents are those of the $U(1)_{\text{top}}$ and $\hat{S}^z$ generators, and are in fact equal to each other.

2.3.3.2 $O_L = 120^\circ$ AFM, $O_R = 120^\circ$ AFM: AC Josephson effect

We again consider a junction with two 120° AFMs separated by a DSL. For this configuration, the expectation values of spin triplet monopole operators on either side of the junction are

$$\left\langle \hat{\vec{\Phi}}_L \right\rangle = |\Phi_L| \begin{pmatrix} 1 & i & 0 \end{pmatrix}^T \text{ and } \left\langle \hat{\vec{\Phi}}_R \right\rangle = |\Phi_R| \begin{pmatrix} 1 & i & 0 \end{pmatrix}^T. \tag{2.32}$$

We now propose two scenarios that lead to an AC Josephson effect. The first scenario is analogous to the AC Josephson effect in superconductors obtained by applying a potential difference, a term that couples to the difference in number of particles on the right and left. Analogously, here we can apply the following term to the Hamiltonian that couples to the difference in emergent magnetic flux across the two sides (the conserved $U(1)_{\text{top}}$ charge). On a triangular lattice, we

show in Appendix B.2.1 that such a term takes the form of the sum of staggered spin chiralities

$$\begin{aligned}\hat{H}_\mu &= \sum_{\vec{n}} \mu(x) \left((\hat{\vec{\mathbf{S}}}_{\vec{n}} \times \hat{\vec{\mathbf{S}}}_{\vec{n}+\vec{a}_1}) \cdot \hat{\vec{\mathbf{S}}}_{\vec{n}+\vec{a}_1-\vec{a_2}} - (\hat{\vec{\mathbf{S}}}_{\vec{n}} \times \hat{\vec{\mathbf{S}}}_{\vec{n}+\vec{a}_1}) \cdot \hat{\vec{\mathbf{S}}}_{\vec{n}+\vec{a}_2} \right) \\ &\equiv \sum_{\vec{n}} \mu(x) (\hat{\chi}_{\triangledown,\vec{n}} - \hat{\chi}_{\triangle,\vec{n}}),\end{aligned} \tag{2.33}$$

where $\mu(x)$ has a gradient from L to R such that $\mu_R - \mu_L \equiv \mu$. Now, we will use the formula in Eq. (2.28) to determine the Josephson currents. In this formula, a perturbation in generator $\hat{Q}^s$ is applied and the current in generator $\hat{Q}^r$ is calculated. For the perturbation considered in Eq. (2.33), s corresponds to $U(1)_{\text{top}}$. Using Eq. (2.32) in Eq. (2.28), and noting that $T^s = T\left[\hat{b}_{\text{tot}}\right] = 1$ we see that the channels r in which we get nonzero currents are $U(1)_{\text{top}}$ and $\hat{S}^z_{\text{tot}}$ (i.e. emergent electric field and spin current). Like before, the two are equal.

$$\left\langle \hat{I}[U(1)_{\text{top}}](t) \right\rangle = \left\langle \hat{I}\left[\sigma^3\right](t) \right\rangle = 2\Gamma_S^{\text{eff}} |\Phi_L||\Phi_R| \sin(\mu t). \tag{2.34}$$

Here, we have made use of the observation in Eq. (2.9) and Eq. (2.10) that $\left\langle \hat{\vec{\mathbf{\Phi}}}_L \right\rangle$ and $\left\langle \hat{\vec{\mathbf{\Phi}}}_R \right\rangle$ are both eigenvectors of $T[\sigma^3]$ with eigenvalue 1. The above equation says that a difference in spin chirality terms applied across the two ordered phases leads to a time-dependent spin current and an equal emergent electric field. This is a nontrivial prediction of the theory.

However, applying an external term Eq. (2.33) is not simple experimentally (although there has been a proposal to get a spin chirality term in the effective Floquet Hamiltonian of a spin system driven with a laser [66]). Therefore, we now propose a simpler way to get the same time dependent electric field and spin current as before, but this time exploiting our observation in Eq. (2.9) and Eq. (2.10).

In this second scenario, we apply a Zeeman field gradient across the junction instead of $\hat{H}_\mu$ above, as shown in Fig. 2.4,

$$\hat{H}_h = \sum_{\vec{n}} h(x)\left(\hat{S}^z_{\vec{n}}\right), \tag{2.35}$$

where $h(x)$ has a gradient from L to R such that $h_R - h_L \equiv h$. The only difference now as far as the formula Eq. (2.28) is concerned, is that $T^s = T[\sigma^3]$ instead of 1. But since $T[\sigma^3]\left\langle \hat{\vec{\mathbf{\Phi}}}_{L(R)} \right\rangle = \left\langle \hat{\vec{\mathbf{\Phi}}}_{L(R)} \right\rangle$, this difference does not change the currents. We therefore again obtain an AC spin current *and* an equal AC emergent electric field inside the DSL given by

$$\left\langle \hat{I}[U(1)_{\text{top}}](t) \right\rangle = \left\langle \hat{I}\left[\sigma^3\right](t) \right\rangle = 2\Gamma_S^{\text{eff}} |\Phi_L||\Phi_R| \sin(ht). \tag{2.36}$$

We can understand this physically as follows. The presence of the Zeeman field gradient leads to a precession of the macroscopic 120° order parameter with a different rate on the two sides of the junction, resulting in a spin current. Similar phenomena have been studied theoretically in several works previously, for conventional magnetically ordered systems [67, 68, 69, 70, 71, 72], and ^{3}He and spinor BECs [73, 74, 75].

What is different for our setup is that the proximity to the DSL, and the assumption that the 120° AFMs are close to a phase transition to a DSL imply that the carriers of the spin current in the DSLs are monopole operators. Therefore any time-dependent spin current should be accompanied by a time-dependent monopole current, or an emergent electric field in the DSL.

Describing and probing this electric field is what we will now focus on. What does an emergent electric field mean in the language of microscopic spins? Using the transformation of electric field under microscopic symmetries (see first row of Table B.3 in Appendix B.2), we can

write the following expression for the zero momentum electric field (i.e., integrated over space), keeping only nearest neighbor terms:

$$
\begin{aligned}
(\hat{e}_x)_{\text{tot}} &\equiv \int d^2x \hat{e}_x = v \sum_{\vec{n}} \left(\hat{\vec{\mathbf{S}}}_{\vec{n}} \cdot \hat{\vec{\mathbf{S}}}_{\vec{n}+\vec{\mathrm{a}}_2} - \hat{\vec{\mathbf{S}}}_{\vec{n}} \cdot \hat{\vec{\mathbf{S}}}_{\vec{n}+\vec{\mathrm{a}}_2-\vec{\mathrm{a}}_1} \right) + \ldots, \\
(\hat{e}_y)_{\text{tot}} &\equiv \int d^2x \hat{e}_y = v \sum_{\vec{n}} \frac{1}{\sqrt{3}} \left(2\hat{\vec{\mathbf{S}}}_{\vec{n}} \cdot \hat{\vec{\mathbf{S}}}_{\vec{n}+\vec{\mathrm{a}}_1} - \hat{\vec{\mathbf{S}}}_{\vec{n}} \cdot \hat{\vec{\mathbf{S}}}_{\vec{n}+\vec{\mathrm{a}}_2} - \hat{\vec{\mathbf{S}}}_{\vec{n}} \cdot \hat{\vec{\mathbf{S}}}_{\vec{n}+\vec{\mathrm{a}}_2-\vec{\mathrm{a}}_1} \right) + \ldots,
\end{aligned}
\tag{2.37}
$$

where v is a constant of the order of the Dirac velocity, which in turn is of the order of $J\mathrm{a}$ where J is the exchange coupling strength and a is the lattice spacing. As a consequence of the AC Josephson effect discussed above, we expect

$$
\left(\langle \hat{e}_x(t) \rangle , \langle \hat{e}_y(t) \rangle \right) = \mathcal{E} \sin(ht) \, (\cos\theta, \sin\theta), \tag{2.38}
$$

where θ is the angle made by the electric field with x-axis (the direction of the electric field is tangential to the DSL-AFM boundaries). $\mathcal{E}$ is given by the right-hand side of Eq. (2.14), calculating which is beyond the scope of this work. The key point is that since the DSL is described by a CFT, $\mathcal{E}$ decays only as a power law in the width of the DSL.

We see that the operators $\hat{e}_x$ and $\hat{e}_y$ have a non-trivial spatial structure. In order to detect this "electric field" consistently, we would need a probe that is sensitive to rotational form-factors. Optical probes are well-suited for this purpose because of the control one gets from the direction of polarization of light [76, 77]. We now propose a way to measure the emergent AC electric field inside the DSL using Raman scattering.

2.4 Raman scattering probe of emergent electric field

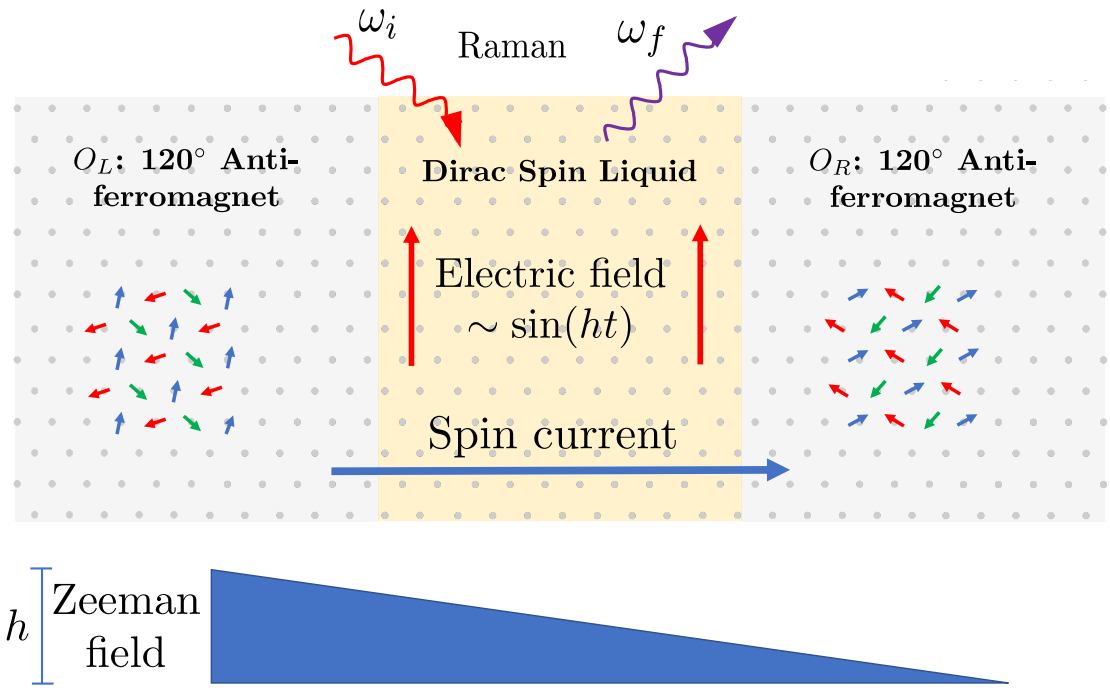

Figure 2.4: The proposed setup (120° AFM — DSL — 120° AFM) to induce and probe the AC Josephson effect. An out of plane (w.r.t. magnetic ordering) Zeeman field gradient of magnitude h is applied across the junction, causing the spins on the left to precess at a different rate than the spins on the right. This precession results in a spin current, whose carriers inside the DSL are monopoles. The resulting emergent electric field within the DSL can be probed via Raman scattering.

Suppose the DSL region is irradiated with a laser of frequency ω_i. A Raman signal corresponds to inelastic scattering of light, i.e. the outgoing photon's frequency ω_f is different from ω_i. We will now argue that the presence of an emergent electric field in the DSL of frequency h, and in particular the one produced in the setup considered in Sec. 2.3.3.2 (see Fig. 2.4), will lead to peaks at Raman frequency shifts $\omega_\Delta \equiv \omega_f - \omega_i = \pm h$.

It was shown in [7, 8] that the Raman scattering rate R for a spin system (not necessarily a spin liquid) is given by the following correlation function calculated in an energy eigenstate of

the spin system $|i\rangle$

$$R = \int_{-\infty}^{\infty} dt e^{i\omega_\Delta t} \langle i|\hat{M}^\dagger_{\vec{q}}(0)\hat{M}_{\vec{q}}(t)|i\rangle \,, \tag{2.39}$$

where $\vec{q} = \vec{q}_f - \vec{q}_i$ is the momentum transferred to the photon. (For simplicity, we will ignore this small momentum transfer from now on.) The operator $\hat{M}$ acts on the Hilbert space of the spin system, and depends on the underlying lattice for the spin system as well as the polarizations and momenta of the incident and scattered light. The operator $\hat{M}$ was calculated for some relevant cases in [7, 54], and we will present the leading-order results later in Eq. (2.41).

However, if the expectation value of some operator (in our case, the emergent electric field) $\langle\psi|\hat{\vec{e}}(t)|\psi\rangle$ in a state $|\psi\rangle$ were to depend sinusoidally on time, then $|\psi\rangle$ is clearly not an energy eigenstate but rather a nonequilibrium state. In such a state, we show in Appendix B.4 that Eq. (2.39) gets modified and the Raman scattering rate now measures the following time-averaged correlation function of the same operator $\hat{M}$:

$$R = \lim_{T\to\infty} \frac{1}{T} \int_{-\frac{T}{2}}^{\frac{T}{2}} dt_0 \int_{-\frac{T}{2}}^{\frac{T}{2}} dt \, \langle\psi|\hat{M}^\dagger(t_0)\hat{M}(t+t_0)|\psi\rangle \, e^{i\omega_\Delta t}. \tag{2.40}$$

We will use the following (Fleury-Loudon [78]) form for $\hat{M}$,

$$\hat{M} = \sum_{\vec{n},\vec{n}'} \frac{2\mathrm{t}^2_{\vec{n},\vec{n}'}\tilde{e}^2}{U-\omega_i} \{\vec{\epsilon}^*_f \cdot (\vec{n}'-\vec{n})\}\{\vec{\epsilon}_i \cdot (\vec{n}'-\vec{n})\}\left(\frac{1}{4} - \hat{\vec{\mathbf{S}}}_{\vec{n}} \cdot \hat{\vec{\mathbf{S}}}_{\vec{n}'}\right), \tag{2.41}$$

which requires a bit of explanation. Here $\vec{\epsilon}_i$ and $\vec{\epsilon}_f$ are the polarizations of the incoming and outgoing photons, respectively. Eq. 2.41 assumes that the spins arise from a single band Hubbard

model at half filling in the large U limit, of the following form

$$\hat{H}_{\text{el}} = -\left(\sum_{\vec{r},\vec{r}',\sigma} \mathrm{t}_{\vec{r},\vec{r}'} \hat{c}^{\dagger}_{\vec{r}\sigma} \hat{c}_{\vec{r}'\sigma} e^{ie\hat{\vec{A}}\left(\frac{\vec{r}+\vec{r}'}{2}\right)\cdot(\vec{r}-\vec{r}')} + \text{h.c.}\right) + U\sum_{\vec{r}} \hat{\mathrm{n}}_{\vec{r},\uparrow}\hat{\mathrm{n}}_{\vec{r},\downarrow}. \tag{2.42}$$

Here $\hat{\vec{A}}(\vec{r})$ is the electromagnetic field and has the following expansion in photon creation and annihilation operators

$$\hat{\vec{A}}(\vec{r}) = \sum_{\vec{k}} \frac{1}{\sqrt{2\varepsilon V \omega_{\vec{k}}}} \left(\vec{\epsilon}_{\vec{k}} \hat{a}_{\vec{k}} + \vec{\epsilon}^{*}_{-\vec{k}} \hat{a}^{\dagger}_{-\vec{k}}\right) e^{i\vec{k}.\vec{r}}, \tag{2.43}$$

where $\vec{\epsilon}_{\vec{k}}$ is the polarization of mode $\vec{k}$, and ε and V are the dielectric constant and laser mode volume respectively. We have defined the coupling constant $\tilde{e}^2 \equiv \frac{e^2 \mathrm{a}^2 \sqrt{\mathcal{N}_i}}{2\varepsilon V \sqrt{\omega_i \omega_f}}$ where e is the electron charge and $\mathcal{N}_i$ is the initial number of photons in the mode of frequency ω_i. The driving is assumed to be near resonance, but at the same time satisfying $\mathrm{t}_{\mathbf{rr}'} \ll |U - \omega_i| \ll U$. Under this assumption, one can calculate the scattering rate perturbatively in both $\mathrm{t}/(\omega_i - U)$ and $\tilde{e}$, the light-matter coupling constant; one obtains Eq. 2.41 at order $\tilde{e}^2 \mathrm{t}^2/(\omega_i - U)$.

It is convenient to decompose the tensor $(\epsilon^j_f)^* \epsilon^k_i$ into two 1-dimensional (A_{1g}, A_{2g}) and one 2-dimensional (E_g) irreducible representations of the triangular lattice point group

$$\begin{aligned} A_1 &\equiv (\epsilon^x_f)^* \epsilon^x_i + (\epsilon^y_f)^* \epsilon^y_i, \\ A_2 &\equiv (\epsilon^x_f)^* \epsilon^y_i - (\epsilon^y_f)^* \epsilon^x_i, \\ \begin{pmatrix} E_1 \\ E_2 \end{pmatrix} &\equiv \begin{pmatrix} -(\epsilon^x_f)^* \epsilon^x_i + (\epsilon^y_f)^* \epsilon^y_i \\ (\epsilon^x_f)^* \epsilon^y_i + (\epsilon^y_f)^* \epsilon^x_i \end{pmatrix}. \end{aligned} \tag{2.44}$$

On the triangular lattice, using this basis reduces Eq. (2.41) to

$$\begin{aligned}
\hat{M} =& \frac{4\mathrm{t}^2\tilde{e}^2}{U-\omega_i}\left(A_1\hat{\mathcal{O}}_{A_1} + E_2\hat{\mathcal{O}}_{E_2} - E_1\hat{\mathcal{O}}_{E_1}\right), \quad \text{where} \\
\hat{\mathcal{O}}_{A_1} =& \sum_{\vec{n}}\left(\hat{\vec{\mathbf{S}}}_{\vec{n}}\cdot\hat{\vec{\mathbf{S}}}_{\vec{n}+\vec{\mathrm{a}}_1} + \hat{\vec{\mathbf{S}}}_{\vec{n}}\cdot\hat{\vec{\mathbf{S}}}_{\vec{n}+\vec{\mathrm{a}}_2} + \hat{\vec{\mathbf{S}}}_{\vec{n}}\cdot\hat{\vec{\mathbf{S}}}_{\vec{n}+\vec{\mathrm{a}}_2-\vec{\mathrm{a}}_1}\right), \\
\hat{\mathcal{O}}_{E_2} =& \frac{\sqrt{3}}{4}\sum_{\vec{n}}\left(\hat{\vec{\mathbf{S}}}_{\vec{n}}\cdot\hat{\vec{\mathbf{S}}}_{\vec{n}+\vec{\mathrm{a}}_2} - \hat{\vec{\mathbf{S}}}_{\vec{n}}\cdot\hat{\vec{\mathbf{S}}}_{\vec{n}+\vec{\mathrm{a}}_2-\vec{\mathrm{a}}_1}\right), \\
\hat{\mathcal{O}}_{E_1} =& \frac{1}{4}\sum_{\vec{n}}\left(2\hat{\vec{\mathbf{S}}}_{\vec{n}}\cdot\hat{\vec{\mathbf{S}}}_{\vec{n}+\vec{\mathrm{a}}_1} - \hat{\vec{\mathbf{S}}}_{\vec{n}}\cdot\hat{\vec{\mathbf{S}}}_{\vec{n}+\vec{\mathrm{a}}_2} - \hat{\vec{\mathbf{S}}}_{\vec{n}}\cdot\hat{\vec{\mathbf{S}}}_{\vec{n}+\vec{\mathrm{a}}_2-\vec{\mathrm{a}}_1}\right).
\end{aligned} \tag{2.45}$$

Up to order $\frac{\mathrm{t}^2\tilde{e}^2}{U-\omega_i}$, there is no term in the A_{2g} channel. For the particular case of a Dirac spin liquid, we can use Eq. (2.37) to relate the emergent electric fields to microscopic quantities. Up to corrections involving longer range terms, we see that $\hat{\mathcal{O}}_{E_2}$ and $\hat{\mathcal{O}}_{E_1}$ are indeed proportional to the emergent electric fields $(\hat{e}_x)_{\mathrm{tot}}$ and $(\hat{e}_y)_{\mathrm{tot}}$ respectively (because the symmetry transformation of the emergent electric fields on the triangular lattice is identical to that of the E_{2g} channel.) On the other hand, $\hat{\mathcal{O}}_{A_1}$ is proportional to the Hamiltonian of the system. This lets us write the above expression as

$$\hat{M} = \frac{4\mathrm{t}^2\tilde{e}^2}{U-\omega_i}\left(\frac{1}{J}A_1\hat{H} + \frac{\sqrt{3}\mathcal{A}}{4v}(E_2\hat{e}_x - E_1\hat{e}_y) + \dots\right), \tag{2.46}$$

where $\mathcal{A}$ is the area of the DSL region. We can now relate the Raman scattering rate in a DSL to correlation functions of the electric field and the Hamiltonian by inserting the above expression into Eq. (2.40).

Before we proceed, we highlight two main differences from previous theoretical literature, arising due to the presence of the AC Josephson effect in the setup in Sec. 2.3.3.2, on Raman scattering. First, the Raman scattering rate is usually derived when the spin system is in an equilibrium state, where one-point functions $\left\langle\hat{\mathcal{O}}(t)\right\rangle$ for interesting operators $\hat{\mathcal{O}}$ typically equal

zero, in which case a correlation function $\left\langle \hat{\mathcal{O}}_1(t_1)\hat{\mathcal{O}}_2(t_2)\right\rangle$ would be given entirely by its connected component. However, in our case, the DSL is in a nonequilibrium steady state where $\left\langle \hat{\vec{e}}(t)\right\rangle \propto \sin(ht)$ (see Eq. 2.38). Hence the correlation function also has a disconnected component. In what follows, we will assume that the contribution to the autocorrelation function coming from the monopole Josephson effect is dominated by the disconnected piece

$$\langle \hat{e}_i(t_1)\hat{e}_j(t_2)\rangle \approx \langle \hat{e}_i(t_1)\rangle \langle \hat{e}_j(t_2)\rangle \,. \tag{2.47}$$

Since

$$\begin{aligned} \lim_{T\to\infty}\frac{1}{T}\int_{-T/2}^{T/2} dt_0 \sin(ht_0)\sin(h(t+t_0)) &= \frac{1}{2}\cos(ht) \text{ and} \\ \lim_{T\to\infty}\frac{1}{T}\int_{-T/2}^{T/2} dt_0 \sin(h(t+t_0)) &= 0, \end{aligned} \tag{2.48}$$

we find that the autocorrelation functions are sharply peaked in frequency as follows

$$\begin{aligned} \lim_{T\to\infty}\frac{1}{T}\int_{-\frac{T}{2}}^{\frac{T}{2}} dt_0 \langle \hat{e}_x(t_0)\hat{e}_x(t_0+t)\rangle &\approx \frac{\mathcal{E}^2\cos^2\theta}{2}\cos(ht), \\ \lim_{T\to\infty}\frac{1}{T}\int_{-\frac{T}{2}}^{\frac{T}{2}} dt_0 \langle \hat{e}_x(t_0)\hat{e}_y(t_0+t)\rangle &\approx \frac{\mathcal{E}^2\sin^2\theta}{2}\cos(ht), \\ \lim_{T\to\infty}\frac{1}{T}\int_{-\frac{T}{2}}^{\frac{T}{2}} dt_0 \langle \hat{e}_x(t_0)\hat{e}_y(t_0+t)\rangle &\approx \frac{\mathcal{E}^2\sin(2\theta)}{4}\cos(ht), \\ \lim_{T\to\infty}\frac{1}{T}\int_{-\frac{T}{2}}^{\frac{T}{2}} dt_0 \left\langle \hat{e}_x(t_0)\hat{H}(t_0+t)\right\rangle &\approx 0. \end{aligned} \tag{2.49}$$

This brings us to the second difference — an equilibrium correlation function in a symmetry preserving state is diagonal in the A_1, A_2, E_2, E_1 basis. But due the monopole Josephson effect, the steady state no longer has rotational symmetry, leading to mixing within the E_g channel, (see

Eq. (2.49)). Now, we are ready to write down the final result for the Raman scattering rate

$$R = \mathcal{K}|E_1 \sin\theta - E_2 \cos\theta|^2 \{\delta(\omega_\Delta - h) + \delta(\omega_\Delta + h)\}, \tag{2.50}$$

where $\mathcal{K} \equiv \frac{3\pi}{2}\mathcal{E}^2\left(\frac{\mathcal{A}}{v}\frac{t^2\tilde{e}^2}{U-\omega_i}\right)^2$ is a constant. By tuning the polarizations of the incoming and detected photons, one can tune the values of A_1, A_2, E_1, E_2. By measuring the scattering rate R for each such choice, one can separately measure the correlation function in each channel, and thus verify the prediction in Eq. (2.50).

We have shown that for a junction with two 120° AFMs separated by a DSL, if we apply a Zeeman field gradient h across the junction, the AC emergent electric field resulting from the monopole Josephson effect produces sharp peaks at Raman frequency shifts $\pm h$ in the E_g channels. The strength of the peak decays as a power law in the width of the junction. The above setup provides a way to induce and directly probe the emergent electric field in a Dirac spin liquid.

2.5 Other monopole Josephson effects

In this section, we present other effects which fall under the general umbrella of monopole Josephson effects.

2.5.1 Josephson energy — Long range phase rigidity

For the DC Josephson current, we assumed that the two 120° orders had an angle misalignment. This misalignment could have arisen due to an external pinning potential, with a strength smaller than the coupling Γ^S_{eff}, so that our assumption that the spin $SO(3)$ is conserved continues

to hold. Here, on the other hand, we suppose that there is no external pinning and we let the relative angle between $\hat{\vec{\mathbf{\Phi}}}_L$ and $\hat{\vec{\mathbf{\Phi}}}_R$ to fluctuate. In other words, if $\left\langle \vec{\mathbf{\Phi}}_L \right\rangle = |\Phi_L| \begin{pmatrix} 1 & i & 0 \end{pmatrix}$ and $\left\langle \vec{\mathbf{\Phi}}_R \right\rangle = e^{i\varphi} |\Phi_R| \begin{pmatrix} 1 & i & 0 \end{pmatrix}$, we let φ be a dynamical degree of freedom.

As a first approximation, one can calculate the energy of such a configuration from the Hamiltonian Eq. (2.15) from just the disconnected piece of the two-monopole correlation function

$$\begin{aligned} E[\varphi] &\approx -\mathcal{E}L\left(\left\langle \hat{\vec{\mathbf{\Phi}}}_L^\dagger \right\rangle \cdot \left\langle \hat{\vec{\mathbf{\Phi}}}_R \right\rangle + \text{ h.c.} \right) \\ &\sim -2\mathcal{E}L|\Phi_L||\Phi_R| \cos(\varphi). \end{aligned} \tag{2.51}$$

This Josephson energy implies that there is a restoring force that tries to align the angles of two 120° AFM puddles separated by a DSL. This restoring force is proportional to $\mathcal{E}$, which we expect to decay only as a power law in the width of the DSL (see Eq. (2.14)) since the DSL is a critical phase. Therefore puddles of ordered phases separated by regions of DSL will display a tendency for their order parameters to align, a behavior we call long-range phase rigidity.

2.5.2 Mixed current: $O_L = 120^\circ$ AFM, $O_R =$ VBS

Consider a junction with a DSL region separating two completely different orders: $O_L = 120^\circ$ AFM and O_R= $\sqrt{12} \times \sqrt{12}$ VBS. Using the parent state picture, we view O_L as the condensate of spin triplet monopoles and O_R as the condensate of spin singlet monopoles, as follows:

$$\begin{aligned} \left\langle \begin{pmatrix} \Phi_1 & \Phi_2 & \Phi_3 & \Phi_4 & \Phi_5 & \Phi_6 \end{pmatrix} \right\rangle_L^T &= |\Phi_L| \begin{pmatrix} 0 & 0 & 0 & 1 & i & 0 \end{pmatrix}^T, \\ \left\langle \begin{pmatrix} \Phi_1 & \Phi_2 & \Phi_3 & \Phi_4 & \Phi_5 & \Phi_6 \end{pmatrix} \right\rangle_R^T &= |\Phi_R| \begin{pmatrix} 1 & i & 0 & 0 & 0 & 0 \end{pmatrix}^T. \end{aligned} \tag{2.52}$$

We now argue that in this configuration, the DSL will have currents of the mixed spin-valley generators of $SO(6)$. As a toy model, we start with the coupling Hamiltonian in Eq. (2.21). This assumes an $SO(6)$ symmetric term for monopole tunneling. In this case, one can directly use Eq. (2.24) to calculate the Josephson currents. We then see that the currents with nonzero expectation value are those for the the mixed $SO(6)$ generators: $\hat{\vec{J}}[\sigma^i\tau^j]$. For the example we picked in Eq. (2.52), $\hat{\vec{J}}^{14} \equiv \hat{\vec{J}}[\sigma^1\tau^1]$ and $\hat{\vec{J}}^{25} \equiv \hat{\vec{J}}[\sigma^2\tau^2]$ are nonzero and equal, and the remaining independent currents are 0.

The presence of these mixed currents can be identified by their symmetry breaking patterns in the bulk of the DSL region. In Appendix B.2, we summarize the symmetry properties of all such currents (Table B.3) on the triangular lattice. We observe that when a general combination of the mixed currents (last three rows of Table B.3) has a nonzero expectation value, time-reversal symmetry is broken and discrete translation symmetry is reduced to translations by 2 lattice spacings along both $\vec{a}_1$ and $\vec{a}_2$, i.e., a 4-site unit cell forms in the DSL region.

We point out, however, that the microscopic model does not have an $SO(6)$ symmetry. Therefore, our assumption above of an $SO(6)$-symmetric coupling at the interface is not strictly justified. Nevertheless, we can qualitatively argue that the physical consequence of having mixed currents in the DSL — unit-cell expansion and time-reversal symmetry breaking (within the DSL bulk) continues to hold. Consider the effective Hamiltonian Eq. (2.18) with a coupling that breaks $SO(6)$ to $SO(3)_{\text{spin}}$. Then we have

$$\begin{aligned}
\left\langle -\dot{\hat{Q}}_L[\sigma^i] \right\rangle &= \left\langle \dot{\hat{Q}}_R[\sigma^i] \right\rangle = 0 \text{ and} \\
\left\langle -\dot{\hat{Q}}_L[\tau^i] \right\rangle &= \left\langle \dot{\hat{Q}}_R[\tau^i] \right\rangle = 0, \text{ while} \\
\left\langle -\dot{\hat{Q}}_L[\sigma^i\tau^j] \right\rangle &\neq \left\langle \dot{\hat{Q}}_R[\sigma^i\tau^j] \right\rangle \text{ but both are nonzero.}
\end{aligned} \tag{2.53}$$

The above equation says that, not surprisingly, the charge of mixed generators lost from side L is not equal to that gained by side R. This leakage however, is localized to the boundaries, because deep inside the DSL, the mixed currents are still conserved. Generically then, the expectation value of some combination of mixed currents in the DSL should still be nonzero. This is true in the limit of $SO(6)$-symmetric coupling, and as we go away from this point, there is no reason for the mixed currents to immediately drop to zero.

2.5.3 Response to $U(1)_{\text{top}}$ flux insertion — lattice dislocation

For the familiar DC Josephson effect, a phase difference between the right (R) and left (L) superconductors is maintained by threading a magnetic flux, like the SQUID geometry shown in Fig. 2.5(a), because the gauge invariant phase difference between points $R1$ and $L1$ is $\theta_{R1} - \theta_{L1} + e\int_{L1}^{R1} \vec{A} \cdot d\vec{r}$. This results in a current between the two superconductors in the tangential direction.

In Fig. 2.5(b), we consider a related configuration involving the DSL. Here ϕ is the flux inserted in $U(1)_{\text{top}}$. For simplicity, we have assumed that the full system is in the DSL phase. An analogous situation for metals is persistent currents in the ground state [79] in the presence of magnetic flux, as required by the Byers-Yang theorem [80]:

$$I[\phi] = -\frac{1}{T}\frac{\partial F[\phi]}{\partial \phi}, \tag{2.54}$$

where I is the equilibrium current, T is the temperature, and F is the free energy. Similar to an electron current in a SQUID, this results in a tangential $U(1)_{\text{top}}$ current, i.e. a radial electric field. But how do we insert a flux in $U(1)_{\text{top}}$? Lattice translations are known to have a nontrivial

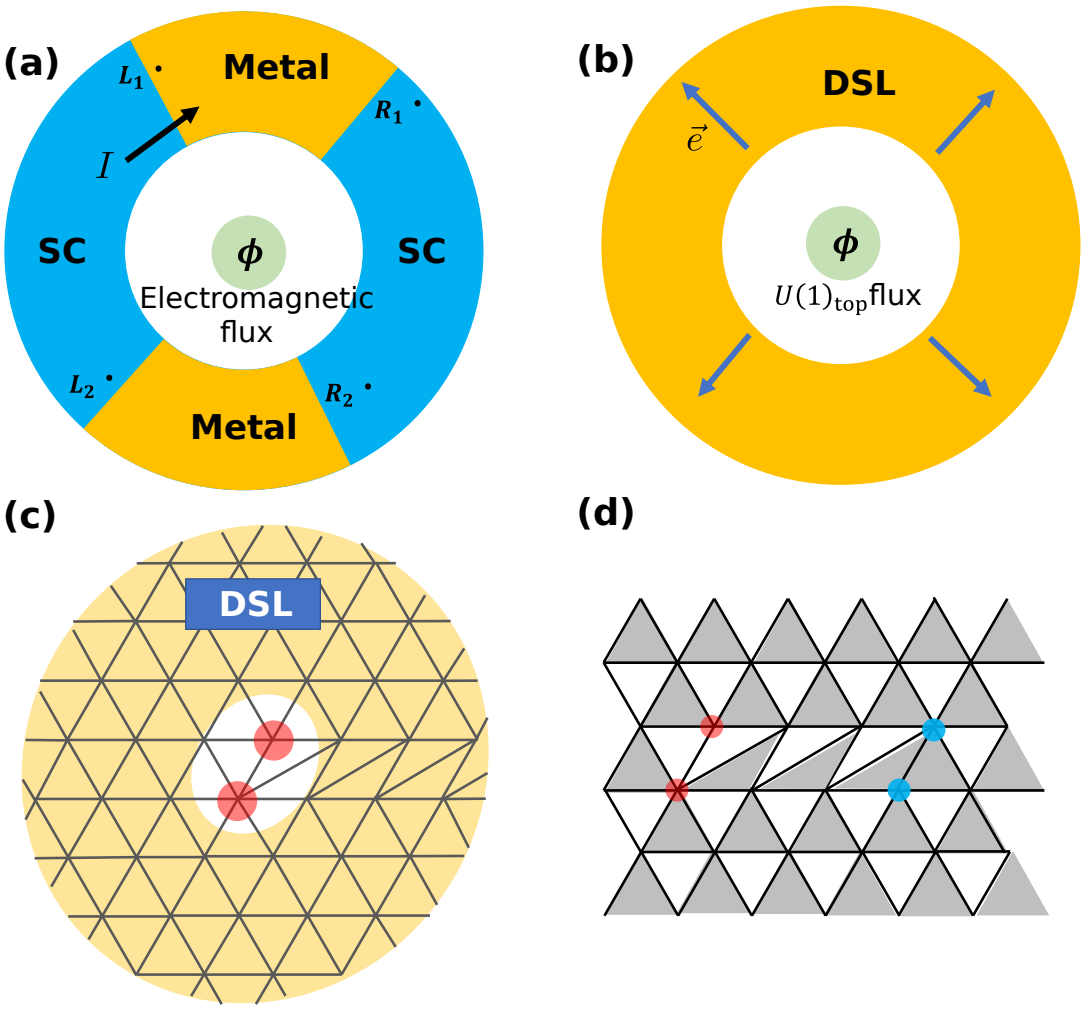

Figure 2.5: (a): In a SQUID geometry (SC-metal-SC-metal), threading a flux ϕ through the center results in a tangential electric current I (black arrow). (b): Similarly, a DSL with a flux ϕ in $U(1)_{\text{top}}$ going through results in an emergent electric field $\langle \hat{\vec{e}} \rangle$ radially outwards (blue arrows). (c): A DSL in the presence of a lattice dislocation. The red circles mark the two lattice sites making up the dislocation. (d): Mean field considered for numerics in the presence of two dislocations with opposite Burger's vectors (red and blue). Grey triangle indicates π flux.

$U(1)_{\text{top}}$ action when embedded into the low-energy symmetry group G_{IR} [24, 57]. Therefore, a symmetry defect of lattice translation, that is, a lattice dislocation (see Fig. 2.5(c)), serves as a $U(1)_{\text{top}}$ flux[4].

Following the above argument, we expect that a lattice dislocation creates a radial electric

[4]In addition to being a $U(1)_{\text{top}}$ symmetry flux, it is also an $SO(6)$ symmetry flux, but this fact does not play a role in the rest of our discussion.

field, which by Gauss's Law results in a *spinon* charge ($U(1)$ gauge charge and *not* a $U(1)_{\text{top}}$ charge) near the dislocation. As a first step, in the parton picture, we can verify this prediction at the mean field level. We consider the mean-field ansatz shown in Fig. 2.5(d) on a lattice with two dislocations with opposite Burger's vectors ($\vec{a}_2$ and $-\vec{a}_2$ respectively) separated by d lattice spacings. The triangles shaded grey have π flux going through them. This ansatz preserves time-reversal but breaks charge-conjugation symmetry. We then numerically diagonalize the corresponding free fermion Hamiltonian on an $L \times L$ torus. The lowest $L^2/2$ levels are filled by both spin $\uparrow$ and $\downarrow$ fermions in the ground state. Then we compute the charge in a region D enclosing the dislocation

$$\langle \hat{q}_{\text{dislo}} \rangle = 2 \sum_{\vec{r} \in D} \left(\sum_{i=1}^{L^2/2} \left(\left| \psi_{\vec{r}}^{i} \right|^2 - \frac{1}{2} \right) \right), \tag{2.55}$$

where $\psi_{\vec{r}}^{i}$ is the single fermion wavefunction of the i^{th} eigenstate (sorted in increasing order of energy) evaluated at $\vec{r}$. For $L = 100$, $d = 50$ and D being a circle of radius 20, we get $q_{\text{dislo}} = 0.297$.

We are unable to determine whether a non-zero spinon charge survives once we include gauge fluctuations. Qualitatively, we expect that the charge gets renormalized due to screening, but may not drop to 0. If the localized spinon charge is indeed nonzero, what it would mean in terms of microscopic spins is an open question. In Eq. (B.8) of Appendix B.2, we have written a nontrivial microscopic operator that is consistent with both the symmetry properties of the field theory spinon charge operator and Gauss's law. How this expression gets modified for a lattice with dislocations, and whether any resulting spinon charge can be computed numerically in candidate DSL wavefunctions [81, 82] is an interesting direction to pursue.

2.6 Discrete Shift and Quantized Electric Polarization in fermionic systems

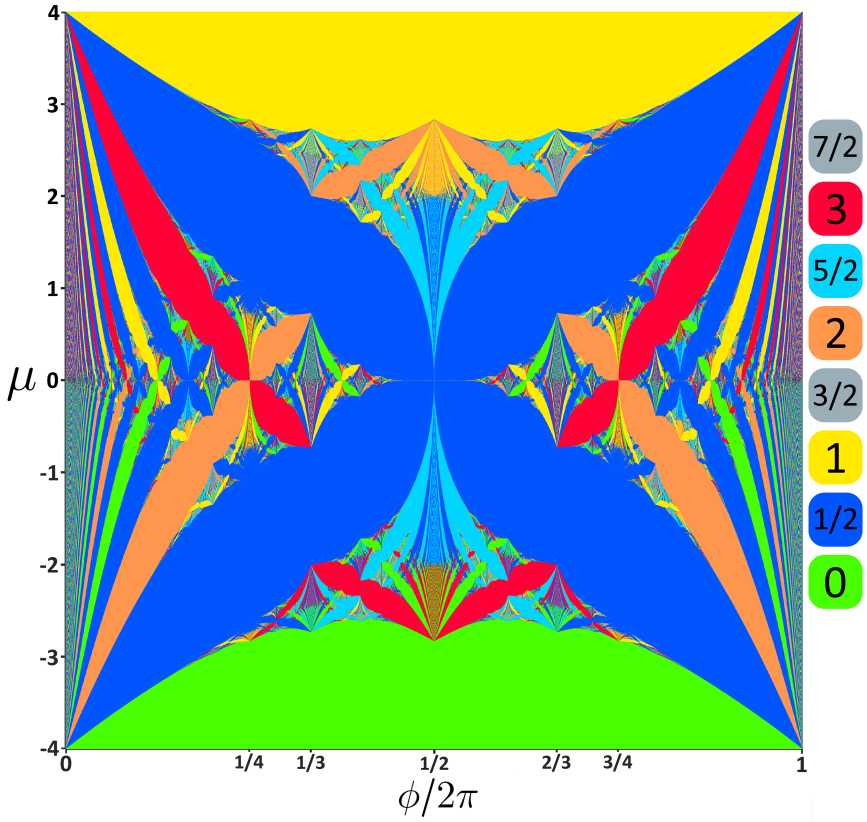

Figure 2.6: Discrete shift $\mathscr{S}$ for Hofstadter model on the square lattice. Each lobe represents a gapped region. The color of a lobe represents the discrete shift of the many-body state obtained by filling all the single particle states below the lobe. Figure from Ref. [2].

Based on the the previous section, we take a short digression. We can make our conclusion on fractional charge more concrete if we directly consider a fermionic system (instead of mean-field partons employed for describing a DSL). In this case, a monopole is an extra 2π magnetic flux inserted. A non-zero momentum of monopole in this context translates to flux insertion being accompanied by addition of nonzero linear momentum. We saw in the previous section that this implies the presence of fractional charge bound to a lattice dislocation. By the same argument, a nonzero angular momentum associated with a 2π flux implies a fractional charge bound to a lattice disclination. If the electronic state is gapped, it can be argued that these charges are

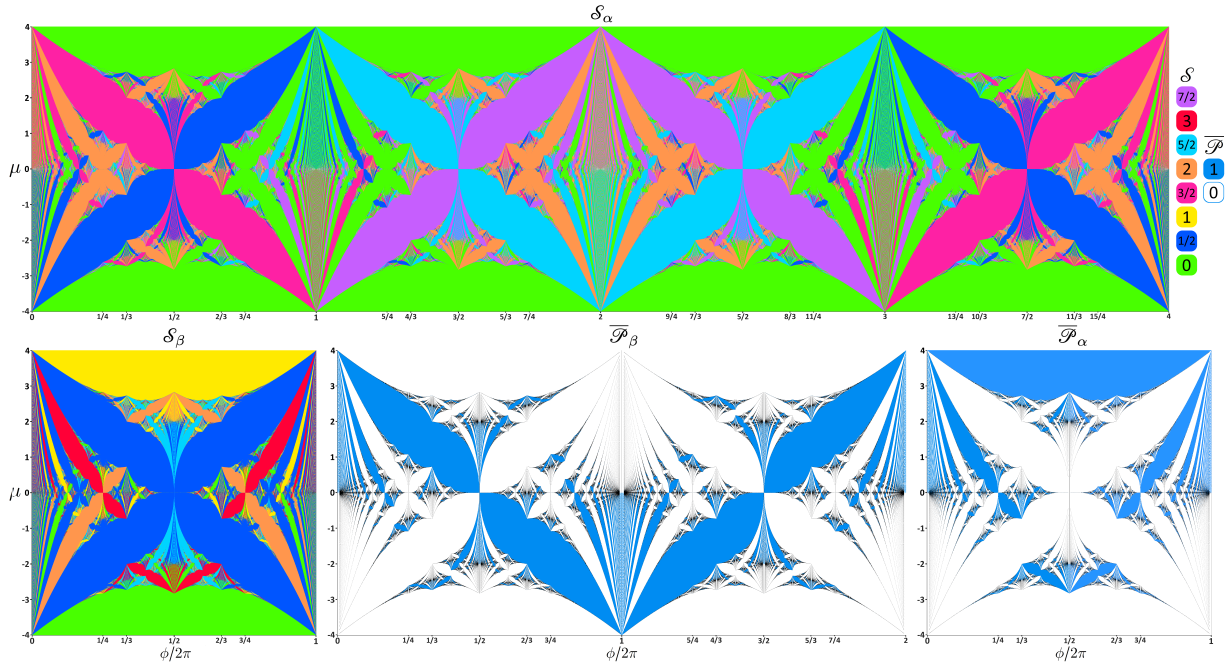

Figure 2.7: A menagerie of butterflies in the spinless square lattice Hofstadter model. α and β represent a plaquette center and vertex respectively. For any C_4 symmetric origin o, $\mathscr{S}_{\rm o}$ has a $\mathbb{Z}_4$ classification, while $\overline{\mathscr{P}}_{\rm o}$ has a $\mathbb{Z}_2$ classification. Figure from Ref. [3].

quantized [2, 3, 83]. The above observations suggest that one should be able to write down mixed Chern Simons like terms that associate electric charge with lattice defects (and therefore, via integration by parts associate linear/angular momenta to magnetic flux). Indeed, such terms were written in Ref. [2, 3, 83]:

$$\mathcal{L} = \frac{C}{4\pi} A \wedge dA + \frac{\mathscr{S}_{\rm o}}{2\pi} A \wedge d\omega + \frac{\vec{\mathscr{P}}_{\rm o}}{2\pi} \cdot A \wedge \vec{T} + \frac{\kappa}{2\pi} A \wedge A_{XY} + \dots \tag{2.56}$$

Here, A is the electromagnetic $U(1)$ gauge field, ω is a discrete spin connection, $\vec{T}$ is translation gauge field (or discrete vielbein), A_{XY} is an area 2-form. Further, C, $\mathscr{S}_{\rm o}$, $\vec{\mathscr{P}}_{\rm o}$, and κ are topological invariants. C is the familiar Chern number. $\mathscr{S}_{\rm o}$, or the discrete shift associates electric charge to lattice disclination (corresponding to a discrete rotation symmetry centered about 'o'). $\vec{\mathscr{P}}_{\rm o}$, or quantized electric polarization associates electric charge to lattice dislocation.

In Ref. [2], we study the Hofstadter model on a square lattice, i.e., electrons hopping on a lattice in a magnetic field. We characterize $\mathscr{S}_{\text{o}}$ (where 'o' is a lattice vertex) throughout the Hofstadter butterfly. The result is shown in Fig. 2.6. In Ref. [3], we study $\vec{\mathscr{P}}_{\text{o}}$ throughout the Hofstadter model, paying special attention to ambiguities in determining the flux through a dislocation. Due to these ambiguities, our results depend on the distribution of flux within each *single* unit cell. Therefore, Fig. 2.7 is periodic under $\phi \to \phi + 8\pi$ and not $\phi \to \phi + 2\pi$.

We have thus made a connection between the DC Monopole Josephson Effect and the characterization of topological phases in the presence of discrete lattice symmetries. Having finished our digression, we now return to Dirac Spin Liquids.

2.7 Discussion

This work uses the viewpoint that certain magnetically ordered states can be obtained upon condensing monopole operators which enter the low energy description of a Dirac spin liquid. We have argued that by using a Josephson junction geometry with two ordered states separated by a DSL, one can induce an emergent electric field (both DC and AC) in the DSL. Further, we have shown that such an AC emergent electric field can be measured optically as a sharp field-tunable peak in Raman scattering. Also, the induced electric field is accompanied by a measurable spin current across the junction that is proportional to the emergent electric field. This serves as an independent check that can be used to validate our first prediction. We have also highlighted other phenomena conceptually related to the monopole Josephson effect, namely long-range phase rigidity between puddles of ordered phases separated by Dirac spin liquids, "mixed currents" across AFM-DSL-VBS junctions and spinon charge bound to lattice dislocations.

In general, an AFM – X – AFM junction, for some unknown phase X and generic details of the interface, will (at least in the short-junction limit) allow monopole tunneling analogous to that of the AFM – DSL – AFM junction. The observation of, for example, a spin current in a DC junction setup is therefore insufficient to claim that the unknown phase X is a DSL. However, two of the effects we propose to measure, namely the field-tunable Raman peak and the power-law dependence of the spin current as a function of junction size, require a conserved monopole current in region X (or equivalently require that the low-energy degrees of freedom of region X include an emergent $U(1)$ electric field). This requirement is satisfied when X is a DSL, but not in ordered phases such as valence bond solids where a spin singlet monopole creation operator acquires nonzero expectation value, and hence the monopole current (electric field) is not a conserved quantity. Therefore, measuring our proposed field-tunable sharp Raman peak in the region X in conjunction with a spin current across the interface, such that both the strength of the Raman peak and the spin current scale as a power law in the width of region X, will be strong evidence that X is a DSL.

We note that our predictions are backed up by writing a phenomenological monopole tunneling Hamiltonian that assumes that a DSL couples to a nearby ordered state chiefly through monopole tunneling terms, since monopoles are the most relevant operators in the DSL. We do not however attempt a full boundary conformal field theory calculation. This is because the current understanding of QED_3 as a CFT (even without boundaries) is still in its nascent stages, although there have been promising recent numerical developments [38, 84, 85]. We also note that due to the Josephson effect, the quantum state of the DSL region differs from the ground state of QED_3. For example, when there is an AC electric field through the DSL, the DSL is in a nonequilibrium state. When there is a mixed spin-valley current, lattice translation symmetry

gets broken. In such cases, whether the framework of DSL theory is still a valid description or not would depend on the strength of coupling between the different regions, size of the DSL region, and temperature. Determining this would again require a detailed boundary CFT calculation, and is beyond the scope of this work.

Our work presents an in-principle method to externally induce and measure emergent gauge field strengths in strongly coupled spin liquids in 2+1 dimensions. In general, one has more control over the degrees of freedom in an ordered state. So looking forward, attempting to probe operators in other spin liquids using more conventional ordered states is a promising direction. We note that Ref. [86] theoretically considered tunneling of spinons between ferromagnets through a quantum spin ice in 3+1D, and is closely related to this idea.

A second interesting direction is in the context of recent developments in Rydberg atom arrays that take us one step closer to realizing a spin liquid in a lab [45]. In these experiments, one can access projections of the microscopic wavefunction in a preferred basis. It will therefore be interesting to come up with signatures of long wavelength operators and non-equilibrium steady state features such as currents, but in the many-body wave function, such that they can be accessed in these experiments.

Chapter 3: Diagnosing Electronic Phases of Matter using Photonic Correlation Functions

3.1 Introduction

Strongly interacting quantum many-body systems can host a variety of exotic phases of matter. However, there exists a gap between theoretical models and experimental observations in terms of accessible physical observables. A hallmark example is topologically ordered phases, beginning with the experimental observation of the Fractional Quantum Hall effect, whose excitations exhibit fractional statistics [87, 88, 89, 90, 91, 92]. There are strong theoretical reasons [46, 47, 93] to expect that spin systems dubbed "quantum spin liquids" also host topological order and other exotic gapless field theories [32, 36, 44, 94, 95, 96, 97]. However, experimental verification of such claims has been extremely challenging. At the same time, other unconventional phases, including high-temperature superconductors and correlated insulators, have been experimentally observed in cuprate-like strongly correlated materials [98], and more recently in moiré materials [99, 100]. While there is a thriving theoretical effort to explain many of these phases, conclusively matching theory to experiment is generally difficult. The main challenge stems from the fact that the nontrivial nature of many of these phases is encoded in correlation functions that are difficult to measure experimentally. Conventionally, probes for accessing electronic corre-

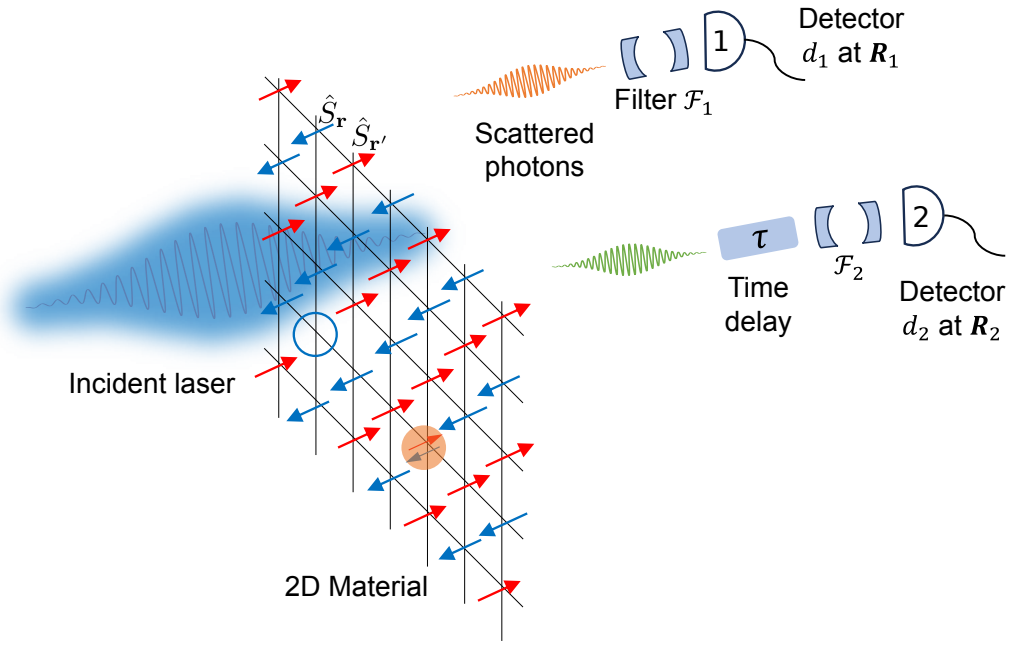

Figure 3.1: A system of itinerant electrons is irradiated with a laser. Conventionally, photodetectors measure the intensity of the scattered photons, and the correlations are ignored. In this paper, we propose a Hanbury Brown-Twiss-type setup to measure correlations between pairs of photons. We allow for frequency filters, $\mathcal{F}_1$ and $\mathcal{F}_2$, before detection, and a time delay, τ, between detection events.

lation functions work within the linear response paradigm. For example, Raman scattering has been employed to study potential spin liquid candidates [1, 7, 8, 54, 76, 77, 101, 102, 103]. However, given how difficult it is to characterize exotic phases, it is important to (1) develop novel experimental protocols to measure a wider class of correlation functions and (2) understand how these new correlation functions can assist in diagnosing the phase of matter under study.

A promising approach is to move beyond the linear-response paradigm by studying the nonlinear response to an external electromagnetic drive [15, 104, 105, 106, 107, 108, 109, 110, 111, 112, 113, 114, 115, 116, 117, 118, 119, 120, 121, 122, 123, 124, 125, 126]. One example is two-dimensional coherent spectroscopy, an extension of pump-probe spectroscopy [127, 128, 129], in which two pump pulses, separated by a fixed time delay, are applied to the sample, followed by a probe measurement at a fixed delay relative to the last pulse. A recent work

predicted that a setup like this can be used to detect anyonic excitations [15, 125]. It is also possible to go beyond the linear-response paradigm by studying higher-order correlations within the output signal generated by external stimuli. A classic example is shot noise in electric current [130] that has been used to detect fractionally charged excitations [131, 132], Cooper pairing in normal state [133, 134] and absence of quasiparticles [135].

Thus, it is intriguing to ask whether quantum correlations between scattered photons could carry useful information beyond what can be obtained from both linear response and pump-probe techniques. It is known in quantum optics that when two or more photons are scattered off an optically nonlinear medium, they can become correlated [136]. Our work demonstrates that when this medium is a strongly correlated electronic system, its nontrivial correlations are inherited by the scattered photons. Therefore, analyzing photonic correlations in the outcome of spectroscopy experiments reveals many-body observables that are not accessible through current linear and nonlinear probes.

The paradigmatic setup for the detection of the photonic correlations consists of a Hanbury Brown-Twiss interferometer where the scattered photons are divided into two separate paths [137] (See Fig. 3.1). Then, the photons are detected in each path separately. In this work, we also allow for the possibility of frequency and polarization filtering before detection. This scheme allows for the measurement of a four-point correlation function $G^{(2)}_{d_1,d_2}(\tau) = \langle \hat{a}^\dagger_{d_1}(0)\hat{a}^\dagger_{d_2}(\tau)\hat{a}_{d_2}(\tau)\hat{a}_{d_1}(0)\rangle$, where $\hat{a}_{d_j}$ are the annihilation operators of the filtered photonic mode in the corresponding (j-th) interferometer arm. τ denotes the time delay between the detection events [1]. We note that in addition to $G^{(2)}$, the described setup allows for the measurement of correlation functions of electromagnetic quadrature including $\langle \hat{a}_{d_1}(0)\rangle$ and $\langle \hat{a}_{d_2}(\tau)\hat{a}_{d_1}(0)\rangle$. This is done by mixing the

[1] The correction due to retardation is clarified in Eq. (3.8) in Sec. 3.3.2.

scattered photons with a strong reference coherent field having a fixed phase.

In this work, we first develop a systematic procedure to map these photonic correlators to dynamical correlation functions of the material in its undriven state. As a specific example, we provide the mapping for a single-band Fermi-Hubbard model at half-filling in a Mott insulator state, where in the limit of strong on-site repulsion, the many-body energy spectrum splits into distinct sectors corresponding to charge and spin degrees of freedom, well-separated by the Mott gap [2]. Furthermore, we demonstrate that the frequency filtering of scattered photons plays a crucial role in our scheme. In particular, it enables the measurement of matter correlations restricted to a particular energy sector of interest, i.e. a pure spin or a mixed spin-charge sector.

We then present several salient applications: (1) We show that by measuring the first-order quadrature of the scattered light and its fluctuations, one can determine the static expectation value of the spin chirality operator on the kagome and triangular lattices, respectively, which is currently inaccessible using current techniques. These operators acquire nonzero expectation values in chiral spin liquids [35, 138, 139, 140, 141, 142, 143], and play the role of chiral mass terms in $U(1)$ Dirac spin liquids [24, 144]. (2) We demonstrate that the correlations of scattered photons can be used to probe the mixed spin-charge correlators, providing insights into the dynamics of a hole and a doubly-occupied site (called a doublon) in a Mott insulator. (3) We derive the contributions to the $G^{(2)}$ correlation functions from non-interacting magnons in a magnetically ordered system. (4) We establish that $G^{(2)}$ can be used to diagnose whether the state in the spin sector is a spin liquid with excitations carrying fractional mutual statistics. For this, we follow the semiclassical argument in Refs. [15, 125] for pump-probe spectroscopy, and show that it also

[2] Strictly speaking, only the many-body states connected through application of local operators on the ground state split into distinct charge and spin sectors.

applies to $G^{(2)}$ spectroscopy.

The rest of the paper is organized as follows. In Sec. 3.2, we provide an overview of the physical setting and the main results of the paper, along with sufficient background and context to allow each of the remaining sections to be read independently. In Sec. 3.3.1, we provide details of the $\hat{\mathcal{T}}$-matrix formalism that we use for describing different scenarios of photon scattering. Sec. 3.3.2 presents a mathematical definition of the photonic correlators studied in this work. Technical details for experimental measurement schemes are provided in Appendix C.4. Next, in Sec. 3.4, we apply the scattering formalism to the Fermi-Hubbard model at half-filling. Given the separation of energy scales discussed in Sec. 3.4.1, we show in Sec. 3.4.2 that correlation functions of photonic operators map to those of pure matter operators denoted as $\hat{R}^{(1)}$ and $\hat{R}^{(2)}$. We study the microscopic structure of these operators in Sec. 3.5, with the technical details provided in Appendix C.3. In Sec. 3.6, we discuss the temporal structure of the matter correlation functions, with the emphasis on the role of frequency filters. Starting from Sec. 3.7, we provide a detailed discussion of the proposed salient applications. First, in Sec. 3.7, we show that by measuring the squeezing spectrum of the scattered photons it is possible to determine the expectation values of the scalar spin chirality operators. Next, in Sec. 3.8, we calculate $G^{(2)}$ of scattered photons for the case when the spin sector has non-interacting bosonic excitations such as magnons. In Sec. 3.9, we discuss the conditions under which their contributions can be filtered out, enabling the measurement of more exotic properties of the matter. In particular, we demonstrate that the presence of anyonic excitations in a spin sector can be established using both conditional $G^{(1)}(\tau)$ and $G^{(2)}$ measurements. In Sec. 3.10, we comment on experimental feasibility. Finally, in Sec. 3.11, we present an outlook.

3.2 Summary of the paper

3.2.1 The setting

We now consider the problem of photon scattering off a 2-dimensional strongly correlated electronic system, as shown in Fig. 3.1. The material, initially prepared in a thermal equilibrium state, is irradiated by a monochromatic laser having polarization $\mathbf{e}_L$ and frequency ω_L. The laser driving is weak, in the sense that $g_L \equiv \sqrt{2\pi I_L \alpha}\mathtt{a}/\omega_L \ll 1$, where I_L is the laser intensity, α is the fine-structure constant and $\mathtt{a}$ is the lattice spacing of the electronic system. Throughout this work, we assume the initial state of the electromagnetic field to be in either a Fock state $|\mathcal{N}_L\rangle = (\mathcal{N}_L!)^{-1/2}(\hat{a}_L^\dagger)^{\mathcal{N}_L}|0\rangle$ or in a coherent state $e^{\phi_L \hat{a}_L^\dagger - \phi_L^* \hat{a}_L}|0\rangle$, where $|0\rangle$ is the vacuum, $\hat{a}_L$ is the annihilation operator of the laser mode (see Appendix C.1 for a more careful treatment of the laser as a wavepacket), and $\phi_L \equiv e^{-i\theta_L}|\phi_L|$. Since the driving is weak, we can restrict our consideration to the subspace containing at most 2 scattered photons [145, 146]. These photons, before being detected, are separated into the two arms of a Hanbury Brown-Twiss interferometer, each containing frequency and polarization filters. We define the filter function in the j-th interferometer arm as $\mathcal{F}_j(\omega)$ and assume that it is centered around frequency ω_j with possibly some spread. Furthermore, we impose the causality condition, i.e. $\tilde{\mathcal{F}}_j(t) \equiv \int_{-\infty}^{\infty} \frac{\mathrm{d}\omega}{2\pi}\mathcal{F}_j(\omega)e^{-i\omega t}$ is 0 for $t < 0$. Then the effective photon annihilation operator corresponding to the detection of a photon in j-th interferometer arm takes the form $\hat{a}_{d_j} \sim i\sum_{\mathbf{k}} \mathcal{F}_j(\omega_{\mathbf{k}})\hat{a}_{\mathbf{k},\mathbf{e}_j}$, i.e., a superposition of normal modes of free space, $\hat{a}_{\mathbf{k},\mathbf{e}_j}$ labeled by momenta $\mathbf{k}$ and polarization $\mathbf{e}_j$ (here, the subscript d_j stands for detector j). For a precise definition of $\hat{a}_{d_j}$, see Eq. (3.9, 3.11). Finally, all measurements are considered to be made in the asymptotic future (formally defined in Sec. 3.3.1).

For the matter side, the general form of our results applies to any correlated insulator with an optical gap. For concreteness, we consider a 2-dimensional system of strongly interacting itinerant electrons in a Mott-insulator state, which we model by the single-band Fermi-Hubbard model at half-filling [147, 148]. In the limit of strong on-site interaction $U \gg \mathtt{t}$, where $\mathtt{t}$ is the tunneling amplitude between nearest sites, the many-body energy spectrum splits into sectors having a definite number of doubly occupied sites ("doublon excitations"). The lowest energy manifold ("spin sector") consists of pure spin excitations described by the Heisenberg model. Depending on the lattice geometry, and strengths of tunnelings between next-nearest-neighbors and beyond, there are several possibilities for the ground state of the spin sector. It could be a magnetically ordered state such as a Néel or a 120° antiferromagnet, in which case its excitations are magnons. It could also be a quantum spin liquid whose excitations are charged under an emergent gauge group, or have fractional statistics or both.

Throughout this work, we assume the incident laser is detuned from the optical gap such that $\mathtt{t} \ll |\omega_L - U| \ll U$. The absorption and emission of photons couples the spin and charge sectors of the system as shown in Fig. 3.2. Furthermore, the photons can be scattered inelastically with their amplitudes being dependent on the finer structure of the spin and charge sectors. We note that in contrast to the conventional Raman spectroscopy, we are interested in the scattering of multiple photons, which, as we demonstrate, provides additional information on the state of the electronic system. The relation between the inelastic photon scattering amplitudes and the matter correlations constitutes the main focus of this work and will be reviewed in the section below.

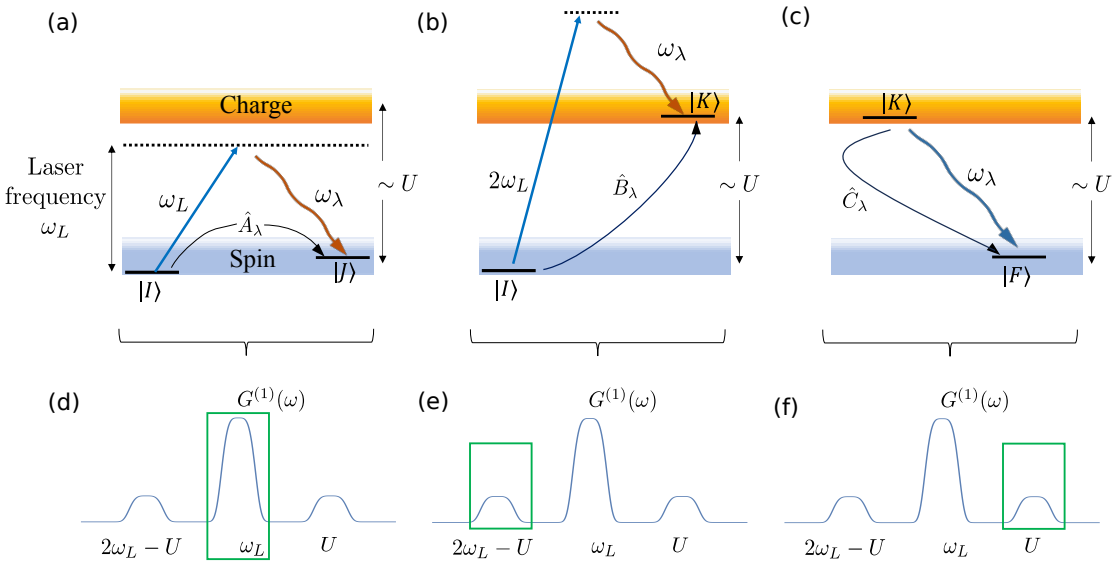

Figure 3.2: Schematic illustration of different photon scattering processes. **(a-c)** The blue- and orange-shaded regions represent the lower and higher energy sectors, respectively, separated by an optical gap of order U. For the Fermi-Hubbard model at half-filling, U corresponds to the on-site repulsion, with the low- and high-energy sectors identified as spin and charge sectors, respectively. More generally, the presented formalism applies to any insulator with an optical gap. The laser frequency ω_L is assumed to be detuned from U. The three terms in $\hat{M}_\lambda$, defined in Eq. (3.2) correspond to different pathways leading to emission of a photon. These three pathways are depicted schematically as follows: **(a)**: Raman process – absorption of a laser photon followed by the emission of a photon with a frequency near ω_L. This process is governed by the effective matter operator $\hat{A}_\lambda$, which mediates transitions from the state $|I\rangle$ to $|J\rangle$ within the same (lower energy) sector. **(b)**: Absorption of two photons followed by emission of a photon of frequency near $2\omega_L - U$. This process involves the effective matter operator $\hat{B}_\lambda$, which transitions the state $|I\rangle$ in the lower energy sector to $|K\rangle$ in the higher energy sector. **(c)**: Emission of a photon of frequency near U originating from a state $|K\rangle$ in the higher energy sector that was previously accessed via process (b). This emission is mediated by the effective matter operator $\hat{C}_\lambda$, which transitions the state $|K\rangle$ to $|F\rangle$ in the lower energy sector. Panels (d-f) illustrate the corresponding intensity versus frequency profiles. Notably, emission into sideband (e) is necessarily accompanied by simultaneous emission into sideband (f).

3.2.2 Mapping between photonic and matter correlators (Input-output relations)

We first summarize the main assumptions in this work:

1. The material is initially in equilibrium at a temperature much smaller than U, the optical gap.

2. $\mathtt{t} \ll |\omega_L - U| \ll U$. More generally, going beyond the single-band Fermi-Hubbard model, this assumption means that the detuning of the drive frequency from the optical gap is much smaller than the optical gap. In addition, the intrinsic coupling scale between different optical sectors is much smaller than the detuning.

3. Weak driving: $g_L \equiv \sqrt{2\pi I_L \alpha}\mathtt{a}/\omega_L \ll 1$. This implies that light-matter scattering processes can be treated order by order in the number of photons involved.

4. The frequencies of detected photons are postselected to be of the order of the drive frequency ω_L up to corrections of order $|U - \omega_L|$. As discussed later (Sec. 3.4.2), this requirement, together with Assumption 2, implies that light scattering processes conserve the total number of photons.

5. Dipole approximation, i.e., momentum exchange between light and matter is neglected (discussed below).

6. We consider a single electronic orbital per lattice site and per spin, and assume that the light-matter coupling in this truncated Hilbert space is given by Peierls' substitution.

Later, in Sec. 3.5, we also assume the absence of spin-orbit coupling for simplicity. But this assumption can be dropped straightforwardly by starting with a spin-orbit coupled microscopic

tunneling Hamiltonian as done in Ref. [149]. We start by providing a qualitative picture of the laser-induced processes. For simplicity we assume the system is initially prepared in the lowest energy sector (for a Mott insulator, this is the spin sector). Emission of a photon by the driven material can result from one of the three pathways shown in Fig. 3.2(a-c). Fig. 3.2(a) depicts the conventional Raman scattering process, where the off-resonant absorption of a single photon is followed by emission at a different frequency, ω_λ. This process is accompanied by the material transitioning from a state $|I\rangle$ to $|J\rangle$ belonging to the same energy sector. Energy conservation implies that $\omega_\lambda = \omega_L + E_I - E_J$, where $E_{...}$ denotes the energy of the state $|\ldots\rangle$. Under our approximations, the emitted photon has a frequency close to ω_L.

At weak driving, Raman scattering involving emission of a single photon represents the leading contribution to photonic observables. However, the Hanbury Brown-Twiss measurement scheme post-selects the scattering amplitudes that necessarily involve two photons. We identify the following main contributions to these amplitudes. (1) Two Raman processes, occurring sequentially, such that both emitted photons have a frequency $\sim \omega_L$ (see Fig. 3.2(d)), and (2) the process shown in Figs. 3.2(b, c) involving the real excitation of an intermediate state $|K\rangle$ within the charge sector (upper Hubbard band).

In the second scenario, after the emission of the first photon, the material transitions from the state $|I\rangle$ in the spin sector to $|K\rangle$ in the charge sector. The frequency of the emitted photon is given by $\omega_\lambda = 2\omega_L + E_I - E_K \sim 2\omega_L - U$. The material can then return to the lowest energy sector by emitting a photon with frequency $E_K - E_F \sim U$. Consequently, the intensity spectrum of scattered light exhibits sidebands at the frequencies $\sim U$ and $2\omega_L - U$, as schematically shown in Figs. 3.2(e, f). At weak driving, these sidebands have a smaller spectral weight compared to the central peak at $\sim \omega_L$ because they involve two-photon emission processes. The microscopic

details of these processes in the correlated insulators described by the Fermi-Hubbard model at half-filling are provided in Sec. 3.5.

Let us now assume that the evolution of light and matter in the absence of light-matter interactions is described by the Hamiltonian $\hat{H}_0$. In the remainder of this Subsection, we provide a quick way to arrive at the mapping between correlation functions of scattered photons and those of matter operators in equilibrium. A more explicit treatment by quantizing the vector potential and using the $\hat{\mathcal{T}}$-matrix formalism to compute scattering amplitudes is provided in Secs. 3.4.2, 3.4.3, and 3.6. To motivate our results here, we directly write down the following effective interaction Hamiltonian that captures all the photon emission processes in Fig. 3.2:

$$\hat{H}^I_{\text{eff}}(t) = \sum_\lambda \hat{M}_\lambda(t)\hat{a}^\dagger_\lambda e^{i\omega_\lambda t} + \text{h.c.}, \tag{3.1}$$

where $\hat{X}(t) \equiv e^{i\hat{H}_0 t}\hat{X}e^{-i\hat{H}_0 t}$. The operator $\hat{a}^\dagger_\lambda$ denotes the photon creation operator in the mode λ, which is a composite index for momentum and polarization. $\hat{M}_\lambda$ is an effective pure matter operator. For now, $\hat{M}_\lambda$ can be thought of as the operator implementing the transitions shown in Fig. 3.2, but we will define $\hat{M}_\lambda$ precisely in Sec. 3.5 and provide intuition in the remainder of this Section. For energy scales considered in this work, the momentum transfer between transverse electromagnetic radiation and electrons is a negligible fraction of the reciprocal lattice momenta. So, we have used the dipole approximation and dropped the spatial dependence of the photon operators – an approximation discussed further in Sec. 3.5.1 and Sec. 3.11. The matter operator $\hat{M}_j$ does depend on the polarization of the absorbed and emitted photons. Through this polarization dependence, $\hat{M}_j$ encodes symmetry properties of light matter interactions, as elaborated later in this Section, and in Sec. 3.7. For the purpose of this section, photon absorption

Photonic correlator	**Matter correlator**
First order quadrature: $e^{i\theta}\left\langle \hat{a}_{d_j}(0)\right\rangle_{\text{out}} + \text{c.c.}$	$e^{i\theta}\mathcal{F}_j(\omega_L)\left\langle \hat{M}_j(0)\right\rangle_0 + \text{c.c.}$
Intensity: $G^{(1)}_{d_j}(0) = \left\langle \hat{a}^\dagger_{d_j}(0)\hat{a}_{d_j}(0)\right\rangle_{\text{out}}$	$\iint_0^\infty \mathrm{d}t\,\mathrm{d}t'\,\tilde{\mathcal{F}}_j(t)\left[\tilde{\mathcal{F}}_j(t')\right]^*\left\langle\left[\hat{M}_j(-t')\right]^\dagger \hat{M}_j(-t)\right\rangle_0$
$G^{(1)}_{d_j}(\tau) = \langle \hat{a}^\dagger_{d_j}(\tau)\hat{a}_{d_j}(0)\rangle_{\text{out}} + \text{c.c.}$	$\left\{\iint_0^\infty \mathrm{d}t\,\mathrm{d}t'\,\tilde{\mathcal{F}}_j(t)\left[\tilde{\mathcal{F}}_j(t')\right]^*\left\langle \hat{M}^\dagger_j(\tau-t')\hat{M}_j(-t)\right\rangle_0\right\} + \text{c.c.}$
Phase-dependent part of the quadrature fluctuations: $e^{2i\theta}\left\langle \hat{a}_{d_2}(\tau)\hat{a}_{d_1}(0)\right\rangle_{\text{out}} + \text{c.c.}$	$\left\{e^{2i\theta}\iint_0^\infty \mathrm{d}t_1\,\mathrm{d}t_2\,\tilde{\mathcal{F}}_1(t_1)\tilde{\mathcal{F}}_2(t_2) \times\left\langle \mathbb{T}\left[\hat{M}_2(\tau-t_2)\hat{M}_1(-t_1)\right]\right\rangle_0\right\} + \text{c.c.}$
Photon-pair correlation function $G^{(2)}_{d_1,d_2}(\tau) = \left\langle \hat{a}^\dagger_{d_1}(0)\hat{a}^\dagger_{d_2}(\tau)\hat{a}_{d_2}(\tau)\hat{a}_{d_1}(0)\right\rangle_{\text{out}}$	$\iiiint_0^\infty \mathrm{d}t_1\,\mathrm{d}t_2\,\mathrm{d}t_1'\,\mathrm{d}t_2'\,\tilde{\mathcal{F}}_1(t_1)\tilde{\mathcal{F}}_2(t_2)[\tilde{\mathcal{F}}_1(t_1')]^*[\tilde{\mathcal{F}}_2(t_2')]^* \times\left\langle \bar{\mathbb{T}}\left[\hat{M}^\dagger_1(-t_1')\hat{M}^\dagger_2(\tau-t_2')\right]\mathbb{T}\left[\hat{M}_2(\tau-t_2)\hat{M}_1(-t_1)\right]\right\rangle_0$
Conditional $G^{(1)}$ defined as $H_{d_1,d_2}(t,\tau) = \langle \hat{a}^\dagger_{d_1}(0)\hat{a}^\dagger_{d_2}(t+\tau)\hat{a}_{d_2}(t)\hat{a}_{d_1}(0)\rangle_{\text{out}}$ +c.c.	$\left\{\iiiint_0^\infty \mathrm{d}t_1\,\mathrm{d}t_2\,\mathrm{d}t_1'\,\mathrm{d}t_2'\,\tilde{\mathcal{F}}_1(t_1)\tilde{\mathcal{F}}_2(t_2)[\tilde{\mathcal{F}}_1(t_1')]^*[\tilde{\mathcal{F}}_2(t_2')]^* \times\left\langle \bar{\mathbb{T}}\left[\hat{M}^\dagger_1(-t_1')\hat{M}^\dagger_2(t+\tau-t_2')\right]\right. \times\mathbb{T}\left.\left[\hat{M}_2(t-t_2)\hat{M}_1(-t_1)\right]\right\rangle_0\right\} + \text{c.c.}$

Table 3.1: Correspondence between the correlation functions of scattered photons (left column) and the matter correlation functions in equilibrium (right column). In the left column, $\langle . \rangle_{\text{out}}$ indicates that the expectation value $\langle \text{out}|.|\text{out}\rangle$ is taken in the full light-matter post-scattering state $|\text{out}\rangle$. In the right column, $\langle . \rangle_0$ indicates that the expectation value is taken in a pure matter energy eigenstate, or more generally in any mixed state diagonal in the energy eigenstate basis. The matter operators $\hat{M}_j$ are defined in Eq. (3.2) and (3.4). $\mathcal{F}_j(\omega_j)$ is the effective filter function, and $\tilde{\mathcal{F}}_j(t)$ is its Fourier transform. Here $\mathbb{T}[\,]$ and $\bar{\mathbb{T}}[\,]$ denote time- and anti-time-ordering respectively. Note that $G^{(1)}_{d_j}(0)$ is the same as intensity of Raman-scattered photons [7, 8]. For measuring the first order quadrature and two-mode squeezing, the output photons are interfered with a strong local oscillator whose frequency is equal to the drive frequency, ω_L, and whose phase *relative* to the drive is θ. We provide a detailed discussion on the above photonic correlators and the experimental schemes to measure them in Sec. 3.3.2 and Appendix C.4.

from the laser is treated classically, while emission is treated quantum mechanically. A full quantum mechanical treatment is provided in Sec. 3.4.3. Under the assumption about energy scales and post-selection discussed above, we can write the matter operator $\hat{M}_\lambda$ as a sum of three terms corresponding to the photon-emission processes in Fig. 3.2 (a), (b) and (c) respectively:

$$\hat{M}_\lambda(t) = \left[e^{-i(\omega_L t+\theta_L)}\hat{A}_\lambda(t) + e^{-2i(\omega_L t+\theta_L)}\hat{B}_\lambda(t) + \hat{C}_\lambda(t)\right] + \text{h.c.}, \tag{3.2}$$

where θ_L is the phase of the drive laser, which we set to zero without loss of generality. Here, the first term corresponds to emission of a photon after absorption of a photon from the laser (hence the factor $e^{-i\omega_L t}$). As shown in Fig. 3.2 (a), the operator $\hat{A}_\lambda$ couples the states $|I\rangle$ and $|J\rangle$ within the spin sector and corresponds to Raman scattering of photons. Operators $\hat{B}_\lambda$ and $\hat{C}_\lambda$ induce transitions between the states belonging to different energy sectors $|I\rangle \to |K\rangle$ and $|K\rangle \to |F\rangle$ (see Figs. 3.2(b, c)). The operator $\hat{B}_\lambda$ is multiplied by $e^{-2i\omega_L t}$ because as shown in Fig. 3.2 (b), a photon is emitted after absorbing two photons from the laser. Operator $\hat{C}_\lambda$, as shown in Fig. 3.2 (c) corresponds to spontaneous emission from the higher energy sector. As a result of the dipole approximation, the matter operators contributing to $\hat{M}_\lambda$ depend only on the polarization of the emitted photons, encoded in λ. For the detection of these photons, their polarization must match that of the filter in the corresponding arm of the interferometer. Accordingly, in the following, we adopt a notation $\hat{M}_j$, where $j = 1, 2$ denotes the polarizations of the detectors in our measurement scheme.

To determine the mapping between photonic and matter correlators, let us consider time evolution under the effective Hamiltonian, Eq. (3.1). From the term $\hat{M}_\lambda(t)\hat{a}^\dagger_\lambda(t)$, we see that the emission of a photon into mode λ is accompanied by application of the matter operator $\hat{M}_\lambda(t)$

on the matter state. This is analogous to photon emission by an oscillating dipole [14] with $\hat{M}_\lambda$ playing the role of an effective dipolar transition operator. Following this analogy, one can also expect the creation/annihilation operators of the scattered photons to be related to that of the matter via the input-output relation:

$$\hat{a}_{d_j}(\tau) \mapsto \int_0^\infty \mathrm{d}t\, \tilde{\mathcal{F}}_j(t) \hat{M}_j(\tau - t). \tag{3.3}$$

In this formula we have also taken into account the modification due to frequency filtering. Physically it means that for a photon to be detected at time τ, it must have been emitted at some earlier time, e.g., $\tau - t$ for $t > 0$, spending the remaining time in the filter. The greater the frequency resolution in the filter, the greater the uncertainty in time t. The complete mapping is summarized in Table 3.1. The left column lists photonic correlators that can be experimentally measured. The subscript 'out' indicates that the measurement is made post scattering in the asymptotic future (as explained in Sec. 3.3.1). When mode $\hat{a}_{d_j}$ corresponds to an inelastically scattered photon, $G^{(1)}_{d_j}$ simply denotes Raman intensity. In Sec. 3.3.2, we explain how the remaining correlators in the left column of Table 3.1 can be measured using standard quantum optics tools, such as homodyne detection and the Hanbury-Brown Twiss setup. The right column maps these photonic correlators to matter correlators in the thermal equilibrium state (in the absence of the laser drive).

To gain some intuition for these matter correlators, let us assume the matter operator $\hat{M}_j(t)$ associated with photon emission creates an excitation. Then two-photon correlations probe the dynamics of pairs of such excitations. One might naïvely think that the retarded delay τ between the detection of the two photons is the same as the delay between the two matter excitation events. However, this is not the case when frequency filtering occurs before detection. The

higher the frequency resolution, the greater the importance of interference between amplitudes for excitations created at different times, and hence, more the uncertainty in time. This motivates the convolution between $\hat{M}_j$ and the Fourier transform of the detector's filter function, i.e., $\tilde{\mathcal{F}}_j$ that appears in Eq. (3.3). Now let us understand the mapping in Table 3.1 and take $G^{(2)}_{d_1,d_2}(\tau)$ as an example. If we naïvely substitute Eq. (3.3) into the photonic correlator, we almost recover the formula in the right column except for the temporal ordering. Physically, this temporal ordering reflects causality of light-matter interaction – the excitation created at the time of the second-photon emission happens after the first. We provide a detailed derivation in Sec. 3.6. Related treatments of theory of time-resolved spectroscopy for intensities were given in Ref. [150, 151].

Now let us summarize the microscopic structure of $\hat{M}_j$ coming from Eq. (3.2). For a detailed explanation, see Sec. 3.5. As shown earlier in Fig. 3.2, the frequency of emitted photons is either around the central peak ω_L, or located in pairs of sidebands, near $2\omega_L - U$ and U. The corresponding matter operators $\hat{A}_j$, $\hat{B}_j$ and $\hat{C}_j$ are studied in detail for the single-band Fermi-Hubbard model in Sec. 3.5. Here, we summarize their key features. The operator $\hat{A}_j$ is a sum of spin singlet terms modulated by the polarizations of the incoming laser and the scattered photon. We define the spin of an electron at site $\mathbf{r}$ as $\hat{\mathbf{S}}_\mathbf{r}$. To leading order in $\mathtt{t}/|\omega_L - U|$, $\hat{A}_j \sim \frac{\mathtt{t}^2}{\omega_L - U} \sum_{\mathbf{r},\boldsymbol{\mu}} (\boldsymbol{\mu}\cdot\mathbf{e}_j^*)(\boldsymbol{\mu}\cdot\mathbf{e}_L) \left(4\hat{\mathbf{S}}_\mathbf{r}\cdot\hat{\mathbf{S}}_{\mathbf{r}+\boldsymbol{\mu}} - 1\right)$, where $\boldsymbol{\mu}$ labels the directions available for electron-tunneling. This is the Loudon-Fleury operator [7, 8, 78], which is defined in detail in Eq. (3.60)). Operator $\hat{A}_j$ can be seen as a sum of 2×2 tensors in the polarization directions, i.e., $(e_j^*)^u(e_L)^v$ for $u, v \in \{x, y\}$. It can thus be decomposed into channels that are irreducible representations of the crystalline point group of the lattice. One can check that at order $\mathtt{t}^2/|\omega_L - U|$, the component of $\hat{A}_j$ in the channel $(e_j^*)^x(e_L)^y - (e_j^*)^y(e_L)^x$ (invariant under spatial rotations but odd under reflection) is zero for all lattices. Ref. [54] showed that on the kagome lattice, the leading nonzero

term for $\hat{A}_j$ in this channel, appearing at order $\mathtt{t}^4/(\omega_L - U)^3$ is a sum of spin chirality operators $\sim \hat{\mathbf{S}}_{\mathbf{r}} \cdot \left(\hat{\mathbf{S}}_{\mathbf{r}'} \times \hat{\mathbf{S}}_{\mathbf{r}''}\right)$.

Next, the operator $\hat{B}_j$ is a mixed spin-charge operator that involves both a spin operator and electron tunneling creating a doublon-hole pair (shown in Fig. 3.9, 3.10, and defined precisely in Eq. (3.61)). Finally, $\hat{C}_j$ is a sum of electron tunneling operators and is proportional to the total electric current (See Eq. (3.62)). Given that $\hat{A}_j$ acts within a single energy sector, while $\hat{B}_j$ and $\hat{C}_j$ couple different ones, it is convenient to treat them separately. Therefore, we focus on the case where the filter functions have enough resolution to distinguish the three peaks in Fig. 3.2, while within each peak, the filter may be either broad or narrow. Then,

$$\hat{M}_j(t) = \begin{cases} e^{-i\omega_L t}\hat{A}_j(t) & \text{if detector } d_j \text{ detects near } \omega_L, \\ e^{-2i\omega_L t}\hat{B}_j(t) & \text{if detector } d_j \\ & \quad \text{detects near } 2\omega_L - U, \\ \hat{C}_j(t) & \text{if detector } d_j \text{ detects near } U. \end{cases} \tag{3.4}$$

Spectral resolution thus enables selection of the energy window of excitations (see Eq. (3.4) above). We thus see that even though light-matter interaction occurred well before photodetection, the frequency filtering during detection can drastically affect the information obtained about the matter. In fact, this is true even for two-photon scattering from a simple two-level system [14, 152, 153]. For example, in the presence of strong frequency filtering, emitted photons can be "stored" in the filter, and therefore the signature anti-bunching may disappear.

3.2.3 Applications

Given the access to new matter correlation functions, what do we learn that cannot be obtained from photon intensity measurements alone? Here, we summarize key applications for Mott insulators. We also show how photonic $G^{(2)}$ and quadrature correlation functions can reveal concrete signatures of spin liquids, which are generally notoriously difficult to observe otherwise.

3.2.3.1 Measuring static spin chirality

A chiral spin liquid is an equivalent of a $1/2$- bosonic fractional quantum Hall state occurring in an electrically neutral system [35]. Spin chirality operators defined earlier ($\sim \hat{\mathbf{S}}_{\mathbf{r}} \cdot (\hat{\mathbf{S}}_{\mathbf{r}'} \times \hat{\mathbf{S}}_{\mathbf{r}''})$) can spontaneously acquire a nonzero expectation value in chiral spin liquids [138, 139, 140, 141, 142, 143]. So far, there are proposals to use neutron [55] and Raman scattering ($G^{(1)}(0)$ in our notation) [54] to measure the fluctuations in spin chirality. Here, we show that quadrature measurements can directly measure the *static* expectation values of spin chirality in both kagome and triangular lattices.

According to Table 3.1 and Eq. (3.4), when the detector frequency filter is tuned near ω_L, the first-order quadrature measurement $\left\langle \hat{a}_{d_j}(0) \right\rangle_{\text{out}}$ directly provides the static expectation value of operator $\hat{A}_j$. As discussed in Ref. [54], on the kagome lattice, the operator $\hat{A}_j$ is equal to the sum of spin chirality terms in the channel $(e_j^*)^x (e_L)^y - (e_j^*)^y (e_L)^x$, termed as A_{2g}. Therefore, the measurement of the quadrature operator allows for the detection of chiral spin liquids.

For the triangular lattice, it was shown in Ref. [54] that the spin chirality terms vanish at order $\mathtt{t}^4/(\omega_L - U)^3$ in the same channel ($(e_j^*)^x (e_L)^y - (e_j^*)^y (e_L)^x$). In this work, we show that the expectation value of the static spin chirality can still be measured using a setup shown in Fig. 3.4,

and described in Sec. 3.3.2 and Appendix C.4. This setup measures the phase-sensitive part of quadrature fluctuations, i.e., two-mode squeezing between photons detected in arms d_1 and d_2. The detected photons should be linearly polarized and the frequency filters in arms d_1 and d_2 should be tuned to the different sidebands of the scattered light, $\sim 2\omega_L - U$ and $\sim U$ respectively. Within each sideband, the filters need to be broadband. Further, the detection events are post-selected such that the retarded time-delay $\tau = 0$. Specifically, we show in Sec. 3.7 that the two-mode squeezing $\mathrm{Im}\left[\langle \hat{a}_{d_2}(0)\hat{a}_{d_1}(0)\rangle_{\mathrm{out}}\right]$ yields $\sim \sum_{\mathbf{r},\mathbf{r}',\mathbf{r}''\in\triangle} \hat{\mathbf{S}}_{\mathbf{r}} \cdot (\hat{\mathbf{S}}_{\mathbf{r}'} \times \hat{\mathbf{S}}_{\mathbf{r}''})$. For measuring this, one should take linear combinations of the experimental data, so as to extract the component along the polarization channels specified in Sec. 3.7 (Eqs. (3.84-3.85)) that are invariant under rotation and odd under reflection. We note that although this type of measurement is accompanied by the real excitation of the charge sector, by post-selecting detection events having no time delay, one ensures that the system leaves this sector immediately, and hence the charge sector does not get entangled with light.

Here, we considered the case $\tau = 0$. Next, we discuss the more general case (when $\tau \neq 0$), in which case, the matter operators whose correlation functions are probed, lie in the charged sector.

3.2.3.2 Charged sector dynamics

By detecting a photon pair in the sidebands, one can extract a mixed spin-charge correlation function. For example, for a Mott insulator, described by the Fermi-Hubbard model at half-filling, the emission of one photon can be accompanied by the creation of a doublon-hole pair at a bond, followed by application of specific spin operators on sites neighboring this bond.

These operators include spin singlet projectors. The doublon-hole pair can then propagate till it is forced to recombine by emitting the second photon. The resulting correlator can potentially capture information about possible bound states in the charge sector called Mott excitons [154, 155, 156, 157, 158, 159, 160, 161, 162, 163, 164, 165, 166, 167] and their dependence on the spin background. We show the general form of such mixed spin-charge operators in Sec. 3.5.3. However, making quantitative predictions for the charged sector of correlated insulators is the subject of future research.

3.2.3.3 $G^{(2)}$ from magnon excitations

In Sec. 3.8, we study the contribution of non-interacting magnon excitations in a spin system to the connected photonic correlator $\mathcal{G}^{(2)}_{d_1,d_2}(\tau) \equiv G^{(2)}_{d_1,d_2}(\tau) - G^{(1)}_{d_1}(0) G^{(1)}_{d_2}(0)$. We demonstrate that $\mathcal{G}^{(2)}_{d_1,d_2}(\tau)$ is zero when the excitations are non-interacting bosons, provided four conditions are met: (1) both the detectors have sharp frequency filters around ω_1 and ω_2 respectively, (2) $\omega_j \neq \omega_L$, i.e., no elastic scattering, (3) $\omega_1 \neq \omega_2$, and (4) the polarization symmetry channels (discussed in Sec. 3.2.2) for the two detectors are distinct. In this limit of sharp spectral resolution, the result is independent of the time delay τ due to energy-time uncertainty. Therefore any nonzero contribution to $\mathcal{G}^{(2)}$ should arise from interactions between magnons or from topological properties of excitations.

3.2.3.4 Anyonic excitations – detecting fractional statistics in spin liquid candidates

If the ground state in the spin sector is topologically ordered, its excitations can have fractional statistics. In this case, the emission of each photon can be accompanied by the creation of an anyon pair. Anyons, created by different photon emissions, can braid nontrivially during their propagation. Nontrivial mutual statistics during such braiding can lead to a nonzero contribution to the connected $\mathcal{G}^{(2)}_{d_1,d_2}$. Using the semiclassical argument developed in [15, 125], in Sec. 3.9.2, we demonstrate that nontrivial braiding leads to a universal singularity in the connected part of the $\mathcal{G}^{(2)}_{d_1,d_2}$ function, depending on the photon filter frequencies. More specifically, we find $G^{(2)}_{d_1,d_2} \sim \theta(\Omega_1 - \Delta_1)\theta(\Omega_2 - \Delta_2)\left[K_2(\Omega_2)(\Omega_1 - \Delta_1)^{-3/2} + (1 \leftrightarrow 2)\right]$, where $\Omega_j = \omega_L - \omega_j$ denotes the Raman shift, $\theta(\omega)$ is the Heaviside step function, Δ_1 and Δ_2 are energy thresholds for creating anyon pairs via operators $\hat{A}_1$ and $\hat{A}_2$ respectively, and $K_j(\Omega_j)$ are system-specific functions. This singularity is a sharp signature of the existence of fractional mutual statistics in a spin liquid candidate.

3.3 The formalism and definitions in detail

In this section, we present the $\hat{\mathcal{T}}$-matrix formalism that we use to model the scattering process. Then we describe in more detail the photonic correlators studied in this work.

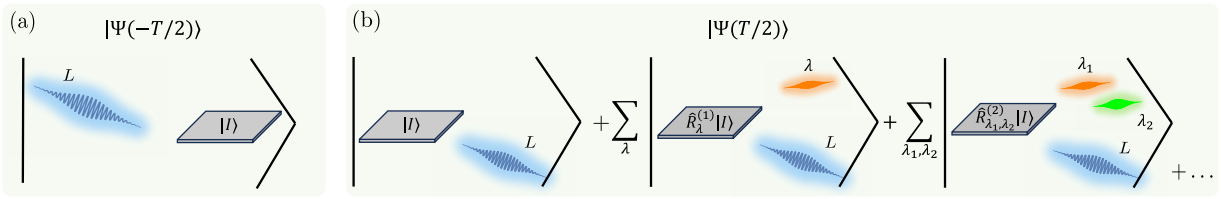

Figure 3.3: Schematic representation of the scattering process. **(a)** The initial state in the asymptotic past (at time $t = -T/2$, in the limit where it approaches $-\infty$), $|\Psi(-T/2)\rangle$ consists of the electromagnetic field in a laser-produced wavepacket state far away from the material. The material is assumed to be in an energy eigenstate $|I\rangle$. Around time $t = 0$, the wavepacket spatially overlaps with the material and interacts with it for a duration proportional to the length of the wavepacket, which we assume to be much larger than its central wavelength **(b)** At $t = T/2$, in the asymptotic future, light and the material are entangled with each other and the resulting superposition is schematically depicted in the figure. The expansion depicted here is in the number of photon modes in the final state. The first term corresponds to the elastic scattering of light. The second set of terms corresponds to the emission of a photon in mode λ, leaving the material in a state $\hat{R}^{(1)}_{\lambda}|I\rangle$, where $\hat{R}^{(1)}_{\lambda}$ is an operator acting purely in the matter sector. For brevity, we have left out energy-conserving δ-functions in the above schematic (for a more careful treatment, see Eq. (3.43)). The third set corresponds to the emission of a pair of photons in modes λ_1 and λ_2. Therefore, correlation functions of photons map to correlation functions of matter operators like $\hat{R}^{(1)}_{\lambda}$ and $\hat{R}^{(2)}_{\lambda_1,\lambda_2}$. In this paper, we present a formalism to derive expressions for these matter correlation functions.

3.3.1 Review of formalism

We model the experimental scenario as a scattering process under a time-independent Hamiltonian $\hat{H} \equiv \hat{H}_0 + \hat{V}$, where $\hat{H}_0$ is the Hamiltonian for light and matter, excluding light-matter interactions, and $\hat{V}$ is the light-matter interaction. The initial state $|\Psi(-T/2)\rangle$ at time $t = -T/2$ (in the limit $T \to \infty$) has light and matter decoupled – with light being in a laser-produced wavepacket state spatially far away from the material (see Fig. 3.3(a)). We assume the initial state of matter is an energy eigenstate $|I\rangle$ of energy E_I. This situation can be readily extended to any mixed initial state diagonal in the eigenstate basis.

Around the time $t = 0$ for a duration proportional to the length of the laser wavepacket (which we later take to ∞), the wavepacket spatially overlaps with the material and interacts

with it. At $t = T/2$, which is in the asymptotic future, the electromagnetic part of the state is once again composed of wavepackets spatially far away from the material. During the scattering, the electromagnetic field becomes entangled with the matter, as schematically shown in Fig. 3.3(b). Optical measurements are assumed to be made at $t = T/2$ in the state $|\Psi(T/2)\rangle \equiv e^{-i\hat{H}T} |\Psi(-T/2)\rangle$.

It is convenient to define $|\text{out}\rangle \equiv e^{i\hat{H}_0 T/2} |\Psi(T/2)\rangle$, $|\text{in}\rangle \equiv e^{-i\hat{H}_0 T/2} |\Psi(-T/2)\rangle$ and the expectation value of energy in the initial state $E^0_{\text{in}} \equiv \langle \text{in}|\hat{H}_0|\text{in}\rangle$. If the experiment duration is sufficiently long, i.e., when the uncertainty in energy $(\delta E_{\text{in}}) \ll 1/T$, we can use the $\hat{\mathcal{T}}$-matrix formalism [168] to approximate $|\text{out}\rangle$. By defining an energy eigenstate (belonging to the full light-matter Hilbert space) of $\hat{H}_0$ with energy E^0_j as $\left|\Psi^0_j\right\rangle$ we get (see Appendix C.1):

$$|\text{out}\rangle = |\text{in}\rangle - \sum_{j,k} 2\pi i \delta(E^0_j - E^0_k) \left|\Psi^0_k\right\rangle \left\langle\Psi^0_k\right| \hat{\mathcal{T}} \left|\Psi^0_j\right\rangle \left\langle\Psi^0_j|\text{in}\right\rangle, \tag{3.5}$$

where the $\hat{\mathcal{T}}$-matrix can be represented as a Dyson series:

$$\begin{aligned} \hat{\mathcal{T}} &= \hat{V} + \hat{V} \frac{1}{E^0_{\text{in}} - \hat{H}_0 - \hat{V} + i0^+} \hat{V} \\ &= \hat{V} + \hat{V}\hat{\mathbb{G}}_0\hat{V} + \hat{V}\hat{\mathbb{G}}_0\hat{V}\hat{\mathbb{G}}_0\hat{V} + \hat{V}\hat{\mathbb{G}}_0\hat{V}\hat{\mathbb{G}}_0\hat{V}\hat{\mathbb{G}}_0\hat{V} + \ldots, \end{aligned} \tag{3.6}$$

with the free propagator denoted as $\hat{\mathbb{G}}_0 \equiv \left(E^0_{\text{in}} - \hat{H}_0 + i0^+\right)^{-1}$. Eq. (3.5) is a generalization of Fermi's Golden rule to all orders in $\hat{V}$. In Appendix C.1, we provide a review of the $\hat{\mathcal{T}}$-matrix formalism along with a derivation of Eq. (3.5).

3.3.2 Definition and measurement of photonic correlation functions

We now consider a wide class of photonic correlation functions (to be introduced in this section) which can be measured in a quantum optical setting. As a specific example, we focus on the setup shown in Fig. 3.1. We assume the detectors d_1 and d_2 are located at $\mathbf{R}_1$ and $\mathbf{R}_2$ respectively (Fig. 3.1). The spatial origin is chosen to be at the center of mass of the material. The positive-frequency part of the filtered electric field operator (in the Interaction Picture) along the direction of the detected polarization $\mathbf{e}_j$, seen by the detector d_j at location $\mathbf{R}_j$ (for $j \in \{1,2\}$), is given by

$$\begin{aligned} &\mathbf{e}_j^* \cdot \hat{\mathbf{E}}^{(+)}\left(\mathbf{R}_j, \tfrac{T}{2}\right) = i \sum_{\mathbf{k}} \sqrt{\frac{\omega_{\mathbf{k}}}{2\varepsilon \mathcal{V}}} \hat{a}_{\mathbf{k},\mathbf{e}_j} e^{i\left(\mathbf{k}\cdot\mathbf{R}_j - \omega_{\mathbf{k}}\frac{T}{2}\right)} f_j(\omega_{\mathbf{k}}), \text{ and} \\ &\hat{\mathbf{E}}^{(-)}(\mathbf{R}_j) \equiv \left[\hat{\mathbf{E}}^{(+)}(\mathbf{R}_j)\right]^\dagger, \end{aligned} \tag{3.7}$$

where $\hat{a}_{\mathbf{k},\mathbf{e}_j}$ is a photon annihilation operator for each orthogonal plane-wave mode of momentum $\mathbf{k}$ and polarization $\mathbf{e}_j$, and $\omega_{\mathbf{k}} = c|\mathbf{k}|$. Here, ε is the dielectric constant and $\mathcal{V}$ is the mode-volume of free-space (which can be taken to infinity at a suitable point). Each detector j could have its own sensitivity profile for modes of different frequencies determined by $f_j(\omega)$, a dimensionless filter function. Causality implies that the poles of $f_j(\omega)$, when seen as a function of complex frequency ω, can only lie in the lower half-plane.

We now assume $|\mathbf{R}_1| = cT/2$ for simplicity. Furthermore, we assume the two detectors $j = 1, 2$ are sensitive to the photons having momenta $\mathbf{k}$ within the thin solid angles δS_j around the directions $\mathbf{R}_j$. We also allow for the time delay between the detection events $\tilde{\tau}$. It is also convenient to introduce the retarded time τ as

$$\tau \equiv \tilde{\tau} - \frac{|\mathbf{R}_2| - |\mathbf{R}_1|}{c}. \tag{3.8}$$

We can now define an effective annihilation operator (which is related to the local electric field) that describes the photodetection by the detector d_j, as follows:

$$\hat{a}_{d_j} \equiv i \sum_{\mathbf{k}}{}' \sqrt{\frac{c\omega_{\mathbf{k}}}{2\mathcal{V}}} f_j(\omega_{\mathbf{k}}) \hat{a}_{\mathbf{k},\mathbf{e}_j}, \tag{3.9}$$

where $\sum_{\mathbf{k}}'$ restricts the direction of $\mathbf{k}$ to be within a solid angle $(\delta S)_j$ around the direction $\mathbf{R}_j$. The sum over $\mathbf{k}$ can be converted into an integral over frequencies $\omega_{\mathbf{k}}$:

$$\sum_{\mathbf{k}}{}' \sqrt{\frac{c\omega_{\mathbf{k}}}{2\mathcal{V}}} \longrightarrow (\delta S)_j \int \mathrm{d}\omega_{\mathbf{k}} \sqrt{\frac{c\omega_{\mathbf{k}}\mathcal{V}}{2}} \rho(\omega_{\mathbf{k}}). \tag{3.10}$$

Here, $\rho(\omega)$ represents the density of states of light modes per unit volume. In free space, $\rho(\omega) = \omega^2/(2\pi c)^3$. More generally, this density can be altered, for example, by the presence of a cavity. The conversion from a summation over wavevectors $\mathbf{k}$ to an integral over frequencies ω is valid because all matrix elements involving $\hat{a}_{\mathbf{k},\mathbf{e}_j}$ depend on $\mathbf{k}$ only through $\omega_{\mathbf{k}}$. We also define an effective filter function (for $j \in \{1, 2\}$):

$$\mathcal{F}_j(\omega) \equiv 2\pi c \rho(\omega) (\delta S)_j f_j(\omega). \tag{3.11}$$

When the filter is represented by a Fabry-Pérot cavity, we get:

$$\mathcal{F}_{j,\,\text{Lorentzian}}(\omega) = \frac{i\mathtt{K}_j \Gamma_j}{\omega - \omega_j + i\Gamma_j}, \tag{3.12}$$

where ω_j denotes the resonant frequency and

$$\mathtt{K}_j \equiv 2\pi c\rho(\omega_j)(\delta S)_j. \tag{3.13}$$

In deriving this expression, we assumed that the photonic density of states remains constant within the frequency window (filter resolution) defined by Γ_j, centered around ω_j. Similarly, other causal effective filter functions with different selectivity profiles could be considered [169].

With this setup in mind, we can provide an explicit mathematical definition of the photonic correlation functions.

3.3.2.1 Photon intensity $G^{(1)}(0)$

The intensity of light measured by the detector d_j of polarization $\mathbf{e}_j$, located at point $\mathbf{R}$ is

$$G^{(1)}_{d_j}(0) \equiv c\varepsilon \left\langle \Psi(T/2) \right| \left(\mathbf{e}_j \cdot \hat{\mathbf{E}}^{(-)}(\mathbf{R})\right) \left(\mathbf{e}_j^* \cdot \hat{\mathbf{E}}^{(+)}(\mathbf{R})\right) \left| \Psi(T/2) \right\rangle . \tag{3.14}$$

Here, the states and operators are represented in the Schrödinger picture. Transitioning to the interaction picture, using the definitions of $|\text{in}\rangle$, $|\text{out}\rangle$, and the mode $\hat{a}_{d_j}$ detected by the detector in (3.9), we can simplify the definition of $G^{(1)}$ to:

$$G^{(1)}_{d_j}(0) = \langle \text{out}| \, \hat{a}^\dagger_{d_j}(0)\hat{a}_{d_j}(0) \, |\text{out}\rangle \equiv \left\langle \hat{a}^\dagger_{d_j}(0)\hat{a}_{d_j}(0) \right\rangle_{\text{out}} . \tag{3.15}$$

Here, we have used the notation $\langle . \rangle_{\text{out}}$ to denote an expectation value taken in state $|\text{out}\rangle$.

3.3.2.2 Photon-pair correlation function $G^{(2)}(\tau)$

$G^{(2)}(\tau)$ characterizes the coincidence detection rate of two photons with a time delay $\tilde{\tau}$ (or τ, as defined in terms of the retarded time in Eq. (3.8)). Let the polarization states selected by the two detectors be $\mathbf{e}_1$ and $\mathbf{e}_2$, respectively. The photon-pair correlation function can then be defined as:

$$\begin{aligned} G^{(2)}_{d_1,d_2}(\tilde{\tau}) = c^2\varepsilon^2 \left\langle \Psi(T/2) \right| \left[\mathbf{e}_1 \cdot \hat{\mathbf{E}}^{(-)}(\mathbf{R}_1)\right] e^{i\hat{H}\tilde{\tau}} \left[\mathbf{e}_2 \cdot \hat{\mathbf{E}}^{(-)}(\mathbf{R}_2)\right] \\ \times \left[\mathbf{e}_2^* \cdot \hat{\mathbf{E}}^{(+)}(\mathbf{R}_2)\right] e^{-i\hat{H}\tilde{\tau}} \left[\mathbf{e}_1^* \cdot \hat{\mathbf{E}}^{(+)}(\mathbf{R}_1)\right] \left| \Psi(T/2) \right\rangle . \end{aligned} \tag{3.16}$$

The exponentials $e^{-i\hat{H}\tilde{\tau}}$ in this expression represent the fact that the whole system continues to evolve between the detection of the first and second photons. Let us suppose that the detection is in the far-field limit, i.e., the distance from the material $L = cT/2$ to the detector is much larger than the wavelengths of incident and scattered light, as well as the correlation length of the sample. Moreover, the time delay between detection events τ should be much smaller than $1/\gamma$, where γ is a relaxation rate of matter excitations, given by the maximum of various contributions such as spontaneous emission and phonon-mediated relaxation. Under these conditions, (see Fig. 3.3(b)), the light-matter interaction $\hat{V}$ has almost zero expectation value in the final state. This is because the light-matter interaction is $\sim \hat{\mathbf{A}}_T(\mathbf{x}) \cdot \hat{\boldsymbol{\mathcal{J}}}(\mathbf{x})$ (where $\hat{\mathbf{A}}_T(\mathbf{x})$ is the transverse part of the electromagnetic field and $\boldsymbol{\mathcal{J}}(\mathbf{x})$ is the electric current), and the support of $\hat{\mathbf{A}}_T(\mathbf{x})$ and that of $\hat{\mathcal{J}}(\mathbf{x})$ are spatially separated. Therefore, $\hat{V}$ does not have any effect after $t = T/2$. One can thus replace $e^{-i\hat{H}\tilde{\tau}}$ with the free evolution $e^{-i\hat{H}_0\tilde{\tau}}$ in Eq. 3.16. This equation can be even further simplified in the interaction picture, by using the retarded time τ (see Eq. 3.8), and using Eq. (3.9) to obtain:

$$G^{(2)}_{d_1,d_2}(\tau) = \left\langle \hat{a}^\dagger_{d_1}(0)\hat{a}^\dagger_{d_2}(\tau)\hat{a}_{d_2}(\tau)\hat{a}_{d_1}(0) \right\rangle_{\text{out}} . \tag{3.17}$$

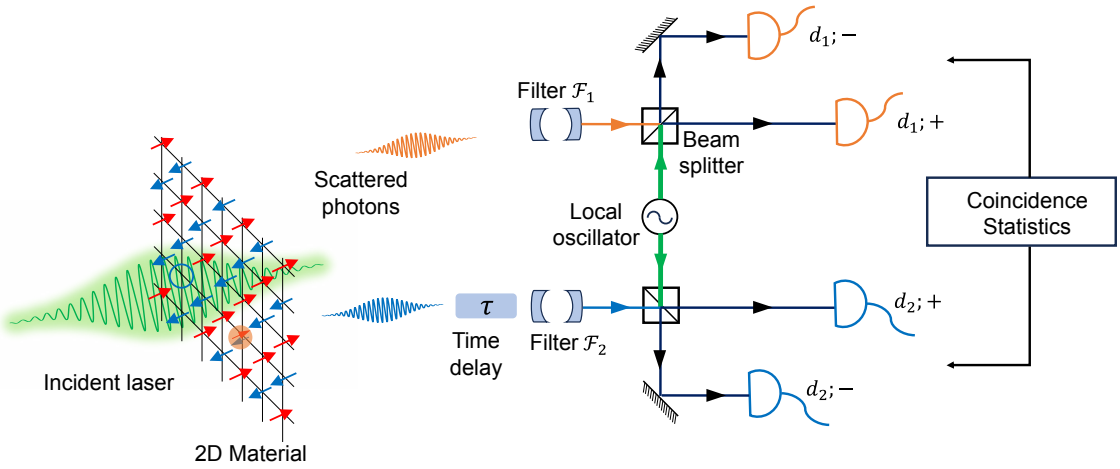

Figure 3.4: Optical scheme for the measurement of the phase-sensitive second-order quadrature correlations between a pair of photons scattered off the material Eq. (3.23). One of the photons (shown as blue) is subjected to an additional (retarded) time delay τ. After both photons pass through the respective frequency filters $\mathcal{F}_j$, each photon is mixed with a strong field of a local oscillator (annihilation operator denoted as $\hat{a}_{\text{L.O.}}$) using a beamsplitter. In our work, we consider the frequency of the local oscillator to be equal to the drive frequency ω_L. The phase difference of the local oscillator with respect to the drive laser can be tuned. If $\hat{a}_{\lambda_j}$ is a scattered photonic mode, then for each of the two beam-splitters, the mode through each of the two output arms, $+1$ and -1 is $\frac{1}{\sqrt{2}}\left(\hat{a}_{\lambda_j} \pm \hat{a}_{\text{L.O.}}\right)$ respectively. First, let us consider the output from just one of the filters $\mathcal{F}_j$. The difference $G^{(1)}_{d_j;+} - G^{(1)}_{d_j;-}$ between the two arms of the beam splitter is proportional to a quadrature measurement $\left\langle \hat{a}_{d_j} \right\rangle e^{i\theta} + \text{c.c.}$ Now, let us consider the output from both the filters $\mathcal{F}_1$ and $\mathcal{F}_2$. We show that by measuring $G^{(2)}$ correlations between the output arms of the beam-splitter and by taking a suitable linear combination [Eq. (3.25)], one can measure phase-sensitive second-order quadrature correlations between the scattered photons $\langle \hat{a}_{d_2}(\tau)\hat{a}_{d_1}(0)\rangle$.

The "connected" component of this correlation function can be defined as:

$$\mathcal{G}^{(2)}_{d_1,d_2}(\tau) \equiv G^{(2)}_{d_1,d_2}(\tau) - G^{(1)}_{d_1}(0)G^{(1)}_{d_2}(0). \tag{3.18}$$

3.3.2.3 Quadrature measurements

So far, we considered the photonic correlation functions $G^{(1)}(0)$ and $G^{(2)}(\tau)$, which are related to photon *number* and its *fluctuations* respectively, and lack information about the phase of the electric field. The phase-sensitive information can be measured by using a homodyne

detection scheme where the scattered photons are mixed with a strong field of a local oscillator (see for example, Chapter 4 of Ref. [170] and Chapter 7 of Ref. [171]). We review below how one can measure an arbitrary "quadrature" of the electric field $\hat{a}_\lambda e^{i\theta} + \text{h.c.}$, for any θ. The setup is shown in Fig. 3.4.

Consider a strong local oscillator $\hat{a}_{\text{L.O.}}$ with the same frequency ω_L as the incoming laser. Here, we will replace $\sqrt{\frac{\omega_L c}{\mathcal{V}}}\hat{a}_{\text{L.O.}}(t)$ by its classical expectation value $-i\sqrt{I_{\text{L.O.}}}e^{-i(\omega_L t+\theta+\theta_L)}$. Here, $I_{\text{L.O.}} \equiv \frac{\langle \hat{a}^\dagger_{\text{L.O.}}\hat{a}_{\text{L.O.}}\rangle \omega_L c}{\mathcal{V}}$ is the intensity of the local oscillator, $\mathcal{V}$ is its mode volume, and θ is the tunable *relative* phase difference between the local oscillator and the drive laser (whose phase is θ_L).

In our proposed setup, each scattered photon after passing through the frequency filter is admixed with the local oscillator using a beamsplitter. If the input modes going into a beamsplitter are $\hat{a}_\lambda$ and $\hat{a}_{\text{L.O.}}$, the output modes are $\frac{1}{\sqrt{2}}(\hat{a}_\lambda \pm \hat{a}_{\text{L.O.}})$. Under filtering followed by admixture with the local oscillator (as shown in Fig. 3.4), the annihilation operator $\hat{a}_{d_j}$ corresponding to detector d_j (defined in Eq. (3.9)) gets transformed as

$$\hat{\mathbb{a}}_{d_j;s}(t) \equiv \frac{\hat{a}_{d_j}(t)}{\sqrt{2}} \pm \frac{\sqrt{I_{\text{L.O.}}}}{2} e^{-i(\omega_L t+\theta+\theta_L)}, \tag{3.19}$$

depending on s, the output arm of the beamsplitter, where s can be $+$ or $-$.

First, one measures $G^{(1)}(0)$ of the transformed modes:

$$G^{(1)}_{d_j;s}(\theta;0;t) = \left\langle \hat{\mathbb{a}}^\dagger_{d_j;s}(t)\hat{\mathbb{a}}_{d_j;s}(t)\right\rangle_{\text{out}}. \tag{3.20}$$

Here, in writing $G^{(1)}_{d_j;s}(0;t)$, the θ in the argument refers to the phase of the local oscillator with

respect to the drive, the 0 implies that the creation and annihilation operators are at equal time, while t denotes the time at which the measurement is done. The t-dependence arises because of the time-dependence of the local oscillator.

By substituting Eq. (3.19) in Eq. (3.20), one can show that

$$G^{(1)}_{d_j;+}(\theta;0;t) - G^{(1)}_{d_j;-}(\theta;0;t) = \sqrt{\frac{I_{\text{L.O.}}}{2}} \left(\left\langle \hat{a}_{d_j}(t) \right\rangle_{\text{out}} e^{i(\omega_L t+\theta)} + \text{c.c.} \right). \tag{3.21}$$

We show in Appendix C.4 that upon time-averaging the above measurement, one can extract the t-independent contribution $\left\langle \hat{a}_{d_j}(0) e^{i\theta} \right\rangle$ + c.c. reported in Table 3.1. By taking appropriate linear combinations of this quantity, one can thus measure:

$$X^{+}_{d_j}(0) = \left\langle \hat{a}_{d_j}(0) \right\rangle_{\text{out}}. \tag{3.22}$$

3.3.2.4 Phase-sensitive second-order quadrature measurements

Furthermore, we show below that the setup in Fig. 3.4 can be used to obtain phase-sensitive second order quadrature correlations:

$$X^{++}_{d_1,d_2}(\tau) = \langle \hat{a}_{d_2}(\tau) \hat{a}_{d_1}(0) \rangle_{\text{out}}. \tag{3.23}$$

To obtain the above, we consider measurements of $G^{(2)}$ between different arms of the beamsplitters:

$$G^{(2)}_{d_1,d_2;s_1,s_2}(\theta;\tau;t) = \left\langle \hat{\mathbb{O}}^{\dagger}_{d_1;s_1}(t) \hat{\mathbb{O}}^{\dagger}_{d_2;s_2}(t+\tau) \hat{\mathbb{O}}_{d_2;s_2}(t+\tau) \hat{\mathbb{O}}_{d_1;s_1}(t) \right\rangle_{\text{out}}. \tag{3.24}$$

By substituting Eq. (3.19) in Eq. (3.24), one can show that (we suppress the indices d_1, d_2 for simplicity):

$$\begin{aligned}&\left(G^{(2)}_{+,+} + G^{(2)}_{-,-} - G^{(2)}_{+,-} - G^{(2)}_{-,+}\right)(\theta;\tau;t)\\ &= \frac{I_{\text{L.O.}}}{2}\left[\left(e^{2i(\omega_L t+\theta)+i\omega_L\tau}\left\langle\hat{a}_{d_2}(t+\tau)\hat{a}_{d_1}(t)\right\rangle_{\text{out}} + e^{-i\omega_L\tau}\langle\hat{a}^\dagger_{d_2}(t+\tau)\hat{a}_{d_1}(t)\rangle_{\text{out}}\right) + \text{c.c.}\right].\end{aligned} \tag{3.25}$$

The above correlation function comprises both a phase-dependent contribution:

$$e^{2i(\omega_L t+\theta)+i\omega_L\tau}\left\langle\hat{a}_{d_2}(t+\tau)\hat{a}_{d_1}(t)\right\rangle_{\text{out}},$$

as well as a phase-independent contribution:

$$e^{-i\omega_L\tau}\langle\hat{a}^\dagger_{d_2}(t+\tau)\hat{a}_{d_1}(t)\rangle_{\text{out}}.$$

These two terms can be experimentally separated out by measuring Eq. (3.25) for different values of θ, because the former depends on θ (the phase of the local oscillator), but the latter does not. In other words, we consider the following difference for different values of θ_A and θ_B:

$$\begin{aligned}&\left(G^{(2)}_{+,+} + G^{(2)}_{-,-} - G^{(2)}_{+,-} - G^{(2)}_{-,+}\right)(\theta_A;\tau;t) - \left(G^{(2)}_{+,+} + G^{(2)}_{-,-} - G^{(2)}_{+,-} - G^{(2)}_{-,+}\right)(\theta_B;\tau;t)\\ =&\frac{I_{\text{L.O.}}}{2}\left[\left(e^{2i\theta_A} - e^{2i\theta_B}\right)e^{i\omega_L(2t+\tau)}\left\langle\hat{a}_{d_2}(t+\tau)\hat{a}_{d_1}(t)\right\rangle_{\text{out}} + \text{ c.c.}\right].\end{aligned} \tag{3.26}$$

Once again, the above equation has a t-dependence. We show in Appendix C.4 that by time-averaging, one can extract the phase-sensitive second order quadrature correlator presented in Table 3.1 and Eq. (3.23).

We note that the above phase-sensitive second order quadrature measurement shown in

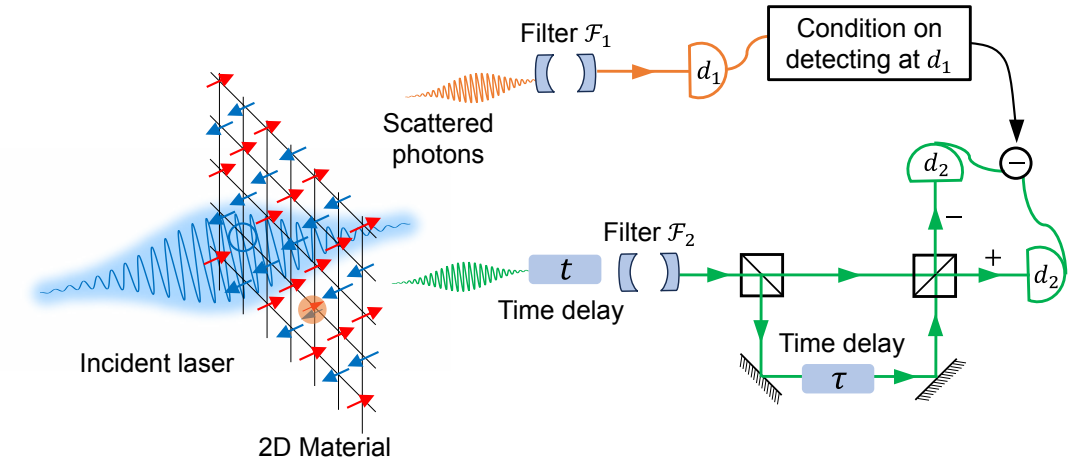

Figure 3.5: Measurement scheme for $H_{d_1,d_2}(t,\tau) \equiv \langle \hat{a}^\dagger_{d_1}(0)\hat{a}^\dagger_{d_2}(t+\tau)\hat{a}_{d_2}(t)\hat{a}_{d_1}(0)\rangle_{\text{out}} + \text{c.c.}$, which can be thought of as a $G^{(1)}(\tau)$ measurement at detector d_2 conditioned on detecting a photon at d_1. The mode shown in green here is split into two paths using a beamsplitter, and one of the paths is given a time delay τ with respect to the other. The two paths are made to interfere, and two $G^{(2)}$ measurements are taken between d_1 and each arm of d_2. We show in Appendix C.4 that the desired correlator can be obtained this way.

Fig. 3.4 is related to two-mode squeezing that has been measured experimentally [172, 173].

3.3.2.5 $G^{(1)}(\tau)$ and Conditional $G^{(1)}(\tau)$

By beating a mode with its own time-delayed counterpart, one can also measure the following correlator:

$$G^{(1)}_{d_j}(\tau) = \langle \hat{a}^\dagger_{d_j}(\tau)\hat{a}_{d_j}(0)\rangle_{\text{out}} + \text{c.c.}. \tag{3.27}$$

In this work, we also consider the following correlation function, obtained by measuring $G^{(1)}(\tau)$ by detector d_2 conditioned on detecting a photon at d_1.

$$H_{d_1,d_2}(t,\tau) = \langle \hat{a}^\dagger_{d_1}(0)\hat{a}^\dagger_{d_2}(t+\tau)\hat{a}_{d_2}(t)\hat{a}_{d_1}(0)\rangle_{\text{out}} + \text{c.c.} \tag{3.28}$$

The corresponding measurement scheme is shown in Fig. 3.5 and described in Appendix C.4.

Having defined the photonic correlators, we now turn to the matter sector in the next section. To establish a connection from the photonic correlators in Eq. (3.15), Eq. (3.17), and Eq. (3.22-3.28), to the corresponding matter correlation functions, it is necessary to know the form of the $\hat{\mathcal{T}}$-matrix that acts on $|\text{in}\rangle$. This requires knowledge of the material's Hamiltonian $\hat{H}_0$ and light-matter interaction $\hat{V}$.

3.4 Light scattering off a single-band Fermi-Hubbard model at half-filling

In this section, we describe the microscopic matter Hamiltonian, light-matter interaction, and the relevant energy scales. We explicitly work out the mapping between photonic and matter correlations when $\hat{H}_0$ is a single-band Fermi-Hubbard model of spin $1/2$ electrons at half-filling, and the light-matter interaction $\hat{V}$ is obtained by Peierls' substitution. Our procedure can then be readily adapted to any other system as long as its ground state is an insulator, i.e., the electrically charged degrees of freedom are gapped. Let us now consider the following Hamiltonian,

$$\hat{H}_0 = \sum_{(\mathbf{r},\boldsymbol{\mu}),\sigma} \left[-\mathtt{t}_{\mathbf{r},\mathbf{r}+\boldsymbol{\mu}} \hat{c}^\dagger_{\mathbf{r}+\boldsymbol{\mu},\sigma} \hat{c}_{\mathbf{r},\sigma}\right] + \text{h.c.} + U \sum_{\mathbf{r}} \hat{n}_{\mathbf{r},\uparrow} \hat{n}_{\mathbf{r},\downarrow} + \sum_{\mathbf{k},\mathbf{e}_\mathbf{k}} \omega_\mathbf{k} \left(\hat{a}^\dagger_{\mathbf{k},\mathbf{e}_\mathbf{k}} \hat{a}_{\mathbf{k},\mathbf{e}_\mathbf{k}} + \frac{1}{2}\right), \tag{3.29}$$

where $\mathtt{t}_{\mathbf{r},\mathbf{r}+\boldsymbol{\mu}}$ is the tunneling coefficient between sites $\mathbf{r}$ and $\mathbf{r}+\boldsymbol{\mu}$. We denote the nearest-neighbor tunneling by $\mathtt{t}$. For example, for a square lattice with nearest-neighbor tunneling, $\boldsymbol{\mu}$ is $\mathtt{a}(1,0)$ or $\mathtt{a}(0,1)$. However, in general, $\boldsymbol{\mu}$ can connect site $\mathbf{r}$ to an arbitrary site $\mathbf{r}+\boldsymbol{\mu}$, if $\mathtt{t}_{\mathbf{r},\mathbf{r}+\boldsymbol{\mu}} \neq 0$, and we say there is a *bond* $(\mathbf{r},\boldsymbol{\mu})$ regardless of whether it is nearest-neighbor. To avoid double counting, $\boldsymbol{\mu}$ runs through half the set of bonds. Operator $\hat{c}^\dagger_{\mathbf{r},\sigma}$ creates an electron of spin $\sigma = \uparrow$ or $\downarrow$ in a Wannier orbital localized at lattice site $\mathbf{r}$. The electronic spin operator is

defined as:

$$\hat{\mathbf{S}}_{\mathbf{r}} = \frac{1}{2} \sum_{\alpha,\beta} \hat{c}^{\dagger}_{\mathbf{r},\alpha} \boldsymbol{\sigma} \hat{c}_{\mathbf{r},\beta}, \tag{3.30}$$

where $\boldsymbol{\sigma}$ is a vector formed by the three Pauli matrices.

Under the Peierls' substitution, the full light-matter Hamiltonian $\hat{H}$ is obtained from $\hat{H}_0$ by substituting $\mathtt{t}_{\mathbf{r},\mathbf{r}+\boldsymbol{\mu}}$ with

$$\mathtt{t}_{\mathbf{r},\mathbf{r}+\boldsymbol{\mu}} \to \mathtt{t}_{\mathbf{r},\mathbf{r}+\boldsymbol{\mu}} e^{iq_e \int_{\mathbf{r}}^{\mathbf{r}+\boldsymbol{\mu}} \mathrm{d}\mathbf{x} \cdot \hat{\mathbf{A}}(\mathbf{x})}, \tag{3.31}$$

where q_e is the charge of the electron, $\hat{\mathbf{A}}(\mathbf{r})$ is the vector potential of the electromagnetic field. By Helmholtz decomposition, any vector field can be decomposed uniquely as a sum of transverse (divergence-free) and longitudinal (curl-free) components. The transverse component of $\hat{\mathbf{A}}(\mathbf{r})$ is invariant under an arbitrary gauge transformation $\mathbf{A}(\mathbf{r}) \to \mathbf{A}(\mathbf{r}) + \boldsymbol{\nabla}\theta(\mathbf{r})$ for some scalar field $\theta(\mathbf{r})$. The transverse component, called $\hat{\mathbf{A}}_T(\mathbf{r})$ can be expanded in terms of the normal modes of radiation in free space, $\hat{a}_{\mathbf{k},\mathbf{e}_\mathbf{k}}$ (introduced in Eq. (3.7)) as:

$$\hat{\mathbf{A}}_T(\mathbf{r}) = \sum_{\mathbf{k},\mathbf{e}_\mathbf{k}} \frac{1}{\sqrt{2\varepsilon \mathcal{V} \omega_\mathbf{k}}} \left(\mathbf{e}_\mathbf{k} \hat{a}_{\mathbf{k},\mathbf{e}_\mathbf{k}} e^{i\mathbf{k}\cdot\mathbf{r}} + \mathbf{e}^*_\mathbf{k} \hat{a}^{\dagger}_{\mathbf{k},\mathbf{e}_\mathbf{k}} e^{-i\mathbf{k}\cdot\mathbf{r}} \right) \tag{3.32}$$

and $\mathbf{e}_\mathbf{k}$ is the mode polarization, and satisfies $\mathbf{k} \cdot \mathbf{e}_\mathbf{k} = 0$. We note that quantizing the transverse part of the vector potential is a gauge-invariant notion. For simplicity, we also choose the Coulomb gauge, i.e.,

$$\mathbf{A}(\mathbf{r}) = \mathbf{A}_T(\mathbf{r}). \tag{3.33}$$

In the Coulomb gauge, longitudinal electric fields are obtained entirely from the scalar potential ϕ as $\mathbf{E}_L(\mathbf{r}) = -\boldsymbol{\nabla}\phi$. Gauss's law implies that $-\boldsymbol{\nabla}^2\phi(\mathbf{x}) = q_e\rho(\mathbf{x})$, where $\rho(\mathbf{x})$ is the electron

density. Integrating out ϕ results in the usual density-density Coulomb interaction found in all electronic systems. For the purpose of this work, this Coulomb interaction can be thought to have been screened leaving behind the on-site Hubbard repulsion in the Hamiltonian Eq. (3.29). Thus, longitudinal electric fields arise purely from matter density fluctuations and not from electromagnetic radiation. Therefore, we can consider light-matter interactions in the Coulomb gauge without loss of generality.

Thus, the light-matter interaction $\hat{V}$ (defined such that the full Hamiltonian $\hat{H} = \hat{H}_0 + \hat{V}$), resulting from Peierls' substitution in Eq. (3.31) is given by:

$$\begin{aligned}\hat{V} = \sum_{(\mathbf{r},\boldsymbol{\mu}),\sigma} \Big\{ & -i \left(\mathtt{t}_{\mathbf{r},\mathbf{r}+\boldsymbol{\mu}} \hat{c}^{\dagger}_{\mathbf{r}+\boldsymbol{\mu},\sigma} \hat{c}_{\mathbf{r},\sigma} - \text{h.c.} \right) \sin\left(q_e \hat{A}_{\mathbf{r},\mathbf{r}+\boldsymbol{\mu}} \right) \\ & + \left(\mathtt{t}_{\mathbf{r},\mathbf{r}+\boldsymbol{\mu}} \hat{c}^{\dagger}_{\mathbf{r}+\boldsymbol{\mu},\sigma} \hat{c}_{\mathbf{r},\sigma} + \text{h.c.} \right) \left[1 - \cos\left(q_e \hat{A}_{\mathbf{r},\mathbf{r}+\boldsymbol{\mu}} \right) \right] \Big\} ,\end{aligned} \tag{3.34}$$

where $\hat{A}_{\mathbf{r},\mathbf{r}+\boldsymbol{\mu}} \equiv \int_{\mathbf{r}}^{\mathbf{r}+\boldsymbol{\mu}} \mathrm{d}\mathbf{x} \cdot \hat{\mathbf{A}}(\mathbf{x}) \approx \hat{\mathbf{A}}\left(\mathbf{r} + \boldsymbol{\mu}/2\right) \cdot \boldsymbol{\mu}$.

A remark is due here regarding Peierls' substitution. The single-band Fermi-Hubbard model should be viewed as the projection of a continuum model into the lowest energy Wannier orbital. Determining the true light-matter coupling term in such projected models is not trivial. The interaction terms could generically be modified [174, 175], for instance, by pair-hopping terms modulated by coupling to the gauge field. In this work, however, following Ref. [7, 8, 54], we restrict ourselves to the toy problem where the light-matter coupling is obtained by Peierls' substitution, which is manifestly gauge-invariant.

3.4.1 Overview of energy scales and sectors

Let us now look at the energy scales in the problem at half-filling (i.e., the number of electrons equals the number of lattice sites) in the limit $\mathtt{t} \ll U$, where the ground state is a Mott-insulator. In this limit, the manifold of energy eigenstates *that can be accessed by applying local operators on the ground state* split up into sectors as shown in Fig. 3.6.

In the lowest energy sector (shaded blue), called the spin sector, or lower Hubbard band, the charge degree of freedom is frozen and the excitations lie purely in the spin sector. If the ground state is a conventionally ordered state, these excitations are magnons and if the ground state is a quantum spin liquid, then these states can be composites of fractionalized excitations. The bandwidth of this sector is of the order of $J \approx \mathtt{t}^2/U$. The sector shaded yellow, roughly separated by an energy U from the spin sector, called the charge sector or upper Hubbard band, consists of states where one site is doubly occupied (called a doublon) and one site is empty (called a hole). The states in this sector include bound-states of doublons and holes, called Mott excitons [154, 155, 156, 157, 158, 159, 160, 161, 162, 163, 164, 165, 166, 167], as well as their scattering states. We expect the bandwidth of this sector to be of order $\mathtt{t}$. The sector shaded red consists of states with two doublon-hole pairs and has an energy of order $2U$ relative to the spin sector.

Similar to Ref. [7, 8, 54], we assume that the laser frequency ω_L satisfies

$$\mathtt{t} \ll |U - \omega_L| \ll U. \tag{3.35}$$

In other words, the laser is detuned from the Fermi-Hubbard repulsion U, and the detuning,

though small compared to U, is large compared to $\mathtt{t}$. This assumption allows us to do perturbation theory in both $\mathtt{t}/|U-\omega_L|$ and $\mathtt{t}/U$.

The second small parameter is the laser-matter coupling that is involved during each photon absorption. Expanding the light-matter interaction from Peierls' substitution in Eq. (3.31) to leading order in q_e, one gets the paramagnetic interaction $q_e\hat{\mathbf{A}}\cdot\hat{\boldsymbol{\mathcal{J}}}$, where $\hat{\boldsymbol{\mathcal{J}}}$ is the electric current. Further, expanding $\hat{\mathbf{A}}$ using Eq. (3.32), we get an interaction term $\sim \mathtt{t}\frac{q_e\mathtt{a}}{\sqrt{2\varepsilon\mathcal{V}\omega_L}}\hat{a}_L\hat{c}^\dagger_{\mathbf{r}}\hat{c}_{\mathbf{r}'}$. If the input state (of the laser field) is a Fock state, the operator $\hat{a}_L$ can be replaced by $\sqrt{\mathcal{N}_L}$, where $\mathcal{N}_L$ is the average number of photons in the laser mode. For a coherent state input $e^{\phi_L a_L^\dagger-\phi_L^* a_L}|0\rangle$ having the amplitude ϕ_L, $N_L=|\phi_L|^2$. Denoting the intensity of the laser as $I_L=\frac{\mathcal{N}_L\omega_L c}{\mathcal{V}}$ and $I_L=\frac{|\phi_L|^2\omega_L c}{\mathcal{V}}$ for the Fock-state and coherent inputs, respectively, we can define a dimensionless light-matter coupling:

$$g_L=\frac{q_e\mathtt{a}\sqrt{\mathcal{N}_L}}{\sqrt{2\varepsilon\mathcal{V}\omega_L}}\equiv\frac{\sqrt{2\pi I_L\alpha}\,\mathtt{a}}{\omega_L}, \tag{3.36}$$

where $\mathtt{a}$ is the lattice spacing and where $\alpha=\frac{q_e^2}{4\pi\varepsilon c}$ is the fine-structure constant. We can also interpret g_L as the ratio of the effective Rabi frequency of the laser drive to the laser frequency ω_L. In this work, we will assume that $g_L\ll 1$.

Similarly, the interaction term corresponding to a photon emission into an unoccupied mode $(\mathbf{k},\mathbf{e}_j)$ is $\sim \mathtt{t}\frac{q_e\mathtt{a}}{\sqrt{2\varepsilon\mathcal{V}\omega_{\mathbf{k}}}}\hat{a}^\dagger_{\mathbf{k},\mathbf{e}_j}\hat{c}^\dagger_{\mathbf{r}}\hat{c}_{\mathbf{r}'}$. This suggests another dimensionless coupling in the problem: $\frac{q_e\mathtt{a}}{\sqrt{2\varepsilon\mathcal{V}\omega_{\mathbf{k}}}}$, which we rewrite as $\sqrt{\pi\alpha}\mathtt{a}\sqrt{\frac{2c}{\omega_{\mathbf{k}}\mathcal{V}}}$. We see from Eq. (3.9),(3.10),(3.11) that the factor $\sqrt{\frac{2c}{\omega_{\mathbf{k}}\mathcal{V}}}$ cancels in the final expressions for $G^{(1)}$ and $G^{(2)}$. Hence we define the following dimensionful light-matter coupling

$$g\equiv\sqrt{\pi\alpha}\mathtt{a}, \tag{3.37}$$

with the understanding that the dimensionless small parameter corresponding to g is essentially

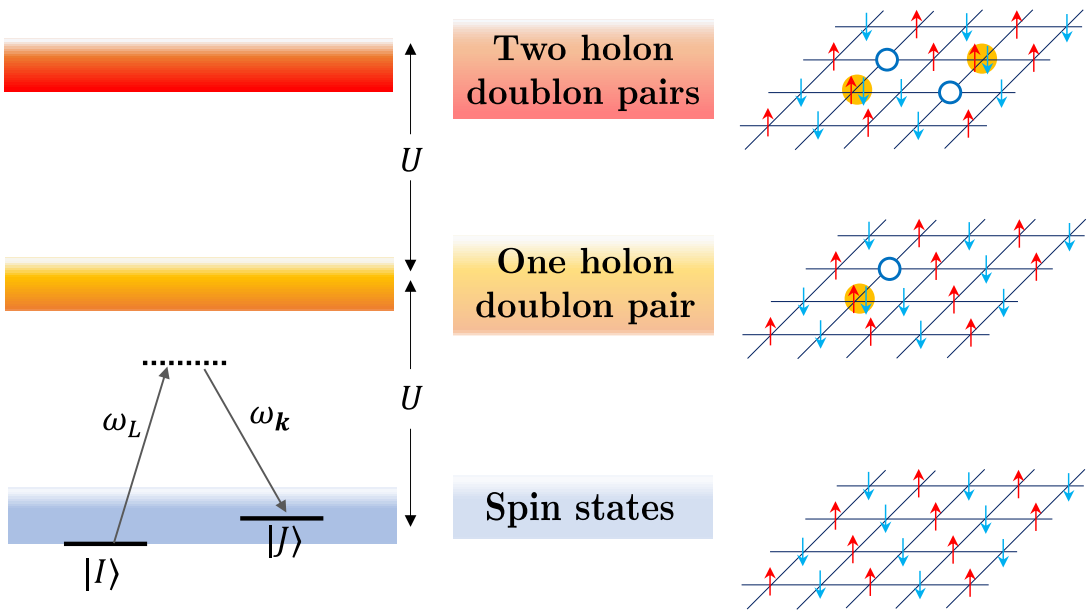

Figure 3.6: Schematic representation of the energy eigenstates accessible by applying local operators to the ground state of the Fermi-Hubbard model at half-filling. The eigenstates are divided into distinct sectors: the lowest-energy sector (light blue) consists of spin states with frozen charge degrees of freedom, while the next two sectors (orange and red) are separated by approximately U and correspond to states with one and two doublon-hole pairs, respectively. A Raman process is illustrated: starting from a state $|I\rangle$ in the spin sector, photon absorption leads to virtual occupation of a state in the one-doublon-hole sector, followed by photon emission into mode $\mathbf{k}$, resulting in the material returning to a potentially different state $|J\rangle$ in the spin sector. Here we use dotted lines to depict virtually occupied states. The dotted line here is placed at the energy $E_I + \omega_L$, even though there is no state at that energy in the matter Hamiltonian.

$\sqrt{\alpha}$.

In the following sections, we present expressions for $G^{(1)}$, $G^{(2)}$, and quadrature correlations, calculated to leading order in the small parameters $\mathtt{t}/U$, $\mathtt{t}/|U - \omega_L|$, g_L, and $\sqrt{\alpha}$.

3.4.2 Form of relevant terms in the $\hat{\mathcal{T}}$-matrix

According to the expansion of the $\hat{\mathcal{T}}$-matrix, the amplitude of the emission of each additional photon is accompanied by a multiplicative factor of g, (and therefore a factor of the small parameter $\sqrt{\alpha}$). Therefore, we can restrict our analysis to processes that result in the emission of

at most two photons, which is the minimal number required for a nonzero $G^{(2)}$.

With this in mind, let us examine the relevant terms in the expression $\hat{\mathcal{T}} = \hat{V} + \hat{V}\hat{\mathbb{G}}_0\hat{V} + \hat{V}\hat{\mathbb{G}}_0\hat{V}\hat{\mathbb{G}}_0\hat{V} + \hat{V}\hat{\mathbb{G}}_0\hat{V}\hat{\mathbb{G}}_0\hat{V}\hat{\mathbb{G}}_0\hat{V} + \ldots$, where $\hat{V}$ is given by Eq. (3.34). We will do a small $\sqrt{\alpha}$ expansion, expanding Eq. (3.34) order by order in $q_e\hat{\mathbf{A}}$. Later, in Sec. 3.5, we provide a discussion about the order at which this expansion can be truncated. But for now, let us make some general conclusions. The (transverse part of) vector potential $\hat{\mathbf{A}}$ can be expanded in terms of $\sim \hat{a}_\lambda + \hat{a}_\lambda^\dagger$, where $\hat{a}_\lambda^\dagger$ is a photon creation operator in mode λ. Thus, each factor of $q_e\hat{\mathbf{A}}$ can lead to either absorption (via $\hat{a}_\lambda$) or emission ($\hat{a}_\lambda^\dagger$) of a photon. In general, one can have arbitrary numbers of photon absorptions and emissions. However, using the energy scales discussed in Sec. 3.4.1, i.e., $\mathtt{t} \ll |U - \omega_L| \ll U$, we can substantially reduce the number of possibilities. Further, we make the approximation that photons can be only absorbed from the laser. Once a photon is emitted into a different mode λ, it never gets absorbed.

With these simplifications, let us consider the part of $\hat{\mathcal{T}}$ leading to the emission of one photon, labeled $\hat{\mathcal{T}}^{(1)}$. As shown in Fig. 3.6, starting from a state in the spin sector, the emission of a photon requires the absorption of a photon from the laser. Consequently, to leading order:

$$\hat{\mathcal{T}}^{(1)} = \sum_{\mathbf{k}} \hat{R}^{(1)}_{(\mathbf{k},\mathbf{e}_j)} \otimes \hat{a}^\dagger_{\mathbf{k},\mathbf{e}_j}\hat{a}_L \sqrt{\frac{2c}{\mathcal{V}\omega_{\mathbf{k}}\mathcal{N}_L}} + \ldots, \tag{3.38}$$

where $\mathbf{e}_j$ is the polarization selected by the detector. The normalization factor $\sqrt{\frac{2c}{\mathcal{V}\omega_{\mathbf{k}}\mathcal{N}_L}}$ is chosen to simplify subsequent expressions.

We now turn to processes that result in the emission of two photons. In this work, we assume that the detector selectively filters photons, allowing only those with frequencies within the range $\omega_L \pm O(|\omega_L - U|)$. For example, as a result, photons with a frequency of $2\omega_L - U$ are

detected, while those with a frequency of $\omega_L/2$ are not. Under these conditions, we can see that: (1) it is sufficient to consider processes where two photons are absorbed, and (2) after absorbing two photons and emitting two photons, the final state of the material is in the spin sector.

Thus, the term in $\hat{\mathcal{T}}$ that contributes to the emission of two photons, which we label as $\hat{\mathcal{T}}^{(2)}$, takes the following form (we use the shorthand notation λ_j for the mode $(\mathbf{k}, \mathbf{e}_{\lambda_j})$ of frequency ω_{λ_j}, where $\mathbf{e}_{\lambda_j}$ is the polarization detected by detector j):

$$\hat{\mathcal{T}}^{(2)} = \sum_{\lambda_1,\lambda_2} \hat{R}^{(2)}_{\lambda_1,\lambda_2} \otimes \frac{\hat{a}^\dagger_{\lambda_1}\hat{a}^\dagger_{\lambda_2}\left(\hat{a}_L\right)^2}{2\sqrt{\mathcal{N}_L(\mathcal{N}_L-1)}} \frac{2c}{\mathcal{V}\sqrt{\omega_{\lambda_1}\omega_{\lambda_2}}} + \dots \tag{3.39}$$

where $\hat{R}^{(2)}_{\lambda_1,\lambda_2}$ is a pure matter operator and will be calculated in the next section. $\hat{R}^{(2)}_{\lambda_1,\lambda_2}$ is symmetric in λ_1 and λ_2. Here, $\hat{a}^\dagger_{\lambda_1}\hat{a}^\dagger_{\lambda_2}\left(\hat{a}_L\right)^2$ signifies that two photons are absorbed from the laser and two photons are emitted into modes λ_1 and λ_2. The remaining factors are due to our normalization convention. We note that while summing over modes λ_1 and λ_2, the polarizations can be fixed to correspond to those selected by the detectors, reducing the summation to the associated momenta only. The full $\hat{\mathcal{T}}$-matrix is the sum $\hat{\mathcal{T}} = \hat{\mathcal{T}}^{(1)} + \hat{\mathcal{T}}^{(2)} + \dots$.

3.4.3 Expressions for photonic correlation functions in terms of matter operators $\hat{R}^{(1)}$ and $\hat{R}^{(2)}$

Recall that the photonic correlations defined in Eqs. (3.15), (3.17), (3.22), (3.23) and (3.27) are expectation values in the $|\text{out}\rangle$ state, which can be determined from the $|\text{in}\rangle$ state using the $\hat{\mathcal{T}}$-matrix. We now use the form of the $\hat{\mathcal{T}}$-matrix in Eqs. (3.38) and (3.39) to express the photonic correlation functions in terms of matter operators $\hat{R}^{(1)}$ and $\hat{R}^{(2)}$. The result of this subsection should be seen as an intermediate step, which will later be used along with more input from

microscopic details to derive the results in Table 3.1.

To begin, let us assume that the $|\text{in}\rangle$ state is a product state between the matter and light degrees of freedom.

$$|\text{in}\rangle = |I\rangle_M \otimes |\psi_L^{(0)}\rangle_R, \tag{3.40}$$

where $|I\rangle_M$ is an energy eigenstate of the matter part of $\hat{H}_0$ (hence subscript M) with energy E_I. $|\psi_L^{(0)}\rangle_R$ is a state in the electromagnetic sector with the laser mode occupied (we use subscript L to denote "laser" and subscript R to denote the "radiation" sector). Since Eq. (3.5) is easiest to apply for an $|\text{in}\rangle$ state that is an eigenstate of $\hat{H}_0$, we can consider $|\psi_L^{(0)}\rangle_R$ to be a Fock state with $\mathcal{N}_L$ photons in laser mode L, a mode with well-defined wavevector and polarization, i.e.,

$$|\psi_L^{(0)}\rangle_R = \frac{1}{\sqrt{\mathcal{N}_L!}} \left(\hat{a}_L^\dagger\right)^{\mathcal{N}_L} |0\rangle_R . \tag{3.41}$$

In Appendix C.2, we show that we can also have the laser mode L to be populated with a coherent state and still be able to calculate $|\text{out}\rangle$ to use Eq. (3.5). In that case,

$$|\psi_L^{(0)}\rangle_R = e^{\phi_L \hat{a}_L^\dagger - \phi_L^* \hat{a}_L} |0\rangle_R . \tag{3.42}$$

Here, $\phi_L \equiv |\phi_L| e^{-i\theta_L}$. Using Eq. (3.38), (3.39) and Eq. (3.5), to leading order in g, we get the $|\text{out}\rangle$ state to be a superposition of the unscattered $|\text{in}\rangle$ state, and states resulting from one and

two-photon scattering:

$$
\begin{aligned}
|\text{out}\rangle &= |I\rangle \otimes |\psi_L^{(0)}\rangle \\
&\quad - 2\pi i \sum_{\lambda} \sum_{F} \delta(E_{FI} + \omega_\lambda - \omega_L)\, |F\rangle \sqrt{\frac{2c}{\mathcal{V}\omega_\lambda}} e^{-i\theta_L} \langle F|\, \hat{R}_\lambda^{(1)}\, |I\rangle \otimes \hat{a}_\lambda^\dagger |\psi_L^{(1)}\rangle \\
&\quad - 2\pi i \sum_{\lambda_1,\lambda_2} \sum_{F} \delta(E_{FI} + \omega_{\lambda_1} + \omega_{\lambda_2} - 2\omega_L)\, |F\rangle \frac{2ce^{-2i\theta_L}}{\mathcal{V}\sqrt{\omega_{\lambda_1}\omega_{\lambda_2}}} \langle F|\, \hat{R}^{(2)}_{\lambda_1,\lambda_2}\, |I\rangle \otimes \frac{\hat{a}^\dagger_{\lambda_1}\hat{a}^\dagger_{\lambda_2}}{2} |\psi_L^{(2)}\rangle.
\end{aligned}
\tag{3.43}
$$

We used the notation $E_{FI} \equiv E_F - E_I$. $|\psi_L^{(n)}\rangle$ is defined as $(\hat{a}_L)^n|\psi_L^{(0)}\rangle$, normalized so that $\langle\psi_L^{(n)}|\psi_L^{(n)}\rangle = 1$. For example, if $|\psi_L^{(0)}\rangle$ is a Fock state as in Eq. (3.41), then $|\psi_L^{(1)}\rangle$ and $|\psi_L^{(2)}\rangle$ are the corresponding Fock states with $\mathcal{N}_L - 1$ and $\mathcal{N}_L - 2$ photons respectively in mode L. On the other hand, if $|\psi_L^{(0)}\rangle$ is a coherent state as in Eq. (3.42), then both $|\psi_L^{(1)}\rangle$ and $|\psi_L^{(2)}\rangle$ are equal to $|\psi_L^{(0)}\rangle$.

It is important to note that the application of photonic annihilation operators to the $|\text{out}\rangle$ state in the phase-sensitive correlation functions $\langle \hat{a}_{d_j} \rangle_{\text{out}}$ and $\langle \hat{a}_{d_2}(\tau)\hat{a}_{d_1}(0)\rangle_{\text{out}}$ changes the total number of photons. In contrast, the $\hat{\mathcal{T}}$-matrix is photon-number preserving, as long as the approximations outlined in Sec. 3.4.1 and Sec. 3.4.2 are applied. Therefore, if the initial state of the laser, i.e., $|\psi_L^{(0)}\rangle$ is a Fock state, then the states $|\text{out}\rangle$ and $\hat{a}_{d_j}|\text{out}\rangle$ are orthogonal. In contrast, they have a finite overlap if $|\psi_L^{(0)}\rangle$ is a coherent superposition of different photon number sectors. Therefore, for quadrature correlators, we assume that the input laser state $|\psi_L^{(0)}\rangle$ is necessarily a coherent state (see Eq. (3.42)). On the other hand, the photonic operators in $G^{(1)}(0)$ [Eq. (3.15)], $G^{(2)}(\tau)$ [Eq. (3.17)], $G^{(1)}(\tau)$ [Eq. (3.27)], and $H_{d_1,d_2}(t,\tau)$ [Eq. (3.28)] do conserve total photon number, so both a coherent state and a Fock state input can lead to a nonzero measurement result.

With this in mind, we can now obtain expressions for photonic correlators in terms of

the matter operators $\hat{R}^{(1)}_{\lambda}$ and $\hat{R}^{(2)}_{\lambda_1,\lambda_2}$. Recall that $G^{(1)}_{d_j} = \langle \text{out}|\hat{a}^{\dagger}_{d_j}(0)\hat{a}_{d_j}(0)|\text{out}\rangle$. Into this, we substitute $|\text{out}\rangle$ [given in Eq. (3.43)], use the definition of operator $\hat{a}_{d_j}$ in Eq. (3.9), the definition of the effective filter function $\mathcal{F}_j(\omega_{\lambda_j})$ [Eq. (3.11)], and use Eq. (3.10) (for converting sums to integrals) to obtain:

$$G^{(1)}_{d_j}(0) \approx \sum_J \left| \int_{-\infty}^{\infty} \mathrm{d}\omega_{\lambda_j}\, \mathcal{F}_j(\omega_{\lambda_j}) \delta\left(E_{JI} + \omega_{\lambda_j} - \omega_L\right) \langle J|\hat{R}^{(1)}_{\lambda_j}(\omega_{\lambda_j})|I\rangle \right|^2 . \tag{3.44}$$

Here, the polarization of mode λ_j is $\mathbf{e}_j$, as set by detector d_j. We also assumed that the dependence of the matter operators $\hat{R}^{(1)}_{\lambda}$ and $\hat{R}^{(2)}_{\lambda_1,\lambda_2}$ on the photonic mode λ is only through its frequency ω_λ and polarization $\mathbf{e}_\lambda$, an assumption that we will justify in Sec. 3.5.1.

For a nonzero time delay, the $G^{(1)}_{d_j}$ function takes the following form:

$$\begin{aligned} G^{(1)}_{d_j}(\tau) &= \left\langle \hat{a}^{\dagger}_{d_j}(\tau)\hat{a}_{d_j}(0)\right\rangle_{\text{out}} \\ &\approx \sum_J \int_{-\infty}^{\infty} \mathrm{d}\omega_{\lambda_j} \left[\mathcal{F}_j(\omega_{\lambda_j})\mathcal{F}^*_j(\omega_{\lambda_j}) e^{i\omega_{\lambda_j}\tau} \delta\left(E_{JI} + \omega_{\lambda_j} - \omega_L\right) \langle I| \left[\hat{R}^{(1)}_{\lambda_j}\right]^{\dagger} |J\rangle\langle J| \hat{R}^{(1)}_{\lambda_j} |I\rangle\right]. \end{aligned} \tag{3.45}$$

Analogously for the $G^{(2)}$ function we get:

$$\begin{aligned} G^{(2)}_{d_1,d_2}(\tau) &\equiv \left\langle \hat{a}^{\dagger}_{d_1}(0)\hat{a}^{\dagger}_{d_2}(\tau)\hat{a}_{d_2}(\tau)\hat{a}_{d_1}(0)\right\rangle_{\text{out}} \\ &\approx \sum_F \left| \iint_{-\infty}^{\infty} \frac{\mathrm{d}\omega_{\lambda_1}\,\mathrm{d}\omega_{\lambda_2}}{(2\pi)} \Big[\mathcal{F}_1(\omega_{\lambda_1})\mathcal{F}_2(\omega_{\lambda_2}) \delta\left(E_{FI} + \omega_{\lambda_1} + \omega_{\lambda_2} - 2\omega_L\right) \right. \\ &\quad \left. \times\, e^{i\omega_{\lambda_1}\tau} \langle F|\hat{R}^{(2)}_{\lambda_1,\lambda_2}(\omega_{\lambda_1},\omega_{\lambda_2})|I\rangle\Big] \right|^2 . \end{aligned} \tag{3.46}$$

The photon in mode λ_2 is detected after time τ following the photon detection in mode λ_1, leading

to the phase $e^{i\omega_{\lambda_1}\tau}$ coming from time- evolution in between. [3]

Finally, we consider phase-sensitive quadrature measurements for a coherent state input. Such correlators can be measured using an interferometric scheme, explained in Sec. 3.3.2.3. The first-order and second-order quadrature correlators are respectively:

$$e^{i(\theta+\theta_L)}\left\langle \hat{a}_{d_j}(0)\right\rangle_{\text{out}} + \text{c.c.} \approx \mathcal{F}_j(\omega_L)e^{i\theta}\,\langle I|\hat{R}^{(1)}_{\lambda_j}(\omega_L)|I\rangle + \text{c.c.}, \text{ and} \tag{3.47}$$

$$\begin{aligned} &e^{2i(\theta+\theta_L)}\left\langle \hat{a}_{d_2}(\tau)\hat{a}_{d_1}(0)\right\rangle_{\text{out}} + \text{c.c.} \\ \approx& i\iint_{-\infty}^{\infty}\frac{\mathrm{d}\omega_{\lambda_1}\,\mathrm{d}\omega_{\lambda_2}}{(2\pi)}\left[e^{-i\omega_{\lambda_2}\tau}\mathcal{F}_1(\omega_{\lambda_1})\mathcal{F}_2(\omega_{\lambda_2})e^{2i\theta}\delta\left(\omega_{\lambda_1}+\omega_{\lambda_2}-2\omega_L\right)\,\langle I|\hat{R}^{(2)}_{\lambda_1,\lambda_2}(\omega_{\lambda_1},\omega_{\lambda_2})|I\rangle\right]. \end{aligned} \tag{3.48}$$

As expected, the final expressions only depend on the *relative* phase difference between the local oscillator (used for measuring the quadrature) and the drive. Further details of the above two correlation functions are provided in Appendix C.4.

3.5 Microscopic structure of matter operators $\hat{R}^{(1)}$ and $\hat{R}^{(2)}$

In this section, we provide the explicit expressions for the matter operators $\hat{R}^{(1)}_{\lambda_1}$ and $\hat{R}^{(2)}_{\lambda_1,\lambda_2}$ for the single-band Fermi-Hubbard model at half-filling defined in Sec. 3.4.

We expand $\hat{\mathcal{T}} = \hat{V} + \hat{V}\hat{\mathbb{G}}_0\hat{V} + \hat{V}\hat{\mathbb{G}}_0\hat{V}\hat{\mathbb{G}}_0\hat{V} + \hat{V}\hat{\mathbb{G}}_0\hat{V}\hat{\mathbb{G}}_0\hat{V}\hat{\mathbb{G}}_0\hat{V} + \ldots$, treating all terms at the same order in $q_e\hat{A}_{\mathbf{r},\mathbf{r}'}$ on equal footing. Recall from the discussion in Sec. 3.4.2 that it suffices to consider processes involving at most two photons being absorbed and at most two photons emitted. So, we should expand the light-matter interaction $\hat{V}$ given in Eq. (3.34) up to fourth order

[3] It may appear from the definition of $G^{(2)}(\tau)$ that this phase is $e^{-i\left(\omega_{\lambda_2}+E_F+(\mathcal{N}_L-2)\omega_L\right)\tau}$. But this reduces to $e^{i\omega_{\lambda_1}\tau}$ after using the δ-function that imposes energy conservation, and after getting rid of overall phases independent of indices F, λ_1, λ_2.

in q_e. The fourth order term $\left(\mathtt{t}_{\mathbf{r},\mathbf{r}+\boldsymbol{\mu}}\hat{c}^\dagger_{\mathbf{r}+\boldsymbol{\mu},\sigma}\hat{c}_{\mathbf{r},\sigma} + \text{h.c.}\right)\left(q_e\hat{A}_{\mathbf{r},\mathbf{r}+\boldsymbol{\mu}}\right)^4$ can however be dropped. The reason is that this term can contribute to processes involving two-photon absorption and two-photon emission at most at linear order in $\hat{V}$. However, the factor $\left(\mathtt{t}_{\mathbf{r},\mathbf{r}+\boldsymbol{\mu}}\hat{c}^\dagger_{\mathbf{r}+\boldsymbol{\mu},\sigma}\hat{c}_{\mathbf{r},\sigma} + \text{h.c.}\right)$ results in the material transitioning out of the spin sector (lower Hubbard band), which we forbid by postselecting the frequencies of detected photons. Therefore, in powers of q_e, the part of $\hat{V}$ [Eq. (3.34)] containing linear or"paramagnetic" ($\hat{V}_P$), quadratic or "diamagnetic" ($\hat{V}_D$), and cubic ($\hat{V}_C$) terms is:

$$\begin{aligned}\hat{V} = \sum_{(\mathbf{r},\boldsymbol{\mu}),\sigma}\Bigg\{ & -i\left(\mathtt{t}_{\mathbf{r},\mathbf{r}+\boldsymbol{\mu}}\hat{c}^\dagger_{\mathbf{r}+\boldsymbol{\mu},\sigma}\hat{c}_{\mathbf{r},\sigma} - \text{h.c.}\right)\left[q_e\hat{A}_{\mathbf{r},\mathbf{r}+\boldsymbol{\mu}} - \frac{\left(q_e\hat{A}_{\mathbf{r},\mathbf{r}+\boldsymbol{\mu}}\right)^3}{6}\right] \\ & + \left(\mathtt{t}_{\mathbf{r},\mathbf{r}+\boldsymbol{\mu}}\hat{c}^\dagger_{\mathbf{r}+\boldsymbol{\mu},\sigma}\hat{c}_{\mathbf{r},\sigma} + \text{h.c.}\right)\frac{\left(q_e\hat{A}_{\mathbf{r},\mathbf{r}+\boldsymbol{\mu}}\right)^2}{2}\Bigg\} \\ \equiv\ & \hat{V}_P + \hat{V}_C + \hat{V}_D.\end{aligned} \tag{3.49}$$

Thus, according to Eq. (3.49), the paramagnetic term $\hat{V}_P$ involves an electron current between a pair of sites by absorbing or emitting a photon. The cubic term $\hat{V}_C$ consists of the same electronic process as $\hat{V}_P$, but involves three photons in total. In this formulation of light-matter interaction, the diamagnetic term $\hat{V}_D$ couples to the point-split local density $\frac{1}{2}\sum_\sigma\left(\mathtt{t}_{\mathbf{r},\mathbf{r}+\boldsymbol{\mu}}\hat{c}^\dagger_{\mathbf{r}+\boldsymbol{\mu},\sigma}\hat{c}_{\mathbf{r},\sigma} + \text{h.c.}\right)$ unlike just the local density in a free-electron gas. $\hat{V}_D$ thus involves hopping of an electron by either absorbing two photons, emitting two photons, or by absorbing one photon along with emitting another.

We now separately study the outcomes where one and two photons are emitted respectively.

3.5.1 Matter operator $\hat{R}^{(1)}_{\lambda}$: Review of Raman scattering

To leading order in g, we consider processes leading to the emission of one photon. Processes involving absorption and emission of two or more photons are of higher order.

At half-filling, electron tunneling results in double occupancy at a site and this costs energy U. Since $\mathtt{t} \ll |U - \omega_L|$, just one insertion of $\hat{V}$ alone cannot result in a photon absorption. But two insertions of $\hat{V}$ via the term $\hat{V}_P \hat{\mathbb{G}}_0 \hat{V}_P$ can result in absorption and emission of a photon. More specifically, this term represents that a laser photon can be absorbed off-resonantly via the paramagnetic term (first arrow from the left in Fig. 3.6). This should then be followed by an electron in the doubly occupied site returning to its empty neighbor by emitting a photon, thus leaving the material in a possibly different state in the spin sector (second arrow from the left in Fig. 3.6). This process can be seen as a photon-assisted superexchange. Therefore, to leading order in light-matter interaction g and $\mathtt{t}/|U - \omega_L|$, the main contribution to $\hat{R}^{(1)}_{\lambda}$ is from such a Raman process [7, 78]. By simplifying the term $\hat{V}_P \hat{\mathbb{G}}_0 \hat{V}_P$, we obtain the Fleury-Loudon operator, a sum of projectors to spin singlets, modulated by the polarizations of the incoming laser and the detected photon [7, 8, 54, 78]:

$$\hat{R}^{(1)}_{(\mathbf{k},\mathbf{e}_j)} \equiv \hat{A}_j = \sum_{(\mathbf{r},\boldsymbol{\mu})} \frac{|\mathtt{t}_{\mathbf{r},\mathbf{r}+\boldsymbol{\mu}}|^2}{g}_L g\omega_L - U\left(4\hat{\mathbf{S}}_{\mathbf{r}} \cdot \hat{\mathbf{S}}_{\mathbf{r}+\boldsymbol{\mu}} - 1\right)\left(\mathbf{e}_j^* \cdot \bar{\boldsymbol{\mu}}\right)\left(\mathbf{e}_L \cdot \bar{\boldsymbol{\mu}}\right) + \dots \tag{3.50}$$

We define $\bar{\boldsymbol{\mu}} \equiv \boldsymbol{\mu}/\mathtt{a}$. In our summation convention, $\sum_{(\mathbf{r},\boldsymbol{\mu})}$ runs through each bond exactly once. The "..." above denotes terms of order $\mathtt{t}^3/|\omega_L - U|^2$ and higher.

In Eq. (3.50) we ignored the momentum transfer between electrons and photons by omitting the $e^{i(\mathbf{k}_L - \mathbf{k})\cdot(\mathbf{r}+\boldsymbol{\mu}/2)}$ factor. This is because ω_L and ω_λ are of order U, the Hubbard interaction. For

typical materials, the corresponding wavelength is equal to several thousand lattice spacings. Hence, throughout this paper, we will ignore the spatial variation of the laser field. Therefore, $\hat{R}^{(1)}_{(\mathbf{k},\mathbf{e}_j)}$ depends on the emitted mode $(\mathbf{k},\mathbf{e}_j)$, only through its polarization $\mathbf{e}_j$ and, in general, the frequency $\omega_{\mathbf{k}}$. In the near future, in systems with much larger lattice spacings, such as moiré materials, significant momentum transfer to electrons may become possible via optical excitation. In this case, our formalism can be adjusted to include finite-momentum matter operators.

3.5.2 Processes leading to the emission of two photons

We now describe the processes that contribute to $\hat{R}^{(2)}$, i.e., lead to the emission of two photons. Unlike the case for $\hat{R}^{(1)}_{\lambda}$, the diamagnetic and cubic terms can also contribute to the emission of two photons. We show that $\hat{R}^{(2)}_{\lambda_1,\lambda_2}$ can be extracted from Eq. (3.39) by expanding $\hat{V}_P\hat{\mathbb{G}}_0\hat{V}_P\hat{\mathbb{G}}_0\hat{V}_P\hat{\mathbb{G}}_0\hat{V}_P + \hat{V}_P\hat{\mathbb{G}}_0\hat{V}_D\hat{\mathbb{G}}_0\hat{V}_P + \hat{V}_C\hat{\mathbb{G}}_0\hat{V}_P + \hat{V}_P\hat{\mathbb{G}}_0\hat{V}_C$. First, we provide a qualitative overview. We then discuss the result for $\hat{R}^{(2)}_{\lambda_1,\lambda_2}$ for the case of the single band Fermi-Hubbard model at half-filling. Explicit details of the derivation are provided in Appendix C.3.

In Fig. 3.7, we schematically show the two-photon scattering processes on the energy diagram. Their microscopic counterparts are provided in Fig. 3.8 for the Fermi-Hubbard model at half-filling. As we explicitly demonstrate in this section below, the photon intensity $G^{(1)}(0)$ as a function of frequency qualitatively resembles the profile in Fig. 3.7(e-f). Specifically, it features a central peak around ω_L with a width of $\sim \mathtt{t}^2/U$ (Fig. 3.7(e)), along with two sidebands near $2\omega_L - U$ and U (Fig. 3.7(f)). The central peak can be anticipated from our previous discussion of Raman scattering, where the emitted photon's frequency deviates from the laser's frequency by an amount of the order of the spin excitation energy scale. Furthermore, in this section, we

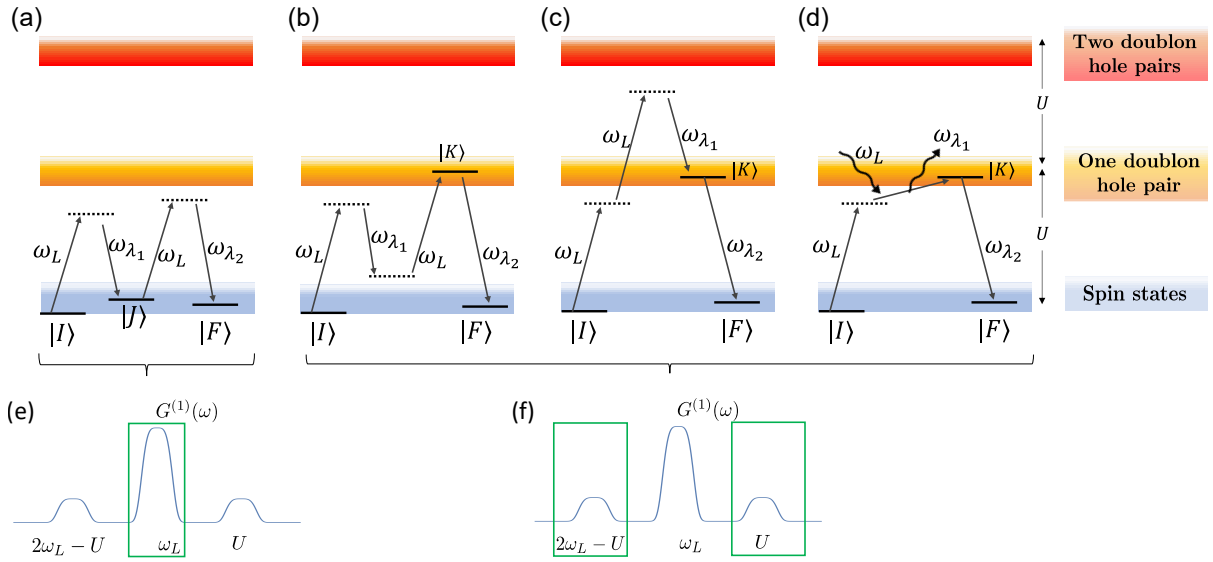

Figure 3.7: (a)-(d) illustrate the four processes contributing to $G^{(2)}(\tau)$ to leading order in g_L and $\mathtt{t}/|\omega_L - U|$. (e) and (f) show a cartoon intensity profile of the emitted photons. Process (a) contributes to the central peak highlighted in (e) and processes (b-d) contribute to the sidebands highlighted in (f). **(a)**: Raman process occurring twice, with the intermediate state $|J\rangle$ being in the spin sector. **(b)**: Scattering of two photons, accompanied with the real, i.e., resonant excitation of a state $|K\rangle$ in the charge sector. This is reminiscent of the sideband process in Ref. [14]. **(c)**: This process corresponds to successive absorption of two photons resulting in virtual occupation of the two-doublon-hole sector, followed by emission of two photons into the sidebands in (f). **(d)**: This process differs from (a), (b) and (c) in that it involves the diamagnetic term. After a photon absorption and virtual occupation of the single doublon-hole sector, the diamagnetic term results in the scattering of a laser photon (wavy line labelled ω_L) into an emitted mode of frequency ω_{λ_1}, which lies in the sideband near $2\omega_L - U$. This results in excitation of a matter state $|K\rangle$ in the single doublon-hole sector. Finally, a photon of frequency ω_{λ_2} is emitted into the sideband around U. **(e)**: The central peak is highlighted, corresponding to photons of frequency around ω_L. **(f)**: The sidebands corresponding to pairs of photons of frequency around $2\omega_L - U$ and U are highlighted.

demonstrate that the sidebands are generated by the processes in Fig. 3.7(b-d) leading to pairs of photons around frequencies $2\omega_L - U$ and U. Let us now study all the processes in Fig. 3.7 one by one.

1. Fig. 3.7(a) shows the Raman process occurring twice in succession. First, a doublon-hole pair is virtually created along a bond by a photon absorption via the paramagnetic term $\hat{V}_P$ (Fig. 3.8(a_1-a_2)). This pair then recombines via a photon emission, with the system

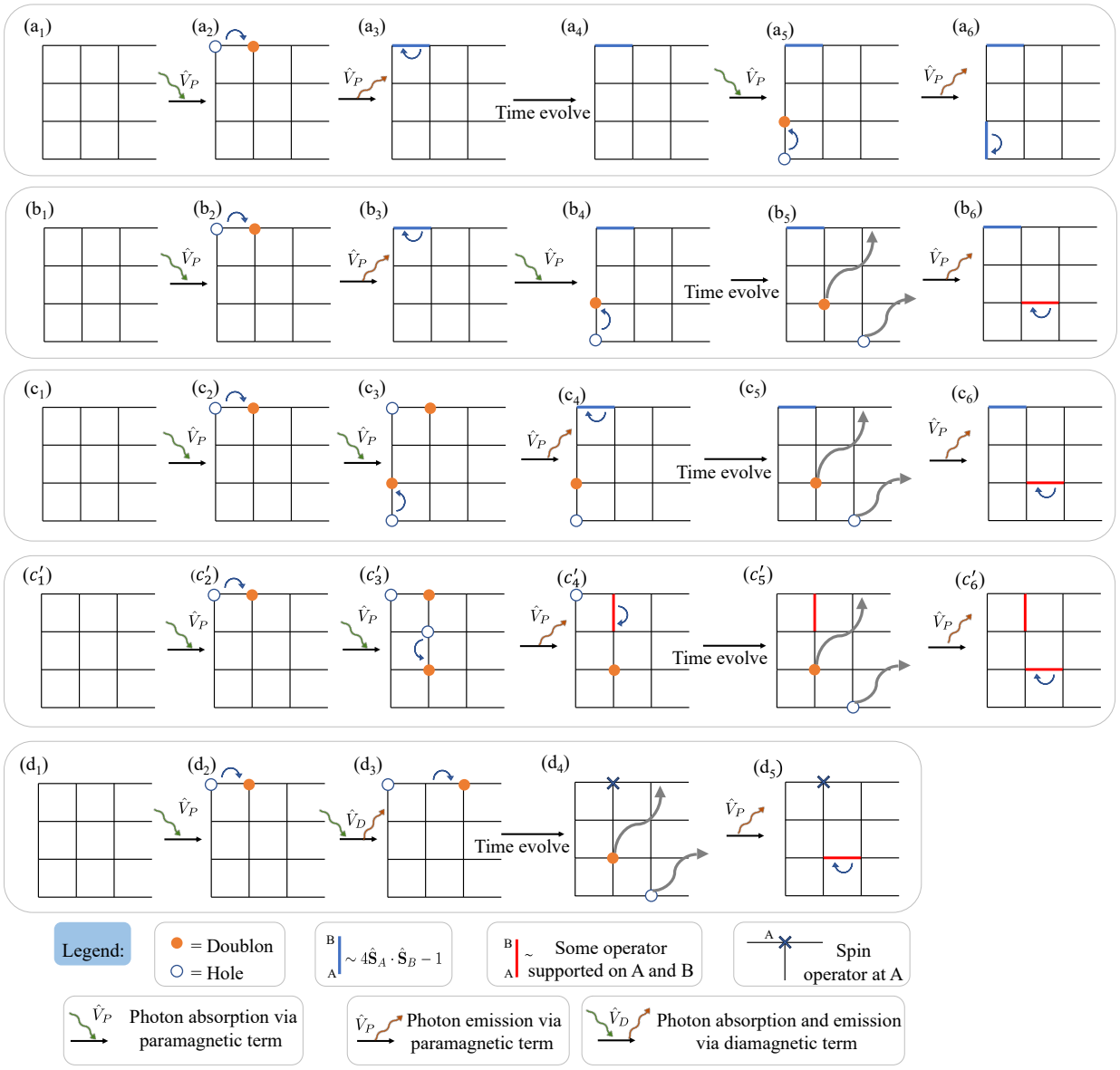

Figure 3.8: Microscopic processes corresponding to Fig. 3.7: We show the square lattice for concreteness, but our results are general. In all the subfigures, a curved blue arrow indicates that an electron *tunneled* from the tail to the head of the arrow, and the configuration shown in a subfigure is a consequence of the hop shown in the *same* subfigure. The legend is provided at the bottom.

returning to the spin sector – in a possibly excited state. This effectively results in the application of a spin operator on the matter state, which to leading order in $\mathtt{t}/|\omega_L - U|$ is the Fleury-Loudon sum of spin singlet projectors [78], $\hat{A}_1$ defined in Eqs. (3.50, 3.60). The system then undergoes a time-evolution until a second Raman process occurs (Fig. 3.8(a_5)), resulting in the application of a second Fleury-Loudon operator $\hat{A}_2$ (See Appendix C.3.1 for technical details).

Both the photons emitted have frequencies close to ω_L (the central peak in Fig. 3.7(e)), and their difference from ω_L is of the order of $J \sim \mathtt{t}^2/U$, i.e., the energy scale of the spin sector.

2. The microscopic process corresponding to Fig. 3.7(b) is shown in Fig. 3.8(b_1-b_6). It starts similarly to the process in Fig. 3.7(a) with the difference being that the two emitted photons have frequencies of order $2\omega_L - U$ and U respectively (belonging to sidebands in Fig. 3.7(e,f)). See also Appendix C.3.1 for technical details.

3. Figure 3.7(c) illustrates a process in which two photons (ω_L) are absorbed sequentially, resulting in the creation of two virtual doublon-hole pairs at different locations (see Fig. 3.8(c_2-c_3, c_2'-c_3')). Subsequently, one of these doublon-hole pairs recombines via the emission of a photon. The recombining pair may consist of one of the initially created pairs (Fig. 3.8(c_4)), in which case the two pairs could have been arbitrarily separated. Alternatively, the recombining pair may involve a doublon from one pair and a hole from the other pair (Fig. 3.8(c_4')). This latter scenario requires the bonds associated with the two pairs to be connected via a third bond (Fig. 3.8(c_3')). The emitted photon in this process has a frequency ω_{λ_1} approximately equal to $2\omega_L - U$.

Following the emission of the first photon, the system transitions to the single-doublon-hole pair sector, where it undergoes time evolution (Fig. 3.8(c_5, c_5')) until a second photon is emitted. This second photon, with a frequency on the order of U, arises from the recombination of the doublon-hole pair, which may have moved to a distant bond (Fig. 3.8(c_6, c_6')). This sequence of events also corresponds to the sidebands depicted in Fig. 3.7(f).

The intermediate state $|K\rangle$, involved in processes shown in Fig. 3.7(b, c), belongs to the single doublon-hole sector. This implies that the scattering of photons in this case, is accompanied by the action of matter operators that induce transitions between energy sectors. We also notice that the elementary processes in Fig. 3.8(b_4-b_6) and 3.8(c_4-c_6) look identical. As a result the contributions to $\hat{R}^{(2)}_{\lambda_1,\lambda_2}$ originating from the scattering amplitudes corresponding to rows (b) and (c) in Fig. 3.8 have opposite signs (arising from opposite signs of two-photon detuning) and nearly cancel each other. The incomplete cancellation can be explained as follows. As shown in Figs. 3.8(b_2) and 3.8(b_4), the two bonds along which light-assisted tunneling occurs, can be arbitrary, and, in principle, can even share a site or coincide. But for two doublon-hole pairs to be created, the bonds in Figs. 3.8(c_2) and 3.8(c_3) must not share sites. The associated effect on the matter state can be mathematically expressed as an application of a sum of local terms. These terms involve a spin-singlet projection along a bond, e.g. $(\mathbf{r}_1, \boldsymbol{\mu}_1)$, followed by electron tunneling along bonds touching the bond $(\mathbf{r}_1, \boldsymbol{\mu}_1)$.

Similarly, the elementary processes depicted in row c' of Fig. 3.8, up to the emission of the first photon, can be described mathematically as the application of a sum of local terms, consisting of a spin operator supported on a bond followed by an electron tunneling oper-

ator supported near that bond.

Finally, the recombination of the doublon-hole pair, accompanied by the emission of the second photon (see Fig. 3.8(b_6, c_6, c_6') and Fig. 3.8(d_5)), is governed by an electron tunneling operator that is proportional to the global electric current.

So far, the considered processes correspond to the action of $\hat{V}_P\hat{\mathbb{G}}_0\hat{V}_P\hat{\mathbb{G}}_0\hat{V}_P\hat{\mathbb{G}}_0\hat{V}_P$ in Eq. (3.39), and do not involve the diamagnetic term.

4. The process depicted in Fig. 3.7(d) involves a contribution from the diamagnetic term and represents the leading-order term in $\mathtt{t}/|U-\omega_L|$. The corresponding elementary steps are schematically illustrated in Fig. 3.8(d_1-d_5). In this sequence, an electron first tunnels by absorbing a photon of frequency ω_L via the paramagnetic term. Subsequently, through the diamagnetic term, another photon of frequency ω_L is absorbed, and a photon with frequency $\omega_{\lambda_1} \sim 2\omega_L - U$ is emitted. Finally, via the paramagnetic term, a photon with frequency $\omega_{\lambda_2} \sim U$ is emitted, returning the material to the spin sector. This process corresponds to the term $\hat{V}_P\hat{\mathbb{G}}_0\hat{V}_D\hat{\mathbb{G}}_0\hat{V}_P$ in Eq. (3.39) and contributes to the sidebands shown in Fig. 3.7(f).

Finally, the processes involving the cubic term $\hat{V}_C$ are explained in Appendix C.3.4.

In summary, all processes contributing to the emission into the sidebands (Fig. 3.7(b, c, d)) involve an intermediate step where the material undergoes a resonant transition to a state $|K\rangle$ in the single doublon-hole sector. In contrast, the process responsible for emission into the central peak (Fig. 3.7(a)) involves only off-resonant excitation of this sector. The physical implication is that, in the cases shown in Fig. 3.7(b, c, d), the scattering of light is governed by mixed spin-charge operators. Meanwhile, the process in Fig. 3.7(a) corresponds to the action of operators

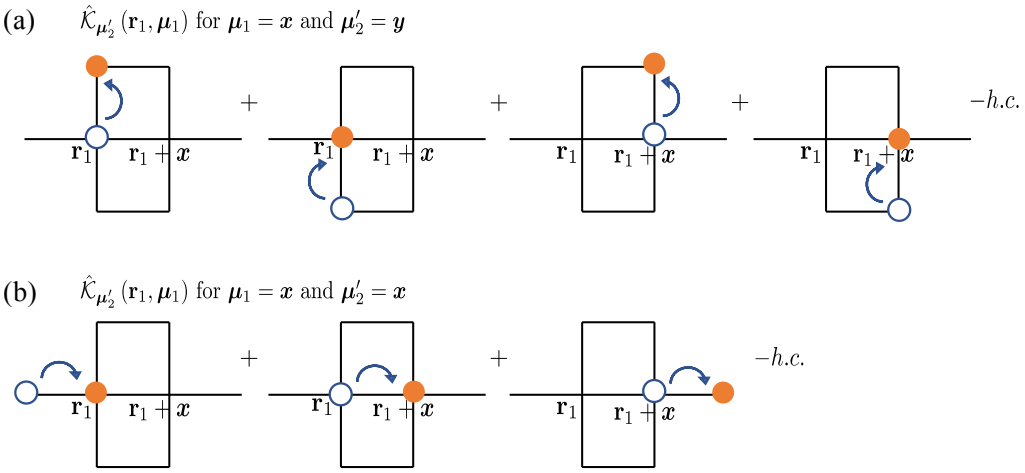

Figure 3.9: A visualization of the definition of the operator $\hat{\mathcal{K}}_{\boldsymbol{\mu}_2'}(\mathbf{r}_1, \boldsymbol{\mu}_1)$ (see Eq. (3.52)) on the square lattice. This is an operator that creates a doublon-hole pair when acting on the spin sector. **(a)**: $\boldsymbol{\mu}_1 = \boldsymbol{x}$ (lattice vector in the x-direction) and $\boldsymbol{\mu}_2' = \boldsymbol{y}$. **(b)**: $\boldsymbol{\mu}_1 = \boldsymbol{x}$ and $\boldsymbol{\mu}_2' = \boldsymbol{x}$.

confined entirely to the spin sector. This distinction is formally demonstrated in Appendix C.3.

3.5.3 Microscopic expression for $\hat{R}^{(2)}$

Following the discussion above, in this subsection, we provide the final expression for the operator $\hat{R}^{(2)}_{\lambda_1,\lambda_2}$ (see Appendix C.3 for a complete derivation using the $\hat{\mathcal{T}}$-matrix formalism). We start by providing several intermediate definitions.

3.5.3.1 Defining operators $\hat{A}_j$, $\hat{B}_j$, and $\hat{C}_j$

We emphasize that throughout this section, bonds $(\mathbf{r}, \mathbf{r}+\boldsymbol{\mu})$ are *not* restricted to be nearest-neighbors. First, let us define

$$\hat{\mathcal{J}}_{\boldsymbol{\mu}} \equiv i \sum_{\mathbf{r},\sigma} \left(\mathtt{t}_{\mathbf{r},\mathbf{r}+\boldsymbol{\mu}} \hat{c}^{\dagger}_{\mathbf{r}+\boldsymbol{\mu},\sigma} \hat{c}_{\mathbf{r},\sigma} - \mathtt{t}^{*}_{\mathbf{r},\mathbf{r}+\boldsymbol{\mu}} \hat{c}^{\dagger}_{\mathbf{r},\sigma} \hat{c}_{\mathbf{r}+\boldsymbol{\mu},\sigma} \right). \tag{3.51}$$

$\hat{\mathcal{J}}_{\boldsymbol{\mu}}$ is related to the global electric current in the direction $\boldsymbol{\mu}$.

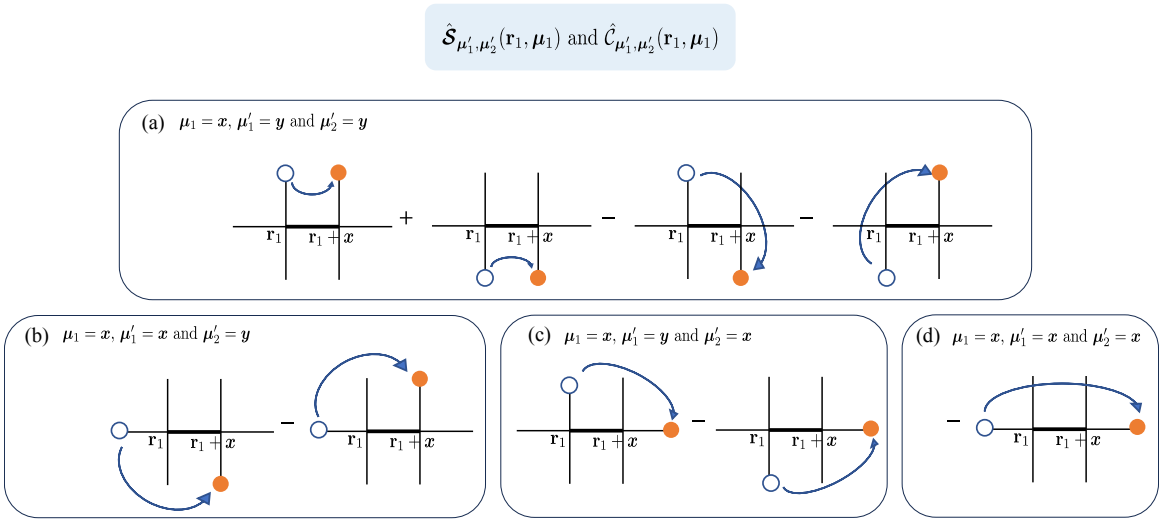

Figure 3.10: A visualization of the definition of the operators $\hat{\boldsymbol{\mathcal{S}}}_{\boldsymbol{\mu}_1',\boldsymbol{\mu}_2'}(\mathbf{r}_1,\boldsymbol{\mu}_1)$ and $\hat{\mathcal{C}}_{\boldsymbol{\mu}_1',\boldsymbol{\mu}_2'}(\mathbf{r}_1,\boldsymbol{\mu}_1)$ (see Eq. (3.56) and Eq. (3.57)). Both the operators create a doublon-hole pair when acting on a state in the spin sector. $\hat{\boldsymbol{\mathcal{S}}}$ is a spin triplet operator, while $\hat{\mathcal{C}}$ is a spin singlet operator. Since this is the only difference between the two, we use the same figure to denote both $\hat{\boldsymbol{\mathcal{S}}}$ and $\hat{\mathcal{C}}$. The operators are specified by a bond $(\mathbf{r}_1,\boldsymbol{\mu}_1)$ and two additional lattice directions $\boldsymbol{\mu}_1'$ and $\boldsymbol{\mu}_2'$. The four subfigures show the definition for different choices of these directions.

Next, we define an operator $\hat{\mathcal{K}}_{\boldsymbol{\mu}_2'}(\mathbf{r}_1,\boldsymbol{\mu}_1)$ which is a sum of operators that induce electron tunneling along the lattice vector $\boldsymbol{\mu}_2'$ with the following additional constraint. As shown in Fig. 3.9, the constituent terms belong to the vicinity of the bond $(\mathbf{r}_1,\boldsymbol{\mu}_1)$, such that each term in $\hat{\mathcal{K}}_{\boldsymbol{\mu}_2'}(\mathbf{r}_1,\boldsymbol{\mu}_1)$ includes the sites $\mathbf{r}_1$ or $\mathbf{r}_1+\boldsymbol{\mu}_1$ as a starting or the ending point of the tunneling. The formal definition is

$$\hat{\mathcal{K}}_{\boldsymbol{\mu}_2'}(\mathbf{r}_1,\boldsymbol{\mu}_1) \equiv i\sum_{\mathbf{r}_2',\sigma_2'} \eta^{(\mathbf{r}_2',\boldsymbol{\mu}_2')}_{(\mathbf{r}_1,\boldsymbol{\mu}_1)} \left(\mathtt{t}_{\mathbf{r}_2',\mathbf{r}_2'+\boldsymbol{\mu}_2'}\hat{c}^\dagger_{\mathbf{r}_2'+\boldsymbol{\mu}_2',\sigma_2'}\hat{c}_{\mathbf{r}_2'\sigma_2'} - \text{h.c.}\right), \tag{3.52}$$

where we have introduced a symbol $\eta^{(\mathbf{r}_2',\boldsymbol{\mu}_2')}_{(\mathbf{r}_1,\boldsymbol{\mu}_1)}$ that is a function of two bonds $(\mathbf{r}_1,\boldsymbol{\mu}_1)$ and $(\mathbf{r}_2',\boldsymbol{\mu}_2')$,

and is symmetric in its two arguments. It is defined as

$$\eta_{(\mathbf{r}_1,\boldsymbol{\mu}_1)}^{(\mathbf{r}_2',\boldsymbol{\mu}_2')} = \begin{cases} 1, \text{ if bonds } (\mathbf{r}_2', \boldsymbol{\mu}_2') \text{ and } (\mathbf{r}_1, \boldsymbol{\mu}_1) \text{ have} \\ \quad \text{at least one site in common.} \\ 0, \text{ otherwise.} \end{cases} \tag{3.53}$$

Now, we define another set of tunneling operators — a spin triplet operator $\hat{\boldsymbol{\mathcal{S}}}_{\boldsymbol{\mu}_1',\boldsymbol{\mu}_2'}(\mathbf{r}_1, \boldsymbol{\mu}_1)$ and a spin singlet operator $\hat{\mathcal{C}}_{\boldsymbol{\mu}_1',\boldsymbol{\mu}_2'}(\mathbf{r}_1, \boldsymbol{\mu}_1)$, shown in Fig. 3.10. They induce an electron tunneling between the two distinct sites adjacent to the bond $(\mathbf{r}_1, \boldsymbol{\mu}_1)$ (see Fig. 3.10). The locations of these two sites can be parametrized as $\mathbf{r}_1 \pm \boldsymbol{\mu}_1'$ and $\mathbf{r}_1 + \boldsymbol{\mu}_1 \pm \boldsymbol{\mu}_2'$. The constraint that these two sites together with $\mathbf{r}_1$ and $\mathbf{r}_1 + \boldsymbol{\mu}_1$ constitute four distinct sites is enforced using the following notation (for nonzero lattice vectors $\boldsymbol{\mu}$, $\boldsymbol{\nu}$ and $\boldsymbol{\rho}$):

$$h(\boldsymbol{\mu}, \boldsymbol{\nu}, \boldsymbol{\rho}) = \begin{cases} 0, \text{ if } \boldsymbol{\mu} + \boldsymbol{\rho} = 0, \\ \quad \text{or if } \boldsymbol{\nu} = \boldsymbol{\mu} \\ \quad \text{or if } \boldsymbol{\mu} + \boldsymbol{\rho} = \boldsymbol{\nu}. \\ 1, \text{ otherwise.} \end{cases} \tag{3.54}$$

Let us also define:

$$\mathtt{t}_{\text{eff}}^3(\boldsymbol{\mu}_1', \boldsymbol{\mu}_2', \mathbf{r}_1, \boldsymbol{\mu}_1) \equiv \mathtt{t}_{\mathbf{r}_1+s_1'\boldsymbol{\mu}_1',\mathbf{r}_1}\mathtt{t}_{\mathbf{r}_1,\mathbf{r}_1+\boldsymbol{\mu}_1}\mathtt{t}_{\mathbf{r}_1+\boldsymbol{\mu}_1,\mathbf{r}_1+\boldsymbol{\mu}_1+s_2'\boldsymbol{\mu}_2'}. \tag{3.55}$$

With this notation, $\hat{\boldsymbol{\mathcal{S}}}_{\boldsymbol{\mu}_1',\boldsymbol{\mu}_2'}(\mathbf{r}_1,\boldsymbol{\mu}_1)$ and $\hat{\mathcal{C}}_{\boldsymbol{\mu}_1',\boldsymbol{\mu}_2'}(\mathbf{r}_1,\boldsymbol{\mu}_1)$ are defined as

$$\begin{aligned}\hat{\boldsymbol{\mathcal{S}}}_{\boldsymbol{\mu}_1',\boldsymbol{\mu}_2'}(\mathbf{r}_1,\boldsymbol{\mu}_1) = \frac{1}{2}\sum_{\substack{s_1'\in\{\pm1\}\\ s_2'\in\{\pm1\}}} s_1's_2'\Bigg\{\Bigg[h\left(\boldsymbol{\mu}_1, s_1'\boldsymbol{\mu}_1', s_2'\boldsymbol{\mu}_2'\right)\\ \times\sum_{\alpha,\beta}\left(\mathtt{t}^3_{\text{eff}}\left(\boldsymbol{\mu}_1',\boldsymbol{\mu}_2',\mathbf{r}_1,\boldsymbol{\mu}_1\right)\hat{c}^\dagger_{\mathbf{r}_1+\boldsymbol{\mu}_1+s_2'\boldsymbol{\mu}_2',\alpha}\boldsymbol{\sigma}_{\alpha\beta}\hat{c}_{\mathbf{r}_1+s_1'\boldsymbol{\mu}_1',\beta}+\text{h.c.}\right)\Bigg]+\left[\boldsymbol{\mu}_1'\leftrightarrow\boldsymbol{\mu}_2'\right]\Bigg\},\text{ and}\end{aligned} \tag{3.56}$$

$$\begin{aligned}\hat{\mathcal{C}}_{\boldsymbol{\mu}_1',\boldsymbol{\mu}_2'}(\mathbf{r}_1,\boldsymbol{\mu}_1) = \frac{i}{2}\sum_{\substack{s_1'\in\{\pm1\}\\ s_2'\in\{\pm1\},\alpha}} s_1's_2'\Bigg\{\Bigg[h\left(\boldsymbol{\mu}_1, s_1'\boldsymbol{\mu}_1', s_2'\boldsymbol{\mu}_2'\right)\\ \times\left(\mathtt{t}^3_{\text{eff}}\left(\boldsymbol{\mu}_1',\boldsymbol{\mu}_2',\mathbf{r}_1,\boldsymbol{\mu}_1\right)\hat{c}^\dagger_{\mathbf{r}_1+\boldsymbol{\mu}_1+s_2'\boldsymbol{\mu}_2',\alpha}\hat{c}_{\mathbf{r}_1+s_1'\boldsymbol{\mu}_1',\alpha}-\text{h.c.}\right)\Bigg]+\left[\boldsymbol{\mu}_1'\leftrightarrow\boldsymbol{\mu}_2'\right]\Bigg\}.\end{aligned} \tag{3.57}$$

Next, we define a symmetric tunneling operator

$$\hat{\mathcal{H}}_{\mathbf{r},s\boldsymbol{\mu},s'\boldsymbol{\mu}'} = \sum_\alpha \mathtt{t}^*_{\mathbf{r},\mathbf{r}+s\boldsymbol{\mu}}\mathtt{t}_{\mathbf{r},\mathbf{r}+s'\boldsymbol{\mu}'}\hat{c}^\dagger_{\mathbf{r}+s'\boldsymbol{\mu}',\alpha}\hat{c}_{\mathbf{r}+s\boldsymbol{\mu},\alpha}+\text{h.c.} \tag{3.58}$$

and a local spin current

$$\hat{\boldsymbol{\mathcal{J}}}^S_{\mathbf{r},s\boldsymbol{\mu},s'\boldsymbol{\mu}'} = i\sum_\alpha\left(\mathtt{t}^*_{\mathbf{r},\mathbf{r}+s\boldsymbol{\mu}}\mathtt{t}_{\mathbf{r},\mathbf{r}+s'\boldsymbol{\mu}'}\hat{c}^\dagger_{\mathbf{r}+s'\boldsymbol{\mu}',\alpha}\boldsymbol{\sigma}_{\alpha\beta}\hat{c}_{\mathbf{r}+s\boldsymbol{\mu},\beta}-\text{h.c.}\right). \tag{3.59}$$

Using these local operators, we now define the following global (zero-momentum) matter operators $\hat{A}_j$, $\hat{B}_j$ and $\hat{C}_j$ that describe photoemission with the polarization matching that of the j-th detector $j\in\{1,2\}$. To leading order in laser-matter coupling g_L and $\mathtt{t}/|\omega_L-U|$, the operators are:

$$\hat{A}_j = \frac{g_L g}{\omega_L-U}\sum_{(\mathbf{r},\boldsymbol{\mu})}\left|\mathtt{t}_{\mathbf{r},\mathbf{r}+\boldsymbol{\mu}}\right|^2\left(4\hat{\mathbf{S}}_\mathbf{r}\cdot\hat{\mathbf{S}}_{\mathbf{r}+\boldsymbol{\mu}}-1\right)\left(\bar{\boldsymbol{\mu}}\cdot\mathbf{e}_L\right)\left(\bar{\boldsymbol{\mu}}\cdot\mathbf{e}_j^*\right), \tag{3.60}$$

The operator $\hat{A}_j$ is therefore equivalent to the Fleury-Loudon operator that describes the conven-

tional Raman scattering (Eq. (3.50)).

In contrast, operator $\hat{B}_j$ is a mixed spin-charge operator that creates a doublon-hole pair and spin excitations. It is defined as (where we make use of the definitions in Eq. (3.58), (3.59), (3.52), (3.56) and (3.57)):

$$\begin{aligned}\hat{B}_j = g_L^2 g \Bigg\{ & \frac{1}{\omega_L - U} \sum_{\mathbf{r},\boldsymbol{\mu}',\boldsymbol{\mu}} \sum_{\substack{s,s'=\pm 1 \\ s\boldsymbol{\mu} \neq s'\boldsymbol{\mu}'}} \Big[\left(s'\bar{\boldsymbol{\mu}}' \cdot \mathbf{e}_L\right) \left(s\bar{\boldsymbol{\mu}} \cdot \mathbf{e}_L\right) \mathbf{e}_j^* \cdot \Big[\left(s\bar{\boldsymbol{\mu}} - s'\bar{\boldsymbol{\mu}}'\right) \hat{\boldsymbol{\mathcal{J}}}^S_{\mathbf{r},s\boldsymbol{\mu},s'\boldsymbol{\mu}'} \cdot \hat{\mathbf{S}}_{\mathbf{r}} \\ & \qquad + \frac{i}{2} \left(s\bar{\boldsymbol{\mu}} + s'\bar{\boldsymbol{\mu}}'\right) \hat{\mathcal{H}}_{\mathbf{r},s\boldsymbol{\mu},s'\boldsymbol{\mu}'} \Big] \Big] \\ & + \frac{1}{(\omega_L - U)^2} \sum_{(\mathbf{r},\boldsymbol{\mu}),\boldsymbol{\mu}'} \Big[\left(\bar{\boldsymbol{\mu}}' \cdot \mathbf{e}_L\right) \left(\bar{\boldsymbol{\mu}} \cdot \mathbf{e}_L\right) \left(\bar{\boldsymbol{\mu}} \cdot \mathbf{e}_j^*\right) \hat{\mathcal{K}}_{\boldsymbol{\mu}'} \left(\mathbf{r}, \boldsymbol{\mu}\right) \left|\mathtt{t}_{\mathbf{r},\mathbf{r}+\boldsymbol{\mu}}\right|^2 \left(4\hat{\mathbf{S}}_{\mathbf{r}} \cdot \hat{\mathbf{S}}_{\mathbf{r}+\boldsymbol{\mu}} - 1\right) \Big] \\ & + \frac{1}{(\omega_L - U)^2} \sum_{\substack{(\mathbf{r},\boldsymbol{\mu}), \\ \boldsymbol{\mu}_1',\boldsymbol{\mu}_2'}} \Big[\left(\bar{\boldsymbol{\mu}}_1' \cdot \mathbf{e}_L\right) \left(\bar{\boldsymbol{\mu}}_2' \cdot \mathbf{e}_L\right) \left(\bar{\boldsymbol{\mu}} \cdot \mathbf{e}_j^*\right) \\ & \qquad \times \Big[i\hat{\boldsymbol{\mathcal{S}}}_{\boldsymbol{\mu}_1',\boldsymbol{\mu}_2'}(\mathbf{r},\boldsymbol{\mu}) \cdot \left(\frac{\hat{\mathbf{S}}_{\mathbf{r}} - \hat{\mathbf{S}}_{\mathbf{r}+\boldsymbol{\mu}}}{2} - i\hat{\mathbf{S}}_{\mathbf{r}} \times \hat{\mathbf{S}}_{\mathbf{r}+\boldsymbol{\mu}} \right) \\ & \qquad + \hat{\mathcal{C}}_{\boldsymbol{\mu}_1',\boldsymbol{\mu}_2'}(\mathbf{r},\boldsymbol{\mu}) \left(\hat{\mathbf{S}}_{\mathbf{r}} \cdot \hat{\mathbf{S}}_{\mathbf{r}+\boldsymbol{\mu}} - \frac{1}{4} \right) \Big] \Big] - \frac{1}{2} \sum_{\boldsymbol{\mu}} \left(\boldsymbol{\mu} \cdot \mathbf{e}_L\right)^2 \left(\boldsymbol{\mu} \cdot \mathbf{e}_j^*\right) \hat{\mathcal{J}}_{\boldsymbol{\mu}} \Bigg\}. \end{aligned} \tag{3.61}$$

The first two lines in Eq. (3.61) come from the process shown in Fig. 3.8(d_1-d_5), and this process involves scattering described by the diamagnetic term. The third line above, involving $\hat{\mathcal{K}}_{\boldsymbol{\mu}'}(\mathbf{r},\boldsymbol{\mu})$ results from the incomplete cancellation of the processes in Fig. 3.8(b_1-b_6) and Fig. 3.8(c_1-c_6) (see Sec. 3.5.2 for a discussion). The last two lines involving $\hat{\boldsymbol{\mathcal{S}}}_{\boldsymbol{\mu}_1',\boldsymbol{\mu}_2'}(\mathbf{r},\boldsymbol{\mu})$ and $\hat{\mathcal{C}}_{\boldsymbol{\mu}_1',\boldsymbol{\mu}_2'}(\mathbf{r},\boldsymbol{\mu})$ originate from the process shown in Fig. 3.8(c_1'-c_6').

Finally, the operators $\hat{C}_j$ that also couple the spin and charge sectors are defined as:

$$\begin{aligned}\hat{C}_j =& ig \sum_{(\mathbf{r},\boldsymbol{\mu}),\sigma} \left(\bar{\boldsymbol{\mu}} \cdot \mathbf{e}_j^*\right) \left(\mathtt{t}_{\mathbf{r},\mathbf{r}+\boldsymbol{\mu}} \hat{c}^\dagger_{\mathbf{r}+\boldsymbol{\mu},\sigma} \hat{c}_{\mathbf{r},\sigma} - \mathtt{t}^*_{\mathbf{r},\mathbf{r}+\boldsymbol{\mu}} \hat{c}^\dagger_{\mathbf{r},\sigma} \hat{c}_{\mathbf{r}+\boldsymbol{\mu},\sigma}\right) \\ \equiv& g \sum_{\boldsymbol{\mu}} \left(\bar{\boldsymbol{\mu}} \cdot \mathbf{e}_j^*\right) \hat{\mathcal{J}}_{\boldsymbol{\mu}}.\end{aligned} \tag{3.62}$$

$\hat{C}_j$ is proportional to the component of the global electron current along the direction of $\mathbf{e}_j^*$.

We can run a sanity check on our expressions Eqs. (3.60-3.62) by performing a symmetry analysis. Specifically, because of the absence of spin-orbit coupling in the microscopic Hamiltonian, all terms should transform as a singlet under spin rotation. One can easily check that this holds for the operators $\hat{A}_j$ and $\hat{C}_j$. This also holds for $\hat{B}_j$. For example, the tunneling operator $\hat{\boldsymbol{\mathcal{S}}}_{\boldsymbol{\mu}'_1,\boldsymbol{\mu}'_2}(\mathbf{r},\boldsymbol{\mu})$ transforms as a triplet, but after taking the scalar product with $\left((\hat{\mathbf{S}}_{\mathbf{r}} - \hat{\mathbf{S}}_{\mathbf{r}+\boldsymbol{\mu}})/2 - i\hat{\mathbf{S}}_{\mathbf{r}} \times \hat{\mathbf{S}}_{\mathbf{r}+\boldsymbol{\mu}}\right)$, the result transforms as a spin singlet. Next, if the input light and the detectors are linearly polarized, one can check that each term in $\hat{B}_j$ and $\hat{C}_j$ is odd under time-reversal transformation. This is also expected from the microscopic form of the light-matter coupling $\sim \hat{\mathbf{A}} \cdot \hat{\boldsymbol{\mathcal{J}}}$ and the fact that the electric current $\hat{\boldsymbol{\mathcal{J}}}$ is odd under time-reversal transformation. Therefore, for linearly polarized input and output, since $\hat{B}_j$ arises from a three-photon process (absorption of two and emission of one), and $\hat{C}_j$ arises from a single-photon process (emission of one), they should both be odd under time-reversal.

We note that in Eq. (3.61), the leading-order terms at face value (in $\mathtt{t}/|\omega_L - U|$), are those in the first line, involving the diamagnetic term. However, after taking the expectation value in a matter state, we expect the contribution from this set of terms to be small. We can directly see that this is the case when the time delay between application of $\hat{B}_1$ and $\hat{C}_2$ on the matter state is

0. This is because when acting on a state in the spin sector,

$$\left(\hat{c}^\dagger_{\mathbf{r}_2,\alpha}\hat{c}_{\mathbf{r}_1,\beta} - \text{h.c.}\right)\left(\hat{c}^\dagger_{\mathbf{r}_2,\beta}\boldsymbol{\sigma}_{\beta\gamma}\hat{c}_{\mathbf{r}_1,\gamma} - \text{h.c.}\right) = 0, \text{ and} \tag{3.63}$$

$$\left(\hat{c}^\dagger_{\mathbf{r}_2,\alpha}\hat{c}_{\mathbf{r}_1,\beta} - \text{h.c.}\right)\left(\hat{c}^\dagger_{\mathbf{r}_2,\beta}\hat{c}_{\mathbf{r}_1,\beta} + \text{h.c.}\right) = 0. \tag{3.64}$$

However, if the time-delay is nonzero, the contribution from the diamagnetic term may be nonzero.

3.5.3.2 Matrix element of $\hat{R}^{(2)}$ in terms of $\hat{A}_j$, $\hat{B}_j$ and $\hat{C}_j$

Using operators Eqs. (3.60-3.62) we now consider the full operator $\hat{R}^{(2)}$ describing the amplitude to absorb two photons and emit two photons. The matrix elements of $\hat{R}^{(2)}$ between matter energy states $|I\rangle$ and $|F\rangle$ (both in the spin sector) have the following form (see Appendix C.3 for further details):

$$\begin{aligned}
&\langle F|\hat{R}^{(2)}_{\lambda_1,\lambda_2}|I\rangle \\
&= -\sum_J \left[\frac{\langle F|\hat{A}_2|J\rangle\ \langle J|\hat{A}_1|I\rangle}{\omega_{\lambda_1} - (\omega_L - E_{JI} + i0^+)} + (1 \leftrightarrow 2)\right] \\
&\quad -\sum_K \left[\frac{\langle F|\hat{C}_2|K\rangle\ \langle K|\hat{B}_1|I\rangle}{\omega_{\lambda_1} - (2\omega_L - E_{KI} + i0^+)} + (1 \leftrightarrow 2)\right],
\end{aligned} \tag{3.65}$$

where $|J\rangle$ and $|K\rangle$ are the intermediate many-body eigenstates, belonging to the spin and charge sectors respectively. E_{JI}, the energy difference between states $|J\rangle$ and $|I\rangle$ is of order $\mathtt{t}^2/U$, while E_{KI} is of order $U \pm$ order($\mathtt{t}$). Therefore, from Eq. (3.65) we explicitly see that the generation of photon pair with frequencies near ω_L (central peak peak in Fig. 3.7(e)) is accompanied by the action of pure spin operators $\hat{A}_j$ on the matter state. In contrast, the sideband emission with the frequencies $2\omega_L - U$ and U(Fig. 3.7(f)), is associated with the action of operators $\hat{B}_j$ and current

operator $\hat{C}_j$ respectively.

The energy dependent factors in Eq. (3.65) can be absorbed into the Heisenberg evolution of the matter operators (see Appendix C.3 for a derivation), and Eq. (3.65) can be written as

$$\begin{aligned}\langle F|\hat{R}^{(2)}_{\lambda_1,\lambda_2}|I\rangle = -i\int_{-\infty}^{\infty} \mathrm{d}t\, e^{-i(\omega_{\lambda_1}-\omega_L)t}\,\langle F|\mathbb{T}\left[\hat{A}_2(0)\hat{A}_1(-t)\right]|I\rangle \\ - i\int_{-\infty}^{\infty}\mathrm{d}t\,\langle F|\left[\theta(t)e^{-i\left(\omega_{\lambda_1}-2\omega_L\right)t}\hat{C}_2(0)\hat{B}_1(-t)+\theta(-t)e^{-i\omega_{\lambda_1}t}\hat{C}_1(-t)\hat{B}_2(0)\right]|I\rangle\,,\end{aligned} \tag{3.66}$$

where $\mathbb{T}[\,]$ denotes time-ordering of operators inside $[\,]$.

Note that the formula for $G^{(2)}(\tau)$ in Eq. (3.46) involves an integral over ω_{λ_1} and ω_{λ_2}, i.e., coherent superpositions of the different $\hat{R}^{(2)}_{\lambda_1,\lambda_2}$'s. Therefore, the frequency filter functions $\mathcal{F}_i(\omega)$ of the detectors play a crucial role in determining $G^{(2)}(\tau)$. With this in mind, in the following section, we investigate the temporal structure of the matter correlation functions inferred from measurement of $G^{(2)}(\tau)$, with an emphasis on their dependence on the frequency filter functions of the detectors.

3.6 Temporal structure of correlation functions

In this section, we combine the results of Sec. 3.5.3 (expressions for matter operators $\hat{R}^{(1)}$ and $\hat{R}^{(2)}$) and Sec. 3.4 (Eqs. (3.44-3.48) to derive the central relations of this work summarized in Table 3.1.

It is convenient to work with the Fourier transform of the filter function defined as $\tilde{\mathcal{F}}_j(t) = \int_{-\infty}^{\infty}\frac{\mathrm{d}\omega}{2\pi}\mathcal{F}_j(\omega)e^{-i\omega t}$. In order to simplify the expressions, we absorb phases such as $e^{-iE_{JI}t}$ into Heisenberg time-evolution of the operators involved in the correlation functions.

3.6.1 Intensity $G^{(1)}(0)$

The expression for $G^{(1)}_{d_j}(0) = \langle \text{out}| \, \hat{a}^\dagger_{d_j}(0)\hat{a}_{d_j}(0) \, |\text{out}\rangle$ in Eq. (3.44) can be simplified to

$$G^{(1)}_{d_j}(0) \approx \iint_{-\infty}^{\infty} \mathrm{d}t \, \mathrm{d}t' \, \tilde{\mathcal{F}}_j(t) \left[\tilde{\mathcal{F}}_j(t')\right]^* e^{i\omega_L(t-t')} \langle I| \left[\hat{A}_j(-t')\right]^\dagger \hat{A}_j(-t)|I\rangle \, , \tag{3.67}$$

where $\hat{A}_j$ is defined in Eq. (3.50). The operators in Eq. (3.67) are represented in the Heisenberg picture such that $\hat{A}(t) \equiv e^{i\hat{H}_0 t}\hat{A}e^{-i\hat{H}_0 t}$. To connect to the known results [7, 8, 54], let us consider the case of a Lorentzian effective filter function, defined in Eq. (3.12) that is peaked in frequency around ω_j with a width Γ_j. In terms of temporal variables, we get:

$$\tilde{\mathcal{F}}_{j,\,\text{Lorentzian}}(t) = \mathtt{K}_j \Gamma_j \theta(t) e^{-i\omega_j t} e^{-\Gamma_j t}, \tag{3.68}$$

where $\mathtt{K}$ is a constant and was defined in Eq. (3.13). In temporal variables, Eq. (3.67) reads:

$$G^{(1)}(\omega_j) \approx |\mathtt{K}_j|^2 \Gamma_j/2 \int_{-\infty}^{\infty} \mathrm{d}t \, e^{-\Gamma_j|t|} e^{i(\omega_L-\omega_j)t} \left\langle \left[\hat{A}_j(t)\right]^\dagger \hat{A}_j(0) \right\rangle_0 , \tag{3.69}$$

As in Eq. (3.67), the expectation value is taken in a matter eigenstate $|I\rangle$ in the spin sector. It can be straightforwardly generalized to any state or a density matrix describing thermal equilibrium (henceforth denoted with a subscript 0 as in Eq. (3.69)) within the spin sector. Eq. (3.67) is equivalent to the results of Ref. [7, 8, 54]. Thus, $G^{(1)}$ measures the dynamical fluctuations of spin singlet projection operators. In the special case of A_{2g} channel for the kagome lattice, it measures the dynamical fluctuations of spin chirality operators.

3.6.2 First-order quadrature correlator X^+

Using Eqs. (3.47,3.50), we get the first-order quadrature operator expectation value:

$$\left\langle \hat{a}_{d_j}(0) \right\rangle_{\text{out}} = \mathcal{F}_j(\omega_L) \left\langle \hat{A}_j(0) \right\rangle_0 . \tag{3.70}$$

It follows that, first, the signal for the quadrature correlator X^+ is sharply peaked at the laser frequency ω_L, corresponding to the *elastic* scattering of photons. Second, this correlator provides a direct measurement of the static expectation value of the operator $\hat{A}_j$, which, in most cases, is a sum of spin-singlet projection operators. However, on the kagome lattice in A_{2g} ($\left(e_j^x\right)^* e_L^y - \left(e_j^y\right)^* e_L^x$) channel, to leading order in $\mathtt{t}/|\omega_L - U|$, this operator is a linear combination of spin chirality operators [54]. While fluctuations of spin chirality have been proposed to be measured via neutron [55] and Raman scattering [54], the first-order photonic quadrature correlator introduced in this work enables a direct measurement of static spin chirality. It is important to note that a nonzero signal in this channel is only possible if the ground state spontaneously breaks reflection and time-reversal symmetries.

3.6.3 Phase-sensitive second order quadrature correlation $X^{++}(\tau)$

Analyzing Eqs. (3.48, 3.46), we find that to derive the matter correlators measured by $X^{++}_{d_1,d_2}(\tau) = \langle \hat{a}_{d_2}(\tau)\hat{a}_{d_1}(0)\rangle_{\text{out}}$ and $G^{(2)}_{d_1,d_2}(\tau) = \langle \hat{a}^\dagger_{d_1}(0)\hat{a}^\dagger_{d_2}(\tau)\hat{a}_{d_2}(\tau)\hat{a}_{d_1}(0)\rangle_{\text{out}}$, we need to express the following term using the expressions for $\hat{A}_j$, $\hat{B}_j$ and $\hat{C}_j$:

$$i\int_{-\infty}^{\infty} \frac{\mathrm{d}\omega_{\lambda_1}}{2\pi} \mathcal{F}_1(\omega_{\lambda_1})\mathcal{F}_2(2\omega_L - \omega_{\lambda_1} - E_{FI}) e^{i\omega_{\lambda_1}\tau} \langle F|\hat{R}^{(2)}_{\lambda_1,\lambda_2}(\omega_{\lambda_1},\omega_{\lambda_2})|I\rangle . \tag{3.71}$$

In the following, we assume that the filters $\mathcal{F}_i(\omega)$ are sensitive enough to distinguish frequencies around ω_L from those around $2\omega_L - U$ and U. Therefore, we ignore any interference between these sets of amplitudes. Without loss of generality, we assume that $\tau > 0$, i.e., detector 2 clicks after detector 1.

Substituting the matrix element $\langle F|\hat{R}^{(2)}_{\lambda_1,\lambda_2}(\omega_{\lambda_1},\omega_{\lambda_2})|I\rangle$ obtained in Eq. (3.66) into the expression in Eq. (3.71), and only keeping the term corresponding to the frequency range of interest, we get:

$$
\begin{aligned}
& i\int_{-\infty}^{\infty}\frac{\mathrm{d}\omega_{\lambda_1}}{2\pi}\mathcal{F}_1(\omega_{\lambda_1})\mathcal{F}_2(2\omega_L-\omega_{\lambda_1}-E_{FI})e^{i\omega_{\lambda_1}\tau}\,\langle F|\hat{R}^{(2)}_{\lambda_1,\lambda_2}|I\rangle \\
&\qquad = e^{i(2\omega_L-E_{FI})\tau}\int_0^{\infty}\int_0^{\infty}\mathrm{d}t_1\,\mathrm{d}t_2\,\tilde{\mathcal{F}}_1(t_1)\tilde{\mathcal{F}}_2(t_2)\,\langle F|\hat{M}^{(2)}_{d_1,d_2}(\tau-t_2,-t_1)|I\rangle\,, \text{ where} \\
& \hat{M}^{(2)}_{d_1,d_2}(\tau-t_2,-t_1) = \begin{cases} e^{i\omega_L(t_1+t_2-\tau)}\mathbb{T}\left[\hat{A}_2(\tau-t_2)\hat{A}_1(-t_1)\right] \\ \qquad \text{if both detectors detect near } \omega_L, \\ e^{2i\omega_L t_1}\theta(t_1+\tau-t_2)\hat{C}_2(\tau-t_2)\hat{B}_1(-t_1) \\ \qquad \text{if } d_1 \text{ detects near } 2\omega_L-U \text{ and } d_2 \text{ detects near } U, \\ e^{2i\omega_L(t_2-\tau)}\theta(t_2-t_1-\tau)\hat{C}_1(-t_1)\hat{B}_2(\tau-t_2) \\ \qquad \text{if } d_1 \text{ detects near } U \text{ and } d_2 \text{ detects near } 2\omega_L-U. \end{cases}
\end{aligned}
\tag{3.72}
$$

The above operator is directly related to the operator $\hat{M}_j(t)$ introduced in Sec. 3.2.2 [see Eq. (3.2)

and Eq. (3.4)] as:

$$\hat{M}^{(2)}_{d_1,d_2}(\tau - t_2, -t_1) = \mathbb{T}\left[\hat{M}_2(\tau - t_2)\hat{M}_1(-t_1)\right]. \tag{3.73}$$

We now substitute Eq. (3.72) in Eq. (3.48) and obtain:

$$\langle \hat{a}_{d_2}(\tau)\hat{a}_{d_1}(0)\rangle_{\text{out}} \approx \iint_{-\infty}^{\infty} \mathrm{d}t_1\, \mathrm{d}t_2\, \tilde{\mathcal{F}}_1(t_1)\tilde{\mathcal{F}}_2(t_2)\left\langle \hat{M}^{(2)}_{d_1,d_2}(\tau - t_2, -t_1)\right\rangle_0, \tag{3.74}$$

where $\hat{M}^{(2)}_{d_1,d_2}(\tau - t_2, -t_1)$ is a time-ordered product of operators, as defined in Eq. (3.72).

Assuming Lorentzian filter functions defined in Eq. (3.68), and taking the large Γ_1, Γ_2 limit, i.e., the limit of frequency selectivity being broad, the above equation becomes

$$\langle \hat{a}_{d_2}(\tau)\hat{a}_{d_1}(0)\rangle_{\text{out}}\Big|_{\Gamma_1,\Gamma_2\to\infty} \approx \mathtt{K}_1\mathtt{K}_2\left\langle \hat{M}^{(2)}_{d_1,d_2}(0, -\tau)\right\rangle_0. \tag{3.75}$$

We remind the reader that measurement of the above correlator requires a phase-sensitive quadrature measurement in which the input drive is in a coherent state. Such a scheme is described in Sec. 3.3.2.3.

3.6.4 Photon pair correlation function $G^{(2)}(\tau)$

Now, we are ready to derive the matter correlator measured by:

$$G^{(2)}_{d_1,d_2}(\tau) = \langle \hat{a}^\dagger_{d_1}(0)\hat{a}^\dagger_{d_2}(\tau)\hat{a}_{d_2}(\tau)\hat{a}_{d_1}(0)\rangle_{\text{out}}.$$

We substitute Eq. (3.72) into Eq. (3.46) and sum over final states $|F\rangle$ to obtain:

$$G^{(2)}_{d_1,d_2}(\tau)$$
$$\approx \int_0^\infty\int_0^\infty \mathrm{d}t_1\,\mathrm{d}t_2\,\mathrm{d}t_1'\,\mathrm{d}t_2'\,\tilde{\mathcal{F}}_1(t_1)\tilde{\mathcal{F}}_2(t_2)[\tilde{\mathcal{F}}_1(t_1')]^*[\tilde{\mathcal{F}}_2(t_2')]^*\,\mathcal{C}^{(2)}_{d_1,d_2}(-t_1',\tau-t_2';\tau-t_2,-t_1), \tag{3.76}$$

where

$$\mathcal{C}^{(2)}_{d_1,d_2}(-t_1',\tau-t_2';\tau-t_2,-t_1)$$
$$= \begin{cases} e^{i\omega_L\left(t_1-t_1'+t_2-t_2'\right)}\left\langle \bar{\mathbb{T}}\left[\hat{A}_1^\dagger(-t_1')\hat{A}_2^\dagger(\tau-t_2')\right]\mathbb{T}\left[\hat{A}_2(\tau-t_2)\hat{A}_1(-t_1)\right]\right\rangle_0 \\ \quad \text{if both detectors detect near } \omega_L, \\ \\ \theta(t_1'+\tau-t_2')\theta(t_1+\tau-t_2)e^{2i\omega_L\left(t_1-t_1'\right)}\left\langle \hat{B}_1^\dagger(-t_1')\hat{C}_2^\dagger(\tau-t_2')\hat{C}_2(\tau-t_2)\hat{B}_1(-t_1)\right\rangle_0 \\ \quad \text{if } d_1 \text{ detects near } 2\omega_L-U \text{ and } d_2 \text{ detects near } U, \\ \\ \theta(t_2-t_1-\tau)\theta(t_2'-t_1'-\tau)e^{2i\omega_L\left(t_2-t_2'\right)}\left\langle \hat{B}_2^\dagger(\tau-t_2')\hat{C}_1^\dagger(-t_1')\hat{C}_1(-t_1)\hat{B}_2(\tau-t_2)\right\rangle_0 \\ \quad \text{if } d_1 \text{ detects near } U \text{ and } d_2 \text{ detects near } 2\omega_L-U. \end{cases} \tag{3.77}$$

Here, the matter operators $\hat{A}_i$, $\hat{B}_j$ and $\hat{C}_i$ are the same as in Eqs. (3.60, 3.61, 3.62), and $\tilde{\mathcal{F}}_j(t_j)$ for detector j is the Fourier transform of the frequency filter function $\mathcal{F}_j(\omega)$.

The temporal structure is illustrated in Fig. 3.11. Given that the photonic correlator is of the form $\sim \left\langle \hat{a}_1^\dagger(0)\hat{a}_2^\dagger(\tau)\hat{a}_2(\tau)\hat{a}_1(0)\right\rangle$, one might expect the matter correlator to be of the form $\sim \left\langle \hat{A}_1^\dagger(0)\hat{A}_2^\dagger(\tau)\hat{A}_2(\tau)\hat{A}_1(0)\right\rangle$. This structure is indeed correct if the filter functions are broad in

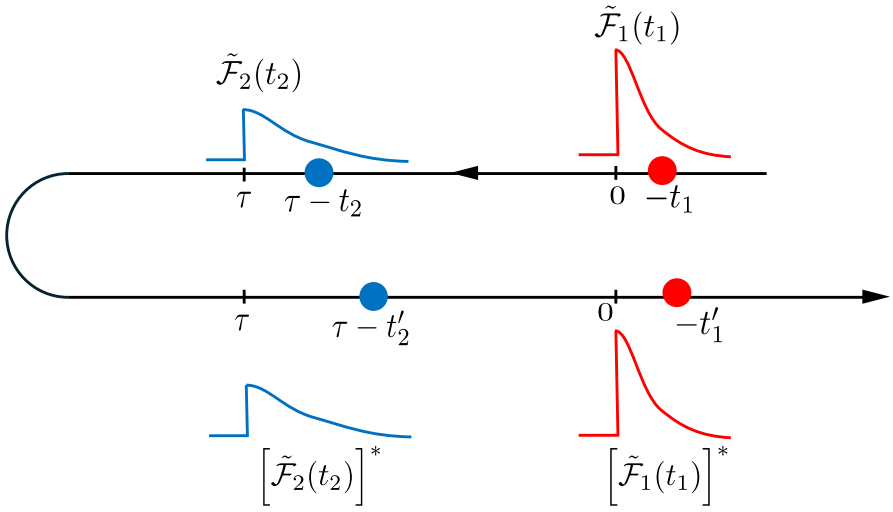

Figure 3.11: Time contour representation of the matter correlation function $G^{(2)}_{d_1,d_2}(\tau)$, given in Eq. (3.76, 3.77). Here, time flows forward from right to left. The red and blue circles denote operators that couple to the photon detected first and second, respectively. The forward time segment of the contour (top) is time-ordered, while the backward time segment (bottom) is anti-time-ordered. The profiles of the Fourier transformed *causal* filter functions $\tilde{\mathcal{F}}_j(t_j)$ are shown schematically.

frequency, and hence narrow in the time domain. However, in a more general scenario, the photon can spend time in the causal filter, say a cavity, before being detected. Consequently, the time delay between the detection events is not necessarily equal to the time interval between the photon emission events. In fact, if the filter's frequency selectivity is narrower than $1/\tau$, its Fourier transform can become sufficiently broad such that the first emitted photon may be detected after the second. Thus, the matter operators must be convolved with the Fourier-transformed filter functions, as expressed in Eqs. (3.76, 3.77).

Let us now consider Lorentzian effective filter functions as defined in Eq. (3.12), i.e., $\mathcal{F}_j(\omega) = i\mathrm{K}\Gamma_j/\left(\omega - \omega_j + i\Gamma_j\right)$, for detectors $j = 1$ and 2 respectively. Substituting its Fourier

transform, Eq. (3.68) into Eq. (3.76), we get:

$$G^{(2)}_{d_1,d_2}(\tau) = |\mathtt{K}_1\mathtt{K}_2\Gamma_1\Gamma_2|^2 \int_0^\infty\int_0^\infty\int_0^\infty\int_0^\infty \mathrm{d}t_1\,\mathrm{d}t_2\,\mathrm{d}t_1'\,\mathrm{d}t_2' \Big[\\ \times e^{-\left[\Gamma_1\left(t_1+t_1'\right)+\Gamma_2\left(t_2+t_2'\right)\right]}\mathcal{C}^{(2)}_{d_1,d_2}(-t_1', \tau-t_2'; \tau-t_2, -t_1)e^{i\omega_1(t_1'-t_1)+i\omega_2(t_2'-t_2)}\Big] \tag{3.78}$$

Let us now look at the different limiting cases of the frequency selectivity being broad (large Γ_j) and narrow (small Γ_j). In the large Γ_j limit, we approximate $\theta(t)\Gamma_j e^{-\Gamma_j t} \approx \delta(t)$ [4].

3.6.4.1 Detector d_1 is broad in frequency

First, let us take the limit $\Gamma_1 \to \infty$, while assuming Γ_2 is finite. Then, Eq. (3.78) yields:

$$G^{(2)}_{d_1,d_2}(\tau)\Big|_{\Gamma_1\to\infty} \approx |\mathtt{K}_1\mathtt{K}_2|^2\Gamma_2^2 \int_0^\infty \mathrm{d}t_2 \int_0^\infty \mathrm{d}t_2'\, e^{-\Gamma_2(t_2+t_2')}e^{i\omega_2(t_2'-t_2)}\mathcal{C}^{(2)}_{d_1,d_2}(0, \tau-t_2'; \tau-t_2, 0). \tag{3.79}$$

Here, the matter operators corresponding to the photon detected first (red dot in Fig. 3.11) are taken at a fixed time 0, while those, corresponding to the second photon (blue dot in Fig. 3.11) can contribute at times earlier than τ.

[4] For Eq. (3.76, 3.77) to hold, we want $\Gamma_j < |\omega_L - U|$, so that the spin operators ($\hat{A}_j$) do not interfere with the charge operators ($\hat{B}_j$, $\hat{C}_j$). Therefore, the approximation $\theta(t)\Gamma_j e^{-\Gamma_j t} \approx \delta(t)$ is justified, only if $|\omega_L - U|$ is much greater than the bandwidth of matter excitations. Since this bandwidth can be at most the tunneling $\mathtt{t}$, the approximation is justified in our setting.

3.6.4.2 Detector d_2 is broad in frequency

Next, let us take the limit $\Gamma_2 \to \infty$, while assuming Γ_1 is finite. Then, Eq. (3.78) yields :

$$G^{(2)}_{d_1,d_2}(\tau)\Big|_{\Gamma_2\to\infty} \approx |\mathtt{K}_1\mathtt{K}_2|^2\Gamma_1^2 \int_0^\infty \mathrm{d}t_1 \int_0^\infty \mathrm{d}t_1'\, e^{-\Gamma_1(t_1+t_1')} \times e^{i\omega_1(t_1'-t_1)}\mathcal{C}^{(2)}_{d_1,d_2}(-t_1', \tau; \tau, -t_1). \tag{3.80}$$

Here, the matter operators corresponding to the photon detected second (blue dots in Fig. 3.11) are taken at a fixed time τ, while those, corresponding to the first photon can contribute earlier than time 0.

3.6.4.3 Both detectors are broad in frequency

Next, let us take the limit where both $\Gamma_1 \to \infty$ and $\Gamma_2 \to \infty$. Then, Eq. (3.78) yields:

$$G^{(2)}_{d_1,d_2}(\tau)\Big|_{\Gamma_1,\Gamma_2\to\infty} \approx |\mathtt{K}_1\mathtt{K}_2|^2\mathcal{C}^{(2)}_{d_1,d_2}(0, \tau; \tau, 0). \tag{3.81}$$

In this limit the photonic correlation function exactly reflects that of the matter.

3.6.4.4 Both detectors are narrow in frequency

Let us consider the opposite limit of sharp frequency resolution, when both Γ_1 and Γ_2 are much less than $1/\tau$. In this limit, $G^{(2)}_{d_1,d_2}(\tau)$ is independent of τ:

$$G^{(2)}_{d_1,d_2}\Big|_{\Gamma_1,\Gamma_2\to 0} \propto \iiint_{-\infty}^{\infty} \mathrm{d}t_2\, \mathrm{d}t_1'\, \mathrm{d}t_2'\, e^{i\omega_1 t_1' + i\omega_2(t_2'-t_2)}\mathcal{C}^{(2)}_{d_1,d_2}(-t_1', -t_2'; -t_2, 0). \tag{3.82}$$

In summary, Eqs. (3.67), (3.70), (3.74), and (3.76), establish a one-to-one correspondence

between the matter and photonic correlation functions. In our derivation, the expectation value $\langle . \rangle_0$ on the right-hand side is evaluated with respect to the unperturbed energy eigenstate $|I\rangle$ of the matter Hamiltonian, within the spin sector. As a corollary, this expectation value can also be taken with respect to a mixed state (within the spin sector) that is diagonal in the energy eigenbasis, such as a thermal state. Consequently, our formalism remains valid at nonzero temperatures, provided that the temperature is much smaller than U.

With this mapping established, we now explore several key applications that enable the characterization of phases in spin systems.

3.7 Application I: Measurement of static spin chirality operators

In this section, we demonstrate that the static spin chirality on the triangular lattice can be probed through the phase-dependent part of fluctuations of the first-order quadrature operators of the scattered photons, i.e. $\mathrm{Im}\,\langle \hat{a}_{d_2}(0)\hat{a}_{d_1}(0)\rangle_{\text{out}}$. For this, the system should be driven by a coherent state input. Additional conditions are that the delay time $\tau = 0$, and the filters should be such that d_1 and d_2 select the sidebands near $2\omega_L - U$, and U respectively, but are broad in their respective sidebands. Also, the polarization of the drive as well as that of the detectors should be linear, i.e., $\mathbf{e}_L$, $\mathbf{e}_1$, and $\mathbf{e}_2$ are all real. The experimental scheme for the photonic measurement is provided in Appendix C.4.

We have shown in Sec. 3.5.3 that the correlations between photons emitted into the sidebands probe correlations between matter operators $\hat{B}_j$ [Eq. (3.61)] and $\hat{C}_j$ [Eq. (3.62)], both of which couple the spin sector to the charge sector. How could we then measure a pure spin correlator via photons in the sidebands? The reason lies in the two conditions we mentioned above.

The absence of filtering implies that photons do not spend any additional time in the filter after they are emitted by the material. Furthermore, $\tau = 0$ implies that the doublon-hole pair formed at the time of the first photon emission should immediately (within a temporal uncertainty $\sim 1/|\omega_L - U|$) recombine to emit the second photon. In other words, the time evolution step between Fig. 3.8(c_4') and (c_5') is not present anymore. Thus, the net result of the two-photon scattering on the material is the application of an operator purely in the spin sector. Further, we are able to circumvent the no-go result in Ref. [54] (where the spin chirality term was zero on the triangular lattice) because we have access to three polarizations $\mathbf{e}_L$, $\mathbf{e}_1$ and $\mathbf{e}_2$.

Using the mapping from photonic to electronic correlator in Eq. (3.75), we have

$$\mathrm{Im}\left\langle \hat{a}_{d_2}(0)\hat{a}_{d_1}(0)\right\rangle_{\text{out}} = \mathtt{K}_1\mathtt{K}_2\,\mathrm{Im}\left\langle \hat{C}_2(0)\hat{B}_1(0)\right\rangle_0 . \tag{3.83}$$

The expression for $\hat{B}_1$ is given in Eq. (3.61). Operator $\hat{C}_2$ is the global electron current along the direction $\mathbf{e}_2$, consisting of nearest-neighbor tunnelings. For the system to return to the spin sector after applying $\hat{C}_2$, the electron tunneling implemented by $\hat{B}_1$ should also be along a nearest-neighbor bond.

We discuss the anticipated form of the spin operators measured by Eq. (3.83) using a symmetry analysis. First, let us examine the terms in Eq. (3.61). Recall from Eqs. (3.63-3.64) in Sec. 3.5.3.1 that the terms in the first line of Eq. (3.61) do not contribute to $\left\langle \hat{C}_2(0)\hat{B}_1(0)\right\rangle$. Furthermore, since $\mathbf{e}_1$, $\mathbf{e}_2$, and $\mathbf{e}_L$ are all real, both $\hat{B}_1(0)$ and $\hat{C}_2(0)$ are odd under time-reversal. So, $\hat{C}_2(0)\hat{B}_1(0)$ is even under time-reversal. Therefore, $-i\left(\hat{C}_2(0)\hat{B}_1(0) - \hat{B}_1^\dagger(0)\hat{C}_2^\dagger(0)\right)/2$ is both a Hermitian operator and odd under time-reversal. It also transforms as a spin singlet under spin rotations since there is no spin-orbit coupling. Since all terms considered in this work are at most

eighth order in fermionic operators, they are at most fourth-order in spin operators. The only possible spin operator compatible with these conditions is a sum of spin chirality terms of the form $\sim \sum \hat{\mathbf{S}}_{\mathbf{r}} \cdot \left(\hat{\mathbf{S}}_{\mathbf{r}'} \times \hat{\mathbf{S}}_{\mathbf{r}''}\right)$ with real coefficients. Specifically, we are interested in scalar spin chirality, which is invariant under lattice rotation and odd under reflection. To isolate the scalar spin chirality, one must take linear combinations of experimental data for different directions of linear polarizations $\mathbf{e}_L$, $\mathbf{e}_1$, and $\mathbf{e}_2$, and expand the result in terms of irreducible representations of the crystalline point group of the triangular lattice. There are two such polarization channels that transform the same way as scalar spin chirality does:

$$\mathcal{A}_a \equiv (e_1^x e_2^y + e_2^x e_1^y)\left[(e_L^x)^2 - (e_L^y)^2\right] - (e_1^x e_2^x - e_1^y e_2^y)\,(2e_L^x e_L^y), \text{ and} \tag{3.84}$$

$$\mathcal{A}_b \equiv (e_1^x e_2^y - e_2^x e_1^y)\left[(e_L^x)^2 + (e_L^y)^2\right]. \tag{3.85}$$

These two channels transform identically as the channel termed A_{2g} in Ref. [54]). Let us now study Eq. (3.83) in each of these channels separately.

We now show that the contribution to channel $\mathcal{A}_a$ arises upon combining the current $\hat{C}_2$ with $i\hat{\boldsymbol{\mathcal{S}}}_{\boldsymbol{\mu}_1,\boldsymbol{\mu}_2}(\mathbf{r},\boldsymbol{\mu}) \cdot \left[\left(\hat{\mathbf{S}}_{\mathbf{r}} - \hat{\mathbf{S}}_{\mathbf{r}+\boldsymbol{\mu}}\right)/2 - i\hat{\mathbf{S}}_{\mathbf{r}} \times \hat{\mathbf{S}}_{\mathbf{r}+\boldsymbol{\mu}}\right]$ from $\hat{B}_1$ (see Eq. (3.61)), thereby yielding a spin operator. Recall that $\hat{\boldsymbol{\mathcal{S}}}_{\boldsymbol{\mu}_1,\boldsymbol{\mu}_2}(\mathbf{r},\boldsymbol{\mu})$ has been defined in Eq. (3.56) and is shown schematically in Fig. 3.10. The contributing process is shown in Fig. 3.7(c) with microscopic counterpart provided in Fig. 3.8(c_1'-c_6'). The same process for the triangular lattice is shown here in Fig. 3.12. In Eq. (3.61), tunneling along $\boldsymbol{\mu}_1'$ after absorbing a laser photon is shown in Fig. 3.12(b). We can now see from Fig. 3.12(c) that the direction of tunneling induced by the first and second photon absorptions are identical, i.e., $\boldsymbol{\mu}_2' = \boldsymbol{\mu}_1'$. The same applies to the photon emission process. We note that Eq. (3.61) holds for arbitrarily long-range fermion tunneling. However, for simplicity,

in Fig. 3.12 and in the expressions below, we restrict to nearest-neighbor tunneling. The term in $\hat{B}_1$ [Eq. (3.61)] which is relevant to Fig. 3.12 is (summation over spin indices of fermionic operators is implicit):

$$\frac{ig_L^2 \mathtt{t}^3 g}{(\omega_L - U)^2} \left(\boldsymbol{a}_1 \cdot \mathbf{e}_L\right)^2 \left(\boldsymbol{a}_2 \cdot \mathbf{e}_1\right) \left(\hat{c}_1^\dagger \boldsymbol{\sigma} \hat{c}_3 + \hat{c}_3^\dagger \boldsymbol{\sigma} \hat{c}_1\right) \cdot \left(\frac{\hat{\mathbf{S}}_0 - \hat{\mathbf{S}}_2}{2} - i\mathbf{S}_0 \times \mathbf{S}_2\right). \tag{3.86}$$

Here, $\boldsymbol{a}_1$ and $\boldsymbol{a}_2$ are lattice vectors $(1, 0)$ and $(1/2, \sqrt{3}/2)$ respectively [See Fig. 3.12(f)]. The subscript for the spins $\hat{\mathbf{S}}$ and fermionic operator $\hat{c}$ is the site index which runs from 0 to 5, the six sites shown in Fig. 3.12. Also, we use the shorthand $\hat{c}_1^\dagger \boldsymbol{\sigma} \hat{c}_3$ to denote $\hat{c}_{1,\alpha}^\dagger \boldsymbol{\sigma}_{\alpha\beta} \hat{c}_{3,\beta}$.

The term from $\hat{C}_2$ [Eq. (3.62)] which is relevant to Fig. 3.12 is:

$$\frac{ig\mathtt{t}}{\omega_L - U} \left(\boldsymbol{a}_2 \cdot \mathbf{e}_2\right) \left(\hat{c}_3^\dagger \hat{c}_1 - \hat{c}_1^\dagger \hat{c}_3\right) \tag{3.87}$$

Now, we can see that the electron tunneling in Eq. (3.86) can be combined with that in Eq. (3.87) to give an operator lying purely in the spin sector. To do so, we use the following identity (for combining a pair of fermionic operators into a spin operator) that holds at half-filling (which can be shown using the definition of spin operators in terms of fermions given in Eq. (3.30)):

$$\left(\hat{c}_3^\dagger \hat{c}_1 - \hat{c}_1^\dagger \hat{c}_3\right) \left(\hat{c}_3^\dagger \boldsymbol{\sigma} \hat{c}_1 + \hat{c}_1^\dagger \boldsymbol{\sigma} \hat{c}_3\right) = 2\left(\hat{\mathbf{S}}_3 - \hat{\mathbf{S}}_1\right) - 4i\hat{\mathbf{S}}_3 \times \hat{\mathbf{S}}_1. \tag{3.88}$$

Using this identity, the contribution from the process shown in Fig. 3.12 to $\hat{C}_2 \hat{B}_1$ is:

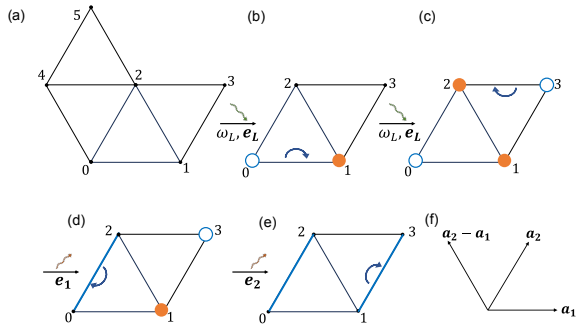

Figure 3.12: Processes leading to spin chirality matter operator: **(a)**: We study this motif because the two orientations of equilateral triangles and all six orientations of isosceles obtuse triangles involving the site labeled 0 can be found in this motif. Any other such triangle can be obtained by translating a triangle from this motif by a lattice vector. A black dot represents a singly occupied electron, i.e., a spin degree of freedom. Blue empty circle is a hole and an orange filled circle is a doubly occupied site (doublon). **(b)**: Upon absorption of a photon, an electron virtually hops from 0 to 1. **(c)**: Upon absorption of a second photon, an electron hops virtually from 3 to 0. **(d)**: The doublon-hole pair recombines along the bond from 2 to 0 by emitting a photon of polarization $\mathbf{e}_1$ and frequency around $2\omega_L - U$. **(e)**: This is similar to the previous step, but the frequency of the second photon is around U. **(f)**: Primitive lattice vectors $\boldsymbol{a}_1$ and $\boldsymbol{a}_2$ of the triangular lattice. Also shown is the linear combination $\boldsymbol{a}_2 - \boldsymbol{a}_1$.

$$\begin{aligned}&\frac{4g_L^2 g^2 \mathfrak{t}^4}{(\omega_L - U)^2} \left(\boldsymbol{a}_1 \cdot \mathbf{e}_L\right)^2 \left(\boldsymbol{a}_2 \cdot \mathbf{e}_1\right) \left(\boldsymbol{a}_2 \cdot \mathbf{e}_2\right) \\ &\times \left(\frac{\hat{\mathbf{S}}_2 - \hat{\mathbf{S}}_0}{2} - i\mathbf{S}_2 \times \mathbf{S}_0\right) \cdot \left(\frac{\hat{\mathbf{S}}_3 - \hat{\mathbf{S}}_1}{2} - i\mathbf{S}_3 \times \mathbf{S}_1\right).\end{aligned} \tag{3.89}$$

Now, for the same set of points $(0, 1, 2, 3)$ [Fig. 3.12], there is an alternative process where the laser-induced tunneling occurs along bonds 02 and 13, while the tunneling during photon emission occurs along the bonds 01 and 23. The resulting contribution to $\hat{C}_2 \hat{B}_1$ is:

$$\begin{aligned}&\frac{4g_L^2 g^2 \mathfrak{t}^4}{(\omega_L - U)^2} \left(\boldsymbol{a}_2 \cdot \mathbf{e}_L\right)^2 \left(\boldsymbol{a}_1 \cdot \mathbf{e}_1\right) \left(\boldsymbol{a}_1 \cdot \mathbf{e}_2\right) \\ &\times \left(\frac{\hat{\mathbf{S}}_3 - \hat{\mathbf{S}}_2}{2} - i\mathbf{S}_3 \times \mathbf{S}_2\right) \cdot \left(\frac{\hat{\mathbf{S}}_1 - \hat{\mathbf{S}}_0}{2} - i\mathbf{S}_1 \times \mathbf{S}_0\right).\end{aligned} \tag{3.90}$$

In addition to the set of points $(0, 1, 2, 3)$ considered above, we have the equivalent of Eq. (3.89) and Eq. (3.90) for the set of points $(0, 1, 2, 4)$ and $(0, 4, 5, 2)$ [Fig. 3.12(a)], thereby leading to

three pairs of terms per motif (shown in Fig. 3.12(a)). We then add up the contribution of each motif that is obtained by a lattice translation of the motif shown in Fig. 3.12(a). From the resulting expression, we isolate the terms corresponding to scalar spin chirality. We find that the result has a nonzero component along channel $\mathcal{A}_a$, but not $\mathcal{A}_b$. The component along the channel $\mathcal{A}_a$ (Eq. (3.84)) is

$$\frac{3\sqrt{3}g_L^2 g^2 \mathtt{K}_1 \mathtt{K}_2 \mathtt{t}^4}{2(\omega_L - U)^2}\chi, \tag{3.91}$$

where

$\chi \equiv$ 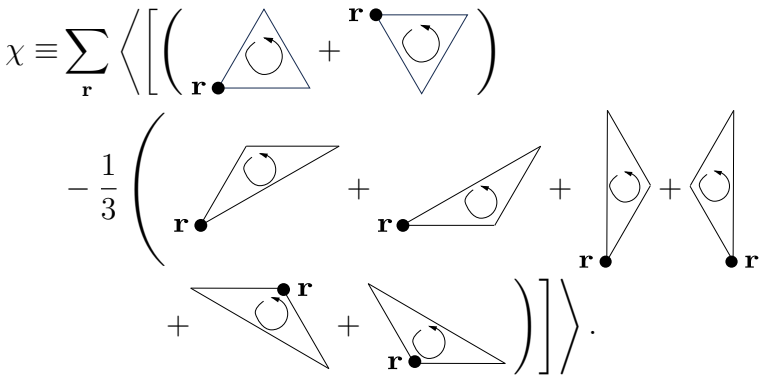 (3.92)

Here, we used the notation  $\equiv \hat{\mathbf{S}}_{\mathbf{r}} \cdot \left(\hat{\mathbf{S}}_{\mathbf{r}+\boldsymbol{a}_1} \times \hat{\mathbf{S}}_{\mathbf{r}+\boldsymbol{a}_2}\right)$.

Similarly, 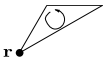 $\equiv \hat{\mathbf{S}}_{\mathbf{r}} \cdot \left(\hat{\mathbf{S}}_{\mathbf{r}+\boldsymbol{a}_1+\boldsymbol{a}_2} \times \hat{\mathbf{S}}_{\mathbf{r}+\boldsymbol{a}_2}\right)$, etc. g_L and g are light-matter couplings defined in Sec. 3.4.1 and $\mathtt{K}_1$ and $\mathtt{K}_2$ are constants related to detector efficiency and photonic density of states, defined in Eq. (3.13).

Next, we show that the contribution to the channel $\mathcal{A}_b$ (Eq. (3.85)) arises from combining the current $\hat{C}_2$ with $\hat{\mathcal{K}}_{\boldsymbol{\mu}'}(\mathbf{r}, \boldsymbol{\mu})\left(4\hat{\mathbf{S}}_{\mathbf{r}} \cdot \hat{\mathbf{S}}_{\mathbf{r}+\boldsymbol{\mu}} - 1\right)$, thereby yielding a spin operator. Recall that $\hat{\mathcal{K}}_{\boldsymbol{\mu}'}(\mathbf{r}, \boldsymbol{\mu})$ (defined in Eq. (3.52) and shown in Fig. 3.9) is a sum of electron tunnelings along bonds in the direction $\boldsymbol{\mu}'$ that also touch the bond $(\mathbf{r}, \boldsymbol{\mu})$. One can see that the result is a sum of

terms of the following form:

$$(4\hat{\mathbf{S}}_{\mathbf{r}} \cdot \hat{\mathbf{S}}_{\mathbf{r}+\boldsymbol{\mu}'} - 1)(4\hat{\mathbf{S}}_{\mathbf{r}} \cdot \hat{\mathbf{S}}_{\mathbf{r}+\boldsymbol{\mu}} - 1)(\bar{\boldsymbol{\mu}} \cdot \mathbf{e}_L)(\bar{\boldsymbol{\mu}} \cdot \mathbf{e}_1)(\bar{\boldsymbol{\mu}}' \cdot \mathbf{e}_L)(\bar{\boldsymbol{\mu}}' \cdot \mathbf{e}_2) \tag{3.93}$$

$$= \Big[-8i\hat{\mathbf{S}}_{\mathbf{r}} \cdot \left(\hat{\mathbf{S}}_{\mathbf{r}+\boldsymbol{\mu}} \times \hat{\mathbf{S}}_{\mathbf{r}+\boldsymbol{\mu}'}\right) - 4\hat{\mathbf{S}}_{\mathbf{r}} \cdot \hat{\mathbf{S}}_{\mathbf{r}+\boldsymbol{\mu}} - 4\hat{\mathbf{S}}_{\mathbf{r}} \cdot \hat{\mathbf{S}}_{\mathbf{r}+\boldsymbol{\mu}'}$$
$$+4\hat{\mathbf{S}}_{\mathbf{r}+\boldsymbol{\mu}} \cdot \hat{\mathbf{S}}_{\mathbf{r}+\boldsymbol{\mu}'} + 1\Big] (\bar{\boldsymbol{\mu}} \cdot \mathbf{e}_L)(\bar{\boldsymbol{\mu}} \cdot \mathbf{e}_1)(\bar{\boldsymbol{\mu}}' \cdot \mathbf{e}_L)(\bar{\boldsymbol{\mu}}' \cdot \mathbf{e}_2). \tag{3.94}$$

The first term in this equation is a spin chirality operator. Performing a summation over bond directions $\boldsymbol{\mu}$ and $\boldsymbol{\mu}'$, and lattice sites $\mathbf{r}$, we find that the resulting component of scalar spin chirality is zero within the channel $\mathcal{A}_a$. In contrast, in channel $\mathcal{A}_b$, we get:

$$-\frac{3\sqrt{3}\mathtt{t}^4 g_L^2 g^2 \mathtt{K}_1 \mathtt{K}_2}{(\omega_L - U)^2}\chi, \tag{3.95}$$

Therefore,

$$\mathrm{Im}\,\langle \hat{a}_{d_2}(0)\hat{a}_{d_1}(0)\rangle_{\text{out}} = \frac{3\sqrt{3}\mathtt{t}^4 g_L^2 g^2 \mathtt{K}_1 \mathtt{K}_2}{2(\omega_L - U)^2}(\mathcal{A}_a - 2\mathcal{A}_b)\chi + \ldots, \tag{3.96}$$

where "..." includes terms in other symmetry channels which can be filtered out by varying the linear polarizations $\mathbf{e}_L$, $\mathbf{e}_1$, $\mathbf{e}_2$, and taking appropriate linear combinations of the experimental data. We note that the sum of coefficients per unit cell in Eq. (3.92) is zero. However, we generically do not expect the spin chirality on an equilateral triangle and an obtuse triangle to cancel out, since the two are unrelated by symmetry. Therefore, we generically expect $\mathrm{Im}\,\langle \hat{a}_{d_2}(0)\hat{a}_{d_1}(0)\rangle_{\text{out}}$ to be nonzero in a chiral spin liquid. While Eq. (3.92) has been written for nearest-neighbor tunneling, we see from Eq. (3.61) that analogous expressions follow for the case of long-range tunneling as well. The main difference will be the addition of spin chirality operators on larger triangles. These new operators have the same symmetry properties as Eq. (3.92) and are again

additional contributions to scalar spin chirality.

In summary, we propose the following experimental protocol to detect scalar spin chirality and identify a chiral spin liquid. (1) The system is driven by a coherent laser beam with a frequency ω_L satisfying $\mathtt{t} \ll |\omega_L - U| \ll U$. (2) The phase-sensitive quadrature fluctuation, $\langle \hat{a}_{d_2}(0)\hat{a}_{d_1}(0)\rangle_{\text{out}}$ of the filtered sidebands of the scattered light is measured. Within each sector of Fig. 3.2, the filters are assumed to be broadband within their respective frequency windows. Linear combinations of $\langle \hat{a}_{d_2}(0)\hat{a}_{d_1}(0)\rangle_{\text{out}}$ at various polarizations are used to extract contributions in the channels $\mathcal{A}_a$ and $\mathcal{A}_b$, as defined in Eqs. (3.84-3.85). A nonzero result directly indicates the presence of scalar spin chirality.

We note that the generation of entangled photons with frequencies $2\omega_L - U$ and U is reminiscent of the four-wave mixing process that naturally occurs in nonlinear media. This process can also be understood as two-mode squeezing of the coherent component of the scattered light [176, 177, 178]. The coherent component corresponds to processes where the matter and light are unentangled after the scattering. In contrast, the incoherent components generate excess noise, which can be probed via measurement of the phase-independent part of the quadrature correlation function, i.e., $G^{(1)}(\tau)$.

If we consider $G^{(2)}_{d_1,d_2}$ instead of the squeezing spectrum, the corresponding matter correlator is the absolute value squared of spin chirality. In this section, we focused on detection near $2\omega_L - U$ and U. Using $G^{(2)}_{d_1,d_2}$, when both the detectors are centered near frequency ω_L, one can already make interesting predictions for the correlators of $\hat{A}_j$, defined in Eq. (3.60). This will be the subject of the next two sections.

3.8 Contribution of noninteracting magnons to $G^{(2)}$

The low-energy Hamiltonian of the Fermi-Hubbard model at half-filling, when projected to the spin sector, yields the Heisenberg model:

$$\hat{H}_{\text{Heisenberg}} = \frac{1}{2}\sum_{\mathbf{r},\mathbf{r}'} J_{\mathbf{r}\mathbf{r}'}\hat{\mathbf{S}}_{\mathbf{r}} \cdot \hat{\mathbf{S}}_{\mathbf{r}'}, \tag{3.97}$$

where $J_{\mathbf{r},\mathbf{r}'} = 4\mathfrak{t}^2_{\mathbf{r},\mathbf{r}'}/U$. Depending on the lattice geometry and the values of couplings beyond nearest-neighbor and next-nearest-neighbor couplings, the Heisenberg model is believed to admit a variety of ground states – both ordered states and spin liquids. If the ground state is magnetically ordered, the excitations are bosonic magnons (which may have a finite lifetime and weak interactions). However, if the ground state is a spin liquid, the excitations can be more exotic, such as anyons with fractional statistics. The goal of this section is to study the contribution to the connected $\mathcal{G}^{(2)}$ from non-interacting magnons. We then determine the conditions under which these contributions can be filtered away, so that any remaining $\mathcal{G}^{(2)}$ signal originates from magnon-magnon interactions or topological contributions.

3.8.1 Quadratic magnon Hamiltonian

Using the standard linearized Holstein-Primakoff and Bogoliubov transformations [179, 180], the Hamiltonian of the Heisenberg model Eq. (3.97) can be written as:

$$\hat{H}_{\text{low}} = \sum_{\mathbf{k}} \xi_{\mathbf{k}} \hat{b}^{\dagger}_{\mathbf{k}} \hat{b}_{\mathbf{k}}, \tag{3.98}$$

where $\hat{b}^\dagger_{\mathbf{k}}$ is the creation operator of a magnon carrying momentum $\mathbf{k}$ and characterized by a dispersion $\xi_{\mathbf{k}}$. In spin variables, $\hat{b}^\dagger_{\mathbf{k}}$ generally corresponds to a superposition of $\hat{S}^+_{\mathbf{k}}$ and $\hat{S}^-_{\mathbf{k}}$, where $\hat{S}^\pm_{\mathbf{k}} = \hat{S}^x_{\mathbf{k}} \pm i\hat{S}^y_{\mathbf{k}}$.

The pure spin sector operators $\hat{A}_j$, which appear in the photonic correlation functions, are defined in Eq. (3.60). As outlined in Sec. 3.5.1, $\hat{A}_j$ can be decomposed into irreducible representations of the crystalline point group. In this section, we assume that this decomposition has been performed (e.g., by taking linear combinations of experimental data corresponding to different polarization directions) and that $\hat{A}_j$ belongs to a specific irreducible representation. We proceed to express $\hat{A}_j$ in terms of magnon operators. Up to second order in magnon operators, we have (in the interaction picture):

$$\begin{aligned}\hat{A}_j(-t) = \sum_{\mathbf{k};k_x\geq 0} \Big\{ &\alpha_j(\mathbf{k}) e^{-2i\xi_{\mathbf{k}}t} \hat{b}^\dagger_{\mathbf{k}} \hat{b}^\dagger_{-\mathbf{k}} + (\alpha'_j(\mathbf{k}))^* \hat{b}_{\mathbf{k}} \hat{b}_{-\mathbf{k}} e^{2i\xi_{\mathbf{k}}t} \\ &+\beta_j(\mathbf{k}) \left(\hat{b}^\dagger_{\mathbf{k}} \hat{b}_{\mathbf{k}} + \hat{b}^\dagger_{-\mathbf{k}} \hat{b}_{-\mathbf{k}} + 1 \right) \Big\} ,\end{aligned} \tag{3.99}$$

where the coefficients $\alpha_j(\mathbf{k})$, $\alpha'_j(\mathbf{k})$ and $\beta_j(\mathbf{k})$ are determined by the same Bogoliubov transformation that diagonalizes the free magnon Hamiltonian. Note that earlier, the subscript j referred to whether the operator $\hat{A}_j$ coupled to a photon mode of detector 1 or 2. In this section, the subscript also labels an irreducible representation of the spatial symmetry group.

The coefficients $\{\alpha_j(\mathbf{k})\}$, $\{\alpha'_j(\mathbf{k})\}$, $\{\beta_j(\mathbf{k})\}$, and their complex conjugates, all transform according to the same irreducible representation as $\hat{A}_j$ does, under spatial rotations and reflection.

Therefore, the following orthogonality conditions hold:

$$\sum_{\mathbf{k}} \left(\alpha'_j(\mathbf{k})\right)^* \alpha_l(\mathbf{k}) = 0, \text{ for } j \neq l, \tag{3.100}$$

$$\sum_{\mathbf{k}} \left(\alpha'_j(\mathbf{k})\right) \alpha_l(\mathbf{k}) = 0, \text{ for } j \neq l, \tag{3.101}$$

$$\sum_{\mathbf{k}} \left(\beta_j(\mathbf{k})\right)^* \beta_l(\mathbf{k}) = 0, \text{ for } j \neq l. \tag{3.102}$$

3.8.2 Contribution of magnons to Raman Scattering, or $G^{(1)}(0)$

Let us now assume the spin system is initially prepared in its ground state. Defining the Raman shift $\Omega_j \equiv \omega_L - \omega_j$. Using Eq. (3.67), we find that the Raman intensity $G^{(1)}$ detected in channel j for a Lorentzian filter (Eq. (3.12)) is given by

$$G^{(1)}_{d_j}(0) = |\mathrm{K}_j|^2 \sum_{\mathbf{k}} \frac{\Gamma_j^2 |\alpha_j(\mathbf{k})|^2}{\Gamma_j^2 + (\Omega_j - 2\xi_{\mathbf{k}})^2}. \tag{3.103}$$

This expression reflects the fact that the photon scattering process can create a magnon pair, and $G^{(1)}(0)$ includes contributions from all magnon pairs with energy $2\xi_{\mathbf{k}}$ equal to the Raman shift Ω_j within an uncertainty Γ_j set by the frequency filter. It is important to note that the equation involves a discrete sum over momenta, with the number of terms governed by the number of lattice sites N illuminated by the laser beam.

We now consider the limits $\Gamma_j \to \infty$ (broad filter) and $\Gamma_j \to 0$ (sharp filter). For a broad filter,

$$G^{(1)}_{d_j}(0) \xrightarrow{\Gamma_j \to \infty} N\mathrm{a}^2 |\mathrm{K}_j|^2 \int_{\text{B.Z.}} \frac{\mathrm{d}^2 k}{(2\pi)^2} |\alpha_j(\mathbf{k})|^2, \tag{3.104}$$

where B.Z. stands for the first Brillouin zone of the lattice. Next, for a sharp filter,

$$G_{d_j}^{(1)}(0) \xrightarrow{\Gamma_j \to 0} N\Gamma_j \mathrm{a}^2 |\mathrm{K}_j|^2 \int_{\mathrm{B.Z.}} \frac{\mathrm{d}^2 k}{4\pi} \delta(2\xi_{\mathbf{k}} - \Omega_j) |\alpha_j(\mathbf{k})|^2. \tag{3.105}$$

We thus find that $G_{d_j}^{(1)}(0)$ reflects the density of states of magnon pairs (of zero total momentum) at Ω_j, modulated by $|\alpha_j(\mathbf{k})|^2$. Note that in the sharp filter limit we assume Γ_j is still greater than the mean energy spacing due to the finite-size quantization. Thus, $\Gamma_j N$ remains nonzero even in the limit $\Gamma_j \to 0$.

3.8.3 Magnon contributions to connected $\mathcal{G}^{(2)}$

Since the magnon Hamiltonian in Eq. (3.98) is quadratic and the input light is Gaussian, one might naïvely expect $G_{d_1,d_2}^{(2)}(0)$ to factorize as $G_{d_1}^{(1)}(0) G_{d_2}^{(1)}(0)$. However, we show here that this is not the case. The reason is that the effective coupling to matter via Eq. (3.99) is nonlinear. This finding is reminiscent of the result of Ref. [177] on single-mode Gaussian states of light.

We consider the connected part of $\mathcal{G}_{d_1,d_2}^{(2)}(\tau) \equiv G_{d_1,d_2}^{(2)}(\tau) - G_{d_1}^{(1)}(0) G_{d_2}^{(1)}(0)$. For a Lorentzian filter, it is given by:

$$\begin{aligned}
\mathcal{G}_{d_1,d_2}^{(2)}(\tau) = |\mathrm{K}_1 \mathrm{K}_2 \Gamma_1 \Gamma_2|^2 \iiiint_0^\infty \mathrm{d}t_1 \, \mathrm{d}t_2 \, \mathrm{d}t_1' \, \mathrm{d}t_2' \\
\times \Big\{ e^{-\left[\Gamma_1(t_1+t_1') + \Gamma_2(t_2+t_2')\right]} e^{i\left[\Omega_1(t_1-t_1') + \Omega_2(t_2-t_2')\right]} \\
\times \Big(\Big\langle \bar{\mathbb{T}} \left[\hat{A}_1^\dagger(-t_1') \hat{A}_2^\dagger(\tau - t_2') \right] \mathbb{T} \left[\hat{A}_2(\tau - t_2) \hat{A}_1(-t_1) \right] \Big\rangle_0 \\
- \left\langle \hat{A}_1^\dagger(-t_1') \hat{A}_1(-t_1) \right\rangle_0 \left\langle \hat{A}_2^\dagger(-t_2') \hat{A}_2(-t_2) \right\rangle_0 \Big) \Big\} .
\end{aligned} \tag{3.106}$$

Starting from the ground state of the spin system, the right-most operator (corresponding to the

earliest photon emission) first creates a magnon pair as shown in Fig. 3.13(a), and the photon emitted is red-detuned with respect to the laser frequency. For $\hat{A}_1$ and $\hat{A}_2$ belonging to the same symmetry channel, $\hat{A}_2$ can annihilate the magnon-pair created by $\hat{A}_1$, leading to the emission of a blue-detuned photon as schematically shown in Fig. 3.13(c). For simplicity, we now assume that operators $\hat{A}_1$ and $\hat{A}_2$ are in different symmetry channels. Then, by the orthogonality relations Eq. (3.100-3.102) the magnon pair created by $\hat{A}_1$ can only be annihilated by $\hat{A}_1^\dagger$ (and not by $\hat{A}_2^\dagger$).

Let us now consider the contribution where $\hat{A}_1$ and $\hat{A}_2$ each create a magnon pair of different momenta as shown in Fig. 3.13(b). Then these pairs are annihilated by $\hat{A}_1^\dagger$ and $\hat{A}_2^\dagger$. The term resulting from this process factorizes as $G^{(1)}_{d_1}(0)G^{(1)}_{d_2}(0)$ and thus contributes only to the disconnected part of the full $G^{(2)}$.

We now describe two classes of terms contributing to the connected part $\mathcal{G}^{(2)}_{d_1,d_2}(0) = G^{(2)}_{d_1,d_2}(0) - G^{(1)}_{d_1}(0)G^{(1)}_{d_2}(0)$.

3.8.3.1 Nonlinear bosonic enhancement

Now, let us consider the scenario where $\hat{A}_1$ and $\hat{A}_2$ create magnon pairs with identical momenta. In this case, the same magnon pair is both created and annihilated twice, as depicted in Fig. 3.13(d). Using the fact that $\langle 0|\hat{b}_{-\mathbf{k}_1}\hat{b}_{\mathbf{k}_1}\hat{b}_{-\mathbf{k}_2}\hat{b}_{\mathbf{k}_2}\hat{b}^\dagger_{-\mathbf{k}_2}\hat{b}^\dagger_{\mathbf{k}_2}\hat{b}^\dagger_{-\mathbf{k}_1}\hat{b}^\dagger_{\mathbf{k}_1}|0\rangle = 4$ for $\mathbf{k}_1 = \mathbf{k}_2$, and 1 for $\mathbf{k}_1 \neq \mathbf{k}_2$, we get the following nonzero contribution to the connected $\mathcal{G}^{(2)}_{d_1,d_2}$:

$$\sum_{\mathbf{k}} \frac{3|\mathtt{K}_1\mathtt{K}_2|^2\Gamma_1^2\Gamma_2^2|\alpha_1(\mathbf{k})\alpha_2(\mathbf{k})|^2}{[\Gamma_1^2+(\Omega_1-2\xi_{\mathbf{k}})^2]\,[\Gamma_2^2+(\Omega_2-2\xi_{\mathbf{k}})^2]}. \tag{3.107}$$

The discrete summation $\sum_{\mathbf{k}}$ can be written in the continuum as $N\mathtt{a}^2\int\frac{\mathrm{d}^2k}{(2\pi)^2}$, where N is the number of lattice sites covered by the incoming laser beam. Let us consider the sharp filter case.

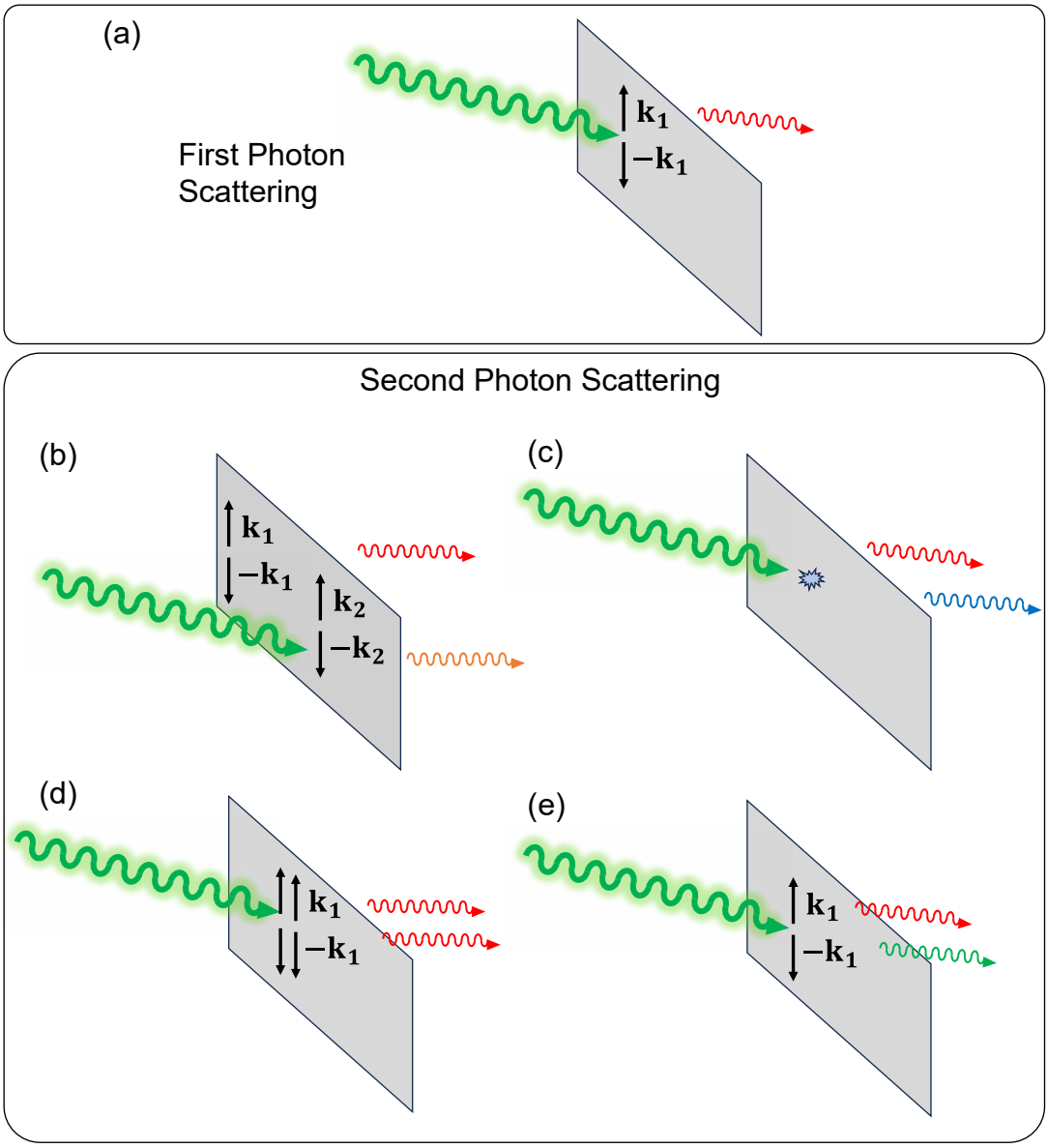

Figure 3.13: Different magnon processes leading to the scattering of two photons: **(a)**: Raman scattering of the first photon leads to the creation of a magnon-pair of momenta $\mathbf{k}_1$ and $-\mathbf{k}_1$. **(b)**: The scattering of the second photon could lead to creation of a different magnon-pair of momenta $\mathbf{k}_2$ and $-\mathbf{k}_2$. In this case, the second photon is also red-detuned with respect to the laser and generically has a frequency different from the first one. **(c)**: Scattering of the second photon leads to the annihilation of the magnon-pair created in (a). The photon is blue-detuned in this case. **(d)**: This is similar to (b), except $\mathbf{k}_2 = \mathbf{k}_1$. This is treated separately here. **(e)**: The second photon is elastically scattered.

Here, we will work in the limit where $\Gamma_1\Gamma_2 N$ is nonzero and finite even as one takes $\Gamma_{1,2} \to 0$. In this limit, using the identity $\lim_{\Gamma\to 0} \frac{\Gamma}{\Gamma^2+x^2} = \pi\delta(x)$, Eq. (3.107) yields:

$$\frac{3|\mathtt{K}_1\mathtt{K}_2|^2(N\Gamma_1\Gamma_2)\mathtt{a}^2}{4}\delta(\Omega_1-\Omega_2)\int \mathrm{d}^2k\,|\alpha_1(\mathbf{k})\alpha_2(\mathbf{k})|^2\delta(\Omega_1-2\xi_{\mathbf{k}}). \tag{3.108}$$

Since this term contains $\delta(\Omega_1 - \Omega_2)$, it can be filtered out by choosing $\omega_1 \neq \omega_2$ (and hence $\Omega_1 \neq \Omega_2$).

3.8.3.2 Elastic scattering

The second contribution to the connected $\mathcal{G}^{(2)}_{d_1,d_2}$ arises from the following scenario: the first photon is inelastically scattered by the material, resulting in the creation of a magnon pair described by the action of $\hat{A}_1$ on the magnon vacuum state $|0\rangle$. The second photon, however, undergoes elastic scattering without generating an additional magnon pair, as illustrated in Fig. 3.13(e). This process is described by the magnon-conserving terms in $\hat{A}_2$ of the form $(\hat{b}^\dagger_{\mathbf{k}}\hat{b}_{\mathbf{k}} + \hat{b}^\dagger_{-\mathbf{k}}\hat{b}_{-\mathbf{k}} + 1)$.

After a lengthy but straightforward algebraic calculation, we arrive at the following contribution to Eq. (3.106), from the integrals over the domains $(t_1 > t_2,\ t_1' > t_2')$ and $(t_1 < t_2,\ t_1' < t_2')$:

$$\sum_{\mathbf{k}}\Bigg\{\frac{|\alpha_1(\mathbf{k})|^2|\beta_2(\mathbf{k})|^2\Gamma_1^2\Gamma_2^2}{[\Gamma_1^2+(2\xi_{\mathbf{k}}-\Omega_1)^2]\,[(\Gamma_1+\Gamma_2)^2+(2\xi_{\mathbf{k}}-\Omega_1-\Omega_2)^2]} + [1\leftrightarrow 2]\Bigg\}\times 9|\mathtt{K}_1\mathtt{K}_2|^2 \tag{3.109}$$

In contrast, the contribution from $(t_1 > t_2,\ t_1' < t_2')$ and $(t_1 < t_2,\ t_1' > t_2')$ in Eq. (3.106) is given

below.

$$\sum_{\mathbf{k}}\Bigg\{\Bigg[\alpha_2^*(\mathbf{k})\beta_1^*(\mathbf{k})\beta_2(\mathbf{k})\alpha_1(\mathbf{k})\frac{\Gamma_1^2\Gamma_2^2 e^{-2i\xi_{\mathbf{k}}\tau}}{(\Omega_2+i\Gamma_2)(\Omega_1-i\Gamma_1)} \times\left(\frac{e^{(i\Omega_2-\Gamma_2)\tau}}{\Omega_1+\Omega_2-2\xi_{\mathbf{k}}+i(\Gamma_1+\Gamma_2)}+\frac{1-e^{(i\Omega_2-\Gamma_2)\tau}}{\Omega_1-2\xi_{\mathbf{k}}+i\Gamma_1}\right) \times\left(\frac{e^{(-i\Omega_1-\Gamma_1)\tau}}{\Omega_1+\Omega_2-2\xi_{\mathbf{k}}-i(\Gamma_1+\Gamma_2)}+\frac{1-e^{(-i\Omega_1-\Gamma_1)\tau}}{\Omega_2-2\xi_{\mathbf{k}}-i\Gamma_2}\right)\Bigg] + \text{ c.c.}\Bigg\}\times 9|\mathtt{K}_1\mathtt{K}_2|^2. \tag{3.110}$$

In Eqs. (3.109) and Eq. (3.110), one factor of $\Gamma_1\Gamma_2$ can be combined with N to give a finite constant while converting the sum to an integral, leaving behind the other factor of $\Gamma_1\Gamma_2$ in the integrand. As we take $\Gamma_1 \to 0$, and $\Gamma_2 \to 0$, regardless of the order, one can check that the expression in Eq. (3.110) goes to 0. On the other hand, for Eq. (3.109), it matters whether one takes $\Gamma_1 \to 0$ first, or $\Gamma_2 \to 0$. If we first take $\Gamma_2 \to 0$ and then $\Gamma_1 \to 0$, then the expression in Eq. (3.109) becomes:

$$\frac{9|\mathtt{K}_1\mathtt{K}_2|^2\mathtt{a}^2 N\Gamma_1\Gamma_2}{4}\delta(\Omega_1)\int \mathrm{d}^2k\,|\alpha_1(\mathbf{k})\beta_2(\mathbf{k})|^2\delta(2\xi_{\mathbf{k}}-\Omega_2). \tag{3.111}$$

On the other hand, if we first take $\Gamma_1 \to 0$ and then $\Gamma_2 \to 0$, then the expression in Eq. (3.109) becomes:

$$\frac{9|\mathtt{K}_1\mathtt{K}_2|^2\mathtt{a}^2 N\Gamma_1\Gamma_2}{4}\delta(\Omega_2)\int \mathrm{d}^2k\,|\alpha_2(\mathbf{k})\beta_1(\mathbf{k})|^2\delta(2\xi_{\mathbf{k}}-\Omega_1). \tag{3.112}$$

Eq. (3.111-3.112) correspond to elastic scattering and by choosing $\Omega_1 = \omega_L - \omega_1 \neq 0$, and $\Omega_2 = \omega_L - \omega_2 \neq 0$, this contribution to $\mathcal{G}^{(2)}_{d_1,d_2}$ can be filtered out.

Therefore, if the filter functions are sharp, any contribution to the connected $\mathcal{G}^{(2)}$ from noninteracting bosonic excitations can be eliminated if we: (1) filter out the case when the two

magnon pairs created are identical by demanding that the frequencies of the detected photons are different (i.e., impose $\omega_1 \neq \omega_2$), and (2) filter out elastic scattering (i.e., impose $\omega_1 \neq \omega_L$ and $\omega_2 \neq \omega_L$).

Once this filtering is implemented, any remaining contribution to the connected $\mathcal{G}^{(2)}$ should thus arise from interactions or topology.

3.9 Application II: Detecting fractional statistics

In this section, we show that if the ground state of the spin sector is topologically ordered, the existence of anyonic excitations with fractional mutual statistics can be detected by measuring photonic correlators of scattered photons. We use the argument from Ref. [15, 125].

We start with an outline of this section. First, in Sec. 3.9.1, we consider the conditional $G^{(1)}(\tau)$ [Eq. (3.28)] and observe that it has the same form as a correlator studied in Ref. [15, 125], allowing us to directly use their results. Next, in Sec. 3.9.2, we propose another approach using the connected $\mathcal{G}^{(2)}$ where one can explicitly filter out the contributions from topologically trivial magnon excitations discussed in Sec. 3.8. The temporal contour of this correlator is slightly different from the one considered in Ref. [15, 125]. So we adapt their arguments for our case. We do not repeat their derivation, but summarize their arguments qualitatively in this subsection. We encourage the reader to refer to Ref. [15, 125] for a treatment of finite temperature effects and for a discussion on ignoring short-range interactions between anyons.

3.9.1 Conditional $G^{(1)}(\tau)$: Signature of existence of fractional statistics

First, let us consider the conditional $G^{(1)}(\tau)$ defined in Eq. (3.28), under the following subtraction scheme:

$$\begin{aligned} &H_{d_1,d_2}(t,\tau) - G^{(1)}_{d_1}(0)G^{(1)}_{d_2}(\tau) \\ =&\langle \hat{a}^\dagger_{d_1}(0)\hat{a}^\dagger_{d_2}(t+\tau)\hat{a}_{d_2}(t)\hat{a}_{d_1}(0)\rangle_{\text{out}} + \text{c.c.} \\ &- \langle \hat{a}^\dagger_{d_1}(0)\hat{a}_{d_1}(0)\rangle_{\text{out}} \left(\langle \hat{a}^\dagger_{d_2}(t+\tau)\hat{a}_{d_2}(t)\rangle_{\text{out}} + \text{c.c.}\right). \end{aligned} \tag{3.113}$$

The experimental scheme to measure this photonic correlator is shown in Fig. 3.5, and explained in detail in Appendix C.4.2. Let us assume that the filter functions are chosen such that they select the window around ω_L (as opposed to the sidebands $2\omega_L - U$ and U), but is broadband with respect to the finer structure within each sector in Fig. 3.2. Then, using the mapping provided in Table 3.1, for $t > 0$ and $\tau > 0$, Eq. (3.113) yields:

$$\begin{aligned} |\mathtt{K}_1\mathtt{K}_2|^2 \Big[&\left\langle \hat{A}^\dagger_1(0)\hat{A}^\dagger_2(t+\tau)\hat{A}_2(t)\hat{A}_1(0)\right\rangle_0 + \text{c.c.} \\ &- \left\langle \hat{A}^\dagger_1(0)\hat{A}_1(0)\right\rangle_0 \left(\left\langle \hat{A}^\dagger_2(t+\tau)\hat{A}_2(t)\right\rangle_0 + \text{c.c.}\right)\Big], \end{aligned} \tag{3.114}$$

where the constants $\mathtt{K}_j$ are defined in Eq. (3.13).

The detection of a photon by detector d_j corresponds to the application of the operator $\hat{A}_j$, (defined in Eq. (3.60)) on the material state. As long as $\hat{A}_j$ does not commute with the Hamiltonian, $\hat{A}_j$ acting on the ground state will create excitations. If the material is topologically ordered, its excitations can be anyonic. We assume that the material is at zero temperature. Now, if $|I\rangle$ is the ground state, then $\hat{A}_j|I\rangle$ would generically have an overlap with a state consisting

of an anyon pair, unless this is ruled out by symmetry. We will therefore suppose that $\hat{A}_1$ and $\hat{A}_2$ create pairs of anyons whose energy gaps are Δ_1 and Δ_2 respectively. For concreteness, if the ground state is a $\mathbb{Z}_2$ spin liquid, one can think of $\hat{A}_1$ and $\hat{A}_2$ as creating e and m anyon pairs respectively. These pairs get annihilated by $\hat{A}_1^\dagger$ and $\hat{A}_2^\dagger$ respectively [5]. We point out that Δ_1 and Δ_2 are the gaps within the spin sector and are much smaller than the optical gap U.

The correlator in Eq. (3.114) is indeed of the same form as the pump-probe susceptibility studied in Ref. [15, 125]. Therefore, using the same argument as Ref. [15, 125] (which we summarize in Sec. 3.9.2), Eq. (3.114) is proportional to $(1-\cos\alpha_{12})\tau^{1/2}$, where $e^{i\alpha_{12}}$ is the braiding phase of an anyon created by $\hat{A}_2$ going around an anyon created by $\hat{A}_1$. This $\tau^{1/2}$ behavior is an experimental signature of the existence of fractional statistics.

One can also look at the following normalized version of the photonic correlator in Eq. (3.113):

$$\bar{H}_{d_1,d_2}(t,\tau) \equiv \frac{H_{d_1,d_2}(t,\tau) - G^{(1)}_{d_1}(0)G^{(1)}_{d_2}(\tau)}{G_{d_2}(\tau)} \tag{3.115}$$

The denominator was shown in Ref. [15] to go as $1/\tau$. Therefore, $\bar{H}_{d_1,d_2}(t,\tau) \sim \tau^{3/2}$ if there are excitations with fractional mutual statistics. The normalized $\bar{H}_{d_1,d_2}(t,\tau) \sim \tau^{3/2}$. It was shown in Ref. [15] to be more robust to thermal fluctuations than Eq. (3.113).

In the next subsection, we show that a similar prediction can be made for the connected $\mathcal{G}^{(2)}_{d_1,d_2}$ correlator instead of Eq. (3.114). $\mathcal{G}^{(2)}_{d_1,d_2}$ offers additional functionality by enabling filtering out contributions from topologically trivial excitations as discussed in Sec. 3.8. Thus, filtering allows us to consider the contribution originating exclusively from the fractional statistics of quasiparticles.

[5] Being in different symmetry channels, $\hat{A}_1^\dagger$ cannot annihilate anyons created by $\hat{A}_2$ and vice-versa.

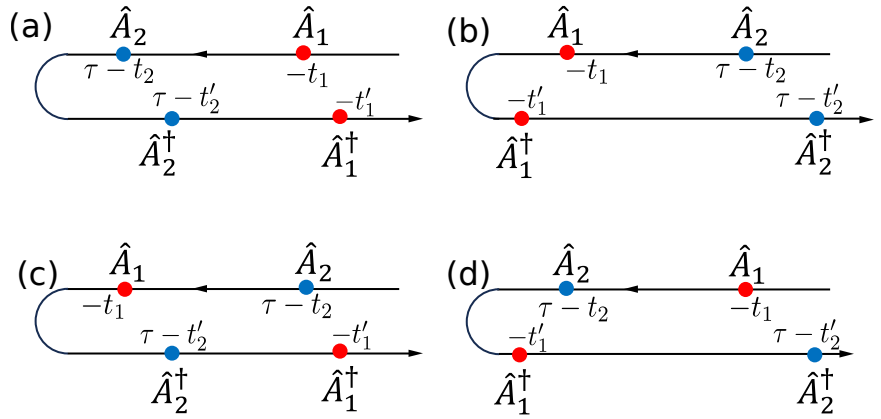

Figure 3.14: Four operator orderings in Eq. (3.106): **(a)**: $\tau - t_2 > -t_1$ and $\tau - t_2' > -t_1'$, **(b)**: $-t_1 > \tau - t_2$ and $-t_1' > \tau - t_2'$, **(c)**: $-t_1 > \tau - t_2$ and $\tau - t_2' > -t_1'$, and **(d)**: $\tau - t_2 > -t_1$ and $-t_1' > \tau - t_2'$.

3.9.2 Connected $\mathcal{G}^{(2)}$: Singularity from fractional statistics

The spin correlator measured by the connected $\mathcal{G}^{(2)}$ is provided in Eq. (3.106). It comprises contributions from different worldlines of anyons obeying the constraint that the pair created at time $-t_1$ is annihilated at time $-t_1'$, and similarly the pair created at $\tau - t_2$ is annihilated at $\tau - t_2'$. Among these are those worldlines where one anyon *braids* nontrivially with another. Such paths come with an extra braiding phase. In this section, we show that nontrivial mutual statistics leads to a singularity in the connected $\mathcal{G}^{(2)}$ as well: $\mathcal{G}^{(2)}_{d_1,d_2}(\Omega_1,\Omega_2) \sim \theta(\Omega_1 - \Delta_1)\theta(\Omega_2 - \Delta_2)\left[K_2(\Omega_2)(\Omega_1 - \Delta_1)^{-3/2} + (1 \leftrightarrow 2)\right]$, where $K_j(\Omega_j)$ are system-specific functions (recall that $\Omega_j = \omega_L - \omega_j$). In the limit of sharp frequency filters, we expect the dependence of $G^{(2)}$ on τ to drop out. Hence, we can set $\tau = 0$ from the outset.

We adapt the geometric argument in Ref. [15, 125] to show the above result. There is one difference in our case: due to the frequency-filtering, the time at which the first anyon pair is created need not be equal to the time when it is annihilated.

The spin correlator extracted from $\mathcal{G}^{(2)}$, i.e., Eq. (3.106) is a sum of terms with four different

operator orderings depending on the ordering within the pairs $(-t_1, -t_1')$, and $(-t_2, -t_2')$. These orderings are (suppressing the time arguments): $\left\langle \hat{A}_1^\dagger \hat{A}_2^\dagger \hat{A}_2 \hat{A}_1 \right\rangle$, $\left\langle \hat{A}_2^\dagger \hat{A}_1^\dagger \hat{A}_1 \hat{A}_2 \right\rangle$, $\left\langle \hat{A}_1^\dagger \hat{A}_2^\dagger \hat{A}_1 \hat{A}_2 \right\rangle$, and $\left\langle \hat{A}_2^\dagger \hat{A}_1^\dagger \hat{A}_2 \hat{A}_1 \right\rangle$ [Fig. 3.14 (a), (b), (c), (d) respectively].

First, let us consider the operator ordering in Fig. 3.14(a), i.e., $\left\langle \hat{A}_1^\dagger(-t_1') \hat{A}_2^\dagger(-t_2') \hat{A}_2(-t_2) \hat{A}_1(-t_1) \right\rangle$. In this correlator, first $\hat{A}_1$ and then $\hat{A}_2$ each create anyon pairs at time $-t_1$ and $-t_2$ respectively (shown as red and blue respectively in Fig. 3.15). The blue pair gets destroyed by $\hat{A}_2^\dagger$ at time $-t_2'$, and lastly, at time $-t_1'$, the red anyon pair gets destroyed by $\hat{A}_1^\dagger$. If one ignores anyon-anyon interactions, the contributions from worldlines without any braiding get canceled when we look at the connected $\mathcal{G}^{(2)}$ (as shown in Sec. 3.8). Furthermore, the argument in Ref. [15] about the contribution from short-ranged interactions being less singular than the contribution from fractional statistics also applies in our setting. Therefore, we will only study worldlines involving nontrivial braiding of otherwise "non-interacting" anyons. Each such worldline contributes a topological factor of $(1 - \cos \alpha_{12})$ where $e^{i\alpha_{12}}$ is the braiding phase of a blue anyon going around the red one.

The connected part can be written as a path integral over all trajectories where the blue anyon pair braids around one of the red anyons. Recall that here, $t_1 - t_2 > 0$, and $t_1' - t_2' > 0$, but the orderings within the pairs (t_1, t_1'), and (t_2, t_2') are left unspecified. For the recombination of the second (blue) anyon pair between t_2 and t_2', it is not sufficient to consider the ballistic propagation and wavepacket spreading has to be taken into account (see Fig. 3.15). The amplitude of recombination of the blue pair due to quantum wavepacket spreading is $\sim |t_2 - t_2'|^{-d/2}$ where spatial dimension $d = 2$.

To study the first (red) anyon pair, following Ref. [15, 125], one can perform a semiclassical analysis in the limit where the time it takes for an anyon pair to recombine is much less than the time difference between creating the first and second anyon pairs, i.e., $|t_1 - t_2| \gg |t_2 - t_2'|$,

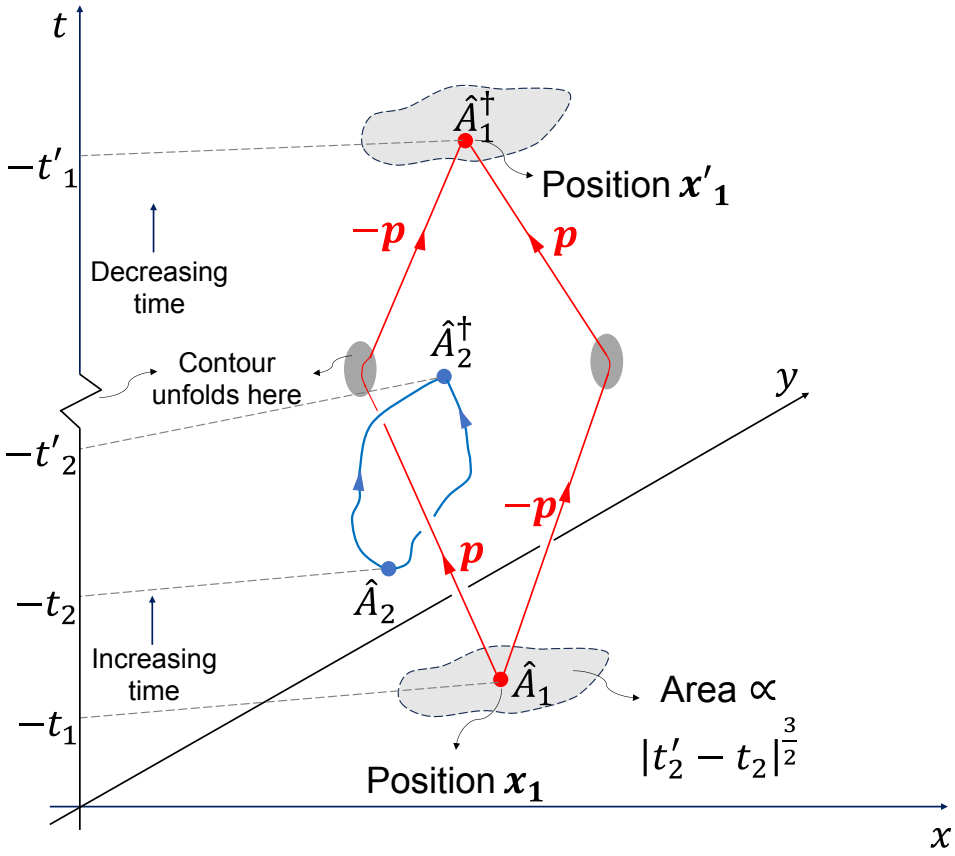

Figure 3.15: This figure is similar to Fig. 1 of Ref. [15], except the backward propagation is unfolded here. Without loss of generality, in this figure, $t_2 > t'_2$. In our time axis, from $-t'_2$, onwards, time decreases in the upward direction. For the operator ordering in Fig. 3.14(a), we depict a history of anyons that contributes to the connected $\mathcal{G}^{(2)}$. At time $-t_1$, operator $\hat{A}_1$ creates an anyon pair (red) at spatial point $\mathbf{x}_1$. Since $\hat{A}_1$ is a zero-momentum operator, $\mathbf{x}_1$ is integrated over the whole area of irradiation. At time $-t_2$, operator $\hat{A}_2$ (blue) creates a second anyon pair that recombines at $-t'_2$ due to wavepacket spreading. Let us consider a fixed worldline loop of the second pair. A path integral over all possible worldlines of the red anyons is dominated by those trajectories where a red anyon ballistically propagates through the blue loop till time $-t'_2$, and then turns around to recombine at time $-t'_1$. For a fixed momentum $\mathbf{p}$ of the red anyon, it has been shown geometrically that $\mathbf{x}_1$ can only be from an area $\sim |t'_2 - t_2|^{3/2}$ [15]. Since $-t'_1$ and $-t_1$ are not necessarily equal, classically, the red anyons will not recombine if they exactly retrace their path during backward propagation. However, due to quantum wavepacket spreading, there is a nonzero amplitude of recombination, which we conjecture to be independent of t_2 and t'_2.

$|t_1' - t_2'| \gg |t_2 - t_2'|$, and $|t_1' - t_2'| \gg |t_1 - t_1'|$. In principle, we also need to evaluate correlators outside this limit, since t_j and t_j' are integrated over. But as a first approximation, we obtain the correlator by extrapolating the expressions found in this limit.

The path integral is then dominated by those trajectories where one anyon from the red pair propagates ballistically with momentum $\mathbf{p}$ and passes through the closed worldline of the blue anyon pair [15, 125]. At time $-t_2'$, the red anyons turn around to recombine at time $-t_1'$ (here, $\mathbf{p}$ is integrated over). One such trajectory is shown in Fig. 3.15. It was shown in Ref. [15, 125] that for a fixed momentum $\mathbf{p}$ of a red anyon, it can braid through the blue pair only if its starting location $\mathbf{x}_1$, i.e., the spatial position of creation of the red anyon pair, belongs to an area that scales as $\sim |t_2' - t_2|^{3/2} F_1(p)$. Computing the function $F_1(p)$ is beyond the scope of this work, and its specific form is not important for our results. Combining all the factors, the overall amplitude for braiding scales as $\sim (1 - \cos\alpha_{12})|t_2 - t_2'|^{1/2} F_1(p) e^{i\Delta_2(t_2' - t_2)}$.

One caveat in our case is that since $t_1' \neq t_1$, we need to consider wavepacket spreading even in the red anyon pair to ensure recombination after backward propagation. We conjecture that this recombination amplitude only depends on $(t_1 - t_1')$, and is independent of t_2 or t_2'. We present a semiclassical argument for this. The center of mass position of the red anyon pair should remain unchanged at the saddle point level, because the blue pair does not impart center of mass momentum to the red pair. If we consider the two red anyons to be moving with equal and opposite momenta $\mathbf{p}$ and $-\mathbf{p}$, each momentum $\mathbf{p}$ contributes an amplitude $e^{i(\frac{p^2}{m_1} + \Delta_1)(t_1' - t_1)}$ towards recombination, where m_1 is the effective mass of a red anyon. This factor is independent

of t_2 and t_2'. Combining all the above factors, we get

$$\sim(1-\cos\alpha_{12})|t_2-t_2'|^{1/2}e^{i\left(\frac{p^2}{m_1}+\Delta_1\right)(t_1'-t_1)}F_1(p)e^{i\Delta_2(t_2'-t_2)} \tag{3.116}$$

While the geometric argument captures the scaling $|t_2-t_2'|^{1/2}$, it does not capture a phase jump $e^{i\frac{\pi}{4}\text{sign}(t_2-t_2')}$ when t_2 and t_2' are exchanged. The phase jump is important to capture the Heaviside step functions $\theta(\Omega_1-\Delta_1)\theta(\Omega_2-\Delta_2)$ in our final result. Fixing the phase requires consideration of the $t_2-t_2'\sim 0$ limit, which is beyond the scope of the scaling approach. In order to make progress, we employ an analyticity argument. For this, it is convenient to consider the correlator $\left\langle\hat{A}_1^\dagger(-t_1')\hat{A}_2^\dagger(-t_2')\hat{A}_2(-t_2)\hat{A}_1(-t_1)\right\rangle$ as an analytic continuation of a Euclidean-time correlation function. Therefore, we consider the analytic continuation defined as:

$$t_j\to t_j+i\epsilon_j\equiv iu_j \text{ and } t_j'\to t_j'+i\epsilon_j'\equiv iu_j', \tag{3.117}$$

such that $0<\epsilon_1<\epsilon_2<\epsilon_2'<\epsilon_1'\to 0^+$. This order of limits is required because a zero temperature correlation function $\left\langle\hat{P}_1(-iu_n)\hat{P}_2(-iu_{n-1})\ldots\hat{P}_n(-iu_1)\right\rangle$ is well-defined only if the operators are time-ordered with respect to the arguments $\text{Re}\,u_n,\text{Re}\,u_{n-1},\ldots,\text{Re}\,u_1$, i.e., if $\text{Re}\,u_n>\text{Re}\,u_{n-1}>\ldots>\text{Re}\,u_1$. Here, we use the convention $\hat{P}_n(-iu_n)\equiv e^{u_n\hat{H}_0}\hat{P}_ne^{-u_n\hat{H}_0}$. Now, we know that the correlation function we are computing here is an analytic function of u_2 and u_2' when $\text{Re}\,u_2'>\text{Re}\,u_2$, i.e., $\epsilon_2'>\epsilon_2$. The factor of $\sim|t_2-t_2'|^{1/2}$ obtained above should thus be replaced by $(u_2'-u_2)^{1/2}$, such that the branch-cut is in the unphysical region where

$\mathrm{Re}(u_2' - u_2) < 0$. This method is agnostic to the ordering between real times t_2 and t_2'.

$$\begin{aligned}&\left\langle \hat{A}_1^\dagger(-iu_1')\hat{A}_2^\dagger(-iu_2')\hat{A}_2(-iu_2)\hat{A}_1(-iu_1)\right\rangle \\ &\sim N\mathsf{a}^2(1-\cos\alpha_{12})e^{-\Delta_1(u_1'-u_1)-\Delta_2(u_2'-u_2)}(u_2'-u_2)^{1/2}\int\frac{\mathrm{d}^2p}{(2\pi)^2}e^{-\frac{p^2}{m_1}(u_1'-u_1)}F_1(p).\end{aligned} \tag{3.118}$$

Analytic continuing back to real-time, while maintaining $\mathrm{Re}(u_1' - u_1) > 0$ and $\mathrm{Re}(u_2' - u_2) > 0$, we get

$$\begin{aligned}&\left\langle \hat{A}_1^\dagger(-t_1')\hat{A}_2^\dagger(-t_2')\hat{A}_2(-t_2)\hat{A}_1(-t_1)\right\rangle \\ &\sim N\mathsf{a}^2|t_2-t_2'|^{1/2}e^{i\frac{\pi}{4}\mathrm{sign}(t_2-t_2')}e^{i\Delta_2(t_2'-t_2+i0^+)} \\ &\quad\times(1-\cos\alpha_{12})\int\frac{\mathrm{d}^2p}{(2\pi)^2}e^{i\left(\frac{p^2}{m_1}+\Delta_1\right)(t_1'-t_1+i0^+)}F_1(p),\end{aligned} \tag{3.119}$$

If we insert this expression into Eq. (3.106), and perform the Fourier transform, we obtain that the contribution of the contour in Fig. 3.14(a) to the connected $\mathcal{G}^{(2)}$ is $N\theta(\Omega_1 - \Delta_1)\theta(\Omega_2 - \Delta_2)K_1(\Omega_1)(\Omega_2 - \Delta_2)^{-3/2}$. Here, $K_1(\Omega_1)$ is a function obtained by integrating over momenta $\mathbf{p}$ of the red anyon and performing the Fourier-transform with respect to $t_1' - t_1$. One can now observe that the result for the contour in Fig. 3.14(b) can be obtained by swapping the roles of the red and blue anyons in the above calculation. The resulting contribution is $N\theta(\Omega_1 - \Delta_1)\theta(\Omega_2 - \Delta_2)K_2(\Omega_2)(\Omega_1 - \Delta_1)^{-3/2}$. The physical origin of this singularity in frequency can be traced back to the result in Ref. [15, 125] that the amplitude for recombination of one pair of anyons, conditioned on braiding through the other pair of anyons grows as $|t_2 - t_2'|^{1/2}$ in time. This growth is in turn due to the fact that the amplitude for one anyon to braid around the other grows with the area enclosed by one anyon loop. We note that the mutual statistics phase α_{12} itself gets absorbed into non-universal factors here, and only the *existence* of fractional statistics can be tested for in this approach.

Now, we consider the contour in Fig. 3.14(c). Here, the blue anyon pair is created before the red pair and is also annihilated before the red pair. In this case, neither anyon can be treated ballistically. If one tries to naïvely apply the semiclassical argument from Ref. [15, 125], the location of creation of the red anyon pair is drawn from an area scaling as $(u_2' - u_1)(u_2' - u_2)^{1/2}$. This area is smaller than the factor $(u_2' - u_2)^{3/2}$ we found for the contour in Fig. 3.14(a). Thus, the resulting contribution to the connected $\mathcal{G}^{(2)}$ from the ordering of Fig. 3.14(c) should also be less singular than that from Fig. 3.14(a). The same applies to the contribution shown in Fig. 3.14(d). Therefore, our final estimate for the singular part of $\mathcal{G}^{(2)}$ is

$$\mathcal{G}^{(2)}_{d_1,d_2}(\Omega_1, \Omega_2) \sim N\theta(\Omega_1 - \Delta_1)\theta(\Omega_2 - \Delta_2)\left[K_2(\Omega_2)(\Omega_1 - \Delta_1)^{-3/2} + (1 \leftrightarrow 2)\right]. \tag{3.120}$$

In conclusion, in this section, we demonstrated that the measurement of correlation functions of the photons scattered off the material enables the detection of the existence of fractional statistics of quasiparticles. We note that the derivation of Eq. (3.120) involved an assumption that the extent of wavepacket spreading of the first anyon pair is independent of the time at which the second pair was created, as long as the two creation events are sufficiently spaced apart temporally. This assumption should be examined more carefully in future work.

We also note that in Eq. (3.120), $\mathcal{G}^{(2)}_{d_1,d_2}(0)$ is proportional to N, i.e., the number of sites illuminated by the input laser. Similarly, our results for $\mathcal{G}^{(2)}_{d_1,d_2}$ in Sec. 3.8, i.e., Eqs. (3.108, 3.111, 3.112) are all proportional to N. In contrast, $G^{(1)}_{d_1}(0)G^{(1)}_{d_2}(0)$ is proportional to N^2. Hence, the normalized $\mathcal{G}^{(2)}_{d_1,d_2}(0)/G^{(1)}_{d_1}(0)G^{(1)}_{d_2}(0)$ would be proportional to $1/N$. This calls into question whether our prediction in Eq. (3.120) will result in a detectable signal. One way the signal can be detected is if the $(\Omega_j - \Delta_j)^{-3/2}$ singularity makes up for the $1/N$ suppression. Finding whether

this is indeed the case requires an explicit microscopic calculation of $\mathcal{G}^{(2)}_{d_1,d_2}$. This is a subject for future work. Another way is if N (proportional to the area of the input light beam) is small enough to overcome the $1/N$ suppression, but large enough for many-body effects to be observed. It is interesting to ask if such a suitable range of N can be achieved using recent advances in near-field spectroscopy [181].

3.10 Potential experimental realization

Our approach is immediately applicable to any correlated material where the system and its optical response can be captured within a Fermi-Hubbard or a generalized Heisenberg model such that the charge gap is in the IR/optical range. Sr_2IrO_4 is an example of such a transition metal oxide. As shown in Ref. [182], after taking into account spin-orbit coupling and crystal field splitting, among the ten available $5d$ orbital states, there is a doubly degenerate subspace of effective total angular momentum $J_{\text{eff}} = 1/2$. This provides an $SU(2)$-symmetric Hamiltonian in terms of pseudospins. As long as the drive frequency (chosen to be of the order of U) is far from gaps to all other orbitals, pseudospin-orbit coupling (and not spin-orbit coupling) can be ignored, and the system is approximately described by Eq. (3.29). In Sr_2IrO_4, U is of the order of 100 meV [182].

Furthermore, the expressions Eq. (3.60), (3.61), (3.62) hold for arbitrarily long-range fermion tunneling. By building on existing literature, our formalism can straightforwardly be extended to systems with spin-orbit coupling [149], and with multiple orbitals per site [174, 175]. To do so, there should be no few-photon resonances between the ground state sector and the higher orbitals.

Moreover, our formalism is applicable to any system in which there are two sectors of states separated by an optical gap. For concreteness, we considered them to be lower Hubbard band (spin sector) and upper Hubbard band (charge sector) (see Fig. 3.2). But our calculation can be adapted to other scenarios. For example, we can modify Fig. 3.2 so that the lower and higher energy sectors are valence and conduction bands respectively in a correlated TMD heterobilayer, such as WS_2/ WSe_2. In this case, a single sector consists of both the upper Hubbard band and lower Hubbard band within the valence/conduction band [183]. In such systems, the emission of photons is strongly susceptible to the nature of the underlying electronic states [184]. For example, it has been observed via photoluminescence (PL) measurements that the diffusion of excitons is affected strongly depending on whether the underlying electronic states are metallic, a Generalized Wigner Crystal or a Mott insulator. In such systems, U is typically a few tens of meV [184, 185, 186, 187, 188]. Therefore, detection of many-body correlations from PL at temperatures much smaller than U is experimentally accessible. Consequently, it is a promising direction to investigate correlations between emitted photons from such systems. For example, our results from Sec. 3.7 can be relevant to the proposal to realize a chiral spin liquid in TMD heterostructures [189].

Furthermore, all photonic correlators in Table 3.1 are either routinely measured in the quantum optics setting or can be measured with existing technology. For example, the phase-sensitive second-order quadrature measurement shown in Fig. 3.4 is related to two-mode squeezing that has been measured experimentally [172, 173]. $G^{(2)}$ measurements have been used experimentally to study non-classical features of phonons in condensed matter systems [190].

In optical experiments probing 2D materials, the materials are typically placed on substrates. The laser frequency is far detuned from any resonances within device substrates. There-

fore, optical coupling to substrates can be ignored as is done routinely in such experiments [188, 191].

Now, we address the effects of nonzero temperatures in our work. In Eq. (3.40), we started with the matter in an arbitrary energy eigenstate $|I\rangle$. As a corollary, our mapping in Table 3.1 holds for the matter starting in any mixed state that is diagonal in the energy eigenbasis, and in particular, for a thermal state. However, we require the temperature to be much smaller than the optical gap U, so that we can assume that the matter starts in the spin sector (lower Hubbard band). Further, the mapping from phase-sensitive second-order quadrature correlation to scalar spin chirality in Sec. 3.7 is purely at the operator level and is agnostic to temperature and the nature of the ground state in the spin sector. Regarding Sec. 3.9 on the detection of the existence of fractional statistics, at non-zero temperatures, there is a finite thermal population of anyons. The resulting effect on the nonlinear matter correlator was considered in Ref. [15]. The same analysis applies to our results in Sec. 3.9, i.e., the $\tau^{3/2}$ growth in Eq. (3.115) is cut off by a thermal timescale, and similarly, the $(\Omega_i - \Delta_i)^{-3/2}$ singularity in Sec. 3.9.2 gets broadened.

3.11 Conclusions and Outlook

In this work, we have proposed a novel probe of many-body states of matter based on the measurement of the quantum statistical properties of scattered light. Furthermore, we demonstrated that it can be used to diagnose exotic properties of strongly correlated electronic systems such as fractional statistics of excitations and scalar spin chirality.

One important aspect that will be subject to future research concerns the inherent complexity of the electronic band structure. In particular, while this work focused on the single-band

Fermi-Hubbard model, many realistic materials, such as cuprates (charge transfer insulators) or insulators based on transition metal dichalcogenides, possess multiple bands. In this case, the specific form of the light-matter interaction, projected to the relevant bands, must account for the orbital structure of the corresponding Bloch wavefunctions.

The formalism developed in this work relies only on the existence of the optical gap and is agnostic to the details of the Hamiltonian describing the low-energy physics. We note that, for a known Hamiltonian, the ground state of a correlated system is not a priori obvious (what symmetries it spontaneously breaks, whether it is a spin liquid, etc.), even if the microscopic Hamiltonian is known. It would thus be interesting to investigate the different ground state ansatzes and the corresponding excitations, with the aim of identifying the distinctive signatures in the photon scattering data corresponding to the different many-body states of matter. The extension of these ideas to cold atom systems is also intriguing [192].

In this work, we ignored the momentum transfer between electrons and photons. However, in the absence of strong Coulomb binding in photo-excited electron-hole pairs, the dipole approximation can be violated for itinerant electrons, and photon momentum and angular momentum can be imparted to electrons [193, 194]. Moreover, given the recent development of near-field spectroscopy [181], it is intriguing to explore spatially and spectrally resolved correlations. This question may be especially relevant today in the context of moiré materials which come with a much enlarged lattice spacing.

The protocol developed in this work is primarily based on classical driving, and correlations between photons are induced by the nonlinearity of the matter. As a future research direction, it would be of interest to identify scenarios where an additional advantage could be obtained by using input light prepared in squeezed coherent [195] or non-Gaussian states.

Chapter 4: Quantum Spin Ice in Three-Dimensional Rydberg Atom Arrays

4.1 Introduction

Traditionally, the main search space for spin liquids has comprised of solid state systems. While consistent progress has been made [20, 44], conclusive evidence for spin liquids is still lacking in these systems. One reason is that the same feature that makes spin liquids interesting—being characterized by non-local order parameters—also makes them hard to detect. Meanwhile, over the past decade, Rydberg atom arrays have emerged as a promising platform for engineering interacting Hamiltonians [196, 197, 198, 199, 200, 201, 202, 203, 204, 205, 206, 207, 208, 209, 210, 211, 212, 213, 214, 215, 216, 217]. Rydberg states have large principal quantum number n ($\sim 20 - 100$), and the van der Waals interaction between them scales as n^{11}. The strong tunable interactions, along with the ability to customize the lattice of atoms, locally control qubits, and take wavefunction snapshots, make Rydberg atom arrays a competitive platform to explore quantum many-body physics. Furthermore, the energy scales in Rydberg atom arrays are orders of magnitude larger than in optical lattices, enabling observation of quantum effects at much higher temperatures in Rydberg atom arrays than in optical lattices. Following theory proposals [218, 219], promising signs of $\mathbb{Z}_2$ topological order have been observed experimentally on this platform [207]. This has sparked a lot of activity over the past few years in the general direction of proposing ways to realize exotic states on quantum devices using analogue quantum

simulation [220, 221, 222, 223, 224, 225, 226, 227], digital quantum simulation [228], and projective measurements [229, 230]. However, all of these proposals have been for two-dimensional Rydberg atom arrays.

Our work is a proposal for realizing a $U(1)$ quantum spin liquid, described by the deconfined phase of a compact $U(1)$ gauge theory on three-dimensional Rydberg atom arrays, with an eye towards accessing the confinement-deconfinement transition. With our proposal, we intend to push the search for a $U(1)$ quantum spin liquid, which has traditionally remained limited to solid state systems, in the direction of three-dimensional Rydberg atom arrays. The connection between Rydberg-atom arrays and Abelian gauge theories in one dimension and two dimensions has been studied in depth in the literature before [231, 232, 233, 234]; however, this connection in three dimensions has remained unexplored. It is known that gauge theories in three dimensions can have a significantly different behavior than those in two dimensions. This is illustrated by the compact $U(1)$ gauge theory. It was shown by Polyakov [235, 236] that compact $U(1)$ gauge theory in 2+1 dimensions is always in the confined phase in the thermodynamic limit due to a proliferation of monopole events. Therefore we turn to 3+1 dimensions, where Polyakov argued [236] for the existence of both deconfined and confined phases separated by a transition driven by monopole excitations. The deconfined phase consists of gapless "photons", gapped "monopoles" and gapped "charge" excitations. In the early 2000s, lattice models of spins [6] and dimers [237] on corner-sharing polyhedra were constructed that were strongly argued to realize this phase—a $U(1)$ spin liquid, using perturbation theory, solvable limits [6] and later Quantum Monte Carlo simulations [16, 238]. Our work is based on a spin model with easy-axis antiferromagnetic interactions introduced by Hermele et al. [6] on the pyrochlore lattice consisting of corner-sharing tetrahedra (see Fig. 4.1). The classical Ising limit of this model is the widely

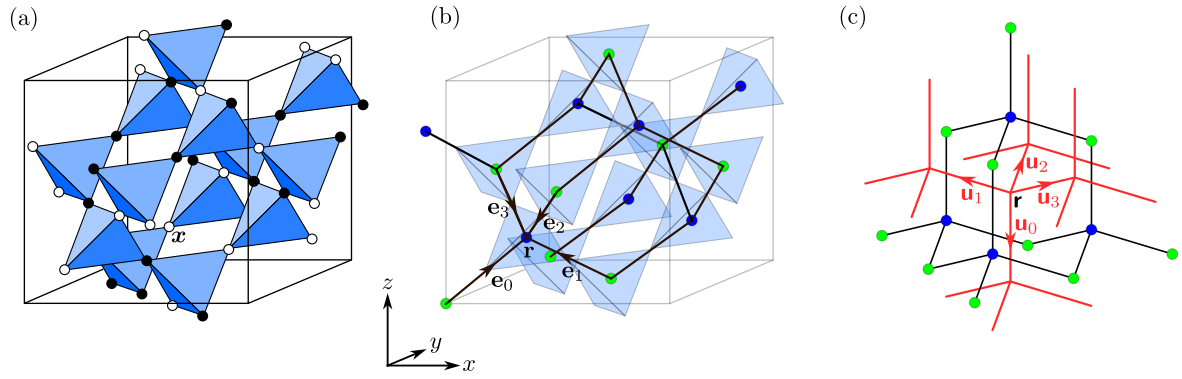

Figure 4.1: (a) The pyrochlore lattice. White circles denote atoms in the ground state, while black circles denote atoms in the Rydberg state. The configuration shown satisfies $n_{\triangle} = 2$ on each tetrahedron. The label $\boldsymbol{x}$ is used to denote the sites of the pyrochlore lattice. (b) The diamond lattice. It is the bipartite lattice formed by the centers of the tetrahedra marked by green (A sublattice) and blue (B sublattice) dots. $\mathbf{e}_\mu$ for $\mu \in \{0, 1, 2, 3\}$ label the vectors joining an A site to its neighboring B sites. The label $\mathbf{r}$ is used to denote the sites of the diamond lattice. (c) The red links are the edges of the lattice dual to the diamond lattice shown in (b). This lattice is also a diamond lattice, and we refer to it as the "dual diamond lattice" in this chapter to distinguish it from the "diamond lattice" in (b). The sites of the dual diamond lattice are centers of the "polyhedra" formed by four puckered hexagons of the diamond lattice. $\mathbf{u}_\mu$ for $\mu \in \{0, 1, 2, 3\}$ label the vectors joining an A site to its neighboring B sites on the dual diamond lattice. The label $\mathbf{r}$ [notice the difference in the font as compared to $\mathbf{r}$ in (b)] is used to denote the sites of the dual diamond lattice.

studied classical spin ice [239, 240, 241, 242, 243], which has a large residual entropy at low temperatures similar to water-ice [21]. This is because the ground states form an exponentially degenerate set of states obeying the "ice rule" (see Sec. 4.2). The quantum model in Ref. [6] has also been a subject of intense study in the context of pyrochlore materials like $Yb_2Ti_2O_7$ and $Er_2Ti_2O_7$ as potential quantum spin ice (another name for the $U(1)$ spin liquid) candidates [244].

It was observed in Ref. [245] that the Hamiltonian in Ref. [6] can be viewed as that of hard-core bosons hopping on an optical lattice with nearest-neighbor repulsion, thus extending its relevance to the cold atom setting. Ref. [246] studied a similar model of hard-core bosons *hopping* on a two-dimensional checkerboard lattice. In Ref. [246], the atom's internal state was largely the ground state, but a dressing with Rydberg states was used to engineer interactions between atoms.

Later, Ref. [247] showed that dimer models in two dimensions can be implemented on configurable Rydberg arrays—where the atoms themselves are stationary but can internally be either in a ground state or in a Rydberg state. In this setting, the atoms are driven with a laser (or a pair of lasers making a two-photon transition) that is detuned from the ground to Rydberg transition. The Rydberg interactions and the detuning define a (frustrated) "classical" energy landscape. The laser driving induces quantum fluctuations controlled by the Rabi frequency, leading (perturbatively) to dimer moves or ring exchange terms that are required to deconfine a gauge theory. The proposal [218] and experiment [207] mentioned above worked in the same setting. Our work is also based on this setting in which the atom array is configured in a 3D pyrochlore lattice. While Ref. [245] proposes to realize a $U(1)$ quantum spin liquid in a 3D optical lattice, our proposal focuses on Rydberg atom arrays where the energy scales involved are several orders of magnitude larger than those in optical lattices. Typical van der Waals interaction strengths in Rydberg atom arrays are on the order of GHz [207], while the on-site interaction strengths in optical lattices are on the order of kHz [248, 249, 250]. For an observation of the $U(1)$ quantum spin liquid, the temperature of the system must be much smaller than the spinon and the monopole gaps. The large energy scales of Rydberg atom arrays make them more favorable than optical lattices to realize a quantum spin liquid. Furthermore, our focus on experimentally measurable correlators goes beyond previous proposals to realize a $U(1)$ quantum spin liquid in atomic, molecular, and optical systems.

In Sec. 4.2, we explain our proposal. We show that within a window of laser detunings, the classical landscape is identical to the set of ice rule obeying states. Our Hamiltonian, when restricted to nearest-neighbor interactions, is equivalent to the transverse-field Ising model on the pyrochlore lattice. In the limit of small Rabi frequencies, it is perturbatively equivalent to the

model in [6], which was argued to have a spin liquid ground state. Away from the perturbative limit, there is numerical evidence for a spin liquid phase [18]. However, once we include the long-range $1/r^6$ interactions beyond nearest-neighbor, the classical landscape is no longer degenerate, and it is a priori unclear if the spin liquid survives as the ground state. We attempt to answer this in Sec. 4.3 by first identifying the classical ground state in the presence of long-range interactions, which we find to be a "chain state" [251]. Then we compare its energy to the energy of an ansatz wave function for the spin liquid. Within our approximation, we find a window of Rabi frequencies for which the system is in the quantum spin liquid phase. By dialing up the Rabi frequency, for fixed detuning and interaction strength, one goes through a confinement-deconfinement transition from an ice rule obeying ferromagnetic state into a deconfined spin liquid phase. Then, by further increasing the Rabi frequency, one goes through a Higgs transition from the spin liquid to a transverse-field-polarized state (see Sec. 4.3.2). Thus both the deconfinement-confinement and the Higgs transitions of the compact $U(1)$ gauge theory can be accessed by changing the Rabi frequency in our model. They have also considered effective gauge theories without Lorentz invariance and shown that the real-space version can be used to diagnose deconfinement. While the analysis till this point focuses on the ground state, in Sec. 4.3.3, we comment on the role played by dynamical state-preparation in deciding the nature of the state prepared in experiment. In Sec. 4.4, we present correlation functions that distinguish the spin liquid from the confined phases, and provide experimental protocols for measuring them. We explain the behavior of the correlation functions in each phase of the phase diagram, and provide protocols to measure them, which we expect be useful for experiments. Some of these correlators are nonlocal in nature and are qualitatively different from the typically considered pinch-point singularities in local correlators. Finally, in Sec. 4.5, we present general discussions and conclusions.

4.2 Proposal to realize a $U(1)$ quantum spin liquid using Rydberg atoms

In this section, we describe our proposal to realize a $U(1)$ Quantum Spin Liquid (QSL) in Rydberg atom arrays. Consider a 3D Rydberg array in which the atoms are positioned on the sites of the pyrochlore lattice [see Fig. 4.1(a)]. Each of the atoms can either be in the ground state $|g\rangle$ or in the Rydberg state $|r\rangle$. In the rotating wave approximation and in a rotating frame, the Hamiltonian is

$$\begin{aligned}\hat{H}_{\text{ryd}} = &-\delta \sum_i \hat{n}_i + \frac{V}{2} \sum_{i \neq j} \left(\frac{a}{|\boldsymbol{x}_i - \boldsymbol{x}_j|} \right)^6 \hat{n}_i \hat{n}_j \\ &+ \frac{\Omega}{2} \sum_i (\hat{b}_i + \hat{b}_i^\dagger),\end{aligned} \tag{4.1}$$

where $\hat{b}_i = |g_i\rangle \langle r_i|$, $\hat{n}_i = \hat{b}_i^\dagger \hat{b}_i$, Ω is the Rabi frequency, δ is the laser detuning, V is the nearest-neighbor van der Waals interaction strength, and a is the distance between two neighboring atoms. The summation $\sum_{i \neq j}$ is over distinct sites i and j of the pyrochlore lattice (each pair is being counted twice), and $\sum_i$ is over sites i. Below, we briefly describe the pyrochlore lattice.

The pyrochlore lattice is a face-centred cubic (FCC) lattice with a four-site basis formed by the four vertices of an up-pointing tetrahedron. (Since each lattice site belongs to one up-pointing tetrahedron and one down-pointing tetrahedron, the down-pointing tetrahedra are formed automatically once we create the up-pointing tetrahedra.) In Cartesian coordinates, the primitive vectors of the FCC lattice are

$$\begin{aligned}\mathbf{a}_1 &= \sqrt{2}a(0,1,1), \\ \mathbf{a}_2 &= \sqrt{2}a(1,0,1), \\ \mathbf{a}_3 &= \sqrt{2}a(1,1,0).\end{aligned} \tag{4.2}$$

The pyrochlore lattice sites are physically located at $\mathbf{r} + \mathbf{e}_\mu/2$ [and labeled $(\mathbf{r}, \mu)$], where $\mathbf{r}$ is an

FCC lattice vector, and the vectors $\mathbf{e}_\mu$ for $\mu \in \{0,1,2,3\}$ are defined as [see Fig. 4.1(b)]

$$\begin{aligned}
\mathbf{e}_0 &= \frac{a}{\sqrt{2}}(1,1,1) = \frac{1}{4}(\mathbf{a}_1+\mathbf{a}_2+\mathbf{a}_3),\\
\mathbf{e}_1 &= \frac{a}{\sqrt{2}}(1,-1,-1),\\
\mathbf{e}_2 &= \frac{a}{\sqrt{2}}(-1,1,-1),\\
\mathbf{e}_3 &= \frac{a}{\sqrt{2}}(-1,-1,1).
\end{aligned} \tag{4.3}$$

We map the two levels of the atoms to spins-1/2s: $|g\rangle \to |\downarrow\rangle$, $|r\rangle \to |\uparrow\rangle$, $\hat{n}_i \to \hat{S}_i^z + 1/2$ and $\hat{b}_i + \hat{b}_i^\dagger \to 2\hat{S}_i^x$. The term $\hat{n}_i\hat{n}_j$ therefore maps to an $\hat{S}_i^z\hat{S}_j^z$ interaction in addition to a Zeeman term $\hat{S}_i^z$. Written in terms of spins, the Hamiltonian, up to an additive constant, is

$$\begin{aligned}
\hat{H}_{\text{ryd}} = &-h\sum_i \hat{S}_i^z + \frac{V}{2}\sum_{i\neq j}\left(\frac{a}{|\boldsymbol{x}_i-\boldsymbol{x}_j|}\right)^6 \hat{S}_i^z\hat{S}_j^z\\
&+\Omega\sum_i \hat{S}_i^x,
\end{aligned} \tag{4.4}$$

where

$$h = \delta - \frac{V}{2}\sum_{i\neq 0}\left(\frac{a}{|\boldsymbol{x}_i-\boldsymbol{x}_0|}\right)^6, \tag{4.5}$$

and is independent of the choice of $\boldsymbol{x}_0$ for an infinite lattice. Evaluating this sum numerically for the pyrochlore lattice, we obtain $h = \delta - 3.46V$. It is useful to separate the total Hamiltonian, Eq. (4.4), into three parts, $\hat{H}_{\text{ryd}} = \hat{H}_0 + \hat{H}_\Omega + \hat{H}_{\text{LR}}$, where

$$\begin{aligned}
\hat{H}_0 =& \frac{V}{2}\sum_{\langle i,j\rangle}\hat{S}_i^z\hat{S}_j^z - h\sum_i \hat{S}_i^z,\\
\hat{H}_\Omega =& \Omega\sum_i \hat{S}_i^x, \text{ and } \hat{H}_{\text{LR}} = \frac{V}{2}{\sum_{i\neq j}}'\left(\frac{a}{|\boldsymbol{x}_i-\boldsymbol{x}_j|}\right)^6 \hat{S}_i^z\hat{S}_j^z,
\end{aligned} \tag{4.6}$$

where $\sum_{\langle i,j\rangle}$ is over nearest-neighbor pairs and $\sum'_{i\neq j}$ in $\hat{H}_{\rm LR}$ is over the remaining pairs that are not nearest-neighbor (in both $\sum$ and $\sum'$, each pair is counted twice). Since the interaction drops very rapidly with distance, we will drop $\hat{H}_{\rm LR}$ for the rest of this section because doing so allows us to connect to some previously known results [6, 16, 17]. We will study the effect of the long-range van der Waals interaction $\hat{H}_{\rm LR}$ in Sec. 4.3.

Since the pyrochlore lattice is made of corner-sharing tetrahedra, we see that $\hat{H}_0$ can be written up to an additive constant as (for convenience, in the expression below, we switch back to the hard-core boson notation)

$$\hat{H}_0 = \frac{V}{2} \sum_{\text{△}_{\mathbf{r}}} \left(\hat{n}_{\text{△}_{\mathbf{r}}} - \rho \right)^2 , \tag{4.7}$$

where the sum is over all tetrahedra, $\rho = \frac{1}{2}\left(4 + \frac{h}{V}\right) = \frac{1}{2}\left(0.54 + \frac{\delta}{V}\right)$, and $\hat{n}_{\text{△}_{\mathbf{r}}} = \sum_{i\in \text{△}_{\mathbf{r}}} \hat{n}_i$ denotes the total number of atoms in the excited state on a given tetrahedron $\text{△}_{\mathbf{r}}$. Minimizing $\hat{H}_0$ to obtain the classical ground state imposes a constraint on $n_{\text{△}}$ for each tetrahedron depending on the value of ρ:

$$n_{\text{△}} = \begin{cases} 0 & \text{if } \rho < 1/2, \\ \text{floor}\left(\rho + \frac{1}{2}\right) & \text{if } 1/2 < \rho < 7/2, \\ 4 & \text{if } 7/2 < \rho. \end{cases} \tag{4.8}$$

The classical ground state is unique for $n_{\text{△}} = 0$ and $n_{\text{△}} = 4$, while it is exponentially degenerate (in system size) for $n_{\text{△}} = 1, 2, 3$. The number of states satisfying the constraint $n_{\text{△}} = 2$, is approximately $(3/2)^{N_{\text{tetrahedra}}}$ (where $N_{\text{tetrahedra}}$ is the number of tetrahedra) [252]. This is based on an argument similar to the one given by Pauling to explain the residual entropy of water-ice at zero

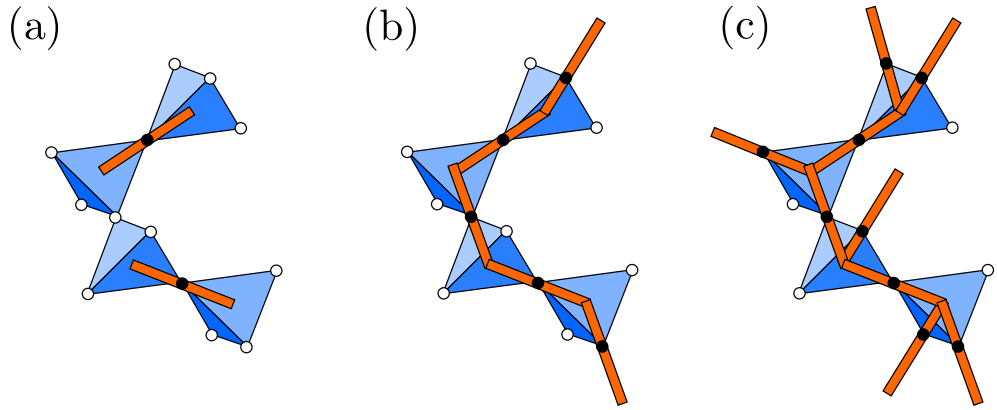

Figure 4.2: Mapping between Rydberg array configurations and dimer configurations. A Rydberg atom (black dot) is mapped to the presence of a dimer (orange bar), while a ground state atom (white dot) is mapped to the absence of a dimer. (a), (b), and (c) show example dimer configurations corresponding to $n_{\triangle} = 1$, 2, and 3, respectively. In each case, $n_{\triangle}$ many dimers touch the center of each tetrahedron (the centers of the tetrahedra form the diamond lattice).

temperature [21]. From now on, we will refer to the condition $n_{\triangle} = 2$ as the "ice rule". An ice rule obeying configuration is shown in Fig. 4.1(a). In these non-trivial cases, the configurations with fixed $n_{\triangle}$ can be mapped to configurations of dimers on the bipartite diamond lattice formed by the centers of tetrahedra of the pyrochlore lattice [Fig. 4.1(b)], with exactly $n_{\triangle}$ many dimers touching each diamond site (see Fig. 4.2). The A and B sites of the diamond lattice are located at $\mathbf{n}$ and $\mathbf{n} + \mathbf{e}_0$, respectively, where $\mathbf{n}$ is an FCC lattice vector. For later use in this chapter, we also show the lattice dual to this diamond lattice in Fig. 4.1(c) (also a diamond lattice, which we call the "dual diamond lattice"). An atom in the Rydberg state on site i is mapped to a dimer on the corresponding link of the diamond lattice, while an atom in the ground state is mapped to no dimer. Such dimer models have been studied extensively in both two and three dimensions [6, 253, 254, 255].

In the limit $\Omega \ll V$, $\hat{H}_\Omega$ leads to quantum fluctuations that break the exponential degeneracy of the low-energy manifold. We will study this effect perturbatively in the following section (Sec. 4.2.1). Classically, the energy gap between the degenerate ground state space and

the lowest excited states corresponding to two tetrahedra violating Eq. (4.8) by either $+1$ or -1 is $2V \times \min\left(\{\rho + 1/2\}, 1 - \{\rho + 1/2\}\right)$. Here, $\{x\} \equiv x - \text{floor}(x)$ is the fractional part of x. It should be noted that, in the borderline cases when $\rho = m + 1/2$ with $m \in \{0, 1, 2, 3\}$, the energy gap closes and our perturbative analysis cannot be used. We assume going forward that ρ is away from these borderline values.

4.2.1 Perturbation theory

We work in the limit $\Omega \ll V$ and treat $\hat{H}_\Omega$ as a perturbation over $\hat{H}_0$, ignoring for now $\hat{H}_{LR}$ whose effects will be considered later in Sec. 4.3. We calculate the effective Hamiltonian within the ground state manifold of $\hat{H}_0$ using the Schrieffer-Wolff formulation of perturbation theory. For simplicity, we present the calculation of the effective Hamiltonian only for $n_{\triangle} = 2$ here. The only difference between these three cases will be the Hilbert space on which the Hamiltonian acts. Calculating, at k^{th} order in perturbation theory, the matrix element of the effective Hamiltonian between two states $|n\rangle$ and $|m\rangle$ lying in the degenerate manifold involves starting from $|m\rangle$, applying the perturbation k times, and reaching the state $|n\rangle$. Since $\hat{H}_\Omega$ changes the particle number by ± 1, the corrections at all odd orders are zero.

Acting with $\frac{\Omega}{2}(\hat{b}_i + \hat{b}_i^\dagger)$ on an ice rule obeying state creates two excited tetrahedra (whose common site is i), which violate the constraint $n_{\triangle} = 2$. Therefore, the only second-order process that takes us back to the ice manifold (the degenerate manifold of the ice rule obeying states) is the one in which two excited tetrahedra are created and annihilated, as illustrated in Figs. 4.3(a) and (b).

Since such processes are present for all the states of the ice manifold, they contribute only

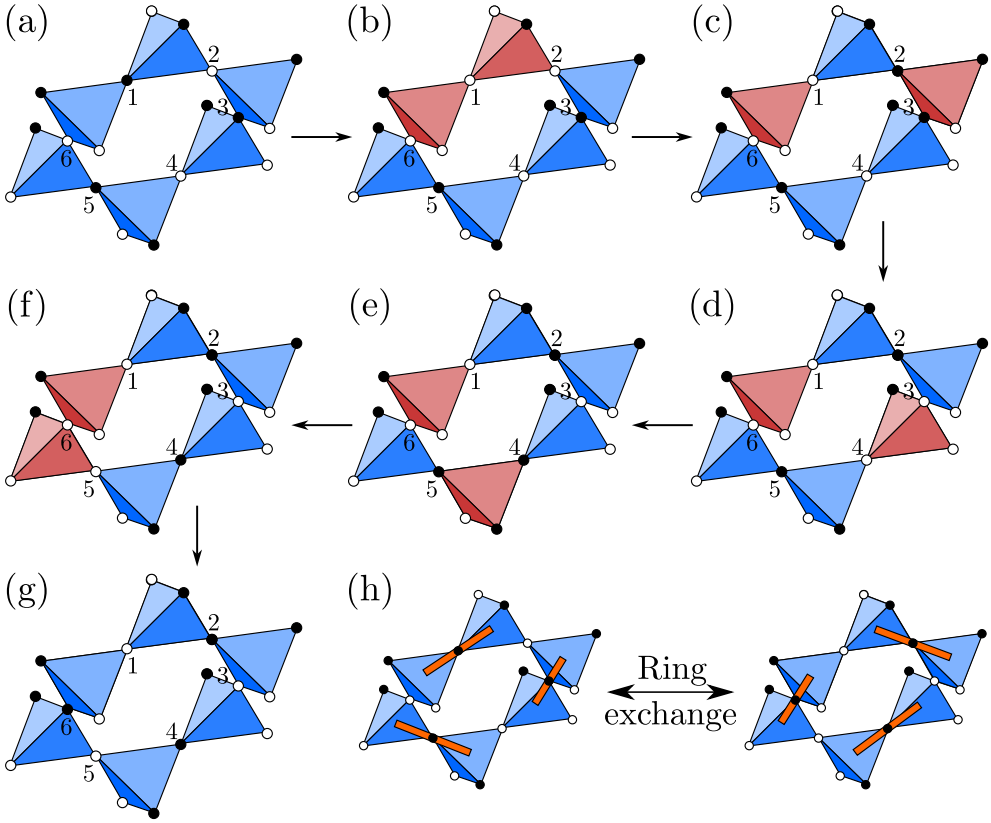

Figure 4.3: (a) and (b) constitute a virtual process at second order in perturbation theory in Ω/V. Starting from (a) which is a configuration that satisfies $n_{\triangle} = 2$ on all sites, $\hat{b}_1 + \hat{b}_1^\dagger$ is applied giving (b). To complete the second order process, $\hat{b}_1 + \hat{b}_1^\dagger$ is applied to (b) giving back (a). Tetrahedra for which $n_{\triangle} \neq 2$ are shaded in red. Sub-figures (a)–(g) constitute a sixth-order process in the perturbation theory that contributes to the ring exchange term in the effective Hamiltonian, Eq. (4.9). Starting from (a), the perturbation $\hat{b}_i + \hat{b}_i^\dagger$ is applied sequentially on sites $i = 1, 2, \ldots, 6$. At the end of the six steps, a configuration with $n_{\triangle} = 2$ is obtained as shown in (g). Note that the configuration of the atoms on the hexagon is flipped in (g) as compared to (a) thereby producing the effect of a ring exchange. Other sixth-order processes where the perturbation is not applied sequentially also contribute to Eq. (4.9), but are not shown here. (h) Ring exchange process which appears in the effective Hamiltonian Eq. (4.9). A flippable configuration is mapped to the complimentary flippable configuration.

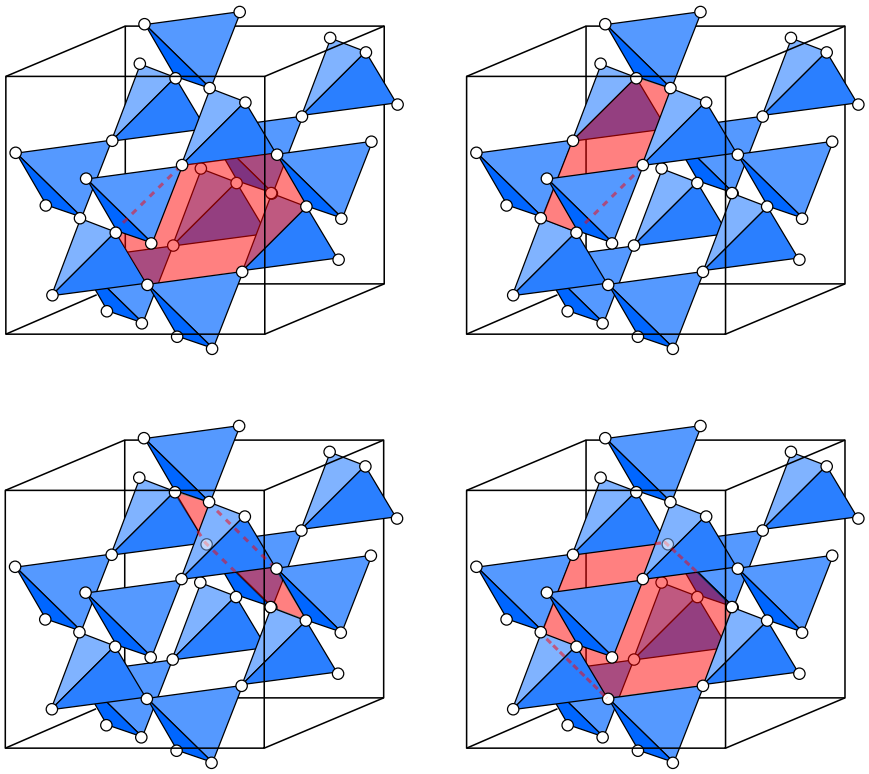

Figure 4.4: Shaded in red are the four nonequivalent hexagonal plaquettes of the pyrochlore lattice.

a constant energy shift and can be ignored. The same is true for the fourth-order processes. Now, the pyrochlore lattice has hexagonal plaquettes, some of which are shown in Fig. 4.4. This allows for non-trivial processes to exist at sixth order. In fact, non-trivial ring exchange over hexagonal plaquettes of the pyrochlore lattice is obtained by the process shown in Figs. 4.3(a)–(g) (some sixth-order processes also result in a constant energy shift which we neglect). A flippable configuration—one in which atoms on a hexagonal plaquette are alternately in the ground and Rydberg states—is mapped to the complementary flippable configuration by the ring exchange process as illustrated in Fig. 4.3(h). Thus, the effective Hamiltonian consists of ring exchange terms:

$$\hat{H}_{\text{eff}} = -J_{\text{ring}}(\rho) \sum_{\hexagon} |\hexagon\rangle\langle\hexagon| + \text{H.c.}, \tag{4.9}$$

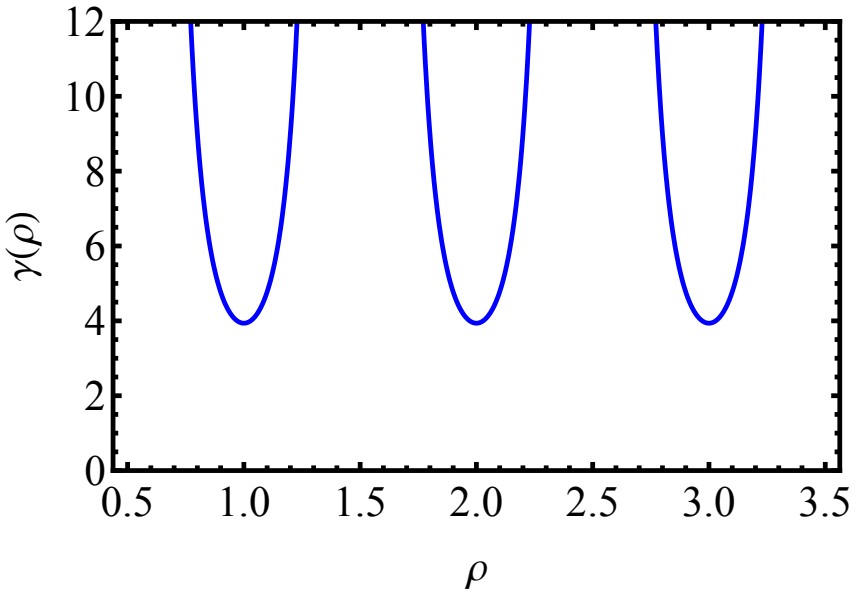

Figure 4.5: Plot showing the variation of $\gamma(\rho)$ (which is the proportionality constant in $J_{\text{ring}}(\rho) = \gamma(\rho)\Omega^6/V^5$) as a function of ρ. For $\rho = 0.5, 1.5, 2.5$, and 3.5, the energy gap between the low-energy and the high-energy sectors closes and $\gamma(\rho)$ diverges.

where $J_{\text{ring}}(\rho) = \gamma(\rho)\Omega^6/V^5$, the sum is over all hexagonal plaquettes of the pyrochlore lattice, and $\gamma(\rho)$ is a dimensionless number obtained by summing over virtual processes and is plotted as a function of ρ in Fig. 4.5 . We note that, when ρ is an integer, the value of $\gamma(\rho)$ is $63/16$ and is the same as the one appearing in Refs. [256, 257]. Although the effective Hamiltonian was derived here assuming $n_{\triangle} = 2$, the effective Hamiltonian we obtain for $n_{\triangle} = 1, 3$ is also given by Eq. (4.9).

In terms of dimers on the diamond lattice, the effective Hamiltonian Eq. (4.9) corresponds to a kinetic energy of the dimers. It is well known that dimer models can be made exactly solvable by adding a potential energy V_{RK} for the dimers and tuning to a special point $V_{RK} = J_{\text{ring}}$ called the Rokhsar-Kivelson (RK) point [253]. The Hamiltonian with such a potential energy term takes

the form

$$\hat{H}_{\text{dimer}} = -J_{\text{ring}}(\rho) \sum_{\hexagon} |\hexagon\rangle\langle\hexagon| + \text{H.c.} \tag{4.10}$$
$$+ V_{RK} \sum_{\hexagon} |\hexagon\rangle\langle\hexagon| + |\hexagon\rangle\langle\hexagon| .$$

The Rydberg system we are interested in [Eq. (4.9)] is obtained from Eq. (4.10) by setting $V_{RK} = 0$.

4.2.2 $U(1)$ quantum spin liquid—relation to Hermele-Fisher-Balents [6]

The Hamiltonian in Eq. (4.10) was also derived by Hermele, Fisher and Balents in Ref. [6] starting from the Heisenberg model on the pyrochlore lattice and taking the easy-axis limit where the Hamiltonian is

$$\hat{H}_{\text{easy-axis}} = \frac{1}{2} \sum_{\langle i,j \rangle} \left[J_z \hat{S}_i^z \hat{S}_j^z + J_\perp \left(\hat{S}_i^x \hat{S}_j^x + \hat{S}_i^y \hat{S}_j^y \right) \right], \tag{4.11}$$

where $J_z \gg J_\perp > 0$. When $J_\perp = 0$, the ground state is exponentially degenerate with $S^z_{\triangle} = 0$ on each tetrahedron, which is equivalent to $n_{\triangle} = 2$. The $J_\perp$ term was treated as a perturbation over the J_z term, and at third order, a ring exchange term identical to Eq. (4.9) was obtained. Written in terms of the spins, the ring-exchange term is

$$\hat{H}_{\text{eff}} = -J_{\text{ring}} \sum_{\hexagon} \hat{S}_1^+ \hat{S}_2^- \hat{S}_3^+ \hat{S}_4^- \hat{S}_5^+ \hat{S}_6^- + \text{H.c.}, \tag{4.12}$$

where the sum is over hexagonal plaquettes of the pyrochlore lattice. The RK potential term was added by hand in Ref. [6] giving Eq. (4.10).

Hermele et al. then go to the quantum rotor variables $n_{\mathbf{r}\mathbf{r}'} \in \mathbb{Z}$ and $\theta_{\mathbf{r}\mathbf{r}'} \in [-\pi, \pi)$, which live on the links $\mathbf{r}\mathbf{r}'$ of the diamond lattice (equivalently, sites of the pyrochlore lattice) and satisfy the canonical commutation relations $[\hat{n}_{\mathbf{r}\mathbf{r}'}, \hat{\theta}_{\mathbf{r}\mathbf{r}'}] = i$:

$$\hat{S}^z \to \hat{n} - \frac{1}{2}, \quad \hat{S}^{\pm} \to e^{\pm i\hat{\theta}}. \tag{4.13}$$

The constraint $n = 0$ or 1 is imposed by adding a term to the Hamiltonian that energetically penalizes states violating this constraint:

$$\hat{H}_{\text{eff}} = \frac{U}{2} \sum_{\langle \mathbf{r}\mathbf{r}' \rangle} \left(\hat{n}_{\mathbf{r}\mathbf{r}'} - \frac{1}{2} \right)^2 \tag{4.14}$$

$$- 2J_{\text{ring}} \sum_{\hexagon_p} \cos \left(\hat{\theta}_{\mathbf{r}_1\mathbf{r}_2} - \hat{\theta}_{\mathbf{r}_2\mathbf{r}_3} + \hat{\theta}_{\mathbf{r}_3\mathbf{r}_4} - \hat{\theta}_{\mathbf{r}_4\mathbf{r}_5} + \hat{\theta}_{\mathbf{r}_5\mathbf{r}_6} - \hat{\theta}_{\mathbf{r}_6\mathbf{r}_1} \right), \tag{4.15}$$

where the first sum is over all the links $\langle \mathbf{r}\mathbf{r}' \rangle$ of the diamond lattice. The second sum is over the puckered hexagonal plaquettes of the diamond lattice $\hexagon_p$ whose vertices are $\mathbf{r}_1, \mathbf{r}_2, \ldots, \mathbf{r}_6$. In the limit $U \to \infty$, Eq. (4.14) reduces to the effective Hamiltonian Eq. (4.12).

The local constraint, $S^z_{\tetrahedron_{\mathbf{r}}} = 0$ for each tetrahedron, gives a gauge structure to the effective Hamiltonian where the gauge transformations are generated by $\hat{S}^z_{\tetrahedron_{\mathbf{r}}}$. The presence of this local symmetry motivated Hermele et al. to write Eq. (4.14) as a lattice $U(1)$ gauge theory. The electric

field and the vector potential were defined as

$$\hat{e}_{\mathbf{r}\mathbf{r}'} = \pm\left(\hat{n}_{\mathbf{r}\mathbf{r}'} - \frac{1}{2}\right), \quad \hat{a}_{\mathbf{r}\mathbf{r}'} = \pm\hat{\theta}_{\mathbf{r}\mathbf{r}'}. \tag{4.16}$$

The positive (negative) sign is chosen if $\mathbf{r}$ belongs to A (B) sublattice of the diamond lattice. The Hamiltonian written in terms of the electric field and the vector potential takes the form of a compact $U(1)$ lattice gauge theory [235, 258]:

$$\hat{H}_{\text{eff}} = \frac{U}{2}\sum_{\langle \mathbf{r},\mathbf{r}'\rangle} \hat{e}^2_{\mathbf{r}\mathbf{r}'} - 2J_{\text{ring}}\sum_{\hexagon} \cos\left((\text{curl}\ \hat{a})_{\hexagon}\right), \tag{4.17}$$

where the second summation is over hexagonal plaquettes of the diamond lattice and

$$(\text{curl}\ \hat{a})_{\hexagon} = \sum_{\mathbf{r},\mathbf{r}'\in\hexagon} \hat{a}_{\mathbf{r}\mathbf{r}'}, \equiv \hat{B}_{\mathbf{r},\mu} \tag{4.18}$$

where $\sum_{\mathbf{r},\mathbf{r}'\in\hexagon}$ is a sum along the directed bonds of a hexagonal plaquette of the diamond lattice. Such a plaquette can be uniquely defined by $(\mathbf{r},\mu)$, where $\mathbf{r}$ belongs to the dual lattice and $\mathbf{u}_\mu$ for $\mu \in \{1,2,3,4\}$ gives the plaquette orientation [as defined in Fig. 4.1(c)], and $\hat{B}_{\mathbf{r},\mu}$ is the magnetic field operator at that plaquette. The adjective "compact" refers to the vector potential $\hat{a}_{\mathbf{r}\mathbf{r}'}$ being an angular variable. There is an important difference between the above gauge theory and the compact $U(1)$ gauge theory studied by Polyakov [235, 236, 259]—the gauge theory obtained by Hermele et al. is an odd gauge theory, i.e., electric fields are half-integers, $e_{\mathbf{r}\mathbf{r}'} \in \mathbb{Z} + 1/2$, while the gauge theory studied by Polyakov was an even gauge theory, i.e., the electric fields were integers, $e_{\mathbf{r}\mathbf{r}'} \in \mathbb{Z}$. Because of this difference, the phases of the two theories differ. For

readers familiar with the Schwinger model, we point out that the even and odd compact $U(1)$ gauge theories are reminiscent of gauge theories with a θ-term in $1+1$ dimensions at $\theta = 0$ and $\theta = \pi$, respectively.

The phases of a gauge theory can be characterized by the interaction between two externally added opposite electric charges separated by a distance R. If the potential between charges goes to zero (or increases as at most $\log R$ in $2+1$D) as $R \to \infty$, then the gauge theory is in the deconfined phase. On the other hand, if the potential increases linearly with R or faster, then these opposite charges cannot be separated, and the gauge theory is in the confined phase. In the limit $U \to \infty$, the even gauge theory was shown to be in the confined phase in Refs. [235, 258], while the odd gauge theory can be in either the confined phase or the deconfined phase [6]. This can be understood intuitively as follows.

In the even gauge theory, in the limit $U \to \infty$, the electric fields are forced to be 0, $e_{\mathbf{r}\mathbf{r}'} = 0$, to minimize the energy in the absence of any external charges. However, in the presence of two opposite external charges, the Gauss's law requires that the electric field can no longer be zero everywhere. The spreading of the electric field is, however, penalized by the term $\frac{U}{2}\sum_{\langle \mathbf{r},\mathbf{r}'\rangle} \hat{e}^2_{\mathbf{r}\mathbf{r}'}$. This forces the electric field to be nonzero only in a narrow tube joining the two charges, leading to a linearly rising potential between the two charges. Thus, in the limit $U \to \infty$, the even gauge theory is in a confined phase, and there is no deconfined phase in this limit. This confinement of charges has been shown in Refs. [235, 236, 258, 260].

On the other hand, in an odd gauge theory, in the limit $U \to \infty$, the electric field can take two values, $e_{\mathbf{r}\mathbf{r}'} = \pm 1/2$. This results in frustration, i.e., allows for many configurations of the electric field, so that the ground state in this limit is non-trivial. When two external charges are introduced, the electric field is not necessarily confined in a string between the charges, but can

spread in space similar to the familiar Coulomb-law field lines of a non-compact $U(1)$ gauge theory. This suggests that it is possible for the odd gauge theory to be in the deconfined phase even in the $U \to \infty$ limit. In fact, the odd gauge theory on the pyrochlore lattice (4.14) is indeed in the deconfined phase in the $U \to \infty$ limit [16, 17, 238].

Hermele et al. have shown that the dimer model with the Hamiltonian Eq. (4.10) is described by the deconfined phase of the underlying compact $U(1)$ gauge theory close to the RK point (for V_{RK} smaller than J_{ring} but close to J_{ring}). This phase is the $U(1)$ quantum spin liquid. It has three types of emergent excitations—gapless photons, gapped magnetic monopoles and gapped fractionalized electric charges, also called as spinons. The spinons are the tetrahedra which violate the constraint on $n_{\triangleleft\!\triangleright}$, Eq. (4.8).

4.2.3 Previous numerical work

In this section, we summarize some of the known work on the dimer model with the Hamiltonian Eq. (4.10) and on the nearest-neighbor transverse-field Ising model on the pyrochlore lattice.

Using quantum Monte Carlo simulations, Refs. [16] and [17] studied the range of V_{RK} [see Eq. (4.10)] over which the $U(1)$ spin liquid exists. They found that the spin liquid is present in the range $-0.5 J_{\text{ring}} < V_{RK} < J_{\text{ring}}$ for the dimer model with $n_{\triangleleft\!\triangleright} = 2$ and in the range $0.77 J_{\text{ring}} < V_{RK} < J_{\text{ring}}$ for the dimer model with $n_{\triangleleft\!\triangleright} = 1$. The dimer model with $n_{\triangleleft\!\triangleright} = 3$ is equivalent to the one with $n_{\triangleleft\!\triangleright} = 1$ by a particle-hole transformation. These numerical results are summarized in Fig. 4.6.

While a theory proposal to realize the RK potential exists [247], the RK potential is a six-

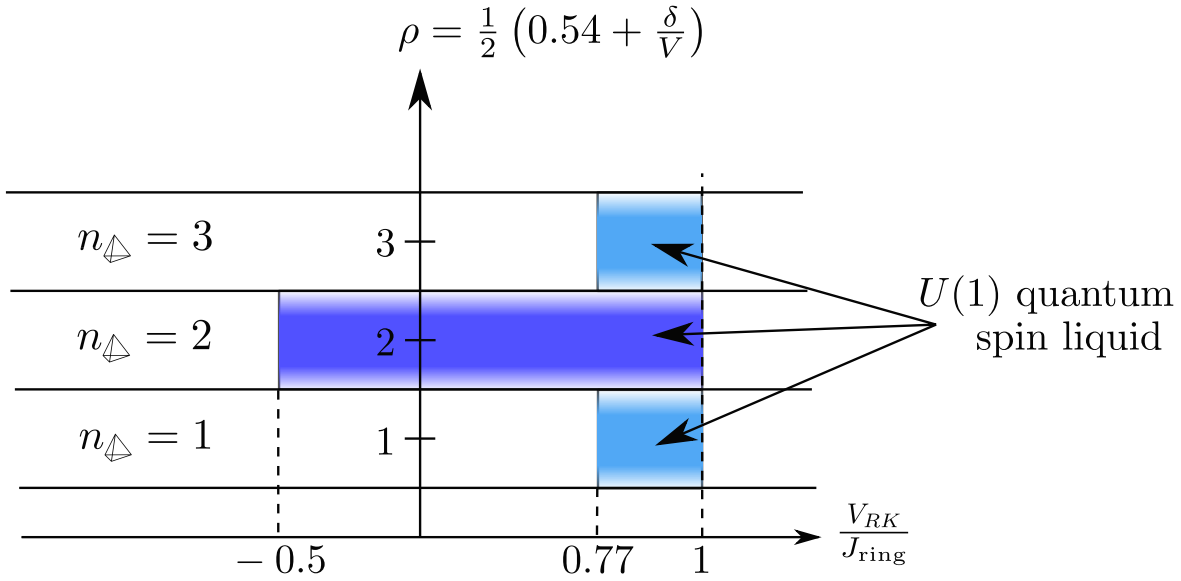

Figure 4.6: For $\rho \in (3/2, 5/2)$, corresponding to $n_{\triangle} = 2$, the system is in the $U(1)$ spin liquid phase at $V_{RK} = 0$ [16]. On the other hand, for $\rho \in (1/2, 3/2)$ and $\rho \in (5/2, 7/2)$, corresponding to $n_{\triangle} = 1$ and 3, respectively, the system is in an ordered phase at $V_{RK} = 0$ [17]. Note that for $\rho = 1/2$, $3/2$, and $5/2$, the perturbation theory described in Sec. 4.2.1 does not apply, and we cannot comment on the phase of the system.

body term for the pyrochlore lattice and is difficult to engineer experimentally. Thus, we focus on the case where $V_{RK} = 0$. From Fig. 4.6, we see that to obtain a spin liquid phase for $V_{RK} = 0$, one must have $n_{\triangle} = 2$, which corresponds to $3/2 < \rho < 5/2$. In the cases $n_{\triangle} = 1$ and 3, the system is in an ordered state when $V_{RK} = 0$. Hence, in conclusion, assuming the long-range interactions $\hat{H}_{LR}$ can be ignored, we expect that, in the limit $\Omega \ll V$, the Rydberg system will be in a $U(1)$ quantum spin liquid phase for $3/2 < \rho < 5/2$.

When $\rho = 2$, or equivalently $h = 0$, and the long-range interactions $\hat{H}_{LR}$ are ignored, the Hamiltonian of the system $\hat{H}_0 + \hat{H}_\Omega$ in Eq. (4.6) is the transverse field Ising model on the pyrochlore lattice. For $\Omega \ll V$, we know from the perturbative analysis of Sec. 4.2.1 and Ref. [17] that the system is in the $U(1)$ quantum spin liquid phase. For large Ω/V, where perturbation theory cannot be applied, Ref. [18] found using quantum Monte Carlo calculations that the $U(1)$ spin liquid exists in the region $\Omega < 0.55(5)V$, while, for $\Omega > 0.55(5)V$, the system is in a

transverse-field-polarized (TFP) phase, which extends to $\Omega/V \to \infty$ where the ground state is polarized in the x-direction. This transition was also studied in Ref. [261] using perturbation theory, where a transition was found at $\Omega \approx 0.6V$.

The effects of adding a third nearest-neighbor interaction, V_{3NN}, to the dimer model were considered in Ref. [262]. It was found that the quantum spin liquid transitioned into an ordered state (antiferromagnet [263]) at $V_{\text{3NN}} \approx J_{\text{ring}}$. Thus non-nearest-neighbor interactions can destabilize the quantum spin liquid. In fact, in a 2D model with neutral atoms located on the bonds of a kagome lattice (same as the sites of a ruby lattice), a spin liquid ground state was found if the interactions were short-ranged using DMRG on cylinders [207, 218]. However, with the full long-range van der Waals interactions, the spin liquid ceased to be the ground state [207, 218]. While these works suggest that long-range interactions could destabilize the quantum spin liquid and favor an ordered state, it is not always the case as was discovered in Ref. [264], where the degeneracy of the ice manifold was preserved despite the introduction of a dipolar-like long-range interaction. We note that, despite the faster decay of van der Waals interactions compared to dipolar-like interactions of Ref. [264], the former splits the degeneracy of the ice manifold (see Sec. 4.3.1.2). Thus, in our work, it is important to study the effects of the van der Waals interaction more closely. In the following section, we will study the phase diagram of Hamiltonian (4.6) in the presence of long-range interactions, using approximate methods.

4.3 Phase Diagram—Approximate Methods

The goal of this section is to study the ground state phase diagram of Hamiltonian (4.4) for $\delta = 3.46V$ (which corresponds to $\rho = 2$) including long-range interactions $\hat{H}_{\text{LR}}$.

4.3.1 Confinement-deconfinement transition—Monte Carlo assisted perturbation theory

Consider the full Hamiltonian $\hat{H} = \hat{H}_0 + \hat{H}_\Omega + \hat{H}_{\text{LR}}$ from Eq. (4.6) in the case $\rho = 2$ [see Eq. (4.7)]:

$$\begin{aligned} \hat{H}_0 =& \frac{V}{2} \sum_{\text{⏢}_{\mathbf{r}}} \left(\sum_{i \in \text{⏢}_{\mathbf{r}}} \hat{S}_i^z \right)^2, \\ \hat{H}_\Omega =& \Omega \sum_i \hat{S}_i^x, \text{ and } \hat{H}_{\text{LR}} = \frac{V}{2} {\sum_{i \neq j}}' \left(\frac{a}{|\boldsymbol{x}_i - \boldsymbol{x}_j|} \right)^6 \hat{S}_i^z \hat{S}_j^z. \end{aligned} \tag{4.19}$$

The long-range interaction $\hat{H}_{\text{LR}}$ splits the exponential degeneracy of the ice manifold, and selects one configuration diagonal in the $\hat{S}^z$ basis as the ground state of $\hat{H}_0 + \hat{H}_{\text{LR}}$, which we call the "ordered state". On the other hand, $\hat{H}_\Omega$ prefers superpositions of ice rule obeying states, the $U(1)$ quantum spin liquid (QSL) being one such superposition. Further, we also note that quantum fluctuations around the "ordered state" due to $\hat{H}_\Omega$ may also lead to a change in its energy relative to the QSL. It is this competition between kinetic energy and long-range interactions that we will study in this section.

We first show that the ground state in the classical limit $\Omega = 0$ is the zero-momentum state satisfying the ice rule which we call the "ice ferromagnet". We assume that, as one increases Ω, there is no phase transition to a different ordered state before the putative transition to a QSL. In order to determine whether a QSL phase exists and, if yes, at what Ω the transition to the QSL occurs, one needs to compare the energies of ansatz wavefunctions of the QSL and the ordered state. When $\Omega \neq 0$, such wavefunctions would necessarily involve configurations that violate the ice rule. We incorporate the effect of nonzero Ω on the wavefunction using perturbation theory. Our strategy is as follows. We treat $\hat{H}_1 \equiv \hat{H}_\Omega + \hat{H}_{\text{LR}}$, i.e., both the laser driving term and the

long-range interactions, as a perturbation to $\hat{H}_0$ (unlike Sec. 4.2.1, where we dropped $\hat{H}_{\text{LR}}$). We perturbatively find an effective Hamiltonian $\hat{H}_{\text{eff}}$ acting on the low-energy ice manifold. We then compare the expectation value of $\hat{H}_{\text{eff}}$ in candidate wavefunctions that live entirely in this low-energy space. Since a QSL wavefunction is a linear superposition of exponentially (in system size) many ice rule obeying states, we calculate $\left\langle \hat{H}_{\text{eff}} \right\rangle$ numerically using classical Monte Carlo sampling (code available online, see [265]).

4.3.1.1 Expression for $\hat{H}_{\text{eff}}$

We perform a Schrieffer-Wolff transformation

$$\hat{\tilde{H}} = \hat{U}_S \hat{H} \hat{U}_S^\dagger = \hat{U}_S \left(\hat{H}_0 + \hat{H}_\Omega + \hat{H}_{\text{LR}} \right) \hat{U}_S^\dagger, \tag{4.20}$$

for a unitary $\hat{U}_S = e^{\hat{S}}$, where $\hat{S}$ is an anti-hermitian operator chosen to make $\hat{\tilde{H}}$ block-diagonal in the (degenerate) eigenbasis of $\hat{H}_0$, i.e.,

$$\hat{\tilde{H}} = \hat{\mathcal{P}} \hat{\tilde{H}} \hat{\mathcal{P}} + (1 - \hat{\mathcal{P}}) \hat{\tilde{H}} (1 - \hat{\mathcal{P}}), \tag{4.21}$$

where $\hat{\mathcal{P}}$ projects onto the ice manifold. In the remainder of this chapter, we will restrict ourselves to the low-energy sector and therefore only consider the $\hat{H}_{\text{eff}} \equiv \hat{\mathcal{P}} \hat{\tilde{H}} \hat{\mathcal{P}}$ term above. We calculate $\hat{H}_{\text{eff}}$ perturbatively in $\hat{H}_1 = \hat{H}_\Omega + \hat{H}_{\text{LR}}$ (see Appendix B of Ref. [266] for general expressions of $\hat{H}_{\text{eff}}$). As we saw in Sec. 4.2.1, if we consider only $\hat{H}_\Omega$ as the perturbation, then the first

non-trivial term appearing in $\hat{H}_{\text{eff}}$ is $-J_{\text{ring}} \sum_{\hexagon} |$  $\rangle \langle$$| + \text{H.c.}$, where

$$J_{\text{ring}} = \frac{63}{16}\frac{\Omega^6}{V^5} + \Theta\left(\frac{\Omega^8}{V^7}\right). \tag{4.22}$$

Since we are performing perturbation theory in two operators $\hat{H}_\Omega$ and $\hat{H}_{LR}$, each of them comes with its own small parameter. Since the perturbative expansion will involve polynomials in these two small parameters, there is some arbitrariness in deciding how to compare the two parameters relative to each other and thus in how to truncate the expansion. In our calculation, we follow an operational scheme of keeping all the terms up to sixth order in $\hat{H}_\Omega + \hat{H}_{\text{LR}}$. Following this truncation scheme, we get (up to additive constants)

$$\begin{aligned}
\hat{H}_{\text{eff}} \approx & -J_{\text{ring}} \sum_{\hexagon} |\text{}\rangle \langle \text{}| + \text{H.c.} \\
& + \left(1 - \frac{\Omega^2}{V^2} - \frac{61}{18}\frac{\Omega^4}{V^4}\right)\hat{H}_{\text{LR}} \\
& - \frac{\Omega^2}{V}\left(\hat{W}^{(2)}_{\text{LR}} + \hat{W}^{(3)}_{\text{LR}} + \hat{W}^{(4)}_{\text{LR}}\right) \\
& - \frac{\Omega^4}{V^3}\left(\frac{152}{27}\hat{W}^{(2)}_{\text{LR}} - \hat{L}^{(2)}_{\text{LR}} + \hat{M}^{(2)}_{\text{LR}}\right),
\end{aligned} \tag{4.23}$$

where

$$\hat{W}^{(2)}_{\text{LR}} \equiv \frac{1}{4}\sum_{j}\sum_{\substack{k_1\neq j\\ k_2\neq j}} v_{j,k_1}v_{j,k_2}\hat{S}^z_{k_1}\hat{S}^z_{k_2}, \tag{4.24}$$

$$\hat{L}^{(2)}_{\text{LR}} \equiv \frac{109}{432}\sum_{\substack{j_1\neq k_1\\ j_2\neq k_2}} \delta_{\langle j_1,j_2\rangle} v_{j_1,k_1}v_{j_2,k_2}\hat{S}^z_{k_1}\hat{S}^z_{k_2}, \tag{4.25}$$

$$\hat{M}^{(2)}_{\text{LR}} \equiv \frac{20}{27}\sum_{\substack{j_1\neq k_1\\ j_2\neq k_2}} \delta_{\langle j_1,j_2\rangle} v_{j_1,k_1}v_{j_2,k_2}\hat{S}^z_{j_1}\hat{S}^z_{k_1}\hat{S}^z_{j_2}\hat{S}^z_{k_2}, \tag{4.26}$$

$$\hat{W}^{(3)}_{\text{LR}} \equiv \frac{1}{2}\sum_{j}\sum_{\substack{k_1\neq j\\ k_2\neq j\\ k_3\neq j}} v_{j,k_1}v_{j,k_2}v_{j,k_3}\hat{S}^z_{k_1}\hat{S}^z_{k_2}\hat{S}^z_{k_3}\hat{S}^z_{j}, \tag{4.27}$$

$$\hat{W}^{(4)}_{\text{LR}} \equiv \frac{1}{4}\sum_{j}\sum_{\substack{k_1\neq j\\ k_2\neq j\\ k_3\neq j\\ k_4\neq j}} v_{j,k_1}v_{j,k_2}v_{j,k_3}v_{j,k_4}\hat{S}^z_{k_1}\hat{S}^z_{k_2}\hat{S}^z_{k_3}\hat{S}^z_{k_4}, \tag{4.28}$$

$$\text{and } v_{i,j} \equiv \begin{cases} \frac{a^6}{|\boldsymbol{x}_i-\boldsymbol{x}_j|^6} \text{ if } \boldsymbol{x}_i, \boldsymbol{x}_j \text{ are not nearest neighbors,} \\ 0 \qquad\quad \text{otherwise.} \end{cases} \tag{4.29}$$

In the above equations, $\delta_{\langle i,j\rangle}$ enforces i and j to be nearest neighbors.

The expectation value of the Hamiltonian (4.6) in a given state $|\Psi\rangle$ is

$$\langle\Psi|\hat{H}|\Psi\rangle = \left(\langle\Psi|\hat{U}_S^\dagger\right)\left(\hat{U}_S\hat{H}\hat{U}_S^\dagger\right)\left(\hat{U}_S|\Psi\rangle\right). \tag{4.30}$$

Suppose $\hat{U}_S|\Psi\rangle$ (i.e., $|\Psi\rangle$ transformed by the Schrieffer-Wolff transformation) lies entirely in the ice manifold, then using Eq. (4.20), we get

$$\langle\Psi|\hat{H}|\Psi\rangle = \left(\langle\Psi|\hat{U}_S^\dagger\right)\hat{H}_{\text{eff}}\left(\hat{U}_S|\Psi\rangle\right). \tag{4.31}$$

For the ground state, $|\Psi_g\rangle$ of the full Hamiltonian $\hat{H}$, $\hat{U}_S|\Psi_g\rangle$ lies entirely in the ice manifold. Thus, we pick an ansatz wavefunction for $\hat{U}_S|\Psi\rangle$ that also lies entirely in the ice manifold and compute the expectation value of $\hat{H}_{\text{eff}}$ in our ansatz state to get the energy. Before describing our ansatz states in Sec. 4.3.1.3, we first consider the limit $\Omega = 0$ in the next section.

4.3.1.2 Classical ground state of the long-range Hamiltonian

Here, we will find the ground state selected by long-range interactions in the limit $\Omega = 0$ where there are no quantum fluctuations. The Hamiltonian is $\hat{H}_{\text{cl}} = \hat{H}_0 + \hat{H}_{LR}$. We find the ground state by going to the Fourier space. Since the pyrochlore lattice is an FCC lattice with a four-site basis, we use the notation $\hat{S}^z_{\mathbf{r},\mu}$ for spins where $\mathbf{r}$ is an FCC lattice vector and $\mu \in \{0,1,2,3\}$ labels the sites within the basis. The spin $\hat{S}^z_{\mathbf{r},\mu}$ is physically located at $\mathbf{r} + \mathbf{e}_\mu/2$ where $\mathbf{e}_\mu$ are the vectors joining a diamond A site to a neighboring diamond B site. (See Fig. 4.1(b) for the precise definition.) Using the Luttinger-Tisza method [267, 268, 269], we are able to determine the exact ground state of the classical Hamiltonian at $\Omega = 0$. We explain this calculation below. As we are considering the classical limit in this section, we drop hats on quantities which would otherwise be operators. The Fourier transform of $S^z_{\mathbf{r},\mu}$ is

$$S^z_{\mathbf{r},\mu} = \frac{1}{\sqrt{N_{\text{u.c.}}}} \sum_{\mathbf{k}} e^{i\mathbf{k}\cdot\mathbf{r}} S^z_{\mathbf{k},\mu}, \tag{4.32}$$

where $N_{\text{u.c.}}$ is the number of FCC unit cells. Substituting this in H_{cl}, we get

$$H_{\text{cl}} = \sum_{\mu,\nu,\mathbf{k}} V_{\mu\nu,\mathbf{k}} S^z_{\mathbf{k},\mu} S^z_{-\mathbf{k},\nu}, \tag{4.33}$$

where $\mathbf{k}$ is a vector in the Brillouin zone of the FCC lattice and $V_{\mu\nu,\mathbf{k}}$ is the Fourier transform of the van der Waals potential:

$$V_{\mu\nu,\mathbf{k}} = \frac{V}{2} \sum_{\mathbf{r}} e^{i\mathbf{k}\cdot\mathbf{r}} \left(\frac{a}{|\mathbf{r} + (\mathbf{e}_\mu - \mathbf{e}_\nu)/2|} \right)^6 . \tag{4.34}$$

Diagonalizing the matrix $V_{\mu\nu,\mathbf{k}}$ for each $\mathbf{k}$ gives

$$H_{\text{cl}} = \sum_{\mu,\mathbf{k}} \varepsilon_{\mathbf{k},\mu} |S'^{z}_{\mathbf{k},\mu}|^2, \tag{4.35}$$

where $S'^{z}_{\mathbf{k},\mu}$ is related to $S^{z}_{\mathbf{k},\nu}$ through a multiplication by a unitary matrix $U_{\mu\nu,\mathbf{k}}$ which diagonalizes $V_{\mu\nu,\mathbf{k}}$: $S'^{z}_{\mathbf{k},\mu} = \sum_\nu U_{\mu\nu,\mathbf{k}} S^{z}_{\mathbf{k},\nu}$. Recall that $S^{z}_{\mathbf{r},\mu}$ is either $+1/2$ or $-1/2$. This imposes the following constraint:

$$\sum_{\mathbf{k},\mu} |S'^{z}_{\mathbf{k},\mu}|^2 = \sum_{\mathbf{k},\mu} |S^{z}_{\mathbf{k},\mu}|^2 = \sum_{\mathbf{r},\mu} \left(S^{z}_{\mathbf{r},\mu}\right)^2 = N_{\text{u.c.}}. \tag{4.36}$$

From Eq. (4.35), the energy can be interpreted as a weighted sum of $\varepsilon_{\mathbf{k},\mu}$ with the corresponding weights being $|S'^{z}_{\mathbf{k},\mu}|^2$. Because of the constraint in Eq. (4.36), the energy is minimized by having the full weight on the smallest $\varepsilon_{\mathbf{k},\mu}$ and no weight on the rest of the $\varepsilon_{\mathbf{k},\mu}$. This holds provided that such a configuration of $S'^{z}_{\mathbf{k},\mu}$ in the momentum space corresponds to some configuration in the real space where $S^{z}_{\mathbf{r},\mu}$ are $\pm 1/2$.

Calculating the Fourier transform of the long-range potential, Eq. (4.34), and its eigenvalues $\varepsilon_{\mathbf{k},\mu}$, we find that the minimum of $\varepsilon_{\mathbf{k},\mu}$ occurs for $\mathbf{k} = \mathbf{0}$ and is triply degenerate. In

particular,

$$V_{\mu\nu,\mathbf{k}=\mathbf{0}} = \begin{pmatrix} v_1 & v_2 & v_2 & v_2 \\ v_2 & v_1 & v_2 & v_2 \\ v_2 & v_2 & v_1 & v_2 \\ v_2 & v_2 & v_2 & v_1 \end{pmatrix}, \tag{4.37}$$

where $v_1 = 0.113V$ and $v_2 = 1.12V$. Its eigenvalues are $\varepsilon_{\mathbf{0},0} = 3.46V$ and $\varepsilon_{\mathbf{0},1} = \varepsilon_{\mathbf{0},2} = \varepsilon_{\mathbf{0},3} = -1.004V$. The unitary that diagonalizes the above matrix also relates $S'^z_{\mathbf{0},\mu}$ to $S^z_{\mathbf{0},\nu}$ as

$$\begin{pmatrix} S'^z_{\mathbf{0},0} \\ S'^z_{\mathbf{0},1} \\ S'^z_{\mathbf{0},2} \\ S'^z_{\mathbf{0},3} \end{pmatrix} = \frac{1}{2} \begin{pmatrix} 1 & 1 & 1 & 1 \\ 1 & 1 & -1 & -1 \\ 1 & -1 & 1 & -1 \\ 1 & -1 & -1 & 1 \end{pmatrix} \begin{pmatrix} S^z_{\mathbf{0},0} \\ S^z_{\mathbf{0},1} \\ S^z_{\mathbf{0},2} \\ S^z_{\mathbf{0},3} \end{pmatrix}. \tag{4.38}$$

Since $\varepsilon_{\mathbf{0},1}, \varepsilon_{\mathbf{0},2}$ and $\varepsilon_{\mathbf{0},3}$ are the minimum eigenvalues, the energy is minimized by having all the weight distributed between $S'^z_{\mathbf{0},1}, S'^z_{\mathbf{0},2}$ and $S'^z_{\mathbf{0},3}$ and no weight on the remaining $S'^z_{\mathbf{k},\mu}$, that is, $S'^z_{\mathbf{k}\neq\mathbf{0},\mu} = 0$ and $S'^z_{\mathbf{0},0} = 0$. There indeed exist states satisfying these two conditions. The first condition, $S'^z_{\mathbf{k}\neq\mathbf{0},\mu} = 0$, implies that the ground state is a $\mathbf{k} = \mathbf{0}$ state, while the second condition, $S'^z_{\mathbf{0},0} = 0$, implies that the ground state satisfies the ice rule (so that the total spin, which is $S'^z_{\mathbf{0},0}$ is 0), see Eq. (4.38). There are six such states, and we refer to them as the "ice ferromagnet" or "ice FM" states. One of these is shown in Fig. 4.7. We note that ice ferromagnet is one of the "chain states" that were described in Ref. [251]. We here point out an interesting question: if we add a next-nearest-neighbor $\hat{S}^z\hat{S}^z$ interaction to $\hat{H}_{\text{cl}}$, do the ground states of this new Hamiltonian

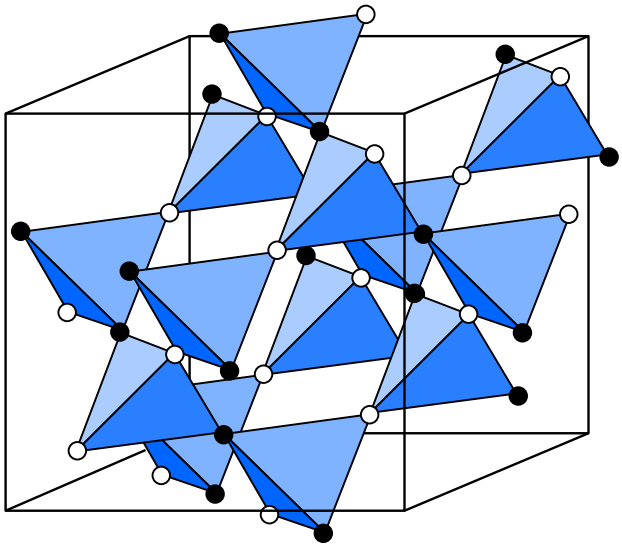

Figure 4.7: An ice ferromagnet state. It is an ice rule obeying state (i.e., $n_{\triangle} = 2$ on every tetrahedron) with $\mathbf{k} = \mathbf{0}$. All the up-pointing tetrahedra are copies of each other. The same is true for the down-pointing tetrahedra. There are six (${}^4C_2$) such states, and together they make up the ground subspace of $\hat{H}_{\text{cl}}$.

satisfy the ice rule and are they also "chain states" as described in Ref. [251]? We leave it for future work to answer this question.

4.3.1.3 Ansatz wavefunctions for the ordered state and for the quantum spin liquid

We now assume that, as one increases Ω starting from $\Omega = 0$, the ground state remains adiabatically connected to the ice ferromagnet derived in the previous section till the point where it undergoes the putative phase transition to the QSL. Therefore, our ansatz for the ordered state is

$$|\Psi_{\text{ord}}\rangle = \hat{U}_S^\dagger |\Psi_{\text{IFM}}\rangle \,, \tag{4.39}$$

where $|\Psi_{\text{IFM}}\rangle$, a product state in the $\hat{S}^z$ basis, is the $\mathbf{k} = \mathbf{0}$ ice ferromagnet defined Sec. 4.3.1.2. This configuration is given by $S^z_{\mathbf{r},\mu} = \frac{1}{2}\varepsilon_\mu$ (independent of $\mathbf{r}$), where $(\varepsilon_0, \varepsilon_1, \varepsilon_2, \varepsilon_3) \equiv (1, 1, -1, -1)$.

We note that there are six such choices for ε_μ that satisfy the ice rule. We pick one such choice, but our calculations are not sensitive to which one we pick. $|\Psi_{\text{IFM}}\rangle$ lives entirely in the ice manifold. Left-multiplication by $\hat{U}_S^\dagger$ takes it back to the original Hilbert space with ice rule violations.

Our ansatz wave function for the spin liquid state is

$$|\Psi_{\text{QSL}}\rangle = \hat{U}_S^\dagger |\Psi_{\text{RK}}\rangle \,, \tag{4.40}$$

where $|\Psi_{\text{RK}}\rangle$ is a uniform superposition of all dimer coverings [253] of the diamond lattice (with $n_{\text{hexagon}} = 2$). $|\Psi_{\text{RK}}\rangle$ lives in the ice manifold. Like before, we left-multiply it by $\hat{U}_S^\dagger$ to take it back to the original Hilbert space. The justification for our choice is the following. $|\Psi_{\text{RK}}\rangle$ is the ground state of the dimer model at the RK point [see Eq. (4.10)]. When the RK potential is zero, $|\Psi_{\text{RK}}\rangle$ has an energy expectation value of $-4N_{\text{u.c.}}J_{\text{ring}}\overline{n}_{\text{flip}}$, where $\overline{n}_{\text{flip}}$ is the average fraction of flippable hexagons in the RK wavefunction. We find numerically that $\overline{n}_{\text{flip}} = 0.1757$ (also calculated in Ref. [6]). Therefore, the energy of $|\Psi_{\text{RK}}\rangle$ is $-0.7028J_{\text{ring}}N_{\text{u.c.}}$ which is not too far from the ground state energy of the dimer model (4.12) found in Ref. [16] to be $-0.756J_{\text{ring}}N_{\text{u.c.}}$. Even though $|\Psi_{\text{RK}}\rangle$ has slightly higher energy, it has the advantage of being simpler to sample by classical Monte Carlo. This explains our choice.

For comparison, we will also calculate the energy of a different ordered state $|\Psi'_{\text{ord}}\rangle = \hat{U}_S^\dagger |\Psi_{\text{IAFM}}\rangle$ that we call an ice antiferromagnet. Here $|\Psi_{\text{IAFM}}\rangle$ is an ice rule obeying state with ordering wave vector $\mathbf{k} = \pi(\mathbf{b}_1 + \mathbf{b}_2)$, where $\mathbf{b}_1$, $\mathbf{b}_2$ and $\mathbf{b}_3$ are primitive reciprocal lattice vectors of the FCC lattice satisfying $\mathbf{a}_i \cdot \mathbf{b}_j = \delta_{ij}$. This state is known elsewhere in literature as the $2\pi(001)$ state (this nomenclature uses an enlarged cubic unit cell of the FCC lattice) [263, 270, 271].

Operator	$\lvert\Psi_{\text{RK}}\rangle$	$\lvert\Psi_{\text{IFM}}\rangle$	$\lvert\Psi_{\text{IAFM}}\rangle$
$\hat{R}$	$0.70288(4)N_{\text{u.c.}}$	0	0
$\hat{H}_{\text{LR}}$	$2.6037(1)\times 10^{-2}N_{\text{u.c.}}$	$-0.4002\times 10^{-2}N_{\text{u.c.}}$	$3.8722\times 10^{-2}N_{\text{u.c.}}$
$\hat{W}^{(2)}_{\text{LR}}$	$1.11778(1)\times 10^{-3}N_{\text{u.c.}}$	$0.01642\times 10^{-3}N_{\text{u.c.}}$	$1.4994\times 10^{-3}N_{\text{u.c.}}$
$\hat{L}^{(2)}_{\text{LR}}$	$-2.7467(3)\times 10^{-4}N_{\text{u.c.}}$	$-0.0829\times 10^{-4}N_{\text{u.c.}}$	$-7.5662\times 10^{-4}N_{\text{u.c.}}$
$\hat{M}^{(2)}_{\text{LR}}$	$2.96(3)\times 10^{-3}N_{\text{u.c.}}$	$0.073\times 10^{-3}N_{\text{u.c.}}$	$6.66\times 10^{-3}N_{\text{u.c.}}$
$\hat{W}^{(3)}_{\text{LR}}$	$5.25(4)\times 10^{-5}N_{\text{u.c.}}$	$-0.00665\times 10^{-5}N_{\text{u.c.}}$	$5.81\times 10^{-5}N_{\text{u.c.}}$
$\hat{W}^{(4)}_{\text{LR}}$	$-3.57(2)\times 10^{-6}N_{\text{u.c.}}$	$-0.0309\times 10^{-6}N_{\text{u.c.}}$	$-5.35\times 10^{-6}N_{\text{u.c.}}$

Table 4.1: The expectation values of the operators in the left column in ansatz wavefunctions $\lvert\Psi_{\text{RK}}\rangle$, $\lvert\Psi_{\text{IFM}}\rangle$ and $\lvert\Psi_{\text{IAFM}}\rangle$ respectively. The operator $\hat{R}$ is defined as $\hat{R}=\sum_{\hexagon}$  + H.c. In the RK wavefunction, $\langle\Psi_{\text{RK}}|\hat{R}|\Psi_{\text{RK}}\rangle = 4\bar{n}_{\text{flip}}N_{\text{u.c.}}$. To calculate expectation values in $\lvert\Psi_{\text{RK}}\rangle$, we have used classical Monte Carlo sampling.

4.3.1.4 Numerical results—energy expectation values and phase diagram

We now describe our computation of the expectation value of $\hat{H}_{\text{eff}}$ [see Eq. (4.23)] in $\lvert\Psi_{\text{RK}}\rangle$, $\lvert\Psi_{\text{IFM}}\rangle$ and in $\lvert\Psi_{\text{IAFM}}\rangle$. While the expectation value in $\lvert\Psi_{\text{IFM}}\rangle$ and $\lvert\Psi_{\text{IAFM}}\rangle$ can be computed straightforwardly, the expectation value in $\lvert\Psi_{\text{RK}}\rangle$ requires classical Monte Carlo sampling. We use a system with $8\times 8\times 8$ unit cells (i.e., containing 2048 pyrochlore sites) with periodic boundary conditions in the $\mathbf{a}_1$, $\mathbf{a}_2$, and $\mathbf{a}_3$ directions. We restrict our sampling to sectors in which the total electric flux piercing through any 2D torus cross-section (as defined in Sec. IV B of Ref. [6]) is 0. Our sampling is done using loop moves as described in Refs. [6, 270, 271] – in each Monte Carlo run, we perform $512\times 500,000$ loop moves. We calculate $\bar{n}_{\text{flip}}$, H_{LR}, $W^{(2)}_{\text{LR}}$ and $L^{(2)}_{\text{LR}}$ after every 512 loop moves, i.e., we take 500,000 data points. We calculate $M^{(2)}_{\text{LR}}$, $W^{(3)}_{\text{LR}}$, and $W^{(4)}_{\text{LR}}$ after every $512\times 10,000$ loop moves, i.e. we take 50 data points. We repeat this procedure for 9 independent runs in order to calculate the uncertainties. Our results are summarized in Table 4.1. With these values at hand, we calculate the expectation value of $\hat{H}_{\text{eff}}$ using Eq. (4.23)

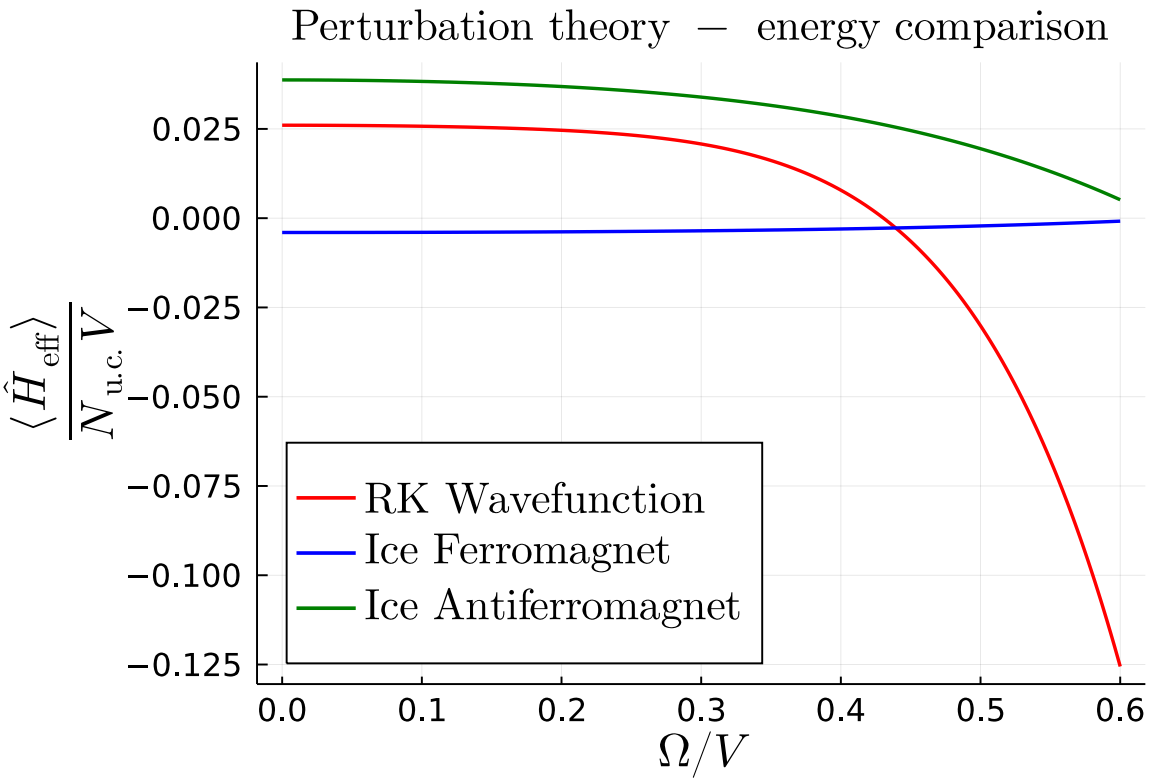

Figure 4.8: $\langle \hat{H}_{\text{eff}} \rangle$ in $|\Psi_{\text{RK}}\rangle$, $|\Psi_{\text{IFM}}\rangle$, and $|\Psi_{\text{IAFM}}\rangle$ calculated by inserting the values in Table 4.1 in Eq. (4.23).

in $|\Psi_{\text{RK}}\rangle$, $|\Psi_{\text{IFM}}\rangle$, and $|\Psi_{\text{IAFM}}\rangle$, and the result is plotted in Fig. 4.8. As we turn on Ω, the transition point Ω_C can be determined within our approximation as the Ω for which the energy of the ice ferromagnet becomes higher than that of the RK wavefunction, as calculated using Eq. (4.23). We find

$$\Omega_C = 0.43927(1)V. \tag{4.41}$$

We note that there are three sources of uncertainty: (1) truncation of the perturbation series in Eq. (4.23), (2) evaluating energies in ansatz state $|\Psi_{\text{RK}}\rangle$ instead of the true eigenstate of $\hat{H}_{\text{eff}}$, and (3) the uncertainty in the Monte Carlo calculation. The uncertainty reported in Eq. (4.41) is only the uncertainty arising from the Monte Carlo calculation.

There is an important question on whether our use of perturbation theory is justified. First,

we argue that treating $\hat{H}_{\text{LR}}$ perturbatively is justified. $\left\{\hat{H}_{\text{LR}}\right\}$, $\left\{\hat{W}^{(2)}_{\text{LR}}, \hat{L}^{(2)}_{\text{LR}}, \hat{M}^{(2)}_{\text{LR}}\right\}$, $\left\{\hat{W}^{(3)}_{\text{LR}}\right\}$, and $\left\{\hat{W}^{(4)}_{\text{LR}}\right\}$ are sets of operators that are first, second, third, and fourth order respectively in $\hat{H}_{\text{LR}}$. As we can see from Table 4.1, the expectation values of these operators in $|\Psi\rangle_{\text{RK}}$ drops by an order of magnitude each time one goes one order higher in $\hat{H}_{\text{LR}}$. Next, is perturbation theory in $\hat{H}_{\Omega}$ justified, given that our calculated Ω_C is outside the $\Omega \ll V$ regime? We observe that the leading contribution to J_{ring} that we dropped, $\frac{33833}{2592}\frac{(\Omega_C)^8}{V^7} = 0.018V$ [261], is smaller than the one we kept, $\frac{63}{16}\frac{(\Omega_C)^6}{V^5} = 0.028V$. If we had kept higher order contributions to J_{ring}, it would only decrease the energy of the QSL relative to the ice ferromagnet and ice antiferromagnet. Further, the energy of the QSL that we present is a conservative estimate since we used the RK wavefunction which has higher energy than the true ground state of Hamiltonian (4.9). This gives us hope that our result obtained using perturbation theory is qualitatively correct. In Appendix D.1, we further address the issue of convergence of the perturbation theory by calculating the Borel-Padé approximants of the perturbative energies of the three ansatz states. We find that using the Borel-Padé approximants for the ice FM and the ice antiferromagnet does not change the phase diagram qualitatively, while the Borel-Padé approximant for the RK wavefunction does not capture the energy reduction coming from quantum fluctuations. However, rigorously ascertaining the convergence of our perturbative expansion is beyond the scope of this work.

Within our approximation, for $\Omega < \Omega_C$, the ground state is an ice ferromagnet, an ordered state satisfying the ice rule. For $\Omega > \Omega_C$ but also close to Ω_C, the ground state is in the QSL phase, i.e., the deconfined phase of a $U(1)$ gauge theory. From the point of view of the QSL, the ordered ice ferromagnet state is obtained when monopole excitations of the spin liquid proliferate, and the monopole-antimonopole string operator, to be defined in Sec. 4.4.2, Eq. (4.74), acquires an expectation value. As a consequence of this, the fractional "electric charges", or spinons, get

confined [235, 236]. The monopole creation operator (see Sec. 4.4.2 and Ref. [6]) is diagonal in the $\hat{S}^z$ basis, and acts in the sector that obeys the ice rule. It is thus plausible that the confined phase is indeed the ice ferromagnet. While our calculation provides microscopic intuition for this transition, we emphasize that, to prove the existence of, locate and characterize this transition accurately, one needs to do a more careful quantum Monte Carlo calculation.

4.3.2 Large Ω—Higgs transition

From the Hamiltonian in Eq. (4.6), it is clear that, in the limit $\Omega \gg V$, the ground state is a transverse-field-polarized (TFP) state, i.e., a product state of $(|g\rangle - |r\rangle)_i$ at each site i. Thus, as Ω is increased away from Ω_C, the system should eventually go through a phase transition from the putative QSL phase into the TFP phase. From the point of view of the QSL, this is a Higgs transition because the operator $\hat{S}^x$ that acquires expectation value in the TFP phase creates a pair of "electric"-charge excitations in the spin liquid. The perturbation theory in Ω/V that we performed in Sec. 4.3.1 relies on the ability to go to a basis where the Hilbert space decouples into ice rule obeying and ice rule disobeying sectors separated by an energy gap of V. But the ground state in the $\Omega \gg V$ limit (TFP) straddles both of these sectors. So we do not expect perturbation theory in Ω/V to capture the phase transition into the TFP phase that contains the $\Omega \to \infty$ ground state. Hence, we will present an indirect reasoning below. In the $\Omega \ll V$ limit, $\hat{H}_{\text{LR}}$ was important, since it was the dominant term splitting the degeneracy in the ice manifold. On the other hand, in the vicinity of the putative Higgs transition, $\hat{H}_{\text{LR}}$ may not be as important since the largest term in $\hat{H}_{\text{LR}}$ has magnitude $V/27$, and as justified above using Table 4.1, the effect of $\hat{H}_{\text{LR}}$ is indeed perturbative. Therefore, we drop $\hat{H}_{\text{LR}}$ as a zeroth-order approximation

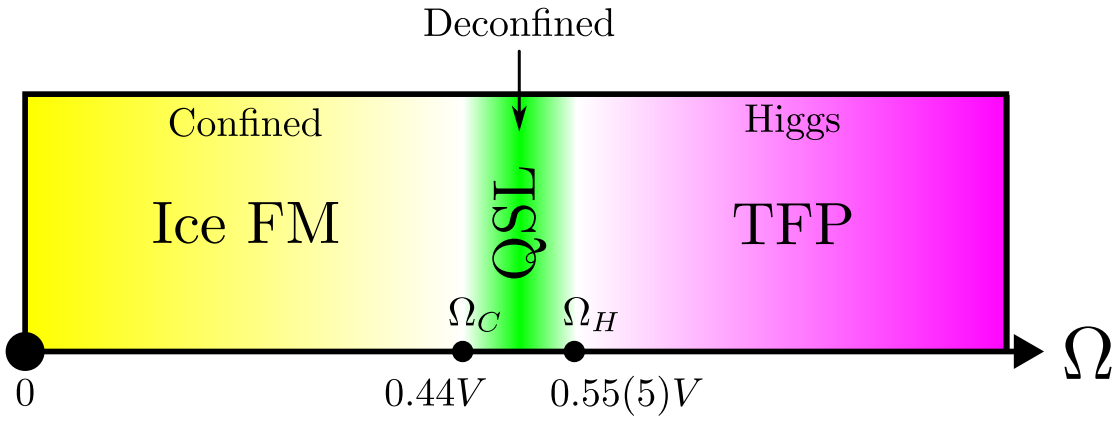

Figure 4.9: Approximate ground state phase diagram of the Hamiltonian in Eq. (4.6). The ground state for $\Omega = 0$ was calculated exactly to be an ice ferromagnet (ice FM) in Sec. 4.3.1.2. We assume that, as Ω is increased, no phase transition occurs to a different ordered state. The transition point from the ice ferromagnet (confined phase) to the QSL (deconfined phase) at $\Omega_C \approx 0.44V$ is obtained by comparing energies of ansatz wavefunctions in the effective Hamiltonian obtained using perturbation theory in $\hat{H}_\Omega$ and $\hat{H}_{LR}$. For the Higgs transition to the TFP phase, we make an approximation by dropping $\hat{H}_{LR}$, in which case Ω_H was calculated in Ref. [18] to be 0.55(5).

for calculating the Higgs transition point. The resulting Hamiltonian is the transverse field Ising model on the pyrochlore lattice. Refs. [18] and [261] studied this model and found the transition point Ω_H to be at $\Omega_H = 0.55(5)V$ and $0.6V$ respectively. This leads us to expect that, in the window $0.44 < \Omega < 0.55$, the ground state may be a QSL, leading us to sketch the phase diagram shown in Fig. 4.9. Within our approximation, $\Omega_C < \Omega_H$ and there is a window where the QSL is the ground state. However, the introduction of $\hat{H}_{\text{LR}}$ may result in a lowering of the energy of the TFP state relative to the QSL. Calculating this effect and verifying that this does not bring down Ω_H far enough to destroy the QSL phase requires a more careful calculation which is beyond the scope of this work. We note that, to be certain about the existence of all the phases we found and about not missing any additional phases, a more detailed quantum Monte Carlo study is required, and we leave it for future work.

In the remainder of this section, we provide some intuition for the Higgs transition by performing a gauge mean field theory (gMFT) calculation introduced in Ref. [272].

4.3.2.1 Gauge mean field theory—Higgs transition

The main idea of this approach is to first recast the microscopic Hamiltonian as an exact gauge theory by introducing ancillary degrees of freedom followed by a mean-field decoupling of the interactions. This theory involves bosonic charges hopping in the presence of a fluctuating gauge field whose mean-field value is chosen self-consistently. If this mean-field gauge-field configuration is such that the hopping amplitudes of the bosonic charges is 0, then the theory is in a confined phase. If not, the theory is in the deconfined phase as long as the bosons do not condense. If the bosonic charges condense, then the theory is in a Higgs phase, which is adiabatically connected to the TFP state.

Concretely, the construction is as follows. For $\mathbf{r} \in A$, where A is a sublattice of the diamond lattice,

$$\hat{S}^{+}_{\mathbf{r}\to\mathbf{r}+\mathbf{e}_\mu} = \hat{\Phi}^{\dagger}_{\mathbf{r}} \hat{\mathsf{s}}^{+}_{\mathbf{r}\to\mathbf{r}+\mathbf{e}_\mu} \hat{\Phi}_{\mathbf{r}+\mathbf{e}_\mu}, \tag{4.42}$$

where $\hat{S}^{+}_{\mathbf{r}\to\mathbf{r}+\mathbf{e}_\mu} \equiv \hat{S}^{+}_{\mathbf{r}+\mathbf{e}_\mu/2} = \hat{S}^{+}_{\mathbf{r},\mu}$ (and similarly $\hat{\mathsf{s}}^{+}_{\mathbf{r}\to\mathbf{r}+\mathbf{e}_\mu} \equiv \hat{\mathsf{s}}^{+}_{\mathbf{r}+\mathbf{e}_\mu/2} = \hat{\mathsf{s}}^{+}_{\mathbf{r},\mu}$) lives on a bond of the diamond lattice connecting sites $\mathbf{r}$ and $\mathbf{r}+\mathbf{e}_\mu$ (recall that centers of the bonds of the diamond lattice are sites of the pyrochlore lattice). $\hat{\mathsf{s}}^{z}$ is also a spin-1/2 operator and has eigenvalues $\pm 1/2$. Here, $\hat{\Phi}^{\dagger}_{\mathbf{r}}$ serves as a raising operator for $\hat{Q}_{\text{△}_{\mathbf{r}}} \equiv \eta_{\mathbf{r}}(\hat{n}_{\text{△}_{\mathbf{r}}} - 2)$, where $\eta_{\mathbf{r}} = 1$ for $\mathbf{r} \in A$ and $\eta_{\mathbf{r}} = -1$ for $\mathbf{r} \in B$. For convenience, we drop the symbol △ from now on. $\hat{Q}_{\mathbf{r}}$ and $\hat{\Phi}^{\dagger}_{\mathbf{r}}$ satisfy the commutation relation: $\left[\hat{Q}_{\mathbf{r}}, \hat{\Phi}^{\dagger}_{\mathbf{r}}\right] = \hat{\Phi}^{\dagger}_{\mathbf{r}}$. Note that $\hat{\Phi}_{\mathbf{r}}$ is not a canonical boson but a rotor satisfying

$$\hat{\Phi}^{\dagger}_{\mathbf{r}} \hat{\Phi}_{\mathbf{r}} = 1. \tag{4.43}$$

To recover the original spin Hilbert space, one imposes the constraint that the total gauge charge

at $\mathbf{r}$ is

$$\hat{Q}_{\mathbf{r}} = \eta_{\mathbf{r}} \sum_{\mu} \hat{\mathsf{s}}^{z}_{\mathbf{r}+\eta\mathbf{e}_{\mu}/2}. \tag{4.44}$$

Rewriting the Hamiltonian (4.6) in terms of the fictitious variables, $\hat{Q}_{\mathbf{r}}$, $\hat{\Phi}_{\mathbf{r}}$ and $\hat{\mathsf{s}}_{\mathbf{r},\mu}$ we get

$$\begin{aligned}\hat{H} =& \frac{V}{2} \sum_{\mathbf{r}\in A,B} \hat{Q}^{2}_{\mathbf{r}} - \frac{\Omega}{2} \sum_{(\mathbf{r}\in A),\mu} \left(\hat{\Phi}^{\dagger}_{\mathbf{r}} \hat{\mathsf{s}}^{+}_{\mathbf{r}\to\mathbf{r}+\mathbf{e}_{\mu}} \hat{\Phi}_{\mathbf{r}+\mathbf{e}_{\mu}} + \text{H.c.} \right) \\ &+ \frac{1}{2} \sum_{\mathbf{r},\mathbf{r}'\in A} \sum_{\mu,\nu} V_{\mu\nu}(\mathbf{r}-\mathbf{r}') \hat{\mathsf{s}}^{z}_{\mathbf{r}\mu} \hat{\mathsf{s}}^{z}_{\mathbf{r}',\nu},\end{aligned} \tag{4.45}$$

where $V_{\mu\nu}(\mathbf{r}-\mathbf{r}') = V \left(\frac{a}{\mathbf{r}-\mathbf{r}'+\mathbf{e}_{\mu}/2-\mathbf{e}_{\nu}/2} \right)^{6}$ whenever $(\mathbf{r},\mu)$ and $(\mathbf{r}',\nu)$ are distinct and are not nearest-neighbors. $V_{\mu\nu}(\mathbf{r}-\mathbf{r}')$ is 0 otherwise.

Following Ref. [272], we perform the zeroth-order mean-field decoupling: $\hat{\Phi}^{\dagger}\hat{\Phi}\hat{\mathsf{s}} \to \hat{\Phi}^{\dagger}\hat{\Phi} \langle \hat{\mathsf{s}} \rangle + \left\langle \hat{\Phi}^{\dagger}\hat{\Phi} \right\rangle \hat{\mathsf{s}} - \left\langle \hat{\Phi}^{\dagger}\hat{\Phi} \right\rangle \langle \hat{\mathsf{s}} \rangle$ and $\hat{\mathsf{s}}\hat{\mathsf{s}} \to \hat{\mathsf{s}} \langle \hat{\mathsf{s}} \rangle + \langle \hat{\mathsf{s}} \rangle \hat{\mathsf{s}} - \langle \hat{\mathsf{s}} \rangle \langle \hat{\mathsf{s}} \rangle$ (where $\hat{\mathsf{s}}$ could either be $\hat{\mathsf{s}}^{+}$, $\hat{\mathsf{s}}^{-}$, or $\hat{\mathsf{s}}^{z}$). Upon doing so, the Hamiltonian decouples into a Hamiltonian of bosons hopping on the diamond lattice and a Hamiltonian of spins in an external field, which itself is set self-consistently by the Green's function of the bosons. Before solving the resulting theory, one needs to enforce the constraints (4.43) and (4.44) using Lagrange multipliers $\lambda_{\mathbf{r}}$ and $v_{\mathbf{r}}$, respectively. Within the mean-field theory, it is assumed that these Lagrange multipliers take a spatially homogeneous value at the saddle point. We then find the minimum value of Ω_H^{MF} such that, for any $\Omega > \Omega_H^{\text{MF}}$, it is possible to self-consistently choose λ only by macroscopically occupying a boson mode. This Ω_H^{MF} marks the location of the Bose-Einstein-condensation transition (or Higgs transition within the mean-field theory). We find $\Omega_H^{\text{MF}} \approx 0.7V$. In Appendix D.2, we present more details of this calculation. An artifact of this technique is that, although we include long-range interactions in our calculation, they do not play any role at the saddle point near the Higgs transition. Therefore, the final steps

and result of our calculation are identical to the ones carried out in [256].

In Appendix D.2, we also point out a major limitation of this technique in the small-Ω limit that may not have been appreciated in previous literature on gauge mean field theory.

4.3.3 Comments on dynamical state preparation

So far, we have focused on the nature of the ground state of Hamiltonian (4.6) as a function of Ω/V. However, what is often experimentally relevant is the nature of the state prepared by a ramping of parameters in a finite amount of time. In the context of the experiment in Ref. [207], it was shown in Ref. [273, 274] that a state in the same phase as the $\mathbb{Z}_2$ gauge theory can be prepared by a non-equilibrium time evolution starting from a trivial state. In the context of the experiment in Ref. [207], it was shown numerically in Ref. [273] that a state with a large overlap with the RVB state can be prepared by a non-equilibrium time evolution. The question of dynamical state preparation was also studied in Ref. [274]. Here, we will present an adaptation of the conclusions of Ref. [274] to our setting.

The excitations of a $U(1)$ QSL are gapless "photons", magnetic monopoles, and "electric charges" (spinons). The transition of a QSL to an ice ferromagnet is driven by the condensation of monopoles, while the transition to the TFP phase is driven by the condensation of spinons. The gapless "photons" are not directly involved in these transitions. Also, a state with "photon" modes excited on top of a QSL state is still in the deconfined phase of the $U(1)$ gauge theory. This allows us to ignore "photons" in this section. Since the confined phase, ice ferromagnet has an extensive number of monopoles, we use the difference per unit cell between the energies of the QSL and ice ferromagnet states as a proxy for the monopole energy scale. At $\Omega = 0$, this

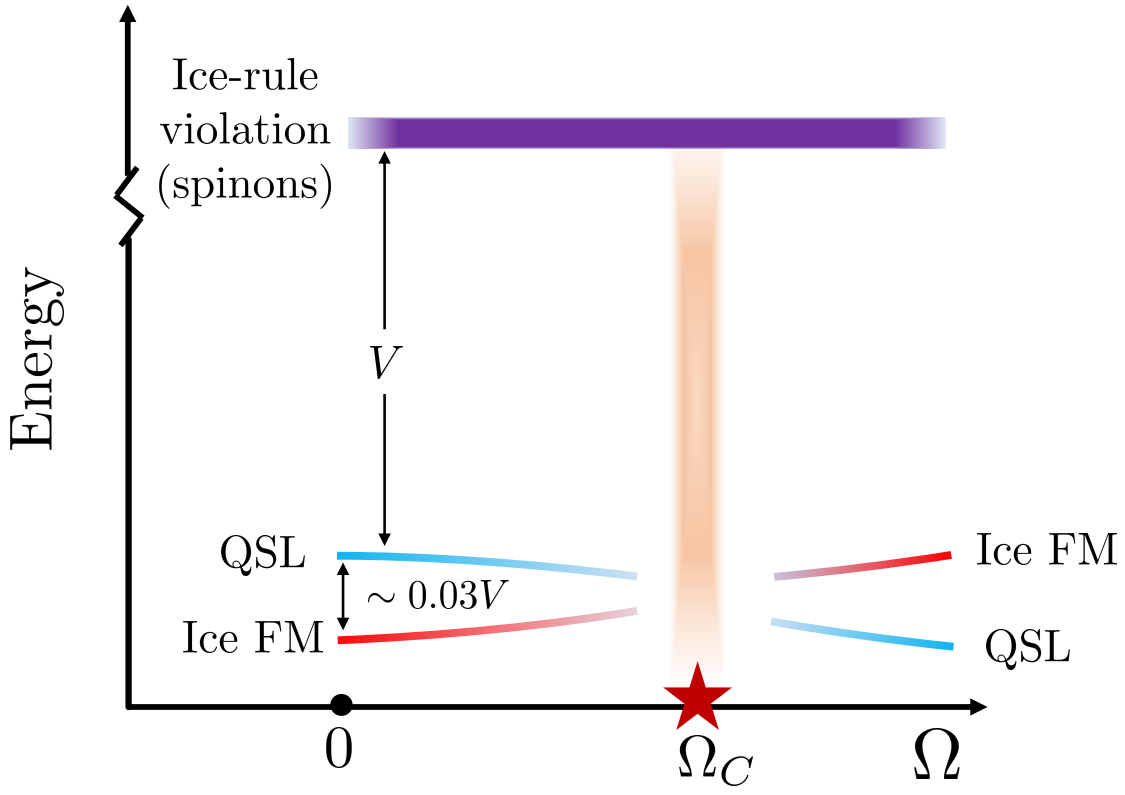

Figure 4.10: A qualitative sketch of the energy scales (per unit cell) in our problem. For $\Omega > \Omega_C$, the ground state is a $U(1)$ QSL. Ice ferromagnet is the ordered state obtained when monopoles proliferate, i.e., the ice ferromagnet has an extensive number of monopoles. We therefore use the energy difference per unit cell between the QSL and the ice ferromagnet at $\Omega = 0$, obtained in Table 4.1, as a proxy for the monopole energy scale. This scale $\sim 0.03V$ is much smaller than the spinon energy scale ("electric charge"), which is $\sim$ V.

difference is $\left(\left\langle \hat{H}_{\text{LR}}\right\rangle_{\text{QSL}} - \left\langle \hat{H}_{\text{LR}}\right\rangle_{\text{IFM}}\right)/N_{\text{u.c.}} \approx 0.03V$ (see Table 4.1), which is much smaller than the spinon energy scale (see Fig. 4.10 for a sketch). Suppose one starts with an initial state (for a small $\epsilon \sim \Omega/V$)

$$\left|\Psi_{(t=0)}\right\rangle = \otimes_i \left(|g\rangle_i + \epsilon\,|r\rangle_i\right), \tag{4.46}$$

which is the ground state in the limit of large negative δ/V and small Ω/V. As shown in Sec. 4.2, the classical ground state lies in the ice manifold when $\delta \in (2.46V, 4.46V)$. Now suppose that δ is ramped up from its initial large negative value to a value in this range such that the ramp is adiabatic with respect to the spinon gap V, but is sudden with respect to the monopole scale

$\sim 0.03V$, while keeping $\Omega/V \ll 1$. Using arguments in Ref. [274], this protocol will not prepare the ground state, which, from Fig. 4.9, is an ice ferromagnet. Instead, it will (approximately) project out violations of the ice rule (due to adiabaticity with respect to the spinon scale) from the initial state $\left|\Psi_{(t=0)}\right\rangle$. The resulting final state is

$$|\Psi_{\text{final}}\rangle \approx \hat{\mathcal{P}}\left\{\otimes_i \left(|g\rangle_i + \epsilon\,|r\rangle_i\right)\right\} = |\Psi_{\text{RK}}\rangle\,, \tag{4.47}$$

where $\hat{\mathcal{P}}$ is the projector onto the ice manifold. The projected wavefunction is an equal-weight superposition of all coverings, which is simply the RK wavefunction and which lies in the QSL phase [6]. There is one catch to the above argument—the spinon gap closes during the above ramp. So it is impossible to be sudden with respect to the monopole scale and yet be strictly adiabatic with respect to the spinon gap throughout the ramp. For a short duration (while the ramp is going through the spinon gap closing), adiabaticity with respect to the spinon gap will be violated. By the Kibble-Zurek mechanism, the resulting state is composed of finite-size puddles of QSL-like regions with a nonzero density of spinons interspersed [274, 275, 276, 277]. Thus, in summary, there are two different ways in which one can prepare a $U(1)$ QSL-like state in experiment and study a confinement-deconfinement transition[1].

1. $\underline{\Omega/V \ll 1}$: Perform a ramp of δ starting from a large negative value and ending in the range $(2.46V, 4.46V)$ for a fixed $\Omega/V \ll 1$ such that the ramp is adiabatic with respect to V (spinon gap) but sudden with respect to the monopole scale ($\sim 0.03V$). Even though the ground state is not a QSL for these parameters, this procedure would create puddles

[1]We note that the confinement-deconfinement transition of $U(1)$ gauge theory in 3+1D is strictly speaking, a ground state transition [259, 278]. Therefore, in this chapter, when we use the phrase confinement-deconfinement transition, we mean signatures of this transition in a finite-size state prepared in finite time.

of QSL-like regions by the argument in Ref. [274]. To see a deconfinement-confinement transition, the ramp of δ should be slowed down and, once it is adiabatic with respect to the monopole gap, an ordered, i.e. confined state will be prepared.

2. Adiabatic: Perform a ramp of δ starting from a large negative value and ending in the range $(2.46V, 4.46V)$ and a ramp in Ω starting from $\Omega/V \ll 1$ and ending in a final value Ω_f, such that both ramps are adiabatic with respect to the monopole scale always. The two ramps can be performed simultaneously, or such that the ramp in δ precedes the ramp in Ω. This would approximately create the ground state of Hamiltonian (4.6). As the final value Ω_f goes through Ω_C (Ω_H), the nature of the final state prepared this way goes through a confinement-deconfinement (Higgs) transition.

We note that the first method above can prepare a state with a large overlap with the RK wavefunction even if the true ground state of the system is not in the QSL phase. Once a state is prepared by either of the above schemes, one needs to devise measurements that can tell whether the state is in the confined phase or in the deconfined phase. We address this in the following section.

4.4 Diagnosis of the quantum spin liquid

Access to wavefunction snapshots in the $\hat{S}^z$ basis, combined with access to unitary evolution, allows one to use the Rydberg-atom platform to measure non-local observables, a feature generally unavailable in traditional condensed matter systems. In this section, we describe some measurable correlators which can be used to observe the signatures of a quantum spin liquid state. In this section, we assume that the detuning is chosen such that $\rho = 2$.

4.4.1 Plaquette-plaquette correlators

The plaquette operators are off-diagonal in the $\hat{S}^z$ basis. Thus they can distinguishing a coherent quantum superposition from a classical admixture of states. We define two plaquette operators $\hat{X}_P$ and $\hat{Y}_P$ for a hexagonal plaquette P of the pyrochlore lattice as

$$\begin{aligned} \hat{X}_P &= \prod_{i=1}^{6} \left(2\hat{S}_i^x\right), \\ \hat{Y}_P &= \prod_{i=1}^{3} \left(2\hat{S}_{2i-1}^x\right)\left(2\hat{S}_{2i}^y\right), \end{aligned} \tag{4.48}$$

where $1, 2, \ldots, 6$ denote the sites around a plaquette P. We are interested in the following two connected correlators of the plaquette operators:

$$\begin{aligned} \langle \hat{X}_P \hat{X}_{P'} \rangle_c &= \langle \hat{X}_P \hat{X}_{P'} \rangle - \langle \hat{X}_P \rangle \langle \hat{X}_{P'} \rangle, \\ \langle \hat{Y}_P \hat{Y}_{P'} \rangle_c &= \langle \hat{Y}_P \hat{Y}_{P'} \rangle - \langle \hat{Y}_P \rangle \langle \hat{Y}_{P'} \rangle, \end{aligned} \tag{4.49}$$

where P and P' denote two plaquettes of the pyrochlore lattice (see Fig. 4.11).

Either of the two correlators, $\langle \hat{X}_P \hat{X}_{P'} \rangle_c$ and $\langle \hat{Y}_P \hat{Y}_{P'} \rangle_c$, can distinguish a QSL phase from other phases including a classical spin ice (see Table 4.2).

We compare the two correlators and provide protocols to measure them. We assume throughout that the two plaquettes P and P' do not have any sites in common. We now explain the behavior of these plaquette correlators in the ice FM, QSL, and TFP phases.

Correlator	Confined (Ice FM)	Deconfined (QSL)	Higgs (TFP)	Classical Spin Ice
$\langle \hat{X}_P \hat{X}_{P'} \rangle_c$	Exp. or faster decay	$1/\mathsf{R}^8$	$1/\mathsf{R}^{12}$	Exp. or faster decay
$\langle \hat{Y}_P \hat{Y}_{P'} \rangle_c$	Exp. or faster decay	$1/\mathsf{R}^4$	$1/\mathsf{R}^6$	Exp. or faster decay
$\left\langle \hat{\mathcal{M}}^\dagger \hat{\mathcal{M}}(\mathbf{r}_1 \to \mathbf{r}_2) \right\rangle$	Nonzero const.	Exp. decay	Exp. decay	Exp. or faster decay
$\chi_{\mathcal{C}}^E$	Nonzero const.	Exp. or faster decay	Nonzero const.	Exp. or faster decay
$\chi_{\mathcal{C}}^M$	Nonzero const.	Exp. or faster decay	Nonzero const.	Exp. or faster decay
$\langle \hat{S}^z_{\mathbf{r}i} \hat{S}^z_{\mathbf{r}'j} \rangle$	Nonzero const.	$1/R^4$	$1/R^6$	$1/R^4$

Table 4.2: Behavior of various correlators. $\hat{X}_P$ and $\hat{Y}_P$ are plaquette operators defined in Eq. (4.48). $\hat{\mathcal{M}}^\dagger \hat{\mathcal{M}}(\mathbf{r}_1 \to \mathbf{r}_2)$ is a monopole string operator defined in Eq. (4.74). $\chi_{\mathcal{C}}^E$ and $\chi_{\mathcal{C}}^M$ are Fredenhagen-Marcu order parameters defined in Eq. (4.82) and Eq. (4.87), respectively. In this table, we have omitted the form factors multiplying $1/R^4$ and $1/R^8$ that are provided in Eqs. (4.66) and (4.93).

4.4.1.1 Plaquette correlators in the ice FM phase

We will determine the behavior of the correlators deep inside the ice FM phase, that is, for $\Omega \ll V$. In this limit, the ice FM phase is a product state in the $\hat{S}^z$ basis with perturbative corrections on top of it produced by $\hat{H}_\Omega$. Our ansatz for the ice FM state is given by $|\Psi_{\text{ord}}\rangle = \hat{U}_S^\dagger |\Psi_{\text{IFM}}\rangle$, where $\hat{U}_S^\dagger$ is the unitary that performs the Schrieffer-Wolff transformation [see Eq. (4.20)], and $|\Psi_{\text{IFM}}\rangle$ is a product state in the $\hat{S}^z$ basis described in Sec. 4.3.1.2 and shown in Fig. 4.7.

At zeroth order in Ω/V, $\hat{U}_S = \hat{1}$ implying $\langle \hat{X}_P \hat{X}_{P'} \rangle_c = 0$ because the diagonal components of $\hat{X}_P$ in the $\hat{S}^z$ basis are zero. Similarly, $\langle \hat{Y}_P \hat{Y}_{P'} \rangle_c = 0$ at zeroth order. A nonzero contribution to the connected correlators is obtained only by terms in perturbation theory that are of an order proportional to R/a. Thus, the plaquette correlators decay exponentially with distance in the ice FM phase.

4.4.1.2 Plaquette correlators in the QSL phase

Here we provide alternative plaquette correlators which agree with the plaquette correlators defined in Eq. (4.49) up to sixth order in Ω/V. We then interpret them in terms of the gauge theory to understand their behavior in the QSL phase.

Let $|\Psi_g\rangle$ be the ground state of the system and let $\hat{U}_S = e^{\hat{S}}$ be the operator that implements the Schrieffer–Wolff transformation so that $\hat{U}_S \hat{H} \hat{U}_S^\dagger$ is the effective Hamiltonian in the ice manifold. We use the same notation as Sec. 4.3.1.1 here. Thus $|\Psi_0\rangle = \hat{U}_S |\Psi_g\rangle$ is the ground state of the effective Hamiltonian and lies in the ice manifold. Consider two new plaquette X and Y operators defined as

$$\begin{aligned} \hat{\tilde{X}}_P &= \left(\hat{S}_1^+ \hat{S}_2^- \hat{S}_3^+ \hat{S}_4^- \hat{S}_5^+ \hat{S}_6^- + \text{H.c.} \right), \\ \hat{\tilde{Y}}_P &= -i \hat{S}_1^+ \hat{S}_2^- \hat{S}_3^+ \hat{S}_4^- \hat{S}_5^+ \hat{S}_6^- + \text{H.c.}, \end{aligned} \tag{4.50}$$

First, note that

$$\langle \Psi_0 | \hat{X}_P \hat{X}_{P'} | \Psi_0 \rangle = \langle \Psi_0 | \hat{\tilde{X}}_P \hat{\tilde{X}}_{P'} | \Psi_0 \rangle. \tag{4.51}$$

This can be seen by writing $2\hat{S}_i^x = \hat{S}_i^+ + \hat{S}_i^-$ and noticing that the only terms that preserve the ice rule are ring exchanges over P and P'. When the remaining terms act on a state in the ice manifold, they either take it outside of the ice manifold or annihilate it. Thus the expectation value

of these remaining operators in $|\Psi_0\rangle$ is zero. For example, $\hat{S}_1^+ \hat{S}_2^+ \hat{S}_3^+ \hat{S}_4^- \hat{S}_5^- \hat{S}_6^- \hat{S}_7^+ \hat{S}_8^- \hat{S}_9^+ \hat{S}_{10}^- \hat{S}_{11}^+ \hat{S}_{12}^-$ acting on a state in the ice manifold would either annihilate this state or give a state that violates the ice rule on four of the tetrahedra surrounding P. An identity similar to Eq. (4.51) also holds for the expectation value for a single plaquette X operator:

$$\langle \Psi_0 | \hat{X}_P | \Psi_0 \rangle = \langle \Psi_0 | \hat{\tilde{X}}_P | \Psi_0 \rangle. \tag{4.52}$$

Equations analogous to Eqs. (4.51,4.52) also hold true for the plaquette Y operator. Now, $|\Psi_g\rangle = |\Psi_0\rangle + \mathcal{O}(\Omega/V)$, where the corrections of order Ω/V come from the perturbation $\hat{H}_\Omega$. Thus, one would expect $\langle \hat{X}_P \hat{X}_{P'} \rangle_{c,|\Psi_g\rangle} = \langle \hat{\tilde{X}}_P \hat{\tilde{X}}_{P'} \rangle_{c,|\Psi_g\rangle}$ up to first order in Ω/V (The expectation values are calculated in $|\Psi_g\rangle$ here). However, in Appendix D.3, we show that this is true up to sixth order:

$$\langle \hat{X}_P \hat{X}_{P'} \rangle_c = \langle \hat{\tilde{X}}_P \hat{\tilde{X}}_{P'} \rangle_c + \Theta\left((\Omega/V)^6\right), \tag{4.53}$$

$$\langle \hat{Y}_P \hat{Y}_{P'} \rangle_c = \langle \hat{\tilde{Y}}_P \hat{\tilde{Y}}_{P'} \rangle_c + \Theta\left((\Omega/V)^6\right), \tag{4.54}$$

where the expectation values are again calculated in $|\Psi_g\rangle$. We will ignore these sixth-order corrections and now move on to understanding the behavior of $\langle \hat{\tilde{X}}_P \hat{\tilde{X}}_{P'} \rangle_c$ and $\langle \hat{\tilde{Y}}_P \hat{\tilde{Y}}_{P'} \rangle_c$ in the QSL phase by mapping the operators $\hat{\tilde{X}}_P$ and $\hat{\tilde{X}}_{P'}$ to gauge fields.

Using the mapping between the spins and the effective $U(1)$ gauge theory from Eq. (4.13), we see that the operators $\hat{\tilde{X}}_P$ and $\hat{\tilde{Y}}_P$ are equal to (twice) the cosine and the sine of the magnetic

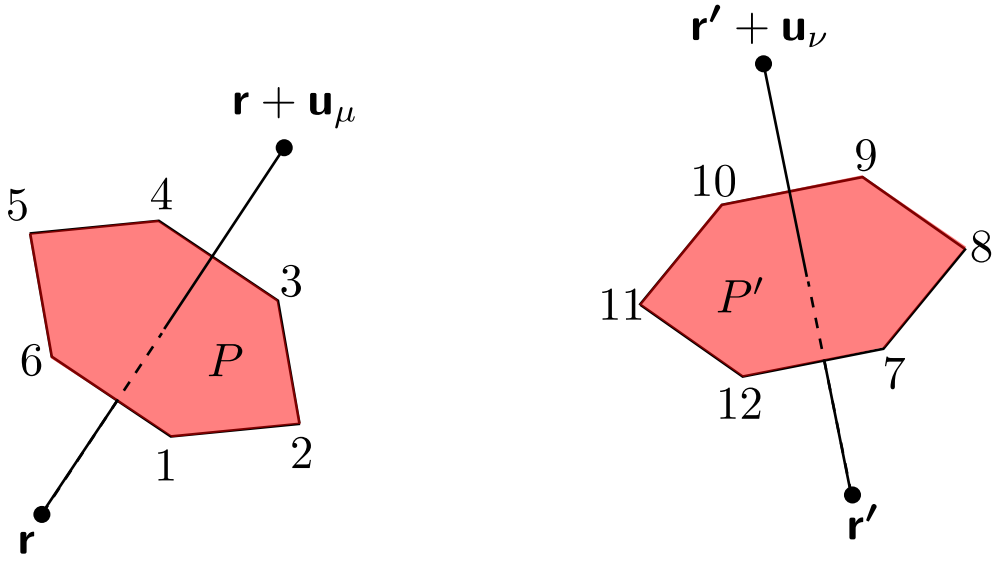

Figure 4.11: Notation for the plaquette correlators. P and P' are two hexagonal plaquettes of the pyrochlore lattice. $\mathbf{r}, \mathbf{r}'$, $\mathbf{r}+\mathbf{u}_\mu$, and $\mathbf{r}'+\mathbf{u}_\nu$ are the sites of the dual diamond lattice. $\mathbf{u}_\mu$ and $\mathbf{u}_\nu$ are vectors perpendicular to P and P'.

field operator $\hat{B}_{\mathbf{r},\mu}$, respectively:

$$\begin{aligned}\hat{\tilde{X}}_P &= 2\cos\left(\hat{\theta}_1-\hat{\theta}_2+\hat{\theta}_3-\hat{\theta}_4+\hat{\theta}_5-\hat{\theta}_6\right)=2\cos\left(\hat{B}_{\mathbf{r},\mu}\right),\\ \hat{\tilde{Y}}_P &= 2\sin\left(\hat{\theta}_1-\hat{\theta}_2+\hat{\theta}_3-\hat{\theta}_4+\hat{\theta}_5-\hat{\theta}_6\right)=2\sin\left(\hat{B}_{\mathbf{r},\mu}\right),\end{aligned} \tag{4.55}$$

where $\mathbf{r}$ belongs to the dual diamond lattice [see Fig. 4.1(c)], and $\mu \in \{0,1,2,3\}$ labels the direction of magnetic field. $\hat{B}_{\mathbf{r},\mu}$ is along $\mathbf{u}_\mu$, which are vectors joining an A site of the dual diamond lattice to its neighboring B sites. These vectors are perpendicular to the plaquettes of the pyrochlore lattice, see Fig. 4.11. The effective theory in the deconfined phase (QSL) is Maxwell electromagnetism. Thus the distance dependence of the plaquette correlators can be determined from the magnetic field correlator in the 3+1D continuum Maxwell electromagnetism.

Note that, for the plaquette correlators, we need the correlator of the magnetic field along the normal to the plaquettes, $\mathbf{u}_\mu$ and $\mathbf{u}_\nu$ (see Fig. 4.11). This can be calculated by first calculating the correlators of the Cartesian components of the magnetic field $\hat{B}_{\mathbf{r},i}$ for $i \in \{x,y,z\}$ and ap-

propriately projecting them on $\mathbf{u}_\mu$ and $\mathbf{u}_\nu$. In the $3+1$D continuum Maxwell electromagnetism, the correlator of the Cartesian components of the magnetic field can be evaluated analytically [6] and we explain it here for completeness.

We first express the magnetic field in terms of the gauge field $\hat{A}_\mu(\mathbf{r})$:

$$\hat{B}_{\mathbf{r},i}(t) = \sum_{j,k\in\{x,y,z\}} \epsilon_{ijk} \left(\partial_j \hat{A}_k(\mathbf{r},t) - \partial_k \hat{A}_j(\mathbf{r},t)\right), \tag{4.56}$$

where $i \in \{x,y,z\}$. Then we express the magnetic field in momentum space:

$$\hat{B}_{\mathbf{k},i}(\mathsf{k}_0) = i \sum_{j,k\in\{x,y,z\}} \epsilon_{ijk} \left(\mathbf{k}_j \hat{A}_k(\mathbf{k},\mathsf{k}_0) - \mathbf{k}_k \hat{A}_j(\mathbf{k},\mathsf{k}_0)\right). \tag{4.57}$$

Now the photon propagator in the Maxwell electrodynamics is given by

$$\langle \hat{A}_i(\mathbf{k},\mathsf{k}_0)\hat{A}_j(-\mathbf{k},-\mathsf{k}_0)\rangle_0 = \frac{1}{\mathsf{k}^2+\mathsf{k}_0^2}\left(\delta_{i,j} - \frac{\mathsf{k}_i\mathsf{k}_j}{\mathsf{k}^2+\mathsf{k}_0^2}\right), \tag{4.58}$$

where $\langle\cdot\rangle_0$ is the expectation value with respect to the Gaussian Maxwell action. Using Eqs. (4.57) and (4.58), the correlator of the magnetic fields in frequency-momentum space is

$$\langle \hat{B}_{\mathbf{k},i}(\mathsf{k}_0)\hat{B}_{-\mathbf{k},i}(-\mathsf{k}_0)\rangle_0 = \frac{\mathsf{k}^2\delta_{i,j} - \mathbf{k}_i\mathbf{k}_j}{\mathsf{k}^2+\mathsf{k}_0^2}. \tag{4.59}$$

Finally, the correlator in real space is obtained by performing a Fourier transform of the above momentum space correlator. The equal-time real-space magnetic-field correlator is given by [6]

$$\langle \hat{B}_{\mathbf{0},i}\hat{B}_{\mathbf{R},j}\rangle_0 \propto \frac{1}{\mathsf{R}^4}\left(2\frac{\mathsf{R}_i\mathsf{R}_j}{\mathsf{R}^2} - \delta_{ij}\right) \equiv \mathcal{C}^B_{ij}(\mathbf{R}). \tag{4.60}$$

Having obtained the correlator of the Cartesian components of the magnetic field, we now project the magnetic fields along the normals $\mathbf{u}_\mu$ and $\mathbf{u}_\nu$ to obtain the correlator of the magnetic fields along the plaquette normals. Thus the correlator of the magnetic field operators $\hat{B}_{\mathbf{r},\mu}$ for $\mu \in \{0,1,2,3\}$ on the pyrochlore plaquettes is

$$\langle \hat{B}_{\mathbf{0},\mu} \hat{B}_{\mathbf{R},\nu} \rangle_0 \propto \frac{1}{\mathsf{R}^4} \sum_{k,l \in \{x,y,z\}} (\mathbf{u}_\mu)_k (\mathbf{u}_\nu)_l \left(2\frac{\mathsf{R}_l \mathsf{R}_k}{\mathsf{R}^2} - \delta_{k,l} \right), \tag{4.61}$$

where $\hat{B}_{\mathbf{0},\mu}$ is the magnetic field along the normal vector $\mathbf{u}_\mu$.

Now we return to the plaquette correlators and determine their behaviors in the QSL phase:

$$\begin{aligned} \langle \hat{\tilde{X}}_P \hat{\tilde{X}}_{P'} \rangle &= \left\langle \cos\left(\hat{B}_{\mathbf{r},\mu}\right) \cos\left(\hat{B}_{\mathbf{r'},\nu}\right) \right\rangle_0 \\ &= e^{-\langle \hat{B}^2 \rangle_0} \cosh \left\langle \hat{B}_{\mathbf{r},\mu} \hat{B}_{\mathbf{r'},\nu} \right\rangle_0 . \end{aligned} \tag{4.62}$$

Similarly,

$$\begin{aligned} \langle \hat{\tilde{Y}}_P \hat{\tilde{Y}}_{P'} \rangle &= \left\langle \sin\left(\hat{B}_{\mathbf{r},\mu}\right) \sin\left(\hat{B}_{\mathbf{r'},\nu}\right) \right\rangle_0 \\ &= e^{-\langle \hat{B}^2 \rangle_0} \sinh \left\langle \hat{B}_{\mathbf{r},\mu} \hat{B}_{\mathbf{r'},\nu} \right\rangle_0 . \end{aligned} \tag{4.63}$$

The connected correlators thus become

$$\begin{aligned} \langle \hat{\tilde{X}}_P \hat{\tilde{X}}_{P'} \rangle_c &= e^{-\langle \hat{B}^2 \rangle_0} \left(\cosh \left\langle \hat{B}_{\mathbf{r},\mu} \hat{B}_{\mathbf{r'},\nu} \right\rangle_0 - 1 \right) \\ &\approx \frac{e^{-\langle \hat{B}^2 \rangle_0}}{2} \left\langle \hat{B}_{\mathbf{r},\mu} \hat{B}_{\mathbf{r'},\nu} \right\rangle_0^2 \end{aligned} \tag{4.64}$$

and

$$\langle \hat{\tilde{Y}}_P \hat{\tilde{Y}}_{P'} \rangle_c \approx \frac{e^{-\langle \hat{B}^2 \rangle_0}}{2} \left\langle \hat{B}_{\mathbf{r},\mu} \hat{B}_{\mathbf{r'},\nu} \right\rangle_0 . \tag{4.65}$$

Thus the connected plaquette correlators in the QSL phase vary as

$$\begin{aligned}\langle \hat{\tilde{X}}_P \hat{\tilde{X}}_{P'} \rangle_c &\propto \frac{1}{\mathsf{R}^8} \left[\sum_{k,l} (\mathbf{u}_\mu)_k (\mathbf{u}_\nu)_l \left(2\frac{\mathsf{R}_l \mathsf{R}_k}{\mathsf{R}^2} - \delta_{k,l} \right) \right]^2, \\ \langle \hat{\tilde{Y}}_P \hat{\tilde{Y}}_{P'} \rangle_c &\propto \frac{1}{\mathsf{R}^4} \left[\sum_{k,l} (\mathbf{u}_\mu)_k (\mathbf{u}_\nu)_l \left(2\frac{\mathsf{R}_l \mathsf{R}_k}{\mathsf{R}^2} - \delta_{k,l} \right) \right],\end{aligned} \tag{4.66}$$

where the summation is over $k, l \in \{x, y, z\}$, $\mathbf{R} = \mathbf{r} - \mathbf{r}'$, and R is assumed to be large compared to the monopole correlation length. The factors inside the square brackets are geometric factors, which depend on the direction of the vectors $\mathbf{u}_\mu$, $\mathbf{u}_\nu$, and $\mathbf{R}$, but are independent of the distance R between the two plaquettes. Ref. [6] also separately studied the correlators precisely at the RK point (which sits at the phase boundary between deconfined and confined phases) where the effective field theory differs from the regular Maxwell theory. In the RK wavefunction, while the behavior of the plaquette correlators differs from Eq. (4.66), it is still a power law with a slower decay [6]. We note that, if the experimentally prepared state is close to an RK wavefunction (see discussion in Sec. 4.3.3), then this distinction will be important.

4.4.1.3 Plaquette correlators in the TFP phase

Now we calculate the dependence of the two-plaquette correlators deep inside the TFP phase, that is for $\Omega \gg V$. Our strategy is to treat the van der Waals interactions, which we denote in this section as $\hat{H}_V = \hat{H}_0 + \hat{H}_{\text{LR}}$ as a perturbation over $\hat{H}_\Omega$ using perturbation theory. Recall that $\hat{H}_V$ is given by

$$\hat{H}_V = \frac{V}{2} \sum_{i \neq j} \frac{\hat{S}_i^z \hat{S}_j^z}{|\boldsymbol{x}_i - \boldsymbol{x}_j|^6}. \tag{4.67}$$

The unperturbed ground state is simply the product state

$$|-\rangle = \bigotimes_i \left|\hat{S}_i^x = -1/2\right\rangle . \tag{4.68}$$

$\hat{H}_V$ flips two spins at $\boldsymbol{x}_i$ and $\boldsymbol{x}_j$ with an amplitude proportional to $V\left(a/|\boldsymbol{x}_i - \boldsymbol{x}_j|\right)^6$. The first-order correction from perturbation theory is

$$|\chi_1\rangle = -\frac{V}{8\Omega} \sum_{\text{pairs } i,j} \left(\frac{a}{|\boldsymbol{x}_i - \boldsymbol{x}_j|}\right)^6 |i,j\rangle , \tag{4.69}$$

where the summation is over all distinct pairs of sites i, j and

$$|i,j\rangle \equiv \left|\hat{S}_i^x = 1/2\right\rangle \left|\hat{S}_j^x = 1/2\right\rangle \bigotimes_{k\neq i,j} \left|\hat{S}_k^x = -1/2\right\rangle . \tag{4.70}$$

We find that the first-order terms in $\langle \hat{X}_P \hat{X}_{P'} \rangle_c$ are 0 and, up to second order in perturbation theory (see Appendix D.4 for derivation),

$$\langle \hat{X}_P \hat{X}_{P'} \rangle_c \propto \frac{V^2 a^{12}}{\Omega^2} \sum_{i\neq j} \frac{\langle i,j| \left(\hat{X}_P - 1\right)\left(\hat{X}_{P'} - 1\right) |i,j\rangle}{|\boldsymbol{x}_i - \boldsymbol{x}_j|^{12}}. \tag{4.71}$$

The matrix element in Eq. (4.71) is nonzero only if $i \in P$ and $j \in P'$ or $i \in P'$ and $j \in P$. If the distance between the plaquettes R is large, then we find

$$\left\langle \hat{X}_P \hat{X}_{P'} \right\rangle_c \propto \frac{V^2}{\Omega^2} \left(\frac{a}{\mathsf{R}}\right)^{12}. \tag{4.72}$$

Now consider the connected plaquette Y correlator. Note that the Hamiltonian Eq. (4.6)

has a global $\mathbb{Z}_2$ symmetry: $\hat{S}^z \to -\hat{S}^z$, $\hat{S}^x \to \hat{S}^x$, and $\hat{S}^y \to -\hat{S}^y$ for $h = 0$. Under this symmetry, $\hat{Y}_P \to -\hat{Y}_P$, implying $\langle \hat{Y}_P \rangle = 0$. However, the product $\hat{Y}_P \hat{Y}_{P'}$ is $\mathbb{Z}_2$-symmetric, and its expectation value need not be zero.

Note that $\hat{Y}_P \hat{Y}_{P'}$ flips three spins of P and three spins of P', where the spins are assumed to be in the eigenbasis of $\hat{S}^x$. On the other hand, the perturbation $\hat{H}_V$ flips two spins in $\hat{S}^x$ basis. Thus the first nonzero contribution in the perturbation series for $\langle \hat{Y}_P \hat{Y}_{P'} \rangle_c$ can only be obtained at third order or higher in perturbation theory. For a large distance between the plaquettes, the dominant contribution to the plaquette Y correlator will come from the process where two spins of P are flipped by one application of $\hat{H}_V$, two spins of P' are flipped by another application of $\hat{H}_V$, and one spin of P and another of P' are flipped by the third application of $\hat{H}_V$. Such a process will give a contribution that will fall off with distance as $(a/\mathsf{R})^6$. Overall, in the TFP phase,

$$\left\langle \hat{Y}_P \hat{Y}_{P'} \right\rangle_c \propto \frac{V^3}{\Omega^3} \left(\frac{a}{\mathsf{R}} \right)^6 . \tag{4.73}$$

Since the plaquette correlators involve off-diagonal operators, they cannot be read out directly from the snapshots of a Rydberg-atom array. However, we show that they can be measured by evolving the system under a modified Hamiltonian for a specific time duration followed by measurement of a diagonal operator [207, 218]. We describe the protocols to measure both plaquette X and plaquette Y correlators in the sections below.

4.4.1.4 Measurement of the plaquette correlators

To measure the plaquette X correlator, one simply needs to change the basis from $\hat{S}^x$ to $\hat{S}^z$ on every site. This can be accomplished by abruptly changing the phase and the amplitude of

the Rabi frequency, so that the new Hamiltonian is $\hat{H}_{\mathrm{Y}} \approx \Omega_Y \sum_i \hat{S}_i^y$ with $\Omega_Y \gg V$. (Achieving $\Omega_Y \gg V$ may require working with atom spacings that are sufficiently large and/or with Rydberg principal quantum numbers that are sufficiently low, but not low enough to make Rydberg lifetime a problem.) It is assumed that this change of the Hamiltonian is done sufficiently rapidly so that the sudden approximation is valid and the state of the system does not change. Then evolve the system under $\hat{H}_Y$ for a time $t_Y = \pi/(2\Omega_Y)$, which amounts to a $\pi/2$ pulse about the y-axis, transforming $\hat{S}_i^x$ into $\hat{S}_i^z$. Finally, measure all the atoms in the $\{|g\rangle, |r\rangle\}$ basis and get $\left\langle \hat{S}_i^z \right\rangle$ in the final state, which is the same as the $\left\langle \hat{S}_i^x \right\rangle$ of the state right before the sudden change of the Hamiltonian. The connected plaquette X correlator can be calculated using these values of $\left\langle \hat{S}_i^x \right\rangle$.

The procedure to measure the connected plaquette Y correlator is similar to the procedure for measuring the plaquette X correlator, except that now the $\pi/2$ pulses on sites $2i$ for $i = 1, 2, \ldots, 6$ are about the x-axis on the Bloch sphere while the $\pi/2$ pulses on sites $2i - 1$ for $i = 1, 2, \ldots, 6$ are around the y-axis, where the sites 1 to 6 are on P and those from 7 to 12 are on P'. These pulses transform $\hat{S}_{2i}^x \to \hat{S}_{2i}^z$ and $\hat{S}_{2i-1}^y \to \hat{S}_{2i-1}^z$. After applying these $\pi/2$ pulses, $\left\langle \hat{S}_i^z \right\rangle$ is measured by taking snapshots of the array and the connected plaquette Y correlator is calculated from it.

We note that the power-law decays of the plaquette correlators in the QSL and the TFP phases are very rapid, and it might be difficult practically to distinguish them from an exponential decay. This connected plaquette Y correlator has an advantage over the connected plaquette X correlator with regards to this issue because the power law decays of the plaquette Y correlator are slower. The disadvantage of the of the plaquette Y correlator is that measuring it requires control over individual sites.

4.4.2 Monopole-monopole correlator

In the deconfined phase, monopoles are gapped. Therefore, the expectation value of an (equal-time) operator that creates a string with a monopole and antimonopole at its endpoints should decay exponentially with the length of the string. On the other hand, in the confined phase, monopoles are condensed, and hence the expectation value should approach a nonzero constant as the length of the string increases. In the continuum, the following operator inserts a string that creates a monopole at $\mathbf{r}_1$ and an antimonopole at $\mathbf{r}_2$ [6]:

$$\hat{\mathcal{M}}^\dagger \hat{\mathcal{M}}(\mathbf{r}_1 \to \mathbf{r}_2) \sim e^{i \int \mathrm{d}^3 \mathbf{r}' \mathcal{A}(\mathbf{r}') \cdot \hat{\mathbf{e}}(\mathbf{r}')}. \tag{4.74}$$

Here $\mathcal{A}(\mathbf{r}')$ is a classical (non single-valued) vector potential such that the flux ϕ_Σ of $\mathcal{B} = \boldsymbol{\nabla} \times \mathcal{A}$ through a closed surface Σ is

$$\phi_\Sigma \equiv \oint_\Sigma \mathcal{B} \cdot d\mathbf{S} = 2\pi q Q_\Sigma, \tag{4.75}$$

where $Q_\Sigma = 1$ when Σ encloses $\mathbf{r}_1$ and not $\mathbf{r}_2$, $Q_\Sigma = -1$ when Σ encloses $\mathbf{r}_2$ and not $\mathbf{r}_1$, and $Q_\Sigma = 0$ otherwise. q is an integer and denotes the "charge" of the monopole string. For simplicity, we will set $q = 1$ in this section. We clarify that $\mathcal{B}$ and ϕ_Σ are classical numbers and are different from $\hat{\mathbf{b}}$ and $\hat{\Phi}_\Sigma$ which are operators. $\hat{\mathbf{b}} \equiv \boldsymbol{\nabla} \times \hat{\mathbf{a}}$, for gauge-field (operator) $\hat{\mathbf{a}}$, and $\hat{\Phi}_\Sigma$ is defined as

$$\hat{\Phi}_\Sigma \equiv \oint_\Sigma \hat{\mathbf{b}} \cdot d\mathbf{S} = 2\pi \hat{m}, \tag{4.76}$$

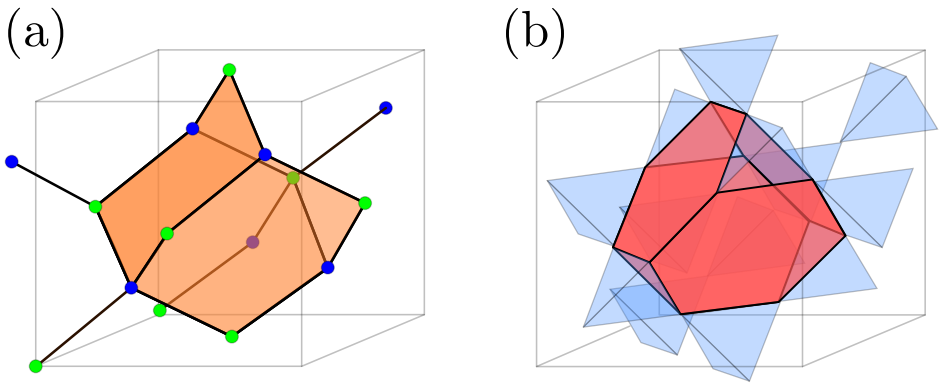

Figure 4.12: (a) The "polyhedron" formed by four puckered hexagons of the diamond lattice is shown in orange. The centers of these "polyhedra" form the dual diamond lattice. (b) The center of the "polyhedron" in (a) is also the center of a truncated tetrahedron (shown in red) of the pyrochlore lattice.

where $\hat{m}$ takes integer eigenvalues. The form of the monopole string operator is chosen so that it increases the flux through Σ by $2\pi Q_\Sigma$, i.e.,

$$\left[\hat{\Phi}_\Sigma, \hat{\mathcal{M}}^\dagger \hat{\mathcal{M}}(\mathbf{r}_1 \to \mathbf{r}_2)\right] = 2\pi Q_\Sigma \hat{\mathcal{M}}^\dagger \hat{\mathcal{M}}(\mathbf{r}_1 \to \mathbf{r}_2). \tag{4.77}$$

We now adapt this operator to the Rydberg setting. Consider the diamond lattice formed by the centers of tetrahedra of the pyrochlore lattice, Fig. 4.1(b). Unlike the continuum, it is now important to specify that the endpoints of the monopole string $\mathbf{r}_1$ and $\mathbf{r}_2$ belong to the dual diamond lattice [see Fig. 4.1(c)], whose sites are centers of "polyhedra" made of four puckered-hexagonal "plaquettes" of the diamond lattice[2], see Fig. 4.12(a). Let $\boldsymbol{x} \equiv \mathbf{r} + \mathbf{e}_\mu/2$ be a site on the pyrochlore lattice, where $\mathbf{r}$ is an A-site of the diamond lattice. $\mathcal{A}_{\boldsymbol{x}} \equiv \mathcal{A}_{\mathbf{r},\mathbf{r}+\mathbf{e}_\mu}$ is the discrete version of $\mathcal{A}$ integrated (Fig. 4.1(b) shows the vectors $\mathbf{e}_\mu$) along the line pointing from the center of an A tetrahedron (centred at $\mathbf{r}$) to the B tetrahedron (centred at $\mathbf{r} + \mathbf{e}_\mu$) such that the two tetrahedra touch at $\boldsymbol{x}$.

[2]In terms of the original pyrochlore lattice, the vertices of the dual diamond lattice are centers of the truncated tetrahedra [see Fig. 4.12(b)] which fill the voids between the tetrahedra.

$\mathcal{A}_{\boldsymbol{x}}$ is required to satisfy the discrete version of Eq. (4.75), and hence depends on $\mathbf{r}_1$, $\mathbf{r}_2$, the "magnetic field" configuration $\mathcal{B}$ and the gauge choice for $\mathcal{A}_{\boldsymbol{x}}$. For the pyrochlore lattice, we have

$$\hat{\mathcal{M}}^\dagger \hat{\mathcal{M}}(\mathbf{r}_1 \to \mathbf{r}_2) = e^{i \sum_{\boldsymbol{x} \in \text{pyrochlore}} \mathcal{A}_{\boldsymbol{x}} (\hat{n}_{\boldsymbol{x}} - 1/2)}. \tag{4.78}$$

This operator is purely diagonal in the $\hat{n}_{\boldsymbol{x}}$ basis (i.e., in the $\hat{S}^z$-basis). So, experimentally, one can calculate this phase for each snapshot and average over shots.

Theoretically, one expects

$$\left| \left\langle \hat{\mathcal{M}}^\dagger \hat{\mathcal{M}}(\mathbf{r}_1 \to \mathbf{r}_2) \right\rangle \right| \sim \begin{cases} e^{-|\mathbf{r}_2 - \mathbf{r}_1|/\lambda}, & \text{deconfined phase,} \\ \text{constant}, & \text{confined phase,} \end{cases} \tag{4.79}$$

where λ is a correlation length that depends on the monopole gap and the "photon" velocity. In Fig. 4.13, we provide an example of one configuration of the classical numbers $\mathcal{A}_{\boldsymbol{x}}$ that defines a monopole string operator. Below, we comment on the freedom in choosing $\mathcal{A}_{\boldsymbol{x}}$.

4.4.2.1 Choice of $\mathcal{A}$

The classical numbers $\mathcal{A}_{\boldsymbol{x}}$ should of course obey the constraint that the flux of $\boldsymbol{\nabla} \times \mathcal{A}$ through a closed surface Σ is $2\pi Q_\Sigma$, as mentioned above. However, one still has a freedom in the choice of $\mathcal{A}$ in the following two respects:

1. Freedom in the arrangement of the field lines of $\boldsymbol{\nabla} \times \mathcal{A}$. For example, they can be confined to a thin tube connecting $\mathbf{r}_1$ and $\mathbf{r}_2$, or be spread out according to Coulomb's law, or be something in between. Different such arrangements, due to their different energy costs,

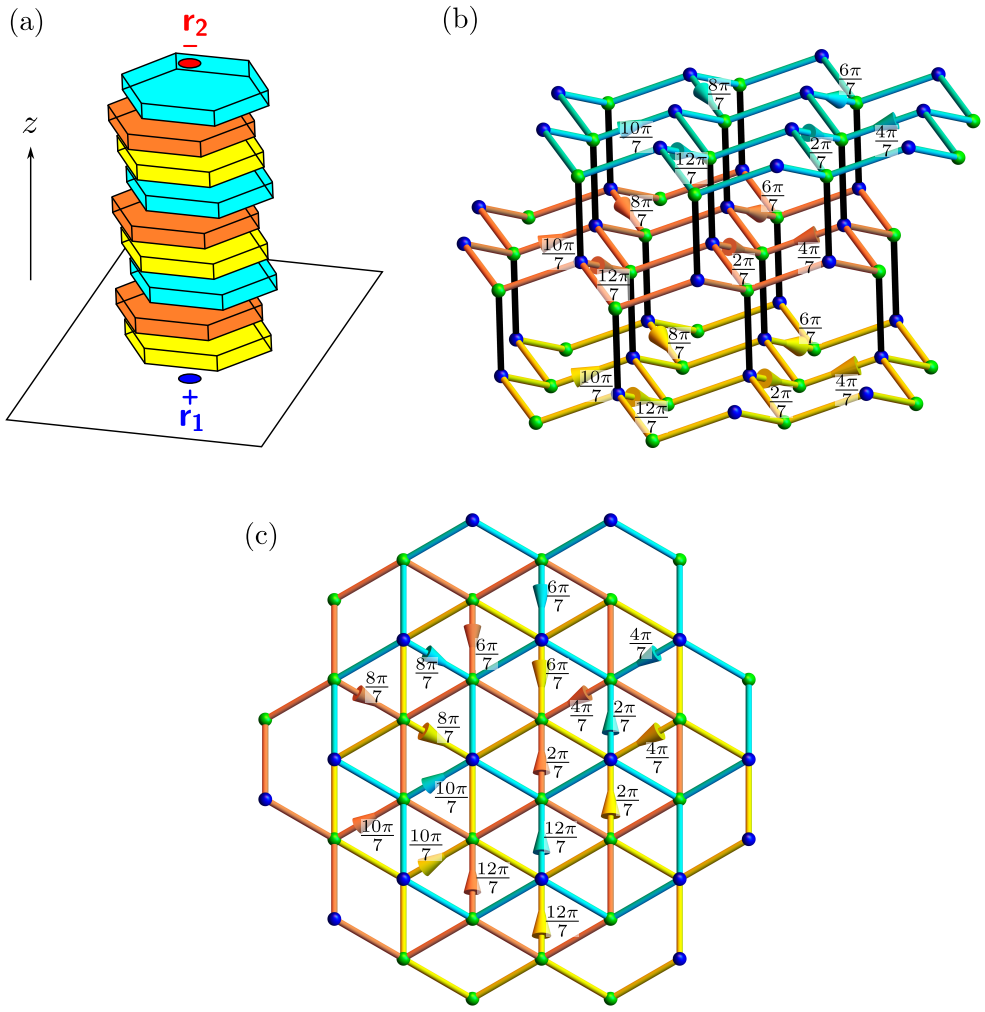

Figure 4.13: An example of the monopole string operator $\hat{\mathcal{M}}^\dagger\hat{\mathcal{M}}(\mathbf{r}_1 \to \mathbf{r}_2)$ for which we provide $\mathcal{A}_{\boldsymbol{x}}$ explicitly. In our example, the string carries 2π flux through a tube with a width of 7 puckered hexagons of the diamond lattice. The tube runs along the $z-$direction. (a) A schematic of the tube running along the z-direction. The diamond lattice (whose vertices are centers of tetrahedra of the pyrochlore lattice) can be seen as ABC stacking of layers of "honeycomb" lattices made of chair-like puckered hexagons. The tube consists of three types of layers shown in yellow, orange, and cyan. Each layer is made of 7 puckered hexagons. To convey a sketch, we depict such a layer by a big hexagon with some thickness. (b) A side view of the stack showing three of its layers, where each layer is made of 7 puckered hexagons of the diamond lattice. The bonds within each of these layers are colored in yellow, orange, and cyan. The bonds (of the diamond lattice) connecting sites of two different layers are shown in black. These layers are repeated in the z direction to get the entire string. For bonds $\boldsymbol{x}$ with (conical) arrows, the value of $\mathcal{A}_{\boldsymbol{x}}$ is written next to the bond. For bonds $\boldsymbol{x}$ without arrows, $\mathcal{A}_{\boldsymbol{x}} = 0$. The two sub-lattices of the diamond lattice are represented by blue and green sites. (c) Top view of three of the layers of the stack. It can be seen from all three sub-figures (a)-(c) that the flux through any closed surface Σ that completely encloses an integer number of layers, such that the bottom layer is included but not the top, is 2π. However, if Σ partially encloses a layer, then Φ_Σ is 0.

would differ in sub-leading corrections to the exponentially decaying behavior, but the leading behavior would be unchanged. In Fig. 4.13, we provide a choice of $\mathcal{A}$, such that the monopole string is localized to a thin tube.

2. For a fixed choice of field lines, we still have a gauge choice for $\mathcal{A}$. Consider a gauge transformation $\mathcal{A}_{\mathbf{r},\mathbf{r}+\mathbf{e}_\mu} \to \mathcal{A}_{\mathbf{r},\mathbf{r}+\mathbf{e}_\mu} + \lambda_{\mathbf{r}+\mathbf{e}_\mu} - \lambda_{\mathbf{r}}$, where $\lambda_{\mathbf{r}}$ is an $\mathbf{r}$-dependent real number. It results in

$$\hat{\mathcal{M}}^\dagger \hat{\mathcal{M}}(\mathbf{r}_1 \to \mathbf{r}_2) \to \hat{\mathcal{M}}^\dagger \hat{\mathcal{M}}(\mathbf{r}_1 \to \mathbf{r}_2) e^{-i\sum_{\mathbf{r}} \lambda_{\mathbf{r}} \eta_{\mathbf{r}} (\hat{n}_{\mathbf{r}} - 2)}, \tag{4.80}$$

where $\eta_{\mathbf{r}} = 1$ for $\mathbf{r} \in A$ and $\eta_{\mathbf{r}} = -1$ for $\mathbf{r} \in B$. In the $\Omega/V \ll 1$ limit, we have $\hat{n}_{\triangle_{\mathbf{r}}} = 2$, so the expectation value is invariant under the gauge transformation. Away from this limit, a gauge transformation on $\mathcal{A}_{\mathbf{r},\mathbf{r}+\mathbf{e}_\mu}$ generically results in a physical transformation on the monopole string operator. However, as long as the external field $h = 0$ [h is defined in Eq. (4.5)], by particle-hole symmetry, we have $\left\langle \hat{n}_{\triangle_{\mathbf{r}}} \right\rangle = 2$. Since the variance $\left\langle (\hat{n}_{\triangle_{\mathbf{r}}} - 2)^2 \right\rangle$ is bounded, we do not expect the gauge transformation on $\mathcal{A}_{\mathbf{r},\mathbf{r}+\mathbf{e}_\mu}$ to qualitatively change the behavior of Eq. (4.79). But this question needs to be studied more closely in future work.

4.4.2.2 Monopole correlator in the ice FM phase

When $\Omega = 0$, the ground state is a product state in which each spin is in an eigenstate of $\hat{S}^z$, as discussed in Sec. 4.3.1.2, and the monopole correlator, $\left\langle \hat{\mathcal{M}}^\dagger \hat{\mathcal{M}}(\mathbf{r}_1 \to \mathbf{r}_2) \right\rangle$, evaluates to a single phase (as opposed to a sum of phases for a state that is a superposition of the basis states). Thus $\left| \left\langle \hat{\mathcal{M}}^\dagger \hat{\mathcal{M}}(\mathbf{r}_1 \to \mathbf{r}_2) \right\rangle \right| = 1$ and does not decay with the length of the string. For $\Omega \ll V$, $\left| \left\langle \hat{\mathcal{M}}^\dagger \hat{\mathcal{M}}(\mathbf{r}_1 \to \mathbf{r}_2) \right\rangle \right|$ will not be equal to 1, but we expect it to saturate to a nonzero constant for

large strings because the monopoles are condensed in the ice FM phase.

4.4.2.3 Monopole correlator in the QSL phase

The monopole correlator at the RK point and away from it in the QSL phase was calculated by Hermele et. al. in Ref. [6] using perturbation theory and field theory techniques. They showed that the correlator decays exponentially with the distance between the monopole and the antimonopole. They also verified the exponential decay numerically at the RK point.

4.4.2.4 Monopole correlator in the TFP phase

In this section, we show that the monopole correlator decays exponentially with the length of the string deep inside the TFP phase, that is for $\Omega \gg V$. We start by rewriting the monopole correlator from Eq. (4.78) as

$$\hat{\mathcal{M}}^\dagger \hat{\mathcal{M}}(\mathbf{r}_1 \to \mathbf{r}_2) = \bigotimes_{i \in \text{string}} \left[\cos\left(\frac{\mathcal{A}_i}{2}\right) + 2i \sin\left(\frac{\mathcal{A}_i}{2}\right) \hat{S}_i^z \right], \tag{4.81}$$

where the tensor product is over the string between $\mathbf{r}_1$ and $\mathbf{r}_2$, and one choice of $\mathcal{A}_i$ is shown in Fig. 4.13.

For $V = 0$, the ground state is $|-\rangle$ (see Eq. (4.68) for its definition), and it can be easily seen that each of the factors of the tensor product in Eq. (4.81) has an expectation value whose absolute value is less than 1. Thus $\left| \left\langle \hat{\mathcal{M}}^\dagger \hat{\mathcal{M}}(\mathbf{r}_1 \to \mathbf{r}_2) \right\rangle \right|$ decays exponentially with the string length. For $V \ll \Omega$, at first order in perturbation theory, only two spins are flipped (in the $\hat{S}^x$ basis). Since the monopole correlator involves a product of a number of terms proportional to the length of the string, only two of which are altered by the perturbation, we expect that the

monopole correlator will decay exponentially even at first order in perturbation theory. Thus the monopole correlator decays exponentially in the TFP phase.

4.4.3 Fredenhagen-Marcu order parameters

It is known that the confined and deconfined phases of a gauge theory without matter fields can be distinguished by the scaling of the Wilson loops $W_{\mathcal{L}} = \left\langle e^{i \oint_{\mathcal{L}} A_\mu dx^\mu} \right\rangle$, where A_μ is the gauge field and $\mathcal{L}$ is a closed loop. In the deconfined phase, the Wilson loop follows the perimeter law, $W_{\mathcal{L}} \propto e^{-\text{Perimeter of } \mathcal{L}}$, while in the confined phase, it follows the area law, $W_{\mathcal{L}} \propto e^{-\text{Area of } \mathcal{L}}$. However, in the presence of matter fields (which are generically always present), the Wilson loop follows the perimeter law in the confined phase as well [279, 280] because of the screening of the confining forces by matter field fluctuations. Thus the Wilson loops cannot be used to distinguish the phases. In such cases, the Fredenhagen-Marcu (FM) order parameters can be used since it has a different behavior in the two phases [207, 218, 281, 282, 283, 284, 285, 286]. In its original formulation [281], the FM order parameters involved expectation values of operators in space-time. Later, Fredenhagen and Marcu proposed that a real-space version of these order parameters could also diagnose deconfinement [283]. In the context of condensed matter physics, Ref. [286] (sections 5.1 and 8.2) demonstrated that these real-space FM order parameters can be used to detect deconfinement in $\mathbb{Z}_2$ and $U(1)$ gauge theories with matter. They have also considered effective gauge theories without Lorentz invariance and shown that the real-space version can be used to diagnose deconfinement. They further suggested that these real-space correlators could help identify phases in quantum dimer models with gapped spinons. More recent works [218, 287] have continued to use real-space versions as diagnostics for deconfinement. Here, we adopt

the real-space FM order parameters because they are simpler to measure experimentally than their space-time counterparts. The Fredenhagen-Marcu order parameter, denoted here by $\chi^E_{\mathcal{C}}$, is defined as

$$\chi^E_{\mathcal{C}} = \frac{\left|\left\langle e^{i\sum_{\mathcal{C}} \hat{a}_{\mathbf{r}\mathbf{r}'}} + \text{H.c.}\right\rangle\right|}{\sqrt{\left|\left\langle e^{i\sum_{\mathcal{L}} \hat{a}_{\mathbf{r}\mathbf{r}'}} + \text{H.c.}\right\rangle\right|}}, \tag{4.82}$$

where $\mathcal{C}$ is an open curve and $\mathcal{L}$ is the closed loop formed by combining $\mathcal{C}$ with its mirror image about a plane that intersects $\mathcal{C}$ only at its end points. This order parameter detects long-range order in the "electric charge"-creation string. In the Higgs phase, "electric charges" are condensed, and hence $\chi^E_{\mathcal{C}}$ approaches a nonzero constant. In the deconfined phase, the numerator in Eq. (4.82) (calculated on an open curve) decays to zero faster than the denominator (calculated on a closed loop, giving the Wilson loop), as the length of $\mathcal{C}$ is increased. Therefore, in the deconfined phase, $\chi^E_{\mathcal{C}}$ goes to 0 as the length of $\mathcal{C}$ is increased. In the confined phase, it was argued in Ref. [282] that while both the numerator and the denominator go to zero as the length of $\mathcal{C}$ is increased, the limit of their ratio approaches a constant. Another way to understand the FM order parameters is that they determine if the perimeter law of the Wilson loop is arising from matter fluctuations or gauge field fluctuations. If it is arising from matter fluctuations in the confined phase, the numerator and the denominator decay at the same rate and their ratio is a constant. If it is partially arising from gauge fluctuations in the deconfined phase, then the denominator decays slower than the numerator and the FM order parameters go to zero [281]. This argument is also applicable to real-space Wilson loops [218, 283, 286, 287]. We point out that distinguishing a nonzero constant from zero in finite systems for finite length of $\mathcal{C}$ may be difficult. Below we explain how to measure $\chi^E_{\mathcal{C}}$.

Using the mapping from spin operators to gauge fields, Eqs. (4.13) and (4.16), we see that

$$e^{i\sum_{\mathcal{C}}\hat{a}_{\mathbf{r}\mathbf{r}'}} \simeq \hat{S}_1^+\hat{S}_2^-\hat{S}_3^+\cdots, \tag{4.83}$$

where the product of $\hat{S}^+$ and $\hat{S}^-$ operators is over the sites on the curve $\mathcal{C}$. The denominator in $\chi_{\mathcal{C}}^E$ has a similar expression in terms of spin operators. Thus, $\chi_{\mathcal{C}}^E$ is given by

$$\chi_{\mathcal{C}}^E = \frac{\left|\left\langle \hat{S}_1^+\hat{S}_2^-\hat{S}_3^+\cdots + \text{H.c.}\right\rangle\right|}{\sqrt{\left|\left\langle \hat{S}_1^+\hat{S}_2^-\hat{S}_3^+\cdots + \text{H.c.}\right\rangle\right|}}, \tag{4.84}$$

where the product in the numerator is along the open curve $\mathcal{C}$ and the one in the denominator is along the closed loop $\mathcal{L}$.

From the point of view of measurement, it is more convenient to consider another quantity, which has the same behavior as $\chi_{\mathcal{C}}^E$ in the three phases, defined as:

$$\tilde{\chi}_{\mathcal{C}}^E \equiv \frac{\left|\left\langle \prod_{i\in\mathcal{C}}\hat{S}_i^x\right\rangle\right|}{\sqrt{\left|\left\langle \prod_{i\in\mathcal{L}}\hat{S}_i^x\right\rangle\right|}}, \tag{4.85}$$

In the transverse-field-polarized (Higgs) phase, $\tilde{\chi}_{\mathcal{C}}^E$ approaches a nonzero constant, just like $\chi_{\mathcal{C}}^E$. Now, we argue that even in the QSL and confined phases, $\tilde{\chi}_{\mathcal{C}}^E$ and $\chi_{\mathcal{C}}^E$ have the same behavior. For a state $|\Psi\rangle$ that dominantly lies in the ice manifold, with corrections from outside the ice manifold being of order Ω/V (such as the ground state $|\Psi_g\rangle$), we have

$$\begin{aligned}&\langle\Psi|\hat{S}_1^+\hat{S}_2^-\hat{S}_3^+\cdots + \text{H.c.}|\Psi\rangle\\ &\qquad = \langle\Psi|(2\hat{S}_1^x)(2\hat{S}_2^x)(2\hat{S}_3^x)\cdots|\Psi\rangle + \Theta\left((\Omega/V)^L\right),\end{aligned} \tag{4.86}$$

where L is the number of sites on $\mathcal{C}$. The correction is of order $(\Omega/V)^L$ by an argument similar to the one used to show that the error is sixth order in the protocol to measure the plaquette X correlator (see Appendix D.3). Thus, for small Ω/V, $\chi_{\mathcal{C}}^E$ and $\tilde{\chi}_{\mathcal{C}}^E$ are equal up to order $(\Omega/V)^L$.

The numerator and the denominator of $\tilde{\chi}_{\mathcal{C}}^E$ can be measured by applying $\pi/2$ pulses about the y-axis and measuring, from the snapshots, products of $\hat{S}^z$ along $\mathcal{C}$ and $\mathcal{L}$. This procedure is similar to the protocol to measure the plaquette X correlator, described in Sec. 4.4.1.4.

The operator $e^{i\sum_{\mathcal{C}}\hat{a}_{\mathbf{r}\mathbf{r}'}}$ creates two opposite "electric charges" at the endpoints of $\mathcal{C}$. So a magnetic analogue of $\chi_{\mathcal{C}}^E$ can also be defined, where the numerator is the expectation value of the operator that creates a monopole and an antimonopole at the endpoints of $\mathcal{C}$. Such an order parameter, $\chi_{\mathcal{C}}^M$, detects long-range order in the monopole string operator and is given by

$$\chi_{\mathcal{C}}^M = \frac{\sqrt{\left\langle \hat{\mathcal{M}}^\dagger \hat{\mathcal{M}}\left(\mathbf{r}_1 \xrightarrow{\mathcal{C}_a} \mathbf{r}_2\right)\right\rangle \left\langle \hat{\mathcal{M}}^\dagger \hat{\mathcal{M}}\left(\mathbf{r}_1 \xrightarrow{\mathcal{C}_b} \mathbf{r}_2\right)\right\rangle}}{\sqrt{\left\langle \hat{\mathcal{M}}^\dagger \hat{\mathcal{M}}\left(\mathbf{r}_1 \xrightarrow{\mathcal{L}} \mathbf{r}_1\right)\right\rangle}}, \tag{4.87}$$

where $\hat{\mathcal{M}}^\dagger\hat{\mathcal{M}}(\mathbf{r}_1 \xrightarrow{\mathcal{C}_a} \mathbf{r}_2)$ inserts a monopole-antimonopole string along $\mathcal{C}_a$ and was defined in Eq. (4.78). The open strings $\mathcal{C}_a$, $\mathcal{C}_b$ and the closed loop $\mathcal{L}$ are chosen so that $\mathcal{L}$ is obtained upon joining $\mathcal{C}_a$ and $\mathcal{C}_b$. In this section, we use the notation where the path of the monopole-antimonopole string is explicitly written in the argument of $\hat{\mathcal{M}}^\dagger\hat{\mathcal{M}}$. Since this operator is diagonal in the $\hat{S}^z$ basis, it can be measured straightforwardly from the snapshots of the Rydberg-atom array.

In the confined phase, monopoles are condensed, so $\chi_{\mathcal{C}}^M$ should be a nonzero constant. In the deconfined phase, by the argument of Ref. [282], the numerator of Eq. (4.87) decays to zero faster than the denominator as the length of $\mathcal{C}$ increases. Therefore, in the deconfined phase,

$\chi_{\mathcal{C}}^{M}$ goes to zero as the length of $\mathcal{C}$ increases. In the Higgs phase, even though there is no long-range order in the monopole string and both the numerator and denominator go to zero, by the argument in Ref. [282], the ratio (i.e. $\chi_{\mathcal{C}}^{M}$) approaches a nonzero constant as the length of $\mathcal{C}$ increases. But distinguishing this nonzero constant from zero in finite-size numerics and experiment may be challenging (similar to the situation for $\chi_{\mathcal{C}}^{E}$ in the confined phase). The behavior of the Fredenhagen-Marcu order parameters in various phases is summarized in Table 4.2.

Before proceeding, we note that our protocols to measure the plaquette correlators and the Fredenhagen-Marcu order parameter $\chi_{\mathcal{C}}^{E}$ work in the limit $\Omega/V \ll 1$, which is outside the window in which the ground state of Hamiltonian (4.6) is a QSL. However, we explained in Sec. 4.3.3 that it is possible to dynamically prepare finite puddles of QSL regions even in the $\Omega/V \ll 1$ limit when the ground state is not a QSL. Our protocols can then be applicable.

4.4.3.1 Fredenhagen-Marcu order parameters in the ice FM phase

We argued in Sec. 4.4.2.2 that $\left|\left\langle \hat{\mathcal{M}}^{\dagger}\hat{\mathcal{M}}\left(\mathbf{r}_1 \xrightarrow{\mathcal{C}} \mathbf{r}_2\right)\right\rangle\right|$ approaches a nonzero constant for large open curves $\mathcal{C}$ in the ice FM phase. By the same reasoning, we expect $\left|\left\langle \hat{\mathcal{M}}^{\dagger}\hat{\mathcal{M}}\left(\mathbf{r}_1 \xrightarrow{\mathcal{L}} \mathbf{r}_2\right)\right\rangle\right|$ to approach a nonzero constant for large closed loops $\mathcal{L}$, implying that $\chi_{\mathcal{C}}^{M}$ approaches a nonzero constant for large loops.

Now we consider the behavior of $\chi_{\mathcal{C}}^{E}$ in the ice FM phase. For $\Omega \ll V$, the ground state will be $|\Psi_{\text{IFM}}\rangle$ plus perturbative corrections in Ω/V on top of it coming from $\hat{H}_{\Omega}$. The ground state in the ice FM phase can be written as $|\Psi_{\text{ord}}\rangle = \hat{U}_S^{\dagger}|\Psi_{\text{IFM}}\rangle$ [see Eq. (4.20)]. Also, call the operator in the numerator of $\chi_{\mathcal{C}}^{E}$ as $\hat{\chi}_{\mathcal{C},\text{num}}^{E} \equiv \hat{S}_1^{+}\hat{S}_2^{-}\hat{S}_3^{+}\cdots + \text{H.c.}$, where the product is over the $\hat{S}^{\pm}$ operators of sites on $\mathcal{C}$. The factor in the numerator of $\chi_{\mathcal{C}}^{E}$ in the ice FM phase can thus be

written as $\left|\langle\Psi_{\text{IFM}}|\hat{U}_S\hat{\chi}^E_{\mathcal{C},\text{num}}\hat{U}_S^\dagger|\Psi_{\text{IFM}}\rangle\right|$. Let $|\mathcal{C}|$ be the length of $\mathcal{C}$. Now, acting on a basis state in which spins along $\mathcal{C}$ are alternating, $\hat{\chi}^E_{\mathcal{C},\text{num}}$ flips these $|\mathcal{C}|$ spins along $\mathcal{C}$. To compensate, the same number of flips must come from $\hat{U}_S$ and $\hat{U}_S^\dagger$ combined. This happens at order $|\mathcal{C}|$ in perturbation theory. Thus for a fixed and small Ω (as compared to V), the numerator of $\chi^E_{\mathcal{C}}$ will be proportional to $(\Omega/V)^{|\mathcal{C}|}$. By a similar argument, we conclude that the denominator of $\chi^E_{\mathcal{C}}$ will be proportional to $(\Omega/V)^{|\mathcal{L}|/2}$. Since the loop $\mathcal{L}$ is formed by joining $\mathcal{C}$ and its mirror image, we have $|\mathcal{L}| = 2|\mathcal{C}|$, and the two exponential decays cancel out. Thus $\chi^E_{\mathcal{C}}$ approaches a nonzero constant in the ice FM phase.

4.4.3.2 Fredenhagen-Marcu order parameters in the QSL phase

Our ansatz for the QSL phase is $|\Psi_{\text{QSL}}\rangle = \hat{U}_S^\dagger|\Psi_{\text{RK}}\rangle$ [see Eq. (4.40)]. The numerator of $\chi^E_{\mathcal{C}}$ is $\left|\langle\Psi_{\text{RK}}|\hat{U}_S\hat{\chi}^E_{\mathcal{C},\text{num}}\hat{U}_S^\dagger|\Psi_{\text{RK}}\rangle\right|$. By an argument similar to the one in Sec. 4.4.3.1, we expect that the numerator is $\propto (\Omega/V)^{|\mathcal{C}|}$. However, unlike the case of Sec. 4.4.3.1, the denominator of $\chi^E_{\mathcal{C}}$ for the QSL phase has a nonzero contribution even at zeroth order in Ω/V. We can estimate the size of the denominator of $\chi^E_{\mathcal{C}}$ in $|\Psi_{\text{RK}}\rangle$ by a simple argument.

Let us call the operator in the denominator of $\chi^E_{\mathcal{C}}$ as $\hat{\chi}^E_{\mathcal{C},\text{den}} \equiv \hat{S}_1^+\hat{S}_2^-\hat{S}_3^+\cdots + \text{H.c.}$, where the product is over the $\hat{S}^\pm$ operators of sites on $\mathcal{L}$. Now we know that the number of dimer configurations on a lattice with N lattice sites grows exponentially with N. Say this number is κ^N. (We know from Pauling's estimate for the residual entropy of water-ice that $\kappa \approx \sqrt{3/2}$ [21]). Now $\hat{\chi}^E_{\mathcal{C},\text{den}}$ has a nonzero expectation value in a basis state only if the loop $\mathcal{L}$ is flippable. If we fix the spins on the loop to be in a flippable configuration, the number of dimer coverings with the remaining $N - |\mathcal{L}|$ spins will be approximately $\kappa^{N-|\mathcal{L}|}$. Thus the expectation value of $\hat{\chi}^E_{\mathcal{C},\text{den}}$ in

the RK wavefunction will be approximately proportional to $\kappa^{-|\mathcal{L}|}$. If we include the perturbative corrections, then the denominator of $\chi_{\mathcal{C}}$ will be $\sqrt{(\text{const.})\kappa^{-|\mathcal{L}|} + \mathcal{O}\left(\Omega/V\right)}$.

Combining the numerator and the denominator, we have

$$\chi^E_{\mathcal{C}} \propto \frac{(\Omega/V)^{-|\mathcal{C}|}}{\sqrt{\kappa^{-|\mathcal{L}|} + \mathcal{O}(\Omega/V)}}. \tag{4.88}$$

Since $|\mathcal{L}| = 2|\mathcal{C}|$, for small enough Ω/V, $\chi^E_{\mathcal{C}}$ decays exponentially with the length of $\mathcal{C}$. Note that this is consistent with our expectation from field theory—the Fredenhagen-Marcu order parameter is supposed to go to zero as the loop size is increased in the deconfined phase of a gauge theory [281, 283].

For the Fredenhagen-Marcu order parameter corresponding to the monopoles, we do not have an argument based on the microscopics of our model which shows that the order parameter decays exponentially with loop length. However, we expect this is the case based on the result that the Fredenhagen-Marcu order parameter goes to zero in the deconfined phase of a gauge theory [281, 282, 283]. Verifying this within the field theory and numerically for the microscopic model is an open problem.

4.4.3.3 Fredenhagen-Marcu order parameters in the TFP phase

We first calculate the two Fredenhagen-Marcu order parameters for the ground state when $V = 0$, which is $|-\rangle$ defined in Eq. (4.68), and later we will consider the perturbative corrections coming from a small, but nonzero, V.

Using the expression from Eq. (4.84), using $\left| \left\langle \hat{S}^x = -1/2 \middle| \hat{S}^{\pm} \middle| \hat{S}^x = -1/2 \right\rangle \right| = 1/2$, and

calculating the expectation value in the $|-\rangle$ state, we find

$$\chi_{\mathcal{C}}^{E} = \frac{2 \times (1/2)^{|\mathcal{C}|}}{\sqrt{2 \times (1/2)^{|\mathcal{L}|}}} = \sqrt{2}, \tag{4.89}$$

where we have used the fact that $|\mathcal{L}| = 2|\mathcal{C}|$. Similarly, for the Fredenhagen-Marcu order parameter corresponding to the monopole-antimonopole string, $\chi_{\mathcal{C}}^{M}$., we have

$$\chi_{\mathcal{C}}^{M} = \frac{\sqrt{\left|\prod_{i\in\mathcal{C}_a} \cos\left(\frac{\mathcal{A}_i}{2}\right)\right| \left|\prod_{i\in\mathcal{C}_b} \cos\left(\frac{\mathcal{A}_i}{2}\right)\right|}}{\sqrt{\left|\prod_{i\in\mathcal{L}} \cos\left(\frac{\mathcal{A}_i}{2}\right)\right|}} = 1, \tag{4.90}$$

i.e., the exponential decay of the numerator cancels the exponential decay of the denominator to give 1. For a small but nonzero value of V, the ground state up to first order in perturbation theory is $|-\rangle + |\chi_1\rangle$, where $|\chi_1\rangle$ is given in Eq. (4.69). Using perturbation theory, the first-order correction to the numerator of Eq. (4.84) is $\langle -|\hat{\mathcal{M}}^{\dagger}\hat{\mathcal{M}}(\mathbf{r}_1 \xrightarrow{\mathcal{C}} \mathbf{r}_2)|\chi_1\rangle \propto (1/2)^{|\mathcal{C}|}\mathcal{O}(V/\Omega)$. An analogous expression is true for the denominator with $\mathcal{C}$ replaced by $\mathcal{L}$. Thus we have

$$\chi_{\mathcal{C}}^{E} = \frac{2(1/2)^{|\mathcal{C}|}\left(1 + \mathcal{O}\left(\frac{V}{\Omega}\right)\right)}{\sqrt{2(1/2)^{|\mathcal{L}|}\left(1 + \mathcal{O}\left(\frac{V}{\Omega}\right)\right)}}, \tag{4.91}$$

and $\chi_{\mathcal{C}}^{E}$ approaches a nonzero constant for large loops. Similarly, for the $\chi_{\mathcal{C}}^{M}$ correlator for a nonzero but small V, we have

$$\chi_{\mathcal{C}}^{M} = \frac{\sqrt{\prod_{\alpha=a,b}\left|\prod_{i\in\mathcal{C}_\alpha} \cos\left(\frac{\mathcal{A}_i}{2}\right)\left(1 + \mathcal{O}\left(\frac{V}{\Omega}\right)\right)\right|}}{\sqrt{\left|\prod_{i\in\mathcal{L}} \cos\left(\frac{\mathcal{A}_i}{2}\right)\left(1 + \mathcal{O}\left(\frac{V}{\Omega}\right)\right)\right|}}, \tag{4.92}$$

and $\chi_{\mathcal{C}}^{M}$ also remains a nonzero constant for large loops. This completes our discussion of the Fredenhagen-Marcu correlators in the TFP phase.

4.4.4 Two-point $\hat{S}^z$ correlator

Consider two spins $\hat{S}^z_{\mathbf{r},\mu}$ and $\hat{S}^z_{\mathbf{r}',\nu}$ located on the sites $\mathbf{r} + \mathbf{e}_\mu/2$ and $\mathbf{r}' + \mathbf{e}_\nu/2$, where $\mathbf{r}$ and $\mathbf{r}'$ are the centers of two up-pointing tetrahedra and $\mu, \nu \in \{0, 1, 2, 3\}$ label the sites of the tetrahedra (see Fig. 4.14). From the mapping of spins to gauge theory, Eqs. (4.13) and (4.16), it can be seen that the two-point correlator of these two spins $\langle \hat{S}^z_{\mathbf{r},\mu} \hat{S}^z_{\mathbf{r}',\nu} \rangle$ is the same as the two-point correlator of the electric field. Since $\hat{S}^z_{\mathbf{r},\mu} \hat{S}^z_{\mathbf{r}',\nu}$ is a diagonal operator, its correlator can be measured experimentally by capturing snapshots of the Rydberg-atom array and averaging over them.

4.4.4.1 Two-point $\hat{S}^z$ correlator in the ice FM phase

For $\Omega \ll V$, the ground state of the system is $\hat{U}_S^\dagger |\Psi_{\text{IFM}}\rangle$, and the two-point $\hat{S}^z$ correlator is $\langle \Psi_{\text{IFM}} | \hat{U}_S \hat{S}^z_{\mathbf{r},\mu} \hat{S}^z_{\mathbf{r}',\nu} \hat{U}_S^\dagger | \Psi_{\text{IFM}} \rangle$. Up to zeroth order in Ω/V, $\hat{U}_S = \hat{1}$. Since $|\Psi_{\text{IFM}}\rangle$ is a product state in the $\hat{S}^z$ basis, $\left| \langle \Psi_{\text{IFM}} | \hat{S}^z_{\mathbf{r},\mu} \hat{S}^z_{\mathbf{r}',\nu} | \Psi_{\text{IFM}} \rangle \right| = (1/2)^2$. After taking into account corrections in Ω/V, we still expect that $\langle \hat{S}^z_{\mathbf{r},\mu} \hat{S}^z_{\mathbf{r}',\nu} \rangle$ will approach a nonzero constant for large separation $|\mathbf{r} - \mathbf{r}'|$.

4.4.4.2 Two-point $\hat{S}^z$ correlator in the QSL phase

The effective theory in the deconfined phase is the Maxwell electromagnetism. By a derivation analogous to the derivation of Eq. (4.60), one can show that in $3 + 1$D continuum Maxwell electromagnetism, the correlator of the Cartesian components of the electric field $\hat{e}_{\mathbf{r},i}$ for $i \in \{x, y, z\}$ is given by [6]

$$\langle \hat{e}_{\mathbf{0},i} \hat{e}_{\mathbf{R},j} \rangle_0 \propto \frac{1}{R^4} \left(2 \frac{R_i R_j}{R^2} - \delta_{ij} \right), \tag{4.93}$$

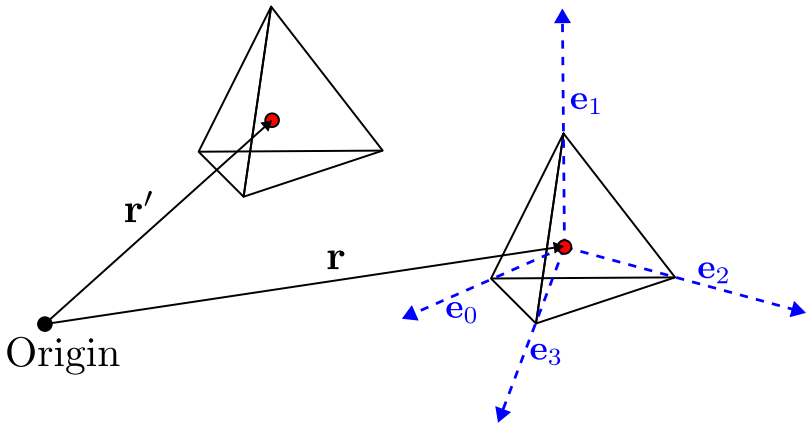

Figure 4.14: Notation for the two-point $\hat{S}^z$ correlator. $\mathbf{r}$ and $\mathbf{r}'$ are the positions of the centers of the tetrahedra. $\mathbf{e}_\mu$ are the vectors joining the center of an up-pointing tetrahedron to the centers of its neighboring down-pointing tetrahedra.

where $\langle\cdot\rangle_0$ denotes expectation value with respect to the Maxwell action. Eq (4.93) is the electric analogue of Eq (4.60). Now the correlator of the electric field operators $\hat{e}_{\mathbf{r},\mu}$ for $\mu \in \{0,1,2,3\}$ along the links of the diamond lattice are obtained from Eq. (4.93) by taking components of the Cartesian electric field along the vectors $\mathbf{e}_\mu$. Thus

$$\langle \hat{S}^z_{\mathbf{r},\mu} \hat{S}^z_{\mathbf{r}',\nu} \rangle = \sum_{k,l\in\{x,y,z\}} (\mathbf{e}_\mu)_k (\mathbf{e}_\nu)_l \langle \hat{e}_{\mathbf{r},k} \hat{e}_{\mathbf{r}',l} \rangle_0, \tag{4.94}$$

4.4.4.3 Two-point $\hat{S}^z$ correlator in the TFP phase

For $V = 0$, the ground state is $|-\rangle$ and $\langle -|\hat{S}^z_{\mathbf{r},\mu}\hat{S}^z_{\mathbf{r}',\nu}|-\rangle = 0$. The first-order correction to the ground-state wavefunction from the perturbation $\hat{H}_V$ is given by $|\chi_1\rangle$ defined in Eq. (4.69). The first-order correction to the two-point $\hat{S}^z$ correlator is

$$\langle -|\hat{S}^z_{\mathbf{r},\mu}\hat{S}^z_{\mathbf{r}',\nu}|\chi_1\rangle + \text{H.c.} \propto \frac{V}{\Omega}\left(\frac{a}{R}\right)^6. \tag{4.95}$$

Thus, in the TFP phase, the two-point $\hat{S}^z$ correlator is proportional to $\frac{V}{\Omega}\left(\frac{a}{R}\right)^6$.

4.5 Discussion

In this work, we have presented a proposal to prepare and detect the deconfined phase of the $U(1)$ gauge theory in 3+1 dimensions on a Rydberg atom simulator. We first showed that laser-driven neutral atoms trapped in a pyrochlore lattice using optical tweezer arrays naturally realise a $U(1)$ quantum spin liquid as the ground state when the laser detuning lies in a specified window and the interactions between Rydberg atoms are restricted to nearest-neighbor. We then studied the effect of van der Waals interactions beyond nearest-neighbor. In the classical limit obtained by dropping the Rabi frequency term, we showed that long-range interactions break the degeneracy to select an ice ferromagnet as the ground state. We then studied the competition between the long-ranged interactions that prefer an ordered state and quantum fluctuations that prefer a QSL state, by calculating the energies in ansatz wavefunctions using perturbation theory. We found that, for Rabi frequencies greater than $\Omega_C \approx 0.44V$, the ground state is a QSL within our approximation. When Ω is increased further, we argued that the QSL goes into a transverse-field-polarized state via a Higgs transition. While we have focused on the ground state, we also commented on the effect of dynamical state preparation in deciding the nature of the prepared state. We then provided experimental protocols for measuring the plaquette correlators, Bricmont-Frölich-Fredenhagen-Marcu order parameters, the monopole-monopole correlator, and the "electric field" correlator that can distinguish a QSL phase from ordered phases.

Our ground state phase diagram is the result of an approximate calculation. A quantum Monte Carlo calculation is required to firmly establish the phase diagram, and we leave it to

future work. While it is possible that the true phase diagram differs from what we found, we note that there are other knobs one can tune to get a desired phase diagram. Dressed states created from multiple Rydberg and possibly ground levels can be used to customize the interactions away from the isotropic $1/r^6$ form we considered in this chapter [288, 289, 290, 291, 292, 293]. It is also possible to engineer interactions that are strongly peaked in distance [294, 295] which could allow the nearest-neighbor interactions to be much stronger than the interactions at other distances, and potentially make the QSL more stable. Designing a dressing scheme compatible with the symmetries of the pyrochlore lattice and exploring the resulting phase diagrams is an interesting direction for future work. It is known that dipolar-like interactions can preserve the degeneracy of the ice manifold [264]. The QSL region can potentially be extended to smaller Rabi frequencies by making the Rydberg atoms interact via dipolar interactions either by applying a DC electric field or microwave-dressing a Rydberg s state with one or more Rydberg p states [293]. We also note that our proposal requires two Rydberg excitations per tetrahedron, meaning that it lies outside of the Rydberg-blockade regime and is therefore sensitive to imperfections and thermal fluctuations in nearest-neighbor spacing. It will therefore be useful to extend our proposal to the blockade regime of one excitation per tetrahedron. While previous numerical work on dimer models have required a nonzero RK potential (6-body term) to achieve this, it will be worthwhile to study if one can engineer long-range Rydberg interactions that stabilize a spin-liquid in the blockade regime.

One can also look for other lattices that could realize a $U(1)$ QSL ground state. One such possibility is a lattice of corner-sharing tetrahedra where all up-pointing tetrahedra (and separately all down-pointing tetrahedra) form a hexagonal close-packed lattice shown in Fig. 4.15. If only nearest-neighbor interactions are considered between atoms positioned on the sites of this

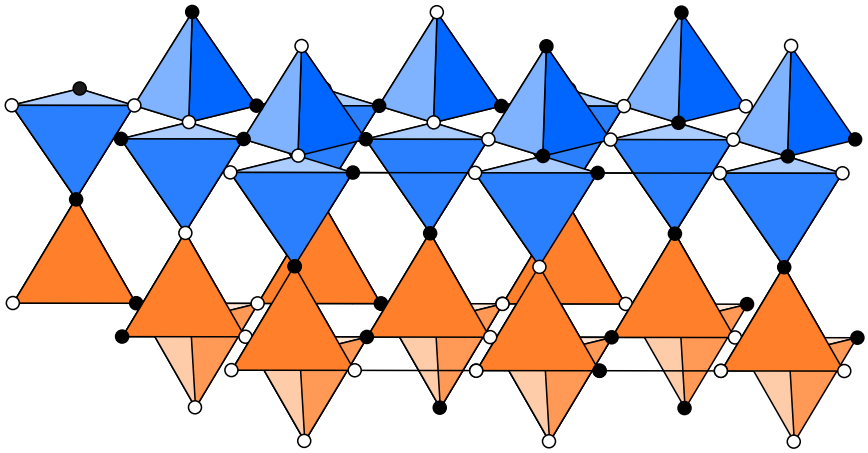

Figure 4.15: A lattice made of corner-sharing tetrahedra different from the pyrochlore lattice. The lattice consists of $ABAB\ldots$ stacking of the blue (A) and the orange (B) layers. A configuration satisfying $n_{\triangle} = 2$ is shown here.

lattice, then, by perturbation theory in Ω/V for a particular range of detunings, one gets ring exchange terms similar to the ones obtained in Sec. 4.2.1, and the system maps onto a dimer model. It is not known if this dimer model is in the QSL phase when the RK potential is zero and long range van der Waals interactions are included. Another open problem is to construct lattices where a dimer model can be realized within the blockade regime without the RK potential.

Next, we note that, formally, a distinction between the confined and deconfined phases exists only in the thermodynamic limit. Experimentally, there are two finiteness effects that can be important. First, a realistic three dimensional Rydberg array will likely have a relatively small linear dimension. Some of the correlators presented in Sec. 4.4 require asymptotic behavior in distance to distinguish different phases. Second, as found in Ref. [274] and mentioned in Sec. 4.3.3, a finite-time state preparation scheme would generically prepare puddles of spin-liquid regions as opposed to an entire spin liquid. It is therefore necessary to quantitatively study how the behavior of the correlators is modified under these conditions. One must also estimate the size of the puddles of the QSL and compare them to the length scale at which the asymptotic

behavior of the correlators is observed. We leave this for future work.

We also note that, to translate field-theory observables into microscopic variables, we relied on the perturbative limit of small Ω/V. However in the phase diagram that we found, the region where the spin liquid is a ground state does not satisfy $\Omega/V \ll 1$. Understanding how the field-theory operators (e.g. plaquette, monopole, and electric-field operators) get renormalized away from the perturbative limit is important both from fundamental and practical standpoints.

Our work is a proposal to prepare a gapless $U(1)$ spin liquid using unitary evolution. An interesting research direction would be to come up with schemes that also use projective measurements to expedite the state preparation along the lines of Refs. [229, 296]. One can also explore how other exotic phases of matter such as fractons and 3+1D topological order can potentially be realized on a Rydberg simulator.

Appendix A: Chapter 1

A.1 Compact $U(1)$ gauge theory – partition function

Let us consider compact $U(1)$ gauge theory on a hypercubic lattice of spacetime dimension D. For simplicity, we will assume the same lattice spacing a in all four directions. We will work in Euclidean spacetime unless mentioned otherwise. The gauge fields $A_\mu(\mathbf{r})$ live on the links of the lattice [see Fig. A.1] and is a compact variable in the sense that aA_μ and $aA_\mu + 2n\pi$ are equivalent for all integers n.[1] If $\mathbf{r}$ is a lattice site, then $A_\mu(\mathbf{r})$ lives at $\mathbf{r} + \mathbf{e}_\mu/2$, where $\mathbf{e}_\mu$ is a unit vector in the direction μ. A gauge-field configuration $aA_\mu(\mathbf{r})$ is said to be gauge-equivalent to a configuration $aA'_\mu = aA_\mu(\mathbf{r}) + (\Delta_\mu\phi)(\mathbf{r}) \equiv aA_\mu(\mathbf{r}) + \phi(\mathbf{r}+\mathbf{e}_\mu) - \phi(\mathbf{r})$, for any compact (defined mod 2π) scalar $\phi(\mathbf{r})$ that lives on the lattice sites $\mathbf{r}$.

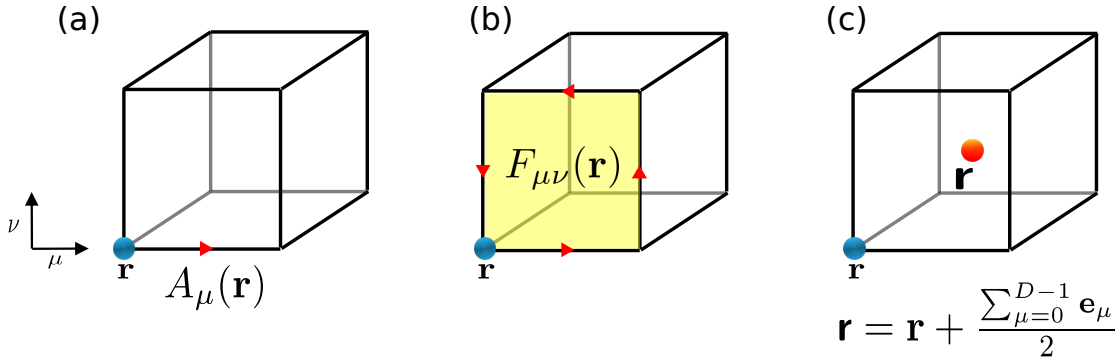

Figure A.1: (a) $\mathbf{r}$ lives on the sites of the lattice. $A_\mu(\mathbf{r})$ lives on the link joining $\mathbf{r}$ and $\mathbf{r} + \mathbf{e}_\mu$. (b) The oriented plaquette corresponding to $F_{\mu\nu}(\mathbf{r})$. (c) Dual lattice site $\mathbf{r} = \mathbf{r} + \frac{\sum_{\mu=0}^{D-1} \mathbf{e}_\mu}{2}$.

[1] The factor of a is just our normalization convention chosen to make converting sums to integral easier.

A compact gauge theory has (1) only gauge-invariant quantities as its degrees of freedom, and (2) is invariant under $aA_\mu(\mathbf{r}) \to aA_\mu(\mathbf{r}) + 2n\pi$. What can an action for such theory be a function of? Consider a linear function of the gauge fields $a\sum_{\mathbf{r}} q_\mu(\mathbf{r})A_\mu(\mathbf{r})$.[2] It can be gauge-invariant if and only if $a(\Delta_\mu q_\mu)(\mathbf{r}) = 0$ for all $\mathbf{r}$, i.e., for a hypercubic lattice, $\sum_{\mu=0}^{D-1}(q_\mu(\mathbf{r}) - q_\mu(\mathbf{r}-\mathbf{e}_\mu)) = 0$. Further, for this function to respect compactness of the gauge field, $q_\mu(\mathbf{r})$ must be an integer. Therefore, the action in a compact gauge theory can only be a periodic function (with a periodicity of $2n\pi$ where $n \geq 1$ is an integer) of the quantity:

$$W_{\{q_\mu(\mathbf{r})\}}\left[\{A_\mu(\mathbf{r})\}\right] \equiv a\sum_{\mathbf{r},\mu} q_\mu(\mathbf{r})A_\mu(\mathbf{r}) \tag{A.1}$$

for a configuration of integers living on the links of the lattice, $q_\mu(\mathbf{r})$ that is divergence-free everywhere, i.e., $\Delta_\mu q_\mu(\mathbf{r}) = 0$. Any such divergence-free configuration of integers can be written as a linear superposition of loop configurations of integers. The simplest such loop configuration is when the loop is supported along the links of an elementary plaquette of the lattice. The function $W_{\{q_\mu(\mathbf{r})\}}\left[\{A_\mu(\mathbf{r})\}\right]$ for such an elementary plaquette is defined as the flux through it, i.e., $a^2F_{\mu\nu}(\mathbf{r})$ [see Fig. A.1].[3] It conventionally lives on the plaquette centre, i.e., at $\mathbf{r} + (\mathbf{e}_\mu + \mathbf{e}_\nu)/2$ and is antisymmetric in its indices μ, ν:

$$a^2F_{\mu\nu}(\mathbf{r}) \equiv aA_\mu(\mathbf{r}) + aA_\nu(\mathbf{r}+\mathbf{e}_\mu) - aA_\mu(\mathbf{r}+\mathbf{e}_\nu) - aA_\nu(\mathbf{r}) \equiv a\Delta_\mu A_\nu(\mathbf{r}) - a\Delta_\nu A_\mu(\mathbf{r}) \tag{A.2}$$

[2] Throughout this chapter, we use the Einstein summation convention where repeated indices of multiplied symbols are summed over. So $q_\mu(\mathbf{r})A_\mu(\mathbf{r})$ means $\sum_{\mu=0}^{D-1} q_\mu(\mathbf{r})A_\mu(\mathbf{r})$. Since, we work in Euclidean spacetime, we do not distinguish between upper and lower indices.

[3] For reference to quantities more familiar to us, we note that in the continuum limit in $D = 3+1$, $F_{\mu\nu}(\mathbf{r})$ approaches the continuum electromagnetic field strengths up to proportionality constants, i.e., for $i, j \neq 0$, $F_{0i} = (c\,\delta t)a\ E^i(\mathbf{r})$ and $F_{ij} = -a^2\ \epsilon_{ijk}B^k(\mathbf{r})$, where $E^i(\mathbf{r})$ and $B^k(\mathbf{r})$ are electric and magnetic field components respectively, a is the lattice spacing, c is the speed of photon and δt is the time-Trotterization unit.

The traditional action for compact $U(1)$ lattice gauge theory [56**?**] is a function of just these field strengths and is chosen so as to reduce to the familiar Maxwell's theory in the long-distance limit for small couplings g_0:

$$S_{\text{cosine}} = \sum_{\mathbf{r},\mu,\nu} \frac{1}{2g_0^2}(1 - \cos\big(a^2 F_{\mu\nu}(\mathbf{r})\big)) \tag{A.3}$$

The cosine function is nonlinear, and hence this is not a free theory. For small g_0^2, we see that $1 - \cos(a^2 F_{\mu\nu}(\mathbf{r}))$ is forced to be small. On first thought, one may think that one could approximate it with $a^4 F_{\mu\nu}^2/2$. But this is not okay since the quadratic function is not periodic. What one can still do however, is to take e^{-S} and expand it about all its maxima that occur at $a^2 F_{\mu\nu} = 2n_{\mu\nu}\pi$ on equal footing (for integers $n_{\mu\nu}$). This approximation, shown explicitly below, is called the Villain approximation:

$$e^{-S_{\text{cosine}}} \to e^{-S_{\text{Villain}}} \equiv \sum_{\{n_{\mu\nu}(\mathbf{r})\in\mathbb{Z}\}} \exp\left[-\frac{1}{4g_0^2}\sum_{\mathbf{r},\mu,\nu}\big(a^2 F_{\mu\nu}(\mathbf{r}) - 2\pi n_{\mu\nu}(\mathbf{r})\big)^2\right]. \tag{A.4}$$

Here, $n_{\mu\nu}(\mathbf{r})$ is also defined at the plaquette centre $(\mathbf{r}+(\mathbf{e}_\mu+\mathbf{e}_\nu)/2)$ and is antisymmetric in μ and ν. Note that we have been using a notation of double counting. For instance, $a^2 F_{12}(\mathbf{r}) - 2\pi n_{12}(\mathbf{r})$ enters the expression as $\exp\left[(-1/2g_0^2)(a^2 F_{12}(\mathbf{r}) - 2\pi n_{12}(\mathbf{r}))^2\right]$. We are interested in studying the long distance physics of this theory, so the microscopic action could very well have been S_{Villain} to begin with. This is what we will assume from now on.

The partition function for this Villain model is

$$Z\left[\{j_\mu(\mathbf{r})\}\right] = \int \left[\mathcal{D}A_\mu(\mathbf{r})\right] \sum_{\{n_{\mu\nu}(\mathbf{r})\in\mathbb{Z}\}} \exp\left[-\frac{1}{4g_0^2}\sum_{\mathbf{r},\mu,\nu}\left(a^2F_{\mu\nu}(\mathbf{r}) - 2\pi n_{\mu\nu}(\mathbf{r})\right)^2 + ia^D\sum_{\mathbf{r}} j_\mu(\mathbf{r})A_\mu(\mathbf{r})\right]. \tag{A.5}$$

Here, $[\mathcal{D}A_\mu(\mathbf{r})]$ means that aA_μ for each link is integrated from $-\pi$ to π, such that each gauge-nonequivalent configuration is counted only once. $\left\{a^{D-1}j_\mu(\mathbf{r})\right\}$ is a divergence-free configuration of integers living on the links of the lattice ($\Delta_\mu j_\mu(\mathbf{r}) = 0$). Therefore,

$$\left\langle e^{ia^D\sum_{\mathbf{r}} A_\mu(\mathbf{r})j_\mu(\mathbf{r})}\right\rangle = \frac{Z\left[\{j_\mu(\mathbf{r})\}\right]}{Z[0]} \tag{A.6}$$

Here, we have used $Z[0]$ to denote $Z\left[j_\mu(\mathbf{r}) = 0\right]$. By appropriately choosing the configuration of $j_\mu(\mathbf{r})$, one can calculate correlation functions of all gauge-invariant quantities using Eq. (A.6). For example, if $j_\mu(\mathbf{r})$ corresponds to a single connected loop, then the above expression gives the expectation value of a Wilson loop. If instead, $j_\mu(\mathbf{r})$ corresponds to two connected loops, then the above expression computes the correlation function of two Wilson loops, and so on. In particular, let us say we want to compute the correlation function between the field strengths $\sin\left(a^2F_{\mu\nu}(\mathbf{r})\right)$ and $\sin\left(a^2F_{\mu'\nu'}(\mathbf{r}')\right)$ at two different points (recall that the field strengths are compact variables). This correlation function is readily obtained from Eq. (A.6) by choosing $\{j_\mu\}$ to be supported exactly on the links of the elementary plaquettes $(\mathbf{r},\mu\nu)$ and $(\mathbf{r}',\mu'\nu')$, and linearly combining the results for each of the four different combinations of orientation of the two plaquettes. With this motivation, let us now try to simplify the right hand side (RHS) of Eq. (A.6).

The first simplification we will make is in the limits of integration for $aA_\mu(\mathbf{r})$. First, note

that the range $(-\pi, \pi]$ is arbitrary. If one shifts the variable $aA_\mu(\mathbf{r})$ for each link independently by an integer multiple of 2π, the integrand in Eq. (A.5) remains unchanged. So, formally, if we extend the limits of integration to $(-N\pi, N\pi)$ for $N \to \infty$, one is essentially adding up an infinite number of copies of the same integral. This is okay because doing so results in both $Z\left[\{j_\mu(\mathbf{r})\}\right]$ and $Z[0]$ getting multiplied by the same number N (that we later take to ∞), leaving the ratio unchanged.

Next, we change the variable of integration from $aA_\mu(\mathbf{r})$ to $a^2F_{\mu\nu}(\mathbf{r})$. We are allowed to do so for Abelian gauge theories since $a^2F_{\mu\nu}$ is linearly related to aA_μ. By the argument in the previous paragraph, we can also extend the range of integration over $a^2F_{\mu\nu}(\mathbf{r})$ to $(-\infty, \infty)$. Since $a^2F_{\mu\nu}$ is gauge-invariant, one no longer needs to worry about the constraint of integrating over gauge-nonequivalent configurations of aA_μ. However, because $a^2F_{\mu\nu}$ is defined to be $a\left(\Delta_\mu A_\nu(\mathbf{r}) - \Delta_\nu A_\mu(\mathbf{r})\right)$, we must respect the following constraint.

$$\begin{aligned} \frac{1}{2}\epsilon_{\nu\lambda\rho}\Delta_\nu F_{\lambda\rho}(\mathbf{r}) \equiv \frac{1}{2}\epsilon_{\nu\lambda\rho}\left[F_{\lambda\rho}(\mathbf{r}+\mathbf{e}_\nu) - F_{\lambda\rho}(\mathbf{r})\right] = 0, \text{ for } D = 3 \text{ and} \\ \frac{1}{2}\epsilon_{\mu\nu\lambda\rho}\Delta_\nu F_{\lambda\rho}(\mathbf{r}) \equiv \frac{1}{2}\epsilon_{\mu\nu\lambda\rho}\left[F_{\lambda\rho}(\mathbf{r}+\mathbf{e}_\nu) - F_{\lambda\rho}(\mathbf{r})\right] = 0, \text{ for } D = 4. \end{aligned} \tag{A.7}$$

These conditions are saying that $F_{\mu\nu}$ as defined above is a closed 2-form (in other words, is divergence free). Also, to set up notation for later, note that in $D = 3$, $\frac{1}{2}\epsilon_{\nu\lambda\rho}\Delta_\nu F_{\lambda\rho}(\mathbf{r})$ lives on the sites of the "dual lattice" formed by the centres of the cubes of the original lattice, i.e., on $\mathbf{r} \equiv \mathbf{r} + \sum_{\mu=0}^{2} \frac{\mathbf{e}_\mu}{2}$. Similarly, in $D = 4$, $\frac{1}{2}\epsilon_{\nu\lambda\rho}\Delta_\nu F_{\lambda\rho}(\mathbf{r})$ lives on the links of the dual lattice formed by $\mathbf{r} \equiv \mathbf{r} + \sum_{\mu=0}^{3} \frac{\mathbf{e}_\mu}{2}$. [4] The above constraint needs to be enforced by hand when integrating over

[4] In fact, In the centres of these links of the dual lattice live on the centres of the three dimensional cubes of the original lattice.

$F_{\mu\nu}(\mathbf{r})$.

Next, to make sure the entire integrand is written in terms of $F_{\mu\nu}$, we introduce a set of integers $J_{\mu\nu}(\mathbf{r})$ antisymmetric in μ, ν, determined completely by the external current configuration $\{j_\mu(\mathbf{r})\}$ such that

$$\frac{1}{2}\sum_{\mathbf{r}} F_{\mu\nu}(\mathbf{r}) J_{\mu\nu}(\mathbf{r}) = \sum_{\mathbf{r}} j_\mu(\mathbf{r}) A_\mu(\mathbf{r}) \tag{A.8}$$

$$\implies \frac{1}{2a}\sum_{\mathbf{r}} \left[\Delta_\mu A_\nu(\mathbf{r}) - \Delta_\nu A_\mu(\mathbf{r})\right] J_{\mu\nu}(\mathbf{r}) = \sum_{\mathbf{r}} j_\mu(\mathbf{r}) A_\mu(\mathbf{r})$$

$$\implies \sum_{\mathbf{r}} \left[\Delta_\nu J_{\mu\nu}(\mathbf{r})\right] A_\mu(\mathbf{r}) = a \sum_{\mathbf{r}} j_\mu(\mathbf{r}) A_\mu(\mathbf{r}) \text{ for any choice of } A_\mu(\mathbf{r})$$

$$\implies \Delta_\nu J_{\mu\nu}(\mathbf{r}) = a j_\mu(\mathbf{r}) \tag{A.9}$$

Thus, $a^{D-2} J_{\mu\nu}(\mathbf{r})$ form a set of integers determined (non-uniquely) by the source currents j_μ. One solution for $J_{\mu\nu}(\mathbf{r})$ in $D = 3$ and $D = 4$ is

$$J_{\mu\nu}(\mathbf{r}) = -a\delta_{\mu,0} \sum_{n=0}^{\infty} j_\nu(\mathbf{r} - n\mathbf{e}_0) + a\delta_{\nu,0} \sum_{n=0}^{\infty} j_\mu(\mathbf{r} - n\mathbf{e}_0) \tag{A.10}$$

This solution is not unique. In $D = 4$, for a given solution $J_{\mu\nu}(\mathbf{r})$, we can find a family of solutions $J_{\mu\nu}(\mathbf{r}) + \frac{1}{a^2}\epsilon_{\mu\nu\rho\lambda}\Delta_\rho l_\lambda(\mathbf{r})$ for $l_\lambda(\mathbf{r}) \in \mathbb{Z}$. In $D = 3$, we have a similar family of solutions $J_{\mu\nu}(\mathbf{r}) + \frac{1}{a}\epsilon_{\mu\nu\rho}\Delta_\rho l(\mathbf{r})$ for $l(\mathbf{r}) \in \mathbb{Z}$. This non-uniqueness of $J_{\mu\nu}$ is not a concern for us presently because we can just choose one and proceed.

With these simplifications, we can proceed with rewriting the partition function. We will do this, first for $D = 4$. The derivation for $D = 3$ is outlined in Appendix. A.2.

A.1.1 Partition function in $D = 4$: Lattice Sine-Gordon loop model

$$
\begin{aligned}
&Z\left[\{j_\mu(\mathbf{r})\}\right] \\
&= \left[\prod \int_{-\infty}^{\infty} \mathrm{d}F_{\mu\nu}(\mathbf{r})\right] \sum_{\{n_{\mu\nu}(\mathbf{r})\in\mathbb{Z}\}} \exp\left[-\frac{1}{4g_0^2}\sum_{\mathbf{r},\mu,\nu}\left(a^2F_{\mu\nu}(\mathbf{r}) - 2\pi n_{\mu\nu}(\mathbf{r})\right)^2 + \frac{i}{2}\sum_{\mathbf{r}} J_{\mu\nu}(\mathbf{r})F_{\mu\nu}(\mathbf{r})\right] \\
&\quad \times \prod_{\mathbf{r},\mu} \delta\left(\frac{a^2}{2}\epsilon_{\mu\nu\lambda\rho}\Delta_\nu F_{\lambda\rho}(\mathbf{r})\right)
\end{aligned}
\tag{A.11}
$$

Let us do a change of variables

$$
F_{\mu\nu} = \tilde{F}_{\mu\nu} + 2\pi n_{\mu\nu}. \tag{A.12}
$$

Since $J_{\mu\nu}(\mathbf{r})$'s are integers, we get

$$
\begin{aligned}
Z\left[\{j_\mu(\mathbf{r})\}\right] = \left[\prod \int_{-\infty}^{\infty} \mathrm{d}\tilde{F}_{\mu\nu}(\mathbf{r})\right] \sum_{\{n_{\mu\nu}(\mathbf{r})\in\mathbb{Z}\}} \exp\left[-\frac{a^4}{4g_0^2}\sum_{\mathbf{r},\mu,\nu}\left(\tilde{F}_{\mu\nu}(\mathbf{r})\right)^2 + \frac{i}{2}\sum_{\mathbf{r}} J_{\mu\nu}(\mathbf{r})\tilde{F}_{\mu\nu}(\mathbf{r})\right] \\
\times \prod_{\mathbf{r},\mu} \delta\left(\frac{a^2}{2}\epsilon_{\mu\nu\lambda\rho}\Delta_\nu \tilde{F}_{\lambda\rho}(\mathbf{r}) + \frac{2\pi}{2}\epsilon_{\mu\nu\lambda\rho}\Delta_\nu n_{\lambda\rho}(\mathbf{r})\right).
\end{aligned}
\tag{A.13}
$$

We can now restructure the above equation by defining $\frac{1}{2}\epsilon_{\mu\nu\lambda\rho}\Delta_\nu n_{\lambda\rho}(\mathbf{r}) \equiv -a^3 m_\mu(\mathbf{r})$. Note that this definition implies that

$$
\Delta_\mu m_\mu(\mathbf{r}) = 0. \tag{A.14}
$$

In other words, $m_\mu(\mathbf{r})$ forms closed loops. The factor of a^3 is just our normalization convention. Here, $a^3 m_\mu(\mathbf{r})$ is an integer. Physically, $m_\mu(\mathbf{r})$ is the monopole $4-$current, i.e. m_0 is the

monopole density and m_1, m_2, and m_3 are the monopole currents. Using this definition,

$$
\begin{aligned}
Z\left[\{j_\mu(\mathbf{r})\}\right] = \left[\prod \int_{-\infty}^{\infty} \mathrm{d}\tilde{F}_{\mu\nu}(\mathbf{r})\right] \sum_{\substack{\{m_\mu(\mathbf{r})\in\mathbb{Z}\} \\ \Delta_\mu m_\mu(\mathbf{r})=0}} \exp\left[-\frac{a^4}{4g_0^2}\sum_{\mathbf{r},\mu,\nu}\left(\tilde{F}_{\mu\nu}(\mathbf{r})\right)^2 + \frac{i}{2}\sum_{\mathbf{r}} J_{\mu\nu}(\mathbf{r})\tilde{F}_{\mu\nu}(\mathbf{r})\right] \\
\times \prod_{\mathbf{r},\mu} \delta\left(\frac{a^2}{2}\epsilon_{\mu\nu\lambda\rho}\Delta_\nu \tilde{F}_{\lambda\rho}(\mathbf{r}) - 2\pi a^3 m_\mu(\mathbf{r})\right) \\
\times \left[\sum_{\{n_{\mu\nu}(\mathbf{r})\in\mathbb{Z}\}} \delta\left(\frac{1}{2}\epsilon_{\mu\nu\lambda\rho}\Delta_\nu n_{\lambda\rho}(\mathbf{r}) + a^3 m_\mu(\mathbf{r})\right)\right].
\end{aligned}
\tag{A.15}
$$

For every choice of $n_{\mu\nu}(\mathbf{r})$ satisfying $\Delta_\nu n_{\lambda\rho}(\mathbf{r}) = -a^3 m_\mu(\mathbf{r})$, we have a family of solutions $n_{\mu\nu}(\mathbf{r}) + \Delta_\mu l_\nu(\mathbf{r}) - \Delta_\nu l_\mu(\mathbf{r})$ for a set of integers $l_\mu(\mathbf{r})$. Thus, the sum over $n_{\mu\nu}$ in square brackets of Eq. A.15 gives an infinite factor independent of $\{m_\mu(\mathbf{r})\}$.[5] As before, the same factor appears in both the numerator and denominator of $Z\left[\{j_\mu(\mathbf{r})\}\right]/Z[0]$ and we will thus drop it.

We can enforce the $\delta-$function using a Lagrange multiplier $\chi_\mu(\mathbf{r})$ that lives on the links of the dual lattice. In other words, we use

$$
\begin{aligned}
&\delta\left(\frac{a^2}{2}\epsilon_{\mu\nu\lambda\rho}\Delta_\nu \tilde{F}_{\lambda\rho}(\mathbf{r}) - 2\pi a^3 m_\mu(\mathbf{r}))\right) \\
=&\frac{1}{(2\pi)^2}\int_{-\infty}^{\infty} \mathrm{d}\left(a\chi_\mu(\mathbf{r})\right) \exp\left\{-i\frac{a\chi_\mu(\mathbf{r})}{2\pi}\left[\frac{a^2}{2}\epsilon_{\mu\nu\lambda\rho}\Delta_\nu \tilde{F}_{\lambda\rho}(\mathbf{r}) - 2\pi a^3 m_\mu(\mathbf{r}))\right]\right\}
\end{aligned}
\tag{A.16}
$$

Finally, the integral in Eq. (A.15) is Gaussian in $\tilde{F}_{\mu\nu}$, and thus $\tilde{F}_{\mu\nu}$ can be integrated out. Doing

[5] This should not be surprising because we earlier traded in an infinite factor which we are now being forced to trade out.

so gives:

$$Z\left[\{j_\mu(\mathbf{r})\}\right] = \prod_{\mathbf{r},\mu}\left[\int_{-\infty}^{\infty} \mathrm{d}\chi_\mu(\mathbf{r})\right] \exp\left[-\frac{g_0^2}{16\pi^2}\sum_{\mathbf{r},\mu,\nu}\left(\epsilon_{\mu\nu\lambda\rho} a\Delta_\lambda \chi_\rho(\mathbf{r}) - 2\pi a^2 J_{\mu\nu}(\mathbf{r})\right)^2\right] \times \sum_{\substack{\{m_\mu(\mathbf{r})\in\mathbb{Z}\} \\ \Delta_\mu m_\mu(\mathbf{r})=0}} \exp\left[ia^4\sum_{\mathbf{r}}\chi_\mu(\mathbf{r})m_\mu(\mathbf{r})\right]. \tag{A.17}$$

Here $\prod_{\mathbf{r},\mu}\left[\int_{-\infty}^{\infty}\mathrm{d}\chi_\mu(\mathbf{r})\right]$ should again be integral over nonequivalent configurations of $\chi_\mu(\mathbf{r})$, where $a\chi_\mu(\mathbf{r})$ and $a\chi_\mu(\mathbf{r}) + \Delta_\mu\phi(\mathbf{r})$ (for a real-valued field $\phi(\mathbf{r})$) are defined to be equivalent. While this requirement is not obvious in the previous step, it follows because the integrand in Eq. (A.17) remains unchanged under redefining $a\chi_\mu$ to $a\chi_\mu + \Delta_\mu\phi$. Therefore, if we had not enforced this requirement, we would have infinite copies of the same integral.

Recall that $J_{\mu\nu}$ can be obtained from j_μ using Eq. (A.10) and $Z[0]$ is obtained by setting every $J_{\mu\nu}(\mathbf{r})$ to 0. For completeness, let us come back to the freedom of transforming $a^2 J_{\mu\nu}(\mathbf{r})$ to $a^2 J_{\mu\nu}(\mathbf{r}) + \epsilon_{\mu\nu\rho\lambda}\Delta_\rho l_\lambda(\mathbf{r})$. This transformation can be undone in Eq. (A.17) by transforming $a\chi_\mu$ to $a\chi_\mu - 2\pi l_\mu$ which leaves rest of the integrand unchanged. So, Eq. (A.17) is indeed indifferent to the particular choice of $\{J_{\mu\nu}\}$ we use for a given current configuration $\{j_\mu\}$.

A.2 Partition function of compact $U(1)$ gauge theory in $D = 3$: Lattice Sine-Gordon Model

For completeness, let us also write down the result for $U(1)$ gauge theory in $D = 3$ (in the Villain form). The derivation proceeds almost exactly like the derivation leading to Eq. (A.17) for $D = 4$. Let us go back to Eq. (A.3). The steps from Eq. (A.3) to Eq. (A.3) in $D = 4$ are in fact identical to those in $D = 3$. In $D = 3$, we satisfy the constraint in Eq. (A.13) by defining

$\frac{1}{2}\sum_{\nu,\lambda}\epsilon_{\nu\lambda\rho}\Delta_\nu n_{\lambda\rho}(\mathbf{r}) \equiv -m(\mathbf{r})$. So, the difference here is that $m(\mathbf{r})$ lives on the sites dual to the dual cubic lattice in $D = 3$ instead of the links of the dual hypercubic lattice. The partition function can then be written as

$$Z\left[\{j_\mu(\mathbf{r})\}\right] = \prod_{\mathbf{r}}\left[\int_{-\infty}^{\infty} \mathrm{d}\chi(\mathbf{r})\right] \exp\left[-\frac{g_0^2}{8\pi^2}\sum_{\mathbf{r},\mu}\left(\Delta_\mu\chi(\mathbf{r}) - \pi\sum_{\nu,\lambda}\epsilon_{\mu\nu\lambda}J_{\nu\lambda}(\mathbf{r})\right)^2\right] \times \sum_{\{m(\mathbf{r})\in\mathbb{Z}\}} \exp\left[i\sum_{\mathbf{r}}\chi(\mathbf{r})m(\mathbf{r})\right], \tag{A.18}$$

where $J_{\nu\lambda}(\mathbf{r})$ is determined by the configuration of source currents $\{j_\mu\}$ by the constraint Eq. (A.9) and can be chosen to obey Eq. (A.10). Therefore compact $U(1)$ gauge theory in $D = 3$ maps to a lattice Sine-Gordon model [56, 297].

Appendix B: Chapter 2

B.1 Review of stability of DSL

If the DSL were to be a stable CFT, then it should contain no relevant (scaling dimension $\Delta > 3$) symmetry allowed operators. In Table B.1 , we summarize the scaling dimensions Δ of some of the important operators derived by references [9, 10, 11, 12] in the large N_f limit.

Operator	Δ_{N_f}	$\Delta_{N_f=4}$
Monopoles		
$\hat{\mathbf{\Phi}}_{2\pi}$	$0.2651N_f - 0.0381 + \mathcal{O}(1/N_f)$	1.022
$\hat{\mathbf{\Phi}}_{4\pi}$	$0.6731N_f - 0.1934 + \mathcal{O}(1/N_f)$	2.499
$\hat{\mathbf{\Phi}}_{6\pi}$	$1.1864N_f - 0.4211 + \mathcal{O}(1/N_f)$	4.325
Fermion bilinears		
$\bar{\psi}\sigma^\alpha\tau^\beta\psi$, ($\alpha, \beta$ are not both 0)	$2 - \frac{64}{3\pi^2 N_f} + \mathcal{O}(\frac{1}{N_f^2})$	1.46
$\bar{\psi}\psi$	$2 + \frac{128}{3\pi^2 N_f} + \mathcal{O}(\frac{1}{N_f^2})$	3.08
Conserved charges and currents		
$\hat{b}, \hat{e}_i, \hat{Q}\left[\sigma^\alpha\tau^\beta\right]$, $\hat{\vec{J}}\left[\sigma^\alpha\tau^\beta\right]$	2	2

Table B.1: Scaling dimensions Δ_{N_f} of some important primary operators in QED_3, calculated in the large N_f limit, compiled from [9, 10, 11, 12]. An operator with $\Delta > 3$ is relevant in the RG sense.

Ref. [57] determined the symmetry properties of monopole operators for various lattices:

1. Bipartite lattices: There is a symmetry allowed 2π monopole which is relevant according

to the large N_f analysis summarized in Table B.1. Hence a DSL cannot be a stable phase on bipartite lattices.

2. Kagome lattice: There is a symmetry allowed 4π monopole, which is likely relevant ($\Delta \approx 2.5$) according to the large N_f calculation.

3. Triangular lattice: $\hat{\mathbf{\Phi}}_{2\pi}$ and $\hat{\mathbf{\Phi}}_{4\pi}$ break translation symmetry and hence are symmetry-forbidden. (We will provide a more microscopic motivation for this fact in Sec. B.2.2.) A 6π monopole operator is symmetry allowed, but is irrelevant ($\Delta = 4.322$) according to the large N_f calculation. This suggests that a DSL could indeed be a stable phase on the triangular lattice.

So, in this work, whenever we refer to microscopic operators, we will assume a triangular lattice for concreteness. However, our general idea applies to any lattice which can realize a DSL as a stable phase.

B.2 Microscopic expressions for field theory operators

In this section, we construct microscopic operators corresponding to operators in the effective field theory. For a given field theory operator $\hat{\mathcal{O}}_{\text{tot}} \equiv \int d^2x \hat{\mathcal{O}}(x)$, we construct the microscopic operator

$$\hat{\mathcal{O}}_{\mathbb{tot}} = \sum_{\vec{n}} e^{i\vec{Q}.\vec{n}} \hat{\mathcal{O}}_{\vec{n}}, \tag{B.1}$$

where we have allowed for $\hat{\mathcal{O}}_{\mathbb{tot}}$ to have momentum $\vec{Q}$ at the lattice scale. We use the following procedure [23, 24, 298]:

1. Find how $\hat{\mathcal{O}}_{\mathbb{tot}}$ transforms under the microscopic symmetries. For operators that can be

written in terms of fermionic partons, this can be done using information obtained by expanding around Dirac points [299]. We tabulate the transformation properties of the conserved charges of G_{IR} in Table B.2, and conserved currents in Table B.3.

2. Construct operators order by order in size (maximum of weight, i.e., number of spins in the support of a local term, and diameter, i.e., extent of a local term) transforming identically as $\hat{\mathcal{O}}_{\mathbb{tot}}$.

We do this for the emergent electric and magnetic fields and spinon charge density in Sec. B.2.1. For monopole operators, this procedure is harder, and requires information at the lattice scale. Ref. [57] did this using a Wannier center calculation. In Sec. B.2.2, we will motivate their result using an independent approach involving the algebra of operators.

Charge	$SO(3)$	$\mathcal{T}$	T_1	T_2	C_6	R_x
$\hat{b}_{\mathbb{tot}}$	S	-1	1	1	-1	1
$\hat{Q}[\sigma^i]$	T	-1	1	1	1	1
$\hat{Q}[\tau^1]$	S	-1	-1	-1	$\hat{Q}[\tau^2]$	$\hat{Q}[\tau^3]$
$\hat{Q}[\tau^2]$	S	-1	1	-1	$-\hat{Q}[\tau^3]$	$-\hat{Q}[\tau^2]$
$\hat{Q}[\tau^3]$	S	-1	-1	1	$-\hat{Q}[\tau^1]$	$\hat{Q}[\tau^1]$
$\hat{Q}[\sigma^i\tau^1]$	T	1	-1	-1	$-\hat{Q}[\sigma^i\tau^2]$	$-\hat{Q}[\sigma^i\tau^3]$
$\hat{Q}[\sigma^i\tau^2]$	T	1	1	-1	$Q[\sigma^i\tau^3]$	$\hat{Q}[\sigma^i\tau^2]$
$\hat{Q}[\sigma^i\tau^3]$	T	1	-1	1	$\hat{Q}[\sigma^i\tau^1]$	$-\hat{Q}[\sigma^i\tau^1]$

Table B.2: Symmetry properties of conserved charges of G_{IR}. $SO(3)$ is spin-rotation (S and T stand for singlet and triplet under spin-rotation respectively.). $\mathcal{T}$ is time-reversal. T_1 and T_2 are lattice translations about $\vec{\mathbb{a}}_1$ and $\vec{\mathbb{a}}_2$ respectively. C_6 is rotation by $2\pi/6$ about a vertex. R_x is reflection about $\vec{\mathbb{a}}_1$.

Current	$SO(3)$	$\mathcal{T}$	T_1	T_2	C_6	R_x
$\frac{\epsilon^{ij}}{2\pi}\hat{e}^j$	S	1	1	1	$-V$	$-V$
$\hat{\vec{J}}[\sigma^i]$	T	1	1	1	V	V
$\hat{\vec{J}}[\tau^1]$	S	1	-1	-1	V as $\hat{\vec{J}}[\tau^2]$	V as $\hat{\vec{J}}[\tau^3]$
$\hat{\vec{J}}[\tau^2]$	S	1	1	-1	V as $-\hat{\vec{J}}[\tau^3]$	V as $-\hat{\vec{J}}[\tau^2]$
$\hat{\vec{J}}[\tau^3]$	S	1	-1	1	V as $-\hat{\vec{J}}[\tau^1]$	V as $\hat{\vec{J}}[\tau^1]$
$\hat{\vec{J}}[\sigma^i\tau^1]$	T	-1	-1	-1	V as $-\hat{\vec{J}}[\sigma^i\tau^2]$	V as $-\hat{\vec{J}}[\sigma^i\tau^3]$
$\hat{\vec{J}}[\sigma^i\tau^2]$	T	-1	1	-1	V as $\hat{\vec{J}}[\sigma^i\tau^3]$	V as $\hat{\vec{J}}[\sigma^i\tau^2]$
$\hat{\vec{J}}[\sigma^i\tau^3]$	T	-1	1	-1	V as $\hat{\vec{J}}[\sigma^i\tau^1]$	V as $-\hat{\vec{J}}[\sigma^i\tau^1]$

Table B.3: Symmetry properties of conserved currents of $U(1)_{\text{top}}$ and $SO(6)$. Notation: "V" means "transforms as a vector", "$-V$" means transforms as a vector except for a factor of -1. "V as $\hat{\vec{J}}[\sigma^i\tau^j]$" means the current's spatial indices are transformed as a vector while the $SO(6)$ indices are rotated to $\sigma^i\tau^j$, possibly with an overall sign.

B.2.1 Emergent electric and magnetic field

The generator of $U(1)_{\text{top}}$ is the total emergent magnetic flux $\hat{b}_{\text{tot}} \equiv \frac{1}{2\pi}\int d^2x \hat{b}(x)$. Because $\hat{b}_{\text{tot}}$ is odd under time-reversal (see Table B.2), and singlet under spin rotation, the lowest weight term is a 3-spin spin chirality: $\hat{\chi}_{\triangledown,\vec{n}} \equiv (\hat{\vec{\mathbf{S}}}_{\vec{n}} \times \hat{\vec{\mathbf{S}}}_{\vec{n}+(1,-1)}) \cdot \hat{\vec{\mathbf{S}}}_{\vec{n}+(1,0)}$ and $\hat{\chi}_{\triangle,\vec{n}} \equiv (\hat{\vec{\mathbf{S}}}_{\vec{n}} \times \hat{\vec{\mathbf{S}}}_{\vec{n}+(1,0)}) \cdot \hat{\vec{\mathbf{S}}}_{\vec{n}+(0,1)}$. Here, we have used the notation $(n_1, n_2) \equiv n_1\vec{\mathfrak{a}}_1 + n_2\vec{\mathfrak{a}}_2$. If we only keep (1) elementary triangles ($\triangle$) and (2) triangles whose 2 edges are nearest-neighbour ($\triangleright$), then the only term consistent with symmetries is

$$\hat{b}_{\text{tot}} = \sum_{\vec{n}} (\hat{\chi}_{\triangledown,\vec{n}} - \hat{\chi}_{\triangle,\vec{n}}) + \dots \tag{B.2}$$

.

Since the total emergent magnetic flux is the $U(1)_{\text{top}}$ charge density, it follows from Faraday's law that the emergent electric field $\hat{\vec{e}}$ is the $U(1)_{\text{top}}$ conserved current rotated by $90°$.

If we consider all operators for $\hat{\vec{e}}$ made of terms with 2 spins (both nearest neighbor and next-nearest-neighbor), then (in the notation: $\hat{\vec{e}} \equiv \hat{e}_1 \vec{\mathfrak{a}}_1 + \hat{e}_2 \vec{\mathfrak{a}}_2$),

$$\hat{e}_i = \alpha_1 (\hat{e}_i)^{(1)} + \alpha_2 (\hat{e}_i)^{(2)} + \dots \quad \text{for } i = 1, 2, \tag{B.3}$$

where

$$(\hat{e}_1)^{(1)} = \sum_{\vec{n}} \vec{n} \quad , \quad (\hat{e}_2)^{(1)} = \sum_{\vec{n}} \vec{n} \quad , \tag{B.4}$$

$$(\hat{e}_1)^{(2)} = \sum_{\vec{n}} \quad , \quad (\hat{e}_2)^{(2)} = \sum_{\vec{n}} \quad , \tag{B.5}$$

with the notation

$$\begin{aligned} &\equiv \hat{\vec{\mathbf{S}}}_1 \cdot \hat{\vec{\mathbf{S}}}_2 - \hat{\vec{\mathbf{S}}}_0 \cdot \hat{\vec{\mathbf{S}}}_1 \text{ and} \\ &\equiv \hat{\vec{\mathbf{S}}}_0 \cdot \hat{\vec{\mathbf{S}}}_1 - \hat{\vec{\mathbf{S}}}_0 \cdot \hat{\vec{\mathbf{S}}}_3, \end{aligned} \tag{B.6}$$

Note that $\hat{e}_1$ and $\hat{e}_2$ are not orthogonal. $\hat{e}_x$ and $\hat{e}_y$ are related to $\hat{e}_1$ and $\hat{e}_2$ as $\hat{e}_x = \hat{e}_1$ and $\hat{e}_y = \frac{1}{\sqrt{3}}(-\hat{e}_1 + 2\hat{e}_2)$.

From the above expression for electric field, one can compute the local divergence of the electric field, which is proportional to the spinon charge by Gauss's law:

$$\hat{q} = \frac{1}{g^2} \mathbb{div} \hat{\vec{e}} \tag{B.7}$$

We see that only $\hat{\vec{e}}^{(2)}$ contributes to $\hat{q}$, and not $\hat{\vec{e}}^{(1)}$. Therefore, $\hat{\vec{e}}^{(1)}$ is the transverse electric field and $\hat{\vec{e}}^{(2)}$ is the longitudinal electric field. $\hat{q}$ at site i is given by

$$\hat{q}_i = \quad + \ldots \equiv \Big(\hat{\vec{\mathbf{S}}}_i \cdot \hat{\vec{\mathbf{S}}}_1 - \hat{\vec{\mathbf{S}}}_i \cdot \hat{\vec{\mathbf{S}}}_2 + \tag{B.8}$$

$$+\hat{\vec{\mathbf{S}}}_i \cdot \hat{\vec{\mathbf{S}}}_3 - \hat{\vec{\mathbf{S}}}_i \cdot \hat{\vec{\mathbf{S}}}_4 + \hat{\vec{\mathbf{S}}}_i \cdot \hat{\vec{\mathbf{S}}}_5 - \hat{\vec{\mathbf{S}}}_i \cdot \hat{\vec{\mathbf{S}}}_6\Big) + \ldots$$

By construction, we see that the sum of spinon charge enclosed in a region D is an operator with support localized to the boundary of D. This is consistent with Gauss's law. It also satisfies $\langle \hat{q}_i \rangle = 0$ by symmetry.

B.2.2 Monopole operators from commutation relations

The symmetry properties of monopole operators were calculated in [24, 57] and reported in Table 2 of Ref. [57]. The $SO(6)$ contribution was calculated using Step 1 (beginning of Appendix B.2). The $U(1)_{\text{top}}$ contribution was calculated using a Wannier center calculation of the free fermion bands for the mean field ansatz. Here, we attempt an alternative approach to calculate the $U(1)_{\text{top}}$ contribution. While our calculation involves an uncontrolled approximation, it provides an independent motivation for the result in Ref. [24].

The principle behind our approach is that the algebra of G_{IR} has to be obeyed down to the microscopic level because we are dealing with operators of the form $\hat{\mathcal{O}}_{\text{tot}}$ here, which have the

longest possible wavelength (allowed by their symmetry properties):

$$\left[\hat{Q}^{ab}_{\mathbb{tot}}, \hat{Q}^{cd}_{\mathbb{tot}}\right] = i\Big(\delta_{bc}\hat{Q}^{da}_{\mathbb{tot}} - \delta_{ac}\hat{Q}^{db}_{\mathbb{tot}} + \delta_{ad}\hat{Q}^{cb}_{\mathbb{tot}} - \delta_{bd}\hat{Q}^{ca}_{\mathbb{tot}}\Big), \tag{B.9}$$

$$\left[\hat{b}_{\mathbb{tot}}, \hat{Q}^{ab}_{\mathbb{tot}}\right] = 0. \tag{B.10}$$

Here $\{\hat{Q}^{ab}\}$ (antisymmetric in a, b with a, b running from 1 to 4) are the 15 generators of $SO(6)$ and $\hat{b}_{\mathbb{tot}}$ is the generator of $U(1)_{\text{top}}$ (see Appendix B.2.4 for the notation).

Next, 2π monopole operators that are charged under G_{IR} have to obey the algebra

$$\left[\hat{b}_{\mathbb{tot}}, (\hat{\Phi}^{\dagger}_{j})_{\mathbb{tot}}\right] = (\hat{\Phi}^{\dagger}_{j})_{\mathbb{tot}}, \tag{B.11}$$

$$\left[\hat{Q}^{bc}_{\mathbb{tot}}, (\hat{\Phi}^{\dagger}_{j})_{\mathbb{tot}}\right] = \sum_{i=1}^{6} (\hat{\Phi}^{\dagger}_{i})_{\mathbb{tot}} \left(T^{bc}\right)_{ij}. \tag{B.12}$$

where, T^{bc}, a matrix of c-numbers, is the generator of $\hat{Q}^{bc}_{\mathbb{tot}}$ acting on $\mathbb{C}^6$, and the matrix elements are given by

$$\left(T^{bc}\right)_{ij} = -i(\delta_{cj}\delta_{ib} - \delta_{bj}\delta_{ic}). \tag{B.13}$$

This suggests a general procedure:

1. Suppose $\hat{\mathcal{O}}_{\mathbb{tot}} = \sum_{\vec{n}} e^{i\vec{Q}.\vec{n}}\hat{\mathcal{O}}_{\vec{n}}$ If we now expand $\hat{\mathcal{O}}_{\vec{n}}$ in operators of increasing "size" s,

$$\hat{\mathcal{O}}_{\vec{n}} = \sum_{s=1}^{\infty} C_s\Big(\hat{\mathcal{O}}_{\vec{n}}\Big)_s. \tag{B.14}$$

Here, each $\left(\hat{\mathcal{O}}_{\vec{n}}\right)_s$ is chosen to respect the symmetry properties obtained just from the low energy theory.

2. Demand Eq. (B.9)-(B.10), (B.11)-(B.12) order by order in size s, and obtain constraints on C_s.

Here we will only perform this calculation at the lowest order in size by enforcing Eq. (B.11) up to a proportionality constant.

$$\left[\hat{b}_{\mathbb{t}\circ\mathbb{t}}, \hat{\vec{\mathbf{\Phi}}}^{\dagger}_{\text{tot}}\right] = \mathcal{K}\hat{\vec{\mathbf{\Phi}}}^{\dagger}_{\text{tot}}, \tag{B.15}$$

where $\mathcal{K}$ is a positive constant. Let us assume that the monopole inserting 2π flux is "simpler", i.e., has a lower leading operator size than the one inserting 4π or 6π flux. Then we ask what the "simplest" spin triplet monopole operator is. We start with operators with size 1.

$$\hat{\vec{\mathbf{\Phi}}}^{\dagger}_{\text{tot}} = \sum_{\vec{n}} e^{i\vec{Q}\cdot\vec{n}}\hat{\vec{\mathbf{S}}}_{\vec{n}} + \dots \tag{B.16}$$

From compatibility of translation symmetry with rotation symmetry, $\vec{Q}$ is either $(0,0)$ or $\pm(2\pi/3, -2\pi/3)$ [24]. Using identity Eq. (B.30), we evaluate the commutator in Eq. (B.15) using the lowest order expression for $\hat{b}^{(1)}_{\mathbb{t}\circ\mathbb{t}}$ in Eq. (B.2). Each single-spin term in $\hat{\vec{\mathbf{\Phi}}}^{\dagger}_{\text{top}}$ fails to commute with exactly 6

triangles in $\hat{b}^{(1)}_{\mathbb{tot}}$. After evaluating each of these commutators, we get

$$\begin{aligned}
&\left[\hat{b}^{(1)}_{\mathbb{tot}}, \vec{\mathbf{\Phi}}^{\dagger}_{\text{tot}}\right] = \\
&-i\sum_{\vec{n}} e^{i\vec{Q}\cdot\vec{n}}\hat{\vec{\mathbf{S}}}_{\vec{n}}\Big\{(e^{-iQ_1}-e^{-iQ_2})(\hat{\vec{\mathbf{S}}}_{\vec{n}_6}\cdot\hat{\vec{\mathbf{S}}}_{\vec{n}_1}) \\
&+(e^{i(Q_1-Q_2)}-e^{iQ_2})(\hat{\vec{\mathbf{S}}}_{\vec{n}_1}\cdot\hat{\vec{\mathbf{S}}}_{\vec{n}_2}) \\
&+(e^{i(Q_1-Q_2)}-e^{iQ_1})(\hat{\vec{\mathbf{S}}}_{\vec{n}_2}\cdot\hat{\vec{\mathbf{S}}}_{\vec{n}_3}) \\
&+(e^{iQ_2}-e^{iQ_1})(\hat{\vec{\mathbf{S}}}_{\vec{n}_3}\cdot\hat{\vec{\mathbf{S}}}_{\vec{n}_4}) \\
&+(e^{iQ_2}-e^{i(Q_2-Q_1)})(\hat{\vec{\mathbf{S}}}_{\vec{n}_4}\cdot\hat{\vec{\mathbf{S}}}_{\vec{n}_5}) \\
&(e^{-iQ_1}-e^{i(Q_2-Q_1)})(\hat{\vec{\mathbf{S}}}_{\vec{n}_5}\cdot\hat{\vec{\mathbf{S}}}_{\vec{n}_6})\Big\}+\ldots,
\end{aligned} \tag{B.17}$$

where $\vec{n}_1 \equiv \vec{n}+(0,-1)$, $\vec{n}_2 \equiv \vec{n}+(1,-1)$, $\vec{n}_3 \equiv \vec{n}+(1,0)$, $\vec{n}_4 \equiv \vec{n}+(0,1)$, $\vec{n}_5 \equiv \vec{n}+(-1,1)$ and $\vec{n}_6 \equiv \vec{n}+(0,-1)$. From this, it is clear that $(Q_1,Q_2)=(0,0)$ will give 0 as the commutator. Therefore if the monopole operator is to have single spin terms as its leading order term, then $\vec{Q} = \pm(2\pi/3,-2\pi/3)$. For $\mathcal{K}$ in Eq. (B.15) to be positive, we choose $\vec{Q}=(2\pi/3,-2\pi/3)$. Here, we have made use of the fact that the DSL is a ground-state of an antiferromagnetic Heisenberg-like Hamiltonian where $\left\langle \hat{\vec{\mathbf{S}}}_i \cdot \hat{\vec{\mathbf{S}}}_j \right\rangle < 0$ for nearest neighbors i and j. So, $(Q_1,Q_2)=(2\pi/3,-2\pi/3)$. With this choice, the Eq. (B.17) becomes

$$\left[\hat{b}^{(1)}_{\text{tot}}, \vec{\mathbf{\Phi}}^{\dagger}_{\text{tot}}\right] = -\sqrt{3}\sum_{\vec{n}} e^{i\vec{Q}\cdot\vec{n}}\hat{\vec{\mathbf{S}}}_{\vec{n}}\left(\quad\right)+\ldots, \tag{B.18}$$

where we use the notation,

$$\begin{aligned} \text{ 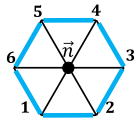 } &\equiv \hat{\vec{\mathbf{S}}}_1 \cdot \hat{\vec{\mathbf{S}}}_2 + \hat{\vec{\mathbf{S}}}_2 \cdot \hat{\vec{\mathbf{S}}}_3 + \hat{\vec{\mathbf{S}}}_3 \cdot \hat{\vec{\mathbf{S}}}_4 + \hat{\vec{\mathbf{S}}}_4 \cdot \hat{\vec{\mathbf{S}}}_5 \\ &+ \hat{\vec{\mathbf{S}}}_5 \cdot \hat{\vec{\mathbf{S}}}_6 + \hat{\vec{\mathbf{S}}}_6 \cdot \hat{\vec{\mathbf{S}}}_1 \equiv \hat{\bigcirc}_{\vec{n}}. \end{aligned} \tag{B.19}$$

To our guess for $\hat{\vec{\Phi}}^{\dagger}_{\text{top}}$, we now add the RHS obtained above.

$$\hat{\vec{\mathbf{\Phi}}}^{\dagger}_{\text{tot}} = \beta_1 \hat{\vec{\mathbf{\Phi}}}^{\dagger(1)} + \beta_2 \hat{\vec{\mathbf{\Phi}}}^{\dagger(2)} + \dots, \tag{B.20}$$

where

$$\hat{\vec{\mathbf{\Phi}}}^{\dagger(1)} = \sum_{\vec{n}} e^{i\vec{Q}\cdot\vec{n}} \hat{\vec{\mathbf{S}}}_{\vec{n}}, \text{ and } \hat{\vec{\mathbf{\Phi}}}^{\dagger(2)} = \sum_{\vec{n}} e^{i\vec{Q}\cdot\vec{n}} \hat{\vec{\mathbf{S}}}_{\vec{n}} \hat{\bigcirc}_{\vec{n}}. \tag{B.21}$$

We can use the commutators Eq. (B.30,B.31,B.32,B.33) to get

$$\begin{aligned} \left[\hat{b}^{(1)}_{\mathbb{tol}}, \hat{\vec{\mathbf{\Phi}}}^{\dagger(1)}\right] &= -\sqrt{3}\hat{\vec{\mathbf{\Phi}}}^{\dagger(2)} \text{ and} \\ \left[\hat{b}^{(1)}_{\mathbb{tol}}, \hat{\vec{\mathbf{\Phi}}}^{\dagger(2)}\right] &= -\sqrt{3}\left(\frac{3}{4}\hat{\vec{\mathbf{\Phi}}}^{\dagger(1)} - \hat{\vec{\mathbf{\Phi}}}^{\dagger(2)} + \dots\right). \end{aligned} \tag{B.22}$$

Using the above equation, truncating at terms supported on at most elementary triangles, we get

$$\hat{\vec{\mathbf{\Phi}}}^{\dagger}_{\text{tot}} = \sum_{\vec{n}} e^{i\vec{Q}.\vec{n}} \left(\hat{\vec{\mathbf{S}}}_{\vec{n}} - \frac{4}{3}\hat{\vec{\mathbf{S}}}_{\vec{n}}\hat{\bigcirc}_{\vec{n}} + \dots\right), \tag{B.23}$$

where $\vec{Q} = (2\pi/3, -2\pi/3)$.

B.2.2.1 Spin singlet monopoles

Having determined the momentum of the spin-triplet 2π-monopoles, the momenta of spin-singlet monopoles can be fixed by the low energy theory since the embedding of the space-group symmetries into $SO(3)_{\text{valley}}$ can be computed purely from low energy information. Doing so results in Table 2 of Ref. [24]. Here, we will write microscopic expressions for them.

The spin singlet monopoles are time-reversal even. Here, we will only keep the lowest weight terms that are dot products of neighbouring spins:

$$\hat{\Phi}_i^\dagger = v_1 \hat{\Phi}_i^{\dagger(1)} + v_2 \hat{\Phi}_i^{\dagger(2)} \quad \text{for } i \in \{1,2,3\}, \text{ where} \tag{B.24}$$

$$\begin{aligned}
\hat{\Phi}_1^{\dagger(1)} &= e^{-i\frac{\pi}{3}} \sum_{\vec{n}} e^{i(-\frac{\pi}{3},\frac{\pi}{3})\cdot\vec{n}} \Big(\vec{n} \bigtriangledown \Big), \\
\hat{\Phi}_2^{\dagger(1)} &= e^{i\frac{\pi}{3}} \sum_{\vec{n}} e^{i(\frac{2\pi}{3},\frac{\pi}{3})\cdot\vec{n}} \Big(\vec{n} \bigtriangledown \Big), \\
\hat{\Phi}_3^{\dagger(1)} &= -\sum_{\vec{n}} e^{i(-\frac{\pi}{3},-\frac{2\pi}{3})\cdot\vec{n}} \Big(\vec{n} \bigtriangledown \Big),
\end{aligned} \tag{B.25}$$

$$\begin{aligned}
\hat{\Phi}_1^{\dagger(2)} &= \sum_{\vec{n}} e^{i(-\frac{\pi}{3},\frac{\pi}{3})\cdot\vec{n}} \Big\{ -i \Big(\vec{n} \bigtriangledown \Big) + e^{-i\frac{\pi}{6}} \Big(\vec{n} \bigtriangledown \Big) \Big\}, \\
\hat{\Phi}_2^{\dagger(2)} &= \sum_{\vec{n}} e^{i(\frac{2\pi}{3},\frac{\pi}{3}).\vec{n}} \Big\{ e^{i\frac{\pi}{6}} \Big(\vec{n} \bigtriangledown \Big) + i \Big(\vec{n} \bigtriangledown \Big) \Big\}. \\
\hat{\Phi}_3^{\dagger(2)} &= \sum_{\vec{n}} e^{i(-\frac{\pi}{3},-\frac{2\pi}{3}).\vec{n}} \Big\{ e^{-i\frac{5\pi}{6}} \Big(\vec{n} \bigtriangledown \Big) + e^{i\frac{5\pi}{6}} \Big(\vec{n} \bigtriangledown \Big) \Big\},
\end{aligned} \tag{B.26}$$

where we use the notation,

$$\overset{0}{\bigtriangledown}\!\!\overset{2}{\underset{1}{}} = \hat{\vec{\mathbf{S}}}_0 \cdot \hat{\vec{\mathbf{S}}}_1 \tag{B.27}$$

We can now use the identity Eq. (B.34) to get

$$\begin{aligned}
\left[\hat{b}^{(1)}_{\mathbb{tot}}, \hat{\Phi}^{\dagger(1)}_i\right] &= \frac{1}{2}\hat{\Phi}^{\dagger(2)}_i + \dots, \\
\left[\hat{b}^{(1)}_{\mathbb{tot}}, \hat{\Phi}^{\dagger(2)}_i\right] &= \hat{\Phi}^{\dagger(1)}_i - \frac{\sqrt{3}}{2}\hat{\Phi}^{\dagger(2)}_i + \dots, \\
\implies \left[\hat{b}^{(1)}_{\mathbb{tot}}, v_1\hat{\Phi}^{\dagger(1)}_i + v_2\hat{\Phi}^{\dagger(2)}_i\right] &= v_2\hat{\Phi}^{\dagger(1)}_i + \\
&+ \left(\frac{1}{2}v_1 - \frac{\sqrt{3}}{2}v_2\right)\hat{\Phi}^{\dagger(2)}_i + \dots .
\end{aligned} \tag{B.28}$$

If we demand proportionality already to this order, then we obtain $\mathcal{K} = v_2/v_1 = 0.396$. In contrast, $\mathcal{K}$ for the spin triplet monopole in Eq. B.23 is $\sqrt{3}$, although in theory they should be the same. The discrepancy is the result of our uncontrolled approximation to drop higher size terms, since the commutator of two high size operators can give a lower size operator (for example, Eq. (B.31)). Nevertheless, using this approach we have been able to motivate why the $U(1)_{\text{top}}$ contribution to monopole momentum is $(2\pi/3, -2\pi/3)$.

It could be a fruitful direction to assume that the coefficients C_s do decay with operator size s and self-consistently solve for C_s using the general approach described above. Since the generators $\hat{Q}^{ab}$ are generators for emergent global *internal* symmetries, naïvely, one would expect that $\hat{Q}^{ab}$ is a sum of approximately local terms, and C_s decays exponentially with size s. It will be interesting to verify that this is indeed the case, and if so, to determine what sets the decay length when the IR theory is conformally invariant. If this approach succeeds, it would help one to study DSLs without resorting to parton construction, and serve as a technique complementary to the one explored in [300].

B.2.3 List of useful commutation relations

Here, we list some useful commutation relations of various spin operators with the spin chirality, i.e. commutators of the form

$$\Big[\hat{\mathcal{O}}\big(\{\vec{\mathbf{S}}_i\}\big), (\hat{\vec{\mathbf{S}}}_1 \times \hat{\vec{\mathbf{S}}}_2)\cdot\hat{\vec{\mathbf{S}}}_3\Big] \tag{B.29}$$

where $\hat{\mathcal{O}}\left[\{\vec{S}_i\}\right]$ is a local operator made of spins.

$\hat{\mathcal{O}}$: Spin triplet made of single spin

$$\Big[\hat{\vec{\mathbf{S}}}_1, (\hat{\vec{\mathbf{S}}}_1 \times \hat{\vec{\mathbf{S}}}_2)\cdot\hat{\vec{\mathbf{S}}}_3\Big] = i\Big((\hat{\vec{\mathbf{S}}}_1\cdot\hat{\vec{\mathbf{S}}}_2)\hat{\vec{\mathbf{S}}}_3 - (\hat{\vec{\mathbf{S}}}_1\cdot\hat{\vec{\mathbf{S}}}_3)\hat{\vec{\mathbf{S}}}_2\Big) \tag{B.30}$$

$\hat{\mathcal{O}}$: Spin triplet made of 3 spins

$$\begin{aligned}\Big[(\hat{\vec{\mathbf{S}}}_1\cdot\hat{\vec{\mathbf{S}}}_2)\hat{\vec{\mathbf{S}}}_3, (\hat{\vec{\mathbf{S}}}_1 \times \hat{\vec{\mathbf{S}}}_2)\cdot\hat{\vec{\mathbf{S}}}_3\Big] &= -\frac{i}{8}(\hat{\vec{\mathbf{S}}}_1 - \hat{\vec{\mathbf{S}}}_2) + \\ &+ \frac{i}{4}\Big((\hat{\vec{\mathbf{S}}}_2\cdot\hat{\vec{\mathbf{S}}}_3)\hat{\vec{\mathbf{S}}}_1 - (\hat{\vec{\mathbf{S}}}_1\cdot\hat{\vec{\mathbf{S}}}_3)\hat{\vec{\mathbf{S}}}_2\Big)\end{aligned} \tag{B.31}$$

$$\Big[(\hat{\vec{\mathbf{S}}}_1\cdot\hat{\vec{\mathbf{S}}}_2)\hat{\vec{\mathbf{S}}}_3, (\hat{\vec{\mathbf{S}}}_1 \times \hat{\vec{\mathbf{S}}}_2)\cdot\hat{\vec{\mathbf{S}}}_4\Big] = -\frac{i}{2}(\hat{\vec{\mathbf{S}}}_1\cdot\hat{\vec{\mathbf{S}}}_4 - \hat{\vec{\mathbf{S}}}_2\cdot\hat{\vec{\mathbf{S}}}_4)\hat{\vec{\mathbf{S}}}_3 \tag{B.32}$$

$$\begin{aligned}\Big[(\hat{\vec{\mathbf{S}}}_1\cdot\hat{\vec{\mathbf{S}}}_2)\hat{\vec{\mathbf{S}}}_3, (\hat{\vec{\mathbf{S}}}_1 \times \hat{\vec{\mathbf{S}}}_3)\cdot\hat{\vec{\mathbf{S}}}_4\Big] &= \frac{i}{2}\Big((\hat{\vec{\mathbf{S}}}_2\cdot\hat{\vec{\mathbf{S}}}_4)\hat{\vec{\mathbf{S}}}_1 + \\ &+(\hat{\vec{\mathbf{S}}}_3\cdot\hat{\vec{\mathbf{S}}}_4)\hat{\vec{\mathbf{S}}}_2 - (\hat{\vec{\mathbf{S}}}_2\cdot\hat{\vec{\mathbf{S}}}_3)\hat{\vec{\mathbf{S}}}_4 - (\hat{\vec{\mathbf{S}}}_1\cdot\hat{\vec{\mathbf{S}}}_4)\hat{\vec{\mathbf{S}}}_2\Big)\end{aligned} \tag{B.33}$$

$\hat{\mathcal{O}}$: Spin singlet made of two spins

$$\Big[\hat{\vec{\mathbf{S}}}_1\cdot\hat{\vec{\mathbf{S}}}_2, (\hat{\vec{\mathbf{S}}}_1 \times \hat{\vec{\mathbf{S}}}_2)\cdot\hat{\vec{\mathbf{S}}}_3\Big] = -\frac{i}{2}(\hat{\vec{\mathbf{S}}}_1\cdot\hat{\vec{\mathbf{S}}}_3 - \hat{\vec{\mathbf{S}}}_2\cdot\hat{\vec{\mathbf{S}}}_3) \tag{B.34}$$

B.2.4 Remarks on notation

We write the generator corresponding to the charge/current in square brackets. Eg: $\hat{Q}[\sigma^i\tau^j]$ and $\hat{Q}[U(1)_{\text{top}}]$.

Correspondence between the notations $\hat{Q}^{ab}$ and $\hat{Q}_{\mathbb{tot}}[\sigma^i\tau^j]$:

$$\hat{Q}_{\mathbb{tot}}\left[\sigma^1\right] = \hat{Q}^{56}, \quad \hat{Q}_{\mathbb{tot}}\left[\sigma^2\right] = \hat{Q}^{64}, \quad \hat{Q}_{\mathbb{tot}}\left[\sigma^3\right] = \hat{Q}^{45} \tag{B.35}$$

$$\hat{Q}_{\mathbb{tot}}\left[\tau^1\right] = \hat{Q}^{23}, \quad \hat{Q}_{\mathbb{tot}}\left[\tau^2\right] = Q^{31}, \quad Q\left[\tau^3\right]_{\mathbb{tot}} = \hat{Q}^{12} \tag{B.36}$$

$$\hat{Q}_{\mathbb{tot}}\left[\sigma^i\tau^j\right] = \hat{Q}^{3+i,j} \text{ for } 1 \leq i,j \leq 3 \tag{B.37}$$

B.3 Ignoring source terms for spin singlet monopoles

In this section, we argue why source terms for spin singlet monopoles potentially arising due to spatial symmetry breaking near the boundaries (see Eq. (2.17)), do not significantly affect the $U(1)_{\text{top}}$ Josephson current between two 120° AFMs. For simplicity, let us work with the effective Hamiltonian in terms of the ordered phases alone, with the DSL integrated out, as we did in Eq. (2.18). The source term, localized to the boundaries modifies Eq. (2.18) as follows:

$$\hat{H}_{\text{new}} = \hat{H}_{\text{eff}} + \sum_{i=1}^{3} \sum_{P=L,R} \left(V_{i,P}^{\text{eff}} \hat{\Phi}_{i,P}^{\dagger} + \text{ h.c.} \right) \tag{B.38}$$

Note that $V_{i,P}^{\text{eff}}$ is a coupling arising under RG flow in the effective field theory due to the boundaries breaking spatial symmetries. Hence, it is small when compared to $\Gamma_S^{\text{eff}} \left\langle \hat{\vec{\Phi}}_{L/R} \right\rangle$, which in contrast is macroscopic in the 120° AFM. The source term leads to the following extraneous

contribution to the $U(1)_{\text{top}}$ current:

$$\begin{aligned} -\left(\frac{\mathrm{d}\hat{b}_{\text{tot},L}}{\mathrm{d}t}\right)_{\text{extra}} &= i\left[\hat{b}_{\text{tot},L}, \sum_{i=1}^{3}\left(V_{i,L}^{\text{eff}}\hat{\Phi}_{iL}^{\dagger} + \text{ h.c.}\right)\right] \\ &= i\sum_{i=1}^{3}\left(V_{i,L}^{\text{eff}}\hat{\Phi}_{iL}^{\dagger} - \text{ h.c.}\right) \end{aligned} \tag{B.39}$$

Now, we take expectation value of the above expression. The result is proportional to the expectation value of a spin singlet monopole at the boundary of a 120° AFM phase. The only reason this expectation value is nonzero is because of $V_{i,L}^{\text{eff}}$. Hence, $\left\langle\hat{\Phi}_{iL}\right\rangle$ is first order in $V_{i,L}^{\text{eff}}$. Therefore, $\left\langle -\left(\frac{\mathrm{d}\hat{b}_{\text{tot},L}}{\mathrm{d}t}\right)_{\text{extra}}\right\rangle$ is second order in $V_{i,L}^{\text{eff}}$, which we neglect due to the assumption that $V_{i,L}^{\text{eff}}$ is small.

B.4 Formula for Raman scattering off a non-equilibrium state

In this appendix, we will derive Eq. (2.40) for the Raman scattering rate when the spin system is not in an energy eigenstate, but in a nonequilibrium steady state. While we will have Raman scattering in mind for the sake of concreteness, our derivation applies for any scattering process. We have two systems — light and matter. Light is used to probe matter (the DSL in our case). The full time-independent Hamiltonian is

$$\hat{H} = \hat{H}_0 + \hat{V} \tag{B.40}$$

where $\hat{H}_0$ is the Hamiltonian for the matter and light fields separately and $\hat{V}$ is the light matter coupling. Suppose that at time $t = 0$, the system is in state $|\psi\rangle \otimes |n_i; 0\rangle$, i.e. the matter part of the state is $|\psi\rangle \equiv \sum_l \psi_l |l\rangle$ (where $|l\rangle$ is an energy eigenstate of the matter Hamiltonian) and the

light part has n_i photons in a mode of frequency ω_i and 0 photons in mode ω_f. In the final state, at time T, the light part is in the state $|n_i - 1; 1\rangle$, while the matter part is in an unknown state $|f\rangle$. The scattering rate is given by

$$\begin{aligned} R &= \frac{1}{T}\sum_f \left|(\langle f| \otimes \langle n_i - 1; 1|)\hat{U}(T)(|\psi\rangle \otimes |n_i; 0\rangle)\right|^2 \\ &= \frac{1}{T}\sum_f \left|\sum_l \psi_l(\langle f| \otimes \langle n_i - 1; 1|)\hat{U}(T)(|l\rangle \otimes |n_i; 0\rangle)\right|^2 \end{aligned} \tag{B.41}$$

where $\hat{U}(T) \equiv e^{-i(\hat{H}_0+\hat{V})T}$ is the time-evolution operator. For ease of notation, we now define

$$|L\rangle \equiv |l\rangle \otimes |n_i; 0\rangle \text{ and } H_0|L\rangle = E_L|L\rangle$$
$$\text{where } E_L \equiv E_l + n_i\omega_i \tag{B.42}$$

$$|F\rangle \equiv |f\rangle \otimes |n_i - 1; 1\rangle \text{ and } H_0|F\rangle = E_F|F\rangle$$
$$\text{where } E_F \equiv E_f + (n_i - 1)\omega_i + \omega_f \tag{B.43}$$

So, Eq. (B.41) becomes

$$R = \frac{1}{T}\sum_f \left|\sum_l \psi_l \langle F|\hat{U}(T)|L\rangle\right|^2. \tag{B.44}$$

For $T > 0$,

$$\hat{U}(T) = i\hat{G}_R(T) = i\int_{-\infty}^{\infty}\frac{d\omega}{2\pi}\hat{G}_R(\omega)e^{-i\omega T}, \tag{B.45}$$

where $\hat{G}_R(\omega)$ is the retarded Green's function for the full system (light + matter). Using the standard T-matrix formalism, we can write

$$\hat{G}_R(\omega) = \hat{G}^0_R(\omega) + \hat{G}^0_R(\omega)\hat{\mathcal{T}}_R(\omega)\hat{G}^0_R(\omega) \tag{B.46}$$

where $\hat{G}_R^0(\omega) = \frac{1}{\omega^+ - \hat{H}_0}$ (here, $\omega^+ \equiv \omega + i0^+$) and $\hat{\mathcal{T}}_R(\omega) = \hat{V} + \hat{V}\hat{G}_R^0(\omega)\hat{V} + \hat{V}\hat{G}_R^0\hat{V}\hat{G}_R^0\hat{V} + \ldots$.

Clearly, $\hat{G}_R^0$ cannot induce a transition that changes the number of photons; only the second term involving $\hat{\mathcal{T}}_R$ can do so. Thus, we get the following scattering amplitude

$$\langle F|\hat{U}(T)|L\rangle = i\int_{-\infty}^{\infty}\frac{d\omega}{2\pi}e^{-i\omega T}\frac{\langle F|\hat{\mathcal{T}}_R(\omega)|L\rangle}{(\omega^+ - E_F)(\omega^+ - E_L)} \tag{B.47}$$

The ω integral should be closed in the lower half plane for convergence. This integral will pick up poles at $E_F - i0^+$ and $E_L - i0^+$. The poles of $\hat{\mathcal{T}}_R(\omega)$ will not play a role under the assumption $T \gg 1/(E_F - E_M)$, which is the regime of interest since we wish to consider the large T limit. Here, E_M is the total energy (light + matter) of any level M such that $\langle F|\hat{V}|M\rangle \neq 0$. In such a large T limit, one can expand out $\hat{\mathcal{T}}_R(\omega)$ and see that our assumption is justified. So, we get

$$\begin{aligned}\langle F|\hat{U}(T)|L\rangle =& -2ie^{-i(E_F+E_L)T/2}\,\frac{\sin((E_F - E_L)T/2)}{E_F - E_L}\\ &\times\ \langle F|\hat{\mathcal{T}}_R(\omega = E_F)|L\rangle \qquad \text{(B.48)}\\ \approx& -2\pi i e^{-iE_FT}\delta(E_f + \omega_f - E_l - \omega_i)\\ &\times\ \langle F|\hat{\mathcal{T}}_R(\omega = E_F)|L\rangle \qquad \text{(B.49)}\end{aligned}$$

Now, $\langle F|\hat{\mathcal{T}}_R(\omega = E_F)|L\rangle$ is the same operator that appears in the equilibrium calculation in [7, 54]. As shown there, up to a constant of proportionality

$$\langle F|\hat{\mathcal{T}}_R(\omega = E_F)|L\rangle = \langle f|\hat{M}|l\rangle \tag{B.50}$$

i.e. the above matrix element for the full system is proportional to a matrix element of the matter

part alone. $\hat{M}$ has been calculated in [7, 54] and depends on the initial and final polarizations of light, momentum transferred by light and the lattice of the matter system. We have presented the leading order expression for $\hat{M}$ in Eq. (2.41). Substituting Eq. (B.49) into Eq. (B.41), we get

$$\begin{aligned}
R \approx & \frac{1}{T}\sum_{f}\sum_{l,l'}\psi_{l'}^{*}\psi_{l}(4\pi)^{2}\delta(E_f+\omega_f-E_l-\omega_i) \\
& \times \delta(E_f+\omega_f-E_{l'}-\omega_i)\,\langle l'|\hat{M}^{\dagger}|f\rangle\;\langle f|\hat{M}|l\rangle \\
= & \frac{1}{T}\sum_{f}\sum_{l,l'}\psi_{l'}^{*}\psi_{l}(4\pi)^{2}\delta(E_f+\omega_f-E_l-\omega_i) \\
& \times \delta(E_{l'}-E_l)\,\langle l'|\hat{M}^{\dagger}|f\rangle\;\langle f|\hat{M}|l\rangle \qquad \text{(B.51)} \\
= & \lim_{T\to\infty}\frac{1}{T}\sum_{f}\int_{-\frac{T}{2}}^{\frac{T}{2}}dt_0 e^{i(E_{l'}-E_l)t_0} \\
& \times \int_{-\infty}^{\infty}dt e^{i(E_f+\omega_f-E_l-\omega_i)t} \\
& \times \sum_{l,l'}\psi_{l'}^{*}\psi_{l}\,\langle l'|\hat{M}^{\dagger}|f\rangle\;\langle f|\hat{M}|l\rangle \qquad \text{(B.52)}
\end{aligned}$$

where in the last equation, we used the Fourier representation of the δ function. Now, we can associate the phases in the above equation with the phases coming from time evolution to simplify it as follows:

$$\begin{aligned}
R = & \lim_{T\to\infty}\frac{1}{T}\sum_{f}\sum_{l,l'}\int_{-T/2}^{T/2}dt_0\int_{-\infty}^{\infty}dt e^{i(\omega_f-\omega_i)t} \\
& \times \psi_{l'}^{*}\psi_{l}\,\langle l'|\hat{M}^{\dagger}e^{i\hat{H}_0 t_0}|f\rangle\;\langle f|e^{i\hat{H}_0 t}Me^{-i\hat{H}_0(t+t_0)}|l\rangle \\
= & \lim_{T\to\infty}\frac{1}{T}\int_{-T/2}^{T/2}dt_0\int_{-\infty}^{\infty}dt e^{i(\omega_f-\omega_i)t} \\
& \times \langle\psi|\hat{M}^{\dagger}(t_0)\hat{M}(t+t_0)|\psi\rangle \qquad \text{(B.53)}
\end{aligned}$$

where $\hat{M}(t) = e^{i\hat{H}_0 t}\hat{M}e^{-i\hat{H}_0 t}$. This completes the derivation of Eq. (2.40).

Appendix C: Chapter 3

C.1 Review of $\hat{\mathcal{T}}$-matrix formalism

In this appendix, we review scattering theory using the $\hat{\mathcal{T}}$-matrix formalism. This review is loosely based on Chapter 3 of Ref. [168]. The key takeaway from this appendix is Eq. (3.5) which serves as a generalization of Fermi's Golden Rule that works to all orders in perturbation theory.

Consider a Hamiltonian

$$\hat{H} = \hat{H}_0 + \hat{V}. \tag{C.1}$$

For concreteness, one can imagine $\hat{H}_0$ to be the full Hamiltonian of light and matter separately, and $\hat{V}$ is the light-matter interaction. But this formalism is applicable to any quantum scattering problem. At time $-T/2$, we start with a state $|\Psi(-T/2)\rangle$ in the full (light + matter) Hilbert Space. Around $t = 0$, light and matter are interacting, and the scattered light is observed at $t = T/2$. The final state is $|\Psi(T/2)\rangle \equiv e^{-i\hat{H}T}|\Psi(-T/2)\rangle$. We are interested in the limit when $T \to \infty$. The final state will have several terms with oscillating prefactors of the type $e^{i(E_m^0 - E_n^0)T}$ where E_m^0 and E_n^0 are the energy eigenstates of $\hat{H}_0$. But we are interested in the limit $T \gg 1/(\delta E_{\text{in}})$, ($\delta E_{\text{in}}$ being the uncertainty in energy of the initial state) where terms like $e^{i(E_m^0 - E_n^0)T}$ are fast-oscillating and average out to 0. Therefore, it is useful to have a formalism

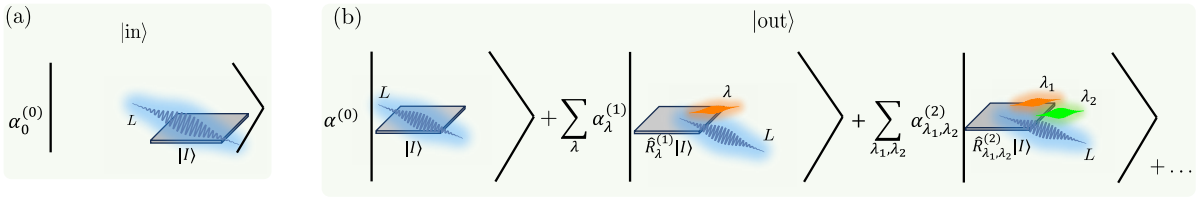

Figure C.1: **Fig. 3.3 in Interaction Picture**: Schematic depiction of (a) $|\text{in}\rangle \equiv e^{-i\hat{H}_0 T/2}\,|\Psi(t=-T/2)\rangle$ and (b) $|\text{out}\rangle \equiv e^{i\hat{H}_0 T/2}\,|\Psi(t=T/2)\rangle$. This is a mathematical trick used to bring all wavepackets to where they should have been at $t=0$, according to the noninteracting Hamiltonian $\hat{H}_0$. The states (a) and (b) are respectively obtained by evolving the initial and final states shown in Fig. 3.3(a) and 3.3(b) forward and backward respectively in time till $t=0$. States $|\text{in}\rangle$ and $|\text{out}\rangle$ are identical to Fig. 3.3(a) and (b) respectively, except that the light wavepackets have been shifted so as to be in the vicinity of the material. Further, upon doing so, the individual terms may have picked up additional phases $\alpha_\lambda^{(1)}$ etc. (compared to the corresponding terms in Fig. 3.3) due to time-evolution.

that directly computes the time-evolved state with such fast-oscillating terms filtered away. This is what the $\hat{\mathcal{T}}$-matrix formalism does.

We define states $|\text{in}\rangle$ and $|\text{out}\rangle$ as follows:

$$|\Psi(-T/2)\rangle \equiv e^{-i\hat{H}_0(-T/2)}\,|\text{in}\rangle \tag{C.2}$$

$$\langle\Psi(T/2)| \equiv \langle\text{out}|\,e^{i\hat{H}_0 T/2}. \tag{C.3}$$

The purpose of this trick is to allow one to define Heisenberg operators in terms of the eigenstates of $\hat{H}_0$ with respect to time $t=0$, which is a time when the photon wave-packet and the material are already interacting. So $|\text{in}\rangle$ is defined as the initial state evolved forward in time till $t=0$ by the noninteracting Hamiltonian $\hat{H}_0$. In this state, the laser wavepacket spatially overlaps with the material [Fig. C.1(a)]. Similarly, $|\text{out}\rangle$ is defined by evolving the final state backward in time till $t=0$ by the noninteracting Hamiltonian $\hat{H}_0$ [Fig. C.1(b)]. We suppose the state $|\text{in}\rangle$ is a wave-packet with a narrow spread of energy with respect to $\hat{H}_0$ such that the energy is centred around E^0_{in}. For the wavepacket to be far away from the material at $t=-T/2$, it necessarily has

a non-zero width in momentum (and therefore energy). Generically, a narrow wavepacket gets wider with time (in real space). Since light is relativistic (i.e., the magnitude of velocity of all the component waves of the wavepacket are equal, so the uncertainty in velocity comes solely in its direction), the velocity of this spreading is maximum in the direction perpendicular to the velocity of the centre of the wavepacket. This spreading velocity has magnitude $\sim c\frac{\sigma_p}{p}$ where p is the mean momentum of the wavepacket and σ_p is its uncertainty in momentum. For small enough $\frac{\sigma_p}{p}$, the spreading of the wavepacket fails to catch up with the center itself. Therefore, in the rest of this section, we will ignore wavepacket spreading. (Similar reasoning can also be used to neglect wavepacket spreading in the case of a non-relativistic scatterer.)

Consider the state at time $t = 0$:

$$|\Gamma_-\rangle \equiv e^{-i\hat{H}T/2} e^{i\hat{H}_0 T/2} |\text{in}\rangle \,. \tag{C.4}$$

Now, let us view $|\Gamma_-\rangle$ as a function of the initial time $-T/2$. We rewrite the above expression by first differentiating with respect to t' (supposing $t' = -T/2$ in the above equation) and then integrating over t' from $-T/2$ to 0.

$$\partial_{t'} |\Gamma_-\rangle = i e^{i\hat{H}t'} \hat{V} e^{-i\hat{H}_0 t'} |\text{in}\rangle \tag{C.5}$$

$$\implies |\Gamma_-\rangle = |\text{in}\rangle - i \int_{-T/2}^{0} \text{d}t' e^{i\hat{H}t'} \hat{V} e^{-i\hat{H}_0 t'} |\text{in}\rangle \tag{C.6}$$

The advantage of rewriting $|\Gamma_-\rangle$ as above is that it makes evident the fact that $|\Gamma_-\rangle$ does not depend on $-T/2$ (as long as $-T/2$ is sufficiently negative). The reason is that $\hat{V}$ acting on $e^{-i\hat{H}_0 t'} |\text{in}\rangle$ returns 0 unless the wavepacket of the photon has some spatial overlap with the ma-

terial. This observation is the key physics input in the $\hat{\mathcal{T}}$-matrix formalism. In the setting we are imagining, the laser beam comes close to the material only around $t = -t_C < 0$ for some time scale $t_C \ll T/2$. Whatever happens before $-t_C$ does not contribute to the above equation. We will soon use this useful fact. Let us suppose

$$|\text{in}\rangle = \sum_j \phi_j^{\text{in}} \left|\Psi_j^0\right\rangle \text{ and } |\text{out}\rangle = \sum_j \phi_j^{\text{out}} \left|\Psi_j^0\right\rangle \tag{C.7}$$

where $\left|\Psi_j^0\right\rangle$ is an eigenstate of $\hat{H}_0$ with energy E_j^0. We assume that the ϕ_j's are narrowly peaked around energy $E_{\text{in},0}$. Also inserting into Eq. (C.6) a resolution of identity in terms of $|\Psi_J\rangle$ which are eigenstates of $\hat{H}$ with eigenvalue $\mathcal{E}_J$, i.e., $\sum_J |\Psi_J\rangle \langle\Psi_J|$, we get:

$$\begin{aligned}
|\Gamma_-\rangle &= |\text{in}\rangle - i \sum_j \phi_j^{\text{in}} \sum_J |\Psi_J\rangle \left\langle \Psi_J \middle| \hat{V} \middle| \Psi_j^0 \right\rangle \\
&\qquad \times \int_{-T/2}^{0} \mathrm{d}t' e^{i(\mathcal{E}_J - E_j^0)t'} \\
&= |\text{in}\rangle + \sum_j \sum_J |\Psi_J\rangle \left\langle \Psi_J \middle| \hat{V} \middle| \Psi_j^0 \right\rangle \phi_j^{\text{in}} \\
&\quad \times \frac{2\sin^2\left[\frac{(\mathcal{E}_J - E_j^0)T/2}{2}\right] + i \sin\left[(\mathcal{E}_J - E_j^0)T/2\right]}{E_j^0 - \mathcal{E}_J}
\end{aligned} \tag{C.8}$$

Let us now simplify the following expression from Eq. (C.8):

$$\frac{2\sin^2((\mathcal{E}_J - E_j^0)T/4) + i \sin\big((\mathcal{E}_J - E_j^0)T/2\big)}{E_j^0 - \mathcal{E}_J} \tag{C.9}$$

Let us suppose that $T/2 \gg \frac{1}{\delta E_{\text{in}}^0}$, (where δE_{in}^0 is the spread in E_{in}^0), i.e., $T/2$ is so large that as E_j^0 runs through the different eigen-components of the $|\text{in}\rangle$ state, the real part of the numerator of Eq. (C.9) goes through several cycles of the $\sin^2()$ function. Let us consider two limits for

$\left|E_j^0 - \mathcal{E}_J\right|$. The first limit is when $\left|E_j^0 - \mathcal{E}_J\right| \gg \delta E_{\text{in}}^0$ (consequently $\left|E_j^0 - \mathcal{E}_J\right| \gg 2/T$). Then the fluctuations in the numerator of Eq. (C.9) are much stronger than the fluctuations of the denominator. Hence, we can replace the real part of the numerator by its average which is $2\times 1/2$. Thus, the real part of the expression is $1/(E_j^0 - \mathcal{E}_J)$. But in the opposite limit, when $\left|E_j^0 - \mathcal{E}_J\right| \ll 2/T$, the real part of Eq. (C.9) tends to 0. Hence the real part can be approximated by $\mathcal{P}\frac{1}{E_j^0 - \mathcal{E}_J}$ for large $T/2$. Here, $\mathcal{P}$ stands for principal value and $\mathcal{P}\frac{1}{z}$ is defined as $\lim_{\eta\to 0}\frac{1}{2}\left(\frac{1}{z+i\eta} + \frac{1}{z-i\eta}\right)$. Next, we consider the imaginary part of Eq. (C.9), i.e., $-\frac{\sin\left((\mathcal{E}_J - E_j^0)T/2\right)}{\mathcal{E}_J - E_j^0}$. As $T/2$ increases, this function becomes sharply peaked around $E_j^0 - \mathcal{E}_J = 0$. As $T/2 \to \infty$, it becomes $-\pi\delta(E_j^0 - \mathcal{E}_J)$. Thus, in Eq. (C.8), we can make the following replacement

$$\begin{aligned}
&\frac{2\sin^2\left[\frac{(\mathcal{E}_J - E_j^0)T/2}{2}\right] + i\sin\left[(\mathcal{E}_J - E_j^0)T/2\right]}{E_j^0 - \mathcal{E}_J} \\
\to &\mathcal{P}\frac{1}{E_j^0 - \mathcal{E}_J} - i\pi\delta(E_j^0 - \mathcal{E}_J) \\
= &\lim_{\eta\to 0^+}\frac{1}{E_j^0 - \mathcal{E}_J + i\eta}.
\end{aligned} \tag{C.10}$$

This agrees with the intuition provided above that $|\Gamma_-\rangle$ should not depend on $T/2$ as long as it is sufficiently large. Thus, we get:

$$|\Gamma_-\rangle = \sum_j \phi_j^{\text{in}}\left(\left|\Psi_j^0\right\rangle + \frac{1}{E_j^0 - \hat{H} + i0^+}\hat{V}\left|\Psi_j^0\right\rangle\right). \tag{C.11}$$

Now, we need to evolve $|\Gamma_-\rangle$ forward in time till $t = T/2$ using $\hat{H}$. This is simple because $\left|\Psi_j^0\right\rangle + \frac{1}{E_j^0 - \hat{H} + i0^+}\hat{V}\left|\Psi_j^0\right\rangle$ is actually an eigenstate of $\hat{H}$ with eigenvalue E_j^0. To see this, if we

replace $\hat{V}$ with $\hat{H} - \hat{H}_0$, then we get

$$\begin{aligned}
&\left|\Psi_j^0\right\rangle + \frac{1}{E_j^0 - \hat{H} + i0^+}\hat{V}\left|\Psi_j^0\right\rangle \\
&= \lim_{\eta\to 0^+} \frac{i\eta}{E_j^0 - \hat{H} + i\eta}\left|\Psi_j^0\right\rangle \\
&= \lim_{\eta\to 0^+} \sum_J \frac{i\eta}{E_j^0 - \mathcal{E}_J + i\eta}\left|\Psi_J\right\rangle\left\langle\Psi_J\middle|\Psi_j^0\right\rangle .
\end{aligned} \tag{C.12}$$

We see that as we take the limit $\eta \to 0^+$, the only J's that survive are those with $\mathcal{E}_J = E_j^0$. Thus we get

$$\begin{aligned}
&\left|\Psi_j^0\right\rangle + \frac{1}{E_j^0 - \hat{H} + i0^+}\hat{V}\left|\Psi_j^0\right\rangle \\
&= \sum_J \delta_{\mathcal{E}_J = E_j^0}\left|\Psi_J\right\rangle\left\langle\Psi_J\middle|\Psi_j^0\right\rangle
\end{aligned} \tag{C.13}$$

Therefore,

$$\begin{aligned}
&e^{-i\hat{H}T/2}\left|\Gamma_-\right\rangle \\
&= \sum_j \phi_j^{\text{in}} \left\{ e^{-iE_j^0 T/2}\left(\left|\Psi_j\right\rangle + \frac{1}{E_j^0 - \hat{H} + i0^+}\hat{V}\left|\Psi_j\right\rangle \right) \right\}
\end{aligned} \tag{C.14}$$

Before proceeding, we make one more formal manipulation (in the style of Dyson equations):

$$\begin{aligned}
&(E_j^0 - \hat{H} + i0^+)^{-1} \\
&= \left(E_j^0 - \hat{H}_0 + i0^+\right)^{-1}\left\{\hat{1} + \hat{V}(E_j^0 - \hat{H} + i0^+)^{-1}\right\}
\end{aligned} \tag{C.15}$$

Therefore,

$$\begin{aligned}
&\frac{1}{E_j^0 - \hat{H} + i0^+}\hat{V} \\
&= \frac{1}{E_j^0 - \hat{H}_0 + i0^+}\left\{\hat{V} + \hat{V}\frac{1}{E_j^0 - \hat{H} + i0^+}\hat{V}\right\} .
\end{aligned} \tag{C.16}$$

We now define the $\hat{\mathcal{T}}$-matrix as

$$\begin{aligned}\hat{\mathcal{T}} \equiv & \hat{V}+\hat{V}\frac{1}{E_{\text{in}}^{0}-\hat{H}+i0^{+}}\hat{V} \\ \equiv & \hat{V}+\hat{V}\frac{1}{E_{\text{in}}^{0}-\hat{H}_{0}-\hat{V}+i0^{+}}\hat{V}\end{aligned} \tag{C.17}$$

where E_{in}^{0} is the energy of the eigenstate of $\hat{H}_0$ appearing in the expansion of $|\text{in}\rangle$ on which $\hat{\mathcal{T}}$ is acting. For example, in the above equation, $\hat{\mathcal{T}}$ is acting on $\left|\Psi_{j}^{0}\right\rangle$ and hence we should use $E_{\text{in}}^{0}=E_{j}^{0}$. With this definition at hand, we rewrite Eq. (C.14) as

$$\begin{aligned}& e^{-i\hat{H}T/2}\left|\Gamma_{-}\right\rangle \\ & =\sum_{j}\phi_{j}^{\text{in}}e^{-iE_{j}^{0}T/2}\left(\left|\Psi_{j}^{0}\right\rangle+\frac{1}{E_{j}^{0}-\hat{H}_{0}+i0^{+}}\hat{\mathcal{T}}\left|\Psi_{j}^{0}\right\rangle\right).\end{aligned} \tag{C.18}$$

Recall that we are interested in calculating $|\text{out}\rangle=e^{i\hat{H}_{0}T/2}e^{-i\hat{H}T/2}\left|\Gamma_{-}\right\rangle$. We have

$$\begin{aligned}& |\text{out}\rangle \\ & =\sum_{j,k}\left|\Psi_{k}^{0}\right\rangle\phi_{j}^{\text{in}}\left\{\delta_{kj}+\frac{e^{-i(E_{j}^{0}-E_{k}^{0})T/2}}{(E_{j}^{0}-E_{k}^{0})+i0^{+}}\left\langle\Psi_{k}^{0}\right|\hat{\mathcal{T}}\left|\Psi_{j}^{0}\right\rangle\right\}\end{aligned} \tag{C.19}$$

Now, by the same argument used before to show that $|\Gamma_{-}\rangle$ is independent of $-T/2$, the above state, i.e., $|\text{out}\rangle=e^{i\hat{H}_{0}T/2}e^{-i\hat{H}T/2}\left|\Gamma_{-}\right\rangle$ should be independent of $T/2$ when $T/2\gg1/(\delta E_{\text{out}}^{0})$.

Therefore, let us extract the $T/2$-independent piece from the above Eq. (C.19).

$$\begin{aligned}
&\frac{e^{-i(E_j^0-E_k^0)T/2}}{(E_j^0-E_k^0)+i0^+} \\
&= e^{-i(E_j^0-E_k^0)T/2}\mathcal{P}\frac{1}{(E_j^0-E_k^0)} - i\pi\delta(E_j^0-E_k^0) \\
&= \mathcal{P}\frac{\cos\left((E_j^0-E_k^0)T/2\right)}{(E_j^0-E_k^0)} - i\frac{\sin\left((E_j^0-E_k^0)T/2\right)}{(E_j^0-E_k^0)} \\
&\quad - i\pi\delta(E_j^0-E_k^0)
\end{aligned} \tag{C.20}$$

In the limit $T/2 \to \infty$, the first term above averages to 0, and hence does not contribute to the T-independent piece. The second term goes to $-i\pi\delta(E_j^0-E_k^0)$. Therefore, in the large $T/2$ limit,

$$\frac{e^{-i(E_j^0-E_k^0)T/2}}{(E_j^0-E_k^0)+i0^+} \to -2\pi i\delta(E_j^0-E_k^0). \tag{C.21}$$

Therefore,

$$\begin{aligned}
&|\text{out}\rangle \\
&= |\text{in}\rangle - \sum_{j,k} 2\pi i\delta(E_j^0-E_k^0)\left|\Psi_k^0\right\rangle\left\langle\Psi_k^0\right|\hat{\mathcal{T}}\left|\Psi_j^0\right\rangle\left\langle\Psi_j^0|\text{in}\right\rangle.
\end{aligned} \tag{C.22}$$

The above equation is a generalization of Fermi's Golden Rule that works to all orders in $\hat{V}$.

C.2 When the incoming laser is modeled as a coherent state instead of a Fock state

In Eq. (3.40) of the main text, we supposed that the radiation part of the $|\text{in}\rangle$ state was in a Fock state (photon-number eigenstate) with $\mathcal{N}_L$ photons in mode L. In this appendix, we examine the case when the initial state of the radiation sector is a coherent state. Our purpose is

two-fold – to clarify the definition of the coupling constant g_L and to write an expression for the $|\text{out}\rangle$ state.

Let us define a coherent state in the radiation sector $|\phi_L\rangle$ as:

$$|\phi_L\rangle \equiv e^{\phi_L \hat{a}_L^\dagger - \phi_L^* \hat{a}_L} |0, \dots, 0\rangle \,. \tag{C.23}$$

Then the full $|\text{in}\rangle$ state is

$$|\text{in}\rangle = |I\rangle_M \otimes e^{\phi_L \hat{a}_L^\dagger - \phi_L^* \hat{a}_L} |0, \dots, 0\rangle \tag{C.24}$$

$$= |I\rangle_M \otimes e^{-\frac{|\phi_L|^2}{2}} \sum_{\mathcal{N}_L} \frac{(\phi_L)^{\mathcal{N}_L}}{\sqrt{\mathcal{N}_L!}} |0, \dots, \mathcal{N}_L, \dots 0\rangle \,. \tag{C.25}$$

In Eq. (3.6), when introducing the $\hat{\mathcal{T}}$ matrix machinery, we assumed an $|\text{in}\rangle$ state that was an eigenstate of $\hat{H}_0$. When $|\text{in}\rangle$ is not an energy eigenstate, as is the case above, one can decompose it into its energy eigenstates, and for each of them, linearly add up the corresponding $|\text{out}\rangle$ states.

We argued in the main text that within our approximation, the only processes contributing to $G^{(1)}$ that we keep are those where exactly one photon is absorbed from the laser and one photon is emitted into a different mode. Similarly, the only processes that we keep for $G^{(2)}$ are those where exactly two photons are absorbed from the laser and two are emitted. Therefore, the matrix elements of $\frac{1}{E_{\text{in}}^0 - \hat{H}_0}$ are independent of the number of photons $\mathcal{N}_L$ in the initial state. The only dependence of $|\text{out}\rangle$ on the initial state thus comes from the action of $\hat{a}_L$. Therefore, if we make a replacement from a Fock state to a coherent state, we just need to replace $\sqrt{\mathcal{N}_L}$ by ϕ_L in expressions for $G^{(1)}$ and $\sqrt{\mathcal{N}_L(\mathcal{N}_L - 1)}$ by ϕ_L^2 in expressions for $G^{(2)}$. For a Fock state, we used $I_L = \frac{\mathcal{N}_L \omega_L c}{\mathcal{V}}$. For a coherent state, we can instead use $I_L = \frac{|\phi_L|^2 \omega_L c}{\mathcal{V}}$.

Now, we come to the laser-matter coupling. For a Fock state input, in expressions for $G^{(2)}$, we make the identification

$$g_L^2 \leftrightarrow \frac{\sqrt{\mathcal{N}_L(\mathcal{N}_L-1)}q_e^2\mathtt{a}^2}{2\varepsilon\mathcal{V}\omega_L}. \tag{C.26}$$

On the other hand, for expressions for $G^{(1)}$, we make the identification

$$g_L \leftrightarrow \frac{\sqrt{\mathcal{N}_L}q_e\mathtt{a}}{\sqrt{2\varepsilon\mathcal{V}\omega_L}}. \tag{C.27}$$

This means that for Fock state input, our definition of g_L is slightly different for $G^{(1)}$ when compared to $G^{(2)}$. But for a coherent state input, the effective laser-matter coupling constants agree.

Now, we are in a position to write an expression for the $|\text{out}\rangle$ state that works for both a Fock state and a coherent state input. We suppose $|\text{in}\rangle = |I\rangle_M \otimes |\psi_L^{(0)}\rangle_R$, as defined in Eq. (3.40) in the main text. Recall from Eq. (3.5) and (3.6), that $|\text{out}\rangle$ can be computed using the $\hat{\mathcal{T}}$-matrix. In Eq. (3.38) and Eq. (3.39), we simplified the terms of the $\hat{\mathcal{T}}$-matrix for processes corresponding to absorption and emission of one and two photons respectively. Combining these with the discussion in the above paragraph, we get Eq. (3.43) in the main text.

C.3 Explicit calculation for matter operator $\hat{R}^{(2)}$

Our goal here is to calculate $\hat{R}^{(2)}_{\lambda_1,\lambda_2}$ defined in Eq. (3.39) by expanding $\hat{V}_P\hat{\mathbb{G}}_0\hat{V}_P\hat{\mathbb{G}}_0\hat{V}_P\hat{\mathbb{G}}_0\hat{V}_P + \hat{V}_P\hat{\mathbb{G}}_0\hat{V}_D\hat{\mathbb{G}}_0\hat{V}_P + \hat{V}_C\hat{\mathbb{G}}_0\hat{V}_P + \hat{V}_P\hat{\mathbb{G}}_0\hat{V}_C$, as promised in Sec. 3.5. Recall that $\hat{\mathbb{G}}_0 = \left(E_{\text{in}} - \hat{H}_0\right)^{-1}$.

Also, recall that within the dipole approximation,

$$\hat{V}_P \approx -\sum_{\boldsymbol{\mu}} \left[\hat{\mathcal{J}}_{\boldsymbol{\mu}} \bar{\boldsymbol{\mu}} \cdot \sum_{\lambda} \frac{g\sqrt{2c}}{\sqrt{\mathcal{V}\omega_\lambda}} \left(\mathbf{e}_\lambda \hat{a}_\lambda + \mathbf{e}_\lambda^* \hat{a}_\lambda^\dagger \right) \right], \tag{C.28}$$

where $\hat{\mathcal{J}}_{\boldsymbol{\mu}}$ was defined in Eq. (3.51), $g = \sqrt{\pi\alpha}\mathtt{a}$ and we use a convention for summation over $\mathbf{r}$ and $\boldsymbol{\mu}$, so that each bond $(\mathbf{r}, \boldsymbol{\mu})$ is counted exactly once (and not double-counted).

Similarly, the diamagnetic term is

$$\hat{V}_D \approx \frac{1}{2} \sum_{(\mathbf{r},\boldsymbol{\mu})} \left\{ \left(\mathtt{t}_{\mathbf{r},\mathbf{r}+\boldsymbol{\mu}} \hat{c}^\dagger_{\mathbf{r}+\boldsymbol{\mu},\sigma} \hat{c}_{\mathbf{r},\sigma} + \text{h.c.} \right) \left[\bar{\boldsymbol{\mu}} \cdot \sum_{\lambda} \frac{g\sqrt{2c}}{\sqrt{\mathcal{V}\omega_\lambda}} \left(\mathbf{e}_\lambda \hat{a}_\lambda + \mathbf{e}_\lambda^* \hat{a}_\lambda^\dagger \right) \right]^2 \right\}, \tag{C.29}$$

and the cubic term is

$$\hat{V}_C \approx \frac{1}{6} \sum_{\boldsymbol{\mu}} \hat{\mathcal{J}}_{\boldsymbol{\mu}} \left[\bar{\boldsymbol{\mu}} \cdot \sum_{\lambda} \frac{g\sqrt{2c}}{\sqrt{\mathcal{V}\omega_\lambda}} \left(\mathbf{e}_\lambda \hat{a}_\lambda + \mathbf{e}_\lambda^* \hat{a}_\lambda^\dagger \right) \right]^3. \tag{C.30}$$

In the $\hat{\mathcal{T}}$-matrix, each insertion of $\hat{V}_P$ can lead to a photon emission ($\hat{a}_\lambda^\dagger$) or absorption ($\hat{a}_\lambda$). Let us write $\hat{V}_P \equiv \hat{V}_P^+ + \hat{V}_P^-$, where $\hat{V}_P^+$ only consists of photon creation operators and $\hat{V}_P^-$ only consists of photon annihilation operators. Similarly, $\hat{V}_D \equiv \hat{V}_D^{+-} + \hat{V}_D^{++} + \hat{V}_D^{--}$, where $\hat{V}_D^{+-}$ is of the form $\hat{a}_\lambda^\dagger \hat{a}_{\lambda'}$ and so on. Then we see that Fig. 3.7(a) and 3.7(b) correspond to $\hat{V}_P^+ \hat{\mathbb{G}}_0 \hat{V}_P^- \hat{\mathbb{G}}_0 \hat{V}_P^+ \hat{\mathbb{G}}_0 \hat{V}_P^-$. Let us denote the contribution from this process to $R^{(2)}_{\lambda_1,\lambda_2}$ as $\hat{R}^{(2)}_{\lambda_1,\lambda_2}\Big|_{a+b}$. Similarly, Fig. 3.7(c) corresponds to $\hat{V}_P^+ \hat{\mathbb{G}}_0 \hat{V}_P^+ \hat{\mathbb{G}}_0 \hat{V}_P^- \hat{\mathbb{G}}_0 \hat{V}_P^-$. Let us denote the contribution from this process as $\hat{R}^{(2)}_{\lambda_1,\lambda_2}\Big|_c$. Fig. 3.7(d) corresponds to $\hat{V}_P^+ \hat{\mathbb{G}}_0 \hat{V}_D^{+-} \hat{\mathbb{G}}_0 \hat{V}_P^-$ and we denote its contribution to $R^{(2)}_{\lambda_1,\lambda_2}$ as $\hat{R}^{(2)}_{\lambda_1,\lambda_2}\Big|_d$. Finally the contribution from the process in Fig. C.5 coming from $\hat{V}_P \hat{\mathbb{G}}_0 \hat{V}_C$ and $\hat{V}_C \hat{\mathbb{G}}_0 \hat{V}_P$ are

denoted $\hat{R}^{(2)}_{\lambda_1,\lambda_2}\Big|_e$ and $\hat{R}^{(2)}_{\lambda_1,\lambda_2}\Big|_{e'}$ respectively. Therefore,

$$\hat{R}^{(2)}_{\lambda_1,\lambda_2} = \hat{R}^{(2)}_{\lambda_1,\lambda_2}\Big|_{a+b} + \hat{R}^{(2)}_{\lambda_1,\lambda_2}\Big|_{c} + \hat{R}^{(2)}_{\lambda_1,\lambda_2}\Big|_{d} + \hat{R}^{(2)}_{\lambda_1,\lambda_2}\Big|_{e} + \hat{R}^{(2)}_{\lambda_1,\lambda_2}\Big|_{e'}. \tag{C.31}$$

C.3.1 Processes in Fig. 3.7(a) and 3.7(b)

These processes are shown pictorially in Fig. 3.8(a_1-a_6). Let us first expand out $\hat{V}_P^+\hat{\mathbb{G}}_0\hat{V}_P^-\hat{\mathbb{G}}_0\hat{V}_P^+\hat{\mathbb{G}}_0\hat{V}_P^-$, keeping the terms that will contribute to $G^{(2)}$:

$$\begin{aligned}
&\hat{V}_P^+\hat{\mathbb{G}}_0\hat{V}_P^-\hat{\mathbb{G}}_0\hat{V}_P^+\hat{\mathbb{G}}_0\hat{V}_P^- \\
&= g^4\frac{(2c)^2}{\mathcal{V}^2\omega_L}\sum_{\boldsymbol{\mu}_1,\boldsymbol{\mu}_2,\boldsymbol{\mu}_1',\boldsymbol{\mu}_2'}(\bar{\boldsymbol{\mu}}_1'\cdot\mathbf{e}_L)\,(\bar{\boldsymbol{\mu}}_2'\cdot\mathbf{e}_L)\,\hat{a}_L^2 \\
&\times\sum_{\substack{\lambda_1,\lambda_2\\K,J,K',F}}\left\{\frac{\hat{a}^\dagger_{\lambda_2}\hat{a}^\dagger_{\lambda_1}}{\sqrt{\omega_{\lambda_1}\omega_{\lambda_2}}}\frac{\left(\bar{\boldsymbol{\mu}}_1\cdot\mathbf{e}^*_{\lambda_1}\right)\left(\bar{\boldsymbol{\mu}}_2\cdot\mathbf{e}^*_{\lambda_2}\right)}{\omega_L-E_{K'I}+i0^+}\right. \\
&\left.\times\frac{|F\rangle\langle F|\,\hat{\mathcal{J}}_{\boldsymbol{\mu}_2}\,|K\rangle\langle K|\,\hat{\mathcal{J}}_{\boldsymbol{\mu}_2'}\,|J\rangle\langle J|\,\hat{\mathcal{J}}_{\boldsymbol{\mu}_1}\,|K'\rangle\langle K'|\,\hat{\mathcal{J}}_{\boldsymbol{\mu}_1'}}{(\omega_L-E_{JI}-\omega_{\lambda_1}+i0^+)\,(2\omega_L-E_{KI}-\omega_{\lambda_1}+i0^+)}\right\}.
\end{aligned} \tag{C.32}$$

See Eq. (3.51) for the definition of $\hat{\mathcal{J}}_{\boldsymbol{\mu}}$. Here, we sum over $|J\rangle$, $|K'\rangle$, $|K\rangle$ and $|F\rangle$ that are many-body energy eigenstates of the Fermi-Hubbard model. For convenience, we have defined $E_{JI}\equiv E_J-E_I$. The overall energy-conservation constraint for each λ_1 and λ_2, imposed by the δ-function in Eq. (3.46) is

$$E_I+2\omega_L = E_F+\omega_{\lambda_1}+\omega_{\lambda_2}. \tag{C.33}$$

Now consider the three energy dependent factors $(2\omega_L-E_{KI}-\omega_{\lambda_1}+i0^+)^{-1}$, $(\omega_L-E_{JI}-\omega_{\lambda_1}+i0^+)^{-1}$ and $(\omega_L-E_{K'I}+i0^+)^{-1}$. Of these, the first two factors contain ω_{λ_1}, a variable that we integrate over, so we cannot estimate them just yet. But we can

estimate the third factor – it is dominated by states $|K'\rangle$ in the single doublon-hole sector. For such states, the factor is of order $1/(\omega_L - U)$. Within this sector, relative variations in this factor are of order $\mathtt{t}/|\omega_L - U|$ that we neglect. We drop contributions from outside this sector because they come with an additional suppression of order $|U - \omega_L|/U$ (see Fig. 3.7). Since Eq. (C.32) now becomes independent of $E_{K'}$, we can replace $\sum_{K'} |K'\rangle\langle K'|$ by the identity operator. Next, to ensure that $|J\rangle$ is in the spin sector, the bond $(\mathbf{r}_1', \boldsymbol{\mu}_1')$ along which the first hop occurs should be the same as the bond $(\mathbf{r}_1, \boldsymbol{\mu}_1)$ along which the second hop occurs. Using this fact, we can use the identities (C.34) and (C.35) given below to simplify the expression in Eq. (C.32):

$$\hat{c}_\alpha^\dagger \hat{c}_\beta = \delta_{\beta\alpha}\frac{\hat{n}}{2} + \left(\hat{\mathbf{S}}\cdot\boldsymbol{\sigma}\right)_{\beta\alpha} \tag{C.34}$$

$$\hat{c}_\alpha \hat{c}_\beta^\dagger = \delta_{\alpha\beta}\left(1 - \frac{\hat{n}}{2}\right) - \left(\hat{\mathbf{S}}\cdot\boldsymbol{\sigma}\right)_{\alpha\beta}. \tag{C.35}$$

We then arrive at the following relation

$$\begin{aligned} &- \langle J|\hat{\mathcal{J}}_{\boldsymbol{\mu}}\hat{\mathcal{J}}_{\boldsymbol{\mu}'}|I\rangle \\ &\approx \langle J|\,\delta_{\boldsymbol{\mu},\boldsymbol{\mu}'}\sum_{\mathbf{r}} |\mathtt{t}_{\mathbf{r},\mathbf{r}+\boldsymbol{\mu}}|^2\left(4\hat{\mathbf{S}}_{\mathbf{r}}\cdot\hat{\mathbf{S}}_{\mathbf{r}+\boldsymbol{\mu}} - 1\right)|I\rangle \end{aligned} \tag{C.36}$$

if both $|I\rangle$ and $|J\rangle$ are in the spin sector.

Using this in Eq. (C.32), then symmetrizing the resultant expression between indices λ_1 and λ_2, we can read off $\hat{R}^{(2)}_{\lambda_1,\lambda_2}$ [defined in Eq. (3.39)]. Due to our choice of definition of $\hat{R}^{(2)}_{\lambda_1,\lambda_2}$, all the

factors of $\sqrt{2c}/\sqrt{\mathcal{V}\omega_\lambda}$ cancel out. We obtain:

$$\begin{aligned}
&\langle F|\hat{R}^{(2)}_{\lambda_1,\lambda_2}\Big|_{a+b}|I\rangle \\
&= -\frac{g_L^2 g^2}{\omega_L - U}\sum_{(\mathbf{r}_1,\boldsymbol{\mu}_1)}\sum_{\boldsymbol{\mu}_2,\boldsymbol{\mu}_2'}\sum_{K,J}\Bigg\{|\mathtt{t}_{\mathbf{r}_1,\mathbf{r}_1+\boldsymbol{\mu}_1}|^2 \\
&\times\Bigg[\frac{\left(\bar{\boldsymbol{\mu}}_2'\cdot\mathbf{e}_L\right)\left(\bar{\boldsymbol{\mu}}_2\cdot\mathbf{e}^*_{\lambda_2}\right)}{\omega_{\lambda_1}-(2\omega_L - E_{KI}+i0^+)}\,\frac{1}{\omega_{\lambda_1}-(\omega_L-E_{JI}+i0^+)} \\
&\qquad + \left(\lambda_1 \leftrightarrow \lambda_2\right)\Bigg]\times\langle F|\,\hat{\mathcal{J}}_{\boldsymbol{\mu}_2}\,|K\rangle\langle K|\,\hat{\mathcal{J}}_{\boldsymbol{\mu}_2'}\,|J\rangle \\
&\times\langle J|\left(4\hat{\mathbf{S}}_{\mathbf{r}_1}\cdot\hat{\mathbf{S}}_{\mathbf{r}_1+\boldsymbol{\mu}_1}-1\right)\left(\bar{\boldsymbol{\mu}}_1\cdot\mathbf{e}^*_{\lambda_1}\right)\left(\bar{\boldsymbol{\mu}}_1\cdot\mathbf{e}_L\right)\Bigg\}|I\rangle\,.
\end{aligned} \tag{C.37}$$

The first term here has two poles, one at $\omega_{\lambda_1} = 2\omega_L - E_{KI} + i0^+$, which corresponds to Fig. 3.7(a), i.e., the central peak and another at $\omega_{\lambda_1} = \omega_L - E_{JI} + i0^+$, which corresponds to Fig. 3.7(b), i.e., the sidebands. The two poles here are reminiscent of the fluorescent triplet of a two-level system studied in Ref. [14]. Our first [Fig. 3.7(a)] and second [Fig. 3.7(b)] set of poles are analogous to the double Rayleigh process and sidebands respectively of Ref. [14]. The point where the analogy with Ref. [14] breaks is that state $|J\rangle$ in Fig. 3.7(a) is generically different from $|I\rangle$, and therefore Fig. 3.7(a) is technically not a double Rayleigh process.

Coming back to our calculation, recall from Eq. (3.46) that the quantity we are interested in is Eq. (C.37) multiplied by $\mathcal{F}_1(\omega_{\lambda_1})\mathcal{F}_2(\omega_{\lambda_2})e^{i\omega_{\lambda_1}\tau}$ and integrated over ω_{λ_1} and ω_{λ_2} with the constraint $2\pi\delta\left(E_{FI}+\omega_{\lambda_1}+\omega_{\lambda_2}-2\omega_L\right)$. In this work, we will assume that the filter function $\mathcal{F}_i(\omega)$ is narrow enough to prevent the central peak and sidebands from interfering. In this case, we can expand the above expression around the individual poles of ω_{λ_1} (and similarly, of ω_{λ_2}),

i.e.,

$$\begin{aligned}&\frac{1}{\omega_{\lambda_1}-(2\omega_L-E_{KI}+i0^+)}\frac{1}{\omega_{\lambda_1}-(\omega_L-E_{JI}+i0^+)}\\ \approx&\frac{1}{\omega_L-U}\left[\frac{1}{\omega_{\lambda_1}-(\omega_L-E_{JI}+i0^+)}-\frac{1}{\omega_{\lambda_1}-(2\omega_L-E_{KI}+i0^+)}\right].\end{aligned}\tag{C.38}$$

The upshot is that we only need to look at Eq. (C.37) around the two poles, corresponding to either the central peak or the sidebands. With this understanding, we can write $\hat{R}^{(2)}_{\lambda_1,\lambda_2}\Big|_{a+b}$ as a sum of two terms: $\hat{R}^{(2)}_{\lambda_1,\lambda_2}\Big|_a$ and $\hat{R}^{(2)}_{\lambda_1,\lambda_2}\Big|_b$, near the first and second pole respectively. Let us look at them one by one.

C.3.1.1 Process in Fig. 3.7(a)

Since $\hat{R}^{(2)}_{\lambda_1,\lambda_2}\Big|_a$ is evaluated near $\omega_{\lambda_1}=\omega_L-E_{JI}$, the factor $[\omega_{\lambda_1}-(2\omega_L-E_{KI}+i0^+)]^{-1}$ becomes $[E_{KI}-\omega_L]^{-1}$. This can be approximated as $(U-\omega_L)^{-1}$. Then, the dependence on E_K drops out and we can replace $\sum_K|K\rangle\langle K|$ by the identity operator. Then, following the same reasoning explained in the paragraph below Eq. (C.33), we can simplify the fermionic terms into a spin singlet projection operator. Doing so, we get

$$\begin{aligned}\langle F|\hat{R}^{(2)}_{\lambda_1,\lambda_2}\Big|_a|I\rangle=&\frac{-g_L^2g^2}{(\omega_L-U)^2}\sum_{\substack{(\mathbf{r}_1,\boldsymbol{\mu}_1)\\(\mathbf{r}_2,\boldsymbol{\mu}_2)}}|\mathtt{t}_{\mathbf{r}_2,\mathbf{r}_2+\boldsymbol{\mu}_2}|^2|\mathtt{t}_{\mathbf{r}_1,\mathbf{r}_1+\boldsymbol{\mu}_1}|^2\\ \times\sum_J\Big\{\Big\{&\frac{1}{\omega_{\lambda_1}-(\omega_L-E_{JI}+i0^+)}\\ \times\langle F|&\left(4\hat{\mathbf{S}}_{\mathbf{r}_2}\cdot\hat{\mathbf{S}}_{\mathbf{r}_2+\boldsymbol{\mu}_2}-1\right)(\bar{\boldsymbol{\mu}}_2\cdot\mathbf{e}_L)\left(\bar{\boldsymbol{\mu}}_2\cdot\mathbf{e}^*_{\lambda_2}\right)|J\rangle\\ \times\langle J|&\left(4\hat{\mathbf{S}}_{\mathbf{r}_1}\cdot\hat{\mathbf{S}}_{\mathbf{r}_1+\boldsymbol{\mu}_1}-1\right)(\bar{\boldsymbol{\mu}}_1\cdot\mathbf{e}_L)\left(\bar{\boldsymbol{\mu}}_1\cdot\mathbf{e}^*_{\lambda_1}\right)\Big\}|I\rangle+\{\lambda_1\leftrightarrow\lambda_2\}\Big\},\end{aligned}\tag{C.39}$$

where $|J\rangle$ lies in the spin sector. ($|I\rangle$ and $|F\rangle$ lie in the spin sector, as usual.) As anticipated in Sec. 3.5.2, the process in Fig. 3.7(a) involves operators entirely in the spin sector.

C.3.1.2 Process in Fig. 3.7(b)

Along similar lines, one can simplify $\hat{R}^{(2)}_{\lambda_1,\lambda_2}\Big|_b$, which is evaluated near $\omega_{\lambda_1} = 2\omega_L - E_{KI}$. As we would expect, this time, it is not possible to rewrite all the fermionic operators in terms of spins. Instead, we get

$$\begin{aligned}\langle F|\hat{R}^{(2)}_{\lambda_1,\lambda_2}\Big|_b|I\rangle = \sum_K \sum_{(\mathbf{r}_1,\boldsymbol{\mu}_1)} \Bigg\{ & -\frac{g_L^2 g^2 |\mathtt{t}_{\mathbf{r}_1,\mathbf{r}_1+\boldsymbol{\mu}_1}|^2}{(\omega_L - U)^2} \\ & \times \frac{\langle F|\sum_{\boldsymbol{\mu}_2} \left(\bar{\boldsymbol{\mu}}_2 \cdot \mathbf{e}^*_{\lambda_2}\right) \hat{\mathcal{J}}_{\boldsymbol{\mu}_2}|K\rangle \langle K| \sum_{\boldsymbol{\mu}'_2} \left(\bar{\boldsymbol{\mu}}'_2 \cdot \mathbf{e}_L\right) \hat{\mathcal{J}}_{\boldsymbol{\mu}'_2}}{\omega_{\lambda_1} - (2\omega_L - E_{KI} + i0^+)} \\ & \times \left(4\hat{\mathbf{S}}_{\mathbf{r}_1} \cdot \hat{\mathbf{S}}_{\mathbf{r}_1+\boldsymbol{\mu}_1} - 1\right) \left(\bar{\boldsymbol{\mu}}_1 \cdot \mathbf{e}_L\right) \left(\bar{\boldsymbol{\mu}}_1 \cdot \mathbf{e}^*_{\lambda_1}\right) \Bigg\} |I\rangle + \{\lambda_1 \leftrightarrow \lambda_2\}\,,\end{aligned} \tag{C.40}$$

where $|K\rangle$ is an energy eigenstate in the single doublon-hole sector. ($|I\rangle$ and $|F\rangle$ lie in the spin sector, as usual.) Therefore, the process in Fig. 3.7(b) necessarily includes operators in the charge sector.

C.3.2 Process in Fig. 3.7(c)

We show this process pictorially in Fig. 3.8(c_1-c_6'). This process, whose energy level schematic is in Fig. 3.7(c), arises from the term $\hat{V}_P^+ \hat{\mathbb{G}}_0 \hat{V}_P^+ \hat{\mathbb{G}}_0 \hat{V}_P^- \hat{\mathbb{G}}_0 \hat{V}_P^-$. Expanding it out,

$$\begin{aligned}
&\hat{V}_P^+ \hat{\mathbb{G}}_0 \hat{V}_P^+ \hat{\mathbb{G}}_0 \hat{V}_P^- \hat{\mathbb{G}}_0 \hat{V}_P^- \\
&= g^4 \sum_{\boldsymbol{\mu}_1, \boldsymbol{\mu}_1', \boldsymbol{\mu}_2, \boldsymbol{\mu}_2'} \left(\bar{\boldsymbol{\mu}}_1' \cdot \mathbf{e}_L\right) \left(\bar{\boldsymbol{\mu}}_2' \cdot \mathbf{e}_L\right) \hat{a}_L^2 \\
&\times \sum_{\substack{\lambda_1, \lambda_2 \\ K, \tilde{J}, K', F}} \left\{ \frac{\hat{a}_{\lambda_2}^\dagger \hat{a}_{\lambda_1}^\dagger \left(\bar{\boldsymbol{\mu}}_1 \cdot \mathbf{e}_{\lambda_1}^*\right) \left(\bar{\boldsymbol{\mu}}_2 \cdot \mathbf{e}_{\lambda_2}^*\right)}{\omega_L - E_{K'I} + i0^+} \right. \\
&\left. \times \frac{|F\rangle\langle F| \hat{\mathcal{J}}_{\boldsymbol{\mu}_2} |K\rangle\langle K| \hat{\mathcal{J}}_{\boldsymbol{\mu}_1} \left|\tilde{J}\right\rangle\left\langle\tilde{J}\right| \hat{\mathcal{J}}_{\boldsymbol{\mu}_2'} |K'\rangle\langle K'| \hat{\mathcal{J}}_{\boldsymbol{\mu}_1'}}{\left(2\omega_L - E_{\tilde{J}I} + i0^+\right) \left(2\omega_L - E_{KI} - \omega_{\lambda_1} + i0^+\right)} \right\},
\end{aligned} \tag{C.41}$$

where $|K'\rangle$ and $|K\rangle$ are in the single doublon-hole sector, $\left|\tilde{J}\right\rangle$ is in the two doublon-hole sector, and $|I\rangle$ and $|F\rangle$ are in the spin sector. Like before, $(\omega_L - E_{K'I})^{-1}$ can be approximated as $(\omega_L - U)^{-1}$. Also, $(2\omega_L - E_{\tilde{J}I})^{-1}$ can be approximated as $(2\omega_L - 2U)^{-1}$. Then the dependence

on both $E_{K'}$ and $E_{\tilde{J}}$ drop out. Thus,

$$\begin{aligned}
&\langle F|\hat{R}^{(2)}_{\lambda_1,\lambda_2}\Big|_c|I\rangle = \frac{ig_L^2 g^2}{2\left(\omega_L - U\right)^2} \\
&\times \Bigg\{\sum_K \Bigg[\frac{\langle F|\sum_{\boldsymbol{\mu}_2}\left(\bar{\boldsymbol{\mu}}_2\cdot\mathbf{e}^*_{\lambda_2}\right)\hat{\mathcal{J}}_{\boldsymbol{\mu}_2}|K\rangle\langle K|}{\omega_{\lambda_1} - (2\omega_L - E_{KI} + i0^+)} \\
&\quad\times \sum_{\mathbf{r}_1,\boldsymbol{\mu}_1,\sigma_1}\left(\bar{\boldsymbol{\mu}}_1\cdot\mathbf{e}^*_{\lambda_1}\right)\left(\mathtt{t}_{\mathbf{r}_1,\mathbf{r}_1+\boldsymbol{\mu}_1}\hat{c}^\dagger_{\mathbf{r}_1+\boldsymbol{\mu}_1,\sigma_1}\hat{c}_{\mathbf{r}_1\sigma_1} - \text{h.c.}\right)\tilde{\sum}_{\tilde{J}}\left|\tilde{J}\right\rangle\!\left\langle\tilde{J}\right| \\
&\quad\times \sum_{\substack{\mathbf{r}'_2,\boldsymbol{\mu}'_2,\\ \sigma'_2}}\left(\bar{\boldsymbol{\mu}}'_2\cdot\mathbf{e}_L\right)\left(\mathtt{t}_{\mathbf{r}'_2,\mathbf{r}'_2+\boldsymbol{\mu}'_2}\hat{c}^\dagger_{\mathbf{r}'_2+\boldsymbol{\mu}'_2,\sigma'_2}\hat{c}_{\mathbf{r}'_2\sigma'_2} - \text{h.c.}\right) \\
&\times \sum_{\substack{(\mathbf{r}'_1,\boldsymbol{\mu}'_1),\\ \sigma'_1}}\left(\bar{\boldsymbol{\mu}}'_1\cdot\mathbf{e}_L\right)\left(\mathtt{t}_{\mathbf{r}'_1,\mathbf{r}'_1+\boldsymbol{\mu}'_1}\hat{c}^\dagger_{\mathbf{r}'_1+\boldsymbol{\mu}'_1,\sigma'_1}\hat{c}_{\mathbf{r}'_1\sigma'_1} - \text{h.c.}\right)|I\rangle\Bigg] + [\lambda_1 \leftrightarrow \lambda_2]\Bigg\},
\end{aligned} \tag{C.42}$$

where $\tilde{\sum}_{\tilde{J}}\left|\tilde{J}\right\rangle\!\left\langle\tilde{J}\right|$ is a projector onto the sector with two doublons and two holes. Consider the first three hops – the first one along bond $(\mathbf{r}'_1, \boldsymbol{\mu}'_1)$, the second one along bond $(\mathbf{r}'_2, \boldsymbol{\mu}'_2)$, and the third along $(\mathbf{r}_1, \boldsymbol{\mu}_1)$. At the end of the second hop, there are two doublons and two holes. At the end of the third hop, there is one doublon and one hole. This can only happen in the two qualitatively distinct ways shown in Fig. C.2 and Fig. C.3. First, in Fig. C.2, the third hop annihilates the doublon-hole pair created in either the first hop or the second hop.

In contrast, in the process shown in Fig. C.3, the two doublon-hole pairs created by the first two hops are on neighbouring bonds. The third hop then annihilates a doublon-hole pair, not along either of the previous two bonds, but instead along the bond connecting the first two hops.

Let us analyze the process in Fig. C.2 first. Here, the bond $(\mathbf{r}_1, \boldsymbol{\mu}_1)$ is identical to either $(\mathbf{r}'_1, \boldsymbol{\mu}'_1)$ [Fig. C.2(e)] or $(\mathbf{r}'_2, \boldsymbol{\mu}'_2)$ [Fig. C.2 (d)]. Let us go with the former first. In this case, the bond $(\mathbf{r}'_2, \boldsymbol{\mu}'_2)$ corresponding to the second hop should share no site in common with the bond

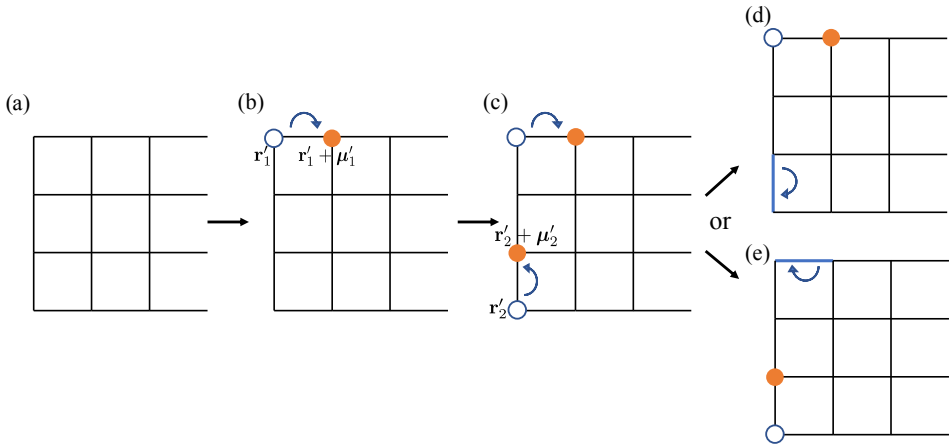

Figure C.2: First class of processes contributing to Fig. 3.7(c). For figures in this paper, an empty circle denotes a hole at the lattice site and a filled circle denotes a doublon. The absence of any circle denotes a spin (whose state is left unspecified). We use a curved blue arrow to denote an electron hopping from the tail to the head of the arrow. The configuration shown in each figure is the *result* of such a hop shown by the arrow on the *same* figure. Here, we show a square lattice for concreteness. But our results hold for any lattice. We suppose $\boldsymbol{\mu}'_1$ and $\boldsymbol{\mu}'_2$ are in the x and y directions respectively. **(a)**: One starts with a spin state. **(b)**: Through a photon absorption, an electron hops from $\mathbf{r}'_1$ to $\mathbf{r}'_1+\boldsymbol{\mu}'_1$. **(c)**: Through a photon absorption, an electron hops from $\mathbf{r}'_2$ to $\mathbf{r}'_2+\boldsymbol{\mu}'_2$. At this point, there are two doublon-hole pairs as shown. Now there are two choices of doublon-hole pairs to annihilate via a photon emission – either **(d)**: the one created second, or **(e)**: the one created first.

$(\mathbf{r}_1,\boldsymbol{\mu}_1)$. Therefore, we can replace $i\sum_{\mathbf{r}'_2,\sigma'_2}\left(\mathtt{t}_{\mathbf{r}'_2,\mathbf{r}'_2+\boldsymbol{\mu}'_2}\hat{c}^\dagger_{\mathbf{r}'_2+\boldsymbol{\mu}'_2,\sigma'_2}\hat{c}_{\mathbf{r}'_2\sigma'_2}-\text{h.c.}\right)$ by

$$\mathcal{J}_{\boldsymbol{\mu}'_2}-i\sum_{\mathbf{r}'_2,\sigma'_2}\eta^{(\mathbf{r}'_2,\boldsymbol{\mu}'_2)}_{(\mathbf{r}_1,\boldsymbol{\mu}_1)}\left(\mathtt{t}_{\mathbf{r}'_2,\mathbf{r}'_2+\boldsymbol{\mu}'_2}\hat{c}^\dagger_{\mathbf{r}'_2+\boldsymbol{\mu}'_2,\sigma'_2}\hat{c}_{\mathbf{r}'_2\sigma'_2}-\text{h.c.}\right),$$

where the symbol $\eta^{(\mathbf{r}'_2,\boldsymbol{\mu}'_2)}_{(\mathbf{r}_1,\boldsymbol{\mu}_1)}$ is a function of two bonds $(\mathbf{r}_1,\boldsymbol{\mu}_1)$ and $(\mathbf{r}'_2,\boldsymbol{\mu}'_2)$, and was defined in Eq (3.53). Once we enforce this constraint, we can drop the projector to the two doublon-hole sector, $\sum_{\tilde{J}}\left|\tilde{J}\right\rangle\!\left\langle\tilde{J}\right|$ in Eq. (C.42), since the projector is enforced automatically. Now, we can commute the bond $(\mathbf{r}_1,\boldsymbol{\mu}_1)$ to the right in Eq. (C.42) through the bond $(\mathbf{r}'_2,\boldsymbol{\mu}'_2)$. Then the resulting expression has the currents through two identical bonds next to each other, and we replace it with $\left|\mathtt{t}_{\mathbf{r}_1,\mathbf{r}_1+\boldsymbol{\mu}_1}\right|^2(\bar{\boldsymbol{\mu}}_1\cdot\mathbf{e}_L)\left(\bar{\boldsymbol{\mu}}_1\cdot\mathbf{e}^*_{\lambda_1}\right)\left(4\hat{\mathbf{S}}_{\mathbf{r}_1}\cdot\hat{\mathbf{S}}_{\mathbf{r}_1+\boldsymbol{\mu}_1}-1\right)$. It is easy to see that the second option

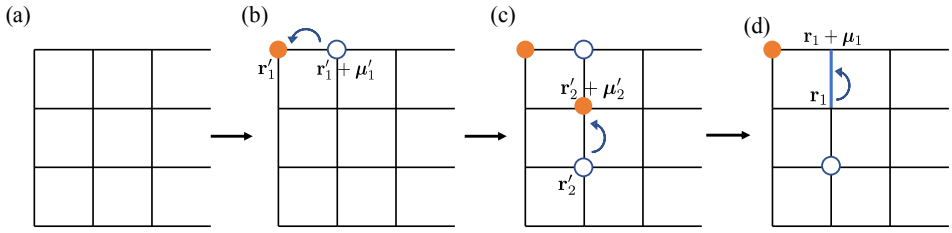

Figure C.3: Second class of processes contributing to Fig. 3.7(c). Here, the doublon-hole pair that is annihilated differs from either of the two pairs that were created, but is instead made of one hole and one doublon from each pair. For this to be possible, the two bonds along which the doublon-hole pairs were created should be connected to each other by another bond. **(a)**: Spin state. **(b)**: Creation of first doublon-hole pair. **(c)**: Creation of second doublon-hole pair. **(d)**: Annihilation of a doublon-hole pair.

[Fig. C.2 (d)] gives the same result. Let us denote the sum of contributions shown in Fig. C.2 (d) and Fig. C.2 (e) by $\langle F|\hat{R}^{(2)}_{\lambda_1,\lambda_2}\Big|_{c_1}|I\rangle$. It thus equals

$$\begin{aligned}
&\langle F|\hat{R}^{(2)}_{\lambda_1,\lambda_2}\Big|_{c_1}|I\rangle = \frac{g_L^2 g^2}{(\omega_L-U)^2} \\
&\times\Bigg\{\sum_K\Bigg\{\frac{\langle F|\sum_{\boldsymbol{\mu}_2}\left(\bar{\boldsymbol{\mu}}_2\cdot\mathbf{e}^*_{\lambda_2}\right)\hat{\mathcal{J}}_{\boldsymbol{\mu}_2}|K\rangle\langle K|}{\omega_{\lambda_1}-(2\omega_L-E_{KI}+i0^+)} \\
&\times\sum_{\mathbf{r}_1,\boldsymbol{\mu}_1}\Bigg[\sum_{\boldsymbol{\mu}'_2}\left(\bar{\boldsymbol{\mu}}'_2\cdot\mathbf{e}_L\right)\left(\mathcal{J}_{\boldsymbol{\mu}'_2}-\hat{\mathcal{K}}_{\boldsymbol{\mu}'_2}(\mathbf{r}_1,\boldsymbol{\mu}_1)\right)|\mathtt{t}_{\mathbf{r}_1,\mathbf{r}_1+\boldsymbol{\mu}_1}|^2 \\
&\quad\times\left(4\hat{\mathbf{S}}_{\mathbf{r}_1}\cdot\hat{\mathbf{S}}_{\mathbf{r}_1+\boldsymbol{\mu}_1}-1\right)\left(\bar{\boldsymbol{\mu}}_1\cdot\mathbf{e}_L\right)\left(\bar{\boldsymbol{\mu}}_1\cdot\mathbf{e}^*_{\lambda_1}\right)\Bigg]\Bigg\}|I\rangle+\{\lambda_1\leftrightarrow\lambda_2\}\Bigg\},
\end{aligned} \tag{C.43}$$

where $\hat{\mathcal{K}}_{\boldsymbol{\mu}'_2}(\mathbf{r}_1,\boldsymbol{\mu}_1)$ is a Hermitian local operator supported near the bond $(\mathbf{r}_1,\boldsymbol{\mu}_1)$ in a way that depends on the direction $\boldsymbol{\mu}'_2$. It was defined in Eq. (3.52) and shown pictorially in Fig. 3.9.

If we now re-examine Eq. (C.40), we find that it actually gets cancelled by part of Eq. (C.43).

Therefore,

$$\begin{aligned}
&\langle F|\hat{R}^{(2)}_{\lambda_1,\lambda_2}\Big|_b + \hat{R}^{(2)}_{\lambda_1,\lambda_2}\Big|_{c_1}|I\rangle = \frac{-g_L^2 g^2}{(\omega_L - U)^2} \\
&\times \Bigg\{\sum_K \Bigg\{ \frac{\sum_{\boldsymbol{\mu}_2}\left(\bar{\boldsymbol{\mu}}_2\cdot\mathbf{e}^*_{\lambda_2}\right)\langle F|\,\hat{\mathcal{J}}_{\boldsymbol{\mu}_2}\,|K\rangle\langle K|}{\omega_{\lambda_1} - (2\omega_L - E_{KI} + i0^+)} \\
&\times \sum_{\mathbf{r}_1,\boldsymbol{\mu}_1}\Bigg[\sum_{\boldsymbol{\mu}'_2}\left(\bar{\boldsymbol{\mu}}'_2\cdot\mathbf{e}_L\right)\hat{\mathcal{K}}_{\boldsymbol{\mu}'_2}\left(\mathbf{r}_1,\boldsymbol{\mu}_1\right)\left(4\hat{\mathbf{S}}_{\mathbf{r}_1}\cdot\hat{\mathbf{S}}_{\mathbf{r}_1+\boldsymbol{\mu}_1} - 1\right) \\
&\times \left|\mathtt{t}_{\mathbf{r}_1,\mathbf{r}_1+\boldsymbol{\mu}_1}\right|^2\left(\bar{\boldsymbol{\mu}}_1\cdot\mathbf{e}_L\right)\left(\bar{\boldsymbol{\mu}}_1\cdot\mathbf{e}^*_{\lambda_1}\right)\Bigg]\Bigg\}|I\rangle + \{\lambda_1\leftrightarrow\lambda_2\}\Bigg\}.
\end{aligned} \tag{C.44}$$

Now, let us consider the contribution from the process shown in Fig. C.3 to Eq. (C.42), that we will denote by $\langle F|\hat{R}^{(2)}_{\lambda_1,\lambda_2}\Big|_{c_2}|I\rangle$. In this process, the bonds $(\mathbf{r}'_2,\boldsymbol{\mu}'_2)$, $(\mathbf{r}_1,\boldsymbol{\mu}_1)$ and $(\mathbf{r}'_1,\boldsymbol{\mu}'_1)$ form a train, when put together successively (see Fig. C.3(d)). The result of this process is a back-and-forth hopping of an electron across the bond $(\mathbf{r}_1,\boldsymbol{\mu}_1)$ as well as the transport of an electron from $\mathbf{r}'_2$ to $\mathbf{r}'_1$ or vice-versa. Thus, the resulting operator only involves spin (and is not charged) at sites $\mathbf{r}_1$ and $\mathbf{r}_1+\boldsymbol{\mu}_1$, but involves charged operators at sites adjacent to the bond $(\mathbf{r}_1,\boldsymbol{\mu}_1)$. Simplifying Eq. (C.42) for this process, we get

$$\begin{aligned}
&\langle F|\hat{R}^{(2)}_{\lambda_1,\lambda_2}\Big|_{c_2}|I\rangle = -\frac{g_L^2 g^2}{(\omega_L - U)^2} \\
&\times \Bigg\{\sum_K \Bigg\{ \frac{\sum_{\boldsymbol{\mu}_2}\left(\bar{\boldsymbol{\mu}}_2\cdot\mathbf{e}^*_{\lambda_2}\right)\langle F|\,\hat{\mathcal{J}}_{\boldsymbol{\mu}_2}\,|K\rangle\langle K|}{\omega_{\lambda_1} - (2\omega_L - E_{KI} + i0^+)} \\
&\times \sum_{(\mathbf{r}_1,\boldsymbol{\mu}_1),\boldsymbol{\mu}'_1,\boldsymbol{\mu}'_2}\Bigg[\left(\bar{\boldsymbol{\mu}}_1\cdot\mathbf{e}^*_{\lambda_1}\right)\left(\bar{\boldsymbol{\mu}}'_1\cdot\mathbf{e}_L\right)\left(\bar{\boldsymbol{\mu}}'_2\cdot\mathbf{e}_L\right) \\
&\times \Bigg(i\hat{\boldsymbol{\mathcal{S}}}_{\boldsymbol{\mu}'_1,\boldsymbol{\mu}'_2}(\mathbf{r}_1,\boldsymbol{\mu}_1)\cdot\left(\frac{\hat{\mathbf{S}}_{\mathbf{r}_1} - \hat{\mathbf{S}}_{\mathbf{r}_1+\boldsymbol{\mu}_1}}{2} - i\hat{\mathbf{S}}_{\mathbf{r}_1}\times\hat{\mathbf{S}}_{\mathbf{r}_1+\boldsymbol{\mu}_1}\right) \\
&+ \hat{\mathcal{C}}_{\boldsymbol{\mu}'_1,\boldsymbol{\mu}'_2}(\mathbf{r}_1,\boldsymbol{\mu}_1)\left(\hat{\mathbf{S}}_{\mathbf{r}_1}\cdot\hat{\mathbf{S}}_{\mathbf{r}_1+\boldsymbol{\mu}_1} - \frac{1}{4}\right)\Bigg)\Bigg]\Bigg\}|I\rangle + \{\lambda_1\leftrightarrow\lambda_2\}\Bigg\},
\end{aligned} \tag{C.45}$$

where $\hat{\boldsymbol{\mathcal{S}}}_{\boldsymbol{\mu}'_1,\boldsymbol{\mu}'_2}(\mathbf{r}_1,\boldsymbol{\mu}_1)$ and $\hat{\mathcal{C}}_{\boldsymbol{\mu}'_1,\boldsymbol{\mu}'_2}(\mathbf{r}_1,\boldsymbol{\mu}_1)$ are operators that result in tunneling of charge from one

site adjacent to the bond $(\mathbf{r}_1, \boldsymbol{\mu}_1)$ to another adjacent to the same bond, for example, from the empty circle to the filled circle in Fig. C.3(d). These operators were defined in Eq. (3.56) and Eq. (3.57), and shown pictorially in Fig. 3.10.

Both of the above operators are symmetric under exchanging the bond directions $\boldsymbol{\mu}_1'$ with $\boldsymbol{\mu}_2'$. Under reversing the orientation of the bond $(\mathbf{r}_1, \boldsymbol{\mu}_1)$, i.e., by replacing it with $(\mathbf{r}_1 + \boldsymbol{\mu}_1, -\boldsymbol{\mu}_1)$, the operator $\hat{\boldsymbol{\mathcal{S}}}_{\boldsymbol{\mu}_1', \boldsymbol{\mu}_2'}(\mathbf{r}_1, \boldsymbol{\mu}_1)$ remains invariant, while $\hat{\mathcal{C}}_{\boldsymbol{\mu}_1', \boldsymbol{\mu}_2'}(\mathbf{r}_1, \boldsymbol{\mu}_1)$ flips sign, as is needed for consistency of Eq. (C.45). Also, note that $\hat{\boldsymbol{\mathcal{S}}}_{\boldsymbol{\mu}_1', \boldsymbol{\mu}_2'}(\mathbf{r}_1, \boldsymbol{\mu}_1)$ and $\hat{\mathcal{C}}_{\boldsymbol{\mu}_1', \boldsymbol{\mu}_2'}(\mathbf{r}_1, \boldsymbol{\mu}_1)$ transform as spin triplet and spin singlet respectively under spin rotation.

C.3.3 Process in Fig. 3.7(d): Diamagnetic term

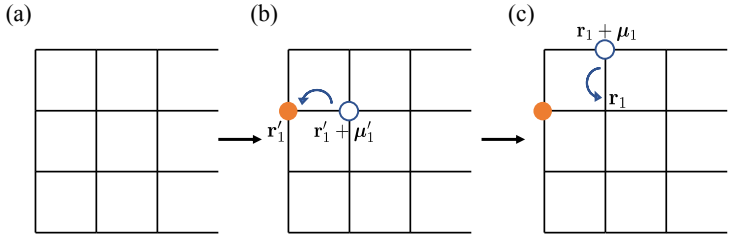

Figure C.4: **(a)**: Spin state. **(b)**: First doublon-hole pair is created via the paramagnetic term. **(c)**: A hole moves via the diamagnetic term.

Let us now look at $\hat{R}^{(2)}_{\lambda_1,\lambda_2}\Big|_d$, i.e., the contribution from $\hat{V}_P^{+}\hat{\mathbb{G}}_0\hat{V}_D^{+-}\hat{\mathbb{G}}_0\hat{V}_P^{-}$, in other words, the process shown in Fig. 3.7(d). This process involves the diamagnetic term, and is illustrated

pictorially in Fig. 3.8(d_1-d_5). We have,

$$\begin{aligned}
&\langle F|\, \hat{R}^{(2)}_{\lambda_1,\lambda_2}\Big|_d\, |I\rangle = i g_L^2 g^2 \\
&\times \sum_{K,K'} \Bigg\{ \sum_{\boldsymbol{\mu}_2} \left(\bar{\boldsymbol{\mu}}_2 \cdot \mathbf{e}^*_{\lambda_2}\right) \langle F|\, \hat{\mathcal{J}}_{\boldsymbol{\mu}_2}\, |K\rangle\langle K| \\
&\times \sum_{\substack{\mathbf{r}_1,\boldsymbol{\mu}_1,\sigma_1 \\ \mathbf{r}'_1,\boldsymbol{\mu}'_1,\sigma'_1}} \frac{\left(\bar{\boldsymbol{\mu}}'_1 \cdot \mathbf{e}_L\right)\left(\bar{\boldsymbol{\mu}}_1 \cdot \mathbf{e}_L\right)\left(\bar{\boldsymbol{\mu}}_1 \cdot \mathbf{e}^*_{\lambda_1}\right)}{\left(\omega_L - E_{K'I} + i0^+\right)\left(2\omega_L - E_{KI} - \omega_{\lambda_1} + i0^+\right)} \\
&\times \left(\mathtt{t}_{\mathbf{r}_1,\mathbf{r}_1+\boldsymbol{\mu}_1}\, \hat{c}^\dagger_{\mathbf{r}_1+\boldsymbol{\mu}_1,\sigma_1}\, \hat{c}_{\mathbf{r}_1,\sigma_1} + \text{h.c.}\right) |K'\rangle\langle K'| \\
&\times \left(\mathtt{t}_{\mathbf{r}'_1,\mathbf{r}'_1+\boldsymbol{\mu}'_1}\, \hat{c}^\dagger_{\mathbf{r}'_1+\boldsymbol{\mu}'_1,\sigma'_1}\, \hat{c}_{\mathbf{r}'_1,\sigma'_1} - \text{h.c.}\right) |I\rangle + \Big[\lambda_1 \leftrightarrow \lambda_2\Big] \Bigg\}.
\end{aligned} \tag{C.46}$$

Here, $|K'\rangle$ and $|K\rangle$ are in the single doublon-hole sector, and $|I\rangle$ and $|F\rangle$ are in the spin sector. Like before, $(\omega_L - E_{K'I})^{-1}$ can be approximated as $(\omega_L - U)^{-1}$. The pattern of electron hopping in this process is depicted in Fig. C.4.

To ensure that the state $|K\rangle$ remains in the single doublon-hole subspace, the process leading from Fig. C.4(b) to (c) should be just a hopping of a doublon or a hole, and should not result in the formation of an additional doublon-hole pair. Therefore, the bonds $(\mathbf{r}_1, \boldsymbol{\mu}_1)$ and $(\mathbf{r}'_1, \boldsymbol{\mu}'_1)$ should have exactly one site in common. Therefore, either $\mathbf{r}'_1 = \mathbf{r}_1$ or $\mathbf{r}'_1 = \mathbf{r}_1 - \boldsymbol{\mu}_1$. This allows

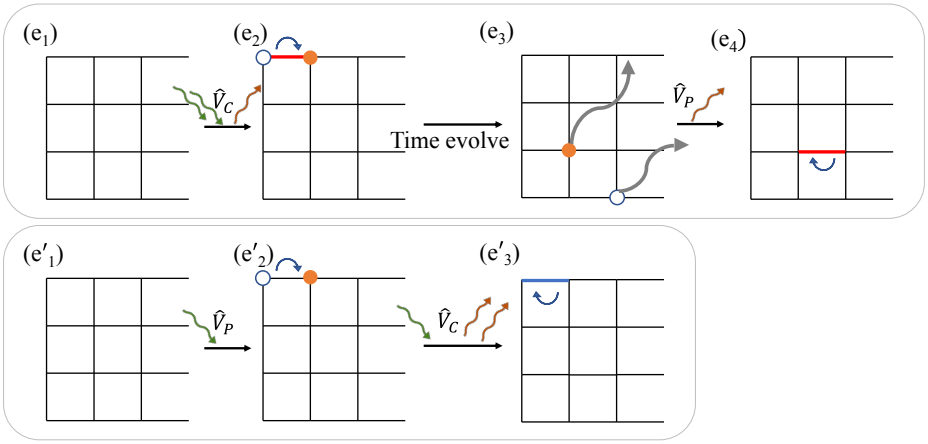

Figure C.5: Microscopic processes involving the cubic term $\hat{V}_C$. This Figure is a continuation of Fig. 3.8, and hence we use (e_j) and (e'_j) as the subfigure indices. ($\mathbf{e}_1$-$\mathbf{e}_4$): Via the $\hat{A}^3$ term, absorption of two photons followed by emission of one results in an electron tunneling across a bond. Then the doublon-hole pair recombines to emit the second photon. This process couples to the charge sector because ($\mathbf{e}'_1$-$\mathbf{e}'_4$): A photon is absorbed via the paramagnetic term leading to off-resonant electron tunneling. Then, two photons are absorbed and one photon is emitted via the $\hat{A}^3$ term resulting in the electron tunneling back.

us to simplify Eq. (C.46) to

$$
\begin{aligned}
\langle F|\, \hat{R}^{(2)}_{\lambda_1,\lambda_2}\Big|_d\, |I\rangle &= \frac{-g_L^2 g^2}{\omega_L - U} \\
\times \Bigg\{ \sum_K \Bigg\{ \sum_{\boldsymbol{\mu}_2} & \frac{\left(\bar{\boldsymbol{\mu}}_2 \cdot \mathbf{e}^*_{\lambda_2}\right) \langle F|\, \hat{\mathcal{J}}_{\boldsymbol{\mu}_2}\, |K\rangle\langle K|}{\omega_{\lambda_1} - (2\omega_L - E_{KI} + i0^+)} \\
& \times \sum_{\mathbf{r},\boldsymbol{\mu}',\boldsymbol{\mu}} \sum_{\substack{s,s'=\pm 1 \\ s\boldsymbol{\mu}\neq s'\boldsymbol{\mu}'}} \Big[\left(s'\bar{\boldsymbol{\mu}}' \cdot \mathbf{e}_L\right) \left(s\bar{\boldsymbol{\mu}} \cdot \mathbf{e}_L\right) \mathbf{e}^*_{\lambda_1} \cdot \\
& \times \Big[\left(s\bar{\boldsymbol{\mu}} - s'\bar{\boldsymbol{\mu}}'\right) \hat{\boldsymbol{\mathcal{J}}}^S_{\mathbf{r},s\boldsymbol{\mu},s'\boldsymbol{\mu}'} \cdot \hat{\mathbf{S}}_{\mathbf{r}} \\
& \quad + \frac{i}{2} \left(s\bar{\boldsymbol{\mu}} + s'\bar{\boldsymbol{\mu}}'\right) \hat{\mathcal{H}}_{\mathbf{r},s\boldsymbol{\mu},s'\boldsymbol{\mu}'} \Big] \Big] \Bigg\} + \{\lambda_1 \leftrightarrow \lambda_2\} \Bigg\}
\end{aligned}
\tag{C.47}
$$

where $\hat{\mathcal{H}}_{\mathbf{r},s\boldsymbol{\mu},s'\boldsymbol{\mu}'}$ and $\hat{\boldsymbol{\mathcal{J}}}^S_{\mathbf{r},s\boldsymbol{\mu},s'\boldsymbol{\mu}'}$ were defined in Eq. (3.58) and (3.59) respectively.

C.3.4 Contribution from the cubic term

Finally, we calculate the contribution from the cubic term $\hat{V}_C$ to the $\hat{\mathcal{T}}$-matrix: $\hat{V}_P\hat{\mathbb{G}}_0\hat{V}_C + \hat{V}_C\hat{\mathbb{G}}_0\hat{V}_P$ (shown in Fig. C.5). First, the contribution from $\hat{V}_P\hat{\mathbb{G}}_0\hat{V}_C$ is:

$$\begin{aligned}\langle F|\,\hat{R}^{(2)}_{\lambda_1,\lambda_2}\Big|_e\,|I\rangle &= \frac{-g_L^2 g^2}{2}\\ &\times\sum_{\boldsymbol{\mu}_1,\boldsymbol{\mu}_2}\Bigg[(\boldsymbol{\mu}_2\cdot\mathbf{e}_L)^2\left(\boldsymbol{\mu}_1\cdot\mathbf{e}^*_{\lambda_1}\right)\left(\boldsymbol{\mu}_2\cdot\mathbf{e}^*_{\lambda_2}\right)\\ &\qquad\times\frac{\langle F|\,\hat{\mathcal{J}}_{\boldsymbol{\mu}_2}\,|K\rangle\,\langle K|\,\hat{\mathcal{J}}_{\boldsymbol{\mu}_1}\,|I\rangle}{2\omega_L - E_{KI} - \omega_{\lambda_1} + i0^+} + [\lambda_1\leftrightarrow\lambda_2]\Bigg].\end{aligned} \tag{C.48}$$

Next, the contribution from $\hat{V}_C\hat{\mathbb{G}}_0\hat{V}_P$ is:

$$\begin{aligned}\langle F|\,\hat{R}^{(2)}_{\lambda_1,\lambda_2}\Big|_{e'}\,|I\rangle &= \frac{g_L^2 g^2}{\omega_L - U}\\ &\times\sum_{(\mathbf{r},\boldsymbol{\mu})}(\bar{\boldsymbol{\mu}}\cdot\mathbf{e}_L)^2\left(\bar{\boldsymbol{\mu}}\cdot\mathbf{e}^*_{\lambda_1}\right)\left(\bar{\boldsymbol{\mu}}\cdot\mathbf{e}^*_{\lambda_2}\right)|\mathtt{t}_{\mathbf{r},\mathbf{r}+\boldsymbol{\mu}}|^2\left(4\hat{\mathbf{S}}_{\mathbf{r}}\cdot\hat{\mathbf{S}}_{\mathbf{r}+\boldsymbol{\mu}} - 1\right).\end{aligned} \tag{C.49}$$

C.3.5 Consolidating all contributions

After all the simplifications in the previous subsection, we are now ready to write an expression for the total two-photon amplitude

$$\begin{aligned}\langle F|\hat{R}^{(2)}_{\lambda_1,\lambda_2}|I\rangle = &\langle F|\,\hat{R}^{(2)}_{\lambda_1,\lambda_2}\Big|_a\,|I\rangle + \langle F|\,\hat{R}^{(2)}_{\lambda_1,\lambda_2}\Big|_b\,|I\rangle\\ &+\langle F|\,\hat{R}^{(2)}_{\lambda_1,\lambda_2}\Big|_c\,|I\rangle + \langle F|\,\hat{R}^{(2)}_{\lambda_1,\lambda_2}\Big|_d\,|I\rangle + \langle F|\,\hat{R}^{(2)}_{\lambda_1,\lambda_2}\Big|_e\,|I\rangle + \langle F|\,\hat{R}^{(2)}_{\lambda_1,\lambda_2}\Big|_{e'}\,|I\rangle.\end{aligned} \tag{C.50}$$

The result leads to Eq. (3.65) in the main text. We discuss below the corrections to Eq. (3.65) due to Eq. (C.49).

$$
\begin{aligned}
&\langle F|\hat{R}^{(2)}_{\lambda_1,\lambda_2}|I\rangle \\
&= -i\int_{-\infty}^{\infty} \mathrm{d}t\, e^{-i(\omega_{\lambda_1}-\omega_L)t}\,\langle F|\mathbb{T}\left[\hat{A}_2(0)\hat{A}_1(-t)\right]|I\rangle \\
&- i\int_{-\infty}^{\infty} \mathrm{d}t\,\langle F|\Big[\theta(t)e^{-i\left(\omega_{\lambda_1}-2\omega_L\right)t}\hat{C}_2(0)\hat{B}_1(-t) \\
&\qquad\qquad +\theta(-t)e^{-i\omega_{\lambda_1}t}\hat{C}_1(-t)\hat{B}_2(0)\Big]\,|I\rangle \\
&+ \frac{1}{\omega_L - U}\,\langle F|\,\hat{D}_{12}\,|I\rangle\,,
\end{aligned}
\tag{C.51}
$$

where $\hat{D}_{12}$ is given by:

$$
\hat{D}_{12} = \sum_{(\mathbf{r},\boldsymbol{\mu})} \left(\mathbf{e}_L\cdot\bar{\boldsymbol{\mu}}\right)^2 \left(\mathbf{e}_1^*\cdot\bar{\boldsymbol{\mu}}\right)\left(\mathbf{e}_2^*\cdot\bar{\boldsymbol{\mu}}\right)\left|\mathtt{t}_{\mathbf{r},\mathbf{r}+\boldsymbol{\mu}}\right|^2\left(4\hat{\mathbf{S}}_{\mathbf{r}}\cdot\hat{\mathbf{S}}_{\mathbf{r}+\boldsymbol{\mu}}-1\right). \tag{C.52}
$$

This contribution arises from the $\hat{A}^3_{\mathbf{r},\mathbf{r}'}$ term in light-matter interactions depicted in Fig. C.5(e_1'-e_4'). $\hat{D}_{12}$ is a pure spin operator, and is hence gauge-invariant. Thus, $\hat{D}_{12}$ is not needed to maintain gauge-invariance of the remaining terms in Eq. (3.66). We now note that the dependence of $\hat{D}_{12}$ on polarizations is fine-tuned, and hence by choosing appropriate polarization channels, the contribution from $\hat{D}_{12}$ can be eliminated. Therefore, in this work, we drop $\hat{D}_{12}$ since it does not affect our main results. Developing a careful understanding of $\hat{D}_{12}$ is a direction for future work.

Thus, Eq. (3.65), combined with the definitions in Eq. (3.60),(3.62) and (3.61), gives the amplitude to find two photons – one in mode λ_1 and another in mode λ_2, entirely in terms of the matrix elements of matter operators between initial matter eigenstate $|I\rangle$ and final matter eigenstate $|F\rangle$. Now, we would like to get rid of the explicit dependence on the intermediate states $|J\rangle$ and $|K\rangle$ in Eq. (3.65). To do so, we use the following identity (for some ω and ω_0): $\frac{1}{\omega-\omega_0-i0^+} = i\int_{-\infty}^{\infty}\mathrm{d}t\,\theta(t)e^{-i(\omega-\omega_0-i0^+)t}$, where $\theta(t)$ is a step function that is 1 for $t > 0$ and

0 otherwise. By using the constraint $\omega_{\lambda_2} = 2\omega_L - \omega_{\lambda_1} - E_{FI}$, Eq. (3.65) can be viewed as a function of only one frequency ω_{λ_1}. We then use the above identity to trade the denominators in Eq. (3.65) in favor of the t-dependent phases. Now, these phases can be absorbed into the Heisenberg evolution of the operators $\hat{A}_j$ and $\hat{B}_j$ (defined as $\hat{A}_j(t) = e^{i\hat{H}_0 t}\hat{A}_j e^{-i\hat{H}_0 t}$). This allows us to rewrite Eq. (3.65) as Eq. (3.66) in the main text.

C.4 Details of measuring phase-sensitive quadrature correlations and Conditional $G^{(1)}$

C.4.1 Time-averaging phase-sensitive quadrature measurements

In Table 3.1 of the main text, we presented phase-sensitive quadrature correlations $\langle \hat{a}_{d_j}(0)\rangle\, e^{i\theta}+$ c.c. and $\langle \hat{a}_{d_2}(\tau)\hat{a}_{d_1}(0)\rangle\, e^{i\theta}+$c.c. In Sec. 3.3.2 and Fig. 3.4 of the main text, we described a setup to measure these. In this Appendix, we address the t-dependence of Eq. (3.21) and Eq. (3.26) of the Main Text. Our goal here is to extract a t-independent piece from them, because fast-oscillating quantities cannot be robustly measured experimentally. Further, we should justify why the matter correlators in Table 3.1 do not depend on t. We do so by time-averaging Eq. (3.21) and Eq. (3.26) over a long time. First, let us consider Eq. (3.21).

$$\begin{aligned}
&\lim_{T\to\infty}\frac{1}{T}\int_{-T/2}^{T/2} \mathrm{d}t\,\left[G^{(1)}_{d_j;+}(\theta;0;t) - G^{(1)}_{d_j;-}(\theta;0;t)\right] \\
&= \lim_{T\to\infty}\frac{1}{T}\int_{-T/2}^{T/2} \mathrm{d}t\,\sqrt{\frac{I_{\text{L.O.}}}{2}}\left(\langle \hat{a}_{d_j}(t)\rangle_{\text{out}}\, e^{i(\omega_L t+\theta)} + \text{c.c.}\right).
\end{aligned} \tag{C.53}$$

From the definition of $\hat{a}_{d_j}$ in Eq. (3.9) of the main text, $\hat{a}_{d_j}(t)e^{i\omega_L t}$ is a sum of terms of the form $e^{i(\omega_L-\omega_{\mathbf{k}})t}$, for each mode of momentum $\mathbf{k}$. The long-time average will select only those modes satisfying $\omega_{\mathbf{k}} = \omega_L$, i.e., elastic scattering. This implies that the energy of the material remains unchanged. Independent of this discussion, we concluded in Eq. 3.47 of Sec. 3.4.3 that in the (leading order) process contributing to $\left\langle \hat{a}_{d_j}(0)\right\rangle_{\text{out}}$, the matter sector remains in the same state $|I\rangle$ after scattering, and the scattered photon has frequency ω_L. In this Appendix, we obtain the same condition from time-averaging. Therefore, combining the two discussions, we conclude that to evaluate the time-average in Eq. C.53, one can simply set $t = 0$, thus justifying why we used $t = 0$ in the Main Text [Eq. (3.22)] for the quadrature measurement.

Next, let us consider the time average of Eq. (3.26) to obtain the phase-sensitive second order quadrature correlator. The relevant integral over t here is $\lim_{T\to\infty} \frac{1}{T}\int_{-T/2}^{T/2} \mathrm{d}t\, e^{2i\omega_L t} \left\langle \hat{a}_{d_2}(t+\tau)\hat{a}_{d_1}(t)\right\rangle_{\text{out}}$. Once again, using Eq. (3.9), we see that $e^{2i\omega_L t}\hat{a}_{d_2}(t+\tau)\hat{a}_{d_1}(t)$ is a sum of terms of the form $e^{i(2\omega_L-\omega_{\mathbf{k}_1}-\omega_{\mathbf{k}_2})t}$. The long-time average selects modes satisfying $2\omega_L = \omega_{\mathbf{k}_1} + \omega_{\mathbf{k}_2}$, therefore implying that the energy of the matter state remains unchanged after scattering. This is once again consistent with our independent conclusion in Eq. (3.48) of Sec. 3.4.3, where we considered $\left\langle \hat{a}_{d_2}(\tau)\hat{a}_{d_1}(0)\right\rangle_{\text{out}}$ and showed that the matter state remains unchanged in processes relevant to this correlator. Therefore, the result of setting $t = 0$, (as in Sec. 3.4.3) is identical to performing a long-time average over t, as in Eq. (3.26).

Finally, we note that by setting $\theta_A = \pi/4$ and $\theta_B = -\pi/4$ in Eq. (3.26), one can measure $\mathrm{Im}\left\langle \hat{a}_{d_2}(0)\hat{a}_{d_1}(0)\right\rangle_{\text{out}}$, as desired in Sec. 3.7.

C.4.2 Measuring Conditional $G^{(1)}$

In this section, we provide the details for the experimental scheme shown in Fig. 3.5 of the Main Text to measure $H_{d_1,d_2}(t,\tau) \equiv \langle \hat{a}^\dagger_{d_1}(0)\hat{a}^\dagger_{d_2}(t+\tau)\hat{a}_{d_2}(t)\hat{a}_{d_1}(0)\rangle_{\text{out}} + \text{c.c.}$. One conditions on a photon detection at detector d_1 (shown in orange in Fig. 3.5) at time 0. The second photon is given a time delay t with respect to the first, and is passed through a beamsplitter. One arm of the beam splitter is given an additional time delay τ with respect to the other, and they are mixed again using a second beamsplitter. The detectors at the two output arms of the second beamsplitters are labeled $d_2;+$ and $d_2;-$. We have:

$$\hat{a}_{d_2;+}(t+\tau) = \frac{1}{\sqrt{2}}\left[\hat{a}_{d_2}(t) + \hat{a}_{d_2}(t+\tau)\right], \tag{C.54}$$

$$\hat{a}_{d_2;-}(t+\tau) = \frac{1}{\sqrt{2}}\left[\hat{a}_{d_2}(t) - \hat{a}_{d_2}(t+\tau)\right]. \tag{C.55}$$

The conditional measurement to be made here is a $G^{(2)}(t+\tau)$ measurement between the pair of detectors $(d_1, d_2; +)$ and $(d_1, d_2; -)$. Let us consider:

$$\begin{aligned}
&G^{(2)}_{d_1,d_2;+}(t+\tau) - G^{(2)}_{d_1,d_2;-}(t+\tau) \\
&= \left\langle \hat{a}^\dagger_{d_1}(0)\hat{a}^\dagger_{d_2;+}(t+\tau)\hat{a}_{d_2;+}(t+\tau)\hat{a}_{d_1}(0)\right\rangle_{\text{out}} - \left\langle \hat{a}^\dagger_{d_1}(0)\hat{a}^\dagger_{d_2;-}(t+\tau)\hat{a}_{d_2;-}(t+\tau)\hat{a}_{d_1}(0)\right\rangle_{\text{out}} \\
&= \left\langle \hat{a}^\dagger_{d_1}(0)\hat{a}^\dagger_{d_2}(t+\tau)\hat{a}_{d_2}(t)\hat{a}_{d_1}(0)\right\rangle_{\text{out}} + \text{ c.c.}
\end{aligned} \tag{C.56}$$

Therefore, the above difference measures the desired correlator.

Appendix D: Chapter 4

D.1 Convergence of the perturbation theory

In this appendix, we examine the issue of the convergence of the Taylor expansion of the perturbational energies of the ice FM, ice antiferromagnet and the RK ansatz wavefunctions. We find that the Padé approximants for the perturbational energies of the ice FM, ice antiferromagnet, and the RK ansatz wavefunctions have spurious singularities in the range $0 < \Omega/V < 0.6$ because of the vanishing of the denominators of the Padé approximants. It is known that such singularities can appear in Padé approximants and can be avoided by the Borel-Padé analysis, and the Borel-Padé approximants obtained from it do not have these spurious singularities. We determine the $[m/n]$ Borel-Padé approximant of a series $f(x)$ by the procedure described in Section 3 of Ref. [301] and we explain it briefly here: first, we perform a Borel transform on the series $f(x)$ giving a new series $\mathcal{B}f(x)$. Then, we calculate the $[m/n]$ Padé approximant of $\mathcal{B}f(x)$ which we denote by $P_{[m/n]}(x)$. Finally, we obtain the $[m/n]$ Borel-Padé approximant by calculating the Laplace transform of $P_{[m/n]}(x)$. Here, $m+n$ should be equal to the degree of the truncated Taylor series.

From the perturbation theory calculation of Sec. 4.3.1.4, we have the Taylor series up to sixth order in Ω/V for the energies of the three ansatz states – ice ferromagnet, ice antiferromagnet, and the RK wavefunction. Thus we have $m+n=6$. We have computed the various $[m/n]$

Borel-Padé approximants and plotted them in Figs. D.1 (a)–(c). Based on these plots, we make the following comments:

- Regarding the ice ferromagnet [Fig. D.1(a)]: We find that the [6/0], [5/1], [4/2], and [3/3] Borel-Padé approximants are equal to the Taylor series while the [2/4] and [1/5] Borel-Padé approximants have a lower energy than the Taylor series. At the transition point, $\Omega_C = 0.43927$, the [2/4] approximant differs from the Taylor series by about 17%. If we use the [2/4] approximant instead of the Taylor series for the ice FM to determine the transition point between ice FM and QSL, it shifts from $\Omega_C = 0.43927V$ to $0.44067V$. This change in the location of the transition point is very small, and using the Borel-Padé approximants instead of the Taylor series does not change the phase diagram qualitatively.

- Regarding the ice antiferromagnet [Fig. D.1(b)]: We again find that the [2/4] and [1/5] approximants are equal to each other and are different from the Taylor series. The other Borel-Padé approximants, namely the [6/0], [5/1], [4/2], and [3/3] approximants are equal to the Taylor series. The [2/4] Borel-Padé approximant differs from the Taylor series at the transition point, $\Omega_C = 0.43927V$, by about 20%. This is not a small amount, but even if we assume that the true energy is lower than the perturbation-theory energy (Taylor series) by 20%, ice antiferromagnet continues to remain an excited state and the phase diagram does not change. This is under the assumption that the energies of the ice ferromagnet and the RK wavefunction are given by their Taylor series.

- Regarding the RK wavefunction [Fig. D.1(c)]: We find that the [4/2], [3/3], [2/4], and [1/5] Borel-Padé approximants are positive for all values of $\Omega/V > 0$, and the phase diagram would not have a QSL if we used these approximants as the energy of the RK

wavefunction. However, we believe this is an artifact of the Borel-Padé approximants and is not representative of the underlying physics. To understand our claim, consider the Hamiltonian without $\hat{H}_{\text{LR}}$, i.e., the transverse-field Ising model. We know from Ref. [18] that the ground state is a QSL for $\Omega < 0.55(5)V$. For $\Omega = 0$, all states in the ice manifold including the RK wavefunction are the ground states. For a nonzero but small Ω/V, the quantum fluctuations are present, and we expect them to decrease the energy of the ground state. In Fig. D.1(d), we show the Taylor series obtained from sixth-order perturbation theory and its Borel-Padé approximants for the Hamiltonian without $\hat{H}_{\text{LR}}$. We see that the Taylor series decreases as Ω/V is increased and captures the energy reduction from quantum fluctuations, however the [2/4], [1/5], [4/2], and [3/3] Borel-Padé approximants remain equal to 0. Thus, the [2/4], [1/5], [4/2], and [3/3] Borel-Padé approximants do not capture the physics. This could be because of the structure of the Taylor series—the sixth-order term has a large coefficient as compared to the zeroth-, second-, and fourth-order terms. (The Taylor series for the RK wavefunction with $\hat{H}_{\text{LR}}$ is $0.026 - 0.027(\Omega/V)^2 - 0.098(\Omega/V)^4 - 2.77(\Omega/V)^6$). However, we are not certain about why the [2/4], [1/5], [4/2], and [3/3] approximants do not capture the energy decrease. Thus the only Borel-Padé approximants we may be able to reliably use with the given data are [6/0] and [5/1], which are the same as the Taylor series. We would obtain the same phase diagram if we were to use the [6/0] or [5/1] approximants.

In summary, we find that using the $[6/0]$ and $[5/1]$ Borel-Padé approximants only changes the critical coupling of the transition, but does not change the phase diagram qualitatively.

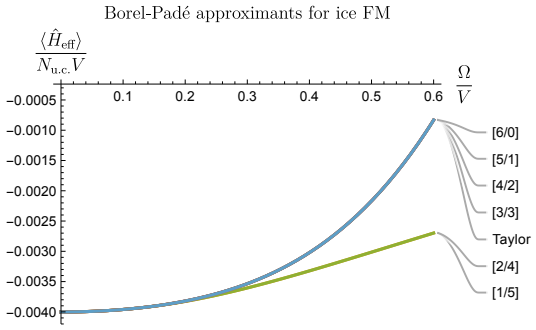

(a) Ice ferromagnet

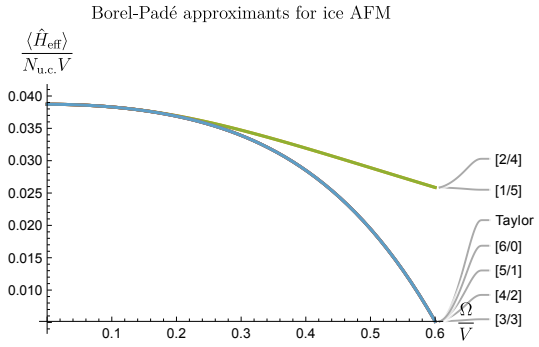

(b) Ice antiferromagnet

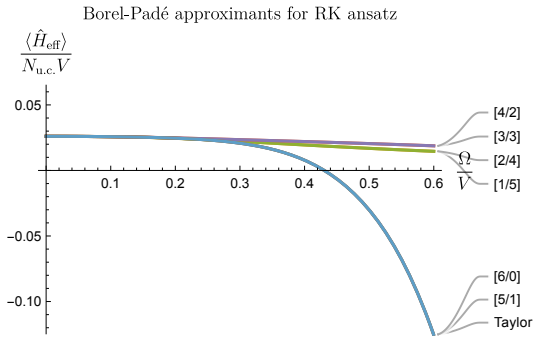

(c) RK wavefunction

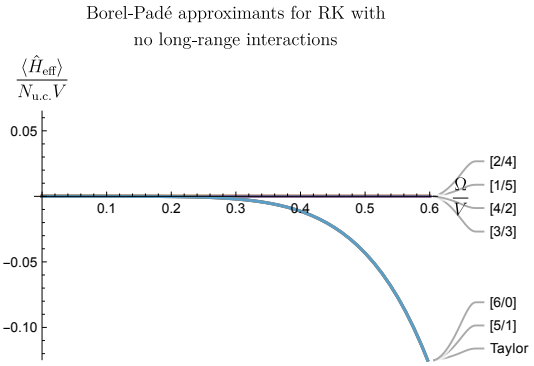

(d) RK wavefunction with long-range interactions turned off

Figure D.1: Sub-figures (a), (b) and (c) show the various Borel-Padé approximants and the Taylor series for the three ansatz states: ice ferromagnet, ice antiferromagnet and the RK wavefunction. Sub-figure (d) shows the Borel-Padé approximants and the Taylor series for the RK wavefunction without the long-range interactions. The curves labelled "Taylor" are the energies of the ansatz states obtained from perturbation theory. The curves labelled by "$[m/n]$" where $m, n \in \{0, 1, ..., 6\}$ such that $m + n = 6$ are the $[m/n]$ Borel-Padé approximants.

D.2 Gauge mean field theory

In this appendix, we first provide details of the gauge mean field theory calculation sketched in Sec. 4.3.2.1, with a focus on capturing the Higgs transition. Then, we attempt to use the same technique in the small-Ω limit to obtain the confinement-deconfinement transition. We find that, in this limit, the technique is fraught with a serious limitation stemming from neglecting gauge fluctuations.

Starting from Eq. (4.45) of Sec. 4.3.2.1 and performing the mean-field decoupling, we get

$$\begin{aligned}
\hat{H}_{\text{MF}} &= \hat{H}_\Phi + \hat{H}_\mathsf{s} + \hat{H}_\text{c}, \text{ where} \\
\hat{H}_\Phi =& \frac{V}{2} \sum_{\mathbf{r}\in A,B} \hat{Q}_\mathbf{r}^2 - \frac{\Omega}{2} \sum_{(\mathbf{r}\in A),\mu} \left(\hat{\Phi}_\mathbf{r}^\dagger \hat{\Phi}_{\mathbf{r}+\mathbf{e}_\mu} \left\langle \hat{\mathsf{s}}^+_{\mathbf{r},\mu} \right\rangle + \text{ H.c.} \right), \\
\hat{H}_\mathsf{s} =& -\frac{\Omega}{2} \sum_{(\mathbf{r}\in A),\mu} \left(\left\langle \hat{\Phi}_\mathbf{r}^\dagger \hat{\Phi}_{\mathbf{r}+\mathbf{e}_\mu} \right\rangle \hat{\mathsf{s}}^+_{\mathbf{r},\mu} + \text{ H.c.} \right) \\
&+ \sum_{(\mathbf{r}\in A),\mu} \hat{\mathsf{s}}^z_{\mathbf{r},\mu} \sum_{(\mathbf{r}'\in A),\nu} \left(V_{\mu\nu}(\mathbf{r}-\mathbf{r}') \left\langle \hat{\mathsf{s}}^z_{\mathbf{r}',\nu} \right\rangle \right), \\
\hat{H}_\text{c} =& \frac{\Omega}{2} \sum_{(\mathbf{r}\in A),\mu} \left(\left\langle \hat{\Phi}_\mathbf{r}^\dagger \hat{\Phi}_{\mathbf{r}+\mathbf{e}_\mu} \right\rangle \left\langle \hat{\mathsf{s}}^+_{\mathbf{r},\mu} \right\rangle + \text{ H.c.} \right) \\
&- \frac{1}{2} \sum_{(\mathbf{r}\in A),\mu} \hat{\mathsf{s}}^z_{\mathbf{r},\mu} \sum_{(\mathbf{r}'\in A),\nu} \left(V_{\mu\nu}(\mathbf{r}-\mathbf{r}') \left\langle \hat{\mathsf{s}}^z_{\mathbf{r}',\nu} \right\rangle \right).
\end{aligned} \tag{D.1}$$

$\hat{H}_\text{c}$ is a constant, and $V_{\mu\nu}(\mathbf{r}-\mathbf{r}')$ was defined in Sec. 4.3.2.1.

$\hat{H}_\mathsf{s}$ above is of the form $-\sum_{(\mathbf{r}\in A),\mu} \left(h^x_{\mathbf{r},\mu} \hat{\mathsf{s}}^x_{\mathbf{r},\mu} + h^z_{\mathbf{r},\mu} \hat{\mathsf{s}}^z_{\mathbf{r},\mu} \right)$, where

$$\begin{aligned}
h^x_{\mathbf{r},\mu} &= \Omega \left\langle \hat{\Phi}_\mathbf{r}^\dagger \hat{\Phi}_{\mathbf{r}+\mathbf{e}_\mu} \right\rangle, \\
h^z_{\mathbf{r},\mu} &= -\sum_{(\mathbf{r}'\in A),\nu} \left(V_{\mu\nu}(\mathbf{r}-\mathbf{r}') \left\langle \hat{\mathsf{s}}^z_{\mathbf{r}',\nu} \right\rangle \right),
\end{aligned} \tag{D.2}$$

and $\left\langle \hat{\Phi}_\mathbf{r}^\dagger \hat{\Phi}_{\mathbf{r}+\mathbf{e}_\mu} \right\rangle$ is calculated in the ground state of $\hat{H}_\Phi$, which in turn depends on $\langle \hat{\mathsf{s}}^+ \rangle$. (We have implicitly assumed here that $\left\langle \hat{\Phi}_\mathbf{r}^\dagger \hat{\Phi}_{\mathbf{r}+\mathbf{e}_\mu} \right\rangle$ is real, which we will show can be assumed self-consistently.) This implies that, in the ground state,

$$\left\langle \hat{\mathsf{s}}^i_{\mathbf{r},\mu} \right\rangle = \frac{h^i_{\mathbf{r},\mu}}{2|\mathbf{h}_{\mathbf{r},\mu}|} \text{ for } i = x, z. \tag{D.3}$$

Our goal is to self-consistently minimize the ground-state energy of the mean-field Hamiltonian

subject to the constraints in Eqs. (4.43) and (4.44). We showed in Sec. 4.3.1.2 that the ordered ground state at $\Omega = 0$ has momentum $\mathbf{k} = \mathbf{0}$. Also, the TFP state in the large-Ω limit is a $\mathbf{k} = \mathbf{0}$ state. So we start with a mean-field ansatz with full translation symmetry (similar to Ref. [272]):

$$\begin{aligned} \left\langle \mathsf{s}^{+}_{\mathbf{r},\mu} \right\rangle &= \frac{1}{2}\cos\theta, \\ \left\langle \mathsf{s}^{z}_{\mathbf{r},\mu} \right\rangle &= \frac{1}{2}\varepsilon_\mu \sin\theta, \end{aligned} \tag{D.4}$$

where $\varepsilon_\mu = 1, 1, -1, -1$ for $\mu = 0, 1, 2, 3$, respectively. To solve the matter sector, it is convenient to deal with the Lagrangian instead of the Hamiltonian. The imaginary-time Lagrangian for the matter sector is

$$\begin{aligned} \mathcal{L} = &\frac{1}{2V}\sum_{\mathbf{r}\in A,B} |(\partial_\tau - i v_{\mathbf{r}})\Phi_{\mathbf{r}}|^2 \\ &- \frac{\Omega\cos\theta}{4}\sum_{(\mathbf{r}\in A),\mu} (\Phi^*_{\mathbf{r}}\Phi_{\mathbf{r}+\mathbf{e}_\mu} e^{i a_{\mathbf{r},\mu}} + \text{ c.c.}) \\ &- i\sum_{\mathbf{r}\in A,B}\left[\eta_{\mathbf{r}} v_{\mathbf{r}}\left(\sum_\mu \mathsf{s}^z_{\mathbf{r}+\eta_{\mathbf{r}}\mathbf{e}_\mu/2}\right) + \tilde{\lambda}_{\mathbf{r}}(|\Phi_{\mathbf{r}}|^2 - 1)\right], \end{aligned} \tag{D.5}$$

where the Lagrange multiplier $\tilde{\lambda}_{\mathbf{r}}$ (which gets integrated over) enforces the constraint $|\Phi_{\mathbf{r}}|^2 = 1$. The Lagrange multiplier $v_{\mathbf{r}}$ enforces the constraint (4.44). To zeroth order, we ignore the gauge fluctuation $a_{\mathbf{r},\mu}$. The matter Lagrangian alone, despite being quadratic in the rotor variables, is nevertheless interacting because a quadratic term in rotor operators is nonlinear in terms of canonical bosons (in other words, it is a cosine term in the phase of the rotor.) In order to make progress, Ref. [272] assumes that, at the saddle point, $\tilde{\lambda}_{\mathbf{r}}$ takes on a spatially uniform and purely imaginary value $i\lambda$, and also implicitly assumes that $v_{\mathbf{r}}$ is 0 at the saddle point. Here, we will follow suit while acknowledging that these approximations are uncontrolled. Making these

simplifications, we obtain

$$\begin{aligned}\mathcal{L} =& \frac{1}{2V}\sum_{\mathbf{r}} |\partial_\tau \Phi_{\mathbf{r}}|^2 - \frac{\Omega\cos\theta}{4}\sum_{(\mathbf{r}\in A),\mu}\left(\Phi^*_{\mathbf{r}}\Phi_{\mathbf{r}+\mathbf{e}_\mu} + \text{ c.c.}\right) \\ &+ \lambda\sum_{\mathbf{r}}(|\Phi_{\mathbf{r}}|^2 - 1).\end{aligned} \tag{D.6}$$

The constraints now simplify to

$$\left\langle \Phi^\dagger_{\mathbf{r}}\Phi_{\mathbf{r}}\right\rangle = 1, \tag{D.7}$$

$$h^x = \Omega\left\langle \Phi^\dagger_{\mathbf{r}}\Phi_{\mathbf{r}+\mathbf{e}_\mu}\right\rangle. \tag{D.8}$$

Now, we have a quadratic Lagrangian, which we solve by Fourier transformation. Our Fourier transformation convention is (for $\alpha \in \{A, B\}$)

$$\Phi_{\mathbf{r},\alpha}(\tau) = T\sum_{\omega_n}\sum_{\mathbf{k}\in BZ}\Phi_{\mathbf{k},\alpha}(\omega_n)e^{i(\mathbf{k}\cdot\mathbf{r}-\omega_n\tau)}, \tag{D.9}$$

where T is the temperature, ω_n are Matsubara frequencies and we eventually take the limit $T \to 0$. Eq. (D.6) becomes

$$\mathcal{L} = T\sum_{\mathbf{k},\omega_n}\begin{pmatrix}\Phi^*_{\mathbf{k},A}(\omega_n) & \Phi^*_{\mathbf{k},B}(\omega_n)\end{pmatrix}\mathcal{G}^{-1}_{\mathbf{k}}(\omega_n)\begin{pmatrix}\Phi_{\mathbf{k},A}(\omega_n)\\ \\ \Phi_{\mathbf{k},B}(\omega_n)\end{pmatrix}, \tag{D.10}$$

where

$$\mathcal{G}^{-1}_{\mathbf{k}}(\omega_n) = \begin{pmatrix}\frac{\omega_n^2}{2V}+\lambda & -\frac{\Omega\cos\theta}{4}f_{\mathbf{k}}\\ -\frac{\Omega\cos\theta}{4}f^*_{\mathbf{k}} & \frac{\omega_n^2}{2V}+\lambda\end{pmatrix}. \tag{D.11}$$

Here,

$$f_{\mathbf{k}} = 1 + e^{-ik_1} + e^{-ik_2} + e^{-ik_3}, \tag{D.12}$$

where $\mathbf{k} \equiv k_1\mathbf{b}_1 + k_2\mathbf{b}_2 + k_3\mathbf{b}_3$, and $\mathbf{b}_1$, $\mathbf{b}_2$ and $\mathbf{b}_3$ are reciprocal lattice vectors of the FCC lattice satisfying $\mathbf{a}_i \cdot \mathbf{b}_j = \delta_{ij}$.

Upon inverting the above matrix, we find that the eigenvalues of $\mathcal{G}_{\mathbf{k}}(\omega_n)$ are $\frac{2V}{\omega_n^2 + \left(\omega_{\mathbf{k}}^{\pm}(\lambda,\theta)\right)^2}$, where the dispersion of the two bosonic bands is

$$\omega_{\mathbf{k}}^{\pm}(\lambda,\theta) = \sqrt{2V\left(\lambda \pm \frac{\Omega\cos\theta}{4}|f_{\mathbf{k}}|\right)}. \tag{D.13}$$

As long as the spinon dispersion is gapped, spinons will not condense. From the dispersion above, we see that the dispersion becomes gapless when $\lambda = \Omega\cos\theta$. However, as we will see below, for fixed θ and Ω, λ is determined by the constraint in Eq. (D.7). Therefore the condition $\lambda = \Omega\cos\theta$ is met for a specific $\Omega = \Omega_H^{\mathrm{MF}}$, which we will calculate below. Before that, will go through a few intermediate steps. First, the matrix form of $\mathcal{G}_{\mathbf{k}}(\omega_n)$ is (assuming $\Omega > 0$)

$$\mathcal{G}_{\mathbf{k}}(\omega_n) = V\begin{pmatrix} \frac{1}{\omega_n^2+(\omega_{\mathbf{k}}^+)^2} + \frac{1}{\omega_n^2+(\omega_{\mathbf{k}}^-)^2} & g_{\mathbf{k}}\left(\frac{1}{\omega_n^2+(\omega_{\mathbf{k}}^+)^2} - \frac{1}{\omega_n^2+(\omega_{\mathbf{k}}^-)^2}\right) \\ g_{\mathbf{k}}^*\left(\frac{1}{\omega_n^2+(\omega_{\mathbf{k}}^+)^2} - \frac{1}{\omega_n^2+(\omega_{\mathbf{k}}^-)^2}\right) & \frac{1}{\omega_n^2+(\omega_{\mathbf{k}}^+)^2} + \frac{1}{\omega_n^2+(\omega_{\mathbf{k}}^-)^2} \end{pmatrix}, \tag{D.14}$$

where

$$g_{\mathbf{k}} = \begin{cases} -\frac{f_{\mathbf{k}}}{|f_{\mathbf{k}}|} & \text{when } 0 \le \theta < \pi/2, \\ 0 & \text{when } \theta = \pi/2. \end{cases} \tag{D.15}$$

With the Green's function in hand, we are now ready to impose the constraints, Eq. (D.7) and Eq. (D.8). First, we calculate equal-time correlation functions of Φ (by performing the Mat-

subara sum on the Green's function). Using these, the constraints in Eq. (D.7) and Eq. (D.8) become, respectively,

$$F_1(\lambda,\theta) \equiv \frac{V}{2N_{\text{u.c.}}} \sum_{\mathbf{k}} \left(\frac{1}{|\omega_{\mathbf{k}}^{+}|} + \frac{1}{|\omega_{\mathbf{k}}^{-}|} \right) = 1, \tag{D.16}$$

$$\Omega F_2(\lambda,\theta) \equiv \Omega \frac{V}{2N_{\text{u.c.}}} \sum_{\mathbf{k}} g_{\mathbf{k}} \left(\frac{1}{|\omega_{\mathbf{k}}^{-}|} - \frac{1}{|\omega_{\mathbf{k}}^{+}|} \right) = h^x. \tag{D.17}$$

Next, by imposing Eq. (D.3) with the help of Eq. (D.2), we get

$$h^z = -\frac{\mathcal{B}\sin\theta}{2}, \text{ where } \mathcal{B} = \frac{\sin\theta}{2} \sum_{(\mathbf{r}'\in A),\nu} V_{0,\nu}(-\mathbf{r}')\varepsilon_{\nu}. \tag{D.18}$$

For a given θ, Eq. (D.16) determines λ. We see that there are three self-consistent solutions for θ:

$$\theta = \begin{cases} 0, \\ \pi/2, \\ \cos^{-1}\left(\frac{2\Omega F_2(\lambda,\theta)}{\mathcal{B}}\right). \end{cases} \tag{D.19}$$

Within gMFT (gauge mean field theory), these three solutions correspond to a QSL, a "Coulomb ferromagnet" (spin liquid with nonzero ice ferromagnetic order parameter), and an ice ferromagnet, respectively [272]. For a fixed parameter Ω, the true solution depends on which of the three solutions above has lower energy with respect to the mean-field Hamiltonian (D.1). Suppose that, for large enough Ω, one is in the QSL phase, i.e., $\theta = 0$ and $\left\langle \hat{\Phi}_{\mathbf{r}} \right\rangle = 0$. Now, the bosons will condense when their dispersion becomes gapless, i.e., $\lambda = \Omega$. Using constraint (D.16), we find that this transition point is $\Omega_{\text{MF}}^{H} \approx 0.7V$, as also found in Ref. [256]. For $\Omega > \Omega_{\text{MF}}^{H}$, the ground

state is in the TFP phase.

Having identified the Higgs transition point, we now attempt to identify the confinement-deconfinement transition for low Ω, i.e., find Ω at which $\theta = 0$ becomes the lowest-energy saddle-point. Using Eq. (D.1), we get the following expression for the mean-field energy:

$$E_{\text{MF}} = K - N_{\text{u.c.}} \left(2\Omega F_2(\lambda, \theta) \cos\theta + \frac{\mathcal{B}}{2} \sin^2\theta \right), \tag{D.20}$$

where K is the total kinetic energy of the bosons and can be calculated to be

$$K = \frac{1}{2} \sum_{\mathbf{k}} \left(\omega_{\mathbf{k}}^{+} + \omega_{\mathbf{k}}^{-} \right). \tag{D.21}$$

In Fig. D.2, we plot the energy E_{MF} for $\theta = 0$ (QSL) and $\theta = \pi/2$ (ice ferromagnet), and find a transition at $\Omega \approx 0.13V$. (The third solution for θ becomes the lowest-energy solution only in a minuscule window around $\Omega \approx 0.13V$, so we ignore it.) However, we will now argue that this result is misleading.

In gMFT, the energy reduction in the QSL phase with respect to the ordered phase (ice ferromagnet) arises from the minimization of kinetic energy of the bosonic charges $\hat{\Phi}_{\mathbf{r}}$ that are allowed to hop. When $\theta = 0$, the hopping coefficient is maximized, while, for $\theta = \pi/2$, the hopping coefficient is 0. However, microscopically, this hopping corresponds to a single spin-flip. A pair of spin-flips at the same site leads to a *constant* reduction of energy coming from second order perturbation theory, given by $-\Omega^2 N_{\text{u.c.}}/V$. It is constant in the sense that this reduction is obtained for *any* state including the QSL and the ice ferromagnet. The mean-field calculation, however, unfairly assigns this reduction to the QSL but not to the ordered state. In

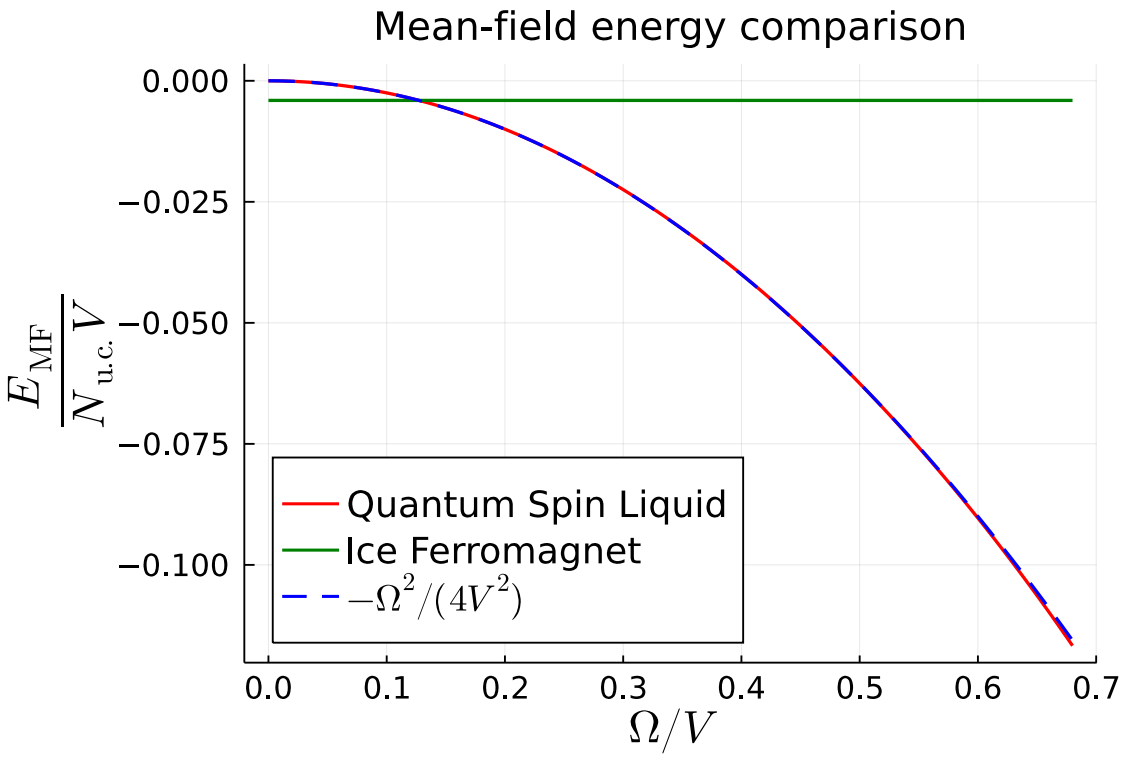

Figure D.2: The energy per unit cell (in units of V) of saddle points $\theta = 0$ (QSL) and $\theta = \pi/2$ (ice ferromagnet) given by Eq. (D.20) up to an overall additive constant that is the same for $\theta = 0$ and $\theta = \pi/2$. We also plot $-\frac{\Omega^2}{4V^2}$ arising from trivial spin-flip pairs: this plot almost overlaps with the energy of the $\theta = 0$ state.

fact, in Fig. D.2, we have also plotted $-\Omega^2/(4V)$ (the factor of 1/4 can perhaps be attributed to using spin-$1/2$ and classical spins at the same time). As can be seen, this plot almost completely overlaps with the energy of the QSL calculated within gMFT. So it is clear that, within gMFT, the difference between the energies of the QSL and the confined phase is quadratic in Ω to leading order even though we know from perturbation theory that the leading order term should be proportional to Ω^6. Hence, gMFT cannot be used in the vicinity of the confinement-deconfinement transition unless gauge-fluctuations are properly taken into consideration.

D.3 Difference between $\langle \hat{X}_P \hat{X}_{P'} \rangle_c$ and $\langle \hat{\tilde{X}}_P \hat{\tilde{X}}_{P'} \rangle_c$

In this appendix, we show that the difference between $\langle \hat{X}_P \hat{X}_{P'} \rangle_c$ and $\langle \hat{\tilde{X}}_P \hat{\tilde{X}}_{P'} \rangle_c$ evaluated in the ground state is of sixth order in Ω/V, that is, derive Eq. (4.53).

Let $|\Psi_g\rangle$ be the ground state of the system. Thus $|\Psi_0\rangle = \hat{U}_S |\Psi_g\rangle$ is in the ice manifold, where $\hat{U}_S$ is the unitary operator that implements the Schrieffer-Wolff transformation (see Sec. 4.3.1.1). We have

$$\langle \Psi_g | \hat{X}_P | \Psi_g \rangle = \langle \Psi_0 | \hat{U}_S \hat{X}_P \hat{U}_S^\dagger | \Psi_0 \rangle. \tag{D.22}$$

At zeroth order in Ω/V, the right-hand side of the above equation is $\langle \Psi_0 | \hat{X}_P | \Psi_0 \rangle$, which we know is equal to $\langle \Psi_0 | \hat{\tilde{X}}_P | \Psi_0 \rangle$ since $|\Psi_0\rangle$ is in the ice manifold [see Eq. (4.52)]. Note that $\hat{U}_S = 1 + \hat{S} + \hat{S}^2/2! + \cdots$. The terms that are of order $(\Omega/V)^i$ flip i spins. When $\hat{U}_S$ and $\hat{U}_S^\dagger$ in Eq. (D.22) are expanded as a power series, the first term whose expectation value is nonzero (other than the zeroth order term) appears at sixth order in Ω/V. This is because $\hat{X}_P$ flips six spins which need to be compensated from another six spin flips coming from six powers of $\hat{S}$. Thus, we have

$$\langle \Psi_0 | \hat{U}_S \hat{X}_P \hat{U}_S^\dagger | \Psi_0 \rangle = \langle \Psi_0 | \hat{X}_P | \Psi_0 \rangle + \Theta\left((\Omega/V)^6\right). \tag{D.23}$$

A similar argument applied to $\langle \hat{\tilde{X}}_P \rangle$ shows that

$$\langle \Psi_0 | \hat{U}_S \hat{\tilde{X}}_P \hat{U}_S^\dagger | \Psi_0 \rangle = \langle \Psi_0 | \hat{\tilde{X}}_P | \Psi_0 \rangle + \Theta\left((\Omega/V)^6\right). \tag{D.24}$$

Using Eq. (4.52), we find that $\langle \hat{\tilde{X}}_P \rangle = \langle \hat{X}_P \rangle + \Theta\left((\Omega/V)^6\right)$. An analogous argument applies to show $\langle \hat{\tilde{X}}_P \hat{\tilde{X}}_{P'} \rangle = \langle \hat{X}_P \hat{X}_{P'} \rangle + \Theta\left((\Omega/V)^{12}\right)$. Finally, putting together all the pieces, we obtain

Eq. (4.53). By similar arguments, Eq. (4.54) can also be derived.

D.4 Plaquette correlators in TFP phase

In this Appendix, we derive the plaquette X correlator deep inside the TFP phase at second order in perturbation theory, treating the van der Waals interaction as the perturbation. That is, we derive Eq. (4.71).

For $\Omega \gg V$, the ground state up to first order in V/Ω is $|\xi\rangle = |-\rangle + |\chi_1\rangle$ [see Eqs. (4.68) and (4.69) for the definitions of $|-\rangle$ and $|\chi_1\rangle$ respectively]. Here $|-\rangle$ is of zeroth order, and $|\chi_1\rangle$ is of first order in Ω/V. The connected plaquette X correlator is

$$\frac{\langle\xi|\hat{X}_P\hat{X}_{P'}|\xi\rangle}{\langle\xi|\xi\rangle} - \frac{\langle\xi|\hat{X}_P|\xi\rangle\langle\xi|\hat{X}_{P'}|\xi\rangle}{\langle\xi|\xi\rangle^2}. \tag{D.25}$$

Since $\langle -|\chi_1\rangle = 0$ and $\hat{X}_P|-\rangle = |-\rangle$, the first-order term in the plaquette X correlator above will be zero. Keeping only terms up to the second order, the plaquette X correlator becomes

$$\begin{aligned}&(1+\langle\chi_1|\hat{X}_P\hat{X}_{P'}|\chi_1\rangle)(1-\langle\chi_1|\chi_1\rangle)\\&-(1+\langle\chi_1|\hat{X}_P|\chi_1\rangle)(1+\langle\chi_1|\hat{X}_{P'}|\chi_1\rangle)(1-2\langle\chi_1|\chi_1\rangle).\end{aligned} \tag{D.26}$$

Simplifying this expression and keeping only terms that are second-order in Ω/V gives

$$\begin{aligned}&\langle\chi_1|\hat{X}_P\hat{X}_{P'}|\chi_1\rangle - \langle\chi_1|\hat{X}_P|\chi_1\rangle - \langle\chi_1|\hat{X}_{P'}|\chi_1\rangle + \langle\chi_1|\chi_1\rangle\\&= \langle\chi_1|(\hat{X}_P-1)(\hat{X}_{P'}-1)|\chi_1\rangle.\end{aligned} \tag{D.27}$$

Substituting the definition of $|\chi_1\rangle$ from Eq. (4.69), we obtain the desired Eq. (4.71).

Bibliography

[1] Gautam Nambiar, Daniel Bulmash, and Victor Galitski. Monopole josephson effects in a dirac spin liquid. *Physical Review Research*, 5(1):013169, 2023.

[2] Yuxuan Zhang, Naren Manjunath, Gautam Nambiar, and Maissam Barkeshli. Fractional disclination charge and discrete shift in the hofstadter butterfly. *Physical Review Letters*, 129(27):275301, 2022.

[3] Yuxuan Zhang, Naren Manjunath, Gautam Nambiar, and Maissam Barkeshli. Quantized charge polarization as a many-body invariant in (2+ 1) d crystalline topological states and hofstadter butterflies. *Physical Review X*, 13(3):031005, 2023.

[4] Gautam Nambiar, Andrey Grankin, and Mohammad Hafezi. Diagnosing electronic phases of matter using photonic correlation functions. *arXiv preprint arXiv:2410.24215*, 2024.

[5] Jeet Shah, Gautam Nambiar, Alexey V. Gorshkov, and Victor Galitski. Quantum spin ice in three-dimensional rydberg atom arrays. *Phys. Rev. X*, 15:011025, Feb 2025.

[6] Michael Hermele, Matthew P. A. Fisher, and Leon Balents. Pyrochlore photons: The $U(1)$ spin liquid in a $S = 1/2$ three-dimensional frustrated magnet. *Phys. Rev. B*, 69(6):064404, February 2004.

[7] B Sriram Shastry and Boris I Shraiman. Theory of Raman scattering in Mott-Hubbard systems. *Physical Review Letters*, 65(8):1068, 1990.

[8] B Sriram Shastry and Boris I Shraiman. Raman scattering in Mott-Hubbard systems. *International Journal of Modern Physics B*, 5(01n02):365–388, 1991.

[9] Vadim Borokhov, Anton Kapustin, and Xinkai Wu. Topological disorder operators in three-dimensional conformal field theory. *Journal of High Energy Physics*, 2002(11):049, 2003.

[10] Ethan Dyer, Márk Mezei, and Silviu S Pufu. Monopole taxonomy in three-dimensional conformal field theories. *arXiv preprint arXiv:1309.1160*, 2013.

[11] Walter Rantner and Xiao-Gang Wen. Electron spectral function and algebraic spin liquid for the normal state of underdoped high t_c superconductors. *Physical review letters*, 86(17):3871, 2001.

[12] Éric Dupuis, Rufus Boyack, and William Witczak-Krempa. Anomalous dimensions of monopole operators at the transitions between dirac and topological spin liquids. *arXiv preprint arXiv:2108.05922*, 2021.

[13] Sophia Tepe. Medium. https://medium.com/betterism/the-blind-men-and-the-elephant-596ec8a72a7d, 2019. Accessed: YYYY-MM-DD.

[14] J Dalibard and S Reynaud. Correlation signals in resonance fluorescence: interpretation via photon scattering amplitudes. *Journal de Physique*, 44(12):1337–1343, 1983.

[15] Max McGinley, Michele Fava, and SA Parameswaran. Anomalous thermal relaxation and pump-probe spectroscopy of two-dimensional topologically ordered systems. *Physical Review B*, 109(7):075108, 2024.

[16] Nic Shannon, Olga Sikora, Frank Pollmann, Karlo Penc, and Peter Fulde. Quantum Ice: A Quantum Monte Carlo Study. *Phys. Rev. Lett.*, 108(6):067204, February 2012.

[17] Olga Sikora, Frank Pollmann, Nic Shannon, Karlo Penc, and Peter Fulde. Quantum Liquid with Deconfined Fractional Excitations in Three Dimensions. *Phys. Rev. Lett.*, 103(24):247001, December 2009.

[18] Patrick Emonts and Stefan Wessel. Monte carlo study of the discontinuous quantum phase transition in the transverse-field Ising model on the pyrochlore lattice. *Phys. Rev. B*, 98:174433, Nov 2018.

[19] Philip W Anderson. Resonating valence bonds: A new kind of insulator? *Mater. Res. Bulletin*, 8(2):153–160, 1973.

[20] Lucile Savary and Leon Balents. Quantum spin liquids: A review. *Rep. Prog. Phys.*, 80(1):016502, January 2017.

[21] Linus Pauling. The Structure and Entropy of Ice and of Other Crystals with Some Randomness of Atomic Arrangement. *J. Am. Chem. Soc.*, 57(12):2680–2684, December 1935.

[22] Todadri Senthil, Ashvin Vishwanath, Leon Balents, Subir Sachdev, and Matthew PA Fisher. Deconfined quantum critical points. *Science*, 303(5663):1490–1494, 2004.

[23] Michael Hermele, T Senthil, and Matthew PA Fisher. Algebraic spin liquid as the mother of many competing orders. *Phys. Rev. B*, 72(10):104404, 2005.

[24] Xue-Yang Song, Chong Wang, Ashvin Vishwanath, and Yin-Chen He. Unifying description of competing orders in two-dimensional quantum magnets. *Nat. Commun.*, 10(1):1–12, 2019.

[25] Gautam Nambiar, Daniel Bulmash, and Victor Galitski. Monopole Josephson effects in a Dirac spin liquid. *Phys. Rev. Res.*, 5:013169, Mar 2023.

[26] Yao-Dong Li and Gang Chen. Symmetry enriched $U(1)$ topological orders for dipole-octupole doublets on a pyrochlore lattice. *Phys. Rev. B*, 95:041106, Jan 2017.

[27] Z. Nussinov, C. D. Batista, B. Normand, and S. A. Trugman. High-dimensional fractionalization and spinon deconfinement in pyrochlore antiferromagnets. *Phys. Rev. B*, 75:094411, Mar 2007.

[28] William Marciano and Heinz Pagels. Quantum chromodynamics. *Phys. Rep.*, 36(3):137–276, 1978.

[29] Hildegard Meyer-Ortmanns. Phase transitions in quantum chromodynamics. *Rev. Mod. Phys.*, 68(2):473, 1996.

[30] John B Kogut. The lattice gauge theory approach to quantum chromodynamics. *Rev. Mod. Phys.*, 55(3):775, 1983.

[31] Lochlainn O'Raifeartaigh and Norbert Straumann. Gauge theory: Historical origins and some modern developments. *Rev. Mod. Phys.*, 72(1):1, 2000.

[32] Patrick A Lee, Naoto Nagaosa, and Xiao-Gang Wen. Doping a Mott insulator: Physics of high-temperature superconductivity. *Rev. Mod. Phys.*, 78(1):17, 2006.

[33] A Yu Kitaev. Fault-tolerant quantum computation by anyons. *Ann. Phys. (N. Y.)*, 303(1):2–30, 2003.

[34] Chetan Nayak, Steven H Simon, Ady Stern, Michael Freedman, and Sankar Das Sarma. Non-abelian anyons and topological quantum computation. *Rev. Mod. Phys.*, 80(3):1083, 2008.

[35] V Kalmeyer and RB Laughlin. Equivalence of the resonating-valence-bond and fractional quantum hall states. *Physical review letters*, 59(18):2095, 1987.

[36] Alexei Kitaev. Anyons in an exactly solved model and beyond. *Annals of Physics*, 321(1):2–111, 2006.

[37] J. Brad Marston and Ian Affleck. Large-n limit of the hubbard-heisenberg model. *Phys. Rev. B*, 39:11538–11558, Jun 1989.

[38] Shai M Chester and Silviu S Pufu. Towards bootstrapping QED3. *Journal of High Energy Physics*, 2016(8):1–30, 2016.

[39] LB Ioffe and AI Larkin. Gapless fermions and gauge fields in dielectrics. *Physical Review B*, 39(13):8988, 1989.

[40] Chetan Nayak and Frank Wilczek. Renormalization group approach to low temperature properties of a non-fermi liquid metal. *Nuclear Physics B*, 430(3):534–562, 1994.

[41] Joseph Polchinski. Low-energy dynamics of the spinon-gauge system. *Nuclear Physics B*, 422(3):617–633, 1994.

[42] BL Altshuler, LB Ioffe, and AJ Millis. Low-energy properties of fermions with singular interactions. *Physical Review B*, 50(19):14048, 1994.

[43] Sung-Sik Lee. Low-energy effective theory of fermi surface coupled with u (1) gauge field in 2+ 1 dimensions. *Physical Review B—Condensed Matter and Materials Physics*, 80(16):165102, 2009.

[44] Johannes Knolle and Roderich Moessner. A field guide to spin liquids. *Annu. Rev. Condens. Matter Phys.*, 10:451–472, 2019.

[45] Giulia Semeghini, Harry Levine, Alexander Keesling, Sepehr Ebadi, Tout T Wang, Dolev Bluvstein, Ruben Verresen, Hannes Pichler, Marcin Kalinowski, Rhine Samajdar, et al. Probing topological spin liquids on a programmable quantum simulator. *Science*, 374(6572):1242–1247, 2021.

[46] Matthew B Hastings. Lieb-Schultz-Mattis in higher dimensions. *Physical review b*, 69(10):104431, 2004.

[47] Elliott Lieb, Theodore Schultz, and Daniel Mattis. Two soluble models of an antiferromagnetic chain. *Annals of Physics*, 16(3):407–466, 1961.

[48] Michael Hermele, T Senthil, Matthew PA Fisher, Patrick A Lee, Naoto Nagaosa, and Xiao-Gang Wen. Stability of $U(1)$ spin liquids in two dimensions. *Physical Review B*, 70(21):214437, 2004.

[49] Nikhil Karthik and Rajamani Narayanan. Scale invariance of parity-invariant three-dimensional QED. *Physical Review D*, 94(6):065026, 2016.

[50] T Senthil and Matthew PA Fisher. Fractionalization in the cuprates: Detecting the topological order. *Physical Review Letters*, 86(2):292, 2001.

[51] Todadri Senthil and Matthew PA Fisher. Fractionalization, topological order, and cuprate superconductivity. *Physical Review B*, 63(13):134521, 2001.

[52] Maissam Barkeshli, Erez Berg, and Steven Kivelson. Coherent transmutation of electrons into fractionalized anyons. *Science*, 346(6210):722–725, 2014.

[53] David Aasen, Roger SK Mong, Benjamin M Hunt, David Mandrus, and Jason Alicea. Electrical probes of the non-Abelian spin liquid in Kitaev materials. *Physical Review X*, 10(3):031014, 2020.

[54] Wing-Ho Ko, Zheng-Xin Liu, Tai-Kai Ng, and Patrick A Lee. Raman signature of the $U(1)$ Dirac spin-liquid state in the spin-1/2 kagome system. *Physical Review B*, 81(2):024414, 2010.

[55] Patrick A Lee and Naoto Nagaosa. Proposal to use neutron scattering to access scalar spin chirality fluctuations in kagome lattices. *Physical Review B*, 87(6):064423, 2013.

[56] Alexander M Polyakov. Quark confinement and topology of gauge theories. *Nuclear Physics B*, 120(3):429–458, 1977.

[57] Xue-Yang Song, Yin-Chen He, Ashvin Vishwanath, and Chong Wang. From spinon band topology to the symmetry quantum numbers of monopoles in Dirac spin liquids. *Physical Review X*, 10(1):011033, 2020.

[58] Shubhayu Chatterjee and Subir Sachdev. Probing excitations in insulators via injection of spin currents. *Physical Review B*, 92(16):165113, 2015.

[59] Chui-Zhen Chen, Qing-feng Sun, Fa Wang, and XC Xie. Detection of spinons via spin transport. *Physical Review B*, 88(4):041405, 2013.

[60] Éric Dupuis, MB Paranjape, and William Witczak-Krempa. Transition from a Dirac spin liquid to an antiferromagnet: monopoles in a QED 3-Gross-Neveu theory. *Physical Review B*, 100(9):094443, 2019.

[61] Yuan-Ming Lu, Gil Young Cho, and Ashvin Vishwanath. Unification of bosonic and fermionic theories of spin liquids on the kagome lattice. *Physical Review B*, 96(20):205150, 2017.

[62] Nikolai Zerf, Rufus Boyack, Peter Marquard, John A Gracey, and Joseph Maciejko. Critical properties of the Néel–algebraic-spin-liquid transition. *Physical Review B*, 100(23):235130, 2019.

[63] Aron J Beekman. Theory of generalized Josephson effects. *Progress of Theoretical and Experimental Physics*, 2020(7):073B09, 2020.

[64] F Paul Esposito, L-P Guay, RB MacKenzie, MB Paranjape, and LCR Wijewardhana. Field theoretic description of the abelian and non-abelian Josephson effect. *Physical review letters*, 98(24):241602, 2007.

[65] Muneto Nitta. Josephson junction of non-abelian superconductors and non-abelian josephson vortices. *Nuclear Physics B*, 899:78–90, 2015.

[66] Martin Claassen, Hong-Chen Jiang, Brian Moritz, and Thomas P Devereaux. Dynamical time-reversal symmetry breaking and photo-induced chiral spin liquids in frustrated Mott insulators. *Nature Communications*, 8(1):1–9, 2017.

[67] D Chassé and A-MS Tremblay. Generalized dc and ac Josephson effects in antiferromagnets and in antiferromagnetic d-wave superconductors. *Physical Review B*, 81(11):115102, 2010.

[68] A Moor, AF Volkov, and KB Efetov. Josephson-like spin current in junctions composed of antiferromagnets and ferromagnets. *Physical Review B*, 85(1):014523, 2012.

[69] Yizhou Liu, Gen Yin, Jiadong Zang, Roger K Lake, and Yafis Barlas. Spin-Josephson effects in exchange coupled antiferromagnetic insulators. *Physical Review B*, 94(9):094434, 2016.

[70] Wei Chen, Peter Horsch, and Dirk Manske. Dissipationless spin current between two coupled ferromagnets. *Physical Review B*, 89(6):064427, 2014.

[71] Andreas Rückriegel and Peter Kopietz. Spin currents, spin torques, and the concept of spin superfluidity. *Physical Review B*, 95(10):104436, 2017.

[72] Premala Chandra, Piers Coleman, and AI Larkin. A quantum fluids approach to frustrated Heisenberg models. *Journal of Physics: Condensed Matter*, 2(39):7933, 1990.

[73] Erkki Thuneberg. Theory of Josephson phenomena in superfluid ^{3}He. In *AIP Conference Proceedings*, volume 850, pages 103–108. American Institute of Physics, 2006.

[74] Ran Qi, Xiao-Lu Yu, ZB Li, and WM Liu. Non-Abelian Josephson effect between two $F = 2$ spinor Bose-Einstein condensates in double optical traps. *Physical review letters*, 102(18):185301, 2009.

[75] T Sh Misirpashaev, GE Volovik, and D PARSONS. Macroscopic Josephson effect in superfluid ^{3}He-B. *JETP Lett*, 56(1), 1992.

[76] Thomas P Devereaux and Rudi Hackl. Inelastic light scattering from correlated electrons. *Reviews of modern physics*, 79(1):175, 2007.

[77] Joji Nasu, Johannes Knolle, Dima L Kovrizhin, Yukitoshi Motome, and Roderich Moessner. Fermionic response from fractionalization in an insulating two-dimensional magnet. *Nature Physics*, 12(10):912–915, 2016.

[78] PA Fleury and R Loudon. Scattering of light by one-and two-magnon excitations. *Physical Review*, 166(2):514, 1968.

[79] AC Bleszynski-Jayich, WE Shanks, B Peaudecerf, E Ginossar, F Von Oppen, L Glazman, and JGE Harris. Persistent currents in normal metal rings. *Science*, 326(5950):272–275, 2009.

[80] N Byers and CN Yang. Theoretical considerations concerning quantized magnetic flux in superconducting cylinders. *Physical review letters*, 7(2):46, 1961.

[81] Yin-Chen He, Michael P Zaletel, Masaki Oshikawa, and Frank Pollmann. Signatures of Dirac cones in a DMRG study of the kagome Heisenberg model. *Physical Review X*, 7(3):031020, 2017.

[82] Shijie Hu, W Zhu, Sebastian Eggert, and Yin-Chen He. Dirac spin liquid on the spin-1/2 triangular Heisenberg antiferromagnet. *Physical review letters*, 123(20):207203, 2019.

[83] Naren Manjunath and Maissam Barkeshli. Crystalline gauge fields and quantized discrete geometric response for abelian topological phases with lattice symmetry. *Physical Review Research*, 3(1):013040, 2021.

[84] Soner Albayrak, Rajeev S Erramilli, Zhijin Li, David Poland, and Yuan Xin. Bootstrapping N f= 4 conformal QED 3. *Physical Review D*, 105(8):085008, 2022.

[85] Yin-Chen He, Junchen Rong, and Ning Su. Conformal bootstrap bounds for the $U(1)$ Dirac spin liquid and $N = 7$ Stiefel liquid. *arXiv preprint arXiv:2107.14637*, 2021.

[86] Sho Nakosai and Shigeki Onoda. Magnetic monopole supercurrent through a quantum spin ice tunnel junction. *Journal of the Physical Society of Japan*, 88(5):053701, 2019.

[87] Daniel Arovas, John R Schrieffer, and Frank Wilczek. Fractional statistics and the quantum hall effect. *Physical review letters*, 53(7):722, 1984.

[88] Xiao-Gang Wen and Qian Niu. Ground-state degeneracy of the fractional quantum hall states in the presence of a random potential and on high-genus riemann surfaces. *Physical Review B*, 41(13):9377, 1990.

[89] Xiao Gang Wen, Elbio Dagotto, and Eduardo Fradkin. Anyons on a torus. *Physical Review B*, 42(10):6110, 1990.

[90] Xiao-Gang Wen. Topological orders and chern-simons theory in strongly correlated quantum liquid. *International Journal of Modern Physics B*, 5(10):1641–1648, 1991.

[91] James Nakamura, Shuang Liang, Geoffrey C Gardner, and Michael J Manfra. Direct observation of anyonic braiding statistics. *Nature Physics*, 16(9):931–936, 2020.

[92] Hugo Bartolomei, Manohar Kumar, Rémi Bisognin, Arthur Marguerite, J-M Berroir, Erwann Bocquillon, Bernard Placais, Antonella Cavanna, Q Dong, Ulf Gennser, et al. Fractional statistics in anyon collisions. *Science*, 368(6487):173–177, 2020.

[93] Masaki Oshikawa. Commensurability, excitation gap, and topology in quantum many-particle systems on a periodic lattice. *Physical review letters*, 84(7):1535, 2000.

[94] Lucile Savary and Leon Balents. Quantum spin liquids: a review. *Reports on Progress in Physics*, 80(1):016502, 2016.

[95] Patrick A Lee. From high temperature superconductivity to quantum spin liquid: progress in strong correlation physics. *Reports on Progress in Physics*, 71(1):012501, 2007.

[96] C Broholm, RJ Cava, SA Kivelson, DG Nocera, MR Norman, and T Senthil. Quantum spin liquids. *Science*, 367(6475):eaay0668, 2020.

[97] Lucy Clark and Aly H Abdeldaim. Quantum spin liquids from a materials perspective. *Annual Review of Materials Research*, 51(1):495–519, 2021.

[98] Bernhard Keimer, Steven A Kivelson, Michael R Norman, Shinichi Uchida, and J Zaanen. From quantum matter to high-temperature superconductivity in copper oxides. *Nature*, 518(7538):179–186, 2015.

[99] Eva Y Andrei, Dmitri K Efetov, Pablo Jarillo-Herrero, Allan H MacDonald, Kin Fai Mak, T Senthil, Emanuel Tutuc, Ali Yazdani, and Andrea F Young. The marvels of moiré materials. *Nature Reviews Materials*, 6(3):201–206, 2021.

[100] Kin Fai Mak and Jie Shan. Semiconductor moiré materials. *Nature Nanotechnology*, 17(7):686–695, 2022.

[101] Dirk Wulferding, Youngsu Choi, Wonjun Lee, and Kwang-Yong Choi. Raman spectroscopic diagnostic of quantum spin liquids. *Journal of Physics: Condensed Matter*, 32(4):043001, 2019.

[102] Yiping Wang, Gavin B Osterhoudt, Yao Tian, Paige Lampen-Kelley, Arnab Banerjee, Thomas Goldstein, Jun Yan, Johannes Knolle, Huiwen Ji, Robert J Cava, et al. The range of non-kitaev terms and fractional particles in α-rucl3. *npj Quantum Materials*, 5(1):14, 2020.

[103] Natalia B. Perkins, Gia-Wei Chern, and Wolfram Brenig. Raman scattering in a heisenberg $s = \frac{1}{2}$ antiferromagnet on the anisotropic triangular lattice. *Phys. Rev. B*, 87:174423, May 2013.

[104] Yuan Wan and NP Armitage. Resolving continua of fractional excitations by spinon echo in thz 2d coherent spectroscopy. *Physical review letters*, 122(25):257401, 2019.

[105] Fahad Mahmood, Dipanjan Chaudhuri, Sarang Gopalakrishnan, Rahul Nandkishore, and NP Armitage. Observation of a marginal fermi glass. *Nature Physics*, 17(5):627–631, 2021.

[106] Michele Fava, Sounak Biswas, Sarang Gopalakrishnan, Romain Vasseur, and SA Parameswaran. Hydrodynamic nonlinear response of interacting integrable systems. *Proceedings of the National Academy of Sciences*, 118(37):e2106945118, 2021.

[107] Wonjune Choi, Ki Hoon Lee, and Yong Baek Kim. Theory of two-dimensional nonlinear spectroscopy for the kitaev spin liquid. *Physical Review Letters*, 124(11):117205, 2020.

[108] Rahul M Nandkishore, Wonjune Choi, and Yong Baek Kim. Spectroscopic fingerprints of gapped quantum spin liquids, both conventional and fractonic. *Physical Review Research*, 3(1):013254, 2021.

[109] Oliver Hart and Rahul Nandkishore. Extracting spinon self-energies from two-dimensional coherent spectroscopy. *Physical Review B*, 107(20):205143, 2023.

[110] EJ König, Piers Coleman, and Alexei M Tsvelik. Spin magnetometry as a probe of stripe superconductivity in twisted bilayer graphene. *Physical Review B*, 102(10):104514, 2020.

[111] Zi-Long Li, Masaki Oshikawa, and Yuan Wan. Photon echo from lensing of fractional excitations in tomonaga-luttinger spin liquid. *Physical Review X*, 11(3):031035, 2021.

[112] GiBaik Sim, Johannes Knolle, and Frank Pollmann. Nonlinear spectroscopy of bound states in perturbed ising spin chains. *Physical Review B*, 107(10):L100404, 2023.

[113] GiBaik Sim, Frank Pollmann, and Johannes Knolle. Microscopic details of two-dimensional spectroscopy of one-dimensional quantum ising magnets. *Physical Review B*, 108(13):134423, 2023.

[114] M Kazem Negahdari and Abdollah Langari. Nonlinear response of the kitaev honeycomb lattice model in a weak magnetic field. *Physical Review B*, 107(13):134404, 2023.

[115] Qi Gao, Yang Liu, Haijun Liao, and Yuan Wan. Two-dimensional coherent spectrum of interacting spinons from matrix product states. *Physical Review B*, 107(16):165121, 2023.

[116] Mark Potts, Roderich Moessner, and Owen Benton. Exploiting polarization dependence in two-dimensional coherent spectroscopy: Examples of ce 2 zr 2 o 7 and nd 2 zr 2 o 7. *Physical Review B*, 109(10):104435, 2024.

[117] Zhuquan Zhang, Frank Y Gao, Jonathan B Curtis, Zi-Jie Liu, Yu-Che Chien, Alexander von Hoegen, Man Tou Wong, Takayuki Kurihara, Tohru Suemoto, Prineha Narang, et al. Terahertz field-induced nonlinear coupling of two magnon modes in an antiferromagnet. *Nature Physics*, pages 1–6, 2024.

[118] SA Parameswaran and Sarang Gopalakrishnan. Asymptotically exact theory for nonlinear spectroscopy of random quantum magnets. *Physical review letters*, 125(23):237601, 2020.

[119] Felix Gerken, Thore Posske, Shaul Mukamel, and Michael Thorwart. Unique signatures of topological phases in two-dimensional thz spectroscopy. *Physical Review Letters*, 129(1):017401, 2022.

[120] Emily Z Zhang, Ciarán Hickey, and Yong Baek Kim. Disentangling spin excitation continua in classical and quantum magnets using 2d nonlinear spectroscopy. *arXiv preprint arXiv:2404.16935*, 2024.

[121] Olesia Krupnitska and Wolfram Brenig. Finite-temperature second harmonic generation in kitaev magnets. *Physical Review B*, 108(7):075120, 2023.

[122] Yoshito Watanabe, Simon Trebst, and Ciarán Hickey. Revealing quadrupolar excitations with non-linear spectroscopy. *arXiv preprint arXiv:2405.14954*, 2024.

[123] Zhanybek Alpichshev, Edbert J Sie, Fahad Mahmood, Gang Cao, and Nuh Gedik. Origin of the exciton mass in the frustrated mott insulator na 2 iro 3. *Physical Review B*, 96(23):235141, 2017.

[124] Thomas P Devereaux, Martin Claassen, Xu-Xin Huang, Michael Zaletel, Joel E Moore, Dirk Morr, Fahad Mahmood, Peter Abbamonte, and Zhi-Xun Shen. Angle-resolved pair photoemission theory for correlated electrons. *Physical Review B*, 108(16):165134, 2023.

[125] Max McGinley, Michele Fava, and SA Parameswaran. Signatures of fractional statistics in nonlinear pump-probe spectroscopy. *Physical Review Letters*, 132(6):066702, 2024.

[126] Wai Ting Tai and Martin Claassen. Quantum-geometric light-matter coupling in correlated quantum materials. *arXiv preprint arXiv:2303.01597*, 2023.

[127] Yuen-Ron Shen. *Principles of nonlinear optics*. Wiley-Interscience, New York, NY, USA, 1984.

[128] Andrius Gelzinis, Ramūnas Augulis, Vytautas Butkus, Bruno Robert, and Leonas Valkunas. Two-dimensional spectroscopy for non-specialists. *Biochimica et Biophysica Acta (BBA)-Bioenergetics*, 1860(4):271–285, 2019.

[129] Christopher L Smallwood and Steven T Cundiff. Multidimensional coherent spectroscopy of semiconductors. *Laser & Photonics Reviews*, 12(12):1800171, 2018.

[130] Kensuke Kobayashi and Masayuki Hashisaka. Shot noise in mesoscopic systems: From single particles to quantum liquids. *Journal of the Physical Society of Japan*, 90(10):102001, 2021.

[131] L Saminadayar, DC Glattli, Y Jin, and B c-m Etienne. Observation of the e/3 fractionally charged laughlin quasiparticle. *Physical Review Letters*, 79(13):2526, 1997.

[132] R De-Picciotto, M Reznikov, Moty Heiblum, V Umansky, G Bunin, and Diana Mahalu. Direct observation of a fractional charge. *Physica B: Condensed Matter*, 249:395–400, 1998.

[133] Koen M Bastiaans, Damianos Chatzopoulos, Jian-Feng Ge, Doohee Cho, Willem O Tromp, Jan M van Ruitenbeek, Mark H Fischer, Pieter J de Visser, David J Thoen, Eduard FC Driessen, et al. Direct evidence for cooper pairing without a spectral gap in a disordered superconductor above t c. *Science*, 374(6567):608–611, 2021.

[134] Panpan Zhou, Liyang Chen, Yue Liu, Ilya Sochnikov, Anthony T Bollinger, Myung-Geun Han, Yimei Zhu, Xi He, Ivan Bozović, and Douglas Natelson. Electron pairing in the pseudogap state revealed by shot noise in copper oxide junctions. *Nature*, 572(7770):493–496, 2019.

[135] Liyang Chen, Dale T Lowder, Emine Bakali, Aaron Maxwell Andrews, Werner Schrenk, Monika Waas, Robert Svagera, Gaku Eguchi, Lukas Prochaska, Yiming Wang, et al. Shot noise in a strange metal. *Science*, 382(6673):907–911, 2023.

[136] Darrick E Chang, Vladan Vuletić, and Mikhail D Lukin. Quantum nonlinear optics—photon by photon. *Nature Photonics*, 8(9):685–694, 2014.

[137] R Hanbury Brown and Richard Q Twiss. Correlation between photons in two coherent beams of light. *Nature*, 177(4497):27–29, 1956.

[138] Xiao-Gang Wen, Frank Wilczek, and Anthony Zee. Chiral spin states and superconductivity. *Physical Review B*, 39(16):11413, 1989.

[139] Shou-Shu Gong, Wei Zhu, and DN Sheng. Emergent chiral spin liquid: Fractional quantum hall effect in a kagome heisenberg model. *Scientific reports*, 4(1):6317, 2014.

[140] Yin-Chen He, DN Sheng, and Yan Chen. Chiral spin liquid in a frustrated anisotropic kagome heisenberg model. *Physical review letters*, 112(13):137202, 2014.

[141] Ciarán Hickey, Lukasz Cincio, Zlatko Papić, and Arun Paramekanti. Haldane-hubbard mott insulator: From tetrahedral spin crystal to chiral spin liquid. *Physical review letters*, 116(13):137202, 2016.

[142] Alexander Wietek and Andreas M Läuchli. Chiral spin liquid and quantum criticality in extended s= 1 2 heisenberg models on the triangular lattice. *Physical Review B*, 95(3):035141, 2017.

[143] Tessa Cookmeyer, Johannes Motruk, and Joel E Moore. Four-spin terms and the origin of the chiral spin liquid in mott insulators on the triangular lattice. *Physical review letters*, 127(8):087201, 2021.

[144] Patrick A Lee and Naoto Nagaosa. Gauge theory of the normal state of high-T_c superconductors. *Physical Review B*, 46(9):5621, 1992.

[145] Mohammad Hafezi, Darrick E Chang, Vladimir Gritsev, Eugene A Demler, and Mikhail D Lukin. Photonic quantum transport in a nonlinear optical fiber. *Europhysics Letters*, 94(5):54006, 2011.

[146] Alexey V Gorshkov, Johannes Otterbach, Michael Fleischhauer, Thomas Pohl, and Mikhail D Lukin. Photon-photon interactions via rydberg blockade. *Physical review letters*, 107(13):133602, 2011.

[147] Daniel P Arovas, Erez Berg, Steven A Kivelson, and Srinivas Raghu. The hubbard model. *Annual review of condensed matter physics*, 13(1):239–274, 2022.

[148] Mingpu Qin, Thomas Schäfer, Sabine Andergassen, Philippe Corboz, and Emanuel Gull. The hubbard model: A computational perspective. *Annual Review of Condensed Matter Physics*, 13(1):275–302, 2022.

[149] Yang Yang, Mengqun Li, Ioannis Rousochatzakis, and Natalia B. Perkins. Non-loudon-fleury raman scattering in spin-orbit coupled mott insulators. *Phys. Rev. B*, 104:144412, Oct 2021.

[150] JK Freericks, HR Krishnamurthy, and Th Pruschke. Theoretical description of time-resolved photoemission spectroscopy:¡? format?¿ application to pump-probe experiments. *Physical review letters*, 102(13):136401, 2009.

[151] Yao Wang, Yuan Chen, Chunjing Jia, Brian Moritz, and Thomas P Devereaux. Time-resolved resonant inelastic x-ray scattering in a pumped mott insulator. *Physical Review B*, 101(16):165126, 2020.

[152] Luke Masters, Xin-Xin Hu, Martin Cordier, Gabriele Maron, Lucas Pache, Arno Rauschenbeutel, Max Schemmer, and Jürgen Volz. On the simultaneous scattering of two photons by a single two-level atom. *Nature Photonics*, 17(11):972–976, 2023.

[153] Venkata Vikram Orre, Elizabeth A Goldschmidt, Abhinav Deshpande, Alexey V Gorshkov, Vincenzo Tamma, Mohammad Hafezi, and Sunil Mittal. Interference of temporally distinguishable photons using frequency-resolved detection. *Physical review letters*, 123(12):123603, 2019.

[154] FB Gallagher and S Mazumdar. Excitons and optical absorption in one-dimensional extended hubbard models with short-and long-range interactions. *Physical Review B*, 56(23):15025, 1997.

[155] Fabian HL Essler, Florian Gebhard, and Eric Jeckelmann. Excitons in one-dimensional mott insulators. *Physical Review B*, 64(12):125119, 2001.

[156] P Wróbel and R Eder. Excitons in mott insulators. *Physical Review B*, 66(3):035111, 2002.

[157] T Tohyama, H Onodera, K Tsutsui, and S Maekawa. Resonant two-magnon raman scattering and photoexcited states in two-dimensional mott insulators. *Physical review letters*, 89(25):257405, 2002.

[158] A Maeda, M Ono, H Kishida, T Manako, A Sawa, M Kawasaki, Y Tokura, and H Okamoto. Third-order nonlinear susceptibility spectra of cuo chain compounds investigated by the z-scan method. *Physical Review B*, 70(12):125117, 2004.

[159] H Matsueda, T Tohyama, and S Maekawa. Excitonic effect on the optical response in the one-dimensional two-band hubbard model. *Physical Review B*, 71(15):153106, 2005.

[160] M Ono, H Kishida, and H Okamoto. Direct observation of excitons and a continuum of one-dimensional mott insulators: A reflection-type third-harmonic-generation study of ni-halogen chain compounds. *Physical review letters*, 95(8):087401, 2005.

[161] T Tohyama. Symmetry of photoexcited states and large-shift raman scattering in two-dimensional mott insulators. *Journal of the Physical Society of Japan*, 75(3):034713, 2006.

[162] A Gössling, R Schmitz, H Roth, MW Haverkort, T Lorenz, JA Mydosh, E Müller-Hartmann, and M Grüninger. Mott-hubbard exciton in the optical conductivity of ytio 3 and smtio 3. *Physical Review B*, 78(7):075122, 2008.

[163] Fabio Novelli, Daniele Fausti, Julia Reul, Federico Cilento, Paul HM Van Loosdrecht, Agung A Nugroho, Thomas TM Palstra, Markus Grüninger, and Fulvio Parmigiani. Ultrafast optical spectroscopy of the lowest energy excitations in the mott insulator compound yvo 3: Evidence for hubbard-type excitons. *Physical Review B*, 86(16):165135, 2012.

[164] Jungho Kim, M Daghofer, AH Said, T Gog, J Van den Brink, G Khaliullin, and BJ Kim. Excitonic quasiparticles in a spin–orbit mott insulator. *Nature communications*, 5(1):4453, 2014.

[165] Sen Zhou, Yupeng Wang, and Ziqiang Wang. Doublon-holon binding, mott transition, and fractionalized antiferromagnet in the hubbard model. *Physical Review B*, 89(19):195119, 2014.

[166] T-S Huang, CL Baldwin, M Hafezi, and V Galitski. Spin-mediated mott excitons. *Physical Review B*, 107(7):075111, 2023.

[167] Omar Mehio, Xinwei Li, Honglie Ning, Zala Lenarčič, Yuchen Han, Michael Buchhold, Zach Porter, Nicholas J Laurita, Stephen D Wilson, and David Hsieh. A hubbard exciton fluid in a photo-doped antiferromagnetic mott insulator. *Nature Physics*, pages 1–7, 2023.

[168] Marvin L Goldberger and Kenneth M Watson. *Collision theory*. Courier Corporation, 2004.

[169] Jacob Peter Kia Ngaha. *Frequency-Filtered Photon Correlations*. PhD thesis, ResearchSpace@ Auckland, 2023.

[170] Marlan O Scully and M Suhail Zubairy. *Quantum optics*. Cambridge university press, 1997.

[171] D. F. Walls and Gerard J Milburn. *Quantum optics*. Springer Berlin, Heidelberg, 2008.

[172] Vincent Boyer, Alberto M Marino, Raphael C Pooser, and Paul D Lett. Entangled images from four-wave mixing. *Science*, 321(5888):544–547, 2008.

[173] Luis EE De Araujo, Zhifan Zhou, Matt DiMario, BE Anderson, Jie Zhao, Kevin M Jones, and Paul D Lett. Characterizing two-mode-squeezed light from four-wave mixing in rubidium vapor for quantum sensing and information processing. *Optics express*, 32(2):1305–1313, 2024.

[174] Jiajun Li, Denis Golez, Giacomo Mazza, Andrew J Millis, Antoine Georges, and Martin Eckstein. Electromagnetic coupling in tight-binding models for strongly correlated light and matter. *Physical Review B*, 101(20):205140, 2020.

[175] Olesia Dmytruk and Marco Schiró. Gauge fixing for strongly correlated electrons coupled to quantum light. *Physical Review B*, 103(7):075131, 2021.

[176] Andreas Christ, Kaisa Laiho, Andreas Eckstein, Katiúscia N Cassemiro, and Christine Silberhorn. Probing multimode squeezing with correlation functions. *New Journal of Physics*, 13(3):033027, 2011.

[177] Marc-Antoine Lemonde, Nicolas Didier, and Aashish A Clerk. Antibunching and unconventional photon blockade with gaussian squeezed states. *Physical Review A*, 90(6):063824, 2014.

[178] A Grankin, E Brion, R Boddeda, S Ćuk, I Usmani, A Ourjoumtsev, and Philippe Grangier. Inelastic photon scattering via the intracavity rydberg blockade. *Physical Review Letters*, 117(25):253602, 2016.

[179] Theodore Holstein and Henry Primakoff. Field dependence of the intrinsic domain magnetization of a ferromagnet. *Physical Review*, 58(12):1098, 1940.

[180] Alexander Altland and Ben D Simons. *Condensed matter field theory*. Cambridge university press, 2010.

[181] Mengkun Liu, Aaron J Sternbach, and DN Basov. Nanoscale electrodynamics of strongly correlated quantum materials. *Reports on Progress in Physics*, 80(1):014501, 2016.

[182] BJ Kim, Hosub Jin, SJ Moon, J-Y Kim, B-G Park, CS Leem, Jaejun Yu, TW Noh, C Kim, S-J Oh, et al. Novel j eff= 1/2 mott state induced by relativistic spin-orbit coupling in sr 2 iro 4. *Physical review letters*, 101(7):076402, 2008.

[183] Tsung-Sheng Huang, Andrey Grankin, Yu-Xin Wang, and Mohammad Hafezi. Optical engineering and detection of magnetism in moir\'e semiconductors. *arXiv preprint arXiv:2504.13758*, 2025.

[184] Pranshoo Upadhyay, Daniel G Suárez-Forero, Tsung-Sheng Huang, Mahmoud Jalali Mehrabad, Beini Gao, Supratik Sarkar, Deric Session, Kenji Watanabe, Takashi Taniguchi, You Zhou, et al. Giant enhancement of exciton diffusion near an electronic mott insulator. *arXiv preprint arXiv:2409.18357*, 2024.

[185] Shengnan Miao, Tianmeng Wang, Xiong Huang, Dongxue Chen, Zhen Lian, Chong Wang, Mark Blei, Takashi Taniguchi, Kenji Watanabe, Sefaattin Tongay, et al. Strong interaction between interlayer excitons and correlated electrons in wse2/ws2 moiré superlattice. *Nature communications*, 12(1):3608, 2021.

[186] Zhen Lian, Yuze Meng, Lei Ma, Indrajit Maity, Li Yan, Qiran Wu, Xiong Huang, Dongxue Chen, Xiaotong Chen, Xinyue Chen, et al. Valley-polarized excitonic mott insulator in ws2/wse2 moiré superlattice. *Nature Physics*, 20(1):34–39, 2024.

[187] Richen Xiong, Jacob H Nie, Samuel L Brantly, Patrick Hays, Renee Sailus, Kenji Watanabe, Takashi Taniguchi, Sefaattin Tongay, and Chenhao Jin. Correlated insulator of excitons in wse2/ws2 moiré superlattices. *Science*, 380(6647):860–864, 2023.

[188] Beini Gao, Daniel G Suárez-Forero, Supratik Sarkar, Tsung-Sheng Huang, Deric Session, Mahmoud Jalali Mehrabad, Ruihao Ni, Ming Xie, Pranshoo Upadhyay, Jonathan Vannucci, et al. Excitonic mott insulator in a bose-fermi-hubbard system of moiré ws2/wse2 heterobilayer. *Nature Communications*, 15(1):2305, 2024.

[189] Clemens Kuhlenkamp, Wilhelm Kadow, Ataç Imamoğlu, and Michael Knap. Chiral pseudospin liquids in moiré heterostructures. *Physical Review X*, 14(2):021013, 2024.

[190] Filippo Glerean, Enrico Maria Rigoni, Giacomo Jarc, Shahla Yasmin Mathengattil, Angela Montanaro, Francesca Giusti, Matteo Mitrano, Fabio Benatti, and Daniele Fausti. Ultrafast pump-probe phase-randomized tomography. *Light: Science & Applications*, 14(1):115, 2025.

[191] Heonjoon Park, Jiaqi Cai, Eric Anderson, Yinong Zhang, Jiayi Zhu, Xiaoyu Liu, Chong Wang, William Holtzmann, Chaowei Hu, Zhaoyu Liu, et al. Observation of fractionally quantized anomalous hall effect. *Nature*, 622(7981):74–79, 2023.

[192] Ruixiao Yao, Sungjae Chi, Mingxuan Wang, Richard J Fletcher, and Martin Zwierlein. Measuring pair correlations in bose and fermi gases via atom-resolved microscopy. *arXiv preprint arXiv:2411.08780*, 2024.

[193] Tobias Graß, Utso Bhattacharya, Julia Sell, and Mohammad Hafezi. Two-dimensional excitons from twisted light and the fate of the photon's orbital angular momentum. *Physical Review B*, 105(20):205202, 2022.

[194] Deric Session, Mahmoud Jalali Mehrabad, Nikil Paithankar, Tobias Grass, Christian J Eckhardt, Bin Cao, Daniel Gustavo Suárez Forero, Kevin Li, Mohammad S Alam, Kenji Watanabe, et al. Optical pumping of electronic quantum hall states with vortex light. *arXiv preprint arXiv:2306.03417*, 2023.

[195] Andrey Grankin, Mohammad Hafezi, and Victor M Galitski. Enhancement of superconductivity with external phonon squeezing. *Physical Review B*, 104(22):L220503, 2021.

[196] Hendrik Weimer, Markus Müller, Igor Lesanovsky, Peter Zoller, and Hans Peter Büchler. A Rydberg quantum simulator. *Nat. Phys.*, 6(5):382–388, 2010.

[197] Sepehr Ebadi, Tout T Wang, Harry Levine, Alexander Keesling, Giulia Semeghini, Ahmed Omran, Dolev Bluvstein, Rhine Samajdar, Hannes Pichler, Wen Wei Ho, et al. Quantum phases of matter on a 256-atom programmable quantum simulator. *Nature*, 595(7866):227–232, 2021.

[198] Xiaoling Wu, Xinhui Liang, Yaoqi Tian, Fan Yang, Cheng Chen, Yong-Chun Liu, Meng Khoon Tey, and Li You. A concise review of Rydberg atom based quantum computation and quantum simulation. *Chin. Phys. B*, 30(2):020305, 2021.

[199] M. Saffman, T. G. Walker, and K. Mølmer. Quantum information with Rydberg atoms. *Rev. Mod. Phys.*, 82(3):2313–2363, August 2010.

[200] M. D. Lukin, M. Fleischhauer, R. Cote, L. M. Duan, D. Jaksch, J. I. Cirac, and P. Zoller. Dipole Blockade and Quantum Information Processing in Mesoscopic Atomic Ensembles. *Phys. Rev. Lett.*, 87(3):037901, June 2001.

[201] Henning Labuhn, Daniel Barredo, Sylvain Ravets, Sylvain de Léséleuc, Tommaso Macrì, Thierry Lahaye, and Antoine Browaeys. Tunable two-dimensional arrays of single Rydberg atoms for realizing quantum Ising models. *Nature*, 534(7609):667–670, June 2016.

[202] D. Jaksch, J. I. Cirac, P. Zoller, S. L. Rolston, R. Côté, and M. D. Lukin. Fast Quantum Gates for Neutral Atoms. *Phys. Rev. Lett.*, 85(10):2208–2211, September 2000.

[203] Antoine Browaeys, Daniel Barredo, and Thierry Lahaye. Experimental investigations of dipole–dipole interactions between a few Rydberg atoms. *J. Phys. B*, 49(15):152001, August 2016.

[204] Daniel Barredo, Sylvain de Léséleuc, Vincent Lienhard, Thierry Lahaye, and Antoine Browaeys. An atom-by-atom assembler of defect-free arbitrary two-dimensional atomic arrays. *Science*, 354(6315):1021–1023, 2016.

[205] L. Béguin, A. Vernier, R. Chicireanu, T. Lahaye, and A. Browaeys. Direct measurement of the van der Waals interaction between two Rydberg atoms. *Phys. Rev. Lett.*, 110(26):263201, June 2013.

[206] Daniel Barredo, Vincent Lienhard, Sylvain de Léséleuc, Thierry Lahaye, and Antoine Browaeys. Synthetic three-dimensional atomic structures assembled atom by atom. *Nature*, 561(7721):79–82, September 2018.

[207] Giulia Semeghini, Harry Levine, Alexander Keesling, Sepehr Ebadi, Tout T. Wang, Dolev Bluvstein, Ruben Verresen, Hannes Pichler, Marcin Kalinowski, Rhine Samajdar, Ahmed Omran, Subir Sachdev, Ashvin Vishwanath, Markus Greiner, Vladan Vuletic, and Mikhail D. Lukin. Probing Topological Spin Liquids on a Programmable Quantum Simulator. *Science*, 374(6572):1242–1247, December 2021.

[208] Hannes Bernien, Sylvain Schwartz, Alexander Keesling, Harry Levine, Ahmed Omran, Hannes Pichler, Soonwon Choi, Alexander S. Zibrov, Manuel Endres, Markus Greiner, Vladan Vuletić, and Mikhail D. Lukin. Probing many-body dynamics on a 51-atom quantum simulator. *Nature*, 551(7682):579–584, November 2017.

[209] Dolev Bluvstein, Harry Levine, Giulia Semeghini, Tout T. Wang, Sepehr Ebadi, Marcin Kalinowski, Alexander Keesling, Nishad Maskara, Hannes Pichler, Markus Greiner, Vladan Vuletić, and Mikhail D. Lukin. A quantum processor based on coherent transport of entangled atom arrays. *Nature*, 604(7906):451–456, April 2022.

[210] Elmer Guardado-Sanchez, Peter T. Brown, Debayan Mitra, Trithep Devakul, David A. Huse, Peter Schauß, and Waseem S. Bakr. Probing the Quench Dynamics of Antiferromagnetic Correlations in a 2D Quantum Ising Spin System. *Phys. Rev. X*, 8(2):021069, June 2018.

[211] Alexander Keesling, Ahmed Omran, Harry Levine, Hannes Bernien, Hannes Pichler, Soonwon Choi, Rhine Samajdar, Sylvain Schwartz, Pietro Silvi, Subir Sachdev, Peter Zoller, Manuel Endres, Markus Greiner, Vladan Vuletić, and Mikhail D. Lukin. Quantum Kibble–Zurek mechanism and critical dynamics on a programmable Rydberg simulator. *Nature*, 568(7751):207–211, April 2019.

[212] Harry Levine, Alexander Keesling, Giulia Semeghini, Ahmed Omran, Tout T. Wang, Sepehr Ebadi, Hannes Bernien, Markus Greiner, Vladan Vuletić, Hannes Pichler, and Mikhail D. Lukin. Parallel Implementation of High-Fidelity Multiqubit Gates with Neutral Atoms. *Phys. Rev. Lett.*, 123(17):170503, October 2019.

[213] Vincent Lienhard, Sylvain de Léséleuc, Daniel Barredo, Thierry Lahaye, Antoine Browaeys, Michael Schuler, Louis-Paul Henry, and Andreas M. Läuchli. Observing the Space- and Time-Dependent Growth of Correlations in Dynamically Tuned Synthetic Ising Models with Antiferromagnetic Interactions. *Phys. Rev. X*, 8(2):021070, June 2018.

[214] Ivaylo S. Madjarov, Jacob P. Covey, Adam L. Shaw, Joonhee Choi, Anant Kale, Alexandre Cooper, Hannes Pichler, Vladimir Schkolnik, Jason R. Williams, and Manuel Endres. High-fidelity entanglement and detection of alkaline-earth Rydberg atoms. *Nat. Phys.*, 16(8):857–861, August 2020.

[215] A. Omran, H. Levine, A. Keesling, G. Semeghini, T. T. Wang, S. Ebadi, H. Bernien, A. S. Zibrov, H. Pichler, S. Choi, J. Cui, M. Rossignolo, P. Rembold, S. Montangero, T. Calarco, M. Endres, M. Greiner, V. Vuletić, and M. D. Lukin. Generation and manipulation of Schrödinger cat states in Rydberg atom arrays. *Science*, 365(6453):570–574, August 2019.

[216] P. Schauß, J. Zeiher, T. Fukuhara, S. Hild, M. Cheneau, T. Macrì, T. Pohl, I. Bloch, and C. Gross. Crystallization in Ising quantum magnets. *Science*, 347(6229):1455–1458, March 2015.

[217] Yunheung Song, Minhyuk Kim, Hansub Hwang, Woojun Lee, and Jaewook Ahn. Quantum annealing of Cayley-tree Ising spins at small scales. *Phys. Rev. Res.*, 3(1):013286, March 2021.

[218] Ruben Verresen, Mikhail D. Lukin, and Ashvin Vishwanath. Prediction of Toric Code Topological Order from Rydberg Blockade. *Phys. Rev. X*, 11(3):031005, July 2021.

[219] Rhine Samajdar, Wen Wei Ho, Hannes Pichler, Mikhail D. Lukin, and Subir Sachdev. Quantum phases of Rydberg atoms on a Kagome lattice. *Proc. Natl. Acad. Sci. U.S.A.*, 118(4):e2015785118, January 2021.

[220] Nayan E Myerson-Jain, Stephen Yan, David Weld, and Cenke Xu. Construction of fractal order and phase transition with Rydberg atoms. *Phys. Rev. Lett.*, 128(1):017601, 2022.

[221] Kevin Slagle, Yue Liu, David Aasen, Hannes Pichler, Roger S. K. Mong, Xie Chen, Manuel Endres, and Jason Alicea. Quantum spin liquids bootstrapped from Ising criticality in Rydberg arrays. *Phys. Rev. B*, 106:115122, Sep 2022.

[222] Giacomo Giudice, Federica Maria Surace, Hannes Pichler, and Giuliano Giudici. Trimer states with $\mathbb{Z}_3$ topological order in Rydberg atom arrays. *Phys. Rev. B*, 106:195155, Nov 2022.

[223] Zheng Zhou, Zheng Yan, Changle Liu, Yan Chen, and Xue-Feng Zhang. Quantum simulation of two-dimensional $\mathrm{U}(1)$ gauge theory in Rydberg atom arrays, 2022.

[224] Poetri Sonya Tarabunga, Giuliano Giudici, Titas Chanda, and Marcello Dalmonte. Classification and emergence of quantum spin liquids in chiral Rydberg models. *Phys. Rev. B*, 108:075118, Aug 2023.

[225] Milan Kornjača, Rhine Samajdar, Tommaso Macrì, Nathan Gemelke, Sheng-Tao Wang, and Fangli Liu. Trimer quantum spin liquid in a honeycomb array of Rydberg atoms. *Commun. Phys.*, 6(1):358, December 2023.

[226] Simon Ohler, Maximilian Kiefer-Emmanouilidis, and Michael Fleischhauer. Quantum spin liquids of Rydberg excitations in a honeycomb lattice induced by density-dependent peierls phases. *Phys. Rev. Res.*, 5:013157, Feb 2023.

[227] Rhine Samajdar, Darshan G. Joshi, Yanting Teng, and Subir Sachdev. Emergent $\mathbb{Z}_2$ gauge theories and topological excitations in Rydberg atom arrays. *Phys. Rev. Lett.*, 130:043601, Jan 2023.

[228] Yu-Jie Liu, Kirill Shtengel, Adam Smith, and Frank Pollmann. Methods for simulating string-net states and anyons on a digital quantum computer. *PRX Quantum*, 3:040315, Nov 2022.

[229] Nathanan Tantivasadakarn, Ruben Verresen, and Ashvin Vishwanath. Shortest route to non-abelian topological order on a quantum processor. *Phys. Rev. Lett.*, 131:060405, Aug 2023.

[230] Ruben Verresen, Nathanan Tantivasadakarn, and Ashvin Vishwanath. Efficiently preparing GHZ, topological and fracton states by measuring cold atoms. *arXiv preprint arXiv:2112.03061*, 2021.

[231] Yanting Cheng and Hui Zhai. Emergent U(1) lattice gauge theory in Rydberg atom arrays. *Nat. Rev. Phys.*, 6(9):566–576, Sep 2024.

[232] Simon Ohler, Maximilian Kiefer-Emmanouilidis, Antoine Browaeys, Hans Peter Büchler, and Michael Fleischhauer. Self-generated quantum gauge fields in arrays of Rydberg atoms. *New J. Phys.*, 24(2):023017, feb 2022.

[233] Federica M. Surace, Paolo P. Mazza, Giuliano Giudici, Alessio Lerose, Andrea Gambassi, and Marcello Dalmonte. Lattice gauge theories and string dynamics in Rydberg atom quantum simulators. *Phys. Rev. X*, 10:021041, May 2020.

[234] Yanting Cheng and Chengshu Li. Gauge theory description of Rydberg atom arrays with a tunable blockade radius. *Phys. Rev. B*, 107:094302, Mar 2023.

[235] A. M. Polyakov. Compact gauge fields and the infrared catastrophe. *Phys. Lett. B*, 59(1):82–84, October 1975.

[236] A.M. Polyakov. Quark confinement and topology of gauge theories. *Nucl. Phys. B*, 120(3):429–458, March 1977.

[237] David A. Huse, Werner Krauth, R. Moessner, and S. L. Sondhi. Coulomb and liquid dimer models in three dimensions. *Phys. Rev. Lett.*, 91(16):167004, October 2003.

[238] Argha Banerjee, Sergei V. Isakov, Kedar Damle, and Yong Baek Kim. Unusual Liquid State of Hard-Core Bosons on the Pyrochlore Lattice. *Phys. Rev. Lett.*, 100(4):047208, January 2008.

[239] Steven T Bramwell and Mark J Harris. The history of spin ice. *J. Condens. Matter Phys.*, 32(37):374010, 2020.

[240] Michel JP Gingras. Spin ice. *Introduction to frustrated magnetism*, pages 293–329, 2011.

[241] Masafumi Udagawa and Ludovic Jaubert. *Spin Ice*. Springer, 2021.

[242] Sandra H Skjærvø, Christopher H Marrows, Robert L Stamps, and Laura J Heyderman. Advances in artificial spin ice. *Nat. Rev. Phys.*, 2(1):13–28, 2020.

[243] Cristiano Nisoli, Roderich Moessner, and Peter Schiffer. Colloquium: Artificial spin ice: Designing and imaging magnetic frustration. *Rev. Mod. Phys.*, 85(4):1473, 2013.

[244] Michel JP Gingras and Paul A McClarty. Quantum spin ice: a search for gapless quantum spin liquids in pyrochlore magnets. *Rep. Prog. Phys.*, 77(5):056501, 2014.

[245] Sumanta Tewari, V. W. Scarola, T. Senthil, and S. Das Sarma. Emergence of artificial photons in an optical lattice. *Phys. Rev. Lett.*, 97:200401, Nov 2006.

[246] A. W. Glaetzle, M. Dalmonte, R. Nath, I. Rousochatzakis, R. Moessner, and P. Zoller. Quantum spin-ice and dimer models with Rydberg atoms. *Phys. Rev. X*, 4:041037, Nov 2014.

[247] Alessio Celi, Benoît Vermersch, Oscar Viyuela, Hannes Pichler, Mikhail D. Lukin, and Peter Zoller. Emerging two-dimensional gauge theories in Rydberg configurable arrays. *Phys. Rev. X*, 10:021057, Jun 2020.

[248] Daniel Adler, David Wei, Melissa Will, Kritsana Srakaew, Suchita Agrawal, Pascal Weckesser, Roderich Moessner, Frank Pollmann, Immanuel Bloch, and Johannes Zeiher. Observation of Hilbert space fragmentation and fractonic excitations in 2D. *Nature*, 636:80–85, Nov 2024.

[249] Julian F. Wienand, Simon Karch, Alexander Impertro, Christian Schweizer, Ewan McCulloch, Romain Vasseur, Sarang Gopalakrishnan, Monika Aidelsburger, and Immanuel Bloch. Emergence of fluctuating hydrodynamics in chaotic quantum systems. *Nat. Phys.*, 20(11):1732–1737, Nov 2024.

[250] Claire K. Thomas, Thomas H. Barter, Tsz-Him Leung, Masayuki Okano, Gyu-Boong Jo, Jennie Guzman, Itamar Kimchi, Ashvin Vishwanath, and Dan M. Stamper-Kurn. Mean-field scaling of the superfluid to mott insulator transition in a 2d optical superlattice. *Phys. Rev. Lett.*, 119:100402, Sep 2017.

[251] P. A. McClarty, O. Sikora, R. Moessner, K. Penc, F. Pollmann, and N. Shannon. Chain-based order and quantum spin liquids in dipolar spin ice. *Phys. Rev. B*, 92:094418, Sep 2015.

[252] P. W. Anderson. Ordering and antiferromagnetism in ferrites. *Phys. Rev.*, 102:1008–1013, May 1956.

[253] Daniel S. Rokhsar and Steven A. Kivelson. Superconductivity and the Quantum Hard-Core Dimer Gas. *Phys. Rev. Lett.*, 61(20):2376–2379, November 1988.

[254] Shankar Balasubramanian, Daniel Bulmash, Victor Galitski, and Ashvin Vishwanath. Interplay of symmetry breaking and deconfinement in three-dimensional quantum vertex models. *Phys. Rev. B*, 110:L180401, Nov 2024.

[255] Shankar Balasubramanian, Victor Galitski, and Ashvin Vishwanath. Classical vertex model dualities in a family of two-dimensional frustrated quantum antiferromagnets. *Phys. Rev. B*, 106:195127, Nov 2022.

[256] Lucile Savary and Leon Balents. Disorder-Induced Quantum Spin Liquid in Spin Ice Pyrochlores. *Phys. Rev. Lett.*, 118(8):087203, February 2017.

[257] Chyh-Hong Chern, Chen-Nan Liao, and Yang-Zhi Chou. Disorder from disorder and confinement in the quantum Ising model in the pyrochlore lattice. *arXiv:1003.4204 [cond-mat]*, August 2010.

[258] Kenneth G. Wilson. Confinement of quarks. *Phys. Rev. D*, 10(8):2445–2459, October 1974.

[259] A. M. Polyakov. Thermal Properties of Gauge fields and Quark Liberation, September 1978.

[260] John B. Kogut. An introduction to lattice gauge theory and spin systems. *Rev. Mod. Phys.*, 51(4):659–713, October 1979.

[261] Julia Röchner, Leon Balents, and Kai Phillip Schmidt. Spin liquid and quantum phase transition without symmetry breaking in a frustrated three-dimensional ising model. *Phys. Rev. B*, 94:201111, Nov 2016.

[262] Salvatore D. Pace, Siddhardh C. Morampudi, Roderich Moessner, and Chris R. Laumann. Emergent Fine Structure Constant of Quantum Spin Ice Is Large. *Phys. Rev. Lett.*, 127(11):117205, September 2021.

[263] Gang Chen. "Magnetic monopole" condensation of the pyrochlore ice $U(1)$ quantum spin liquid: Application to $\mathrm{Pr_2Ir_2O_7}$ and $\mathrm{Yb_2Ti_2O_7}$. *Phys. Rev. B*, 94:205107, Nov 2016.

[264] S. V. Isakov, R. Moessner, and S. L. Sondhi. Why spin ice obeys the ice rules. *Phys. Rev. Lett.*, 95:217201, Nov 2005.

[265] https://github.com/Galitski-theory-group/quantum-spin-ice-rydbergs.

[266] Kevin Slagle and Yong Baek Kim. Fracton Topological Order from Nearest-Neighbor Two-Spin Interactions and Dualities. *Phys. Rev. B*, 96(16):165106, October 2017.

[267] J. M. Luttinger and L. Tisza. Theory of Dipole Interaction in Crystals. *Phys. Rev.*, 70(11-12):954–964, December 1946.

[268] D. H. Lyons and T. A. Kaplan. Method for Determining Ground-State Spin Configurations. *Phys. Rev.*, 120(5):1580–1585, December 1960.

[269] D.B. Litvin. The Luttinger-Tisza method. *Physica*, 77(2):205–219, 1974.

[270] Roger G. Melko, Byron C. den Hertog, and Michel J. P. Gingras. Long-range order at low temperatures in dipolar spin ice. *Phys. Rev. Lett.*, 87:067203, Jul 2001.

[271] Roger G Melko and Michel JP Gingras. Monte Carlo studies of the dipolar spin ice model. *J. Condens. Matter Phys.*, 16(43):R1277, 2004.

[272] Lucile Savary and Leon Balents. Coulombic quantum liquids in spin-$1/2$ pyrochlores. *Phys. Rev. Lett.*, 108:037202, Jan 2012.

[273] Giuliano Giudici, Mikhail D. Lukin, and Hannes Pichler. Dynamical preparation of quantum spin liquids in Rydberg atom arrays. *Phys. Rev. Lett.*, 129:090401, Aug 2022.

[274] Rahul Sahay, Ashvin Vishwanath, and Ruben Verresen. Quantum spin puddles and lakes: NISQ-Era spin liquids from non-equilibrium dynamics. *arXiv preprint arXiv:2211.01381*, 2022.

[275] Wojciech H Zurek. Cosmological experiments in superfluid helium? *Nature*, 317(6037):505–508, 1985.

[276] Thomas WB Kibble. Topology of cosmic domains and strings. *J. Phys. A*, 9(8):1387, 1976.

[277] Adolfo Del Campo and Wojciech H Zurek. Universality of phase transition dynamics: Topological defects from symmetry breaking. *Int. J. Mod. Phys. A*, 29(08):1430018, 2014.

[278] Benjamin Svetitsky. Symmetry aspects of finite-temperature confinement transitions. *Phys. Rep.*, 132(1):1–53, 1986.

[279] Eduardo Fradkin. *Field theories of condensed matter physics*. Cambridge University Press, 2013.

[280] Ramamurti Shankar. *Quantum field theory and condensed matter: An introduction*. Cambridge University Press, 2017.

[281] Klaus Fredenhagen and Mihail Marcu. Charged states in Z_2 gauge theories. *Commun. Math. Phys.*, 92(1):81–119, 1983.

[282] Klaus Fredenhagen and Mihail Marcu. Confinement criterion for QCD with dynamical quarks. *Phys. Rev. Lett.*, 56:223–224, Jan 1986.

[283] Klaus Fredenhagen and Mihail Marcu. Dual interpretation of order parameters for lattice gauge theories with matter fields. *Nucl. Phys. B-Proceedings Supplements*, 4:352–357, 1988.

[284] Mihail Marcu. *(Uses of) An Order Parameter for Lattice Gauge Theories with Matter Fields*, pages 267–278. Springer US, Boston, MA, 1986.

[285] Jean Bricmont and Jürg Frölich. An order parameter distinguishing between different phases of lattice gauge theories with matter fields. *Phys. Lett. B*, 122(1):73–77, 1983.

[286] K Gregor, David A Huse, R Moessner, and Shivaji Lal Sondhi. Diagnosing deconfinement and topological order. *New J. Phys.*, 13(2):025009, 2011.

[287] Wen-Tao Xu, Frank Pollmann, and Michael Knap. Critical behavior of the Fredenhagen-Marcu order parameter at topological phase transitions, 2024.

[288] Sylvain de Léséleuc, Daniel Barredo, Vincent Lienhard, Antoine Browaeys, and Thierry Lahaye. Optical control of the resonant dipole-dipole interaction between Rydberg atoms. *Phys. Rev. Lett.*, 119:053202, Aug 2017.

[289] Alexander W. Glaetzle, Marcello Dalmonte, Rejish Nath, Christian Gross, Immanuel Bloch, and Peter Zoller. Designing frustrated quantum magnets with laser-dressed Rydberg atoms. *Phys. Rev. Lett.*, 114:173002, Apr 2015.

[290] R. M. W. van Bijnen and T. Pohl. Quantum magnetism and topological ordering via Rydberg dressing near Förster resonances. *Phys. Rev. Lett.*, 114:243002, Jun 2015.

[291] David Petrosyan and Klaus Mølmer. Binding potentials and interaction gates between microwave-dressed Rydberg atoms. *Phys. Rev. Lett.*, 113:123003, Sep 2014.

[292] Tobias Graß, Przemyslaw Bienias, Michael J. Gullans, Rex Lundgren, Joseph Maciejko, and Alexey V. Gorshkov. Fractional quantum hall phases of bosons with tunable interactions: From the laughlin liquid to a fractional Wigner crystal. *Phys. Rev. Lett.*, 121:253403, Dec 2018.

[293] Jeremy T. Young, Przemyslaw Bienias, Ron Belyansky, Adam M. Kaufman, and Alexey V. Gorshkov. Asymmetric blockade and multiqubit gates via dipole-dipole interactions. *Phys. Rev. Lett.*, 127:120501, Sep 2021.

[294] Lea-Marina Steinert, Philip Osterholz, Robin Eberhard, Lorenzo Festa, Nikolaus Lorenz, Zaijun Chen, Arno Trautmann, and Christian Gross. Spatially tunable spin interactions in neutral atom arrays. *Phys. Rev. Lett.*, 130:243001, Jun 2023.

[295] Simon Hollerith, Kritsana Srakaew, David Wei, Antonio Rubio-Abadal, Daniel Adler, Pascal Weckesser, Andreas Kruckenhauser, Valentin Walther, Rick van Bijnen, Jun Rui, Christian Gross, Immanuel Bloch, and Johannes Zeiher. Realizing distance-selective interactions in a Rydberg-dressed atom array. *Phys. Rev. Lett.*, 128:113602, Mar 2022.

[296] Ali Lavasani, Zhu-Xi Luo, and Sagar Vijay. Monitored quantum dynamics and the kitaev spin liquid. *Phys. Rev. B*, 108:115135, Sep 2023.

[297] Tom Banks, R Myerson, and John Kogut. Phase transitions in abelian lattice gauge theories. *Nuclear Physics B*, 129(3):493–510, 1977.

[298] Michael Hermele, Ying Ran, Patrick A Lee, and Xiao-Gang Wen. Properties of an algebraic spin liquid on the kagome lattice. *Physical Review B*, 77(22):224413, 2008.

[299] Xiao-Gang Wen. *Quantum field theory of many-body systems: from the origin of sound to an origin of light and electrons*. Oxford University Press on Demand, 2004.

[300] Weicheng Ye, Meng Guo, Yin-Chen He, Chong Wang, and Liujun Zou. Topological characterization of Lieb-Schultz-Mattis constraints and applications to symmetry-enriched quantum criticality. *arXiv preprint arXiv:2111.12097*, 2021.

[301] Ahmad Deeb, Aziz Hamdouni, and Dina Razafindralandy. Comparison between Borel-Padé summation and factorial series, as time integration methods. *Discrete and Continuous Dynamical Systems - Series S*, 9(2):393–408, April 2016.